

EUSKAL HERRIKO UNIBERTSITATEA
THE UNIVERSITY OF THE BASQUE COUNTRY

Department of Electricity and Electronics



CAMPUS OF
INTERNATIONAL
EXCELLENCE

Quantum-mechanical study of optical excitations in nanoscale systems: first-principles description of plasmons, tunneling-induced light emission and ultrastrong light-matter interaction

Thesis by

Unai Muniain Caballero

Supervised by

Dr. Rubén Esteban Llorente

and

Prof. Vyacheslav M. Silkin

Donostia-San Sebastián, September 2023

This PhD thesis has been developed thanks to the financial support of Donostia International Physics Center (DIPC) (Ref. 2018/10), Project No. PI2017-30 of the Departamento de Educación, Política Lingüística y Cultura of the Basque Government, Projects IT1164-19 and IT 1526-22 of the Basque Government for consolidated groups of the Basque University, and Grant No. PID2019-107432GB-I00 funded by MCIN/AEI/10.13039/501100011033/, as well as thanks to the computing facilities of the DIPC.

Etzekoei

ACKNOWLEDGMENTS

Orain dela mende erdi Letek bere kantu batean idatzi zuen bezala, *itsasoan urak handi dire murgildu nahi dutenentzat*. Hitz hauek entzutean, gaur baino bost urte gazteagoa nintzen mutiko hartaz oroitzen naiz, uretan murgiltzeko gogoz eta ilusioz zegoena, benetan ur horiek zenbateriano handi eta sakon izango ziren jakin gabe. Momentu honetan hitz hauek idazten ari banaiz, mundu akademikoaren uretan ito gabe kostaldera iritsi naizelako da. Hori ezinezkoa litzateke jende askorengandik jaso dudan laguntzarik gabe, eta nire bidean edozein ekarpen egin duen jendeari zor diot tesi hau:

Aunque mi inicio oficial en el doctorado fue en octubre de 2018, para el verdadero comienzo de esta historia tenemos que ir un año hacia atrás. Fue en aquel verano de 2017 cuando Rubén me acogió como estudiante de verano. Por aquel entonces yo no era ni graduado en física, y no tenía ni idea de lo que era un plasmón. Desde entonces, al lado de Rubén he creado muchos notebooks de Mathematica, muchas ecuaciones, muchas figuras y muchas (muchísimas) versiones de manuscritos. Pero entre muchas alegrías y frustraciones, tengo claro que he aprendido mucho sobre física, sobre cómo trabajar en el mundo de la ciencia y sobre (no ser tan barroco en la) escritura. Muchas gracias por toda tu paciencia y comprensión, y espero de corazón que todo lo aprendido contigo me sirva en los años próximos.

También le tengo mucho que agradecer a mi otro director, a Slava, al que le conocí ya en el comienzo del doctorado. Al principio no fue fácil entender de dónde venía una descripción del plasmón tan distinta a lo que tenía entendido desde antes, pero al final entre los dos hemos sacado un buen trabajo. Muchas gracias por toda la ayuda con los códigos de Fortran al principio, y con el análisis de resultados después. La mitad de la tesis te la debo completamente a ti.

Tesi honen azalean bere izena ageri ez den arren, bere zati handi bat asko zor dizut zuri ere, Javi. Hirugarren zuzendaria izango bazina bezala, ikuspuntu benetan baliagarria eman didazu. Asko ikasi dut zurekin, bereziki, ikerketan lortutako emaitzak artikuluetan eta ahozko aurkezpenetan nola aurkeztu behar diren. Eskerrik asko nigan izan duzun konfiantzarengatik.

Le tengo mucho que agradecer también a Jean-Jacques por acogerme durante tres meses en su grupo. Gracias por toda tu dedicación durante en esos meses (y también en los siguientes), y por mostrarme otro punto de la vista sobre la ciencia, con mucha claridad, rigurosidad y elegancia a la vez.

Una cosa importante que he aprendido en estos años es que no se puede obtener

éxito en la ciencia sin colaboraciones, y esta tesis tampoco sería posible sin ellas. Muchas gracias a Luis Martín-Moreno por todas las discusiones sobre los modelos del ultrastrong coupling. Y acercándonos a Donostia, no me puedo olvidar de los colaboradores de nanoGUNE. Thanks a lot Luis Hueso and Rainer for all the patience with the work of hBN cavities and all the discussions. I hope that we all learned from each other about why ultrastrong coupling can be interesting and useful. Por terminar, muchas gracias a María por tu paciencia y apoyo. Al empezar con el proyecto, al estar ambos en nuestros inicios, nos costó bastante ver cómo tirar adelante. Pero cada uno con su perspectiva teórica o experimental, creo que llegamos a entendernos bien. Ahora que estamos llegando a nuestro fin bastante a la par también, te deseo muchísima suerte después.

Tampoco puedo olvidar al grupo al que he pertenecido en todos estos años. A pesar de estar físicamente aparte en el despacho, cada vez que he acudido a vosotros a tener conversaciones de ciencia, o simplemente a charlar sobre la vida, he sentido mucho apoyo por vuestra parte. Muchas gracias por vuestra amabilidad a Mattin, Antton, Álvaro, Carlos, Bruno, Roberto, Adri, Jonathan, Mario, Sofía, Xabi, Isa... ha sido verdaderamente un placer estar en el grupo con vosotros y os deseo lo mejor.

En estos cinco años, e incluso durante varios meses antes cuando era estudiante de prácticas, he pasado mucho tiempo en el DIPC, por lo que gran parte de mis agradecimientos van a la gente de allí. Primero, le agradezco mucho al DIPC como institución, por abrirme las puertas desde el principio y por la financiación de esta tesis, de la cual parte le debo de agradecer también al Gobierno Vasco. Muchas gracias a los trabajadores y trabajadoras de administración por vuestra amabilidad en todo momento. Muchas gracias a toda la gente con la que he compartido comidas o cafés: Edu, Verónica, Mikel García, Irián, David... y a mucha gente más que seguro que me olvido. Quiero agradecerles en especial a mis compañeros de despacho: Irene, María, Sofía, Nathaniel, Tim y Antonio. Aparte de despacho hemos compartido también muchas conversaciones, y muchas gracias por vuestro apoyo.

Eskerrak emateko DIPC osotik izen bakarra aipatu beharko banu, zalantzarik gabe zurea litzateke, Mikel. Oraindik nerabe ginela gradua hasi genuenetik, hamarkada bat igaro da dagoeneko, eta batera egin dugu bidea denbora honetan guztian. Gorabeheraz betetako urte hauetan zure laguntza ezinbestekoa izan da niretzat, fisikaren inguruko edozein zalantza argitzeko, elkarren frustrazioak konpartitzeko edo, besterik gabe, edozertaz hitz egiteko lanetik deskonektatu dezagun. Jada gure bideak banatu badira ere, zorterik onena opa dizut mundu akademikoan edo bestela ere iristen zaren lekuan.

Doktoretza egiteko fisikaren munduan jarraitzea erabaki badut, fisika ikasten nabilela alboan izan dudan jendearengatik da, zuei esker segi baitut hemen. Zuei ere zor dizuet, beraz, tesi hau. Mila esker klasekide izan zinetenoi, Unai, Ander, Sagasti, Joseba, Iñigo, Lujua... Muchas gracias también a los que fuisteis compañeros de piso, Álex, Paula, Mikel y Martín. Físicos o no, en aquellos años todos compartimos amistad y afán por la ciencia que aún perdura y que ha sido base importante para la tesis.

Tesiaren emaitzak lortu eta idatzi bitartean Donostian ordu ugari igaro ditudan arren, guztia ez da lana izan, eta fisikariak ez izan arren, Zarautzen izan ditudan lagunak ere parte ezinbesteko izan dira tesi honen garapenean. Mila esker Motxian-kideei, batera egin ditugun saio eta otorduengatik. Nahiz eta ni bapatean egiten saiatzea lortu ez, taldearen parte sentiarazi izan nauzue beti. Eskerrik asko ere Alprojako kide guztiei, izugarrizko plazera baita udaro zuekin elkartzea. Urte (eta antzerki) asko daramatzat zuekin, eta lanetik kanpo arnasa hartzen ikaragarri lagundu didazue urte hauetan guztietan, eta luzaronan hala jarraitzea espero dut.

Nire azken hitzak, nola ez, zuentzat doaz, Oihana, ama eta aita. Bizitza osoan zehar hartu ditudan erabaki guztietan babestu nauzue. Urte gogorrak izan dira azken hauek, etsipen momentu askorekin, eta hor egon zarete beti, ni zutik mantentzen, ekuazio eta artikulatu artean ito ez nadin. Nahiz eta zuentzat tesi honen edukia mundu erabat desberdin batekoa den, hori gutxienezkoa da. Oso ondo dakizue tesia zuena ere badela, eta badakit ni bezain harro egongo zaretela bost urte hauetan lortu dudana guztiaz. Maite zaituztet.

LABURPENA

Zientziaren aurrerakuntzak asko zor dio behaketa hutsez naturan ereduak antzemateko dugun berezko gaitasunari. Esate baterako, abilezia honek historiaurretik eragin ditu aurrerapenak nekazaritzan, urtaroen aldaketak aztertuz. Hala ere, behaketa soilean oinarritutako zientzia giza-begiaren gabeziez mugatuta dago. Argi ikuskorrari dagozkion maiztasunetatik kanpo uhin elektromagnetikoak antzemateko ezintasuna da gabezi horietako bat, begia espektro elektromagnetikoaren zati txiki batera mugatuta baitago. Bestalde, giza begiak ezin ditu urrunegi dauden edo txikiegiak diren objektuak bereizi. XVII. mendean, aurrerakuntza teknologikoak objektu ikuskorren eskalaren mugak zabaltzea ahalbidetu zuen. Garatu ziren gailuen adibide dira teleskopioa, zeinarekin Galileo Galileik Jupiterreko lau satellite handienak behatu zituen [1], eta baita zelulen behaketa posible bilakatu zuen mikroskopioa ere [2]. Aurkikuntza hauei esker, edozein distantziara kokatuta dauden eta edozein tamaina duten objektuak giza begiaren bidez bereiztea noizbait posible izango zela pentsa zitekeen.

Nahiz eta hurrengo mendeetan ohiko mikroskopio optikoez hobekuntza asko izan zituzten, tresna hauen bidez lortu daitekeen tamaina bereizgarriaren muga ehun nanometro inguruan geratu zen, hortik jaitsi ezinik. Muga honen arrazoia ez da egon garapen teknologikoaren esku, argiaren izaera hutsari baitagokio. Argiaren uhin izaerak Abbe-ren difrakzio muga ezartzen du, zeinak ohiko mikroskopikoan bereizmena uhin-luzeraren erdiak ezarritakoa baino hobea izatea eragozten duen [3,4]. Ondorioz, argi ikuskorren kasuan, difrakzio muga 200-400 nm bitartean dago ezarrita. Fenomeno fisiko hau dela eta, argiaren bidez uhin-luzera baino tamaina txikiagoa duten objektuak behatu eta manipulatzeko, ohiko mikroskopio optikoetatik haratago joatea eta metodo berriak bilatzea ezinbestekoa da. Hori horrela izanik, nanofotonikaren arloa argia eremu oso txikietan lokalizatzeke metodoak bilatu asmoz sortu zen.

Adibide gisa, gainazal metalikoez uhin-luzeraren azpitik argia lokalizatzea ahalbidetzen dute [5]. Argiaren lokalizazio hau gainazaleko plasmoi polaritoen (ingelesez *surface plasmon polariton*, SPP) kitzikapenari esker da posible, non uhin elektromagnetikoak metala eta hutsaren arteko interfasean kokatutako kondukziozko elektroien oszilazioekin akoplatzen diren. SPPak argiaren eta elektroien propietate hibridoak dituzten uhinak dira. Hain zuzen ere, gainazal metalikoetan zehar hedatzen dira uhin hauek, eta euren eremu elektrikoa metala eta hutsaren arteko interfasean oso lokalizatua dago, norabide perpendikularrean

esponentzialki jaitsiz. Bestalde, nanofotonikaren arloan interes handia sortu duen beste sistema fisiko bat nanoestruturak metalikoak dira. Tamaina nanometrikoa duten objektu hauetan gainazaleko plasmoi lokalizatuak kitzikatu daitezke, eta plasmoi hauen bidez energia elektromagnetikoa oso bolumen txikian kontzentratu daiteke. Muturreko lokalizazio honek difrakzio muga gainditzen du eta gailu fotonikoen bitartez objektu nanometrikoak bereiztea eta manipulatzeko ahalbidetzen du. Halaber, sistemaren geometriaren arabera, gainazaleko plasmoi lokalizatuek eremu elektriko erasotzailea $\approx 1 - 3$ magnitude-ordenatan areagotu dezakete [6–9].

Metaletako kitzikapen plasmonikoak espektro elektromagnetikoaren maiztasun-tarte ultramorean, ikuskorrean edo infragorri hurbilean daude kokatuta. Era berean, nanofotonikaren arloak beste kitzikapen batzuk ere aztergai ditu, zeinak maiztasun-tarte hauetan eta gainerakoetan ere kokatzen diren. Horren adibide dira material polarretan kitzikatu daitezkeen fonoi polaritoiak [10], eta erdieroaleei dagozkien exzitoi polaritoiak [11]. Kitzikapen hauek induzitzen duten eremu elektriko bortitzaren eta lokalizatuaren ondorioz, espektroskopiaren alorrean zenbait teknikek aurrerapen nabarmenak izan dituzte, hala nola, gainazalak areagotutako Raman espektroskopiak (ingelesez *surface-enhanced Raman spectroscopy*) [12–15] edota gainazalak areagotutako espektroskopia infragorriak (*surface-enhanced infrared spectroscopy*) [16–18]. Are gehiago, eremu elektrikoaren muturreko lokalizazioaren bidez, molekula isolatuak bereiztea ere posible bilakatu da [19–21]. Oro har, material ugariaren kitzipakenean dituzten ezaugarri interesgarriak direla eta, nanofotonika arlo multidisziplinaria da gaur egun [22]. Arlo honek dituen aplikazioen adibide gisa honakoak aipa ditzakegu: eguzki-plaketan energiaren bilketa [23, 24], terapia fototermala medikuntzan [25, 26], drogen detekzioa [27] edo informazio kuantikoaren prozesaketa [28].

Nanofotonikaren arloak tamaina nanometrikoa duten sistema fisikoetan propietate optiko berriak aurkitu ahal izateko metodo ezberdinak garatu ditu, zeinek argiaren eta materiaren elkarrekintza eskala nanometrikoan nola gauzatzen den aztertzen duten. Metodo ugari, elektromagnetismo klasikoaren esparruan kokatuta, Maxwell-en ekuazioetan oinarrituz argiaren uhin izaera deskribatzen dute. Halaber, Maxwell-en ekuazioak ebatzi ahal izateko, beharrezkoa da materialen permitibitatea ezagutzea. Horretarako, esperimentuen bidez lortutako permitibitate lokalak (hau da, uhin-bektorearen menpenkotasunik ez dutenak) edo materia-kitzikapenak deskribatzeko eredu teorikoetan oinarritutako permitibitatearen adierazpen analitikoak erabili ohi dira. Modu honen bidez, argia eta materia deskribatzeko eredu klasikoak konbinatuz, sistema fisikoaren erantzun optikoaren inguruan ezaugarri ugari aurkitu eta ulertu daitezke.

Nahiz eta metodo klasikoek nanofotonikaren alorreko esperimentuetan behatutako fenomeno ugari deskribatu ditzaketan [29], eskala nanometrikoan fisika klasikoaren bitartez azaldu ezin diren zenbait efektu kuantiko ageri dira. Beraz, zenbait kasutan beharrezkoa da argiaren eta materia-kitzikapenaren izaera kuantikoa aintzat hartzea [30–32]. Alde batetik, materia kondentsatuaren fisikak atomoen eta elektroien izaera kuantikoa deskribatzen du egoera solidoko sistematan, Schrödinger-en ekuazioan oinarrituz eta lehen printzipioetatik abiatuz. Nanofotonikaren testuinguruan, ikuspuntu honek permitibitate klasikoek kontuan hartzen ez dituzten

efektu ez-lokalak deskribatu ditzake [33–35], esate baterako. Horretaz gain, material ezberdinen arteko tarte mikroskopikoetan tunel kuantikoaren eraginez sistemaren erantzun kuantikoa nola aldatzen den ere azal dezake [36–38]. Bestalde, optika kuantikoaren esparrua ere oso arrakastatsua izan da nanofotonikaren arloan zenbait efektu kuantiko azaltzeko. Ikuspuntu honek, argiaren eta materia-kitzikapenen kuantizazioan oinarrituz, argiaren egoera ez-klasikoak eta argiaren eta materia-kitzikapenen arteko akoplamenduaren ondorioz agertzen diren fenomeno ez-linealak aztertzen ditu. Adibidez, zenbait atomok fotoi isolatuak igor ditzaketela behatu da [39, 40], eta fenomeno hau azaltzeko guztiz beharrezkoa da optika kuantikoaren ikuspuntua erabiltzea.

Hori guztia dela eta, nanofotonikaren arloak aurrerakuntza nabarmena izan du azken urteotan, materia kondentsatuaren fisikaren eta optika kuantikoaren metodo ezberdinak erabiliz. Tesi hau nanofotonikaren arloan ekarpen bat egiteko asmotan idatzi da, deskribapen kuantikoen garrantzia zehazteko helburuarekin, metodologia klasikoaren mugak eta abantailak ere aztertuz bide honetan. Zehazki esanda, tesi hau hiru zati nagusitan banatu da. Lehenik, sistema metalikoetan plasmioen ezaugarriak aztertu ditugu, materia kondentsatuaren fisikan oinarritutako metodologia erabiliz. Bigarrenik, dielektriko batez banatutako bi metalez osatutako sistematan plasmioen kitzikapenak eragin dezakeen argiaren igorpena dugu aztergai. Amaitzeko, eredu klasiko eta kuantikoek argia eta materiaren arteko elkarrekintza ultrabortitza (ingelesez *ultrastrong coupling*) nola deskribatzen duten ikertu dugu, eredu horien arteko loturak ere ezarriz.

Tesiaren lehen bi kapituluetan, gure analisiaren oinarrian dauden aurretiko ereduak eztabaidatu ditugu. Hasteko, 1. kapituluan, argia eta materia-kitzikapenen arteko elkarrekintza ulertzeko oinarria finkatu dugu. Maxwell-en ekuazioak aztertu ditugu lehenik, eta kitzikapen ezberdinek (hala nola, plasmioiek eta molekulen bibrazioek) materialen permitibitatean duten eragina eztabaidatu dugu gero. Ondoren, argiaren eta materiaren ereduak konbinatu ditugu, ikuspuntu klasikotik abiatuta materia-kitzikapenen eta barrunbe plasmonikoetako edo dielektrikoetako (ingelesez, *plasmonic cavity* eta *dielectric cavity* hurrenez hurren) modu elektromagnetikoen arteko elkarrekintza deskribatu ahal izateko. Zehazki, argia eta materiaren arteko elkarrekintza ahularen (non horien arteko akoplamendu indarra argiaren eta materiaren galera-tasak baino txikiagoa den) eta elkarrekintza bortitzaren (non handiagoa den) [41] arteko desberdintasunetan ipini dugu arreta. Kapituluarekin bukatzeko, barrunbeetako elektrodinamika kuantikoaren (ingelesez *cavity quantum electrodynamics*, *cavity QED*) inguruko sarrera egin dugu, argiaren eta materiaren elkarrekintza optika kuantikoaren ikuspuntutik nola aztertzen den ikusi dezagun. Bestetik, 2. kapituluan materia kondentsatuaren fisikaren ikuspuntua hartu dugu, metalen egitura elektronikoaren deskribapen mikroskopio zehatz bat egiteak sistemaren erantzun optikoaren azterketan duen eragina ikertzeko. Eztabaida hau bi ardatz nagusitan banatu da. Alde batetik, dentsitate funtzionalaren teoriak (ingelesez *Density Functional Theory*, DFT) eta denboraren menpeko dentsitate funtzionalaren teoriak (*Time Dependent Density Functional Theory*, TDDFT) metodo klasikoek baino plasmioen deskribapen zehatzagoa ahalbidetzen dutela aztertu dugu. Bestetik, metal-dielektriko-metal materialez

osatutako tunel-lotuneetan (ingelesez *tunneling junction*) elektroiek dielektrikoa tunel efektuaren bitartez zein tasatan zeharkatzen duten kalkulatu dugu. Tasa hau erabilia, tunel-lotuneetatik igortzen den argiaren intentsitatea kalkulatu daiteke (5. kapituluaren zehaztuko dugun bezala).

Oinarri teorikoa finkatuta, tesi honen ikerketa prozesuan zehar lortutako emaitzak aurkeztu ditugu ondoren. Hasieran, lehen printzipioetatik abiatuta kitzikapen plasmonikoen deskribapena gauzatu dugu. Zehazki, 3. kapituluaren, paladioan ipini dugu arreta eta material honi dagokion (110) norabideko gainazalean zein plasmoi existitzen diren aztertu dugu. Horretarako, DFTn oinarritutako metodologia erabili dugu lehenik gainazaleko banda egitura kalkulatzeko, atomoen sare-egituraren oinarrituta. Ondoren, banda egituraren bidez, sistemaz kanpoko perturbazio ahul batek metalean induzitzen duen dentsitate elektronikoa kalkulatu dugu TDDFTn oinarrituta [42, 43]. Emaitza hauek kitzikapen plasmoniko ezberdinak aztertzeke aukera ematen dute. Horrela, lehendabizi gainazaleko plasmioen ezaugarriak izan ditugu ikergai. Kalkulu teorikoen arabera, limite lokal klasikoan (uhin-bektorearen anplitudea zero egiten den limitean) lortu dugun plasmoiaren maiztasuna bat dator aurretiko esperimenduetan lortutako datuekin. Hala eta guztiz ere, efektu ez-lokalak aztertzerako garaian, dispersioari dagokionez (hau da, maiztasunak uhin-bektorearekiko duen menpekotasunari dagokionez) desadostasun nabarmena lortu dugu esperimenduetako neurketekin. Izan ere, esperimenduetan dispersio negatibo nabarmena neurtu izan den arren uhin-bektorearen modulua 1 nm^{-1} magnitude ordenakoa denean, gure kalkuluen arabera dispersio positibo ahul bat du Pd(110) gainazaleko plasmoiak.

Era berean, Pd(110) gainazalean plasmoi akustikoak existitzen diren ala ez ikertu dugu. Plasmoi hauek interes handia piztu dute, euren dispersio linealaren eraginez, haiei dagozkien uhin-bektoreen anplitudeak gainazaleko plasmioen kasuan baino handiagoak direlako eta, ondorioz, eremu elektrikoa are eskualde murrizagoan lokalizatu dezaketelako [44–46]. Elektroien gas homogeen eta isotropoan oinarritutako eredu teorikoen arabera, gainazaleko plasmoi akustikoak existitu ahal izateko, beharrezkoa da metalaren barnealdean lokalizatutako egoera elektronikoak egotea alde batetik, eta gainazalean lokalizatutakoak, bestetik. Gainera, egoera hauek Fermiren abiadura desberdina izan behar dute bata bestearekiko. Kalkulatu ditugun banda elektronikoen arabera, Pd(110) gainazalak betetzen du baldintza hau. Hori horrela izanik ere, TDDFT bidezko kalkuluak egin ondoren, ez dugu gainazaleko plasmoi akustikoen inolako ezaugarririk behatu gainazalaren erantzun optikoan. Ondorioz, gainazaleko eta bolumeneko egoera elektronikoak egotea ez da nahikoa gainazaleko plasmoi akustikoak existitzeko. Horren ordez, banda egitura konplexuek kitzikapen horren existentzia ukatu dezakete eta, beraz, plasmioen deskribapen zehatz bat egiteko beharrezkoa da metalen banda egitura osoa kontuan hartzea.

Hariarekin jarraituz, 4. kapituluaren, egitura elektronikoaren anisotropiak plasmioen ezaugarrietan duen eragina ikertu dugu. Horretarako, bi dimentsiodun (2D) materialak izan ditugu ikergai. Material hauetako plasmoiak, ohiko gainazaleko plasmoiekin alderatuta, ezaugarri desberdinak dituzte. Esate baterako, dispersioari dagokionez, 2D plasmioen maiztasuna uhin-bektorearen moduluen

erro karratuarekiko proportzionala da, ohiko gainazal metalikoen kasuan gertatzen ez den bezala. Horregatik, 2D plasmioen maiztasuna espektro elektromagnetikoaren THz tartean edo tarte infragorrian egon daiteke, uhin-bektorearen anplitudea handia denean ere. 2D plasmioen dispersioa jadanik neurtu da esperimentuen bitartez [47], eta bi dimentsiodun elektroien gas homogeen eta isotropoaren ereduaren bitartez azaldu daiteke teorikoki [48]. Bestalde, azken urteotan zenbait materialetan banda egitura anisotropoa behatu denez, anisotropia honen geometriaren arabera (hala nola, geometria trianguluarra, karratua eta hexagonala hautatu ditugu) [49–53], 2D materialetan plasmioen ezaugarriak nola aldatzen diren aztertu dugu.

2D plasmioen dispersioa geometriaren arabera nola aldatzen den ikertzeaz gain, bi dimentsioko elektroien gas anisotropoan plasmoi akustikoak daudela behatu dugu, zeinek eremu elektriko oso eskualde txikian lokalizatzea ahalbidetzen duten. Kitzikapen hau ez da 2D material isotropoetan ageri. Bestalde, gure emaitzen arabera, plasmoi akustikoen kopurua geometriaren arabera aldatzen da: hiruki eta lauki formako banda egitura duten materialetan, plasmoi akustiko bakarra dago, eta hexagono formaren kasuan, aldiz, bi. Oro har, plasmoi akustikoen kopurua materialean Fermiren abiadura berdina duten elektroien multzoen kopuruarekin dago lotuta. Aurretik, plasmoi akustikoak soilik bi mota desberdinetako egoera elektronikoak dauden materialetan behatu dira, adibidez, gainazalean lokalizatutako eta metalaren barnealdean lokalizatutako egoera elektronikoak dituzten metaletan. Gure emaitzek erakutsi dutenez, banda egituraren anisotropia plasmoi akustikoak existitzeko beste mekanismo bat da, eta horrela, posible da banda elektroniko bakarra duten materialetan ere plasmoi akustikoak kitzikatzea.

Aurreko kapituluetan, plasmioen propietateak aztertu ditugu sistema ezberdinetan, horiek kitzikatze mekanismoari eta efizientziari arretarik ipini gabe. Honela, 5. kapituluan, tesi honen bigarren gai nagusia garatu dugu: SPPak nola kitzikatu daitezkeen elektroien bitartez metal-dielektriko-metal tunel-lotuneetan potentziala ezarri ondoren, eta prozesu honen bidez tunel-lotunedun gailuek argia nola igortzen duten [54]. Historikoki, SPPen kitzikapena elektrodoen arteko tarte dielektrikoan gauzatzen dela uste izan da, tunel efektu inelastikoaren bitartez [55,56]. Prozesu hau Bardeen-ek sortutako tunel elastikoaren eredutik abiatuta deskribatu da, non elektroien uhin-funtzioek tarte dielektrikoan duten izaera hartzen den kontuan. Hori horrela izanik ere, prozesu honek ez du zenbait esperimentutan detektatu den argi guztia aintzat hartzen [57]. Horregatik, argiaren igorpenaren atzean bigarren prozesu bat gertatzen dela argudiatu zen, non elektro berroek (hau da, elektrodo bati dagokion Fermiren energia baino energia handiagoa duten elektroiek) energia elektrodoan galtzen duten tunel efektu elastikoa gauzatu ondoren, galdutako energiarekin SPPak kitzikatuz.

Testuinguru honetatik abiatuta, kapitulu honetan tunel-lotunedun gailuetatik igortzen den argiaren deskribapen teorikoan sakondu dugu. Hasteko, literaturan SPPen kitzikapen tasa kalkulatzeko sarritan erabiltzen diren bi metodo aztertu ditugu. Horietako bat Fermiren urrezko legean dago oinarrituta eta bestea, aldiz, korrante elektrikoaren fluktuazioek igortzen duten potentziaren kalkuluan. Bi metodo hauen arteko lotura ezarri dugu, bien bitartez emaitza baliokideak lortzen direla frogatuz. Gainera, SPPen kitzikapen tasaren kalkuluan, tunel efektu

inelastikoak elektrodoetako prozesuen ekarpena aintzat hartzen duela erakutsi dugu, elektroien beroen prozesua ereduari sartu beharrik izan gabe. Horretarako, gailuaren soluzio kuantikoaren (ingelesez *quantum device solution*, QDS) metodoa proposatu dugu, non elektroien uhin-funtzioa Schrödinger-en ekuazioaren bidez kalkulatzeko garaian gailu osoa hartzen den kontuan, hau da, bi elektrodo metalikoak eta horien arteko tarte dielektrikoa. Metodo hau sarri erabili izan den Bardeen-en hurbilketa haratago doa, non argiaren igorpenaren kalkulua soilik tarte dielektrikoan egiten den. QDSak Bardeen-en hurbilketa baino kitzikapen tasa nabarmenki handiagoa aurreratu du, SPParen eremu elektrikoa tarte dielektrikotik zenbait nanometrora lokalizatuta dagoen kasuetan. Gainera, QDSak argiaren igorpenaren deskribapen kualitatibo osatuago bat ematen du Bardeen-en hurbilketarekin alderatuta. Izan ere, QDSaren arabera, korrante elektrikoa bortizki korrelazionatuta dago bi elektrodoetan, eta Bardeen-en hurbilketa ezin dezake fenomeno hau azaldu. Eraitza hau tarte dielektrikoan birkonbinatzen den elektroien-hutsune bikote baten ondorioa dela interpretatu dugu. Horrela, birkonbinaketa prozesu honek argiaren igorpenari gainerako ekarpen bat egiten dio, tarte dielektrikoan gertatzen diren prozesuez haratago doana. Gure analisiak tunel-lotunedun gailuetatik argiaren igorpenaren inguruan gaur egun dagoen ikuspuntua zabaltzea ahalbidetzen du.

3., 4. eta 5. kapituluetan materia-kitzikapenen ezaugarriak aztertu ondoren, azken bi kapituluetan kitzikapenen eta modu elektromagnetikoen arteko elkarrekintza nola gauzatzen den izan dugu ikergai. 6. kapituluan, argiaren eta materiaren arteko akoplamendu ultrabortitzaren (non akoplamendu indarra argiaren eta materia-kitzikapenaren maiztasunaren %10 den gutxienez) [58, 59] atzean dauden teoria ezberdinak aztertu ditugu. Azterketa hau bi ikuspuntu ezberdinetatik garatu dugu. Lehen ikuspuntua *cavity* QED alorrari dagokio, zeinetan analisia hamiltondar kuantikoetan oinarrituta egin dugun. Zehazki, literaturako lan batzuetan, argiaren eta materiaren arteko akoplamendua deskribatzeko termino diamagnetiko bat erantsi izan zaio hamiltondarrari, baina beste zenbait kasutan, aldiz, ez. Bestalde, ikuspuntu klasikotik begiraturik, akoplatutako osziladore harmonikoetan oinarrituta dauden eredu klasikoak aztertu ditugu, non osziladore batek modu elektromagnetikoa deskribatzen duen eta beste osziladorea materia-kitzikapenari dagokion [60].

Akoplamenduaren eredu klasiko eta kuantikoak lortzeko, elektrodinamika klasikoaren deskribapen lagrangeartetik abiatu gara. Modu honen bidez, bi ikuspuntu ezberdin horien arteko lotura ezarri dugu, bien bitartez autobalio berdinak lortzen direla frogatuz, eta baita esperimenduetan neurtu daitezkeen behagarrien balio berdinak lortzen direla ere. Bereziki, osziladoreen bi eredu klasikoetan eta *cavity* QED alorreko bi hamiltondar kuantikoetan ipini dugu arreta. Lehen eredu klasikoari malgukien bidezko akoplamendua (ingelesez *spring coupling*, SpC) deitu diogu, zeina malguki batez akoplatutako bi osziladore mekanikoren baliokidea den matematikoki. Eredu honek luzetarako elkarrekintzak deskribatzen dituela frogatu dugu, hala nola, Coulomb elkarrekintzak (adibidez, molekula baten eta nanopartikula plasmoniko baten elkarrekintza hurbilketa kuasi-estatikoan). Era berean, eredu klasiko hau termino diamagnetikoa ez duen *cavity* QED alorreko hamiltondar kuantikoaren baliokidea dela frogatu dugu. Aztertu dugun bigarren

eredu klasikoan, aldiz, akoplamenduaren terminoa osziladoreen abiadurarekiko proportzionala da, SpC ereduan ez bezala, non osziladoreen anplitudearekiko den proportzionala. Horregatik, bigarren ereduari akoplamendu aldatua (ingelesez *modified coupling*, MC) deitu diogu. Gure analisiaren arabera, eredu honek zeharkako uhin elektromagnetikoen eta materia-kitzikapenen arteko akoplamendua deskribatzen du zehazki (adibidez, barrunbe dielektrikoetan), eta bestalde, termino diamagnetikoa ezarrita duen *cavity* QED alorreko hamiltondar kuantikoaren emaitza baliokideak ematen ditu.

Osziladore harmonikoen ereduen baliotasuna ezarri ondoren, 7. kapitulu fonioen eta barrunbe dielektrikoetako modu elektromagnetikoen arteko elkarrekintza aztertzeke erabili ditugu eredu hauek. Ondorioz, kapitulu honek bibrazioen akoplamendu bortitzaren alorrean sakondu du. Alor honek interes handia piztu du, barrunbeetan molekulen bibrazioen eta eremu elektrikoaren hutsaren fluktuazio kuantikoen arteko elkarrekintzak molekulen ezaugarri kimikoak aldatzen dituela behatu zenetik [61, 62]. Orokorrean, molekulaz betetako Fabry-Pérot barrunbeak sistema fisiko egokiak dira akoplamendu bortitza lortu ahal izateko [63, 64]. Hala ere, fonioen oszilazio indarra molekulena baino bortitzagoa denez, fonioen bitartez modu elektromagnetikoekin are akoplamendu bortitzagoa lortu daitekeela espero daiteke. Horregatik, kapitulu honetan material polar bat hartu dugu kontuan, boro nitruro hexagonal (ingelesez *hexagonal boron nitride*, hBN) hain zuzen. Material honen geruzaz beteriko Fabry-Pérot barrunbeak ikertu ditugu material polarretako fonioen eta modu elektromagnetikoen arteko akoplamendua aztertzeke.

Sistema honen bitartez, argiaren eta materiaren arteko akoplamendu erregimen ezberdinak ikertu daitezkeela frogatu dugu. Lehenik, soilik 3 nm-ko lodiera duen hBN geruza batekin akoplamendu bortitza lortu daiteke. Halaber, argiaren eta materiaren arteko akoplamendu indarra nabarmenki igotzen da hBN geruzaren lodiera igo ahala, eta 150 nm-ko lodieradun geruza baten bitartez akoplamendu ultrabortitza lortzen da sisteman. Azkenik, hBN materialaz osorik betetako Fabry-Pérot barrunbe baten kasuan, akoplamendu indarraren balioa fonoiaren maiztasunaren %30 dela erakutsi dugu. Sistema honetan akoplamendu indarrak kalkulatzeko, simulazio elektromagnetikoetan oinarritutako azterketa numeriko bat egiteaz gain, fonioen eta argiaren deskribapen mikroskopikoan oinarritutako eredu bat ere erabili dugu, akoplamendu indarraren adierazpen analitiko bat lortzea ahalbidetzen duena. Horren arabera, osorik beteta dauden barrunbeetan, akoplamendu indarra materialaren ezaugarrien menpekoa da soilik eta, beraz, magnitude fisiko horrek ez du modu elektromagnetikoen ezaugarriekiko menpekotasunik. Hori dela eta, Fabry-Pérot barrunbeetan ez da posible materialaren ezaugarriek mugatutako akoplamendu indarra baino handiagoa den baliorik lortzea. Bestalde, kapitulu honetan frogatu dugunez, akoplamendu ultrabortitzaren ondorioz sortu diren modu hibridoak dispersioa zehazki lotuta dago hBNren permitibitatearekin eta materialaren bolumeneko fonoi polaritoiden dispersioarekin. Aurkikuntza hauek guztiak direla eta, material polarrez betetako mikrobarrunbe eta nanobarrunbeak aproposak dira fonioen eta modu elektromagnetikoen akoplamendu bortitza eta ultrabortitza aztertzeke.

Laburbilduz, tesi hau nanofotonikaren arloan ekarpena egiteko asmoarekin idatzi da, bi helburu nagusirekin. Lehen helburua metodologia klasikoaren eta kuantikoaren inguruan gaur egungo ulermena areagotzea izan da, bai materia kondentsatuaren fisikaren ikuspuntutik eta baita optika kuantikoaren aldetik ere. Horrela, sarri erabiltzen diren metodo ezberdinak aztertu ondoren, horien artean orain arte ezarri gabe zeuden loturak ezarri ditugu. Ondoren, metodo horiek sistema ezberdinetan aplikatu ditugu tesiaren bigarren helburua bete ahal izateko: plasmoiden, tunel inelastikoak induzitutako argiaren igorpenaren, eta argiaren eta materiaren arteko akoplamendu ultrabortitzaren inguruan fenomeno berriak aurkitzea eta aztertzea.

LIST OF ABBREVIATIONS

2DP	Two-dimensional plasmon
ALDA	Adiabatic local density approximation
AP	Acoustic plasmon
DFT	Density functional theory
hBN	Hexagonal boron nitride
HEG	Homogeneous electron gas
KS	Kohn-Sham
LDA	Local density approximation
LO	Longitudinal optical
LSP	Localized surface plasmon
MC	Modified coupling
MIM	Metal-insulator-metal
QDS	Quantum device solution
QED	Quantum electrodynamics
RPA	Random phase approximation
RWA	Rotating-wave approximation
SBZ	Surface Brillouin zone
SpC	Spring coupling
STM	Scanning tunneling microscope
SPP	Surface plasmon polariton
TDDFT	Time-dependent density functional theory
TE	Transverse electric
TM	Transverse magnetic
TO	Transverse optical

CONTENTS

Acknowledgments	v
Laburpena	ix
List of abbreviations	xvii
Introduction	1
1 Descriptions of light-matter interaction in the nanoscale	7
1.1 Classical description of light	8
1.1.1 Maxwell's equations	8
1.1.2 Lagrangian and Hamiltonian formulation of electromagnetic fields	14
1.2 Optical excitations in matter	17
1.2.1 Plasmons	17
1.2.2 Vibrational excitations	26
1.3 Weak, strong and ultrastrong coupling between light and matter	30
1.3.1 Classical harmonic oscillator model	32
1.3.2 Cavity quantum electrodynamics description	35
2 Quantum descriptions of plasmonic excitations and of electron tunneling	39
2.1 Linear response theory	40
2.1.1 Density-density response function	41
2.1.2 Causality and Kramers-Kronig relations	42
2.2 Permittivity of an homogeneous electron gas under the random phase approximation	44
2.2.1 3D homogeneous electron gas	46
2.2.2 2D homogeneous electron gas	49
2.2.3 A 2D layer over a 3D bulk substrate: acoustic surface plasmons	51
2.3 <i>Ab initio</i> methods	54
2.3.1 Density Functional Theory	54
2.3.2 Time-Dependent Density Functional Theory in the linear response framework	60

2.3.3	Computational methods to calculate electronic excitations in metallic surfaces	63
2.4	Bardeen's theory of elastic electron tunneling	68
3	<i>Ab initio</i> description of plasmonic excitations on the Pd(110) surface	75
3.1	Introduction	75
3.2	System and computational details	77
3.3	Electronic band structure of the Pd(110) surface	79
3.4	Excitation spectrum of the Pd(110) surface	81
3.4.1	Surface plasmon	81
3.4.2	Induced density on the Pd(110) surface	85
3.4.3	Additional plasmonic excitations	88
3.5	Summary	89
4	Plasmonic excitations in two-dimensional anisotropic electron systems	91
4.1	Introduction	91
4.2	Details of calculations	93
4.3	Excitation spectra of two-dimensional anisotropic electron gases . .	94
4.3.1	Triangular anisotropy	95
4.3.2	Square anisotropy	99
4.3.3	Hexagonal anisotropy	101
4.3.4	Electron gas with non-ideal anisotropic dispersion	105
4.4	Summary	106
5	Light emission from tunneling junctions	109
5.1	Introduction	109
5.2	Descriptions of elastic tunneling	112
5.3	Descriptions of inelastic tunneling	116
5.3.1	Fermi's golden rule	117
5.3.2	Energy-loss model and Poynting vector flux calculation . .	121
5.3.3	Equivalence of the methods	123
5.3.4	Current-density correlation function	124
5.4	Light emission from planar devices	127
5.4.1	Mode structure of the system	127
5.4.2	Excitation rate of the slow mode	130
5.4.3	Excitation rate of the fast mode	133
5.4.4	Excitation rate of the medium mode	138
5.5	Summary	138
6	Comparison of classical and cavity-QED models in the ultrastrong coupling regime	141
6.1	Introduction	141
6.2	Classical models of coupled harmonic oscillators in nanophotonics .	144

6.3	Derivation of the equations of motion in the classical coupled harmonic oscillator models	150
6.3.1	Spring coupling model with external laser illumination . . .	154
6.4	Comparison between cavity-QED Hamiltonians and classical models	155
6.4.1	Modified coupling model	155
6.4.2	Spring coupling model	159
6.5	Physical observables obtained from classical models	159
6.5.1	A molecular excitation interacting with a transverse mode of a dielectric cavity	160
6.5.2	A molecule interacting with the longitudinal field of a metallic nanoparticle	165
6.5.3	An ensemble of interacting molecules in a Fabry-Pérot cavity	170
6.6	Alternative classical models of coupled harmonic oscillators	172
6.6.1	Interaction of a molecular excitation with a transverse cavity mode described within the Coulomb gauge	173
6.6.2	Interaction of a molecular excitation with a transverse cavity mode described within the dipole gauge	174
6.6.3	Interaction of a molecule with a metallic nanoparticle . . .	175
6.7	Summary	176
7	Microcavity phonon polaritons in the weak, strong and ultrastrong coupling regimes	179
7.1	Introduction	179
7.2	Description of the system	180
7.3	Evolution of the coupling strength with the cavity filling factor . .	183
7.3.1	Transfer-matrix simulations and classical coupled harmonic oscillator model	183
7.3.2	Microscopic model of interaction between phonons and Fabry-Pérot modes	190
7.4	Comparison with experimental reflectivity data	196
7.4.1	Reflectivity of the system under focused illumination	198
7.5	Dispersion relation of microcavity phonon polaritons	202
7.6	Summary	205
	Conclusions and Outlook	207
	Appendices	
A	Origin of the strong current correlations at opposite metals in tunneling junctions	213
B	Classical description of the coupling between a molecule and a plasmonic nanocavity based on their polarizability	217

C Transformation from individual to collective oscillators in the description of homogeneous materials in Fabry-Pérot cavities	219
List of publications	223
Bibliography	225

INTRODUCTION

The progress of science owes much to our innate ability to recognize patterns in nature through simple observation. From prehistoric times, this ability has enabled advances in agriculture, for example, as people observed the changing of the seasons. However, science based solely on visual observation is limited by the capabilities of the human eye. One limitation is based on the inability to detect light waves outside the visible range, which is a small part of the electromagnetic spectrum. Further, objects that are too faint or too small cannot be distinguished by the human eye. In the 17th century, the limits of the scale of visible objects were broadened due to technological advances. The telescope allowed Galileo Galilei to observe the four largest moons of Jupiter [1], while the microscope enabled the observation of cells [2]. These early discoveries opened up the possibility that objects at any distance or of any size could be observed through human eyes.

However, despite improvements in traditional optical microscopes over the following centuries, the limit of the size that could be distinguished remained around hundreds of nanometers. This limitation is not due to technological tools, but to the nature of light itself. The wave behavior of light establishes Abbe's diffraction limit, which forbids to distinguish features in these microscopes at a resolution better than half the wavelength [3, 4]. For visible light, this condition corresponds to a size of 200-400 nm. These sizes also correspond to the maximum field localization possible by focusing light with a lens. To observe and manipulate sub-wavelength objects with light, additional methods are necessary. The field of nanophotonics emerged motivated by the search of these methods.

A particular structure that allows for localization of light in sub-wavelength regions are metallic surfaces [5]. In planar metallic surfaces, electromagnetic radiation can couple with collective oscillations of conduction electrons in the metal-vacuum interface, leading to the emergence of excitations called propagating surface plasmon polaritons (SPPs). These excitations, which have hybrid properties of light and electrons, are waves that propagate along the surface, with electric fields that are highly localized in the interface and decay exponentially through the normal direction. Additionally, metallic nanostructures with nanometric dimensions in all three spatial directions can support localized surface plasmons, which can store electromagnetic energy in very small volumes. This extreme localization overcomes the diffraction limit and enables the design of photonic devices that manipulate light in the nanometric scale. It has been found that, for optimized

geometries, localized surface plasmons can enhance the incident electric field by $\approx 1 - 3$ orders of magnitude [6–9].

Plasmonic excitations in metals lie in the ultraviolet, visible or near infrared ranges of the electromagnetic spectrum, but nanophotonic systems can also exploit other excitations in other materials that occur in these and in other ranges of the electromagnetic spectrum. Some examples are phonon polaritons in polar materials [10] or exciton polaritons in semiconductors [11]. The strong electric fields induced by the excitations in these systems have led to significant improvements in spectroscopy techniques, such as surface-enhanced Raman scattering [12–15] or surface-enhanced infrared spectroscopy [16–18]. Further, the possibility of extreme field confinement has made it possible to even observe objects with molecular resolution [19–21]. More generally, the promising properties of these excitations have led to nanophotonics becoming a multidisciplinary field [22] with possible applications including energy harvesting in solar cells [23,24], photothermal therapy in medicine [25,26], drug detection [27] and quantum information processing [28].

In the search for new properties in nanophotonic systems, various theoretical methods have been developed to study how light interacts with matter excitations on the nanometric scale. A large variety of these methods fall within the framework of classical electromagnetism that describes the wave-like behavior of light through Maxwell’s equations. To solve these equations, the optical response of different materials, as given by their permittivity, must be known together with the geometry of the system. To quantify the permittivity, either experimentally measured local values (i.e. which do not depend on the wavevector) or analytical expressions based on classical local models of matter excitations have been used. Thus, by combining classical descriptions of both light and matter excitations, it is possible to understand many properties of the optical response of the system.

This classical framework has been successful in explaining many features of nanophotonic systems observed in experiments [29]. However, in nanoscale systems, quantum effects can emerge that cannot be accounted for by classical models and that require considering the quantum nature of matter excitations and light [30–32]. On the one hand, the field of condensed matter physics accounts for quantum phenomena by considering accurately the behavior of atoms and electrons according to a description based on first principles of the solid system. In the context of nanophotonics, this approach allows for considering non-local effects in the optical response that are not captured by classical local permittivities [33–35], and to describe how the optical response of systems with subnanometric gaps is modified by considering the tunneling of electrons through the gaps [36–38], for instance. On the other hand, the framework of quantum optics has been also successfully applied to describe many phenomena in nanophotonics. This framework considers the quantization of light and matter excitations, and describes phenomena related to non-classical states of light, or non-linear phenomena emerged due to the coupling of electromagnetic modes with molecular excitations or matter excitations in different materials, among others. For example, it has been observed that single atoms and other systems can emit antibunched light [39,40], which cannot be explained by classical models.

As a consequence, the field of nanophotonics has made significant progress in recent years by adopting different tools from condensed matter physics and quantum optics. This promising context has motivated this thesis, which aims to contribute to the understanding of quantum effects in nanophotonics and to determine the limitations and successes of classical models. The thesis focuses on three key areas that involve i) a first-principles description of plasmonic excitations, ii) how they can be excited and iii) how different matter excitations couple with electromagnetic modes of different cavities. First, the thesis examines how methodologies based on condensed matter theory can accurately describe the (non-local) properties of plasmonic excitations in metallic structures by incorporating the characteristics of the system through first principles. Secondly, we explore how systems formed by metals separated by an insulator of nanometer thickness can emit light due to the SPPs that are excited by electrons via inelastic tunneling. Finally, we investigate the ability of both quantum and classical models to describe light-matter coupling in the ultrastrong coupling regime, and how these different types of models are connected with each other.

The first two chapters of this thesis provide an overview of the fundamental models and principles on which our analysis is based. In [Chapter 1](#), we establish the basics for understanding the interaction between light and matter excitations. We first discuss Maxwell's equations, which describe the dynamics of the electromagnetic fields, and then analyze the classical local permittivity of materials supporting different matter excitations, such as plasmons and molecular vibrations. Then, after this separate description of the properties of light and matter excitations, we introduce the classical interaction between matter excitations and electromagnetic modes in dielectric and plasmonic cavities, focusing on the differences between the weak light-matter coupling regime (where the coupling strength is weaker than the decay rates of light and matter) and the strong coupling regime (where it is larger) [41]. Last, we introduce cavity quantum electrodynamics (QED), which describes light-matter interaction in these coupling regimes within the framework of quantum optics. On the other hand, [Chapter 2](#) adopts the perspective of condensed matter physics to the study of plasmonic systems. Two topics motivate this discussion. First, we examine how a rigorous first-principles description of the electronic properties, based on Density Functional Theory (DFT) and Time Dependent Density Functional Theory (TDDFT), allows for a more accurate description of the properties of plasmonic excitations than possible with classical models. Afterwards, we discuss how solving the Schrödinger equation in metal-insulator-metal tunneling junctions enables the evaluation of the electron tunneling rate between the two metallic electrodes. This tunneling rate is used in [Chapter 5](#) (see below) to calculate the rate of light emission from tunneling junctions.

After establishing the theoretical background, we present the results of the thesis. We first consider the first-principles description of plasmonic excitations using tools of condensed matter physics. In particular, in [Chapter 3](#) we focus on palladium and analyze plasmonic excitations on the (110) surface. With this aim, we first use the methodology of DFT to calculate the band structure of the Pd(110)

surface based on the distribution of the atoms in the lattice. We then use the obtained band structure to calculate the electronic density induced by an external weak probe within TDDFT [42, 43], which allows us to obtain the properties of different matter excitations such as electron-hole pairs or, more importantly, surface plasmons. This study enables the comparison of the theoretical dispersion relation of the surface plasmon (i.e. how the frequency ω of these excitations depends on the wavevector \mathbf{q}) with already published experimental data. Further, studies in recent decades have predicted an alternative excitation called acoustic surface plasmons, where the dispersion relation is linear, i.e. $\omega \propto |\mathbf{q}|$ [44–46]. This excitation is associated with even larger wavevectors than the conventional surface plasmons (so that it can be localized in extremely small dimensions) and it is caused by the existence of electronic states localized in the bulk and in the surface with different Fermi velocities. We analyze whether the electronic structure of the palladium (110) surface enables the existence of these plasmons.

Additionally, we analyze in [Chapter 4](#) the effects of anisotropy at the atomic scale on the plasmonic excitations in metals. In this analysis, we choose two-dimensional (2D) metals, where the plasmonic excitations have different properties than those in the three-dimensional case. Indeed, 2D plasmons typically follow a dispersion relation of the form $\omega \propto \sqrt{|\mathbf{q}|}$, which means that these excitations can reach the mid-infrared and THz parts of the spectrum with very large $|\mathbf{q}|$. This dispersion relation has been measured experimentally [47] and can already be obtained from a simple model of a homogeneous and isotropic electron gas [48]. Motivated by experimental measurements of anisotropic electronic structures in different materials [49–53], we study how different types of anisotropy of the electronic structure in 2D homogeneous electron gases affects the plasmon dispersion compared to the isotropic situation. Notably, we analyze in detail how the existence and number of acoustic plasmons in 2D metals depends on the type of anisotropy.

In the previous chapters, we have analyzed the properties of plasmons in different metallic systems, without paying attention to the excitation mechanism and its efficiency. In [Chapter 5](#), we turn our attention to the second main topic of this thesis: the study of how plasmons can be excited via electrons in metal-insulator-metal tunneling junctions under a bias potential, and how this process leads to light emission [54]. Historically, the excitation of plasmons has been mainly attributed to inelastic tunneling processes occurring in the insulator gap during the tunneling of the electron between the two metallic electrodes [55, 56]. However, it was found that this theoretical description does not account for all the emitted light [57]. Therefore, it was argued that other processes also contribute to light emission, such as the decay of hot electrons (i.e. electrons with larger energy than the Fermi energy of the corresponding metallic electrode) after elastic tunneling. The main objective of [Chapter 5](#) is to show that calculations of inelastic tunneling based on the solution of the Schrödinger equation in the complete metal-insulator-metal device can describe additional light emission (related to that induced by processes in the insulator gap) that is generated in the metallic electrode, without the need of considering additional hot-electron excitation processes. In this context, we consider two different methodologies previously used in the calculation of light

emitted from tunneling junctions, to determine whether they lead to equivalent descriptions and results.

Last, after the study in Chapters 3–5 of the properties of the matter excitations themselves, the final two chapters are devoted to analyzing the coupling between matter excitations and electromagnetic modes in optical cavities. In Chapter 6, we analyze in detail theoretical frameworks that are used to study systems that are in the ultrastrong coupling regime. This regime occurs when the coupling strength between the electromagnetic mode and the matter excitation is comparable to the frequencies of the uncoupled excitations [58, 59]. The first approach is based on cavity QED, where the electromagnetic modes of the cavity and matter excitations are quantized. On the other hand, we also consider classical models of light-matter coupling that are based on two coupled harmonic oscillators. One oscillator represents the matter excitation and the other corresponds to the electromagnetic modes of a cavity [60]. The analysis of this chapter allows us to establish the connection between classical and cavity-QED models in the ultrastrong coupling regime, and to show that both approaches are equivalent for the analysis of typical properties of the coupled system.

Having established in a sound footing the validity of the coupled harmonic oscillator models, we use them in Chapter 7 to explore in detail the interaction between phonons in polar materials and cavity modes. This chapter thus explores the topic of vibrational strong coupling, which has raised considerable interest after the finding that the coupling of molecular vibrations with vacuum fluctuations of the electric field of a cavity mode could modify chemical reactions, without using any external illumination [61, 62]. Typically, the strong coupling regime is achieved by filling a Fabry-Pérot cavity with molecules [63, 64]. However, due to their larger oscillator strength, phonons in polar materials can exhibit an even stronger coupling with the microcavity modes than the molecular vibrations. Accordingly, we analyze Fabry-Pérot microcavities filled with layers of the polar material hexagonal boron nitride (hBN) as a versatile platform to study vibrational coupling with phonons in different coupling regimes.

Hence, the aim of this thesis is to contribute to two main aspects of the field of nanophotonics. The first objective is to advance the current understanding on different classical and quantum methodologies, both within the condensed-matter framework and within cavity QED, exploring the equivalences between different widely-used approaches that were not clearly specified before. We then apply these methodologies to fulfill the second main objective of the thesis, which consists in analyzing new phenomena regarding plasmonic excitations, light emission from tunneling junctions and light-matter interaction in the ultrastrong coupling regime.

DESCRIPTIONS OF LIGHT-MATTER INTERACTION IN THE NANOSCALE

In this thesis, we use quantum and classical frameworks to analyze the properties of matter excitations in nanophotonic systemsⁱ and their interaction with light, and we highlight the differences and similarities between these two types of description. The main goal of this chapter is to present classical descriptions that we use through this thesis, but we also introduce at the end a description of light-matter interaction based on cavity quantum electrodynamics (QED).

In Sec. 1.1, we summarize the theory of classical electrodynamics. Maxwell's equations are presented first in Sec. 1.1.1, where we emphasize that the classical optical response of a bulk material is usually described by its permittivity and that electromagnetic fields must satisfy certain boundary conditions in the interfaces between different materials. We also illustrate in this subsection how to combine the bulk Maxwell's equations and the boundary conditions. With this purpose, we choose a situation of large importance in this thesis, which consists in systems formed by planar layers, and show that the optical response in this situation can be obtained with the transfer-matrix formalism. Further, we outline in Sec. 1.1.2 a description of classical electromagnetism based on the Lagrangian and Hamiltonian formalisms, which is equivalent to Maxwell's equations and will be useful in Chapter 6 to formally derive a cavity-QED framework of light-matter interaction. In Sec. 1.2, we discuss different optical excitations in matter. Specifically, we consider two different types of excitations, collective oscillations of electrons in metals (plasmons, Sec. 1.2.1) and vibrations in polar materials (phonons) or in molecular ensembles (Sec. 1.2.2). We discuss simple models describing the permittivity of these materials

ⁱFor simplicity, in this thesis we use *nanophotonics* as a general term, but some of the discussed approaches are also applied or applicable to systems of micrometer dimensions.

and how different plasmonic and phononic resonances can be present depending on the geometry of the system. Last, in Sec. 1.3 we formalize the description of the light-matter interaction, focusing on the importance of distinguishing between three regimes of interaction: the weak, strong and ultrastrong coupling regimes. We compare the description of these regimes using two alternative models: one based on classical coupled harmonic oscillators (Sec. 1.3.1), and the other on cavity QED (Sec. 1.3.2).

1.1 Classical description of light

1.1.1 Maxwell's equations

The most fundamental description of classical nanophotonics relies on Maxwell's equations, which are differential equations that model the dynamics of electromagnetic fields interacting with any system or material [65–68]. The electric and magnetic degrees of freedom are described by four vector fields, consisting in the electric field \mathbf{E} , the displacement vector \mathbf{D} , the magnetic field \mathbf{B} and magnetic field strength \mathbf{H} . Maxwell's equations connect these magnitudes as

$$\nabla \cdot \mathbf{D} = \rho_f, \quad (1.1a)$$

$$\nabla \cdot \mathbf{B} = 0, \quad (1.1b)$$

$$\nabla \times \mathbf{E} = -\frac{\partial \mathbf{B}}{\partial t}, \quad (1.1c)$$

$$\nabla \times \mathbf{H} = \mathbf{j}_f + \frac{\partial \mathbf{D}}{\partial t}. \quad (1.1d)$$

All the free charges that act as sources of electromagnetic radiation are introduced in terms of the free charge density $\rho_f(\mathbf{r}, t)$ and current density $\mathbf{j}_f(\mathbf{r}, t)$. The conservation of charge is ensured by the continuity equation

$$\nabla \cdot \mathbf{j}_f + \frac{\partial \rho_f}{\partial t} = 0, \quad (1.2)$$

which is obtained by taking the divergence of Eq. (1.1d) and then relating the displacement vector with the free charge density following Eq. (1.1a).

Besides the free charge and current densities, nanophotonic systems have bound charges whose effect on the optical response is described with the (relative) permittivity $\varepsilon(\mathbf{r}, \mathbf{r}', t, t')$ and (relative) permeability $\mu(\mathbf{r}, \mathbf{r}', t, t')$ functions. These functions establish additional relations between the vector fields \mathbf{E} , \mathbf{D} , \mathbf{B} and \mathbf{H} to those given by Maxwell's equations in Eq. (1.1). The permeability relates the fields associated to magnetism, i.e., \mathbf{B} and \mathbf{H} . In this thesis, we consider non-magnetic materials, and thus $\mu(\mathbf{r}, \mathbf{r}', t, t') = 1$ in all cases. Accordingly, these fields are related as $\mathbf{B} = \mu_0 \mathbf{H}$, where μ_0 is the vacuum permeability. The optical response of matter is then fully described with the permittivity, which in a general non-local

description relates \mathbf{E} and \mathbf{D} according to the integral relation

$$\mathbf{D}(\mathbf{r}, t) = \int \int \varepsilon_0 \varepsilon(\mathbf{r}, \mathbf{r}', t, t') \mathbf{E}(\mathbf{r}', t') d\mathbf{r}' dt', \quad (1.3)$$

where ε_0 is the vacuum permittivity. Usually, it is convenient to write this equation in the frequency (ω) domain instead than in the time (t) domain. By considering that the system is invariant to time translations, $\varepsilon(\mathbf{r}, \mathbf{r}', t, t') = \varepsilon(\mathbf{r}, \mathbf{r}', t - t')$, and calculating the Fourier transform of Eq. (1.3), the relation between the electric and displacement fields becomes

$$\mathbf{D}(\mathbf{r}, \omega) = \int \varepsilon_0 \varepsilon(\mathbf{r}, \mathbf{r}', \omega) \mathbf{E}(\mathbf{r}', \omega) d\mathbf{r}'. \quad (1.4)$$

The last relation can be further rewritten by performing the Fourier transform over space, giving the optical response of the material as a function of the wavevector \mathbf{q} with

$$\mathbf{D}(\mathbf{q}, \omega) = \varepsilon_0 \varepsilon(\mathbf{q}, \omega) \mathbf{E}(\mathbf{q}, \omega). \quad (1.5)$$

Hence, in order to fully characterize the optical response of a material, it is necessary to know both the spatial and temporal dispersion of the permittivity $\varepsilon(\mathbf{q}, \omega)$. The spatial nonlocality (given by the dependence with \mathbf{q}) is specially important for phenomena at wavevectors of magnitude $|\mathbf{q}| \gtrsim k_F$, where k_F is the Fermi wavevector of the material. Taking into account that the Fermi wavelength of standard materials is usually less than a nanometer, a non-local description is necessary when the characteristic wavelength of the excitations of the system is comparable to atomic dimensions. We discuss models of non-local permittivity in more detail in Chapter 2.

On the other hand, non-local descriptions are really difficult in most situations. Fortunately, in many systems of nanophotonics, the relevant wavelengths of optical waves are much larger than the atomic dimensions. Therefore, a local classical model of the permittivity, which neglects the dependence on \mathbf{q} in Eq. (1.5), gives a very reliable description that agrees with experimental measurements. This local approximation consists in assuming $\varepsilon(\mathbf{r}, \mathbf{r}', \omega) = \varepsilon(\mathbf{r}, \omega) \delta(\mathbf{r} - \mathbf{r}')$, which leads to the relation

$$\mathbf{D}(\mathbf{r}, \omega) = \varepsilon_0 \varepsilon(\mathbf{r}, \omega) \mathbf{E}(\mathbf{r}, \omega) = \varepsilon_0 \mathbf{E}(\mathbf{r}, \omega) + \mathbf{P}(\mathbf{r}, \omega). \quad (1.6)$$

In the last relation, we have further introduced the polarization density \mathbf{P} , which gives the dipole moment per unit volume at any point \mathbf{r} . While the displacement field is related to free charges as $\nabla \cdot \mathbf{D} = \rho_f$ [Eq. (1.1a)], the polarization density is determined by the bound charge density ρ_b as $\nabla \cdot \mathbf{P} = -\rho_b$ [69]. According to Eq. (1.6), the electric field is therefore related to all (free and bound) charges as $\nabla \cdot \mathbf{E} = \varepsilon_0^{-1}(\rho_f + \rho_b)$. This means that the optical response of a system can be obtained either via the permittivity $\varepsilon(\mathbf{r}, \omega)$ or via implicit treatment of bound charges, but generally the former approach is the simplest one.

Boundary conditions

A bulk material can typically be described by a single permittivity that is spatially constant. However, nanophotonic systems are composed by more than one material with different optical properties, which implies that Maxwell's equations must be solved with a permittivity that depends on the spatial coordinates. In a local description based on classical electromagnetism, the main approach considered is that the change of the permittivity between materials occurs abruptly in space. According to this method, $\varepsilon(\mathbf{r}, \omega)$ is piecewise constant, which allows solving Eqs. (1.1a)-(1.1d) with a constant permittivity for each material. In this case, Maxwell's equations must also be verified at the interfaces between them. In an interface between two materials indexed by numbers 1 and 2, and defining \mathbf{n}_{12} as the unit vector normal to the interface that points from material 1 to 2, Maxwell's equations are satisfied if the fields fulfill the following boundary conditions [66]:

$$\mathbf{n}_{12} \cdot (\mathbf{D}_2 - \mathbf{D}_1) = \rho_s, \quad (1.7a)$$

$$\mathbf{n}_{12} \cdot (\mathbf{B}_2 - \mathbf{B}_1) = 0, \quad (1.7b)$$

$$\mathbf{n}_{12} \times (\mathbf{E}_2 - \mathbf{E}_1) = 0, \quad (1.7c)$$

$$\mathbf{n}_{12} \times (\mathbf{H}_2 - \mathbf{H}_1) = \mathbf{j}_s, \quad (1.7d)$$

where ρ_s and \mathbf{j}_s are the surface charge density and surface current density associated to free charges in the interface, respectively. In the systems analyzed in this thesis, we do not consider any free charges in the interfaces, and thus $\rho_s = \mathbf{j}_s = 0$. Equations (1.7a)-(1.7d) imply in this case the continuity of the normal component of the fields \mathbf{D} and \mathbf{B} , and of the tangential component of the fields \mathbf{E} and \mathbf{H} . Therefore, for nonmagnetic materials the magnetic fields \mathbf{B} and \mathbf{H} are continuous everywhere, but the electric field \mathbf{E} has strong discontinuities at the interfaces where the permittivity changes abruptly.

Application of Maxwell's equations in anisotropic layered media: transfer-matrix formalism

After presenting Maxwell's equations and the boundary conditions in a single interface, we now illustrate the implementation of these equations for a system composed by layers of different materials separated by planar interfaces. This discussion is of great importance for Chapter 7, because there we analyze light-matter interaction in some planar systems. In this situation, the transfer-matrix formalism is an efficient method to obtain the optical response, as described in detail in Ref. [70]. The transfer-matrix formalism allows calculating the total reflection $r_{\text{total}}^{s(p)}$ and transmission $t_{\text{total}}^{s(p)}$ coefficients of a $s(p)$ -polarized planewave for any layered structure, and it can be also applied to calculate the electric and magnetic fields at any point in space. The s and p polarizations are also sometimes referred to as the transverse electric (TE) and transverse magnetic (TM) polarizations, because a planewave is $s(p)$ -polarized when its electric (magnetic) field is parallel to the interfaces.

We consider a system formed by an arbitrary number N_{lay} of layers of different materials separated by planar interfaces that are parallel to the $x - y$ plane. Each layer $i \in \{1, 2, \dots, N_{\text{lay}}\}$ has a finite thickness L_i and permittivity ε_i . The system also contains two semi-infinite layers, where one corresponds to the material from where the incident light comes (this layer is labelled with $i = 0$) and the other is the substrate (labelled by $i = N_{\text{lay}} + 1$). Further, since in Chapter 7 we analyze cavities filled with an anisotropic material, we include the possibility of anisotropic materials in the transfer-matrix formalism by considering that each layer i has a permittivity tensor of the general diagonal form $\overset{\leftrightarrow}{\varepsilon}_i = \text{diag}(\varepsilon_{i,x}, \varepsilon_{i,y}, \varepsilon_{i,z})$. A sketch of the system is shown in Fig. 1.1a.

To obtain the intensities of the light reflected and transmitted by the layered system, we first focus on a single interface between materials i and $i + 1$. In this case, the Fresnel coefficients give the amplitudes of the reflected and transmitted waves of a wave incident in the $x - z$ plane. These coefficients for s - and p -polarized waves are given by [67]

$$r_{i,i+1}^s = \frac{\sqrt{\varepsilon_{i,y} - \xi^2} - \sqrt{\varepsilon_{i+1,y} - \xi^2}}{\sqrt{\varepsilon_{i,y} - \xi^2} + \sqrt{\varepsilon_{i+1,y} - \xi^2}}, \quad (1.8a)$$

$$r_{i,i+1}^p = \frac{\varepsilon_{i+1,x} \sqrt{\varepsilon_{i,x} \left(1 - \frac{\xi^2}{\varepsilon_{i,z}}\right)} - \varepsilon_{i,x} \sqrt{\varepsilon_{i+1,x} \left(1 - \frac{\xi^2}{\varepsilon_{i+1,z}}\right)}}{\varepsilon_{i+1,x} \sqrt{\varepsilon_{i,x} \left(1 - \frac{\xi^2}{\varepsilon_{i,z}}\right)} + \varepsilon_{i,x} \sqrt{\varepsilon_{i+1,x} \left(1 - \frac{\xi^2}{\varepsilon_{i+1,z}}\right)}}, \quad (1.8b)$$

$$t_{i,i+1}^s = \frac{2\sqrt{\varepsilon_{i,y} - \xi^2}}{\sqrt{\varepsilon_{i,y} - \xi^2} + \sqrt{\varepsilon_{i+1,y} - \xi^2}}, \quad (1.8c)$$

$$t_{i,i+1}^p = \frac{2\varepsilon_{i+1,x} \sqrt{\varepsilon_{i,x} \left(1 - \frac{\xi^2}{\varepsilon_{i,z}}\right)}}{\varepsilon_{i+1,x} \sqrt{\varepsilon_{i,x} \left(1 - \frac{\xi^2}{\varepsilon_{i,z}}\right)} + \varepsilon_{i,x} \sqrt{\varepsilon_{i+1,x} \left(1 - \frac{\xi^2}{\varepsilon_{i+1,z}}\right)}}, \quad (1.8d)$$

where $\xi = k_x/k_0$ is the component of the wavevector k_x parallel to the interfaces and normalized with respect to the wavevector in vacuum $k_0 = \omega/c$, where c is the speed of light in vacuum.

For systems with more than one interface, we search for the total transfer matrix $\mathbf{T}^{s(p)}$ that relates the amplitudes of the electromagnetic field in the incident medium ($i = 0$) and the substrate ($i = N_{\text{lay}} + 1$) for $s(p)$ -polarized light as:

$$\begin{pmatrix} A_{0,+}^{s(p)} \\ A_{0,-}^{s(p)} \end{pmatrix} = \mathbf{T}^{s(p)} \begin{pmatrix} A_{N_{\text{lay}}+1,+}^{s(p)} \\ A_{N_{\text{lay}}+1,-}^{s(p)} \end{pmatrix}.$$
 $A_{i,\pm}^s$ and $A_{i,\pm}^p$ correspond to the amplitude of the electric and magnetic field, respectively (i.e. the amplitude of the field parallel to the interface for each polarization), evaluated in the layer $i \in \{0, N_{\text{lay}} + 1\}$ at the position of their corresponding single interface. The second subindex indicates the direction of propagation. The symbol $+$ corresponds to the direction of the incoming planewave (and thus also to the direction of the transmitted light) and,

similarly, the subindex $-$ corresponds to the direction of the reflected light. Further, $A_{N_{\text{lay}}+1,-}^{s(p)} = 0$ because in the substrate the electromagnetic field only propagates in the direction of the transmission. $\mathbf{T}^{s(p)}$ is given by the expression [70]

$$\mathbf{T}^{s(p)} = \mathbf{M}_{0,1}^{s(p)} \mathbf{Q}_1^{s(p)} \mathbf{M}_{1,2}^{s(p)} \mathbf{Q}_2^{s(p)} \mathbf{M}_{2,3}^{s(p)} \dots \mathbf{M}_{N_{\text{lay}}-1,N_{\text{lay}}}^{s(p)} \mathbf{Q}_{N_{\text{lay}}}^{s(p)} \mathbf{M}_{N_{\text{lay}},N_{\text{lay}}+1}^{s(p)}, \quad (1.9)$$

with

$$\mathbf{M}_{i,i+1}^{s(p)} = \frac{1}{t_{i,i+1}^{s(p)}} \begin{pmatrix} 1 & r_{i,i+1}^{s(p)} \\ r_{i,i+1}^{s(p)} & 1 \end{pmatrix}, \quad (1.10a)$$

$$\mathbf{Q}_i^s = \begin{pmatrix} e^{-i\frac{\omega}{c}d_i\sqrt{\varepsilon_{i,y}-\xi^2}} & 0 \\ 0 & e^{i\frac{\omega}{c}d_i\sqrt{\varepsilon_{i,y}-\xi^2}} \end{pmatrix}, \quad (1.10b)$$

$$\mathbf{Q}_i^p = \begin{pmatrix} e^{-i\frac{\omega}{c}d_i\sqrt{\varepsilon_{i,x}\left(1-\frac{\xi^2}{\varepsilon_{i,z}}\right)}} & 0 \\ 0 & e^{i\frac{\omega}{c}d_i\sqrt{\varepsilon_{i,x}\left(1-\frac{\xi^2}{\varepsilon_{i,z}}\right)}} \end{pmatrix}. \quad (1.10c)$$

The matrix $\mathbf{M}_{i,i+1}^{s(p)}$ relates the amplitudes $A_{i,+}^{s(p)}$ and $A_{i+1,+}^{s(p)}$ of the electromagnetic fields propagating both in the $+$ and $-$ directions and evaluated at both sides of the interface between layers i and $i+1$: $\begin{pmatrix} A_{i,+}^{s(p)} \\ A_{i,-}^{s(p)} \end{pmatrix} = \mathbf{M}_{i,i+1}^{s(p)} \begin{pmatrix} A_{i+1,+}^{s(p)} \\ A_{i+1,-}^{s(p)} \end{pmatrix}$. $\mathbf{Q}_i^{s(p)}$ describes the propagation of light through the layer i .

Once the total matrix $\mathbf{T}^{s(p)} = \begin{pmatrix} T_{11}^{s(p)} & T_{12}^{s(p)} \\ T_{21}^{s(p)} & T_{22}^{s(p)} \end{pmatrix}$ is obtained, its matrix elements are used to calculate the total transmission and reflection coefficients of the system as $t_{\text{total}}^{s(p)} = \frac{A_{N_{\text{lay}}+1,+}^{s(p)}}{A_{0,+}^{s(p)}} = \frac{1}{T_{11}^{s(p)}}$ and $r_{\text{total}}^{s(p)} = \frac{A_{0,-}^{s(p)}}{A_{0,+}^{s(p)}} = \frac{T_{21}^{s(p)}}{T_{11}^{s(p)}}$. With these coefficients, we can finally obtain, for instance, the reflectivity spectra $\mathcal{R}^{s(p)}$ of any planar system, which is defined as the ratio between the intensity of the reflected and incident light. It is obtained as $\mathcal{R}^{s(p)} = |r_{\text{total}}^{s(p)}|^2$ ($r_{\text{total}}^{s(p)}$ corresponds to the ratio of the amplitude of the electromagnetic field).

Further, transfer-matrix simulations also allow obtaining the frequencies of the modes in the system, as given by the poles of the Fresnel coefficients $r_{\text{total}}^{s(p)}$ and $t_{\text{total}}^{s(p)}$. The procedure consists in first obtaining the analytical expressions of these coefficients from the transfer matrix $\mathbf{T}^{s(p)}$, and then solving numerically the complex frequencies for which their denominator vanishes. With this aim, it is necessary to extend the permittivities of all materials to complex values of ω . The real part of the obtained complex eigenfrequency is the mode frequency, while the imaginary part is equal to (minus) half the losses of the mode, and also equal to half the full width at half maximum of the corresponding dip or peak in the reflectivity or transmittance spectra.

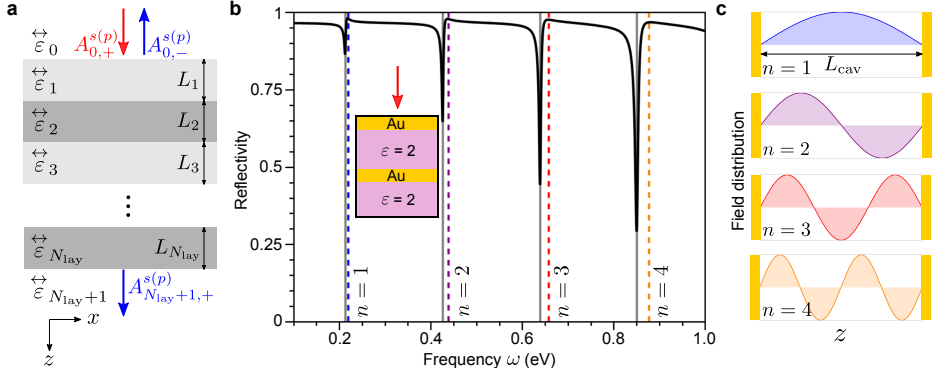


Figure 1.1: Optical response of a layered system: the Fabry-Pérot cavity. a) Sketch of a general layered system with N_{lay} layers. We indicate the coordinates axes and the relevant parameters that need to be introduced in transfer-matrix simulations to obtain the optical response: the thicknesses L_i and permittivity tensors $\overleftrightarrow{\epsilon}_i$ of each layer. The red arrow corresponds to the incident plane wave with amplitude $A_{0,+}^{s(p)}$ for $s(p)$ -polarized light, and the blue arrows to the reflected and transmitted waves with amplitudes $A_{0,-}^{s(p)}$ and $A_{N_{\text{lay}}+1,+}^{s(p)}$ that are obtained with transfer-matrix simulations, respectively. b) Reflectivity spectrum (black line) of a Fabry-Pérot cavity filled with a material of permittivity $\varepsilon = 2$ and thickness $L_{\text{cav}} = 2000$ nm that is placed between two gold mirrors of thickness 20 nm. The reflectivity of the system is obtained with transfer-matrix simulations. Dashed lines indicate the frequencies of the Fabry-Pérot modes in the approximation of perfect mirrors, and the gray lines indicate the mode frequencies according to the poles of the Fresnel coefficients. The inset shows a sketch of the system and the red arrow indicates the normal incidence of light, which implies that the wave can be considered both s - or p -polarized. c) Electric field distribution of the first four Fabry-Pérot modes, calculated with Eq. (1.12) for $n = 1, 2, 3$ and 4. Each mode is evaluated at the frequency indicated in panel (b) by the dashed line of the same color. The yellow slabs indicate the mirrors of the cavity.

To illustrate how the optical response of a planar system is obtained with transfer-matrix simulations, we now choose Fabry-Pérot cavities as a typical example, which we also analyze in detail in Chapters 6 and 7. These cavities are formed by two planar parallel mirrors separated by a distance L_{cav} (i.e., L_{cav} is the thickness of the cavity between the mirrors). Before presenting the results according to the rigorous transfer-matrix simulations, we describe briefly the main principles behind its optical response. For a cavity filled with a material of permittivity ε , the wavevector of light inside the cavity satisfies the dispersion relation $k = \sqrt{|\mathbf{k}_{\parallel}|^2 + k_z^2} = \frac{\omega}{c} \sqrt{\varepsilon}$, where $\mathbf{k}_{\parallel} = (k_x, k_y)$ is the component of the wavevector parallel to the interfaces. Further, mirrors establish the boundary conditions to the modes; under the assumption of perfect mirrors (i.e. considering that the mirrors have an infinite negative permittivity, $\varepsilon(\omega) = -\infty$), the component of the electric field parallel to the interfaces \mathbf{E}_{\parallel} must vanish in the mirror planes according to Eq. (1.7). Consequently, a solution of Maxwell's equation can only exist under the condition

$$k_z L_{\text{cav}} = n\pi, \quad (1.11)$$

for any integer n . The frequencies ω that satisfy Eq. (1.11) for a given parallel wavevector \mathbf{k}_{\parallel} are the resonant frequencies of the Fabry-Pérot cavity. The parallel component of the electric field associated to each mode, determined by the indexes n and \mathbf{k}_{\parallel} , has a standing wave-like pattern of the form

$$\mathbf{E}_{\parallel}(\mathbf{r}) = \mathbf{E}_{\parallel 0} \sin\left(\frac{n\pi z}{L_{\text{cav}}}\right) e^{i\mathbf{k}_{\parallel} \cdot \mathbf{r}_{\parallel}}, \quad (1.12)$$

where $\mathbf{E}_{\parallel 0}$ is the maximum amplitude of the field component.

We next describe this system rigorously using transfer-matrix simulations, for a specific cavity of thickness $L_{\text{cav}} = 2000$ nm, filled with a material of permittivity $\varepsilon = 2$ and placed over a substrate of the same permittivity. Each mirror is composed by a single layer of gold of thickness 20 nm (the permittivity of gold has been taken from the experimental measurements in Ref. [71]). In Fig. 1.1b, we show the reflectivity spectra of this cavity under normal incidence. At most frequencies, the cavity is highly reflecting, but the spectra contains pronounced dips at certain frequencies. We also indicate in the figure with gray lines the frequencies of the modes of the system, as obtained by calculating the poles of the Fresnel coefficients. The frequency of these modes and of the minima of the reflectivity almost coincide, indicating that an experimental measurement of the reflectivity spectra gives precise information about the modes of the system.

Additionally, the frequencies of the Fabry-Pérot modes given by the approximate analytical Eq. (1.11) are indicated by dashed lines in Fig. 1.1b, together with their corresponding electric field distribution given by the simplified Eq. (1.12) in Fig. 1.1c, which indicates that the field of the n^{th} mode contains $n - 1$ nodes. The approximate frequencies are close to the mode frequencies obtained by the transfer-matrix simulations. However, there is a difference between the two because the gold mirrors of the cavity are not perfect (i.e. the mirrors do not have an infinite permittivity and the reflection coefficient is not identical to one) and the corresponding finite value of the metal permittivity shifts the resonant frequencies, an effect not taken into account in Eq. (1.11). Therefore, although the approximate Eq. (1.11) is useful to determine resonances of Fabry-Pérot cavities, the transfer-matrix calculations describe the system more rigorously.

1.1.2 Lagrangian and Hamiltonian formulation of electromagnetic fields

Maxwell's equations describe completely the optical response of nanophotonic systems according to classical electrodynamics. A reformulation of this classical theory is based on the principle of least action and is usually written in terms of a classical Lagrangian or Hamiltonian, as summarized in this section. This approach is considerably less used than Maxwell's equations to obtain the response of a given system, but it is a necessary step to derive a quantized model of light-matter interaction.

To write the classical electromagnetic Lagrangian (which needs to be equivalent

to Maxwell's equations), we first determine the dynamical variables. In this approach, the system is considered to be formed by point charges, where each of them has charge Q_i and is placed at the position \mathbf{r}_i . All these individual charges lead to free charge and current densities following

$$\rho_f(\mathbf{r}) = \sum_i Q_i \delta(\mathbf{r} - \mathbf{r}_i), \quad (1.13a)$$

$$\mathbf{j}_f(\mathbf{r}) = \sum_i Q_i \dot{\mathbf{r}}_i \delta(\mathbf{r} - \mathbf{r}_i), \quad (1.13b)$$

where the dot \cdot denotes the time derivative. Although in the formalism of Maxwell's equations (Sec. 1.1.1) we separated the matter degrees of freedom into free charges [included in the density ρ_f in Eq. (1.1a)] and bound charges (included in ρ_b and determined by the relative permittivity ε and polarization density \mathbf{P}), in this section we consider the materials as a collection of free charges [described within the densities of Eq. (1.13)] over a vacuum background with $\varepsilon(\mathbf{r}, \omega) = 1$.

We now analyze the dynamical variables with which the electromagnetic degrees of freedom are characterized within the classical Lagrangian and Hamiltonian formalisms. With this aim, we start by considering the scalar potential V and the vector potential \mathbf{A} , which are defined so that the electric and magnetic fields satisfy the expressions

$$\mathbf{E} = -\nabla V - \frac{\partial \mathbf{A}}{\partial t}, \quad (1.14a)$$

$$\mathbf{B} = \nabla \times \mathbf{A}. \quad (1.14b)$$

With these definitions, Maxwell's equations (1.1b) and (1.1c) are immediately fulfilled for any V and \mathbf{A} due to the vector identities

$$\nabla \cdot (\nabla \times \mathbf{A}) = 0 \Rightarrow \nabla \cdot \mathbf{B} = 0, \quad (1.15a)$$

$$\nabla \times \left(-\nabla V - \frac{\partial \mathbf{A}}{\partial t} \right) = -\frac{\partial \nabla \times \mathbf{A}}{\partial t} \Rightarrow \nabla \times \mathbf{E} = -\frac{\partial \mathbf{B}}{\partial t}. \quad (1.15b)$$

Further, these potentials are not uniquely defined, because a transformation with an arbitrary function $\mathcal{G}(\mathbf{r}, t)$ of the form

$$V \rightarrow V - \frac{\partial \mathcal{G}}{\partial t}, \quad (1.16a)$$

$$\mathbf{A} \rightarrow \mathbf{A} + \nabla \mathcal{G}, \quad (1.16b)$$

gives the same electric and magnetic field as defined by Eq. (1.14). The exact function \mathcal{G} must be chosen before writing the Lagrangian in terms of the potentials, taking into account that any particular choice of \mathcal{G} gives a different gauge condition. We consider here the Coulomb gauge, according to which the vector potential satisfies the condition $\nabla \cdot \mathbf{A} = 0$. With this choice, the free charge density $\rho_f(\mathbf{r})$ is solely related to the scalar potential, as indicated by the first Maxwell's equation

[Eqs. (1.1a) and (1.14a)] as

$$\nabla \cdot (\varepsilon_0 \mathbf{E}) = \rho_f \Rightarrow \nabla^2 V = -\frac{\rho_f}{\varepsilon_0} \Rightarrow V(\mathbf{r}) = \frac{1}{4\pi\varepsilon_0} \int \frac{\rho_f(\mathbf{r}')}{|\mathbf{r} - \mathbf{r}'|} d\mathbf{r}' = \frac{1}{4\pi\varepsilon_0} \sum_i \frac{Q_i}{|\mathbf{r} - \mathbf{r}_i|}. \quad (1.17)$$

This equation shows that the positions \mathbf{r}_i of all charges fully determine the scalar potential $V(\mathbf{r})$. Therefore, $V(\mathbf{r})$ is a redundant variable and only \mathbf{A} and all \mathbf{r}_i are necessary to describe completely the dynamics of the electromagnetic fields. The resulting Lagrangian, as a function of the variables \mathbf{A} and \mathbf{r}_i and of their velocities, has the form [72, 73]

$$\mathcal{L}_{\text{Cou}} = \sum_i \frac{1}{2} m_i \dot{\mathbf{r}}_i^2 - \sum_{j>i} \sum_i \frac{Q_i Q_j}{4\pi\varepsilon_0 |\mathbf{r}_i - \mathbf{r}_j|} + \int \left[\frac{\varepsilon_0}{2} (|\dot{\mathbf{A}}|^2 - c^2 |\nabla \times \mathbf{A}|^2) + \mathbf{j}_f \cdot \mathbf{A} \right] d\mathbf{r}. \quad (1.18)$$

To prove that the Lagrangian given by Eq. (1.18) does indeed describe classical electrodynamics, we now derive the Euler-Lagrange equations. The equation corresponding to each charge is

$$\begin{aligned} \frac{d}{dt} \frac{\partial \mathcal{L}_{\text{Cou}}}{\partial \dot{\mathbf{r}}_i} - \frac{\partial \mathcal{L}_{\text{Cou}}}{\partial \mathbf{r}_i} &= 0 \\ \Rightarrow m_i \ddot{\mathbf{r}}_i &= Q_i \left[\sum_{j \neq i} \frac{Q_j (\mathbf{r}_i - \mathbf{r}_j)}{4\pi\varepsilon_0 |\mathbf{r}_i - \mathbf{r}_j|^3} - \frac{\partial \mathbf{A}(\mathbf{r}_i, t)}{\partial t} \right] + Q_i \dot{\mathbf{r}}_i \nabla \times (\nabla \times \mathbf{A}(\mathbf{r}_i, t)) \\ \Rightarrow m_i \ddot{\mathbf{r}}_i &= Q_i [\mathbf{E}(\mathbf{r}_i, t) + \dot{\mathbf{r}}_i \times \mathbf{B}(\mathbf{r}_i, t)], \end{aligned} \quad (1.19)$$

which is the same as Newton's equation of motion under the Lorentz force. Further, the equation related to the vector potential reads

$$\frac{d}{dt} \frac{\partial \mathcal{L}_{\text{Cou}}}{\partial \dot{\mathbf{A}}} - \frac{\partial \mathcal{L}_{\text{Cou}}}{\partial \mathbf{A}} = \nabla^2 \mathbf{A} - \frac{1}{c^2} \frac{\partial^2 \mathbf{A}}{\partial t^2} + \mu_0 \mathbf{j}_f = 0, \quad (1.20)$$

which is equivalent to Eq. (1.1d) written in terms of the vector potential. Therefore, the Lagrangian of Eq. (1.18) describes the same physics as classical electrodynamics described by the four Maxwell's equations and the Lorentz force.

Once the electromagnetic Lagrangian \mathcal{L}_{Cou} has been justified, it can be used to derive the classical Hamiltonian of light-matter interaction. To write the Hamiltonian of the electromagnetic fields, the canonical momenta of the charged particles $\mathbf{p}_{\text{Cou},i}$ and of the electromagnetic fields $\mathbf{\Pi}_{\text{Cou}}(\mathbf{r})$ are needed, which are calculated from the Lagrangian as

$$\mathbf{p}_{\text{Cou},i} = \frac{\partial \mathcal{L}_{\text{Cou}}}{\partial \dot{\mathbf{r}}_i} = m_i \dot{\mathbf{r}}_i + Q_i \mathbf{A}(\mathbf{r}_i), \quad (1.21a)$$

$$\mathbf{\Pi}_{\text{Cou}}(\mathbf{r}) = \frac{\partial \mathcal{L}_{\text{Cou}}}{\partial \dot{\mathbf{A}}(\mathbf{r})} = \varepsilon_0 \dot{\mathbf{A}}(\mathbf{r}). \quad (1.21b)$$

The Hamiltonian in the Coulomb gauge is obtained as $\mathcal{H}_{\text{Cou}} = \sum_i \mathbf{p}_{\text{Cou},i} \cdot \dot{\mathbf{r}}_i + \int \mathbf{\Pi}_{\text{Cou}}(\mathbf{r}) \cdot \dot{\mathbf{A}}(\mathbf{r}) d\mathbf{r} - \mathcal{L}_{\text{Cou}}$, which gives

$$\begin{aligned}
 \mathcal{H}_{\text{Cou}} &= \int \left[\frac{|\mathbf{\Pi}_{\text{Cou}}|^2}{2\varepsilon_0} + \frac{\varepsilon_0 c^2}{2} |\nabla \times \mathbf{A}|^2 \right] d\mathbf{r} + \sum_{j>i} \sum_i \frac{Q_i Q_j}{4\pi\varepsilon_0 |\mathbf{r}_i - \mathbf{r}_j|} \\
 &\quad + \sum_i \frac{[\mathbf{p}_{\text{Cou},i} - Q_i \mathbf{A}(\mathbf{r}_i)]^2}{2m_i} \\
 &= \underbrace{\int \left[\frac{|\mathbf{\Pi}_{\text{Cou}}|^2}{2\varepsilon_0} + \frac{\varepsilon_0 c^2}{2} |\nabla \times \mathbf{A}|^2 \right] d\mathbf{r}}_{\mathcal{H}_{\text{Cou}}^{\text{EM}}} + \underbrace{\sum_i \frac{|\mathbf{p}_{\text{Cou},i}|^2}{2m_i} + \sum_{j>i} \sum_i \frac{Q_i Q_j}{4\pi\varepsilon_0 |\mathbf{r}_i - \mathbf{r}_j|}}_{\mathcal{H}_{\text{Cou}}^{\text{mat}}} \\
 &\quad + \underbrace{\sum_i \frac{-Q_i \mathbf{p}_{\text{Cou},i} \cdot \mathbf{A}(\mathbf{r}_i)}{m_i}}_{\mathcal{H}_{\text{Cou}}^{\text{int}}} + \underbrace{\sum_i \frac{Q_i^2 \mathbf{A}(\mathbf{r}_i)^2}{2m_i}}_{\mathcal{H}_{\text{Cou}}^{\text{dia}}}. \tag{1.22}
 \end{aligned}$$

Interestingly, we can divide the Hamiltonian into four contributions. The first two terms, $\mathcal{H}_{\text{Cou}}^{\text{EM}}$ and $\mathcal{H}_{\text{Cou}}^{\text{mat}}$, correspond to the energy associated to the electromagnetic fields and to the charged particles independently. The standard interaction between light and matter is expressed by the term $\mathcal{H}_{\text{Cou}}^{\text{int}}$. Last, $\mathcal{H}_{\text{Cou}}^{\text{dia}}$ is the so-called diamagnetic term, and corresponds to an additional energy of the electromagnetic field proportional to \mathbf{A}^2 and that depends on the magnitudes of all individual charges Q_i . This term is specially important in the description of systems with very strong light-matter interaction, as discussed thoroughly in this thesis. Further, the Hamiltonian of Eq. (1.22) connects classical electrodynamics and quantum optics, as it can be directly quantized following the canonical quantization procedure. We analyze in Chapter 6 in detail how quantum Hamiltonians can be obtained from Eq. (1.22) for different systems and their connection with classical models of light-matter interaction.

1.2 Optical excitations in matter

The permittivity $\varepsilon(\mathbf{r}, \omega)$ introduced in Sec. 1.1.1 results from all excitations within a given bulk material. In this section, we derive simple analytical expressions of the permittivity of metals, ensembles of molecules and polar materials, which are the main materials that we analyze in this thesis. These models are based on classical descriptions of the displacement of electrons or ions in these materials. Further, we discuss the resonant modes of metals induced by the collective oscillations of the free electrons, called plasmons, in different configurations such as in bulk, surfaces and spherical nanoparticles.

1.2.1 Plasmons

Drude model of metals

Metallic systems are widely used to localize light in the nanoscale, and different descriptions of the electronic structure have been studied in order to calculate the permittivity of metals. We analyze in Chapter 2 rigorous approaches, and in this chapter we focus on the simplest description of the optical response of a metal. This description is based on the Drude model, which assumes that the electronic structure of the material is the same as that of a classical homogeneous electron gas.

When an electric field $\mathbf{E}(t) = \mathbf{E}_0 e^{-i\omega t}$ oscillating at frequency ω is applied to the metal, the position \mathbf{r} of each electron of effective mass m_{eff} and charge e is dictated by the equation of motion

$$m_{\text{eff}}\ddot{\mathbf{r}} + m_{\text{eff}}\gamma_p\dot{\mathbf{r}} = e\mathbf{E}_0 e^{-i\omega t}. \quad (1.23)$$

This equation considers the free propagation of the electron driven by the electric field (which induces an external force $\mathbf{F}_{\text{ext}}(t) = e\mathbf{E}_0 e^{-i\omega t}$). Additionally, damping phenomena related to collisions with the nuclei and other processes are phenomenologically included in the decay rate γ_p . Under the ansatz $\mathbf{r}(t) = \mathbf{r}_0 e^{-i\omega t}$, Eq. (1.23) can be solved to obtain the displacement of the electrons induced by the electric field as

$$\mathbf{r}_0(\omega) = -\frac{e}{m_{\text{eff}}\omega(\omega + i\gamma_p)}\mathbf{E}_0(\omega). \quad (1.24)$$

The displacement \mathbf{r}_0 of each electron induces a dipole moment $\mathbf{d} = e\mathbf{r}_0$, and the collective displacement of all electrons thus results in a polarization density $\mathbf{P}(\omega) = \frac{\mathbf{d}}{\mathcal{V}} = \rho_e e\mathbf{r}_0(\omega)$, where ρ_e is the electron density per unit volume \mathcal{V} . By inserting the resulting expression of $\mathbf{P}(\omega)$ into Eq. (1.6), we obtain the permittivity of the Drude model

$$\varepsilon^{\text{Dr}}(\omega) = 1 - \frac{\omega_p^2}{\omega(\omega + i\gamma_p)}, \quad (1.25)$$

with the plasma frequency $\omega_p = \sqrt{\frac{\rho_e e^2}{m_{\text{eff}}\varepsilon_0}}$.

Equation (1.25) has been derived under the assumption that all electrons of the metal are free, and it captures many features of the metallic optical response at low energies [74]. However, interband transitions of electrons bound to nuclei also contribute to the polarization density, and this feature has not been taken into account in the previous derivation. The contribution of these electrons is important at high energies, and corrections to Eq. (1.25) must be done to appropriately describe the permittivity of metals. In this context, the simplest way to obtain better agreement between theory and experimental measurements is to introduce an offset ε_∞ in Eq. (1.25).

Bulk plasmons and bulk plasmon polaritons

The Drude permittivity contains the necessary information to describe the excitations of metallic systems, the simplest configuration being a bulk metal

that extends to infinity. In this case, a longitudinal excitation called bulk plasmon can be excited, which consists in a collective oscillation of the free electrons inside the metal. The properties of this resonance can be obtained directly from Maxwell's equations. In the absence of external charges, the displacement vector follows the equation $\nabla \cdot \mathbf{D}(\omega) = \nabla \cdot [\varepsilon_0 \varepsilon(\omega) \mathbf{E}(\omega)] = 0$ [from Eq. (1.1a)]. This implies that free longitudinal waves (which satisfy $\nabla \cdot \mathbf{E}(\omega) \neq 0$) can only exist in a homogeneous material when the permittivity vanishes. For a metal with permittivity following the Drude model expression of Eq. (1.25) (Drude metal in the following) and neglecting losses ($\gamma_p = 0$), the bulk plasmons occur at frequency $\omega = \omega_p$.

Further, we can also search for transverse electromagnetic modes inside the bulk metal. First, we note that Maxwell's equations admit solutions of the form of propagating transverse waves. By trying solutions of the form $\mathbf{E}(\mathbf{r}, t) = \mathbf{E}_0 e^{i\mathbf{k} \cdot \mathbf{r}} e^{-i\omega t}$ and $\mathbf{B}(\mathbf{r}, t) = \mathbf{B}_0 e^{i\mathbf{k} \cdot \mathbf{r}} e^{-i\omega t}$ into Eq. (1.1) (considering a single bulk material with permittivity $\varepsilon(\omega)$ and no free charges, i.e. $\rho_f = \mathbf{j}_f = 0$), we observe that a non-trivial solution (with $\mathbf{E}_0 \neq 0$ and $\mathbf{B}_0 \neq 0$) only exists if the magnitude of the wavevector $k = |\mathbf{k}|$ and the frequency ω satisfy the dispersion relation

$$\omega = \frac{ck}{\sqrt{\varepsilon(\omega)}}. \quad (1.26)$$

By introducing the Drude permittivity [Eq. (1.25)] into Eq. (1.26), we obtain the condition

$$\omega = \sqrt{\omega_p^2 + c^2 k^2}. \quad (1.27)$$

Propagating modes inside a Drude metal can therefore exist only at frequencies $\omega \geq \omega_p$, i.e. when the Drude permittivity is positive. Transverse modes following the dispersion of Eq. (1.27) are called bulk plasmon polaritons and are a result of the hybridization of light and electronic oscillations. To show that these modes have features of both photons and plasmons, we analyze two opposite limits of Eq. (1.27). On the one hand, at the $k \rightarrow 0$ limit, the transverse mode transforms into a mode that is degenerate with the longitudinal oscillations of electrons at frequency $\omega = \omega_p$. Otherwise, at the opposite $k \rightarrow \infty$ limit, the mode is equivalent to light in vacuum with dispersion $\omega = ck$, without influence of the metal electrons.

Surface plasmons and surface plasmon polaritons

Another type of plasmonic waves called surface plasmon polariton (SPP) appears when a semi-infinite metal is in contact with a semi-infinite insulator (i.e. a dielectric material with $\varepsilon > 0$). These excitations propagate along the metal-insulator interface (which we set at the plane $z = 0$) in the x direction, and have an evanescent tail in the z direction. The electric and magnetic fields at each medium $j \in \{1, 2\}$ therefore have a spatial dependence of the form

$$\mathbf{E}_j(\mathbf{r}) = \mathbf{E}_j e^{ik_{\parallel} x} e^{-k_{zj}|z|}, \quad (1.28a)$$

$$\mathbf{B}_j(\mathbf{r}) = \mathbf{B}_j e^{ik_{\parallel} x} e^{-k_{zj}|z|}. \quad (1.28b)$$

Due to the continuity of the parallel components of the electric and magnetic fields along the interface, the parallel component of the wavevector k_{\parallel} is equal for both materials, while k_{zj} changes as

$$k_{zj} = \sqrt{\frac{\omega^2}{c^2} \varepsilon_j - k_{\parallel}^2}. \quad (1.29)$$

A solution with the form given by Eq. (1.28) only exists if the boundary conditions from Eq. (1.7) are fulfilled. At any given frequency ω , this only occurs for wavevectors that satisfy [67, 75]

$$k_{\parallel}(\omega) = \frac{\omega}{c} \sqrt{\frac{\varepsilon_1 \varepsilon_2}{\varepsilon_1 + \varepsilon_2}}. \quad (1.30)$$

A well-known analytical dispersion relation of SPPs can be obtained by considering that the metal has a Drude permittivity $\varepsilon_1 = \varepsilon^{\text{Dr}}(\omega)$ [Eq. (1.25)] and the insulator is vacuum ($\varepsilon_2 = 1$), leading to the expression

$$\omega_{\text{SPP}}^2 = \omega_{\text{p}}^2 + c^2 k_{\parallel}^2 - \sqrt{\omega_{\text{p}}^4/4 + c^4 k_{\parallel}^4}. \quad (1.31)$$

This dispersion relation is plotted in Fig. 1.2a, and it reveals the hybrid nature of the SPPs, which are a mixture of photons and of the electronic oscillations. This hybrid nature can be appreciated from the behavior of the dispersion relation in limiting cases. While in the $k_{\parallel} \rightarrow 0$ limit SPPs resemble pure photons as Eq. (1.31) approaches the light line ($\omega = ck_{\parallel}$, indicated by the gray line in Fig. 1.2a), on the opposite limit of large wavevectors the SPP frequencies approach the value $\omega_{\text{p}}/\sqrt{2}$ asymptotically (this frequency is plotted by the black line), and thus SPPs acquire an electronic character. The frequency $\omega_{\text{p}}/\sqrt{2}$, which is entirely determined by the electronic structure of the metal, is called the surface plasmon frequency ω_{SP} of a metal. Particularly at frequencies ω close to ω_{SP} , high localizations of the electric field can be obtained in the interface. This feature can be observed in Eqs. (1.29) and (1.30), because the z component of the wavevector k_z can be relatively large in both materials, implying that at these conditions the electric field of the SPP already decays strongly at a small distance from the interface (see Fig. 1.2b for a sketch).

The dispersion relation of SPPs gives additional information about how to excite them, because the frequency ω and parallel wavevector k_{\parallel} must be conserved. As we observe in Fig. 1.2a, the SPP dispersion relation never crosses the light line, and therefore it is impossible to excite SPPs with a conventional beam propagating in vacuum. In order to overcome the mismatch of k_{\parallel} between light and SPPs, several strategies have been proposed along the last decades. On the one hand, glass prisms can be used, either creating a thin air gap between the prism and the metallic surface (Otto configuration [76]) or depositing a thin metallic layer over the prism (Kretschmann configuration [77]). Since the permittivity is larger in glasses ($\varepsilon > 1$) than in vacuum, the light line inside the prisms changes to

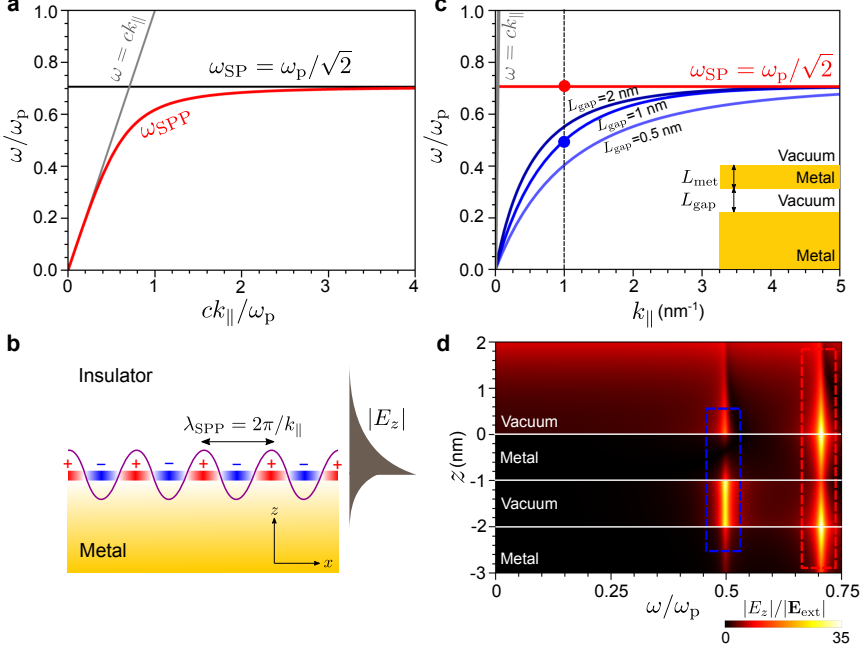


Figure 1.2: Analysis of surface plasmon polaritons (SPPs). a) Dispersion relation of SPPs (red line) in a planar interface between vacuum and a semi-infinite layer of a Drude metal. The light line in vacuum $\omega = ck_{\parallel}$ and the surface plasmon frequency ω_{SP} correspond to the gray and black lines, respectively. b) Sketch of the charge (red and blue regions) and electric field E_z distribution (right) of a SPP. The SPP corresponds to a wave oscillating with wavelength $\lambda_{\text{SPP}} = 2\pi/k_{\parallel}$. We also indicate the coordinate axes that we use in this section and in all panels of this figure. c) Dispersion relation of the two SPPs (red and blue lines) in the system indicated by the inset under the quasistatic approximation. A metallic layer of thickness $L_{\text{met}} = 1$ nm is placed over a substrate of the same metal, with both separated by a gap of thickness $L_{\text{gap}} = 0.5$ nm, 1 nm or 2 nm for each blue line. The metallic layers are formed by a Drude metal and are placed on a vacuum background. The light line in vacuum is indicated by a gray line. d) Spatial distribution of the electric field enhancement $|E_z|/|\mathbf{E}_{\text{ext}}|$ along the z direction perpendicular to all interfaces and as a function of the normalized excitation frequency ω/ω_p , for the same system of panel (c). The gap thickness is $L_{\text{gap}} = 1$ nm. The system is excited by an external potential given by Eq. (1.33) with $k_{\parallel} = 1 \text{ nm}^{-1}$. The electric fields corresponding to the two plasmonic modes are highlighted by the blue and red dashed rectangles, at frequencies indicated in the dispersion of panel (c) by dots. The permittivity of the metals is described by the Drude model with a damping rate $\gamma_p = \omega_p/100$.

$\omega = ck/\sqrt{\epsilon}$, which can match the values of ω and k_{\parallel} needed to excite SPPs in the metal-vacuum interfaces of the mentioned configurations. Further, gratings can be also used [78, 79], because due to the periodicity of these systems they can provide multiples of their reciprocal lattice vectors to reach the necessary value of k_{\parallel} . Last, sharp tips (or other small nanoparticles) can also excite SPPs when placed close to a metal [80–82], because the electric field confined in the small region between the metallic layer and the tip can access the large values of k_{\parallel} of the SPP dispersion relation.

The analysis of SPPs up to this point has been done by considering the full solution of Maxwell's equations. In this approach, the speed of light c is considered to be finite, which causes the hybridization between light and plasmons in the regime $k_{\parallel} \lesssim \omega/c$. Due to the effects of the finite value of c , the excitation following the dispersion relation of Eq. (1.31) is considered to be the retarded SPP. On the other hand, we are sometimes interested in analyzing plasmonic modes with wavelengths comparable to the atomic scale and thus when the relevant wavevectors satisfy the condition $k_{\parallel} \gg \omega/c$. In this non-retarded regime, retardation does not affect the optical response of the system and the $c \rightarrow \infty$ limit can be considered, which simplifies the calculations of the dispersion relation and other properties of the SPPs.

A key quantity that is used to study the optical response of surfaces in the non-retarded regime is the so-called surface response function, defined as [33, 83]

$$\mathbf{g}(\mathbf{k}_{\parallel}, \omega) = \int \rho_{\text{ind}}(z, \mathbf{k}_{\parallel}, \omega) e^{k_{\parallel} z} dz, \quad (1.32)$$

where $\rho_{\text{ind}}(\mathbf{r}, \mathbf{k}_{\parallel}, \omega)$ is the electronic density induced by an external potential of the form

$$V_{\text{ext}}(\mathbf{r}, \mathbf{k}_{\parallel}, \omega) = -\frac{\pi Q^2}{\epsilon_0 k_{\parallel}} e^{k_{\parallel} z} e^{i\mathbf{k}_{\parallel} \cdot \mathbf{r}_{\parallel}} e^{-i\omega t}. \quad (1.33)$$

$V_{\text{ext}}(\mathbf{r}, \mathbf{k}_{\parallel}, \omega)$ corresponds to the two-dimensional (2D) Fourier transform of the Coulomb potential induced by a point charge placed in front of the system at infinite distance, with the charge oscillating in time as $Qe^{-i\omega t}$. In the non-retarded regime, the quasistatic approximation can be used, where the vector potential \mathbf{A} does not vary in timeⁱⁱ. Hence, Eq. (1.14a) indicates that the electric field is fully determined by the scalar potential as $\mathbf{E} = -\nabla V$. Importantly, the surface response function contains information of the electronic excitations of the system, as its imaginary part $\text{Im}[\mathbf{g}(\mathbf{k}_{\parallel}, \omega)]$, which is called the surface loss function, is proportional to the power absorption due to the induced electronic excitations [83]. As a consequence, the dispersion relation of the modes is given by the poles of $\mathbf{g}(\mathbf{k}_{\parallel}, \omega)$.

We illustrate next the usefulness of the classical non-retarded approximation to study plasmonic modes with very small wavelength in more complex systems than a single metal-vacuum interface (quantum treatments of non-local optical response are

ⁱⁱ In the $c \rightarrow \infty$ quasistatic limit, $\omega \ll ck$, so that the electromagnetic field oscillating as $e^{-i\omega t}$ varies very slowly on the scale of time determined by c , justifying the $\frac{\partial \mathbf{A}}{\partial t} = 0$ approximation.

analyzed in Chapters 2, 3 and 4). To analyze classical results, we choose a system formed by a semi-infinite Drude metal and a thin layer of the same material and of thickness $L_{\text{met}} = 1$ nm, both placed over a vacuum background ($\varepsilon = 1$). The thin layer and the semi-infinite substrate are separated by a distance L_{gap} of the order of 1 nm forming a nanogap (see inset in Fig. 1.2c). Despite the considered small thicknesses L_{gap} and L_{met} , the system can be modelled classically, with quantum effects only becoming prominent for even smaller gap and metal thicknesses [84]. Due to the dimensions in this system, the plasmonic modes in the nanogap have extremely small wavelengths (of the order of atomic dimensions), which justifies the non-retarded approximation as the condition $k_{\parallel} \gg \omega/c$ is satisfied.

To obtain the surface response function of this system, we first need to determine the potential induced by the external source [given by Eq. (1.33)]. In the absence of free charges, $\nabla \cdot \mathbf{E} = 0$ [Eq. (1.1a)], and from $\mathbf{E} = -\nabla V$, the potential must satisfy the Laplace equation $\nabla^2 V = 0$. To be consistent with the expression of the external potential, we make the following ansatz for the potential in the j^{th} layer,

$$V_j(\mathbf{r}, \mathbf{k}_{\parallel}, \omega) = -\frac{2\pi}{k_{\parallel}} \{V_{j+}(\mathbf{k}_{\parallel}, \omega)e^{k_{\parallel}z} + V_{j-}(\mathbf{k}_{\parallel}, \omega)e^{-k_{\parallel}z}\} e^{i\mathbf{k}_{\parallel} \cdot \mathbf{r}} e^{-i\omega t}, \quad (1.34)$$

which already satisfies the Laplace equation in each layer. Considering that the oscillating point charge that probes the system is placed in the $j = 1$ layer, we directly obtain $V_{1+} = 1$ by comparing Eqs. (1.33) and (1.34). All other coefficients V_{j+} and V_{j-} are obtained applying boundary conditions [Eq. (1.7)] across all interfaces, which impose that both the potential $V(\mathbf{r}, \mathbf{k}_{\parallel}, \omega)$ and the normal component of the displacement vector $D_z(\mathbf{r}, \mathbf{k}_{\parallel}, \omega) = -\varepsilon(\mathbf{r}, \omega) \frac{\partial V(\mathbf{r}, \mathbf{k}_{\parallel}, \omega)}{\partial z}$ must be continuous.

Once the potential is obtained, Poisson's equation $\nabla^2 V = \rho_{\text{ind}}(\mathbf{r})/\varepsilon_0$ gives the density of the bound charges (given by the polarization density as $\rho_{\text{ind}}(\mathbf{r}) = -\nabla \cdot \mathbf{P}$) induced in the interfaces between materials. Last, inserting $\rho_{\text{ind}}(\mathbf{r})$ into Eq. (1.32) leads to the surface response function of the form

$$\begin{aligned} \mathbf{g}(\mathbf{k}_{\parallel}, \omega) &= \frac{\varepsilon(\omega) - 1}{\varepsilon(\omega) + 1} \\ &\times \frac{(e^{2k_{\parallel}L_{\text{met}}} - 1)[(\varepsilon(\omega) - 1)^2 - e^{2k_{\parallel}L_{\text{gap}}}(\varepsilon(\omega) + 1)^2] - 4\varepsilon(\omega)}{(e^{2k_{\parallel}L_{\text{met}}} + e^{2k_{\parallel}L_{\text{gap}}} - 1)(\varepsilon(\omega) - 1)^2 - e^{2k_{\parallel}(L_{\text{met}} + L_{\text{gap}})}(\varepsilon(\omega) + 1)^2}. \end{aligned} \quad (1.35)$$

The surface response function of Eq. (1.35) contains a pole at the frequency where the permittivity of the metal satisfies $\varepsilon(\omega) = -1$, which for a Drude metal occurs at $\omega_{\text{SP}} = \omega_p/\sqrt{2}$ (indicated by the red line in Fig. 1.2c). This solution corresponds to the surface plasmon resonance of the semi-infinite substrate, which is nondispersive in the non-retarded situation. Since this resonant frequency ω_{SP} is the same as that obtained by taking the $k_{\parallel} \rightarrow \infty$ limit in the retarded expression of Eq. (1.31), we have confirmed that the non-retarded calculation leads to same solutions as the fully-retarded Maxwell's equations in the $k_{\parallel} \gg \omega/c$ limit.

Further, due to the presence of the thin layer over the bulk metal, the system has an additional mode at the frequency given by the second pole of the surface response function, i.e. by the solution of the equation

$$(e^{2k_{\parallel}L_{\text{met}}} + e^{2k_{\parallel}L_{\text{gap}}} - 1)(\varepsilon(\omega) - 1)^2 - e^{2k_{\parallel}(L_{\text{met}}+L_{\text{gap}})}(\varepsilon(\omega) + 1)^2 = 0. \quad (1.36)$$

As opposed to the previous surface plasmon, this mode is dispersive also in the non-retarded description. We plot the dispersion relation given by Eq. (1.36) in Fig. 1.2c by blue lines for gap thicknesses $L_{\text{gap}} = 0.5 \text{ nm}$, 1 nm and 2 nm . The results are very sensitive to L_{gap} , resulting in a smaller plasmonic wavelength (larger k_{\parallel}) for fixed ω with decreasing thickness. The obtained plasmonic wavelengths for all L_{gap} are much smaller than the corresponding value for the retarded SPP of a semi-infinite substrate at any frequency (for $\omega < \omega_{\text{SP}}$), as observed by comparing the corresponding dispersion relations of Fig. 1.2c (blue lines) and Fig. 1.2a (red line)ⁱⁱⁱ.

Additional information about the properties of the modes can be extracted by calculating the induced electric field $\mathbf{E} = -\nabla V$. We plot in Fig. 1.2d the spatial distribution of the electric field (normalized to the external field amplitude $|\mathbf{E}_{\text{ext}}|$) induced by the external potential of Eq. (1.33) with a fixed value $k_{\parallel} = 1 \text{ nm}^{-1}$ and as a function of the excitation frequency ω normalized to the plasmon frequency ω_{p} . For most frequencies, the optical response of the system is weak, but strong field enhancements appear at the frequencies of the two plasmonic modes of this system (highlighted by dashed rectangles and indicated by dots in Fig. 1.2c). In particular, for the lower frequency resonance at $\omega \approx 0.50 \omega_{\text{p}}$, the electric field is mostly trapped in the gap between metals. Therefore, systems with very thin layers have modes that confine light in extremely small dimensions.

Localized surface plasmons

The plasmonic resonances that we have considered up to now correspond to waves that propagate either in the bulk metal or in metal-vacuum interfaces of the system. We focus next on the resonances of metallic objects that are finite in the three dimensions. In these systems, the oscillations of electrons are localized in space. Accordingly, resonances in finite metallic nanostructures are called localized surface plasmons (LSPs). Further, the lack of spatial invariance simplifies the excitation of LSPs. For perfectly planar interfaces SPPs cannot be excited with a light beam propagating in vacuum because the dispersion relations of SPPs do not cross the light line, and thus the wavevector k_{\parallel} cannot be conserved. However, k_{\parallel} does not need to be conserved in the excitation of LSPs in finite objects. Thus a light beam can be used (without any glass prism) to excite plasmonic resonances in this case.

For illustration, here we consider the response of the simple case of a small spherical nanoparticle made by a metal with Drude permittivity $\varepsilon^{\text{Dr}}(\omega)$, which can be described with an analytical solution. For nanoparticles of radius R much

ⁱⁱⁱ The scale of the x axis is different in Figs. 1.2a and c, as can be appreciated by the slope of the light line $\omega = ck_{\parallel}$ in both of them.

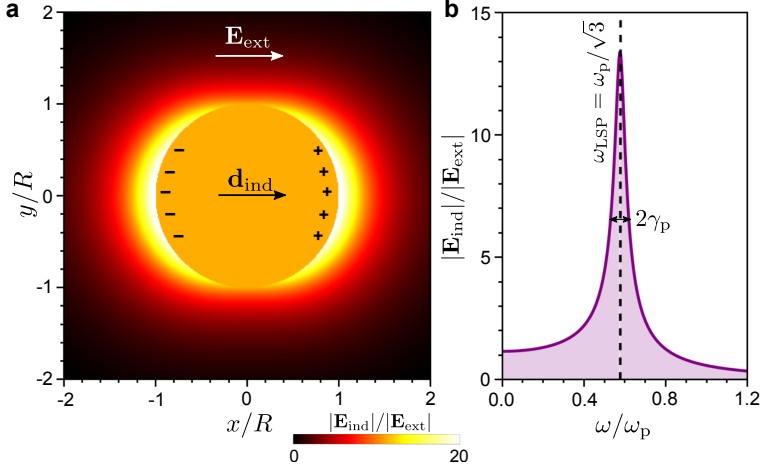


Figure 1.3: Electric field enhancement due to the excitation of LSPs. a) Spatial distribution of the amplitude of the induced electric field $|\mathbf{E}_{\text{ind}}|$, normalized with respect to the amplitude of the external field $|\mathbf{E}_{\text{ext}}|$ for a metallic nanosphere with Drude permittivity. The fields are evaluated at frequency $\omega = \omega_p/\sqrt{3}$, and the permittivity of the metal has a damping parameter of value $\gamma_p = 0.05\omega_p$. The external electric field is polarized along the x direction (indicated by the white arrow). The direction of the dipole induced in the sphere and the induced charges are represented by the black arrow and the black $+$ and $-$ symbols, respectively (in resonance, the induced charges are dephased by $\pi/2$ with respect to the external field \mathbf{E}_{ext}). b) Field enhancement $|\mathbf{E}_{\text{ind}}|/|\mathbf{E}_{\text{ext}}|$ at the point $(x, y) = (1.2R, 0)$ (where the origin is in the center of the sphere), as a function of the normalized excitation frequency ω/ω_p . The black dashed line indicates the resonant frequency of the LSP, $\omega_{\text{LSP}} = \omega_p/\sqrt{3}$.

smaller than the wavelength of the illumination, the quasistatic approximation that neglects retardation effects is valid, because light can be assumed to propagate instantaneously to all points of the nanoparticle. In this context, and since there are no free charges in the system, Maxwell's equation (1.1a) implies the electric field is directly calculated with the scalar potential that is obtained by solving the Laplace equation $\nabla^2 V = 0$ outside and inside the sphere. The potential also needs to satisfy the same boundary conditions discussed in the section of SPPs, i.e. the continuity of the potential and of the normal component of the displacement field across the surface of the nanosphere.

To obtain the response, we first consider that the system is illuminated by a planewave of wavevector \mathbf{k} with spatial distribution $\mathbf{E}_{\text{ext}} e^{i\mathbf{k}\cdot\mathbf{r}} = E_{\text{ext}} e^{i\mathbf{k}\cdot\mathbf{r}} \mathbf{n}_x$, where \mathbf{n}_x is the unit vector in the direction of the x axis. Since the radius R of the sphere is much smaller than the wavelength of the illumination, the phase of the external electric field changes very little inside the system and the illumination can be treated as an uniform electric field \mathbf{E}_{ext} . Consequently, in the non-retarded regime the external potential reads $V_{\text{ext}} = -E_{\text{ext}}x$. We then obtain the total potential $V(\mathbf{r})$ from the solution of the Laplace equation together with the boundary conditions, taking into account that far from the particle the total potential must be equal

to the external contribution, i.e., $V(|\mathbf{r}| \gg R) \approx V_{\text{ext}}$. The potential directly gives the total electric field of the system, $\mathbf{E}(\mathbf{r}) = -\nabla V(\mathbf{r}) = \mathbf{E}_{\text{ext}}(\mathbf{r}) + \mathbf{E}_{\text{ind}}(\mathbf{r})$, where $\mathbf{E}_{\text{ind}}(\mathbf{r})$ is the field induced by the external illumination. This contribution of the electric field reads [60, 85]

$$\mathbf{E}_{\text{ind}}(\mathbf{r}) = \begin{cases} -\frac{\varepsilon^{\text{Dr}}(\omega)-1}{\varepsilon^{\text{Dr}}(\omega)+2}\mathbf{E}_{\text{ext}} & r < R \\ \frac{\varepsilon^{\text{Dr}}(\omega)-1}{\varepsilon^{\text{Dr}}(\omega)+2}\frac{R^3}{r^3}[3(\mathbf{E}_{\text{ext}} \cdot \mathbf{n}_r)\mathbf{n}_r - \mathbf{E}_{\text{ext}}] & r > R, \end{cases} \quad (1.37)$$

where $\mathbf{n}_r = \frac{\mathbf{r}}{|\mathbf{r}|}$ is the unit vector in the radial direction with respect to the center of the sphere.

Interestingly, the electric field of Eq. (1.37) outside the sphere is the same as that created by a dipole at the center of the sphere of dipole moment

$$\mathbf{d}_{\text{ind}} = 4\pi\varepsilon_0 R^3 \frac{\varepsilon^{\text{Dr}}(\omega) - 1}{\varepsilon^{\text{Dr}}(\omega) + 2} \mathbf{E}_{\text{ext}} = 4\pi\varepsilon_0 R^3 \frac{\omega_p^2}{\omega_p^2 - 3\omega(\omega + i\gamma_p)} \mathbf{E}_{\text{ext}}. \quad (1.38)$$

Thus, in many situations where only the electric field outside the sphere is considered, the particle can be replaced by an effective point-like dipole. In the limit of no losses, the induced dipole moment \mathbf{d}_{ind} diverges at frequency $\omega_{\text{LSP}} = \omega_p/\sqrt{3}$, corresponding to the resonant frequency of the LSP in a metallic sphere. We plot in Fig. 1.3a the spatial distribution of the induced electric field [given by Eq. (1.37)] of the system at the resonant frequency ω_{LSP} . The field is mostly enhanced close to the sphere in the x direction (parallel to the external electric field). For the specific metal considered with losses $\gamma_p = 0.05 \omega_p$, the maximum enhancement of the electric field is of about 20. Further, to emphasize the resonant behavior of the system, we show in Fig. 1.3b the field enhancement $|\mathbf{E}_{\text{ind}}|/|\mathbf{E}_{\text{ext}}|$ as a function of the normalized frequency ω/ω_p , evaluated in the point $(x, y) = (1.2R, 0)$ from the center of the sphere. The spectrum is dominated by a sharp peak centered at resonant frequency ω_{LSP} (black dashed line) and of width $2\gamma_p$.

We have focused this discussion on LSPs of spherical particles, but the properties of these excitations depend strongly on the geometry. For example, the resonant frequency can be adjusted by choosing the material and the shape of the structure appropriately [86]. Additionally, larger field enhancements than those analyzed in Fig. 1.3 can also be obtained by engineering the geometry of the system. For instance, by placing two metallic particles close to each other, much larger electric fields can be induced in the gap between the particles compared to the single particle scenario [6, 7].

1.2.2 Vibrational excitations

Molecular vibrations

We consider next a different type of matter excitation that can couple to light, vibrations of molecules at infrared frequencies. In order to understand how these excitations respond to light, the Lorentz oscillator model is typically used. In this

model, the displacement of the ions is evaluated, by considering them as point charges experiencing Coulomb interactions.

The main assumptions of the Lorentz model are that ions are in an equilibrium position, and that they are subjected to a harmonic force $\mathbf{F}_{\text{spr}} = -k_{\text{spr}}\mathbf{r}$ that is linear with respect to the distance $|\mathbf{r}|$ from this equilibrium position, i.e. the force is the same as that exerted by a spring with spring constant k_{spr} according to Hooke's law. A damping force $\mathbf{F}_{\text{damp}} = -m_{\text{eff}}\gamma\dot{\mathbf{r}}$ is also included in the model, where γ is the damping rate and m_{eff} the effective mass of the ions. Last, these particles with charge Q react to an external electric field of amplitude \mathbf{E}_{ext} , which in the Lorentz model is introduced as a time-dependent driving force $\mathbf{F}_{\text{ext}}(t) = Q\mathbf{E}_{\text{ext}}e^{-i\omega t}$. The dynamics of the system under these forces is governed by Newton's law $m_{\text{eff}}\ddot{\mathbf{r}} = \mathbf{F}_{\text{spr}} + \mathbf{F}_{\text{damp}} + \mathbf{F}_{\text{ext}}$, which leads to the equation of motion

$$m_{\text{eff}}\ddot{\mathbf{r}} + m_{\text{eff}}\gamma\dot{\mathbf{r}} + k_{\text{spr}}\mathbf{r} = Q\mathbf{E}_{\text{ext}}e^{-i\omega t}. \quad (1.39)$$

By trying a solution of the form $\mathbf{r}(t) = \mathbf{r}_0e^{-i\omega t}$ in Eq. (1.39), the amplitude of the oscillations for the ions is solved to be

$$\mathbf{r}_0(\omega) = \frac{\frac{Q}{m_{\text{eff}}}}{\frac{k_{\text{spr}}}{m_{\text{eff}}} - (\omega^2 + i\gamma\omega)}\mathbf{E}_{\text{ext}}(\omega). \quad (1.40)$$

When applying the Lorentz model to an ensemble of molecules of density ρ_{mol} , the polarization density $\mathbf{P}(\omega)$ is obtained as $\mathbf{P}(\omega) = \rho_{\text{mol}}Q\mathbf{r}_0(\omega)$. Introducing this polarization density into Eq. (1.6) leads to a permittivity of the form

$$\varepsilon(\omega) = \varepsilon_{\infty} \left(1 + \frac{f}{\omega_{\text{vib}}^2 - \omega^2 - i\omega\gamma} \right), \quad (1.41)$$

where $\omega_{\text{vib}} = \sqrt{\frac{k_{\text{spr}}}{m_{\text{eff}}}}$ is the resonant frequency of the molecular vibrations, and f is an effective oscillator strength. In the simple picture considered in this section, f depends on the charge, effective mass and the density of the molecules as $f = \frac{\rho_{\text{mol}}Q^2}{m_{\text{eff}}\varepsilon_{\infty}}$. However, the rigorous calculation of f for real molecules requires simulations that account for complex interactions between ions. In general, f determines the strength of the optical response at the resonant frequency $\omega \approx \omega_{\text{vib}}$. Last, we note that the term ε_{∞} in Eq. (1.41) is introduced by hand as it does not come directly from the derivation of the Lorentz model. This derivation considers a single vibration that reacts resonantly with light, but molecules exhibit additional resonances at other frequencies that also contribute to the optical response. The high-frequency permittivity ε_{∞} accounts in an effective manner for the mean contribution of all these resonant modes when their resonant frequencies are far from ω_{vib} .

Bulk phonons and bulk phonon polaritons in polar materials

Other materials that support vibrational excitations are polar materials. Their corresponding excitations are phonons, which are collective oscillations of the

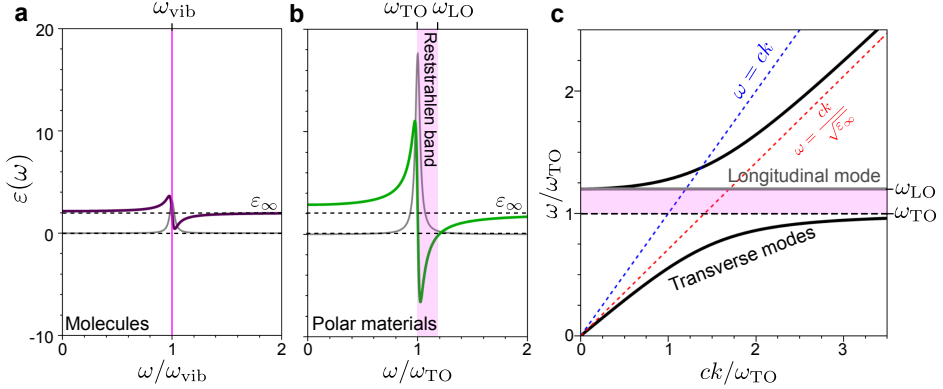


Figure 1.4: Optical response of systems supporting vibrational excitations. a) Real (purple line) and imaginary (gray line) parts of the permittivity of ensembles of molecules [Eq. (1.41)], with oscillator strength $f = 0.08 \omega_{\text{vib}}^2$, high-frequency permittivity $\varepsilon_\infty = 2$ and losses $\gamma = 0.05 \omega_{\text{vib}}$. b) Real (green line) and imaginary (gray line) parts of the permittivity of polar materials [Eq. (1.42)], with LO phonon frequency $\omega_{\text{LO}} = 1.2 \omega_{\text{TO}}$, high-frequency permittivity $\varepsilon_\infty = 2$ and losses $\gamma = 0.05 \omega_{\text{TO}}$. c) Dispersion relation of bulk longitudinal (gray line) and transverse phonon polaritons (black lines), with the same parameters as in panel (b). The light lines corresponding to the vacuum permittivity ($\varepsilon = 1$) and to the high-frequency permittivity of the polar material ($\varepsilon = \varepsilon_\infty = 2$) are plotted by the blue and red dashed lines, respectively. In panels (b) and (c), the Reststrahlen band is highlighted by the pink area.

atoms in the lattice. Some examples of polar materials are hexagonal boron nitride (hBN) [87] and silicon carbide [88]. In these materials, the displacement of the atoms associated with optical phonons create a dipole moment in each unit cell, allowing light to interact with these collective vibrations. Under the approximation that each atom is subjected to a harmonic force, the dynamics of the atoms can be expressed with Eq. (1.39) and therefore the response of the material due to optical excitation is modelled with the Lorentz oscillator model. The standard form to write the permittivity in this context is

$$\varepsilon(\omega) = \varepsilon_\infty \left(1 + \frac{\omega_{\text{LO}}^2 - \omega_{\text{TO}}^2}{\omega_{\text{TO}}^2 - \omega^2 - i\omega\gamma} \right). \quad (1.42)$$

ω_{TO} and ω_{LO} are the frequencies of the transverse optical (TO) and longitudinal optical (LO) phonons, respectively, which are discussed below.

Comparing the permittivity of an ensemble of molecules [Eq. (1.41)] and of a polar material [Eq. (1.42)] we find that, although they are obtained from the same model, they are written in terms of different parameters. To justify this difference, we plot in Figs. 1.4a and b the permittivity of Eq. (1.41) for a typical ensemble of molecules and of Eq. (1.42) for a typical polar material, respectively. In both cases, the imaginary part (gray line) peaks at the corresponding resonant frequency $\omega = \omega_{\text{vib}}$ or $\omega = \omega_{\text{TO}}$. However, the real part of the permittivity shows a key difference between the two situations. For typical molecules (purple line

in panel a), $\text{Re}[\varepsilon(\omega)]$ is always positive due to their relatively small oscillator strength. On the other hand, in the case of polar materials (green line in panel b), $\text{Re}[\varepsilon(\omega)]$ becomes negative for some frequencies. The frequency range of negative permittivities is delimited (for negligible losses) by $\omega_{\text{TO}} \leq \omega \leq \omega_{\text{LO}}$, which is known as the Reststrahlen band (highlighted by the pink area). Since in polar materials the TO and LO phonon frequencies give important information and can be accessed experimentally [89], their corresponding permittivity in Eq. (1.42) is usually written in terms of these frequencies instead of using an effective oscillator strength f .

To analyze further how phonons couple to electromagnetic fields, we obtain next the modes of a bulk polar material by solving Maxwell's equations (losses are neglected for simplicity). First, according to Maxwell's equation $\nabla \cdot [\varepsilon(\omega)\mathbf{E}] = 0$, the longitudinal modes of the system (which need to satisfy the condition $\nabla \cdot \mathbf{E} \neq 0$) only exist when the permittivity vanishes, which occurs at $\omega = \omega_{\text{LO}}$ (gray line in Fig. 1.4). This mode is dispersionless because it cannot couple to transverse light due to its longitudinal nature.

Regarding the transverse modes of the system, we consider again that electromagnetic waves propagating through a material with permittivity $\varepsilon(\omega)$ must satisfy the dispersion relation given by Eq. (1.26). By using the permittivity of polar materials from Eq. (1.42), the dispersion relation can be solved for ω as

$$\omega = \frac{1}{\sqrt{2}} \sqrt{\omega_{\text{LO}}^2 + \frac{c^2 k^2}{\varepsilon_\infty} \pm \sqrt{\left(\omega_{\text{LO}}^2 + \frac{c^2 k^2}{\varepsilon_\infty}\right)^2 - 4 \frac{c^2 k^2}{\varepsilon_\infty} \omega_{\text{TO}}^2}}, \quad (1.43)$$

Equation (1.43) corresponds to the frequencies of new modes of the material, called bulk phonon polaritons, which originate from the coupling of photons and phonons. This dispersion relation is plotted in Fig. 1.4c by black lines for a material with LO phonon frequency $\omega_{\text{LO}} = 1.2 \omega_{\text{TO}}$ and $\varepsilon_\infty = 2$. For each wavevector k , there are two possible values of ω , implying that the dispersion contains two branches. In the $k \rightarrow \infty$ limit, the dispersion relation of the higher-energy transverse branch is very close to the light line determined by the high-frequency permittivity $\omega = \frac{ck}{\sqrt{\varepsilon_\infty}}$ (red dashed line, which we compare with the light line in vacuum $\omega = ck$ indicated by the blue dashed line), while the lower-energy branch approaches the TO phonon frequency. In the $k \rightarrow 0$ limit, the higher-energy and lower-energy branches follow the dispersion relations of the uncoupled LO phonon and the light line determined by ε_∞ , respectively. Importantly, the transverse branches do not cross with each other and their frequencies are always different from those of pure phonons and photons (except in the $k \rightarrow 0$ and $k \rightarrow \infty$ limits), implying that bulk phonon polaritons acquire hybrid properties of both light and matter. The hybridization of the modes is a signature of strong coupling between photons and phonons, as discussed in the next section. Further, the dispersion relation shows that bulk phonon polaritons can be excited at any frequency, except in the Reststrahlen band between ω_{TO} and ω_{LO} . This behavior can be related to the negative value of the permittivity in this frequency range, which forbids the propagation of

electromagnetic fields inside the material.

Last, although we mainly focus on bulk phonon polaritons in this thesis, we note that other types of phononic resonances can be excited in polar materials depending on the geometry of the system. In an analogous way to the plasmonic excitations, surface phonon polaritons can propagate along interfaces between a polar material and an insulator [90], and localized phonon polaritons can be excited in nanoresonators made by this type of materials [91]. These excitations occur in the frequency range $\omega_{\text{TO}} \lesssim \omega \lesssim \omega_{\text{LO}}$, where the permittivity is negative, and support large concentrations of the electric field. Further, polar materials represent a promising alternative to plasmonic materials. On the one hand, while plasmonic resonances are usually excited in the ultraviolet, optical or near infrared spectral ranges, polar crystals are suited to fabricate ultras-small resonators with excitations at smaller energy, reaching the far-infrared range [92]. Additionally, the lifetime of optical phonons (of the order of picoseconds) is considerably larger than for the free electrons (of the order of femtoseconds), and therefore systems supporting phonon polaritons have typically less losses and larger quality factors than the plasmonic counterparts.

1.3 Weak, strong and ultrastrong coupling between light and matter

Matter excitations, such as the molecular vibrations and bulk phonons discussed in Sec. 1.2.2, have well-defined frequencies and lifetimes for each particular system. However, when materials that support any of these or other type of matter excitations are placed inside cavities with resonant electromagnetic modes, the properties of the excitations can be modified due to the light-matter interaction.

To demonstrate the effect of the coupling of matter excitations with electromagnetic modes, we choose as an example a Fabry-Pérot cavity filled with an ensemble of molecules. The reflectivity spectrum of the system is obtained from transfer-matrix simulations (Sec. 1.1.1). Before focusing on the interaction, we analyze the electromagnetic modes of a bare cavity, which consists in a cavity filled with a material of constant permittivity, i.e. without any optically-active excitations. We consider the same Fabry-Pérot cavity analyzed in Fig. 1.1, with thickness $L_{\text{cav}} = 2000$ nm and background permittivity $\varepsilon = 2$. The reflectivity spectra of this cavity is plotted in Fig. 1.5a as a function of the angle θ of the incident light with respect to normal incidence. By modifying θ , the parallel wavevector k_{\parallel} changes, which allows exciting Fabry-Pérot modes at different frequencies. Figure 1.5a indicates the frequency and decay rate (inverse of the lifetime) of the first cavity mode by the frequency and width of the reflectivity dip, respectively. In particular, for the chosen parameters, the dispersion of the first mode varies from $\omega_{\text{cav}} \approx 0.21$

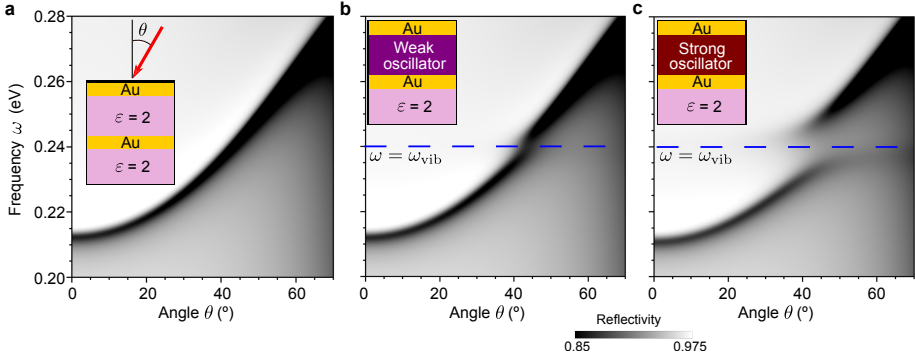


Figure 1.5: Analysis of the interaction between molecular vibrations and Fabry-Pérot cavity modes. Reflectivity spectra of a) a dielectric cavity with constant permittivity $\varepsilon = 2$, b) a cavity filled by molecules with weak oscillator strength ($f = 0.8 \cdot 10^{-4} \text{ eV}^2$) and c) a cavity filled by molecules with strong oscillator strength ($f = 4 \cdot 10^{-4} \text{ eV}^2$). The spectra are plotted as a function of the frequency ω and angle θ of the incident planewave. The insets show a scheme of each cavity, and the blue dashed lines in panels (b) and (c) indicate the vibrational frequency of the molecules $\omega_{\text{vib}} = 0.24 \text{ eV}$. In all cases, the mirrors are two gold layers of 20 nm and the thickness of the cavity is $L_{\text{cav}} = 2000 \text{ nm}$, placed over a substrate of permittivity $\varepsilon = 2$.

eV^{iv} at normal incidence ($\theta = 0^\circ$) to $\omega_{\text{cav}} \approx 0.27 \text{ eV}$ at $\theta \approx 70^\circ$, and the mode has a decay rate $\kappa \approx 0.004 \text{ eV}$.

We illustrate next the effects of light-matter interaction by considering that the cavity is filled with an ensemble of molecules with the permittivity given by Eq. (1.41). As representative values, we choose $\omega_{\text{vib}} = 0.24 \text{ eV}$ (which coincides with the bare cavity frequency ω_{cav} at the angle $\theta \approx 42^\circ$), $\gamma = 0.01 \text{ eV}$ and the high-frequency permittivity $\varepsilon_\infty = 2$, equal to the value used for the bare cavity (so that the dispersion in Fig. 1.5a can be taken as reference). Further, a crucial parameter that governs the light-matter coupling in this system is the oscillator strength f of the molecules. For comparison, we show the reflectivity of a Fabry-Pérot cavity filled by molecules with weak oscillator strength $f = 0.8 \cdot 10^{-4} \text{ eV}^2$ (Fig. 1.5b) and with strong oscillator strength $f = 4 \cdot 10^{-4} \text{ eV}^2$ (Fig. 1.5c).

For the cavity filled with weak oscillators, the reflectivity spectrum is nearly identical to that corresponding to the bare cavity (compare Fig. 1.5b with 1.5a), except for angles $\theta \approx 42^\circ$ where the frequency of the cavity mode ω_{cav} is close to or on resonance with the vibrational frequency of the molecules (indicated by the blue dashed line). Under this condition $\omega_{\text{cav}} \approx \omega_{\text{vib}}$, the dispersion of the mode in the cavity filled with molecules (as given by the reflectivity dips) becomes slightly distorted compared to the smooth dispersion of the bare cavity. However, the change is relatively small and the frequency of the mode of the filled cavity

^{iv} In this thesis, when we use numerical values, we use eV as units of frequency. Although eV is an unit of energy, it allows us to compare easily classical frequencies ω and quantum energies $\hbar\omega$ using the same units. When we refer to classical frequencies, eV has to be understood as a shorthand notation of the actual unit eV/\hbar .

continues varying in a continuous way with the angle θ of the incident light.

On the other hand, for the larger oscillator strength, a very different behavior is observed. The dispersion of the system splits into two branches below and over ω_{vib} instead of being continuous, showing an anticrossing when ω_{cav} approaches ω_{vib} . The very different spectra calculated in Figs. 1.5b and c correspond to two different regimes of light-matter interaction, called weak and strong coupling regimes. To fully understand the boundary between these two regimes and the properties of the modes in each of them, we next consider simple models of light-matter coupling. Specifically, we discuss two different approaches to analyze this coupling, the first based on classical mechanics and the second on cavity QED. The interaction between Fabry-Pérot cavity modes and polar materials is analyzed in much more detail in Chapter 7.

1.3.1 Classical harmonic oscillator model

A canonical system to represent classically the phenomenology behind light-matter interaction consists in coupled harmonic oscillators. In this kind of models, one oscillator is characterized by a displacement $x_{\text{mat}}(t)$ and represents the degrees of freedom of the matter excitation, whose physical origin can be electronic (e.g. molecular excitons) or vibrational, for instance. The electromagnetic mode that couples with the matter excitations is modelled with another oscillator of displacement $x_{\text{cav}}(t)$, and can correspond to a resonance of different types of optical resonators, such as Fabry-Pérot cavities, metallic planar layers supporting SPPs, nanocavities supporting localized plasmon polaritons, photonic crystals... These two oscillators have natural frequencies ω_{cav} and ω_{mat} , and interact with coupling strength g . Further, the losses of the cavity mode and the matter excitations are included as friction terms for the oscillators, with decay rates κ and γ , respectively. There are more than one possible way to describe the coupling between classical oscillators, and Chapter 6 is devoted to a full discussion of these models, including a more careful analysis of the physical interpretation of the displacements x_{cav} and x_{mat} . Focusing here just on the most intuitive model based on classical mechanical springs, the oscillators of this system satisfy the equations of motion [60]

$$\ddot{x}_{\text{cav}} + \kappa\dot{x}_{\text{cav}} + \omega_{\text{cav}}^2 x_{\text{cav}} + 2g\sqrt{\omega_{\text{cav}}\omega_{\text{mat}}}x_{\text{mat}} = 0, \quad (1.44a)$$

$$\ddot{x}_{\text{mat}} + \gamma\dot{x}_{\text{mat}} + \omega_{\text{mat}}^2 x_{\text{mat}} + 2g\sqrt{\omega_{\text{cav}}\omega_{\text{mat}}}x_{\text{cav}} = 0. \quad (1.44b)$$

This system of equations is usually solved in the frequency domain. Under the ansatz $x_{\text{cav}}(t) = x_{\text{cav}}e^{-i\omega t}$ and $x_{\text{mat}}(t) = x_{\text{mat}}e^{-i\omega t}$, Eq. (1.44) transforms to

$$(-\omega^2 - i\omega\kappa + \omega_{\text{cav}}^2)x_{\text{cav}} + 2g\sqrt{\omega_{\text{cav}}\omega_{\text{mat}}}x_{\text{mat}} = 0, \quad (1.45a)$$

$$2g\sqrt{\omega_{\text{cav}}\omega_{\text{mat}}}x_{\text{cav}} + (-\omega^2 - i\omega\gamma + \omega_{\text{mat}}^2)x_{\text{mat}} = 0. \quad (1.45b)$$

Further, classical models of coupled harmonic oscillators are often used in systems with coupling strengths that are small compared to the bare frequencies ω_{mat}

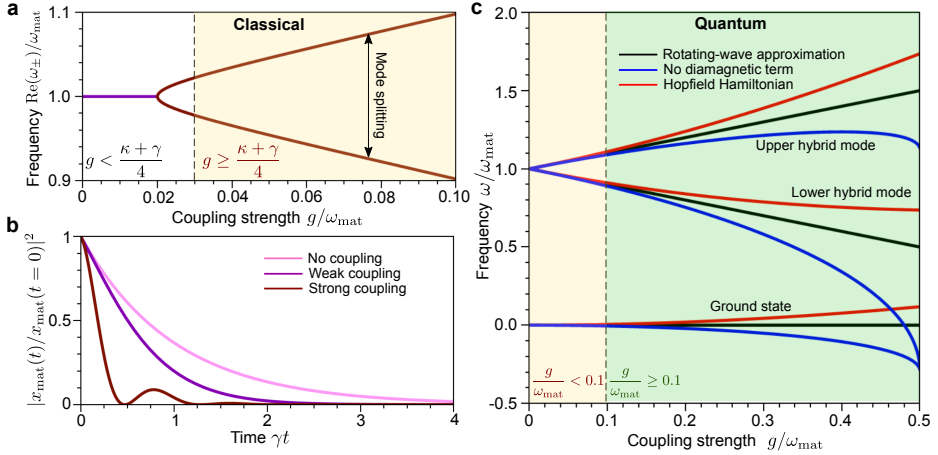


Figure 1.6: Theoretical analysis of the different light-matter coupling regimes. a) Eigenfrequencies $\text{Re}(\omega_{\pm})$ of the classical model of coupled harmonic oscillators [Eq. (1.46)] as a function of the normalized coupling strength g/ω_{mat} . The two oscillators are resonant at the same frequency ($\omega_{\text{cav}} = \omega_{\text{mat}}$) and have decay rates $\kappa = 0.1 \omega_{\text{mat}}$ and $\gamma = 0.02 \omega_{\text{mat}}$. The purple and brown lines represent the eigenfrequencies ω_{\pm} for coupling strengths for which $\text{Re}(\omega_{+}) = \text{Re}(\omega_{-})$ and for which $\text{Re}(\omega_{+}) \neq \text{Re}(\omega_{-})$, respectively. The vertical line indicates the boundary between different coupling regimes. b) Evolution of the magnitude $|x_{\text{mat}}(t)|^2$ under no coupling ($g = 0$, pink line), weak coupling ($g = 0.02 \omega_{\text{mat}}$, purple line) and strong coupling ($g = 0.08 \omega_{\text{mat}}$, brown line). In the three cases, the initial state of the system is $x_{\text{mat}}(t = 0) = 1$ and $x_{\text{cav}}(t = 0) = 0$. c) Eigenfrequencies ω of the Hopfield Hamiltonian as a function of the normalized coupling strength g/ω_{mat} obtained with the RWA (black line), the Hopfield Hamiltonian without the diamagnetic term (blue line) and the complete Hopfield Hamiltonian (red line), without including losses in any of these cases ($\kappa = \gamma = 0$). In panels (a) and (c), the weak coupling regime is highlighted by the white area, the strong coupling regime by the yellow area and the ultrastrong coupling regime by the green area (there is no white area in panel (c) due to the assumption of no losses).

and ω_{cav} . Under these circumstances, the mode frequencies ω of the coupled system do not differ too much from those of the uncoupled oscillators, and thus an approximation of the form $\omega_{\text{cav}} + \omega \simeq 2\omega_{\text{cav}}$ can be done (and the corresponding approximation for ω_{mat}) to simplify Eq. (1.45). The resulting system of linear equations has nonzero solutions for x_{cav} and x_{mat} when its determinant vanishes, which leads to the two complex eigenfrequencies given by

$$\omega_{\pm} = \frac{1}{2}(\omega_{\text{cav}} + \omega_{\text{mat}}) - \frac{i}{2}(\kappa + \gamma) \pm \frac{1}{2}\sqrt{\left(\omega_{\text{cav}} - \omega_{\text{mat}} + i\frac{\gamma - \kappa}{2}\right)^2 + 4g^2}. \quad (1.46)$$

The frequencies of the coupled modes are given by the real part of this expression. We plot $\text{Re}(\omega_{\pm})$ in Fig. 1.6a as a function of the coupling strength, for two oscillators at zero detuning ($\omega_{\text{cav}} = \omega_{\text{mat}}$) and decay rates $\kappa = 0.1 \omega_{\text{mat}}$ and $\gamma = 0.02 \omega_{\text{mat}}$. As can also be obtained from Eq. (1.46), the real part of both eigenfrequencies is equal for coupling strengths satisfying $g \leq \frac{|\kappa - \gamma|}{4}$ (purple line).

Therefore, there is no energy separation (splitting) between the two modes and, when this occurs, the system is in the weak coupling regime.

In contrast, the strong coupling regime corresponds to the situation where the resonant coupling between light and matter leads to the existence of two hybrid modes with different frequencies ω_+ and ω_- from those of the uncoupled constituents ω_{cav} and ω_{mat} . More in detail, several criteria of strong coupling have been discussed. As a first option, any non-zero separation between the frequencies of the two modes can be considered enough for strong coupling, corresponding to the criteria $g \geq \frac{|\kappa - \gamma|}{4}$. However, this condition is often not considered to be sufficient from a practical point of view, because the separation between the modes could be much smaller than the spectral peak widths, a situation where no new phenomenology distinctive of strong coupling is expected. To minimize this issue, the more strict criteria $g \geq \frac{|\kappa + \gamma|}{4}$, $g \geq \frac{|\kappa + \gamma|}{2}$ or $g \geq \sqrt{\frac{\kappa^2 + \gamma^2}{8}}$ have all been considered.

The consequences of weak and strong light-matter coupling can also be analyzed by solving the equations of motion of Eq. (1.44) in time domain, instead of in frequency domain. If the matter excitation is not coupled to any electromagnetic mode ($g = 0$), the dynamics of the matter oscillator is given by $x_{\text{mat}}(t) = x_{\text{mat}}(t=0)e^{-\gamma t/2}e^{-i\omega_{\text{mat}}t}$. Thus, the energy associated to the oscillator, which is proportional to $|x_{\text{mat}}(t)|^2 = |x_{\text{mat}}(t=0)|^2e^{-\gamma t}$, decays at a rate solely determined by the decay rate γ (we plot this solution by the pink line in Fig. 1.6b). By considering the same losses as before and a value of $g = 0.02 \omega_{\text{mat}} = \frac{\kappa + \gamma}{6}$ larger than zero but still corresponding to the weak coupling regime, the dynamics of the oscillator changes. Although such weak coupling strengths do not alter the real part of the oscillator frequencies in Eq. (1.46), the imaginary part, which corresponds to half the decay rate of the eigenstates, does get modified. This change leads to a slower or, typically, faster decay of the matter excitation. We illustrate this effect in Fig. 1.6b for an initial state of $x_{\text{mat}}(t=0) = 1$ and $x_{\text{cav}}(t=0) = 0$. A faster decay of the energy of the matter oscillator $\propto |x_{\text{mat}}(t)|^2$ is indeed observed for such a system (purple line), compared with the uncoupled system ($g = 0$, pink line). This modification of the spontaneous emission rate of the matter excitation is called Purcell effect [93], and the ratio between the modified decay rate and the decay rate in vacuum γ can be related to the quality factor \mathcal{Q} , the effective volume \mathcal{V} and the wavelength λ of the cavity mode as

$$F_{\text{P}} = 1 + \frac{3}{4\pi^2} \frac{\mathcal{Q}}{\mathcal{V}} \lambda^3. \quad (1.47)$$

Last, in the strong coupling regime, the energy of the matter oscillator $\propto |x_{\text{mat}}(t)|^2$ shows several periods of oscillation before it completely dissipates. These oscillations can be observed in the brown curve of Fig. 1.6b, where we plot $|x_{\text{mat}}(t)|^2$ for the same losses and initial state as for the weak coupling situation, but in a system with coupling strength $g = 0.08 \omega_{\text{mat}} = \frac{2}{3}(\kappa + \gamma)$. Besides the oscillations of $|x_{\text{mat}}(t)|^2$, we note that the energy of the cavity mode $\propto |x_{\text{cav}}(t)|^2$ also shows oscillations, where the maxima of the cavity energy coincides with the

minima of the matter energy an vice versa (not shown). This behavior indicates that in the strong coupling regime the matter excitation and the cavity mode interchange energy before they both decay.

1.3.2 Cavity quantum electrodynamics description

An alternative approach to study light-matter interaction is to consider explicitly the quantum nature of the electromagnetic fields and the matter excitations following the framework of cavity QED. Possibly the simplest scenario within cavity QED consists in a matter excitation coupled to a single cavity mode. According to the canonical quantization procedure, the energy of the electromagnetic mode is quantized by using bosonic creation \hat{a}^\dagger and annihilation \hat{a} operators. On the other hand, the matter excitation is quantized using bosonic or fermionic operators depending on its nature. In this thesis we only deal with bosonic systems, and thus the energy associated to the matter is quantized with the creation \hat{b}^\dagger and annihilation \hat{b} operators with the commutation rules $[\hat{b}, \hat{b}^\dagger] = [\hat{a}, \hat{a}^\dagger] = 1$. In this context, the light-matter interaction is expressed with the so-called Hopfield Hamiltonian [94]

$$\hat{\mathcal{H}}_{\text{Hop}} = \underbrace{\hbar\omega_{\text{cav}} \left(\hat{a}^\dagger \hat{a} + \frac{1}{2} \right)}_{\hat{\mathcal{H}}_{\text{Hop}}^{\text{EM}}} + \underbrace{\hbar\omega_{\text{mat}} \left(\hat{b}^\dagger \hat{b} + \frac{1}{2} \right)}_{\hat{\mathcal{H}}_{\text{Hop}}^{\text{mat}}} + \underbrace{\hbar g (\hat{a} + \hat{a}^\dagger)(\hat{b} + \hat{b}^\dagger)}_{\hat{\mathcal{H}}_{\text{Hop}}^{\text{int}}} + \underbrace{\hbar D (\hat{a} + \hat{a}^\dagger)^2}_{\hat{\mathcal{H}}_{\text{Hop}}^{\text{dia}}}. \quad (1.48)$$

The first two terms, $\hat{\mathcal{H}}_{\text{Hop}}^{\text{EM}}$ and $\hat{\mathcal{H}}_{\text{Hop}}^{\text{mat}}$, are associated to the energies of the free oscillators of the cavity mode and the matter excitation. The interaction between light and matter is considered in the term $\hat{\mathcal{H}}_{\text{Hop}}^{\text{int}}$ and it scales with the coupling strength g . Last, the so-called diamagnetic term $\hat{\mathcal{H}}_{\text{Hop}}^{\text{dia}}$ originates from the self-interaction of the cavity mode. However, the necessity to include this term in cavity QED models is still under discussion, and depends on the system under study. Mainly, two different values for the scaling parameter D are considered, $D = 0$ (no diamagnetic term) and $D = \frac{g^2}{\omega_{\text{cav}}}$ (which is established by quantum sum rules [95]). We notice that the operators appearing in the diamagnetic term are only those of the electromagnetic field, but that this term depends on the coupling strength g with the matter excitation. We discuss the Hopfield Hamiltonian and the diamagnetic term in more detail in Chapter 6. Further, we do not consider losses in this analysis because they cannot be included directly in Eq. (1.48) without breaking hermiticity. For small coupling strengths, Lindblad operators include these losses in the context of open quantum systems [96,97]. However, for large coupling strengths, more intricate methods must be used [98,99].

There is no known close solution of the eigenstates of the Hopfield Hamiltonian in Eq. (1.48). However, in the regime of small coupling strengths (compared to the bare frequencies ω_{cav} and ω_{mat}), the rotating-wave approximation (RWA) is usually made, which leads to exact solutions. The RWA takes into account that, for small g , the combined operators $\hat{a}\hat{b}^\dagger$ and $\hat{a}^\dagger\hat{b}$ of the interaction term evolve in

time as $e^{-i(\omega_{\text{cav}} - \omega_{\text{mat}})t}$, whereas the counter-rotating terms $\hat{a}\hat{b}$ and $\hat{a}^\dagger\hat{b}^\dagger$ follow the evolution of the form $e^{-i(\omega_{\text{cav}} + \omega_{\text{mat}})t}$. Close to zero detuning, the contribution of the latter operators averages to zero at relevant time scales, because they oscillate much faster than the former operators. Further, the diamagnetic term scales with g^2 , and it is negligible at first order of g . The RWA thus consists in neglecting the diamagnetic and the counter-rotating terms. The RWA Hamiltonian therefore reads

$$\hat{\mathcal{H}}_{\text{RWA}} = \hbar\omega_{\text{cav}} \left(\hat{a}^\dagger\hat{a} + \frac{1}{2} \right) + \hbar\omega_{\text{mat}} \left(\hat{b}^\dagger\hat{b} + \frac{1}{2} \right) + \hbar g(\hat{a}\hat{b}^\dagger + \hat{a}^\dagger\hat{b}). \quad (1.49)$$

By solving Schrödinger's equation, we obtain that the ground state is at zero energy, while the eigenfrequencies of the first two excited states are

$$\omega_{\pm} = \frac{1}{2}(\omega_{\text{cav}} + \omega_{\text{mat}}) \pm \frac{1}{2}\sqrt{(\omega_{\text{cav}} - \omega_{\text{mat}})^2 + 4g^2}. \quad (1.50)$$

These frequencies are exactly the same as those obtained with the classical coupled harmonic oscillator models for small coupling strength [Eq. (1.46)] and no losses ($\kappa = \gamma = 0$), which points out towards the equivalence of classical and quantum models of these systems (Chapter 6).

After analyzing the eigenfrequencies of the Hopfield Hamiltonian for small coupling strengths, we now compare the results of different methods by extending the calculation to larger values of g . We plot in Fig. 1.6c the eigenfrequencies of the ground state and the two excited states that in the RWA are associated to a single excitation, for zero detuning between the cavity mode and matter excitation. The black line corresponds to the analytical eigenfrequencies obtained with the RWA [Eq. (1.50)], whereas the blue and red lines indicate the numerical eigenfrequencies of the complete Hopfield Hamiltonian with $D = 0$ and $D = \frac{g^2}{\omega_{\text{cav}}}$, respectively. For small g , in the range highlighted by the yellow area, the three lines almost overlap, showing the validity of the RWA (note that since we do not consider losses, the system is always strongly coupled in Fig. 1.6c). However, the three models start to differ at $g \approx 0.1 \omega_{\text{mat}}$, corresponding to the onset of the ultrastrong coupling regime, highlighted by the green area in Fig. 1.6c.

An interesting feature in the ultrastrong coupling regime is that the ground-state energy is shifted from zero when the full Hamiltonian in Eq. (1.48) (without RWA) is considered, including the counter-rotating terms. It becomes negative for $D = 0$ and positive when the diamagnetic term with $D = \frac{g^2}{\omega_{\text{cav}}}$ is included. This shift implies that the ground state is not equal to the vacuum state, and as a consequence, the population of the number operators $\hat{a}^\dagger\hat{a}$ and $\hat{b}^\dagger\hat{b}$ in the ground state is nonzero in the ultrastrong coupling regime. However, the ground state cannot radiate by decaying to a lower-energy state, and since these $\hat{a}^\dagger\hat{a}$ and $\hat{b}^\dagger\hat{b}$ excitations cannot be then detected, they are said to be virtual [100, 101]. Additionally, for the complete Hamiltonian with $D = 0$, the frequency of the lower hybrid mode crosses the ground-state energy at $g = 0.5 \omega_{\text{mat}}$, leading to the superradiant phase transition [102, 103]. In contrast, when $D = \frac{g^2}{\omega_{\text{cav}}}$ is included,

this crossing never occurs, and the system becomes stable with respect to that phase transition.

Last, we note that although the relation between classical and quantum models is well established for small g , their connection within the ultrastrong coupling regime has been much less explored. For example, it becomes necessary to clarify how to include the effects of the diamagnetic term in the classical model. This and other related questions are addressed in Chapter 6.

QUANTUM DESCRIPTIONS OF PLASMONIC EXCITATIONS AND OF ELECTRON TUNNELING

In this chapter, we outline the quantum perspective based on condensed matter theory that we use throughout this thesis. While in the previous chapter we have given a classical description of metals based on a local permittivity, such models fail when dealing with phenomena where charge oscillations of atomic-size wavelength are involved. Therefore, we now go beyond classical descriptions of metallic systems, which allows for an accurate description of the properties of plasmons and of how electrons can excite these plasmons.

First, we focus on the calculation of the excitation spectra in metals. Under the assumption of a weak external perturbation, it is safe to work in the linear response regime, and therefore the properties of metallic excitations can be analyzed within linear response theory. According to this theory, all the information about the response of a system to any external probe is encapsulated in the linear response function. After analyzing the main properties of this function in Sec. 2.1, we use it to calculate the non-local permittivity of a homogeneous electron gas (HEG) in Sec. 2.2. This system is useful for a simple description of electronic excitations in metals, because the permittivity can be obtained analytically under the assumption that electrons in metals behave in the same way as in a HEG. However, in real systems the band structure differs from that of free electrons. In Sec. 2.3, we give the necessary tools to obtain the excitation spectra of real metals in terms of their atomic and electronic structure, under the Density Functional Theory (DFT) and Time-Dependent Density Functional Theory (TDDFT).

After discussing the properties of plasmonic excitations in metallic systems, we describe a mechanism to excite surface plasmon polaritons (SPPs) in such systems

using tunneling electrons. In systems formed by two metallic electrodes separated by an insulator barrier, electrons from one electrode can tunnel through the gap to the other electrode. During the tunneling, electrons lose part of their energy to excite SPPs, and these SPPs can then lead to electromagnetic radiation. In Sec. 2.4, we summarize Bardeen's theory of quantum elastic tunneling, which gives the basic tools to calculate the SPP excitation rate in this context.

2.1 Linear response theory

As the first step towards the extraction of the excitation spectra in metals, we outline the basis of the linear response theory. This theory aims to explain how a system responds to a weak perturbation created by an external probe. The probe is usually represented by a physical magnitude X , and a particular magnitude Y of the system is measured. The response is quantified in terms of the X - Y response function.

In quantum mechanics, the formulation of the linear response theory starts with a time-dependent Hamiltonian that describes the interaction of the system with the probe in the form

$$\hat{H}_{\text{sys-probe}}(t) = \varsigma_{\text{probe}}(t)\hat{Y}_{\text{sys}}(t). \quad (2.1)$$

$\varsigma_{\text{probe}}(t)$ describes the time dependence of the perturbation and depends on the physical quantity X . $\hat{Y}_{\text{sys}}(t)$ is the quantum operator associated to the magnitude Y of the system written in the Heisenberg picture. The objective is to know how the operator $\hat{Y}_{\text{sys}}(t)$ evolves in time. Usually, obtaining the analytical expression of $\hat{Y}_{\text{sys}}(t)$ from Eq. (2.1) is very difficult or even impossible. However, assuming that the response of the system is linear, the solution for the expectation value $\langle \hat{Y}_{\text{sys}}(t) \rangle$ can be written [104, 105]

$$\langle \hat{Y}_{\text{sys}}(t) \rangle = \int \chi_{X \rightarrow Y}(t - t') \varsigma_{\text{probe}}(t') dt'. \quad (2.2)$$

$\chi_{X \rightarrow Y}(t - t')$ is the response function and is invariant to time translations. By performing the Fourier transform of Eq. (2.2), the expression of $\langle \hat{Y}_{\text{sys}} \rangle$ simplifies to

$$\begin{aligned} \langle \hat{Y}_{\text{sys}}(\omega) \rangle &= \int \chi_{X \rightarrow Y}(t - t') \varsigma_{\text{probe}}(t') e^{-i\omega t} dt dt' \\ &= \int \chi_{X \rightarrow Y}(t - t') e^{-i\omega(t-t')} \varsigma_{\text{probe}}(t') e^{-i\omega t'} dt dt' \\ &= \chi_{X \rightarrow Y}(\omega) \varsigma_{\text{probe}}(\omega). \end{aligned} \quad (2.3)$$

Therefore, the response of the system at a particular frequency ω is only affected by the external perturbation $\varsigma_{\text{probe}}(\omega)$ at the same frequency. We next analyze how $\chi_{X \rightarrow Y}(\omega)$ is calculated using the tools of the linear response theory. Further, in this thesis, we are interested in analyzing how the electronic density of a metallic

system is modified due to the interaction with a probe. Thus, from now on, the analysis focuses in the particular case of the density-density response function.

2.1.1 Density-density response function

In the formalism of linear density-density response, the system is characterized with the electronic density $\rho_{\text{ind}}(\mathbf{r}, t)$ induced by the probe. The interaction with the external probe is expressed through the external potential $V_{\text{ext}}(\mathbf{r}, t)$ induced by this probe. To calculate how $V_{\text{ext}}(\mathbf{r}, t)$ affects the system, we consider a single frequency ω in the potential to focus on the evolution of the electronic density just at the same frequency, i.e. $\rho_{\text{ind}}(\mathbf{r}, t) = \rho_{\text{ind}}(\mathbf{r}, \omega)e^{-i\omega t}$. Further, in the linear response regime, the external potential must be turned on adiabatically to ensure that the system reacts slowly. This adiabatic potential can be written as $V_{\text{ext}}(\mathbf{r}, t) = V_{\text{ext}}(\mathbf{r}, \omega)e^{-i\omega t}e^{\eta t}$ (where the potential is turned on at the $t \rightarrow -\infty$ time limit), and this analysis is valid only for small $\eta > 0$ so that the system-probe interaction does not become too strong to leave the linear response regime. Therefore, the $\eta \rightarrow 0$ limit is considered finally.

The density-density response function can be obtained by making the Fourier transform of the system-probe Hamiltonian over spatial variables as

$$\hat{\mathcal{H}}_{\text{sys-probe}} = \int V_{\text{ext}}(\mathbf{r}, t)\rho_{\text{ind}}(\mathbf{r})e^{-i\omega t}d\mathbf{r} = \int V_{\text{ext}}(\mathbf{q}, \omega)\rho_{\text{ind}}^*(\mathbf{q})e^{-i(\omega+i\eta)t}d\mathbf{q}. \quad (2.4)$$

Each \mathbf{q} component of the electronic density responds only to the same \mathbf{q} component of the external potential. Thus, each Fourier component of the response function, according to Eq. (2.2), reads [106]

$$\chi(\mathbf{q}, \omega) = \frac{\rho_{\text{ind}}(\mathbf{q}, \omega)}{V_{\text{ext}}(\mathbf{q}, \omega)}. \quad (2.5)$$

Since we only deal with density-density response functions, we eliminate the subscript $X \rightarrow Y$ from the symbol $\chi_{X \rightarrow Y}$ to simplify the notation.

In order to calculate the response function, the expectation value of the electronic density for the quantum state $|\Psi\rangle$ must be calculated with [106]

$$\rho_{\text{ind}}(\mathbf{q}, \omega) = \langle \Psi | e^{i\mathbf{q}\cdot\mathbf{r}} e^{i\omega t} e^{-\eta t} | \Psi \rangle. \quad (2.6)$$

In this equation, $|\Psi\rangle$ is the solution of the Schrödinger equation

$$[\hat{\mathcal{H}}_{\text{sys}} + V_{\text{ext}}(\mathbf{q}, \omega)\rho_{\text{ind}}^*(\mathbf{q})e^{-i(\omega+i\eta)t}]|\Psi\rangle = i\hbar\frac{\partial|\Psi\rangle}{\partial t}, \quad (2.7)$$

where a single \mathbf{q} term of the Hamiltonian $\hat{\mathcal{H}}_{\text{sys-probe}}$ is considered. Since $\chi(\mathbf{q}, \omega)$ is calculated in the linear response regime, Eq. (2.7) needs to be solved just at first order of perturbation theory. With this aim, we expand $|\Psi\rangle$ over the eigenstates $|\phi_n\rangle$ of the system Hamiltonian $\hat{\mathcal{H}}_{\text{sys}}$ (i.e. which satisfy the equation

$\hat{\mathcal{H}}_{\text{sys}} |\phi_n\rangle = \hbar\omega_n |\phi_n\rangle$), according to the expression

$$|\Psi\rangle = \sum_n a_n(t) e^{-i\omega_n t} |\phi_n\rangle. \quad (2.8)$$

By introducing this expression into Eq. (2.7), the solution needs to satisfy the initial conditions $a_m(-\infty) = 1$ for all the states $|\phi_m\rangle$ that are occupied before the interaction is turned on, and $a_n(-\infty) = 0$ for the unoccupied states $|\phi_n\rangle$. At first-order approximation, the occupation factor of the occupied states can be assumed to remain constant at $a_m(t) = 1$. Subsequently, Eq. (2.7) with these initial conditions gives the coefficients of the unoccupied states, which are

$$a_n(t) = \sum_m^{\text{occ.}} \frac{e^{-i(\omega + i\eta - \omega_m + \omega_n)t}}{\hbar(\omega + i\eta - \omega_m + \omega_n)} V_{\text{ext}}(\mathbf{q}) \langle \phi_n | \rho_{\text{ind}}(\mathbf{q}) | \phi_m \rangle. \quad (2.9)$$

Last, the coefficients $a_n(t)$ give the expectation value of the density with [106]

$$\rho_{\text{ind}}(\mathbf{q}, t) = \sum_m^{\text{occ.}} \sum_n^{\text{unocc.}} a_n(t) e^{i(\omega_m - \omega_n)t} \langle \phi_m | \rho_{\text{ind}}(\mathbf{q}) | \phi_n \rangle + \text{c.c.}, \quad (2.10)$$

where c.c. stands for the complex conjugate. By introducing the coefficients of Eq. (2.9) into this last expression, the response function [Eq. (2.5)] is calculated as

$$\chi(\mathbf{q}, \omega) = \sum_m^{\text{occ.}} \sum_n^{\text{unocc.}} \left[\frac{|\langle \phi_n | \rho_{\text{ind}}(\mathbf{q}) | \phi_m \rangle|^2}{\hbar(\omega + i\eta + \omega_m - \omega_n)} - \frac{|\langle \phi_n | \rho_{\text{ind}}(\mathbf{q}) | \phi_m \rangle|^2}{\hbar(\omega + i\eta - \omega_m + \omega_n)} \right]. \quad (2.11)$$

This result implies that if all eigenvalues $\omega_{m(n)}$ and eigenstates $|\phi_{m(n)}\rangle$ are known for a system, we can calculate the density $\rho_{\text{ind}}(\mathbf{q}, \omega)$ induced in the system by any external perturbative potential $V_{\text{ext}}(\mathbf{q}, \omega)$ using Eq. (2.5).

2.1.2 Causality and Kramers-Kronig relations

From a physical point of view, a response function must satisfy certain properties, such as the preservation of causality. To demonstrate that the response function from Eq. (2.11) is appropriate in regards of this property, we first observe that $\chi(\mathbf{q}, \omega)$ exhibits poles at frequencies $\omega = \pm(\omega_m - \omega_n) - i\eta$. $\chi(\mathbf{q}, \omega)$ is therefore analytic in the upper half of the complex plane but not in the lower half. This property has a significant consequence in the response function in the time domain, which becomes apparent by computing the inverse Fourier transform,

$$\chi(\mathbf{q}, t - t') = \frac{1}{2\pi} \int_{-\infty}^{\infty} \chi(\mathbf{q}, \omega) e^{-i\omega(t-t')} d\omega. \quad (2.12)$$

If $t - t'$ is negative, the contour of this integral can be closed in the upper complex plane (indicated by C_1 in Fig. 2.1a), because the exponential of Eq. (2.12) vanishes

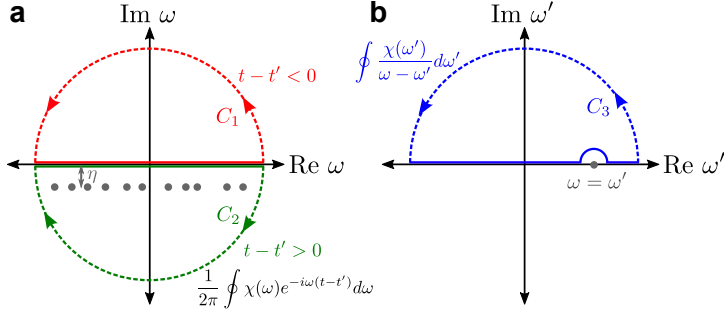


Figure 2.1: Contours of the complex integrals related to the response function $\chi(\mathbf{q}, \omega)$. a) Contours of the integral in Eq. (2.12), for $t - t' < 0$ (C_1 , in red) and for $t - t' > 0$ (C_2 , in green). b) Contour C_3 of the integral in Eq. (2.15). The poles of the integrands are indicated by gray dots in both panels.

in the $|\omega| \rightarrow \infty$ limit. Since $\chi(\mathbf{q}, \omega)$ is analytic inside the contour C_1 , $\chi(\mathbf{q}, t - t')$ must be zero. However, for positive values of $t - t'$, the integral must be evaluated in the lower half plane, where $\chi(\mathbf{q}, \omega)$ is no longer analytic (the corresponding contour is indicated by C_2 in Fig. 2.1a together with the poles of the response function). This analysis leads to the important result

$$\chi(\mathbf{q}, \omega) \text{ analytic for } \text{Im } \omega > 0 \iff \chi(\mathbf{q}, t - t') = 0, \quad t - t' < 0 \\ \neq 0, \quad t - t' > 0. \quad (2.13)$$

Accordingly, the response function $\chi(\mathbf{q}, t - t')$ does not violate causality, because an external perturbation at time t' can only modify the system at later times $t > t'$.

Further, the response function $\chi(\mathbf{q}, t - t')$ is real in the time domain, because the two quantities related by the time-dependent response function in Eq. (2.2), i.e. $\langle \hat{Y}_{\text{sys}}(t) \rangle$ for the system and $\varsigma_{\text{probe}}(t)$ for the probe, are real. This property of the response function implies that its Fourier transform $\chi(\mathbf{q}, \omega)$ in the frequency domain is complex. The mathematical properties of $\chi(\mathbf{q}, \omega)$ give additional information about the processes involved in the response of the system. We consider separately the real and imaginary parts of the frequency-dependent response function as $\chi(\mathbf{q}, \omega) = \chi_{\text{R}}(\mathbf{q}, \omega) + i\chi_{\text{I}}(\mathbf{q}, \omega)$. By using standard properties of the Fourier transform, each of these parts can be written as follows,

$$\chi_{\text{R}}(\mathbf{q}, \omega) = \frac{1}{2} \int_{-\infty}^{+\infty} [\chi(\mathbf{q}, t) + \chi(\mathbf{q}, -t)] e^{i\omega t} dt, \quad (2.14a)$$

$$\chi_{\text{I}}(\mathbf{q}, \omega) = -\frac{i}{2} \int_{-\infty}^{+\infty} [\chi(\mathbf{q}, t) - \chi(\mathbf{q}, -t)] e^{i\omega t} dt. \quad (2.14b)$$

We observe that the real part $\chi_{\text{R}}(\mathbf{q}, \omega)$ accounts for processes that are invariant to the time reversal transformation $t \rightarrow -t$, and thus it is called as the *reactive*

part of the response. On the contrary, the imaginary part $\chi_I(\mathbf{q}, \omega)$ is not invariant with respect to time reversal, making it sensitive to the direction of the arrow of time. Since the physical processes involved in closed microscopic systems are usually invariant to time reversal, $\chi_I(\mathbf{q}, \omega)$ must be related to energy absorption due to the interaction with the environment. As a consequence, $\chi_I(\mathbf{q}, \omega)$ is called the *dissipative* part of the response.

Although $\chi_R(\mathbf{q}, \omega)$ and $\chi_I(\mathbf{q}, \omega)$ describe different phenomena on the response of a system, these two functions are not independent of each other. Indeed, $\chi_R(\mathbf{q}, \omega)$ also contains information about dissipative processes of the system and vice versa for $\chi_I(\mathbf{q}, \omega)$. To analyze this relationship in further detail, let us integrate the function $\frac{\chi(\mathbf{q}, \omega')}{\omega - \omega'}$ with respect to ω' in the closed path C_3 indicated in Fig. 2.1b. Since there is no pole inside the area determined by the path C_3 , the integral over the complete path must vanish. Further, the integral in the big half circle (dashed lines) vanishes in the $|\omega'| \rightarrow \infty$ limit because $\chi(\mathbf{q}, \omega')$ scales with $1/|\omega'|^2$. Therefore, the integral has to be performed in the real line and in the small half circle around the pole $\omega = \omega'$, which evaluates

$$\oint \frac{\chi(\mathbf{q}, \omega')}{\omega - \omega'} d\omega' = PV \left(\int_{-\infty}^{\infty} \frac{\chi(\mathbf{q}, \omega')}{\omega - \omega'} d\omega' \right) + i\pi\chi(\mathbf{q}, \omega) = 0, \quad (2.15)$$

where PV stands for the Cauchy principal value. By taking the real and imaginary parts of Eq. (2.15), we obtain

$$\chi_R(\mathbf{q}, \omega') = -\frac{1}{\pi} PV \left(\int_{-\infty}^{\infty} \frac{\chi_I(\mathbf{q}, \omega')}{\omega - \omega'} d\omega' \right), \quad (2.16a)$$

$$\chi_I(\mathbf{q}, \omega') = \frac{1}{\pi} PV \left(\int_{-\infty}^{\infty} \frac{\chi_R(\mathbf{q}, \omega')}{\omega - \omega'} d\omega' \right). \quad (2.16b)$$

These important results in linear response theory are called the Kramers-Kronig relations [107]. These relations imply that if either the real or imaginary part of $\chi(\mathbf{q}, \omega)$ is known at all frequencies, the other can be calculated directly. In many systems, the imaginary part $\chi_I(\mathbf{q}, \omega)$ can be calculated computationally in a considerably faster way than the real part $\chi_R(\mathbf{q}, \omega)$. In this case, the direct calculation of $\chi_I(\mathbf{q}, \omega)$ and the following use of Kramers-Kronig relations to obtain $\chi_R(\mathbf{q}, \omega)$ can be much more efficient than calculating the complete response function $\chi(\mathbf{q}, \omega)$ from the beginning.

2.2 Permittivity of an homogeneous electron gas under the random phase approximation

The linear response theory outlined in the previous section can be used to derive the non-local permittivity $\varepsilon(\mathbf{q}, \omega)$ of a metal. In this derivation, we start by relating the density-density response function [Eq. (2.11)] with the electromagnetic fields inside the metal. By taking the spatial Fourier transform of Maxwell's equation

(1.1a), we relate the displacement and electric fields with the charge densities of the metal and the probe. First, the displacement field reads [directly from Eq. (1.1a)]

$$i\mathbf{q} \cdot \mathbf{D}(\mathbf{q}, \omega) = \rho_{\text{ext}}(\mathbf{q}, \omega), \quad (2.17)$$

where $\rho_{\text{ext}}(\mathbf{q}, \omega)$ is the charge density of the external probe. By using the relation between the displacement and electric fields $\mathbf{D} = \varepsilon_0 \mathbf{E} + \mathbf{P}$, we obtain that the electric field is written as

$$i\mathbf{q} \cdot \mathbf{E}(\mathbf{q}, \omega) = \frac{1}{\varepsilon_0} [\rho_{\text{ext}}(\mathbf{q}, \omega) + \rho_{\text{ind}}(\mathbf{q}, \omega)], \quad (2.18)$$

where $\rho_{\text{ind}}(\mathbf{q}, \omega) = -i\mathbf{q} \cdot \mathbf{P}(\mathbf{q}, \omega)$ is the induced charge density of the system obtained from the polarization density $\mathbf{P}(\mathbf{q}, \omega)$.

In linear optical response, the electric and displacement fields are related as $\mathbf{D}(\mathbf{q}, \omega) = \varepsilon_0 \varepsilon(\mathbf{q}, \omega) \mathbf{E}(\mathbf{q}, \omega)$ [Eq. (1.5)]. We then obtain the (relative) permittivity $\varepsilon(\mathbf{q}, \omega)$ of the metal by inserting in the left handside of this equation the expression of \mathbf{D} in Eq. (2.17), and in the right handside the expression of \mathbf{E} in Eq. (2.18). We obtain

$$\frac{1}{\varepsilon(\mathbf{q}, \omega)} = 1 + \frac{\rho_{\text{ind}}(\mathbf{q}, \omega)}{\rho_{\text{ext}}(\mathbf{q}, \omega)} = 1 + V_{\text{Coul}}(\mathbf{q}) \chi(\mathbf{q}, \omega). \quad (2.19)$$

In the last step, we have used the definition of the density-density response function given by Eq. (2.5), where the external potential is $V_{\text{ext}}(\mathbf{q}, \omega) = V_{\text{Coul}}(\mathbf{q}) \rho_{\text{ext}}(\mathbf{q}, \omega)$ [108] and $V_{\text{Coul}}(\mathbf{q})$ is the Fourier transform of the Coulomb potential.

We have thus shown that the permittivity of any quantum system can be calculated directly from the response function of Eq. (2.11). However, even for the HEG, which is the simplest model for metals, the calculation of $\chi(\mathbf{q}, \omega)$ is a difficult task. In the derivation of the response function, we have considered the interaction between the system and the probe, but the interaction between all electrons within the system has been neglected. In the most rigorous approach, all the electron-electron interactions should be included in the Schrödinger equation of the system [Eq. (2.7)], in order to obtain all eigenstates $|\phi_n\rangle$ accordingly. Due to the difficulty of solving the complete equation, approximations must be made.

An important approximation used for the HEG is the Random Phase Approximation (RPA). In this approach, the interaction of all the other electrons is treated as an effective *external* potential for each electron. That is, the screening field of the form $V_{\text{Coul}}(\mathbf{q}) \rho_{\text{ind}}(\mathbf{q}, \omega)$ due to the induced density is treated in the same way as the field of the external probe $V_{\text{Coul}}(\mathbf{q}) \rho_{\text{ext}}(\mathbf{q}, \omega)$. Besides the screening field of other electrons, further contributions to the electron-electron interaction (such as exchange and correlation, as explained in Sec. 2.3), are neglected.

As a first step, before calculating the response function of the interacting system according to the RPA, we calculate the response function of a hypothetical system of non-interacting electrons. In this approach, treating the screening potential as an external contribution, the electrons can be considered as being independent of each other. Therefore, each electron is influenced by an effective potential that accounts for both the external potential and screening potential of other electrons.

The response function of this system would be given by Eq. (2.5) with the external potential $V_{\text{ext}}(\mathbf{q}, \omega) = V_{\text{Cou}}(\mathbf{q})\rho_{\text{ext}}(\mathbf{q}, \omega) + V_{\text{Cou}}(\mathbf{q})\rho_{\text{ind}}(\mathbf{q}, \omega)$, i.e.

$$\chi^0(\mathbf{q}, \omega) = \frac{\rho_{\text{ind}}(\mathbf{q}, \omega)}{V_{\text{Cou}}(\mathbf{q})[\rho_{\text{ind}}(\mathbf{q}, \omega) + \rho_{\text{ext}}(\mathbf{q}, \omega)]}. \quad (2.20)$$

In this expression, $\chi^0(\mathbf{q}, \omega)$ is the response function of a non-interacting electron gas, i.e. it is calculated according to Eq. (2.11) with single-electron orbitals $|\phi_n\rangle$. However, $\chi^0(\mathbf{q}, \omega)$ is not the response function of the actual interacting system. We note that the interacting system just reacts to the external potential, because the contribution of the screening would be included in the interaction of the system, not as being an external contribution. That is, the response function of the interacting system satisfies Eq. (2.5) with $V_{\text{ext}}(\mathbf{q}, \omega) = V_{\text{Cou}}(\mathbf{q})\rho_{\text{ext}}(\mathbf{q}, \omega)$, instead of with $V_{\text{ext}}(\mathbf{q}, \omega) = V_{\text{Cou}}(\mathbf{q})\rho_{\text{ext}}(\mathbf{q}, \omega) + V_{\text{Cou}}(\mathbf{q})\rho_{\text{ind}}(\mathbf{q}, \omega)$ as the non-interacting system. From this perspective, we can use $\chi^0(\mathbf{q}, \omega)$ from Eq. (2.20) to obtain the approximate response function $\chi^{\text{RPA}}(\mathbf{q}, \omega)$ of the interacting electron gas according to

$$\chi^{\text{RPA}}(\mathbf{q}, \omega) = \frac{\rho_{\text{ind}}(\mathbf{q}, \omega)}{V_{\text{Cou}}(\mathbf{q})\rho_{\text{ext}}(\mathbf{q}, \omega)} = \frac{\chi^0(\mathbf{q}, \omega)}{1 - V_{\text{Cou}}(\mathbf{q})\chi^0(\mathbf{q}, \omega)}. \quad (2.21)$$

Last, by introducing this expression into Eq. (2.19), the permittivity of a metal can be calculated directly from the non-interacting response function with

$$\varepsilon(\mathbf{q}, \omega) = 1 - V_{\text{Cou}}(\mathbf{q})\chi^0(\mathbf{q}, \omega). \quad (2.22)$$

After obtaining the expression of the permittivity for a general HEG, in the following subsections we analyze in detail the results corresponding to three particular systems.

2.2.1 3D homogeneous electron gas

The first calculation of a permittivity under the RPA was carried out by Lindhard for a three-dimensional (3D) HEG [109]. The Lindhard permittivity $\varepsilon^{\text{Lin}}(\mathbf{q}, \omega) = \varepsilon_{\text{R}}^{\text{Lin}}(\mathbf{q}, \omega) + i\varepsilon_{\text{I}}^{\text{Lin}}(\mathbf{q}, \omega)$ is calculated using the Fourier transform of the Coulomb potential in three dimensions (with $q = |\mathbf{q}|$),

$$V_{\text{Cou}}(\mathbf{q}) = \frac{e^2}{\varepsilon_0 q^2}, \quad (2.23)$$

and computing the non-interacting response function $\chi^0(\mathbf{q}, \omega)$ according to Eq. (2.11). For a metal with Fermi velocity v_{F} , plasma frequency ω_{p} and electron effective mass m_{eff} , the real part of the Lindhard permittivity is

$$\begin{aligned} & \varepsilon_{\text{R}}^{\text{Lin}}(\mathbf{q}, \omega) \\ &= 1 + \frac{3\omega_{\text{p}}^2}{(qv_{\text{F}})^2} \left\{ \frac{1}{2} + \frac{m_{\text{eff}}v_{\text{F}}}{4\hbar q} \left[\left(\frac{(\hbar\omega + \frac{\hbar^2 q^2}{2m_{\text{eff}}})^2}{(\hbar q v_{\text{F}})^2} - 1 \right) \ln \left| \frac{\hbar\omega - \hbar q v_{\text{F}} + \frac{\hbar^2 q^2}{2m_{\text{eff}}}}{\hbar\omega + \hbar q v_{\text{F}} + \frac{\hbar^2 q^2}{2m_{\text{eff}}}} \right| \right] \right\} \end{aligned}$$

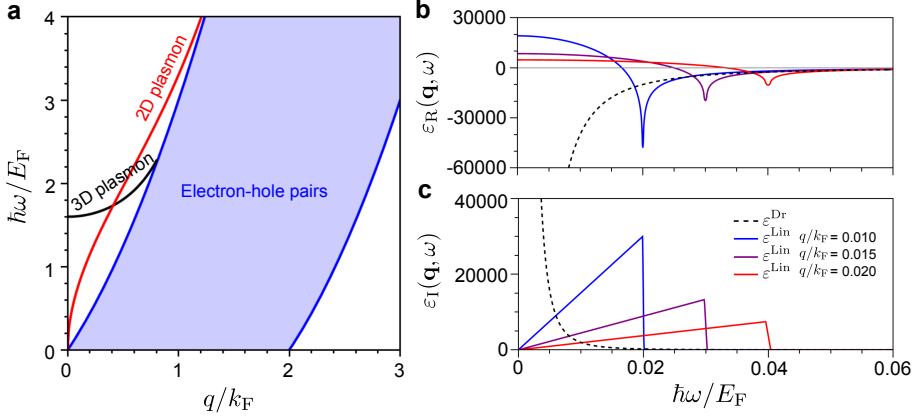


Figure 2.2: Excitation spectra and permittivities according to the RPA. a) Excitation spectra obtained from the RPA. The blue area indicates the momentum-energy region where electron-hole pairs can be excited in 2D and 3D metals. The red and black lines give the dispersion relation of the plasmon in the 2D and 3D HEG, respectively. The energy $\hbar\omega$ and wavevector q are normalized by the Fermi energy E_F and Fermi wavevector k_F , respectively. b) Real part and c) imaginary part of the Lindhard permittivity $\varepsilon^{\text{Lin}}(\mathbf{q}, \omega)$ for $q = 0.01k_F$ (blue), $q = 0.015k_F$ (purple) and $q = 0.02k_F$ (red), for a 3D HEG with plasma energy $\hbar\omega_p = 1.6E_F$. The black dashed line corresponds to the Drude permittivity $\varepsilon^{\text{Dr}}(\omega)$ with plasma energy $\hbar\omega_p = 1.6E_F$ and damping energy $\hbar\gamma = 5 \cdot 10^{-4}E_F$.

$$- \left(\frac{(\hbar\omega - \frac{\hbar^2 q^2}{2m_{\text{eff}}})^2}{(\hbar q v_F)^2} - 1 \right) \ln \left| \frac{\hbar\omega - \hbar q v_F - \frac{\hbar^2 q^2}{2m_{\text{eff}}}}{\hbar\omega + \hbar q v_F - \frac{\hbar^2 q^2}{2m_{\text{eff}}}} \right| \Bigg\}. \quad (2.24)$$

On the other hand, for $\hbar q \leq 2m_{\text{eff}}v_F$, we obtain the imaginary part given by

$$\begin{aligned} \varepsilon_I^{\text{Lin}}(\mathbf{q}, \omega) &= \frac{\pi}{2} \frac{3\omega_p^2}{(q v_F)^2} \frac{\omega}{q v_F}, \quad 0 \leq \hbar\omega \leq -\frac{\hbar^2 q^2}{2m_{\text{eff}}} + \hbar q v_F, \\ &= \frac{\pi}{2} \frac{3\omega_p^2}{(q v_F)^2} \frac{m_{\text{eff}} v_F}{\hbar q} \left[1 - \frac{(\hbar\omega - \frac{\hbar^2 q^2}{2m_{\text{eff}}})^2}{(\hbar q v_F)^2} \right], \quad \hbar q v_F - \frac{\hbar^2 q^2}{2m_{\text{eff}}} \leq \hbar\omega \leq \hbar q v_F + \frac{\hbar^2 q^2}{2m_{\text{eff}}}, \\ &= 0, \quad \hbar q v_F + \frac{\hbar^2 q^2}{2m_{\text{eff}}} \leq \hbar\omega, \end{aligned} \quad (2.25)$$

while for $\hbar q > 2m_{\text{eff}}v_F$, the imaginary part is

$$\begin{aligned} \varepsilon_I^{\text{Lin}}(\mathbf{q}, \omega) &= \frac{\pi}{2} \frac{3\omega_p^2}{(q v_F)^2} \frac{m_{\text{eff}} v_F}{\hbar q} \left[1 - \frac{(\hbar\omega - \frac{\hbar^2 q^2}{2m_{\text{eff}}})^2}{(\hbar q v_F)^2} \right], \quad \frac{\hbar^2 q^2}{2m_{\text{eff}}} - \hbar q v_F \leq \hbar\omega \leq \frac{\hbar^2 q^2}{2m_{\text{eff}}} + \hbar q v_F, \end{aligned}$$

$$= 0, \text{ elsewhere.} \quad (2.26)$$

The permittivity of a material contains information about the electronic excitations that can be directly measured in an experiment. For instance, in electron energy loss spectroscopy, an incident electron can transfer energy $\hbar\omega$ and momentum $\hbar\mathbf{q}$ to an excitation of the system. If this experiment is carried out in bulk, the loss function $-\text{Im}[\varepsilon^{-1}(\mathbf{q}, \omega)]$ is proportional to the differential cross section of electron scattering $\frac{d^2\sigma_{\text{e-ea}}}{d\omega d\Omega_{\theta\phi}}$ per solid angle $\Omega_{\theta\phi}$ [110, 111]. Since the scattering cross section of a bulk material is influenced by its excitations, the loss function can be used to analyze bulk excitations of different materials.

In particular, the loss function $-\text{Im}[\varepsilon^{\text{Lin}}(\mathbf{q}, \omega)^{-1}] = \varepsilon_{\text{I}}^{\text{Lin}}(\mathbf{q}, \omega)/[\varepsilon_{\text{R}}^{\text{Lin}}(\mathbf{q}, \omega)^2 + \varepsilon_{\text{I}}^{\text{Lin}}(\mathbf{q}, \omega)^2]$ is nonzero in the energy-momentum region delimited by the curves $\hbar\omega = \hbar q v_{\text{F}} \pm \hbar^2 q^2 / 2m_{\text{eff}}$ (indicated by the blue area in Fig. 2.2a), where $\varepsilon_{\text{I}}^{\text{Lin}}(\mathbf{q}, \omega)$ is positive. This is the necessary condition to induce a transition for an electron from a state of momentum $\hbar\mathbf{k}$ inside the Fermi's sphere of the metal, leaving a hole in this state, to an unoccupied state of momentum $\hbar(\mathbf{k} + \mathbf{q})$. Therefore, all the excitations measured in a metal for all these values of ω and \mathbf{q} correspond to electron-hole pairs [106].

Moreover, the loss function is also nonzero if both $\varepsilon_{\text{R}}^{\text{Lin}}$ and $\varepsilon_{\text{I}}^{\text{Lin}}$ vanish, and this condition gives raise to a plasmonic collective excitation (we have also justified the condition $\varepsilon = 0$ for a bulk plasmon in Sec. 1.2.1 for classical electrodynamics). The black curve in Fig. 2.2a indicates the dispersion relation $\omega(\mathbf{q})$ of the plasmon, by solving numerically $\varepsilon_{\text{R}}^{\text{Lin}}(\mathbf{q}, \omega) = 0$ in Eq. (2.24) in the region of \mathbf{q} and ω where $\varepsilon_{\text{I}}^{\text{Lin}}(\mathbf{q}, \omega) = 0$. In the $\mathbf{q} \rightarrow 0$ limit of local response, Lindhard's calculation indicates that a bulk plasmon exists at frequency $\omega = \omega_{\text{p}}$, recovering the result obtained within the Drude permittivity (Sec. 1.2.1). In contrast to the Drude model, however, RPA calculations result in a dependence on the frequency ω of the modes with increasing q . At small q , the resulting dispersion can be approximated as

$$\omega(\mathbf{q}) = \omega_{\text{p}} \left[1 + \frac{3}{10} \left(\frac{q v_{\text{F}}}{\omega_{\text{p}}} \right)^2 + \mathcal{O} \left(\frac{q v_{\text{F}}}{\omega_{\text{p}}} \right)^4 \right]. \quad (2.27)$$

In this low- q regime, the plasmonic resonance of a HEG appears as a peak of zero width¹, because the loss function diverges under the condition $\varepsilon_{\text{I}}^{\text{Lin}} = \varepsilon_{\text{R}}^{\text{Lin}} = 0$. However, the plasmon is not undamped for all q . As shown in Fig. 2.2a, the dispersion of the plasmon (black curve) increases slower than the boundary of the region of the electron-hole excitations (blue area). Subsequently, at momenta $\hbar q \gtrsim \frac{\hbar\omega}{v_{\text{F}}}$, electron-hole pairs can be excited at the same frequencies $\omega(\mathbf{q})$ of the plasmon, which opens a decay channel for the collective excitation. Therefore, the

¹ In real metals, plasmonic resonances have a finite linewidth even in the $q \rightarrow 0$ limit. As we discuss thoroughly in Chapter 3, the discrepancy between this theoretical result and reality emerges because the HEG is a too simple model for real metals.

plasmon acquires a finite lifetime under these circumstancesⁱⁱ.

To analyze the relation between the Drude [Eq. (1.25)] and Lindhard permittivities, we plot their real and imaginary parts in Figs. 2.2b and c, respectively. We show $\varepsilon^{\text{Lin}}(\omega)$ at small values of $q = 0.01k_{\text{F}}$ (blue), $0.015k_{\text{F}}$ (purple) and $0.02k_{\text{F}}$ (red), to study the $q \rightarrow 0$ limit of local response. The Drude permittivity $\varepsilon^{\text{Dr}}(\omega)$ is local and does not depend on \mathbf{q} . We observe that the real part of the Lindhard permittivity approaches $\varepsilon_{\text{R}}^{\text{Dr}}(\omega)$ at large frequencies $\omega \gg q/v_{\text{F}}$. By decreasing q , the two permittivities become more similar, and Eq. (2.24) indicates that in the local limit they are indeed equivalent,

$$\lim_{q \rightarrow 0} \varepsilon_{\text{R}}^{\text{Lin}}(\mathbf{q}, \omega) = 1 - \frac{\omega_{\text{p}}^2}{\omega^2} = \varepsilon_{\text{R}}^{\text{Dr}}(\omega). \quad (2.28)$$

From this perspective, the Lindhard permittivity can be understood as a non-local extension of the Drude permittivity.

However, the two models give a very different description of the damping phenomena in a metal, as shown in Fig. 2.2c. As mentioned previously, the imaginary part of the Lindhard permittivity describes the excitation of electron-hole pairs. In the HEG, these excitations are only possible with a finite momentum transfer $\hbar\mathbf{q}$, and therefore, $\varepsilon_{\text{I}}^{\text{Lin}}$ vanishes completely for all frequencies in the $q \rightarrow 0$ limit. In contrast, in the Drude model, the friction parameter γ is introduced to represent the damping of the electrons. We plot the imaginary part of the Drude permittivity in 2.2c for a small damping of value $\hbar\gamma = 5 \cdot 10^{-4}E_{\text{F}}$ (E_{F} being the Fermi energy of the metal), and a completely different dependence on ω is shown as compared to the Lindhard permittivity. Thus, there is no correspondence between the two models according to the imaginary part of the permittivity.

2.2.2 2D homogeneous electron gas

A decade after the publication of the Lindhard permittivity, Stern followed the same approach to calculate the permittivity of a HEG confined in a plane [48]. This work showed that plasmons in 2D electron gases are a very promising alternative to those in bulk metals because of their very different properties. Since then, plasmons have been extensively studied in 2D materials including graphene [112] and in systems exploiting electronic surface states, such as topological insulators [113, 114].

According to the calculation by Stern, the response function of a 2D HEG under

ⁱⁱ Inside the region of electron-hole excitations, the strict condition $\varepsilon^{\text{Lin}}(\mathbf{q}, \omega) = 0$ for the existence of plasmons cannot be satisfied, because the imaginary part of the permittivity is positive, i.e. $\varepsilon_{\text{I}}^{\text{Lin}}(\mathbf{q}, \omega) > 0$. However, the loss function still contains a clear peak of finite linewidth at frequencies where $\varepsilon_{\text{R}}^{\text{Lin}}(\mathbf{q}, \omega) = 0$. Thus, inside the electron-hole region we still consider the existence of plasmons for frequencies where the real part of the permittivity vanishes, even if the imaginary part is nonzero.

the RPA leads to the expression [48]

$$\chi_{\text{R}}^{\text{RPA-2D}}(\mathbf{q}_{\parallel}, \omega) = \frac{m_{\text{eff}}k_{\text{F}}}{\pi\hbar^2q_{\parallel}} \left[-\frac{q_{\parallel}}{k_{\text{F}}} + \Theta(\zeta_{+}^2 - 1)\sqrt{\zeta_{+}^2 - 1} - \text{sgn}(\zeta_{-})\Theta(\zeta_{-}^2 - 1)\sqrt{\zeta_{-}^2 - 1} \right], \quad (2.29\text{a})$$

$$\chi_{\text{I}}^{\text{RPA-2D}}(\mathbf{q}_{\parallel}, \omega) = \frac{m_{\text{eff}}k_{\text{F}}}{\pi\hbar^2q_{\parallel}} \left[\Theta(1 - \zeta_{+}^2)\sqrt{1 - \zeta_{+}^2} - \Theta(1 - \zeta_{-}^2)\sqrt{1 - \zeta_{-}^2} \right], \quad (2.29\text{b})$$

where $q_{\parallel} = |\mathbf{q}_{\parallel}|$ is the magnitude of the 2D wavevector $\mathbf{q}_{\parallel} = (q_x, q_y)$, Θ denotes the Heaviside step function and

$$\zeta_{\pm} = \frac{\omega}{v_{\text{F}}q_{\parallel}} \pm \frac{q_{\parallel}}{2k_{\text{F}}}. \quad (2.30)$$

The permittivity $\varepsilon^{\text{RPA-2D}}(\mathbf{q}_{\parallel}, \omega)$ of these materials is then calculated straightforwardly with Eq. (2.22), using the 2D Fourier transform of the Coulomb potential

$$V_{\text{Cou}}(\mathbf{q}_{\parallel}) = \frac{e^2}{2\varepsilon_0q_{\parallel}}. \quad (2.31)$$

Following the same analysis carried out for 3D metals, the result of the response function allows obtaining the excitation spectra of 2D materials with the loss function $-\text{Im}[\varepsilon^{-1}(\mathbf{q}_{\parallel}, \omega)]$. The momentum $\hbar\mathbf{q}_{\parallel}$ and energy $\hbar\omega$ required to excite electron-hole pairs are determined by the imaginary part of the permittivity under the condition $\varepsilon_{\text{I}}^{\text{RPA-2D}}(\mathbf{q}_{\parallel}, \omega) > 0$. Their corresponding spectrum is delimited by the curves $\hbar\omega = \hbar q_{\parallel}v_{\text{F}} \pm \hbar^2q_{\parallel}^2/2m_{\text{eff}}$, which is exactly the same as for the 3D HEG. Therefore, the properties of the electron-hole pairs do not strongly depend on the dimensionality of the material. More importantly, the dispersion of the plasmons, given by the condition $\varepsilon_{\text{R}}^{\text{RPA-2D}}(\mathbf{q}_{\parallel}, \omega) = 0$, is very different from the 3D counterpart as plotted in Fig. 2.2a (red curve). In the low- q_{\parallel} regime, the dispersion of 2D plasmons (2DP) can be approximated to

$$\omega_{\text{2DP}}^2(\mathbf{q}_{\parallel}) = \frac{e^2E_{\text{F}}}{2\pi\varepsilon_0\hbar^2}q_{\parallel} + \frac{3}{4}v_{\text{F}}^2q_{\parallel}^2 + \mathcal{O}(q_{\parallel}^3). \quad (2.32)$$

Whereas in bulk metals the non-retarded plasmon frequency tends to the finite value ω_{p} in the $q \rightarrow 0$ limit and has a weak dispersion at small q (Fig. 2.2a), the 2D plasmon frequency reaches zero in the $q_{\parallel} \rightarrow 0$ limit and it scales as $\omega_{\text{2DP}} \propto \sqrt{q_{\parallel}}$. According to this dispersion relation, plasmons can be excited even in the THz and far-infrared ranges at relatively large q_{\parallel} , and thus 2D systems increase the range of applicability of this type of excitations from 3D metals.

2.2.3 A 2D layer over a 3D bulk substrate: acoustic surface plasmons

Several metal surfaces, such as those of beryllium or of the noble metals Cu, Ag or Au [115], support electronic states that are strongly localized in the metal-vacuum interface, known as the Shockley surface states. Due to the strong localization of the Shockley states, the electrons that occupy these bands can be considered as forming a 2D gas placed over a semi-infinite 3D HEG. Although a rigorous description of the excitation spectra requires the complete information about the band structure of the corresponding metal surfaces, a simple model based on the RPA already describes some properties of the excitations that have been verified experimentally [45, 116].

We consider a simple model where the gas comprising all bulk electrons is located at $z < 0$, whereas the sheet filled by the electrons in the Shockley states is in the plane $z = z_s$. Following linear response theory, we can relate the induced electronic densities in the 2D ($\rho_{\text{ind}}^{2\text{D}}$) and 3D ($\rho_{\text{ind}}^{3\text{D}}$) gases with their corresponding response functions $\chi^{2\text{D}}(\mathbf{q}_{\parallel}, \omega)$ and $\chi^{3\text{D}}(\mathbf{q}_{\parallel}, \omega)$. We write these expressions by performing the Fourier transform in the direction parallel to the interface (taking advantage of the translational invariance in this direction), but leaving the dependence over z explicitly, which gives [117]

$$\rho_{\text{ind}}^{2\text{D}}(z, \mathbf{q}_{\parallel}, \omega) = \left[V_{\text{ext}}(z, \mathbf{q}_{\parallel}, \omega) + \int V_{\text{Cou}}(z, z', \mathbf{q}_{\parallel}) \rho_{\text{ind}}^{3\text{D}}(z', \mathbf{q}_{\parallel}, \omega) dz' \right] \times \chi^{2\text{D}}(\mathbf{q}_{\parallel}, \omega) \delta(z - z_s), \quad (2.33a)$$

$$\rho_{\text{ind}}^{3\text{D}}(z, \mathbf{q}_{\parallel}, \omega) = \int \left[V_{\text{ext}}(z', \mathbf{q}_{\parallel}, \omega) + \int V_{\text{Cou}}(z', z'', \mathbf{q}_{\parallel}) \rho_{\text{ind}}^{2\text{D}}(z'', \mathbf{q}_{\parallel}, \omega) dz'' \right] \times \chi^{3\text{D}}(z, z', \mathbf{q}_{\parallel}, \omega) dz', \quad (2.33b)$$

with the Fourier transform of the Coulomb potential

$$V_{\text{Cou}}(z, z', \mathbf{q}_{\parallel}) = \frac{e^2}{2\varepsilon_0 q_{\parallel}} e^{-q_{\parallel} |z - z'|}. \quad (2.34)$$

In order to obtain the excitation spectra of the metallic surface, we need to focus on the electronic density of the 2D gas. These electrons are exposed to the external potential and also to the Coulomb interactions from the electrons in the metallic substrateⁱⁱⁱ. By combining Eqs. (2.33a) and (2.33b), we find that the induced density in the 2D HEG is proportional to the effective external potential \tilde{V}_{ext} given by [117]

$$\tilde{V}_{\text{ext}}(z, \mathbf{q}_{\parallel}, \omega) = V_{\text{ext}}(z, \mathbf{q}_{\parallel}, \omega)$$

ⁱⁱⁱ There are also electron-electron interactions within the 2D HEG, but the effects of these interactions are already included into the response function $\chi^{2\text{D}}(\mathbf{q}_{\parallel}, \omega)$ of the 2D system.

$$+ \int \int V_{\text{Cou}}(z, z', \mathbf{q}_{\parallel}) \chi^{3\text{D}}(z', z'', \mathbf{q}_{\parallel}, \omega) V_{\text{ext}}(z'', \mathbf{q}_{\parallel}, \omega) dz' dz''. \quad (2.35)$$

Indeed, the density $\rho_{\text{ind}}^{2\text{D}}$ can be written in terms of this potential as

$$\rho_{\text{ind}}^{2\text{D}}(z, \mathbf{q}_{\parallel}, \omega) = \chi^{\text{eff}}(\mathbf{q}_{\parallel}, \omega) \tilde{V}_{\text{ext}}(z, \mathbf{q}_{\parallel}, \omega) \delta(z - z_s). \quad (2.36)$$

Importantly, the response of the 2D HEG to the effective external potential $\tilde{V}_{\text{ext}}(z, \mathbf{q}_{\parallel}, \omega)$ is fully determined by the effective response function

$$\chi^{\text{eff}}(\mathbf{q}_{\parallel}, \omega) = \frac{\chi^{2\text{D}}(\mathbf{q}_{\parallel}, \omega)}{1 - [W(\mathbf{q}_{\parallel}, \omega) - V_{\text{Cou}}(z_s, z_s, \mathbf{q}_{\parallel})] \chi^{2\text{D}}(\mathbf{q}_{\parallel}, \omega)}, \quad (2.37)$$

where $W(\mathbf{q}_{\parallel}, \omega)$ is the so-called screened interaction. According to the last expression, if the response function of the 2D HEG $\chi^{2\text{D}}(\mathbf{q}_{\parallel}, \omega)$ is known, we can directly obtain the response of the system in the presence of the 3D semi-infinite HEG. However, as discussed in detail above, it is difficult to obtain the response function of an interacting system. To simplify the calculations, we can use the RPA, where Eq. (2.21) gives the relation between the response function of the interacting system $\chi^{2\text{D}}$ and the response function corresponding to the non-interacting system $\chi_{2\text{D}}^0$ (which can be calculated with Eq. (2.11) using single-electron orbitals). With Eq. (2.21), we can simplify Eq. (2.37) to write it in terms of the response function of the non-interacting system $\chi_{2\text{D}}^0$ as

$$\chi^{\text{eff}}(\mathbf{q}_{\parallel}, \omega) = \frac{\chi_{2\text{D}}^0(\mathbf{q}_{\parallel}, \omega)}{1 - W(\mathbf{q}_{\parallel}, \omega) \chi_{2\text{D}}^0(\mathbf{q}_{\parallel}, \omega)}. \quad (2.38)$$

Last, in order to calculate the effective response function with Eq. (2.38), we must know how the screened interaction term $W(\mathbf{q}_{\parallel}, \omega)$ is evaluated. In the absence of the substrate metal, the term $W(\mathbf{q}_{\parallel}, \omega)$ that mediates the interaction between electrons is equal to $V_{\text{Cou}}(\mathbf{q}_{\parallel})$, so that we recover Eq. (2.21). However, by adding the metallic substrate, $W(\mathbf{q}_{\parallel}, \omega)$ transforms to

$$W(\mathbf{q}_{\parallel}, \omega) = V_{\text{Cou}}(z_s, z_s, \mathbf{q}_{\parallel}) + \int \int V_{\text{Cou}}(z_s, z', \mathbf{q}_{\parallel}) \chi^{3\text{D}}(z', z'', \mathbf{q}_{\parallel}, \omega) V_{\text{Cou}}(z'', z_s, \mathbf{q}_{\parallel}) dz' dz''. \quad (2.39)$$

According to this equation, the main effect of the bulk electrons is to screen the interaction between the electrons of the surface, as given by the second term in the right handside. Further, in the same manner as in the derivation of Eq. (2.22), we can describe the excitation spectra of the metallic surface in terms of the screened Coulomb interaction according to the permittivity

$$\varepsilon_{\text{eff}}(\mathbf{q}_{\parallel}, \omega) = 1 - W(\mathbf{q}_{\parallel}, \omega) \chi_{2\text{D}}^0(\mathbf{q}_{\parallel}, \omega). \quad (2.40)$$

As analyzed for the 2D and 3D HEGs, the plasmonic excitations of the system are given by the zeroes of the real part of the permittivity. Interestingly, by placing a 2D layer over a 3D substrate, the effective permittivity $\varepsilon_{\text{eff}}(\mathbf{q}_{\parallel}, \omega)$ has two zeroes in the $q_{\parallel} \rightarrow 0$ limit. The first zero occurs at high frequencies. Under the condition $\omega \gg v_{\text{F}}q_{\parallel}$, the following limits of the response function and the screening interactions are known [117],

$$\lim_{q_{\parallel} \rightarrow 0} \chi_{2\text{D}}^0(\mathbf{q}_{\parallel}, \omega \gg v_{\text{F}}q_{\parallel}) = \frac{1}{V_{\text{Cou}}(\mathbf{q}_{\parallel})} \frac{\omega_{2\text{DP}}^2}{\omega^2}, \quad (2.41\text{a})$$

$$\lim_{q_{\parallel} \rightarrow 0} W(\mathbf{q}_{\parallel}, \omega \gg v_{\text{F}}q_{\parallel}) = V_{\text{Cou}}(\mathbf{q}_{\parallel}) \frac{\omega^2}{\omega^2 - \omega_{\text{SP}}^2}. \quad (2.41\text{b})$$

Thus, the first zero of the permittivity [Eq. (2.40)] occurs at the frequency

$$\omega^2 = \omega_{\text{SP}}^2 + \omega_{2\text{DP}}^2, \quad (2.42)$$

which is associated to in-phase collective oscillations of the surface and bulk electrons.

The other zero of the permittivity is associated to the out-of-phase collective oscillations of these electrons. The dispersion of the second excitation is [117]

$$\omega = \mathbf{a}v_{\text{F}}q_{\parallel}, \quad (2.43)$$

which follows a linear scaling of ω with q_{\parallel} , instead of the $\omega \propto \sqrt{q_{\parallel}}$ dependence observed for the single 2D HEG. Due to the linear dispersion relation of Eq. (2.43), these waves that appear in metallic surfaces with surface and bulk electronic states are called acoustic surface plasmons. The parameter \mathbf{a} that mediates the velocity of these acoustic waves is of the order of 1, and its exact value depends on the electronic structure of the metal and on the position of the 2D sheet with respect to the bulk metal. In the simple model that we have outlined in this section, this value can be written as [117]

$$\mathbf{a} = \sqrt{1 + \frac{\mathcal{I}^2}{\pi[\pi + 2\mathcal{I}]}} \quad (2.44)$$

where $\mathcal{I} = \lim_{q_{\parallel} \rightarrow 0} W(\mathbf{q}_{\parallel}, \omega \rightarrow 0)$ is defined to be the $q_{\parallel} \rightarrow 0$ limit of the static screening (for $\omega = 0$) induced by the bulk particles. $\mathbf{a}v_{\text{F}}$ is much smaller than the speed of light, and thus acoustic surface plasmons have a much larger wavevector than electromagnetic waves in vacuum, and also a larger one than the 2D plasmon with $\omega \propto \sqrt{q_{\parallel}}$ dispersion. Hence, acoustic surface plasmons confine electromagnetic energy in even smaller dimensions than the conventional plasmons.

2.3 *Ab initio* methods

In real metals, electrons do not behave like in a homogeneous gas, but interact with nuclei in a lattice. Thus, a more precise description of the excitation spectra of metals must include the interactions of electrons with other electrons and with the electrostatic potential of the nuclei. Solving the Schrödinger equation to find the wavefunction that depends on the position \mathbf{r}_i of all these $\sim 10^{23}$ particles is impossible with the current technology, so that Density Functional Theory (DFT) is used instead. This theory describes the system through a ground-state electronic density that depends on one position vector \mathbf{r} . Further, Time Dependent Density Functional Theory (TDDFT) can be used to study the response of the metal to a time-dependent external perturbation. This section explains how *ab initio* methods based on TDDFT can be used in the linear regime to calculate the response function $\chi(\mathbf{q}, \omega)$ of metals, which allows us to obtain the properties of excitations in metallic systems.

2.3.1 Density Functional Theory

Born-Oppenheimer approximation

The wavefunction Ψ associated to all particles in a metal is the solution of the time-independent Schrödinger equation

$$\hat{\mathcal{H}}_{\text{met}} \Psi(\mathbf{r}_1, \mathbf{r}_2, \dots, \mathbf{r}_{N_{\text{el}}}, \mathbf{R}_1, \mathbf{R}_2, \dots, \mathbf{R}_{N_{\text{nuc}}}) = \hbar\omega \Psi(\mathbf{r}_1, \mathbf{r}_2, \dots, \mathbf{r}_{N_{\text{el}}}, \mathbf{R}_1, \mathbf{R}_2, \dots, \mathbf{R}_{N_{\text{nuc}}}), \quad (2.45)$$

where \mathbf{r}_i and \mathbf{R}_A are the position coordinates of the N_{el} electrons and N_{nuc} nuclei, respectively. The Hamiltonian of the metal $\hat{\mathcal{H}}_{\text{met}}$ reads

$$\begin{aligned} \hat{\mathcal{H}}_{\text{met}} &= \hat{T}_{\text{el}} + \hat{T}_{\text{nuc}} + \hat{V}_{\text{el-el}} + \hat{V}_{\text{nuc-nuc}} + \hat{V}_{\text{nuc-el}} \\ &= \sum_i -\frac{\hbar^2}{2m_e} \nabla_i^2 - \sum_A \frac{\hbar^2}{2M_A} \nabla_A^2 + \frac{e^2}{4\pi\epsilon_0} \frac{1}{2} \sum_{i \neq j} \frac{1}{|\mathbf{r}_i - \mathbf{r}_j|} \\ &\quad - \frac{e^2}{4\pi\epsilon_0} \sum_{i,A} \frac{Z_A}{|\mathbf{r}_i - \mathbf{R}_A|} + \frac{e^2}{4\pi\epsilon_0} \frac{1}{2} \sum_{A \neq B} \frac{Z_A Z_B}{|\mathbf{R}_A - \mathbf{R}_B|}, \end{aligned} \quad (2.46)$$

where the subindexes i and j refer to electrons, while A and B correspond to nuclei. The first two terms of the Hamiltonian, \hat{T}_{el} and \hat{T}_{nuc} , are the kinetic energy operators of the electrons of mass m_e and of the nuclei with mass M_A and atomic number Z_A , respectively. The other three terms represent the Coulomb interactions between all the particles, where $\hat{V}_{\text{el-el}}$ is the potential energy due to the interactions between different electrons, the term $\hat{V}_{\text{nuc-el}}$ corresponds to the interactions of electrons with nuclei, and the last term $\hat{V}_{\text{nuc-nuc}}$ accounts for the interaction between different nuclei.

The Hamiltonian of Eq. (2.46) is not separable into the single-particle coordinates \mathbf{r}_i or \mathbf{R}_A due to the interaction terms. Even in the simplest

scenario of two interacting electrons in an atom, the Schrödinger equation is not analytically solvable and numerical methods are necessary. The computational cost of this task increases exponentially with the number of particles, and thus further approximations must be made for a metal. As a first step, a widely-used approximation was first proposed by M. Born and R. Oppenheimer [118], by considering that the ratio between the masses of the electrons and of the nuclei is of the order $\frac{m_e}{M_A} \sim 10^{-3}$. The Born-Oppenheimer approximation consists in separating the wavefunctions into two parts, one associated to the electrons and the other one to the nuclei, in the form $\Psi(\mathbf{r}_1, \mathbf{r}_2, \dots, \mathbf{r}_{N_{\text{el}}}, \mathbf{R}_1, \mathbf{R}_2, \dots, \mathbf{R}_{N_{\text{nuc}}}) \approx \phi(\mathbf{r}_1, \mathbf{r}_2, \dots, \mathbf{r}_{N_{\text{el}}})\Phi(\mathbf{R}_1, \mathbf{R}_2, \dots, \mathbf{R}_{N_{\text{nuc}}})$. Due to the large mass of the nuclei, the contribution of their kinetic energy \hat{T}_{nuc} is small, and therefore it is assumed that the electronic part of the wavefunction $\phi(\mathbf{r}_1, \mathbf{r}_2, \dots, \mathbf{r}_{N_{\text{el}}})$ is not affected by the dynamics of the nuclei encoded in the wavefunction $\Phi(\mathbf{R}_1, \mathbf{R}_2, \dots, \mathbf{R}_{N_{\text{nuc}}})$. All the nuclei can therefore be considered to be at fixed positions inside the lattice. Hence, the electronic wavefunction satisfies the Schrödinger equation with the Hamiltonian

$$\hat{\mathcal{H}}_{\text{el}} = \hat{T}_{\text{el}} + \hat{V}_{\text{ext}} + \hat{V}_{\text{el-el}} = -\frac{\hbar^2}{2m_e} \sum_i \nabla_i^2 - \frac{e^2}{4\pi\epsilon_0} \sum_{i,A} \frac{Z_A}{|\mathbf{r}_i - \mathbf{R}_A|} + \frac{e^2}{4\pi\epsilon_0} \frac{1}{2} \sum_{i \neq j} \frac{1}{|\mathbf{r}_i - \mathbf{r}_j|}. \quad (2.47)$$

Since the coordinates \mathbf{R}_A are not longer dynamical variables of the problem, the electrostatic potential caused by the nuclei is treated as an external contribution in \hat{V}_{ext} . However, the term $\hat{V}_{\text{el-el}}$ that connects the positions \mathbf{r}_i of all electrons still remains, which makes further approximations necessary to separate the Hamiltonian into terms with a single position \mathbf{r}_i and to solve the electronic problem.

Hohenberg-Kohn theorems and Kohn-Sham equations

The basic idea of DFT is to describe the system with the ground-state electronic density $\rho_0(\mathbf{r})$ instead of with all the eigenfunctions from the Hamiltonian in Eq. (2.47). This density is defined from the ground-state wavefunction $\phi_0(\mathbf{r}_i)$ as

$$\rho_0(\mathbf{r}) = N_{\text{el}} \int d\mathbf{r}_2 \int d\mathbf{r}_3 \cdots \int d\mathbf{r}_{N_{\text{el}}} |\phi_0(\mathbf{r}, \mathbf{r}_2, \mathbf{r}_3, \dots, \mathbf{r}_{N_{\text{el}}})|^2, \quad (2.48)$$

and is normalized so that the total number of electrons in the system is N_{el} , i.e. it satisfies $\int \rho_0(\mathbf{r}) d\mathbf{r} = N_{\text{el}}$. The importance of this function in the full description of the electronic system is expressed by the two Hohenberg-Kohn theorems [119], the first of which states

- First Hohenberg-Kohn theorem: The external potential (corresponding to the nuclei) of the system is a unique functional of the ground-state density (up to a constant): $\hat{V}_{\text{ext}}[\rho_0(\mathbf{r})]$.

Among the three terms of the electronic Hamiltonian of Eq. (2.47), only the external potential \hat{V}_{ext} depends on the system to be analyzed (i.e. on the position and atomic number of the nuclei), while \hat{T}_{el} and $\hat{V}_{\text{el-el}}$ are universal operators.

According to the first Hohenberg-Kohn theorem, the ground-state density fully determines \hat{V}_{ext} , and thus, there is a one-to-one correspondence between $\rho_0(\mathbf{r})$ and the Hamiltonian $\hat{\mathcal{H}}_{\text{el}}[\rho_0(\mathbf{r})]$. As a consequence, all excited states of the Schrödinger equation are also unique functionals of $\rho_0(\mathbf{r})$ and therefore, all the properties of the system can be extracted from this function. Further, the ground-state density is a much simpler mathematical object than the wavefunctions because it is a function of just a single position vector \mathbf{r} . The method to find $\rho_0(\mathbf{r})$ is specified in the second theorem.

- Second Hohenberg-Kohn theorem: The ground-state energy can be obtained using the variational principle. Accordingly, the actual ground-state density of the system is the function that minimizes the functional of the ground-state energy, $\hbar\omega_0[\rho_0(\mathbf{r})]$.

In order to fulfill this minimization procedure, we first write the ground-state energy in the functional form

$$\hbar\omega_0[\rho_0(\mathbf{r})] = \langle \phi_0 | \hat{T}_{\text{el}} + \hat{V}_{\text{ext}} + \hat{V}_{\text{el-el}} | \phi_0 \rangle = \hat{T}_{\text{el}}[\rho_0(\mathbf{r})] + \hat{V}_{\text{el-el}}[\rho_0(\mathbf{r})] + \int V_{\text{ext}}(\mathbf{r})\rho_0(\mathbf{r})d\mathbf{r}. \quad (2.49)$$

This functional must be minimized under all functions $\rho_0(\mathbf{r})$, with the constraint that $\rho_0(\mathbf{r})$ must be normalized according to $\int \rho_0(\mathbf{r})d\mathbf{r} = N_{\text{el}}$. By using Lagrange multipliers Λ , the ground-state density is given by the equation

$$\frac{\delta}{\delta\rho_0(\mathbf{r})} \left[\hbar\omega_0[\rho_0(\mathbf{r})] - \Lambda \int \rho_0(\mathbf{r}')d\mathbf{r}' \right] = 0 \Leftrightarrow \frac{\delta T_{\text{el}}[\rho_0(\mathbf{r})]}{\delta\rho_0(\mathbf{r})} + \frac{\delta V_{\text{el-el}}[\rho_0(\mathbf{r})]}{\delta\rho_0(\mathbf{r})} + V_{\text{ext}}(\mathbf{r}) = \Lambda. \quad (2.50)$$

The main difficulty of this approach is that the exact analytical form of the electron-electron interaction functional, $V_{\text{el-el}}[\rho_0(\mathbf{r})]$, is unknown. In response to this, W. Kohn and L. J. Sham proposed an alternative approach to the problem based on the Hohenberg-Kohn theorems.

The key idea of the Kohn-Sham (KS) approach [120] is to replace the Hamiltonian of interacting particles [Eq. (2.47)] with an effective Hamiltonian of a fictitious non-interacting system that has the same ground-state density as the original system, given by

$$\hat{\mathcal{H}}_{\text{KS}} = \sum_i \left(-\frac{\hbar^2}{2m_e} \nabla_i^2 + V_{\text{KS}}(\mathbf{r}_i) \right). \quad (2.51)$$

The electron-electron interactions are not completely eliminated because their effects are introduced inside the effective KS potential $V_{\text{KS}}(\mathbf{r})$ to which each electron is subjected. Further, $\hat{\mathcal{H}}_{\text{KS}}$ is separable over all variables \mathbf{r}_i corresponding to individual electrons, and thus the single-particle Schrödinger equation of the KS Hamiltonian gives the single-particle KS orbitals $\phi_i^{\text{KS}}(\mathbf{r})$ and KS energies $\hbar\omega_i^{\text{KS}}$,

$$-\frac{\hbar^2}{2m_e} \nabla^2 \phi_i^{\text{KS}}(\mathbf{r}) + V_{\text{KS}}(\mathbf{r})\phi_i^{\text{KS}}(\mathbf{r}) = \hbar\omega_i^{\text{KS}}\phi_i^{\text{KS}}(\mathbf{r}). \quad (2.52)$$

With these orbitals, all the wavefunctions of the system can be expressed as a Slater determinant evaluated as

$$\phi(\mathbf{r}_1, \mathbf{r}_2, \dots, \mathbf{r}_{N_{\text{el}}}) = \frac{1}{\sqrt{N_{\text{el}}!}} \begin{vmatrix} \phi_1^{\text{KS}}(\mathbf{r}_1) & \phi_2^{\text{KS}}(\mathbf{r}_1) & \cdots & \phi_{N_{\text{el}}}^{\text{KS}}(\mathbf{r}_1) \\ \phi_1^{\text{KS}}(\mathbf{r}_2) & \phi_2^{\text{KS}}(\mathbf{r}_2) & \cdots & \phi_{N_{\text{el}}}^{\text{KS}}(\mathbf{r}_2) \\ \vdots & \vdots & \ddots & \vdots \\ \phi_1^{\text{KS}}(\mathbf{r}_{N_{\text{el}}}) & \phi_2^{\text{KS}}(\mathbf{r}_{N_{\text{el}}}) & \cdots & \phi_{N_{\text{el}}}^{\text{KS}}(\mathbf{r}_{N_{\text{el}}}) \end{vmatrix}. \quad (2.53)$$

In order to find the expression of the KS potential, we need to know the ground-state energy functional $\hbar\omega_0[\rho_0(\mathbf{r})]$ first. We first note that, since the electrons are considered to be independent within the KS approach, the ground-state density is simplified by introducing Eq. (2.53) into Eq. (2.48), which leads to the expression

$$\rho_0(\mathbf{r}) = \sum_i^{\text{occ.}} |\phi_i^{\text{KS}}(\mathbf{r})|^2. \quad (2.54)$$

Thus, the ground-state density of the system is the sum of the probability densities of the occupied individual KS orbitals. With the help of this expression, the functional $\hbar\omega_0^{\text{KS}}[\rho_0(\mathbf{r})]$ under the KS approach can be written as [120–122]

$$\begin{aligned} \hbar\omega_0^{\text{KS}}[\rho_0(\mathbf{r})] = & -\frac{\hbar^2}{2m_e} \int [\phi_i^{\text{KS}}(\mathbf{r})]^* \nabla^2 \phi_i^{\text{KS}}(\mathbf{r}) d\mathbf{r} + \int V_{\text{ext}}(\mathbf{r}) \rho_0(\mathbf{r}) d\mathbf{r} \\ & + \int \frac{\rho_0(\mathbf{r}) \rho_0(\mathbf{r}')}{|\mathbf{r} - \mathbf{r}'|} d\mathbf{r} d\mathbf{r}' + \hbar\omega_{\text{xc}}[\rho_0(\mathbf{r})]. \end{aligned} \quad (2.55)$$

The first term in the right handside corresponds to the kinetic energy of a non-interacting system. The contribution of the external potential (of the nuclei) is included in the second term in the same way as in Eq. (2.49). Part of the potential energy due to electron-electron interactions is introduced within the Hartree energy functional, $\hbar\omega_{\text{Har}}[\rho_0(\mathbf{r})] = \int \frac{\rho_0(\mathbf{r}) \rho_0(\mathbf{r}')}{|\mathbf{r} - \mathbf{r}'|} d\mathbf{r} d\mathbf{r}'$. However, these kinetic and potential functionals do not account for all the effects of electronic interactions, and the remaining contributions are included in the exchange-correlation functional $\hbar\omega_{\text{xc}}[\rho_0(\mathbf{r})]$. This functional is defined to be the necessary term for the ground-state energy functional in Eq. (2.55) to give the actual value of the energy, and thus, the functional of Eq. (2.55) is exact in theory. Nevertheless, the main problem of the KS approach is that the exact form of the exchange-correlation functional is unknown. Thus, in practical calculations we cannot obtain the exact KS orbitals and energies from Eq. (2.55) directly, and we must make approximations for the exchange-correlation term, as we discuss below.

The equations that the KS orbitals must satisfy are obtained by applying the second Hohenberg-Kohn theorem into Eq. (2.55), i.e. these equations are obtained by minimizing the functional of Eq. (2.55) over the ground-state density $\rho_0(\mathbf{r})$. An advantage of the KS approach is that this minimization procedure can be carried out more easily by using single-electron KS orbitals $\phi_i^{\text{KS}}(\mathbf{r})$, because they are related with the ground-state density according to Eq. (2.54). By

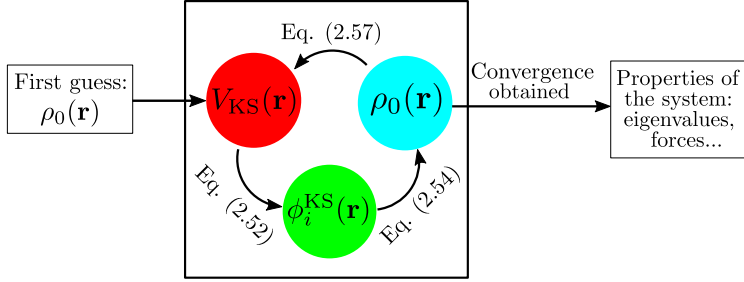


Figure 2.3: Graphical representation of the self-consistent calculations within DFT. An initial guess of the ground-state density $\rho_0(\mathbf{r})$ is introduced in the main self-consistent loop, schematized by the box in the center. In this loop, Eqs. (2.52), (2.54) and (2.57) are solved repeatedly to obtain the actual KS potential $V_{\text{KS}}(\mathbf{r})$, KS orbitals $\phi_i^{\text{KS}}(\mathbf{r})$ and ground-state density $\rho_0(\mathbf{r})$. After obtaining convergence, the last function $\rho_0(\mathbf{r})$ exits the loop and is used to calculate different physical properties of the system.

using the method of Lagrange multipliers (for convenience, we use $\hbar\omega_i^{\text{KS}}$ as multipliers) with the constraint that the KS orbitals must be normalized to unity, i.e. $\int \phi_i^{\text{KS}}(\mathbf{r})[\phi_i^{\text{KS}}(\mathbf{r})]^* d\mathbf{r} = 1$, we obtain [121]

$$\begin{aligned} & \frac{\delta}{\delta[\phi_i^{\text{KS}}(\mathbf{r})]^*} \left[\hbar\omega_0^{\text{KS}}[\rho_0(\mathbf{r})] - \hbar\omega_i^{\text{KS}} \int \phi_i^{\text{KS}}(\mathbf{r})[\phi_i^{\text{KS}}(\mathbf{r})]^* d\mathbf{r} \right] = 0 \\ \Leftrightarrow & -\frac{\hbar^2}{2m_e} \nabla^2 \phi_i^{\text{KS}}(\mathbf{r}) + V_{\text{ext}}(\mathbf{r})\phi_i^{\text{KS}}(\mathbf{r}) + \phi_i^{\text{KS}}(\mathbf{r}) \int \frac{\rho_0(\mathbf{r}')}{|\mathbf{r} - \mathbf{r}'|} d\mathbf{r}' \\ & + \phi_i^{\text{KS}}(\mathbf{r}) \frac{\delta \hbar\omega_{\text{xc}}[\rho_0(\mathbf{r})]}{\delta \rho_0(\mathbf{r})} = \hbar\omega_i^{\text{KS}} \phi_i^{\text{KS}}(\mathbf{r}). \end{aligned} \quad (2.56)$$

By comparing this last expression, obtained by the variational principle, with Eq. (2.52), we observe that the KS orbitals $\phi_i^{\text{KS}}(\mathbf{r})$ satisfy the Schrödinger equation with the KS Hamiltonian $\hat{\mathcal{H}}_{\text{KS}}$ from Eq. (2.51) with the potential given by

$$V_{\text{KS}}(\mathbf{r}) = V_{\text{ext}}(\mathbf{r}) + \underbrace{\int \frac{\rho_0(\mathbf{r}')}{|\mathbf{r} - \mathbf{r}'|} d\mathbf{r}'}_{V_{\text{Har}}[\rho_0(\mathbf{r})]} + \underbrace{\frac{\delta \hbar\omega_{\text{xc}}[\rho_0(\mathbf{r})]}{\delta \rho_0(\mathbf{r})}}_{V_{\text{xc}}[\rho_0(\mathbf{r})]}. \quad (2.57)$$

This effective KS potential contains three terms: the external potential, the Hartree potential $V_{\text{Har}}[\rho_0(\mathbf{r})]$ and the (unknown) exchange-correlation potential $V_{\text{xc}}[\rho_0(\mathbf{r})]$. Although the KS equations [Eq. (2.52)] are now fully determined, they are still very difficult to solve, because the KS potential depends on the ground-state density $\rho_0(\mathbf{r})$. Therefore, all $\phi_i^{\text{KS}}(\mathbf{r})$ orbitals are needed to build the KS potential, but the KS orbitals cannot be known without solving the KS equation itself. To overcome this problem, a self-consistent method is usually used in DFT calculations, as shown by the diagram of Fig. 2.3. Based on the atomic structure

of the system, a first guess of $\rho_0(\mathbf{r})$ is made, which is used to construct the KS potential $V_{\text{KS}}(\mathbf{r})$. Then, Eq. (2.52) is solved, which leads to a new ground-state density that can be different from the initial guess. This new density leads to a new KS potential, and the KS equations are again solved with new solutions. This procedure continues in a self-consistent loop until the ground-state density $\rho_0(\mathbf{r})$ and the KS eigenvalues do not change. When this convergence is fulfilled, the last function $\rho_0(\mathbf{r})$ represents the real ground state of the system, and many properties of the solid system can be calculated from there.

Exchange and correlation

DFT is an exact theory as described up to this point. However, since the exact form of the exchange-correlation potential $V_{\text{xc}}(\mathbf{r})$ is unknown, it must be approximated in order to solve the KS equations. Accordingly, DFT has been successful mainly in systems where electrons are not strongly correlated, and thus where the exchange-correlation energy is small enough for the approximations to be valid. In particular, here we outline the Local Density Approximation (LDA) that is used in the calculations of Chapter 3. This approximation was first proposed by W. Kohn and L. J. Sham [120], and it is still used as a reliable approach for many systems despite its simplicity.

Although the electronic structure of most real systems is highly inhomogeneous, the LDA approximates the exchange-correlation energy of the real system by using the results corresponding to the HEG, which is the simplest system where this energy can be calculated. To obtain the value of the exchange-correlation energy of the real metal, we consider at each point \mathbf{r} , with electronic density $\rho_0(\mathbf{r})$, a HEG with the exact same density $\rho_0(\mathbf{r})$. We discuss below how to obtain the contribution $e_{\text{xc}}^{\text{HEG}}[\rho_0(\mathbf{r})]$ of each point \mathbf{r} to the total energy. With this result, the total energy is then obtained by integrating all contributions over space. With this procedure, the LDA approximation neglects any contribution of the gradients of the density $\nabla\rho_0(\mathbf{r})$ to the exchange-correlation energy. Under these assumptions, the functional form of the exchange-correlation energy is written as

$$\hbar\omega_{\text{xc}}^{\text{LDA}}[\rho_0(\mathbf{r})] = \int \rho_0(\mathbf{r}) e_{\text{xc}}^{\text{HEG}}[\rho_0(\mathbf{r})] d\mathbf{r}. \quad (2.58)$$

In order to obtain the exchange-correlation functional in the HEG, we separate it into two terms as $e_{\text{xc}}^{\text{HEG}}[\rho_0(\mathbf{r})] = e_{\text{x}}^{\text{HEG}}[\rho_0(\mathbf{r})] + e_{\text{c}}^{\text{HEG}}[\rho_0(\mathbf{r})]$, where the first and the second term in the right handside correspond to the exchange and correlation energy, respectively. First, we note that the origin of the exchange energy $\hbar\omega_{\text{x}}$ is the antisymmetrization of the wavefunction in the Slater determinant [Eq. (2.53)], and that it can be exactly calculated in terms of KS orbitals according to the expression [121]

$$\hbar\omega_{\text{x}}[\rho_0(\mathbf{r})] = -\frac{1}{2} \frac{e^2}{4\pi\epsilon_0} \sum_{i,j} \int \int \frac{[\phi_i^{\text{KS}}(\mathbf{r})]^* [\phi_j^{\text{KS}}(\mathbf{r}')]^* \phi_i^{\text{KS}}(\mathbf{r}') \phi_j^{\text{KS}}(\mathbf{r})}{|\mathbf{r} - \mathbf{r}'|} d\mathbf{r} d\mathbf{r}'. \quad (2.59)$$

In the case of a HEG, since the potential is constant over space, the corresponding Schrödinger equation implies that all occupied KS orbitals are planewaves of the form $\phi_i^{\text{KS}}(\mathbf{r}) = \frac{1}{\sqrt{\mathcal{V}}} e^{i\mathbf{k}_i \cdot \mathbf{r}}$, where \mathcal{V} is the volume of the system. The wavevectors \mathbf{k}_i of the occupied states are inside the Fermi's sphere, i.e. with magnitude $|\mathbf{k}| < k_F = (3\pi^2\rho_0)^{\frac{1}{3}}$. Evaluating the integrals of Eq. (2.59) with these wavefunctions, we obtain the expression

$$e_x^{\text{HEG}}[\rho_0(\mathbf{r})] = -\frac{3}{4} \left(\frac{3}{\pi} \right)^{\frac{1}{3}} \rho_0(\mathbf{r})^{\frac{4}{3}}. \quad (2.60)$$

Unfortunately, the functional of the correlation energy is unknown even for the simplest case of the HEG. However, several Monte-Carlo simulations have evaluated this term with high precision, and thus we can find different parametrizations fitting these simulations in the literature. In particular, in Chapter 3 we use the Ceperley-Alder form [123] for the exchange-correlation functional. By combining the correlation term with the exchange term of Eq. (2.60), the exchange-correlation functional and the corresponding potential (evaluated with the functional derivative $V_{\text{xc}}[\rho_0(\mathbf{r})] = \frac{\delta \hbar\omega_{\text{xc}}[\rho_0(\mathbf{r})]}{\delta \rho_0(\mathbf{r})} = \frac{\partial}{\partial \rho_0} [\rho_0 e_{\text{xc}}^{\text{HEG}}(\rho_0)]$), read

$$e_{\text{xc}}^{\text{HEG}}[\rho_0(\mathbf{r})] = \frac{e^2}{4\pi\epsilon_0} \left[\frac{0.458}{r_s} - \frac{\gamma_{\text{xc}}^{\text{HEG}}}{1 + \beta_1\sqrt{r_s} + \beta_2 r_s} \right], \quad (2.61a)$$

$$V_{\text{xc}}^{\text{HEG}}[\rho_0(\mathbf{r})] = \frac{e^2}{4\pi\epsilon_0} \left[-\frac{0.611}{r_s} - \frac{\gamma_{\text{xc}}^{\text{HEG}}(1 + \frac{7}{6}\beta_1\sqrt{r_s} + \frac{4}{3}\beta_2 r_s)}{(1 + \beta_1\sqrt{r_s} + \beta_2 r_s)^2} \right]. \quad (2.61b)$$

The fitting done by Ceperley and Alder gives the parameters $\gamma_{\text{xc}}^{\text{HEG}} = 0.13450 \text{ \AA}^{-1}$, $\beta_1 = 1.4476 \text{ \AA}^{-\frac{1}{2}}$ and $\beta_2 = 0.6302 \text{ \AA}^{-1}$ [124]. The ground-state density is introduced into Eq. (2.61) in terms of the Wigner-Seitz radius, defined as

$$r_s(\mathbf{r}) = \left(\frac{3}{4\pi\rho_0(\mathbf{r})} \right)^{\frac{1}{3}}. \quad (2.62)$$

2.3.2 Time-Dependent Density Functional Theory in the linear response framework

TDDFT is an extension of DFT that analyzes the modification of the electronic density of a system due to a time-dependent external potential [42, 43]. Whereas DFT deals with properties related to the ground state, TDDFT is necessary to study the excited states of the Hamiltonian. The general formulation of TDDFT relies on the Runge-Gross theorem, which is an extension of the Hohenberg-Kohn theorems and states that the electronic density $\rho(\mathbf{r}, t)$ is a unique functional of the external potential $V_{\text{ext}}(\mathbf{r}, t)$ [125]. However, this general approach requires to solve the time-dependent KS equations, which is a more computationally demanding task than obtaining the ground-state density from the time-independent equations.

On the other hand, if the time-dependent external potential is weak, the results of DFT can be combined with linear response theory (Sec. 2.1). Since in this thesis we work in the perturbative regime, in this subsection we outline the procedure to work with TDDFT in the linear response framework.

The standard procedure begins by writing the external potential as $V_{\text{ext}}^{(0)}(\mathbf{r}) + V_{\text{ext}}^{(1)}(\mathbf{r}, \omega)$, where the zeroth-order term $V_{\text{ext}}^{(0)}(\mathbf{r})$ is the static ionic potential (which is the same as the external potential used in Sec. 2.3.1 for DFT) and the much smaller first-order term $V_{\text{ext}}^{(1)}(\mathbf{r}, \omega)$ is the external time-dependent perturbation written in frequency domain (we focus on the contribution to the perturbation at a single frequency ω because in the linear regime each ω component can be considered independently, as discussed in Sec. 2.1). While the static potential $V_{\text{ext}}^{(0)}(\mathbf{r})$ gives the ground-state density $\rho_0(\mathbf{r})$, the inclusion of the time-dependent perturbation induces a charged density as given by the expression $\rho_0(\mathbf{r}) + \rho_1(\mathbf{r}, \omega) + \dots$, where we only focus on the first-order correction of the induced density $\rho_1(\mathbf{r}, \omega)$ neglecting higher-order terms in the expansion. Further, within the KS theory, the electronic density also modifies the Hartree potential in Eq. (2.57) by adding the term

$$V_{\text{Har}}^{(1)}(\mathbf{r}, \omega) = \int \frac{\rho_1(\mathbf{r}', \omega)}{|\mathbf{r} - \mathbf{r}'|} d\mathbf{r}'. \quad (2.63)$$

Further, the modification of the exchange-correlation potential due to the perturbation is expressed as a linear expansion with respect to the electronic density around the ground-state density, i.e.

$$V_{\text{xc}}^{(1)}(\mathbf{r}, \omega) = \int \underbrace{\frac{\delta V_{\text{xc}}(\mathbf{r}, \omega)}{\delta \rho(\mathbf{r}', \omega)} \Big|_{\rho(\mathbf{r}', \omega) = \rho_0(\mathbf{r}')}}_{K_{\text{xc}}(\mathbf{r}, \mathbf{r}', \omega)} \rho_1(\mathbf{r}', \omega) d\mathbf{r}', \quad (2.64)$$

where we define the dynamical exchange-correlation kernel $K_{\text{xc}}(\mathbf{r}, \mathbf{r}', \omega)$.

As explained in Sec. 2.1, the excitation spectrum of a metal is encoded in the response function $\chi(\mathbf{r}, \omega)$ that connects the external potential and the modified density as

$$\rho_1(\mathbf{r}, \omega) = \int \chi(\mathbf{r}, \mathbf{r}', \omega) V_{\text{ext}}^{(1)}(\mathbf{r}', \omega) d\mathbf{r}'. \quad (2.65)$$

However, a direct calculation of this response function [applying Eq. (2.11)] would require all the eigenfunctions of the Hamiltonian of Eq. (2.47), which considers all the electron-electron interactions. We have shown in Sec. 2.3.1 that an equivalent description of the system is to introduce all the interactions effectively inside the KS potential, and to solve the single-electron Schrödinger equation from Eq. (2.52). In the linear regime, a perturbative KS potential acts as an external contribution that modifies the electronic density following

$$\rho_1(\mathbf{r}, \omega) = \int \chi^{\text{KS}}(\mathbf{r}, \mathbf{r}', \omega) V_{\text{KS}}^{(1)}(\mathbf{r}', \omega) d\mathbf{r}'. \quad (2.66)$$

This equation is very helpful because we can evaluate the KS response function $\chi^{\text{KS}}(\mathbf{r}, \mathbf{r}', \omega)$ using Eq. (2.11) with the Kohn-Sham orbitals calculated within DFT.

Nevertheless, Eq. (2.66) does not solve the problem completely, because the objective is to calculate the response of the system just to the external potential $V_{\text{ext}}^{(1)}(\mathbf{r}, \omega)$, and not to the KS potential $V_{\text{KS}}^{(1)}(\mathbf{r}, \omega) = V_{\text{ext}}^{(1)}(\mathbf{r}, \omega) + V_{\text{Har}}^{(1)}(\mathbf{r}, \omega) + V_{\text{xc}}^{(1)}(\mathbf{r}, \omega)$. By noticing that the density $\rho_1(\mathbf{r}, \omega)$ is equal in Eqs. (2.65) and (2.66), and by introducing the expressions of the Hartree potential [Eq. (2.63)] and the exchange-correlation potential [Eq. (2.64)] into Eq. (2.66), one can prove that the response functions associated with the external and KS potential are related according to the integral equation

$$\begin{aligned} \chi(\mathbf{r}, \mathbf{r}', \omega) = & \chi^{\text{KS}}(\mathbf{r}, \mathbf{r}', \omega) \\ & + \int d\mathbf{x} \int d\mathbf{x}' \chi^{\text{KS}}(\mathbf{r}, \mathbf{x}, \omega) \left[\frac{1}{|\mathbf{x} - \mathbf{x}'|} + K_{\text{xc}}(\mathbf{x}, \mathbf{x}', \omega) \right] \chi(\mathbf{x}', \mathbf{r}', \omega), \end{aligned} \quad (2.67)$$

which depends on the dynamical exchange-correlation kernel $K_{\text{xc}}(\mathbf{x}, \mathbf{x}', \omega)$ as defined in Eq. (2.64).

To summarize, we have shown that the procedure to obtain the response function of a metal within TDDFT follows three main steps. First, we need to calculate the KS orbitals from the unperturbed KS Hamiltonian [Eq. (2.52)]. Then, after including the perturbation, the KS response function can be directly calculated by introducing the KS orbitals $\phi_i^{\text{KS}}(\mathbf{r})$ into Eq. (2.11). Last, the needed response function is the solution of Eq. (2.67). However, this integral equation cannot be solved analytically for real systems, and computational methods are needed as explained in Sec. 2.3.3.

Dynamical exchange and correlation kernel

Besides the difficulties of solving an integral equation to obtain $\chi(\mathbf{r}, \mathbf{r}', \omega)$, Eq. (2.67) has the additional problem that it requires the exact form of the dynamical exchange-correlation kernel $K_{\text{xc}}(\mathbf{x}, \mathbf{x}', \omega)$. Since the exchange-correlation potential $V_{\text{xc}}(\mathbf{r})$ is unknown in DFT, the definition from Eq. (2.64) cannot be used directly to obtain the dynamical kernel $K_{\text{xc}}(\mathbf{x}, \mathbf{x}', \omega)$ within the TDDFT formalism. Thus, we must make approximations in the same way as in the time-independent formalism.

In Chapter 3, we use two approximations for $K_{\text{xc}}(\mathbf{x}, \mathbf{x}', \omega)$ that are very common due to their simplicity. The first one is the RPA, which is the crudest approximation that can be made in Eq. (2.67) because it neglects entirely the dynamical kernel: $K_{\text{xc}}(\mathbf{x}, \mathbf{x}', \omega) = 0$. This is a generalization of the RPA that we have discussed for the HEG (Sec. 2.2), where the screening of the electrons is considered inside the Hartree potential and the exchange and correlation are completely neglected. However, the RPA gives more accurate results in the TDDFT approach than for the HEG, because in the former case the exchange and correlation are not fully eliminated: even though $K_{\text{xc}}(\mathbf{x}, \mathbf{x}', \omega)$ is neglected in the dynamical response, the KS orbitals are calculated with the static exchange-correlation potential $V_{\text{xc}}[\rho_0(\mathbf{r})]$.

Therefore, the response function obtained in the TDDFT formalism under the RPA contains some effects of exchange and correlation.

Raising one step in the level of complexity, the next approximation is the Adiabatic Local Density Approximation (ALDA), which is an extension of the LDA of the time-independent DFT. The LDA considers that the ground-state density varies slowly in space (because the contribution of $\nabla\rho_0(\mathbf{r})$ and of all higher-order terms to the exchange-correlation energy are neglected), and the same assumption is made for the perturbed density, so that the ALDA kernel is local in space: $K_{\text{xc}}(\mathbf{r}, \mathbf{r}', t, t') = K_{\text{xc}}(\mathbf{r}, t, t')\delta(\mathbf{r} - \mathbf{r}')$. Further, the adiabatic approximation means that the dynamical kernel is considered to be instantaneous in time, $K_{\text{xc}}(\mathbf{r}, \mathbf{r}', t, t') = K_{\text{xc}}(\mathbf{r}, \mathbf{r}')\delta(t - t')$. This locality in time implies that its Fourier transform is independent of ω , and thus all possible variations of the dynamical exchange and correlation with frequency are neglected. With these assumptions, the ALDA kernel is calculated by introducing the exchange-correlation potential of the HEG [Eq. (2.61b)] in the definition of the exchange-correlation kernel from Eq. (2.64), which leads to the expression

$$K_{\text{xc}}^{\text{ALDA}}(\mathbf{r}, \mathbf{r}', \omega) = \frac{\delta V_{\text{xc}}^{\text{HEG}}[\rho_0(\mathbf{r})]}{\delta\rho_0(\mathbf{r}')} \delta(\mathbf{r} - \mathbf{r}'). \quad (2.68)$$

Due to the adiabatic approximation, this kernel works well in the static $\omega \rightarrow 0$ limit, while the error is considerably larger for high-frequency phenomena. However, the agreement of ALDA with experimental data for the energies of interest in this thesis is remarkably good and better than for the RPA [126–128]. Indeed, ALDA fails mostly in the description of higher-order processes involving multiparticle excitations, but the excitation spectra close to the plasmonic resonances is dominated by single electron-hole excitations. Therefore, for the calculations in this thesis, the RPA and particularly the ALDA are reasonable approximations.

2.3.3 Computational methods to calculate electronic excitations in metallic surfaces

In the DFT and TDDFT approaches, computational methods are necessary to solve the KS equations [Eq. (2.52)] and the integral equation of the response function [Eq. (2.67)]. In the case of bulk (infinite) crystalline materials, the periodicity of the system allows for the transformation of functional equations into matrix equations, for which there are efficient numerical methods available. However, in this thesis we analyze the excitation spectra of metallic surfaces, where the periodicity is broken in one dimension, and this fact must be taken into account in the methodology. In this subsection, we summarize the computational methods to calculate the excitation spectra with DFT and TDDFT in surface systems.

Calculation of the Kohn-Sham orbitals with a plane-wave basis

The computational effort to solve the KS equations can be simplified by expanding the wavefunctions into an appropriate basis. In bulk solid-state crystalline systems (infinite in the three dimensions), we can take advantage of Bloch's theorem to choose the basis. Since the KS potential in crystals has a periodicity given by the lattice vectors \mathbf{R} , i.e. it satisfies the condition $V_{\text{KS}}(\mathbf{r}) = V_{\text{KS}}(\mathbf{r} + \mathbf{R})$, Bloch's theorem implies that the eigenfunctions of the KS Hamiltonian must satisfy the form [129]

$$\phi_{n\mathbf{k}}^{\text{KS}}(\mathbf{r}) = e^{i\mathbf{k}\cdot\mathbf{r}} \mathbf{u}_{n\mathbf{k}}(\mathbf{r}). \quad (2.69)$$

The subindexes n and \mathbf{k} of the KS orbital refer to the associated band index and wavevector, respectively. The function $\mathbf{u}_{n\mathbf{k}}(\mathbf{r}) = \mathbf{u}_{n\mathbf{k}}(\mathbf{r} + \mathbf{R})$ has the same periodicity as the KS potential. Equation (2.69) implies that an appropriate basis for the expansion of KS orbitals are plane waves. Indeed, these orbitals can be expanded as

$$\phi_{n\mathbf{k}}^{\text{KS}}(\mathbf{r}) = \frac{1}{\sqrt{\mathcal{V}}} \sum_{\mathbf{K}} \mathbf{c}_{n\mathbf{k}+\mathbf{K}} e^{i(\mathbf{k}+\mathbf{K})\cdot\mathbf{r}}, \quad (2.70)$$

where \mathbf{K} are reciprocal lattice vectors and the volume \mathcal{V} of the system (which is considered to be very large but finite) acts as a normalization constant.

With the plane-wave basis for the KS orbitals, we do not have to solve the KS equation [Eq. (2.52)] in real space. Instead, by introducing the expansion of Eq. (2.70) into Eq. (2.52), we obtain a linear system for the coefficients $\mathbf{c}_{n\mathbf{k}+\mathbf{K}}$, which can be solved using linear algebra computational methods. All these coefficients are related as

$$\sum_{\mathbf{K}'} \left(-\frac{\hbar^2 |\mathbf{k} + \mathbf{K}'|^2}{2m_e} \delta_{\mathbf{K},\mathbf{K}'} + \langle \mathbf{k} + \mathbf{K} | V_{\text{KS}}(\mathbf{r}) | \mathbf{k} + \mathbf{K}' \rangle \right) \mathbf{c}_{n\mathbf{k}+\mathbf{K}'} = \hbar\omega_{n\mathbf{k}} \mathbf{c}_{n\mathbf{k}+\mathbf{K}}. \quad (2.71)$$

Thus, the band structure of a solid system is obtained by solving Eq. (2.71) for each wavevector \mathbf{k} in the Brillouin zone. Although this equation contains an infinite sum over \mathbf{K} vectors, a finite set is chosen in practice, where the necessary number of vectors depends on the system and on the required accuracy. The choice of the finite set is typically done by considering a cut-off energy $\hbar\omega_{\text{cut-off}}$, where all reciprocal state vectors that satisfy the following condition are used in the system of Eq. (2.71):

$$\frac{\hbar^2 |\mathbf{k} + \mathbf{K}|^2}{2m_e} \leq \hbar\omega_{\text{cut-off}}. \quad (2.72)$$

A main problem of the matrix equation of Eq. (2.71) is that it requires periodicity in the system to have a basis of reciprocal lattice vectors. This requirement is satisfied in solid materials. However, in this thesis we perform DFT and TDDFT calculations in metallic surfaces, and in surface systems formed by a semi-infinite metallic medium and vacuum there is no periodicity in the direction perpendicular to the metal-vacuum interface. In order to apply the described approach in this type of systems, the supercell method is typically used.

For metallic surfaces, this method consists in considering a finite number of atomic layers in the metal. The number of layers must be sufficient to recover the bulk properties of the metal in the innermost layers. All these atoms are introduced in the supercell, and further, an empty space is also considered in the supercell above the topmost atomic layer to model the vacuum. To perform the DFT calculations, an infinite 3D system is created by repeating the supercell periodically. A main drawback of this method is that a large number of atoms is needed for an accurate description of the system. Additionally, the ensuing large cell demands a larger set of reciprocal lattice vectors \mathbf{K} in the matrix to solve Eq. (2.71), because vectors \mathbf{K} associated to large cells have a small magnitude. Thus, in the supercell geometry more \mathbf{K} vectors are needed to satisfy the condition of Eq. (2.72) for the same cut-off energy $\hbar\omega_{\text{cut-off}}$ in comparison to the case of bulk crystalline metals. Due to these drawbacks, DFT calculations in surfaces are quite expensive computationally.

Calculation of the linear response function and surface response function with a planewave basis

Once the KS orbitals are known for a system, the next step to obtain its excitation spectra is the calculation of the linear response function within the TDDFT formalism, as described in Sec. 2.3.2. As done for the KS orbitals, we can expand the response function into the reciprocal lattice vectors \mathbf{K} to simplify the calculations. Further, in this thesis, we are interested in calculating the response of metallic surfaces to the specific external potential $V_{\text{ext}}(\mathbf{q}_{\parallel}, \omega)$ given by (1.33). Since this external potential is given as a function of the wavevector \mathbf{q}_{\parallel} in the plane parallel to the metal-vacuum interface, we are interested in calculating the linear response function in reciprocal space. By expanding the response function $\chi(\mathbf{r}, \mathbf{r}', \omega)$ over the reciprocal lattice vectors \mathbf{K} and performing the Fourier transform, this function is written as

$$\chi(\mathbf{r}, \mathbf{r}', \omega) = \sum_{\mathbf{q}_{\parallel}} \sum_{\mathbf{K}, \mathbf{K}'} \chi_{\mathbf{K}, \mathbf{K}'}(\mathbf{q}_{\parallel}, \omega) e^{i(\mathbf{q}_{\parallel} + \mathbf{K}) \cdot \mathbf{r}} e^{-i(\mathbf{q}_{\parallel} + \mathbf{K}') \cdot \mathbf{r}'}. \quad (2.73)$$

The expansion over reciprocal vectors \mathbf{K} is very helpful, because it allows transforming the integral equation (2.67) for each \mathbf{q}_{\parallel} and ω component of the response function into a matrix equation of the form

$$\chi_{\mathbf{K}, \mathbf{K}'} = \chi_{\mathbf{K}, \mathbf{K}'}^{\text{KS}} + \sum_{\mathbf{K}'', \mathbf{K}'''} \chi_{\mathbf{K}, \mathbf{K}''}^{\text{KS}} [V_{\mathbf{K}'', \mathbf{K}'''}^{\text{Cou}} + K_{\mathbf{K}'', \mathbf{K}'''}^{\text{xc}}] \chi_{\mathbf{K}'', \mathbf{K}'} \quad (2.74)$$

which is considerably easier to solve with computational methods than Eq. (2.67). In this equation, we need the matrix elements of the KS response function $\chi_{\mathbf{K}, \mathbf{K}'}^{\text{KS}}$, which after introducing the KS orbitals $\phi_{n\mathbf{k}_{\parallel}}^{\text{KS}}$ into Eq. (2.11) can be calculated as

$$\chi_{\mathbf{K}, \mathbf{K}'}^{\text{KS}}(\mathbf{q}_{\parallel}, \omega) = \frac{2}{S} \sum_{\mathbf{k}_{\parallel}}^{\text{SBZ}} \sum_m \sum_n \frac{f_{\text{FD}}^{m\mathbf{k}_{\parallel}} - f_{\text{FD}}^{n\mathbf{k}_{\parallel} + \mathbf{q}_{\parallel}}}{\hbar(\omega + i\eta + \omega_{m\mathbf{k}_{\parallel}} - \omega_{n\mathbf{k}_{\parallel} + \mathbf{q}_{\parallel}})}$$

$$\times \left\langle \phi_{m\mathbf{k}_{\parallel}}^{\text{KS}} \left| e^{-i(\mathbf{q}_{\parallel} + \mathbf{K}) \cdot \mathbf{r}} \right| \phi_{n\mathbf{k}_{\parallel} + \mathbf{q}_{\parallel}}^{\text{KS}} \right\rangle \left\langle \phi_{m\mathbf{k}_{\parallel}}^{\text{KS}} \left| e^{i(\mathbf{q}_{\parallel} + \mathbf{K}') \cdot \mathbf{r}} \right| \phi_{n\mathbf{k}_{\parallel} + \mathbf{q}_{\parallel}}^{\text{KS}} \right\rangle, \quad (2.75)$$

where S is the in-plane unit cell area and the factor 2 accounts for the spin. The sum of Eq. (2.75) is performed over all \mathbf{k}_{\parallel} inside the surface Brillouin zone (SBZ). Further, in this equation we have introduced the Fermi-Dirac occupation factor $f_{\text{FD}}^{n\mathbf{k}_{\parallel}}$ of the state in the band n at parallel wavevector \mathbf{k}_{\parallel} . In the derivation of the linear response function of Eq. (2.11), we have assumed that the system is at zero temperature, for which the states are either occupied (with occupation factor 1) or unoccupied (with occupation factor 0). By now including factors $f_{\text{FD}}^{n\mathbf{k}_{\parallel}}$, we generalize the calculation for nonzero temperatures where occupation factors between 0 and 1 are possible.

Last, an important quantity that directly leads to the excitation spectra of metallic surfaces is the surface response function $\mathbf{g}(\mathbf{q}_{\parallel}, \omega)$. This function has been defined in Eq. (1.32), and we have used a classical calculation based on Maxwell's equations to analyze the excitation spectra of planar systems in Sec. 1.2.1. Importantly, we can use the same definition of $\mathbf{g}(\mathbf{q}_{\parallel}, \omega)$ in the quantum approach to obtain the excitation spectra of metallic surfaces. The calculation of $\mathbf{g}(\mathbf{q}_{\parallel}, \omega)$ requires the density induced by the external potential from Eq. (1.33). In the quantum approach, this information is entirely given by the response function $\chi(\mathbf{q}_{\parallel}, \omega)$. Indeed, the surface response function $\mathbf{g}(\mathbf{q}_{\parallel}, \omega)$ can be calculated with the response function obtained from the TDDFT approach. To demonstrate it, we introduce Eq. (2.65) into Eq. (1.32), and we obtain the surface response function

$$\mathbf{g}(\mathbf{q}_{\parallel}, \omega) = -\frac{2\pi}{q_{\parallel}} \int dz \int dz' \chi_{\mathbf{K}_{\parallel}=\mathbf{K}'_{\parallel}=0}(z, z', \mathbf{q}_{\parallel}, \omega) e^{q_{\parallel}(z+z')}, \quad (2.76)$$

where the matrix elements over the parallel component of the reciprocal lattice vectors \mathbf{K}_{\parallel} are defined as

$$\chi_{\mathbf{K}_{\parallel}, \mathbf{K}'_{\parallel}}(z, z', \mathbf{q}_{\parallel}, \omega) = \sum_{K_z, K'_z} \chi_{\mathbf{K}, \mathbf{K}'}(\mathbf{q}_{\parallel}, \omega) e^{iK_z z} e^{-iK'_z z'}. \quad (2.77)$$

Hence, if the KS orbitals $\phi_{n\mathbf{k}_{\parallel}}^{\text{KS}}$ of a system are known, the surface response function $\mathbf{g}(\mathbf{q}_{\parallel}, \omega)$ can be directly calculated within three steps. First, we obtain the matrix elements of the KS response function $\chi_{\mathbf{K}, \mathbf{K}'}^{\text{KS}}$ with Eq. (2.75). After, Eq. (2.74) gives the matrix elements of the response function of the actual interacting system, $\chi_{\mathbf{K}, \mathbf{K}'}$. Last, we perform the integral in Eq. (2.76) to calculate $\mathbf{g}(\mathbf{q}_{\parallel}, \omega)$.

Extraction of the single-slab response function from the supercell geometry

An additional problem of the supercell geometry, beyond the computational cost, is that different slabs interact with each other in the periodic system due to the long-range Coulomb potential. Therefore, each slab is influenced by the external

potential and by the potential induced by the electrons from all the other slabs. However, the objective of our TDDFT calculations is to determine the response of a single slab to the external potential. As a consequence, the inter-slab interactions must be eliminated from the calculation. We now summarize the procedure proposed by Nazarov in Ref. [130], which we use in Chapter 3.

The response function $\tilde{\chi}(\mathbf{q}, \omega)$ of the supercell geometry is the result directly achievable from TDDFT calculations according to the procedure above. The matrix elements of this function connect the external potential with the induced density according to

$$\rho_{1\mathbf{K}}(\mathbf{q}_{\parallel}, \omega) = \sum_{\mathbf{K}'} \tilde{\chi}_{\mathbf{K}, \mathbf{K}'}(\mathbf{q}_{\parallel}, \omega) V_{\mathbf{K}'}^{\text{ext}}(\mathbf{q}_{\parallel}, \omega). \quad (2.78)$$

However, the response function $\chi(\mathbf{q}, \omega)$ of a single slab needs to satisfy the equation

$$\rho_{1\mathbf{K}}(\mathbf{q}_{\parallel}, \omega) = \sum_{\mathbf{K}'} \chi_{\mathbf{K}, \mathbf{K}'}(\mathbf{q}_{\parallel}, \omega) V_{\mathbf{K}'}^{\text{eff}}(\mathbf{q}_{\parallel}, \omega), \quad (2.79)$$

where $V_{\mathbf{K}'}^{\text{eff}}$ are the \mathbf{K} -components of the effective potential $V_{\text{eff}}(\mathbf{r}, \omega)$ to which a single slab is subjected, i.e.

$$V_{\text{eff}}(\mathbf{r}, \omega) = V_{\text{ext}}(\mathbf{r}, \omega) + \underbrace{\frac{e^2}{4\pi\epsilon_0} \int_{\mathbf{r}' \in (\text{other slabs})} \frac{\rho_1(\mathbf{r}', \omega)}{|\mathbf{r} - \mathbf{r}'|} d\mathbf{r}'}_{V_{\text{ind}}(\mathbf{r}, \omega)}. \quad (2.80)$$

The effective potential includes the contribution of the external potential together with the induced potential $V_{\text{ind}}(\mathbf{r}, \omega)$, which consists in the Coulomb interactions caused by the induced charges in all the other slabs.

In order to apply the computational procedure, we need the expansion of the potentials into reciprocal lattice vectors \mathbf{K} . With this aim, we separate the effective potential as $V_{\mathbf{K}}^{\text{eff}}(\mathbf{r}, \omega) = V_{\mathbf{K}}^{\text{ext}}(\mathbf{r}, \omega) + V_{\mathbf{K}}^{\text{ind}}(\mathbf{r}, \omega)$. By performing the Fourier transform of $V_{\mathbf{K}}^{\text{ind}}(\mathbf{r}, \omega)$ in Eq. (2.80) over the \mathbf{r}_{\parallel} direction and performing the integral in the z direction for all slabs, the induced potential can be written in terms of the induced charge density as (see Ref. [130] for a detailed derivation)

$$V_{\mathbf{K}}^{\text{ind}}(\mathbf{q}_{\parallel}, \omega) = \sum_{\mathbf{K}'} \mathcal{C}_{\mathbf{K}, \mathbf{K}'}(|\mathbf{K}_{\parallel} + \mathbf{q}_{\parallel}|) \rho_{1\mathbf{K}'}(\mathbf{q}_{\parallel}, \omega), \quad (2.81)$$

with the matrix elements

$$\mathcal{C}_{\mathbf{K}, \mathbf{K}'}(\beta) = \delta_{\mathbf{K}_{\parallel}, \mathbf{K}'_{\parallel}} \frac{4\pi(\beta^2 - K_z K'_z) \delta_{\mathbf{K}_{\perp}, \mathbf{K}'_{\perp}}}{\beta L_{\text{cell}}(\beta^2 + K_z^2)(\beta^2 + K_z'^2)} \cos \left[\frac{(K_z + K'_z) L_{\text{cell}}}{2} \right] (1 - e^{-\beta L_{\text{cell}}}), \quad (2.82)$$

where L_{cell} is the thickness of each supercell considered in the TDDFT calculations. Last, we introduce the expansion of the effective potential of Eq. (2.81) into Eq. (2.79). By noticing that the density components $\rho_{1\mathbf{K}}$ of Eqs. (2.78) and (2.79) must be equal for every external potential, the relation between the single-slab and

the supercell response functions in matrix notation verifies

$$\chi(\mathbf{q}_{\parallel}, \omega) = \tilde{\chi}(\mathbf{q}_{\parallel}, \omega) [1 - \mathcal{C}(|\mathbf{G}_{\parallel} + \mathbf{q}_{\parallel}|) \tilde{\chi}(\mathbf{q}_{\parallel}, \omega)]^{-1}. \quad (2.83)$$

A crucial characteristic of this last equation is that, although the function $\tilde{\chi}(\mathbf{q}_{\parallel}, \omega)$ depends on L_{cell} (and thus, on the computational details), the function $\chi(\mathbf{q}_{\parallel}, \omega)$ has been verified to be independent of that parameter, as expected from a single surface. Therefore, Eq. (2.83) gives the final result necessary to obtain the excitation spectra of a metallic surface.

2.4 Bardeen's theory of elastic electron tunneling

In nanophotonics, a quantum description of the electron dynamics is not only useful to study the properties of plasmons in metallic systems (as outlined in previous sections of this chapter), but it can also describe how these plasmons can be excited by injecting electrons into the metal. In this context, a particular system of interest are metal-insulator-metal (MIM) tunneling junctions, consisting in two metallic electrodes separated by an insulator nanometric gap. By applying a bias voltage V_{B} to the junction, an excess of energy eV_{B} is induced in the electrons of one of the two metallic electrodes. The electrons of this metal can tunnel elastically through the insulator gap between the electrodes to an unoccupied state in the other metal, generating a direct current. Further, inelastic processes during electron tunneling also occur, where the energy lost by the electrons can result in the excitation of SPPs. Light emission from MIM junctions due to SPP excitation by inelastic tunneling was first measured by Lambe and McCarthy [131]. We discuss how to describe the inelastic tunneling and quantify the excitation rate of SPPs in MIM tunneling junctions in Chapter 5. In this section, we set the foundation of this discussion by introducing the theory originally created by Bardeen to describe elastic tunneling [132].

In order to describe the dynamics of the electrons according to Bardeen's theory of elastic electron tunneling, we define the electronic Hamiltonian $\hat{\mathcal{H}}_{\text{el}}$ as

$$\hat{\mathcal{H}}_{\text{el}} = \frac{-\hbar^2 \nabla^2}{2m_{\text{eff}}} + U(z), \quad (2.84)$$

where the symbol m_{eff} refers to the effective mass of the electrons in the MIM junction. This Hamiltonian is essentially a free electron model supplemented with the description of a potential to account for the barrier. It includes the kinetic energy of the electrons in the metals (first term in the right handside) and the potential energy $U(z)$ (second term in the right handside) [133].

To characterize the potential energy $U(z)$, we first consider that the metals placed on the left and on the right of the insulator gap have Fermi energies E_{F}^{L} and E_{F}^{R} , respectively. If there is no bias potential applied ($V_{\text{B}} = 0$), the system is at equilibrium and the Fermi surfaces of both metals are at the same energy, which we set as the zero energy level. From this reference, the lowest values of

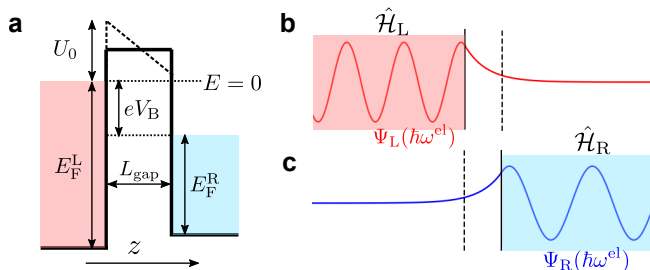


Figure 2.4: Schematics of the description of the MIM junction according to Bardeen's theory. a) Potential energy $U(z)$ of the electrons in the MIM junctions. The dashed lines represent the potential energy $U(z)$ with the linear function $U_{\text{gap}}(z)$ for the gap (of thickness L_{gap}), while solid lines represent the potential energy $U(z)$ under the rectangular approximation that we consider in our calculations. The occupied states of the metals in the left and right are represented by red and blue, respectively. b-c) Electronic wavefunctions $\Psi_{\text{L}}(\mathbf{r})$ and $\Psi_{\text{R}}(\mathbf{r})$ of the Hamiltonians $\hat{\mathcal{H}}_{\text{L}}$ and $\hat{\mathcal{H}}_{\text{R}}$ within Bardeen's approximation, respectively. Solid lines indicate the boundary between the metal considered in the Hamiltonian $\hat{\mathcal{H}}_{\text{L}}$ or $\hat{\mathcal{H}}_{\text{R}}$ and the gap. Dashed lines show the boundary between the gap and the metal that is considered absent in the corresponding Hamiltonian.

the potential energy that electrons can have in the left and right metals are $-E_{\text{F}}^{\text{L}}$ and $-E_{\text{F}}^{\text{R}}$, respectively. The height of the barrier in the gap region is U_0 . For applied bias potentials, the energies of all electrons in one metal are shifted by a value eV_{B} as compared to those in the other electrode (see sketch in Fig. 2.4a). We maintain the zero energy reference in the Fermi energy of the left metal, and thus the minimum potential energy remains here as $U_{\text{L}} = -E_{\text{F}}^{\text{L}}$. In the right metal, this minimum energy shifts to the value $U_{\text{R}} = -E_{\text{F}}^{\text{R}} - eV_{\text{B}}$, while the energy of the highest occupied state becomes $-eV_{\text{B}}$. This shift of the energy levels also affects the work functions of the metals, which causes a modification of the potential inside the insulator barrier. The potential in this region can be described with the linear function $U_{\text{gap}}(z) = U_0 - eV_{\text{B}} \frac{z}{L_{\text{gap}}}$, where z is the perpendicular direction to the interfaces of the junction and L_{gap} is the thickness of the insulator gap (the potential $U(z)$ with the linear function is indicated by dashed lines in the sketch of Fig. 2.4a). However, to obtain simple analytical expressions of the electronic wavefunctions, we use a rectangular approximation for the barrier potential, which takes a constant value determined by the average $U_{\text{gap}}(z) \approx U_0 - \frac{eV_{\text{B}}}{2}$ (we show the rectangular potential energy $U(z)$ in Fig. 2.4a by solid lines).

In Bardeen's theory, the main approximation is that the two metals are considered as two separate entities, and thus the electronic states of each metal are not affected by the other one. The eigenstates of the system are obtained from the separate Hamiltonians of the left ($\hat{\mathcal{H}}_{\text{L}}$) and right ($\hat{\mathcal{H}}_{\text{R}}$) metals. Each of these Hamiltonians includes operators for the kinetic and the potential energy. The potential energy operator considers the energy level of the corresponding metal (U_{L} or U_{R}) and of the insulator barrier (U_{gap}). We illustrate in Figs. 2.4b and c with vertical solid lines the metal-insulator boundary considered in the Hamiltonians $\hat{\mathcal{H}}_{\text{L}}$

and $\hat{\mathcal{H}}_R$, respectively. However, when calculating the wavefunction associated with each electrode, we do not consider the presence of the other one i.e. we extend the gap barrier to infinity (we show in Figs. 2.4b and c the metal-insulator boundary neglected in each Hamiltonian by dashed lines). Following this procedure, and by solving the Schrödinger equation, we obtain the wavefunctions of the states of the left metal (see Fig. 2.4b) [134]:

$$\Psi_L(\mathbf{r}) = \begin{cases} \frac{1}{\sqrt{L_z}} \frac{1}{\sqrt{S}} \left(e^{ik_{zL}z} + \frac{ik_{zL} + k_{z\text{gap}}}{ik_{zL} - k_{z\text{gap}}} e^{-ik_{zL}z} \right) e^{i\mathbf{k}_{\parallel} \cdot \mathbf{r}_{\parallel}} & z \leq 0 \\ \frac{1}{\sqrt{L_z}} \frac{1}{\sqrt{S}} \left(\frac{2ik_{zL}}{ik_{zL} - k_{z\text{gap}}} e^{-k_{z\text{gap}}z} \right) e^{i\mathbf{k}_{\parallel} \cdot \mathbf{r}_{\parallel}} & z > 0 \end{cases}. \quad (2.85)$$

Equivalently, the eigenfunctions corresponding to the right metal have the form (see Fig. 2.4c)

$$\Psi_R(\mathbf{r}) = \begin{cases} \frac{1}{\sqrt{L_z}} \frac{1}{\sqrt{S}} \left(\frac{2ik_{zR}}{ik_{zR} - k_{z\text{gap}}} e^{k_{z\text{gap}}(z - L_{\text{gap}})} \right) e^{i\mathbf{k}_{\parallel} \cdot \mathbf{r}_{\parallel}} & z \leq L_{\text{gap}} \\ \frac{1}{\sqrt{L_z}} \frac{1}{\sqrt{S}} \left(e^{-ik_{zR}(z - L_{\text{gap}})} + \frac{ik_{zR} + k_{z\text{gap}}}{ik_{zR} - k_{z\text{gap}}} e^{ik_{zR}(z - L_{\text{gap}})} \right) e^{i\mathbf{k}_{\parallel} \cdot \mathbf{r}_{\parallel}} & z > L_{\text{gap}} \end{cases}. \quad (2.86)$$

L_z is the (arbitrary) length of the system in the z direction, whereas S is the surface area of the interfaces in the $\mathbf{r}_{\parallel} = (x, y)$ plane. These two parameters act as normalization constants in the wavefunctions. Further,

$$k_{zL(R)}(\omega^{\text{el}}, \mathbf{k}_{\parallel}) = \sqrt{\frac{2m_{\text{eff}}}{\hbar^2} (\hbar\omega^{\text{el}} - U_{L(R)}) - |\mathbf{k}_{\parallel}|^2} \quad (2.87)$$

is the z component of the wavevector of an electron in the left (right) metal. The spatial decay of the wavefunction in the gap region is governed by the value

$$k_{z\text{gap}}(\omega^{\text{el}}, \mathbf{k}_{\parallel}) = \sqrt{\frac{2m_{\text{eff}}}{\hbar^2} (U_{\text{gap}} - \hbar\omega^{\text{el}}) + |\mathbf{k}_{\parallel}|^2}. \quad (2.88)$$

Since the electronic states of Bardeen's theory are localized in a single metal, the occupation of each wavefunction $\Psi_L(\mathbf{r})$ and $\Psi_R(\mathbf{r})$ is dictated by the Fermi-Dirac distribution of its respective metal $f_{\text{FD}}^{L(R)}(\omega^{\text{el}}) = \left[1 + \exp\left(\frac{\hbar\omega^{\text{el}} - E_{\text{F}}^{L(R)}}{k_{\text{B}}T}\right) \right]^{-1}$ at temperature T , with Boltzmann constant k_{B} .

Further, in Bardeen's theory, the interaction between the two metals that leads to elastic tunneling is treated at a perturbative level. Each electron of the left metal is at first in the state $|\Psi_L\rangle$ (with energy $\hbar\omega_L^{\text{el}}$ and parallel component of the wavevector $\mathbf{k}_{\parallel L}$) corresponding to the Hamiltonian $\hat{\mathcal{H}}_L$. The rest of the electronic Hamiltonian of Eq. (2.84), $\hat{\mathcal{H}}_{\text{el}} - \hat{\mathcal{H}}_L$, induces transitions to states of the form $|\Psi_R\rangle$ (with respective values $\hbar\omega_R^{\text{el}}$ and $\mathbf{k}_{\parallel R}$). The assumption of weak tunneling due to a sufficiently thick gap implies that the transition rate between two particular left

and right states is dictated by Fermi's golden rule, as

$$\Gamma_{L \rightarrow R} = \frac{2\pi}{\hbar^2} \delta(\omega_L^{\text{el}} - \omega_R^{\text{el}}) |\langle \Psi_R | \hat{\mathcal{H}}_{\text{el}} - \hat{\mathcal{H}}_L | \Psi_L \rangle|^2. \quad (2.89)$$

We first compute the matrix element of the interaction Hamiltonian $\hat{\mathcal{H}}_{\text{el}} - \hat{\mathcal{H}}_L$. Although the wavefunctions depend on the three spatial coordinates as $\Psi_{L(R)}(\mathbf{r}) = \Psi_{L(R)}(z) e^{i\mathbf{k}_{\parallel L(R)} \cdot \mathbf{r}_{\parallel}}$, the interaction Hamiltonian only depends on z , which allows separating the integral into spatial coordinates:

$$\begin{aligned} & |\langle \Psi_R | \hat{\mathcal{H}}_{\text{el}} - \hat{\mathcal{H}}_L | \Psi_L \rangle|^2 \\ &= \left(\int \Psi_R^*(z) e^{-i\mathbf{k}_{\parallel R} \cdot \mathbf{r}_{\parallel}} (\hat{\mathcal{H}}_{\text{el}} - \hat{\mathcal{H}}_L) [\Psi_L(z) e^{i\mathbf{k}_{\parallel L} \cdot \mathbf{r}_{\parallel}}] d\mathbf{r} \right) \\ &\quad \times \left(\int \Psi_L^*(z') e^{-i\mathbf{k}_{\parallel L} \cdot \mathbf{r}'_{\parallel}} (\hat{\mathcal{H}}_{\text{el}} - \hat{\mathcal{H}}_L) [\Psi_R(z') e^{i\mathbf{k}_{\parallel R} \cdot \mathbf{r}'_{\parallel}}] d\mathbf{r}' \right) \\ &= \left| \int \Psi_R^*(z) (\hat{\mathcal{H}}_{\text{el}} - \hat{\mathcal{H}}_L) \Psi_L(z) dz \right|^2 \int \int e^{-i(\mathbf{k}_{\parallel R} - \mathbf{k}_{\parallel L}) \cdot (\mathbf{r}_{\parallel} - \mathbf{r}'_{\parallel})} d\mathbf{r}_{\parallel} d\mathbf{r}'_{\parallel} \\ &= \left| \int \Psi_R^*(z) (\hat{\mathcal{H}}_{\text{el}} - \hat{\mathcal{H}}_L) \Psi_L(z) dz \right|^2 (2\pi)^2 \delta(\mathbf{k}_{\parallel R} - \mathbf{k}_{\parallel L}) S. \end{aligned} \quad (2.90)$$

Since the Hamiltonian $\hat{\mathcal{H}}_L$ is equal to the complete electronic Hamiltonian $\hat{\mathcal{H}}_{\text{el}}$ in the regions of the left metal and the insulator gap, the integral over z in Eq. (2.90) has to be done just in the right metal. In this region, the complete Hamiltonian $\hat{\mathcal{H}}_{\text{el}}$ is equal to $\hat{\mathcal{H}}_R$, and following the procedure of Bardeen in Ref. [132], we can add the vanishing term $-\Psi_L(z)(\hat{\mathcal{H}}_{\text{el}} - \hat{\mathcal{H}}_R)\Psi_R^*(z)$ to obtain a symmetrical form inside the integral:

$$\begin{aligned} & \int_{-\infty}^{\infty} \Psi_R^*(z) (\hat{\mathcal{H}}_{\text{el}} - \hat{\mathcal{H}}_L) \Psi_L(z) dz \\ &= \int_{L_{\text{gap}}}^{\infty} \Psi_R^*(z) (\hat{\mathcal{H}}_{\text{el}} - \hat{\mathcal{H}}_L) \Psi_L(z) - \Psi_L(z) (\hat{\mathcal{H}}_{\text{el}} - \hat{\mathcal{H}}_R) \Psi_R^*(z) dz \\ &= \int_{L_{\text{gap}}}^{\infty} \Psi_R^*(z) (\hat{\mathcal{H}}_{\text{el}} - \hbar\omega_L^{\text{el}}) \Psi_L(z) - \Psi_L(z) (\hat{\mathcal{H}}_{\text{el}} - \hbar\omega_R^{\text{el}}) \Psi_R^*(z) dz \\ &= \int_{L_{\text{gap}}}^{\infty} \Psi_R^*(z) \left(-\frac{\hbar^2 \nabla^2}{2m_{\text{eff}}} + U(z) \right) \Psi_L(z) - \Psi_L(z) \left(-\frac{\hbar^2 \nabla^2}{2m_{\text{eff}}} + U(z) \right) \Psi_R^*(z) dz \\ &= -\frac{\hbar^2}{2m_{\text{eff}}} \int_{L_{\text{gap}}}^{\infty} \left(\Psi_R^*(z) \frac{\partial^2 \Psi_L(z)}{\partial z^2} - \Psi_L(z) \frac{\partial^2 \Psi_R^*(z)}{\partial z^2} \right) dz. \end{aligned} \quad (2.91)$$

Here, we have taken into account that the energies $\hbar\omega_L^{\text{el}}$ and $\hbar\omega_R^{\text{el}}$ must be equal so that Eq. (2.89) leads to a nonzero value. By noticing that the functions $\Psi_L(z)$ and $\frac{\partial \Psi_L(z)}{\partial z}$ vanish at infinity, we solve the integral using the method of integration

by parts:

$$\begin{aligned}
 & \int \Psi_{\text{R}}^*(z)(\hat{\mathcal{H}}_{\text{el}} - \hat{\mathcal{H}}_{\text{L}})\Psi_{\text{L}}(z)dz \\
 &= -\frac{\hbar^2}{2m_{\text{eff}}} \left(\Psi_{\text{R}}^*(z) \frac{\partial \Psi_{\text{L}}(z)}{\partial z} \Big|_{L_{\text{gap}}}^{\infty} - \int_{L_{\text{gap}}}^{\infty} \frac{\partial \Psi_{\text{L}}(z)}{\partial z} \frac{\partial \Psi_{\text{R}}^*(z)}{\partial z} dz \right. \\
 &\quad \left. - \Psi_{\text{L}}(z) \frac{\partial \Psi_{\text{R}}^*(z)}{\partial z} \Big|_{L_{\text{gap}}}^{\infty} + \int_{L_{\text{gap}}}^{\infty} \frac{\partial \Psi_{\text{L}}(z)}{\partial z} \frac{\partial \Psi_{\text{R}}^*(z)}{\partial z} dz \right) \\
 &= \frac{\hbar^2}{2m_{\text{eff}}} \left(\Psi_{\text{R}}^*(z) \frac{\partial \Psi_{\text{L}}(z)}{\partial z} - \Psi_{\text{L}}(z) \frac{\partial \Psi_{\text{R}}^*(z)}{\partial z} \right) \Big|_{z=L_{\text{gap}}} . \tag{2.92}
 \end{aligned}$$

Equations (2.89), (2.90) and (2.92) lead to the following transition rate between left and right states:

$$\Gamma_{\text{L} \rightarrow \text{R}} = \frac{(2\pi)^3 \hbar^2}{4m_{\text{eff}}^2} S \delta(\omega_{\text{L}}^{\text{el}} - \omega_{\text{R}}^{\text{el}}) \delta(\mathbf{k}_{\parallel \text{R}} - \mathbf{k}_{\parallel \text{L}}) \left| \Psi_{\text{R}}^*(z) \frac{\partial \Psi_{\text{L}}(z)}{\partial z} - \Psi_{\text{L}}(z) \frac{\partial \Psi_{\text{R}}^*(z)}{\partial z} \Big|_{z=L_{\text{gap}}} \right|^2 . \tag{2.93}$$

According to Eq. (2.93), together with the energy $\hbar\omega^{\text{el}}$, the parallel component of the wavevector \mathbf{k}_{\parallel} must also be conserved in the transition due to the homogeneity of the system in the \mathbf{r}_{\parallel} direction. Further, the electronic wavefunctions appear in the expression of the transition rate in the form $\mathbf{j}_{\text{Bar}}(z) = \frac{i\hbar e}{2m_{\text{eff}}} [\Psi_{\text{R}}^*(z) \partial_z \Psi_{\text{L}}(z) - \Psi_{\text{L}}(z) \partial_z \Psi_{\text{R}}^*(z)] \mathbf{n}_z$ (where \mathbf{n}_z is the unit vector in the z direction) evaluated in the boundary between the gap and the right metal. In the original work by Bardeen, this term was associated to the transition current density of elastic tunneling, due to its similar form of the probability current density $\mathbf{j}(z) = \frac{i\hbar e}{2m_{\text{eff}}} [\Psi^*(\mathbf{r}) \nabla \Psi(\mathbf{r}) - \Psi(\mathbf{r}) \nabla \Psi^*(\mathbf{r})]$ of a quantum state.

The current density measured in an experiment is due to all possible transitions from occupied states of the left metal to unoccupied states of the right metal. Thus, the rate $\Gamma_{\text{L} \rightarrow \text{R}}$ must be summed for all these transitions. We first consider the sum over all final states, which leads to the transmission probability for each incident electron through the junction. To characterize the electronic states, we use the Sommerfeld model, where the electrons are considered to be free in a box of dimensions determined by the parameters S (along the \mathbf{r}_{\parallel} plane) and L_z (along the z direction). We further apply periodic boundary conditions in the box. Under these conditions, the states are given by wavevectors of the form $\mathbf{k}_{\text{L(R)}} = \left(\frac{2\pi}{\sqrt{S}} n_x, \frac{2\pi}{\sqrt{S}} n_y, \frac{2\pi}{L_z} n_z \right)$ with integers n_x , n_y and n_z . Considering the large number of states, we can substitute the discrete sum over all final states of wavevectors \mathbf{k}_{R} , $\frac{1}{L_z S} \sum_{\mathbf{k}_{\text{R}}}$, with the integral $\frac{1}{(2\pi)^3} \int d\mathbf{k}_{\text{R}}$, which leads to the expression

$$\Gamma_{\text{L}} = \sum_{\mathbf{k}_{\text{R}}} \Gamma_{\text{L} \rightarrow \text{R}} = \frac{L_z S}{2\pi (2\pi)^2} \int \Gamma_{\text{L} \rightarrow \text{R}} \frac{dk_{z\text{R}}}{d\omega_{\text{el}}^{\text{R}}} d\mathbf{k}_{\parallel \text{R}} d\omega_{\text{R}}^{\text{el}}$$

$$\begin{aligned}
 &= \frac{L_z S^2 \hbar^2}{4m_{\text{eff}}^2} \left. \frac{dk_{zR}}{d\omega_R^{\text{el}}} \right|_{\omega_R^{\text{el}}=\omega_L^{\text{el}}} \\
 &\times \left| \Psi_{R(\mathbf{k}_{\parallel L}, \hbar\omega_L^{\text{el}})}^*(z) \frac{\partial \Psi_{L(\mathbf{k}_{\parallel L}, \hbar\omega_L^{\text{el}})}(z)}{\partial z} - \Psi_{L(\mathbf{k}_{\parallel L}, \hbar\omega_L^{\text{el}})}(z) \frac{\partial \Psi_{R(\mathbf{k}_{\parallel L}, \hbar\omega_L^{\text{el}})}^*(z)}{\partial z} \right|_{z=L_{\text{gap}}}^2.
 \end{aligned} \tag{2.94}$$

The effect of the integral over the final states in Eq. (2.94) is thus to impose that the left and right states have the same parallel wavevector $\mathbf{k}_{\parallel L}$ and energy $\hbar\omega_L^{\text{el}}$, as expected for an elastic process. Further, the term $\frac{dk_{zR}}{d\omega_R^{\text{el}}} = \frac{m_{\text{eff}}}{\hbar k_{zR}}$ includes the density of states in the metal on the right. By introducing the expression of the wavefunctions of Eqs. (2.85) and (2.86) into Eq. (2.94), the transition rate per incident electron is calculated as

$$\Gamma_L = \frac{\hbar}{m_{\text{eff}} L_z} \frac{16k_{zL}^2 k_{zR} k_{z\text{gap}}^2}{(k_{zL}^2 + k_{z\text{gap}}^2)(k_{zR}^2 + k_{z\text{gap}}^2)} e^{-2k_{z\text{gap}} L_{\text{gap}}}. \tag{2.95}$$

The total tunneling rate is obtained after we sum Γ_L over all initial states of the left metal:

$$\begin{aligned}
 \Gamma_{\text{el}} = \sum_{\mathbf{k}_L}^{\text{occ.}} \Gamma_L &= \frac{L_z S}{2\pi (2\pi)^2} \int_0^\infty d\omega_L^{\text{el}} \int_0^{\min_{j \in \{L, R\}} \sqrt{\frac{2m_{\text{eff}}}{\hbar^2} (\hbar\omega_L^{\text{el}} - U_j)}} dk_{\parallel L} \\
 &\left[f_{\text{FD}}^L(\mathbf{k}_L) (1 - f_{\text{FD}}^R(\mathbf{k}_R)) \Gamma_L(\hbar\omega_L^{\text{el}}, k_{\parallel L}) 2\pi k_{\parallel L} \frac{dk_{zL}}{d\omega_L^{\text{el}}} \right].
 \end{aligned} \tag{2.96}$$

We notice that for each energy $\hbar\omega_L^{\text{el}}$, there are electronic states with wavevectors up to a maximal value of $|\mathbf{k}_{\parallel L(R)}| = \sqrt{\frac{2m_{\text{eff}}}{\hbar^2} (\hbar\omega_L^{\text{el}} - U_{L(R)})}$ in the metal on the left and on the right. Due to the conservation of \mathbf{k}_{\parallel} , a transition is valid only if both metals have an electronic state for a vector $\mathbf{k}_{\parallel L(R)}$. Thus, the integral has to be calculated up to the minimum between the two extremal values $|\mathbf{k}_{\parallel L(R)}|$ that accept a state in both metals. Further, in Eq. (2.96) we impose that the initial state of wavevector \mathbf{k}_L must be occupied [with probability given by the Fermi-Dirac occupation factor of the left metal $f_{\text{FD}}^L(\mathbf{k}_L)$] and that the final state of wavevector \mathbf{k}_R must be unoccupied [with probability $1 - f_{\text{FD}}^R(\mathbf{k}_R)$]. The calculation of Eq. (2.96) describes the electronic properties of different junctions, such as how the current intensity is modified according to the applied bias potential V_B .

The elastic tunneling rate Γ_{el} is a very important result of Bardeen's theory, as it allows the characterization of the electronic properties of tunneling junctions. Another important magnitude related to tunneling junctions is the inelastic tunneling rate Γ_{inel} , which quantifies the excitation rate of plasmonic resonances and thus describes how light is emitted from tunneling junctions. We discuss in Chapter 5 how Bardeen's theory describes light emission from tunneling junctions.

Further, we compare this theory with other methodologies and discuss the validity of the approximations involved in the approach of Bardeen.

AB INITIO DESCRIPTION OF PLASMONIC EXCITATIONS ON THE PD(110) SURFACE

3.1 Introduction

The study of surface plasmons in different metals [33, 75, 135, 136] has gained significant interest since Ritchie's first discovery [137]. A particular focus has been placed on understanding how the properties of surface plasmons, such as energy and lifetime, vary with in-plane wavevector \mathbf{q}_{\parallel} . As discussed in Chapter 1, for a metal with Drude permittivity, the energy of the surface plasmon is $\hbar\omega_{\text{SP}} = \hbar\omega_p/\sqrt{2}$ at all \mathbf{q}_{\parallel} (in the non-retarded regime), making it dispersionless. However, this classical Drude model neglects non-local effects. Incorporating these effects can provide more accurate information about the dispersion relation of surface plasmons, as outlined in Chapter 2. Indeed, in a simple model based on the homogeneous electron gas (HEG), Feibelman included the microscopic spatial distribution of the electronic density close to the jellium border of the metal, predicting that the dispersion relation of the surface plasmon in the $|\mathbf{q}_{\parallel}| \rightarrow 0$ limit is given by [138]

$$\hbar\omega_{\text{SP}} = \hbar\omega_{\text{SP}}(\mathbf{q}_{\parallel} = 0) \left(1 - \frac{\text{Re}\{d_{\perp}(\omega_{\text{SP}})\}}{2} |\mathbf{q}_{\parallel}| \right), \quad (3.1)$$

where d_{\perp} is the centroid of the induced electronic density relative to the jellium edge. The parameter d_{\perp} is of the order of 1 Å [139], and thus according to Eq. (3.1) the surface plasmon energy is modified by wavevectors \mathbf{q}_{\parallel} of magnitude of the order of 1 Å⁻¹, which are much larger than those corresponding to the retarded

regime (of the order of 10^{-3} \AA^{-1}). Calculations carried out for the jellium model with the random phase approximation (RPA) [140,141] and adiabatic local density approximation (ALDA) [142,143] show that in metals with typical bulk densities [$r_s = 2 - 6$, as given by Eq. (2.62)], the centroid of the induced density lies outside the jellium border ($d_\perp > 0$). This leads to a negative dispersion in Eq. (3.1). At larger $|\mathbf{q}_\parallel|$, the dispersion becomes positive when higher-order terms are included. This simple picture has been confirmed by several experiments in simple metals such as aluminum or magnesium [144,145].

However, the assumption that electrons behave as in a HEG is a simplistic description of most metals and do not provide accurate predictions for all systems. In fact, for some metals, there is a qualitative discrepancy between theoretical predictions and experimental measurements. For instance, in the case of silver, experimental measurements show a positive dispersion relation [146–149], as opposed to the theoretical prediction of a negative dispersion indicated in Eq. (3.1). This discrepancy is attributed to the presence of totally occupied $4d$ valence bands in silver, which significantly alter the behavior of electrons compared to the HEG [150–152]. Furthermore, the jellium model is inadequate for accurately predicting the lifetime of surface plasmons. In the $|\mathbf{q}_\parallel| \rightarrow 0$ limit, there are no electron-hole transitions in the HEG, and thus the surface plasmon should not decay. According to this model, the lifetime should therefore be infinite at long wavelengths. However, experimental measurements show that usually the lifetime of surface plasmons is of the order of few femtoseconds or shorter, even at low $|\mathbf{q}_\parallel|$.

To accurately describe the phenomena observed in experiments, more advanced and sophisticated descriptions of metals are necessary, for example based on the TDDFT approach (Sec. 2.3). The inclusion of the complete band structure, together with proper exchange-correlation effects, allows for the accurate consideration of all intraband and interband transitions that can modify the optical properties of the metal, such as the frequencies and lifetimes of excitations. In the case of surface plasmons in solids, the TDDFT approach was first successfully applied to the nearly free-electron metal Mg(0001) surface, where the experimental dispersion relation was reproduced with larger accuracy than with the HEG model [153]. *Ab initio* calculations applied to d metals such as silver [154] or gold [155,156] have successfully resolved the qualitative discrepancies of the simple HEG model, leading to the recovery of a positive surface plasmon dispersion.

Based on the success of TDDFT to reproduce the experimental features of surface plasmons in d metals, in the present chapter we use *ab initio* calculations to study the properties of these excitations on the Pd(110) surface. This study is motivated by a lack of accurate analysis of surface plasmons in palladium. We calculate the electronic structure of Pd(110) and then analyze the dispersion relation and damping of the corresponding surface plasmon. Our theoretical results allow for comparison with several experimental works that have obtained slightly different data. For example, electron energy loss spectroscopy experiments have measured surface excitations between 6.8 and 7.0 eV in single-crystal surfaces [157,158], and around 6.5 eV in polycrystalline Pd [159,160]. Other scattering experiments have also detected energy-loss peaks in the 7.2 – 7.5 eV energy range, which may also

be related to the surface plasmon [161, 162]. Further, the dispersion relation of the surface plasmon in palladium has been shown experimentally to depend strongly on the specific surface. While a nondispersive surface plasmon peak with energy 6.6 eV was observed on Pd(111) in Ref. [163], Rocca et al. found that the surface plasmon in Pd(110) exhibits an unusually strong negative linear dispersion in the $|\mathbf{q}_{\parallel}| \rightarrow 0$ limit [164, 165]. The authors proposed that the electronic structure of Pd(110) behaves differently with respect to simple and noble metals. However, no further analysis was conducted, and the results of this chapter could shed light on the discrepancies between different experimental data.

The calculation of the optical response of the Pd(110) surface is also motivated by the search for acoustic surface plasmons. As explained in Section 2.2.3, these excitations have a linear dispersion relation and are associated with considerably larger wavevectors than conventional surface plasmons. In the previous chapter, the dispersion of acoustic surface plasmons has been derived using the RPA in a system consisting of a 3D semi-infinite jellium and a 2D sheet of a HEG. However, this model does not consider the band structure of real metals. To observe acoustic surface plasmons in such systems, it is necessary to have electronic states highly localized in both the bulk and the surface with different Fermi velocities. No acoustic plasmon has been observed on palladium surfaces so far. However, Pd is a promising material for such excitations because it has been shown that several groups of electrons with different Fermi velocities lead to the existence of acoustic plasmons in bulk Pd [166, 167]. Therefore, the analysis of this chapter aims to clarify whether acoustic plasmons in bulk metal have any influence on the optical response of the surface and whether acoustic surface plasmons exist at the interface between Pd(110) and vacuum.

3.2 System and computational details

The objective of this chapter is to analyze the excitation spectra of the Pd(110) surface. To achieve this goal, we calculate the surface loss function $\text{Im}[\mathbf{g}(\mathbf{q}_{\parallel}, \omega)]$ of the system using the methodology described in Chapter 2. We start by self-consistently calculating the band structure using a homemade code [168]. The atomic structure of bulk palladium forms the face-centered cubic lattice. We use the experimental value of $a = 3.89 \text{ \AA}$ for the lattice parameter [169]. However, since the code used for the calculations considers periodic structures, we simulate the Pd(110) surface with a slab consisting of 19 atomic layers, separated by vacuum intervals of thickness corresponding to nine interlayer spacings. To avoid long-range Coulomb interactions between slabs, we use the methodology outlined in Sec. 2.3.3 so that we finally consider the optical response of a single slab without the influence of the other slabs.

In principle, the topmost three atomic layers in the Pd(110) surface have different interlayer distances than those in bulk due to surface relaxation, as reported by a low-energy diffraction experiment [170]. Specifically, the distance between the first two layers is modified by $-5.1 \pm 1.5\%$, and the distance between the second and

third layers is modified by $+2.9 \pm 1.5\%$. However, we have checked that this surface relaxation does not visibly affect the electronic band structure or the excitation spectra of the system. Therefore, we present our results using an ideal surface without any relaxation of atomic positions.

To calculate the electronic band structure, it is necessary to introduce the external potential into Eq. (2.57) to obtain the complete Kohn-Sham (KS) potential. The ionic electrostatic potential diverges at the exact positions of the ions [Eq. (2.47)], which makes the calculation of the KS orbitals computationally complex due to the large basis needed to reproduce these orbitals close to the ionic positions. To simplify this calculation, the method of pseudopotentials is usually used. We consider that the band structure near the Fermi energy is mainly determined by the valence electrons, which interact with the ions and also with the core electrons. To include the effect of the core electrons, we replace the ionic external potential with pseudopotentials. At distances far from the atomic nuclei, the contribution of the core electrons in the potential is negligible, and the pseudopotential is required to be exactly equal to the ionic potential at distances $r > R_c$ from the nuclei, for some defined core radius R_c . The negative charge of the core electrons neutralizes the positive charge of the nuclei, which softens the divergence of the ionic potential in the $r \rightarrow 0$ limit. With a pseudopotential that satisfies these conditions, we obtain a very similar band structure as with the KS equations of the real system, and the corresponding pseudowavefunctions are only modified at $r < R_c$ with respect to the real wavefunctions. In our calculations, we use the Troullier-Martins norm-conserving pseudopotential [171], where the norm of the pseudowavefunctions inside the core ($r < R_c$) is equal to that of the actual wavefunctions. Further, for the exchange-correlation potential in Eq. (2.57), we adopt the Ceperley-Alder form [123], which is based on the Local Density Approximation (LDA) and given by Eq. (2.61b).

Once the band structure of the Pd(110) surface has been obtained, the matrix elements of the non-interacting linear response function $\chi_{\mathbf{K},\mathbf{K}'}^{\text{KS}}$ can be calculated directly with Eq. (2.75) using the KS orbitals and energies [which are the solutions of Eq. (2.52)]. These orbitals are calculated for several \mathbf{k}_{\parallel} wavevectors in the surface Brillouin zone, and then the linear response function is given as a function of the wavevector \mathbf{q}_{\parallel} by summing the contribution of electronic orbitals at all \mathbf{k}_{\parallel} vectors. To account for all interband and intraband transitions, the Fermi-Dirac occupation factors $f_{\text{FD}}^{n\mathbf{k}_{\parallel}}$ for the n band at \mathbf{k}_{\parallel} wavevector must be included in the equation. We calculate these factors for a temperature of 10 meV to reduce noise from the discrete summation over \mathbf{k}_{\parallel} . This summation is performed over a 136×96 grid of \mathbf{k}_{\parallel} wavevectors in the surface Brillouin zone. Further, since the two different wavevectors used in this chapter (\mathbf{k}_{\parallel} , which is associated to the electronic band structure; and \mathbf{q}_{\parallel} , which gives the dispersion relation of the surface loss function, and thus, also of the plasmonic excitations) belong to the same grid, our calculations also set a minimum value of $|\mathbf{q}_{\parallel}^{\text{min}}| = \frac{2\pi}{96a} = 0.017 \text{ \AA}^{-1}$ for \mathbf{q}_{\parallel} accessible to calculate the optical response of the material.

Another important remark about Eq. (2.75) is that the surface response function

depends on an infinitesimal value of η . In practical calculations, a finite value of η must be used to avoid computational issues, resulting in an artificial broadening in the spectra. To avoid such broadening, we follow an alternative formulation. First, the imaginary part of the linear response function is calculated using the method described in Ref. [172], which does not depend on η . Then, the real part is calculated using the Kramers-Kronig relation [Eq. (2.16)]. This approach significantly accelerates the calculations. In order to obtain $\text{Re}[\chi_{\mathbf{K},\mathbf{K}'}^{\text{KS}}(\mathbf{q}_{\parallel},\omega)]$ at a single frequency, it is necessary to know $\text{Im}[\chi_{\mathbf{K},\mathbf{K}'}^{\text{KS}}(\mathbf{q}_{\parallel},\omega)]$ at all ω . With this aim, we consider in our calculations all the Pd valence states with energies up to 25 eV above the Fermi level, which ensures convergence of the results within the range of energies considered in this study.

Next, we calculate the linear response function of the interacting system in the supercell geometry using Eq. (2.67). Subsequently, we use Eq. (2.83) to calculate the linear response function associated with a single slab cutting the interaction with other slabs in the periodic structure. This last result enables us to obtain the surface loss function using Eq. (2.76) and the induced density using Eq. (2.65) [taking into account the external potential described by Eq. (1.33)]. To incorporate dynamical exchange-correlation effects, we use the dynamic exchange-correlation kernel K_{xc} in Eq. (2.67) under two approximations: the RPA and ALDA (Sec. 2.3.2). Previous studies have shown that at low values of $|\mathbf{q}_{\parallel}|$, the excitation spectrum of many metals remains largely unaffected by dynamical exchange and correlation, while the results at larger $|\mathbf{q}_{\parallel}|$ become more significantly affected [43, 173]. In the latter regime, ALDA typically yields better agreement with experimental observations than RPA [153, 174, 175]. Because of this agreement, in this chapter we show mostly results under ALDA, but we have checked the agreement between the results obtained with ALDA and RPA. We further show the comparison between the results under the two approximations. Since it has been shown that ALDA usually describes accurately experimental results in d metals, we expect that more sophisticated methods than using ALDA would not significantly impact our results.

3.3 Electronic band structure of the Pd(110) surface

Figure 3.1 presents the electronic band structure of the 19-atomic Pd(110) slab obtained from the *ab initio* calculations. The $4d$ bands dominate both the occupied and unoccupied valence band structure around the Fermi level, strongly hybridizing with $s - p$ states within the energy interval of -5.5 to 0.5 eV. Notably, the band structure exhibits energy gaps for bulk electronic states (indicated with gray curves in Fig. 3.1). For instance, a wide energy gap ranging from -0.2 to 2.2 eV is located around the $\bar{X}\bar{S}$ and $\bar{S}\bar{Y}$ symmetry directions. Additionally, two other gaps can be observed around the \bar{X} and \bar{Y} high-symmetry points, with the bottom at energies of 3.4 and 1.1 eV, respectively. Some narrow gaps can also be detected in the

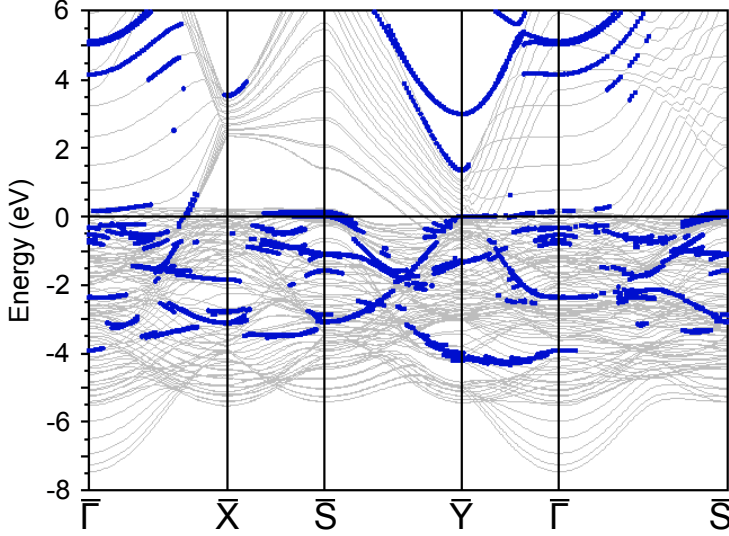


Figure 3.1: Band structure of the 19-atomic Pd(110) slab calculated along the lines of high symmetry in the surface Brillouin zone. The states with strong localization in the surface atomic layer are highlighted by blue dots.

occupied part of the bands.

While most of the bands plotted in Fig. 3.1 are associated to states of bulk palladium, we identify the states that are highly localized on the topmost atomic layer and could influence the excitation spectra of the surface by marking them with blue dots in Fig. 3.1. Interestingly, in the wide gap of bulk states (without blue dots) observed at the \bar{Y} point, we find two clear unoccupied surface states, where one is close to the bottom of the gap at 1.3 eV and the other at 3.0 eV. To verify the existence of these states, we have compared our results with data obtained by an inverse photoemission experiment in Ref. [176]. The experiment shows two surface states at the \bar{Y} point of the Brillouin zone, where one correlates well with the state at 1.3 eV obtained from our calculations, while the other is located at 3.5 eV and has an almost flat dispersion. This dispersion relation does not completely match the parabolic-like dispersion that we observe in Fig. 3.1 around similar energies, but the origin of this discrepancy is not clear. Furthermore, we obtain several other surface states around the $\bar{\Gamma}$ point with free-electron-like dispersion. These states could be the precursors of the image potential states, which are detected at 3.8 eV at the same point of the Brillouin zone in Ref. [176]. We also notice that most of the surface states are found below the Fermi level and are mainly of d type. These states could be related to many interband transitions in the surface region, but the existence of so many states does not allow us to establish any specific role for each of these states in the excitation spectra.

Surface states that are located in the vicinity of the Fermi level can have a particularly relevant contribution to the excitation spectra. In this regard, a surface state of d type is found around the \bar{Y} point, which is unoccupied at this point and has a small dispersion, but upon moving towards \bar{S} , the band crosses the Fermi level and becomes occupied. On the contrary, this state remains above the Fermi level and unoccupied along the $\bar{Y}\bar{T}$ direction. This surface state has been experimentally observed [176] and is also consistent with previous DFT calculations [177, 178]. Another state with similar characteristics is also observed around the \bar{S} point, which gets occupied in the $\bar{S}\bar{Y}$ direction and agrees with previous calculations [178]. The existence of such states around the Fermi level suggests the possibility of acoustic surface plasmons in the Pd(110) surface, arising from out-of-phase collective oscillations of charges involved in these surface states and in bulk. In Section 3.4.3, we analyze whether the band structure plotted in Fig. 3.1 leads to this excitation.

3.4 Excitation spectrum of the Pd(110) surface

3.4.1 Surface plasmon

Figure 3.2 displays the surface loss function $\text{Im}[\mathbf{g}(\mathbf{q}_{\parallel}, \omega)]$ of the Pd(110) surface obtained from the band structure discussed in Section 3.3. We use the ALDA to account for dynamical exchange-correlation effects and calculate the surface loss function at two different directions of \mathbf{q}_{\parallel} : the high-symmetry lines $\bar{\Gamma}\bar{X}$ and $\bar{\Gamma}\bar{Y}$. We find that the surface loss function does not significantly differ for both directions, indicating that the optical response of the Pd(110) surface is highly isotropic. The surface loss function is dominated by a broad surface plasmon peak labeled as SP (yellow-white color in the contour plot of Fig. 3.2). This peak is observed at energies ranging from 7.3 – 7.6 eV for most wavevectors \mathbf{q}_{\parallel} shown in Fig. 3.2. We also observe a shift in the peak for values $|\mathbf{q}_{\parallel}| < 0.1 \text{ \AA}^{-1}$, which occurs because the top and bottom interfaces of the 19-atomic slab interact with each other at such small wavevectors. Therefore, at this range of \mathbf{q}_{\parallel} , the considered system does not accurately represent an ideal surface. To extract the value of the semi-infinite surface plasmon at the $|\mathbf{q}_{\parallel}| \rightarrow 0$ limit, we directly extrapolate the maxima of the loss function from the $|\mathbf{q}_{\parallel}| \approx 0.1 - 0.4 \text{ \AA}^{-1}$ range. This extrapolation yields a value of $\hbar\omega_{\text{SP}}(\mathbf{q}_{\parallel} = 0) = 7.35 \text{ eV}$, which is consistent with the experimental value of $7.37 \pm 0.10 \text{ eV}$ reported by Rocca et al. in Ref. [164].

To confirm that the shift of the SP maxima at low $|\mathbf{q}_{\parallel}|$ is due to the finite thickness of the slab, we consider the classical dispersion of surface hybrid plasmons in a thin slab. Specifically, we analyze a slab composed of a Drude metal with a surface plasmon energy of $\hbar\omega_{\text{SP}} = \hbar\omega_p/\sqrt{2}$ and thickness L_{met} , for which the energies of the two non-retarded plasmonic modes are [33, 75, 137]

$$\hbar\omega_{\text{SP}}^{\pm} = \hbar\omega_{\text{SP}}(\mathbf{q}_{\parallel} = 0) \sqrt{1 \pm e^{-|\mathbf{q}_{\parallel}|L_{\text{met}}}}. \quad (3.2)$$

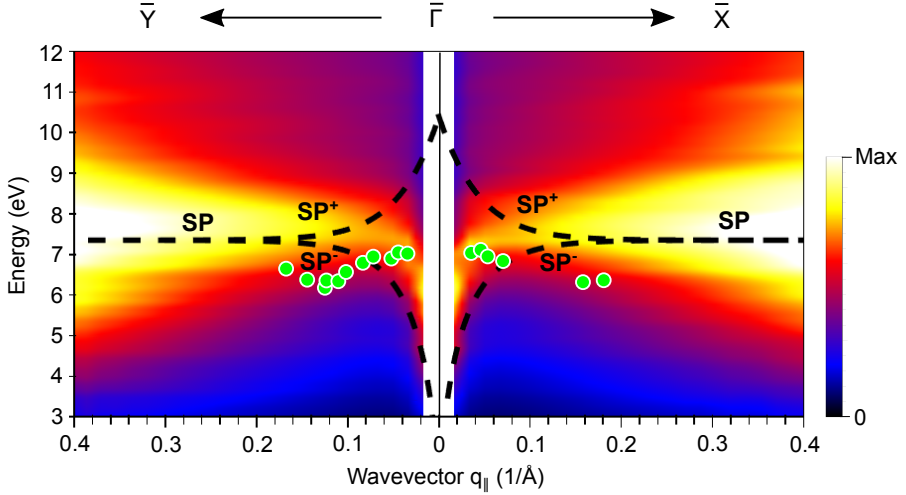


Figure 3.2: Surface loss function $\text{Im}[g(\mathbf{q}_{\parallel}, \omega)]$ of the 19-atomic Pd(110) slab along the lines of high symmetry $\overline{\Gamma\bar{X}}$ and $\overline{\Gamma\bar{Y}}$ in the surface Brillouin zone, calculated with ALDA. The dashed lines show the classical dispersion relation for surface modes in a thin film of a Drude metal [given by Eq. (3.2)], where the surface plasmon SP splits into two hybrid surface modes indicated by SP^+ and SP^- at small $|\mathbf{q}_{\parallel}|$. The green dots indicate the experimental data points of the surface plasmon dispersion reported in Ref. [164].

The classical dispersions of these two hybrid modes are depicted as dashed lines in Fig. 3.2, with the value $\hbar\omega_{\text{SP}}(\mathbf{q}_{\parallel} = 0) = 7.35$ eV obtained from the extrapolation. When $|\mathbf{q}_{\parallel}| \gg 1/L_{\text{met}}$, the two interfaces are decoupled, and the two modes are degenerate, with each mode corresponding to the surface plasmon of a single interface. At $|\mathbf{q}_{\parallel}| \approx 0.1 \text{ \AA}^{-1}$, the two modes start to split, and at lower wavevectors, we observe that the maximum of the surface loss function obtained with the full *ab initio* calculations follows a similar tendency as the classical dispersion labeled by SP^- , which corresponds to in-phase oscillations of electrons at both interfaces [179]. However, the surface plasmon peak obtained from TDDFT calculations displays a higher energy than the prediction of the Drude model. We attribute this effect to interband transitions involving *d* valence states, which are not included in the dispersion of Eq. (3.2). In fact, previous studies have shown that even in relatively simple metals, such as lead, the band structure effects can deviate the excitation spectra from the prediction of Eq. (3.2) [179].

Although the surface plasmon dispersion resulting from the TDDFT calculations agrees reasonably with the classical dispersion SP^- , no discernible feature is observed at energies above 7.35 eV marked by the dashed line labeled with SP^+ . This line corresponds to the antisymmetric mode where electronic charges of the two interfaces oscillate out of phase. The absence of a distinct peak in the surface loss function associated with a collective resonance suggests that interband

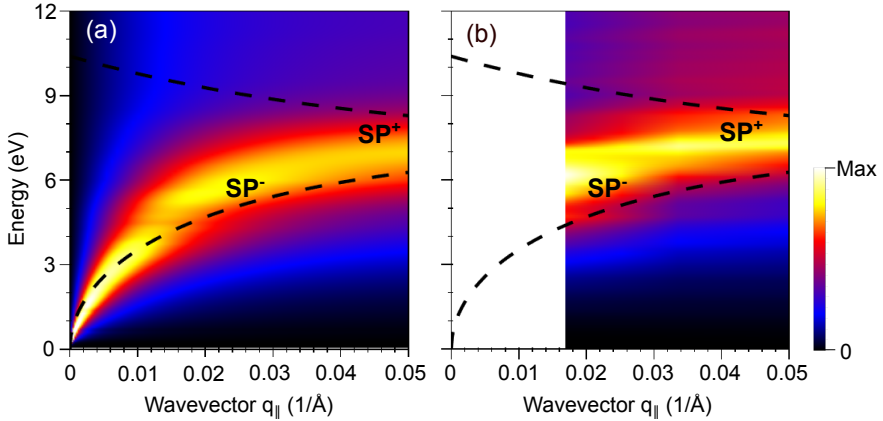


Figure 3.3: Surface loss function of the Pd(110) surface at low momentum transfers. a) $\text{Im}[g(\mathbf{q}_{\parallel}, \omega)]$ calculated for a Pd(110) slab of thickness equivalent to a 19-atomic slab obtained with classical electromagnetism under the non-retarded approximation. We use the bulk permittivity of Pd reported in Ref. [180]. b) $\text{Im}[g(\mathbf{q}_{\parallel}, \omega)]$ calculated for a 19-atomic Pd(110) slab within the *ab initio* approach along the $\bar{\Gamma}\bar{X}$ line (zoom in of Fig. 3.2). The dashed lines show the classical dispersion of the two hybrid surface modes SP^{-} and SP^{+} [Eq. (3.2)]. The white region in panel (b) at $|\mathbf{q}_{\parallel}| < 0.017 \text{ \AA}^{-1}$ is inaccessible in our *ab initio* calculations.

transitions dominate the spectra in this energy range. To support this explanation, we plot in Fig. 3.3a the surface loss function obtained from a classical non-retarded electromagnetic calculation using the experimental bulk permittivity of palladium of Ref. [180]. Within the range of $|\mathbf{q}_{\parallel}|$ considered in the figure, the SP^{-} hybrid mode dominates the spectra, while the intensity of the upper-energy SP^{+} peak is negligible. Furthermore, when performing corresponding calculations using the Drude permittivity instead of the experimental one, both SP^{+} and SP^{-} peaks become clearly visible with similar intensities (not shown). Notably, the classical calculation in Fig. 3.3a also demonstrates a deviation in the SP^{-} peak dispersion from the prediction of Eq. (3.2), as also observed in the results obtained with the TDDFT calculations (Figure 3.3b zooms in on the surface loss function plotted in Fig. 3.2 for the low- $|\mathbf{q}_{\parallel}|$ range). This comparison confirms that the Drude permittivity fails to account for the strong influence of d electrons at small wavevectors, which suppresses the SP^{+} mode and modifies moderately the dispersion of the SP^{-} mode.

We now shift our focus to the regime of large $|\mathbf{q}_{\parallel}|$. In this case, according to Eq. (3.2) and as also depicted in Fig. 3.2, the influence of the finite thickness of the film diminishes significantly, and therefore the results can be interpreted as being very close to those of a semi-infinite substrate. As previously discussed, the loss function exhibits a peak at an (extrapolated) energy of approximately 7.35 eV for low $|\mathbf{q}_{\parallel}|$, in agreement with experimental data from the same surface reported in Ref. [164].

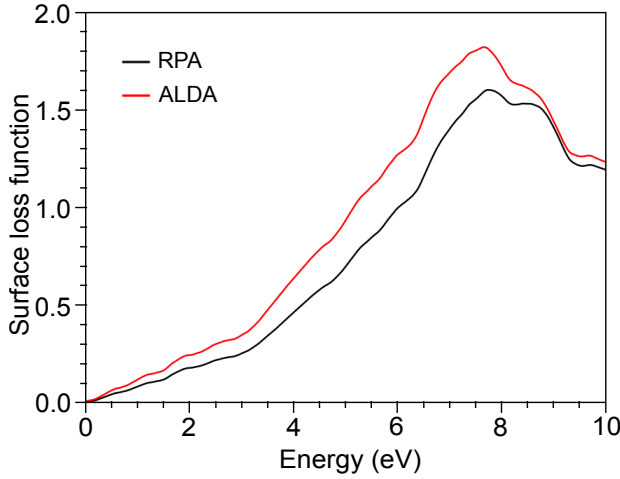


Figure 3.4: Surface loss function of Pd(110) calculated at $|\mathbf{q}_{\parallel}| = 0.370 \text{ \AA}^{-1}$ along the $\overline{\Gamma X}$ line using RPA (black line) and ALDA (red line).

However, when observing the behavior of the surface plasmon for increasing $|\mathbf{q}_{\parallel}|$, the agreement between our theoretical predictions and the experimental data is not so satisfactory. The experimental dispersion shows a negative trend up to 0.16 \AA^{-1} along the $\overline{\Gamma X}$ direction and up to 0.12 \AA^{-1} along the $\overline{\Gamma Y}$ direction, with an unusually large slope, even for materials that exhibit negative dispersion [153]. Subsequently, the dispersion becomes positive, at least up to the maximum value of $|\mathbf{q}_{\parallel}| = 0.18 \text{ \AA}^{-1}$ reported in the experiment. On the contrary, the surface loss function peak in our calculations displays a weak increase as a function of $|\mathbf{q}_{\parallel}|$, extending up to the maximum explored $|\mathbf{q}_{\parallel}|$. This behavior aligns more closely with the absence of dispersion observed for Pd(111) by Netzer and El Gomani [163]. However, the measured energy of 6.6 eV in that experiment significantly deviates from our calculations and the more recent experimental results reported by Rocca et al. in Ref. [164]. These discrepancies strongly suggest that band effects play a crucial role in determining the energy and dispersion of the surface plasmon, emphasizing the need for further analysis.

To evaluate the impact on the excitation spectrum of the approximations used in the dynamical exchange-correlation kernel K_{xc} , we compare the results obtained with ALDA (as discussed thus far) to those obtained with the simpler RPA. Initially, we have checked that for low $|\mathbf{q}_{\parallel}|$ the calculated surface loss function $\text{Im}[\mathbf{g}(\mathbf{q}_{\parallel}, \omega)]$ is nearly identical for both approximations. However, differences become apparent as $|\mathbf{q}_{\parallel}|$ increases, with ALDA generally yielding larger values of $\text{Im}[\mathbf{g}(\mathbf{q}_{\parallel}, \omega)]$ compared to RPA. The most significant differences occur on the low-energy side of the surface plasmon peak. To illustrate this, Fig. 3.4 presents the results obtained using both approximations for one of the largest $|\mathbf{q}_{\parallel}|$ values in our

calculations ($|\mathbf{q}_{\parallel}| = 0.370 \text{ \AA}^{-1}$ in the $\overline{\Gamma X}$ high-symmetry line), which corresponds to the regime where the most pronounced deviations between RPA and ALDA are observed. In this context, the RPA calculations indicate a surface loss function peak centered at $\hbar\omega_{\text{SP}} \approx 7.7 \text{ eV}$, while ALDA shifts the peak to slightly lower energies, placing it at $\hbar\omega_{\text{SP}} \approx 7.6 \text{ eV}$. Importantly, the relative difference between the two approximations is much smaller than the width of the peak itself. This finding indicates that dynamical exchange-correlation effects beyond the RPA have minimal influence on the description of surface plasmons in metals with high valence charge density, such as Pd. It is worth noting that for other metallic surfaces, such as those corresponding to the simple Mg, these effects are more significant [153], highlighting the dependence on the specific material under consideration.

In addition to providing information about the dispersion of the surface plasmon, the surface loss function also reveals its decay rate, which is directly linked to the linewidth of the peak calculated by the full width at half maximum. Interestingly, the value of the linewidth remains relatively large even at small $|\mathbf{q}_{\parallel}|$ values. For instance, at $|\mathbf{q}_{\parallel}| = 0.05 \text{ \AA}^{-1}$, both RPA and ALDA calculations yield a linewidth of $\approx 1.8 \text{ eV}$. This significant value can be attributed to the efficient decay of the surface plasmon into electron-hole pairs involving valence states of the d bands and highlights the necessity of considering real band structure effects. In contrast, the simple HEG model, which neglects these states, would predict a very narrow linewidth for the mode due to the absence of interband transitions. Furthermore, the linewidth broadens as the wavevector $|\mathbf{q}_{\parallel}|$ increases, indicating an increased decay into incoherent electron-hole pairs. At the largest $|\mathbf{q}_{\parallel}|$ value considered ($|\mathbf{q}_{\parallel}| = 0.4 \text{ \AA}^{-1}$), we obtain a linewidth of 3.3 eV for RPA and 4.9 eV for ALDA. This observation aligns with previous calculations demonstrating that, in general, ALDA predicts a more efficient decay into electron-hole pairs compared to RPA [128, 181]. Despite the large linewidth of the surface plasmon peak, this plasmon remains the dominant feature in the surface loss function for all the \mathbf{q}_{\parallel} vectors shown in Fig. 3.2. Consequently, the surface plasmon does not become completely suppressed by electron-hole decay within this range of wavevectors.

3.4.2 Induced density on the Pd(110) surface

To gain further insights into the nature of the peak observed in the surface loss function of Fig. 3.2, we now analyze the distribution of the induced charge density $\rho_{\text{ind}}(z, \mathbf{q}_{\parallel}, \omega)$. This density is induced by the external potential $V_{\text{ext}}(z, \mathbf{q}_{\parallel}, \omega)$, which is given by Eq. (1.33) and represents the Coulomb potential of an oscillating point charge placed at infinity. In Figs. 3.5a and b, we present the real and imaginary parts of $\rho_{\text{ind}}(z, \mathbf{q}_{\parallel}, \omega)$, respectively, as a function of energy and the spatial coordinate z (perpendicular to the surface) for a specific wavevector with a magnitude of $|\mathbf{q}_{\parallel}| = 0.084 \text{ \AA}^{-1}$ along the $\overline{\Gamma X}$ symmetry direction. Interestingly, near the energy $\hbar\omega_{\text{SP}} = 7.35 \text{ eV}$ corresponding to the surface loss function peak, $\text{Im}[\rho_{\text{ind}}(z, \mathbf{q}_{\parallel}, \omega \approx \omega_{\text{SP}})]$ (Fig. 3.5b) exhibits a dominant maximum positioned above the topmost atomic layer of palladium (atomic layers are indicated by

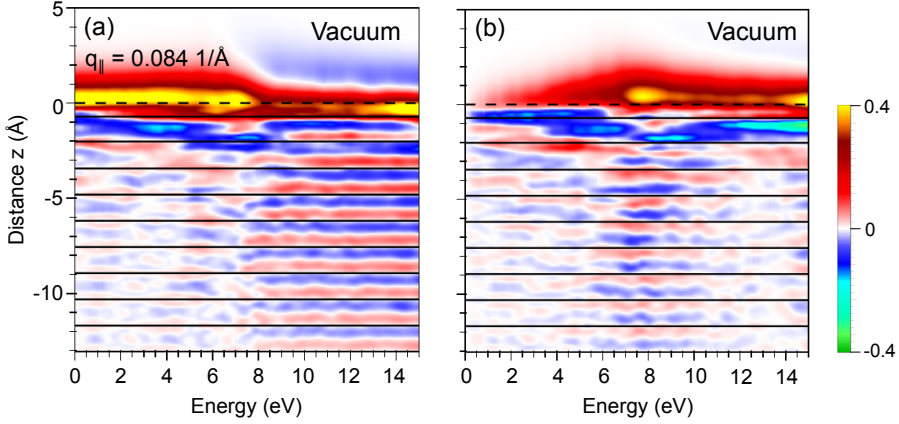


Figure 3.5: Spatial distribution for $|\mathbf{q}_{\parallel}| = 0.084 \text{ \AA}^{-1}$ along the $\overline{\Gamma X}$ direction of the a) real and b) imaginary parts of the charge density $\rho_{\text{ind}}(z, \mathbf{q}_{\parallel}, \omega)$ induced by the external potential $V_{\text{ext}}(z, \mathbf{q}_{\parallel}, \omega)$, plotted as a function of energy. The results are calculated using ALDA. The origin of the z coordinate corresponds to the geometrical surface position (dashed lines). Solid lines indicate the positions of the palladium atomic layers.

solid horizontal lines in the figure). This strong localization of the density close to the interface supports our assertion that the maximum of the surface loss function is associated with the surface plasmon. Additionally, due to the relatively small wavevector considered, the induced density penetrates deeply into the metal, displaying a relatively slow decay in amplitude while exhibiting oscillations with the same periodicity as the crystal lattice. Further, for energies exceeding $\hbar\omega_{\text{SP}} = 7.35$ eV, it is shown in Fig. 3.5a that $\text{Re}[\rho_{\text{ind}}(z, \mathbf{q}_{\parallel}, \omega)]$ presents an undamped oscillatory behavior. Thus, Pd(110) demonstrates at these energies a considerably larger optical transparency than for the $\hbar\omega_{\text{SP}} < 7.35$ eV range, where the decay of the induced density is stronger. This observation implies that at energies $\hbar\omega_{\text{SP}} > 7.35$ eV the electrons are less effective at screening the external electric field.

A significant aspect related to the induced density is the centroid position when a surface plasmon is excited, which is calculated by the first moment of $\rho_{\text{ind}}(z, \mathbf{q}_{\parallel}, \omega \approx \omega_{\text{SP}})$. This centroid is directly related to the Feibelman parameter d_{\perp} presented in Eq. (3.1), which gives the relative position of the centroid from the geometric position of the surface, and is calculated as

$$d_{\perp} = \frac{\int_{-\infty}^{\infty} z \rho_{\text{ind}}(z) dz}{\int_{-\infty}^{\infty} \rho_{\text{ind}}(z) dz}. \quad (3.3)$$

At the energy of $\hbar\omega_{\text{SP}} = 7.35$ eV, we determine the centroid for various small values of $|\mathbf{q}_{\parallel}|$ and find that the average centroid position is 0.635 \AA above the geometric surface position of the metal. This geometric surface is defined as to be above

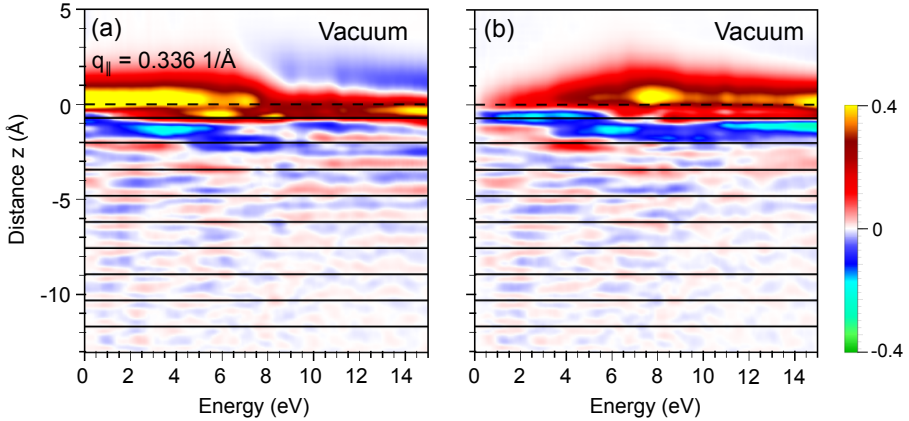


Figure 3.6: Spatial distribution for $|\mathbf{q}_{\parallel}| = 0.336 \text{ \AA}^{-1}$ along the $\overline{\Gamma X}$ direction of the a) real and b) imaginary parts of the charge density $\rho_{\text{ind}}(z, \mathbf{q}_{\parallel}, \omega)$ induced by the external potential $V_{\text{ext}}(z, \mathbf{q}_{\parallel}, \omega)$, plotted as a function of energy. The results are calculated using ALDA. The origin of the z coordinate corresponds to the geometrical surface position (dashed lines). Solid lines indicate the positions of the palladium atomic layers.

the topmost atomic layer at half the distance between atomic layers (indicated by dashed lines in Fig. 3.5, where we establish the $z = 0$ origin in this figure). Therefore, the centroid of the induced charge density is located outside the surface, contrary to the behavior observed in Ag and Au, where the influence of d electrons pushes the charge centroid inwards the metal [33]. In this regard, the placement of the induced charge centroid in palladium corresponds to the scenario exhibited by simple metals. However, our calculations also present differences with simple metals. For example, simple metals exhibit a negative dispersion at small $|\mathbf{q}_{\parallel}|$, while we obtain a weak positive dispersion for Pd(110).

According to this discussion, the electronic structure of Pd(110) exhibits two contrasting features: the presence of d electrons, which are considered to contribute to a positive dispersion of the surface plasmon [33], and the centroid position of the induced charge density outside the metal, which suggests a negative dispersion [Eq. (3.1) with $d_{\perp}(\omega_{\text{SP}}) > 0$]. Figure 3.2 shows that the overall effect is a positive dispersion with a considerably weaker slope compared to Au and Ag. This less pronounced surface plasmon dispersion in Pd could be attributed to the more delocalized nature of the d states. However, it is important to note that this conclusion is based solely on the surface loss function peak positions at $|\mathbf{q}_{\parallel}|$ values larger than approximately 0.05 \AA^{-1} . An accurate determination of the peak position at smaller $|\mathbf{q}_{\parallel}|$ values requires considering significantly thicker slabs of Pd(110) in TDDFT calculations, which would increase the computational cost.

We explore next how the induced charge density is modified with increasing wavevector. With this aim, we plot in Figs. 3.6a and b $\text{Re}[\rho_{\text{ind}}(z, \mathbf{q}_{\parallel}, \omega)]$ and

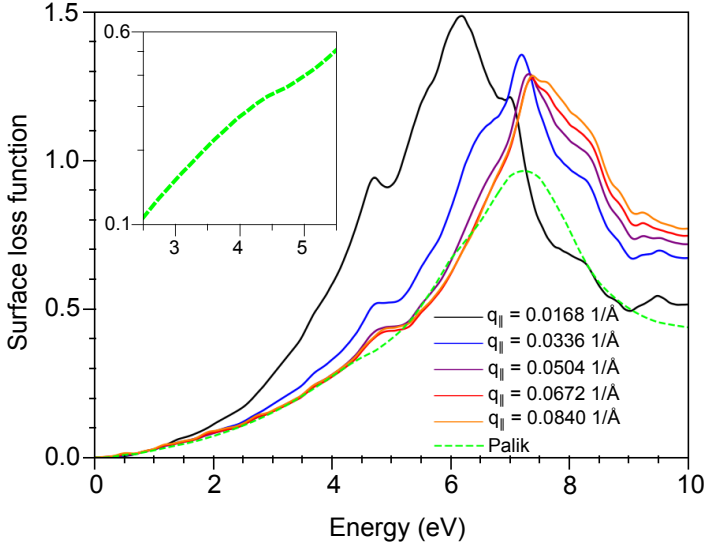


Figure 3.7: Surface loss function of the 19-atomic Pd(110) slab calculated with ALDA for the five smallest values of $|\mathbf{q}_{\parallel}|$ considered in our calculations along the $\bar{\Gamma}\bar{X}$ direction: 0.0168 \AA^{-1} (black solid line), 0.0336 \AA^{-1} (blue solid line), 0.0504 \AA^{-1} (purple solid line), 0.0672 \AA^{-1} (red solid line) and 0.0840 \AA^{-1} (orange solid line). The dashed green line shows the surface loss function calculated at $\mathbf{q}_{\parallel} = 0$ employing classical electromagnetic calculations with the experimental bulk permittivity of Pd reported in Ref. [180] by Palik. For the latter, the inset shows a zoom in the 2.5 – 5.5 eV interval.

$\text{Im}[\rho_{\text{ind}}(z, \mathbf{q}_{\parallel}, \omega)]$, respectively, evaluated at $|\mathbf{q}_{\parallel}| = 0.336 \text{ \AA}^{-1}$ along the $\bar{\Gamma}\bar{X}$ direction. We observe a clear peak in $\text{Im}[\rho_{\text{ind}}(z, \mathbf{q}_{\parallel}, \omega)]$ at energies around 7.6 eV, which correlates well with the peak observed in the surface loss function. The behavior of the induced density near the surface plasmon energy is similar to the case of low wavevectors (Fig. 3.5), but it presents some notable distinctions. As $|\mathbf{q}_{\parallel}|$ increases, the region influenced by the external field diminishes, resulting in a decreased efficiency in exciting the electrons within the bulk and a stronger confinement of the electronic density of the surface plasmon close to the vacuum-Pd(110) interface.

3.4.3 Additional plasmonic excitations

Although the surface plasmon peak dominates the surface loss function of Pd(110), a closer examination of Fig. 3.2 at low values of $|\mathbf{q}_{\parallel}|$ reveals a subtle peak around 4.9 eV. To provide a clearer illustration, we show in Fig. 3.7 the surface loss function at the five lowest $|\mathbf{q}_{\parallel}|$ values accessible in our TDDFT calculations along the $\bar{\Gamma}\bar{X}$ direction (which correspond to vertical cuts in Fig. 3.2). The small peak observed at 4.9 eV increases in energy and diminishes in spectral weight as $|\mathbf{q}_{\parallel}|$ increases

until it eventually disappears at 5.0 eV for $|\mathbf{q}_{\parallel}| = 0.17 \text{ \AA}^{-1}$. The impact of this excitation can also be observed in the induced density shown in Fig. 3.5, where the real part (panel a) exhibits weak resonating behavior around 4.9 eV within the crystal, and a weak oscillating feature along z is discernible in the imaginary part (panel b) at the same energy. Liu and Brown [182, 183] detected a similar mode at an energy of 5.2 eV without resolving its dispersion and interpreted it as a surface feature. Given that we observe this excitation in the surface loss function $\text{Im}[\mathbf{g}(\mathbf{q}_{\parallel}, \omega)]$, its effects are indeed influenced by the surface. However, the presence of resonances associated with the induced density inside the bulk suggests that the origin of this excitation lies in the bulk properties of Pd. To validate this, in Fig. 3.7 we indicate by the green dashed line the classical surface loss function at $\mathbf{q}_{\parallel} = 0$ obtained using the experimental bulk permittivity of palladium reported in Ref. [180]. A weak feature around 4.5 eV can be distinguished (see inset for a zoom), and we attribute it to the excitation obtained in our TDDFT calculations. Consequently, we have established that the bulk permittivity of Pd already encompasses this excitation.

Hence, the surface loss function primarily exhibits two notable features: the dominant surface plasmon peak and a relatively smaller peak around 4.9 eV. Apart from these excitations, no other significant features are observed in the surface loss function, regardless of whether ALDA or RPA is employed. The absence of any prominent peak at low energies (below 4 eV) indicates that our calculations do not provide evidence of low-energy interband plasmons or acoustic surface plasmons. This lack of evidence may be due to the abundance of surface states in the valence band structure of Pd(110), as observed in Fig. 3.1. Although the presence of surface states near the Fermi level should, in principle, facilitate the occurrence of acoustic surface plasmons with linear dispersion, the numerous amount of transitions involving surface states discourages the formation of well-defined resonances corresponding to collective excitations. This stands in contrast to the situation in the bulk [166, 167]. Consequently, our calculations suggest that the Pd(110) surface may represent a scenario where the mere existence of distinct electronic states localized in the bulk and on the surface is insufficient to generate a surface collective mode with a linear dispersion.

3.5 Summary

In this chapter, we have presented the TDDFT-based calculations of the excitation spectra of the Pd(110) surface. The surface loss function presents a prominent feature corresponding to the surface plasmon, which manifests at an energy of 7.35 eV for small wavevectors. This result aligns with existing experimental data for this surface at low $|\mathbf{q}_{\parallel}|$. However, as $|\mathbf{q}_{\parallel}|$ increases, our TDDFT calculations predict a weak positive dispersion of the surface plasmon up to approximately $|\mathbf{q}_{\parallel}| = 0.4 \text{ \AA}^{-1}$. This finding contradicts the electron energy-loss experiments conducted on this surface, as reported in Ref. [164], where a pronounced negative dispersion of the surface plasmon was observed at low $|\mathbf{q}_{\parallel}|$. Hence, the excitation spectrum of the

Pd(110) surface exhibits a substantial discrepancy between the *ab initio* surface response calculations and the electron energy-loss experiments. Accordingly, further experimental and theoretical investigations are required to discover the origin of such discrepancy. From a theoretical viewpoint, it is important to acknowledge that the present calculations are conducted by considering the response of the surface to an external static charge, and a more accurate theoretical description of the experiment could be achieved by surpassing this assumption. In this respect, the dynamics of the incident probing electron should be also considered quantum mechanically in the same way as the free electrons in the metal [184, 185].

The calculations presented in this chapter highlight the significance of considering accurately the electronic structure of metals, emphasizing the limitations of a classical Drude description. In contrast to the Drude model, which predicts two modes in the low- $|\mathbf{q}_{\parallel}|$ region, the *ab initio* calculations demonstrate a modified dispersion for the mode at low energies, while no evidence of the upper mode is observed due to the impact of band structure effects. Therefore, interband and intraband transitions within the metal can significantly perturb the excitation spectra from the simplest description of free particles in a HEG. Further, a local description is not valid in the range of wavevectors \mathbf{q}_{\parallel} considered in this chapter. Therefore, only a quantum non-local description based on the atomic structure of the material can give accurately the dispersion relation of the surface plasmon and the density induced by an external potential.

On the other hand, *ab initio* calculations performed in other metals previously revealed an important feature that the Drude model cannot describe: the existence of acoustic surface plasmons resulting from the out-of-phase collective excitations of surface and bulk electrons. However, the calculated surface loss function exhibits a robust resonant response only at ultraviolet energies and no signature of low-energy collective excitations is found, despite the presence of surface states near the Fermi level. While the coexistence of free-electron-like states in both the surface and bulk enables the formation of acoustic surface plasmons (Sec. 2.2.3), our findings suggest that an abundance of surface states can impede the emergence of well-defined collective excitations. Adopting a quantum perspective that accounts for free electrons alone is also insufficient for an accurate description of acoustic surface plasmons, because this model only considers a single electronic band for the surface electrons. Therefore, a thorough analysis of the band structure is necessary to determine whether a particular system can support these acoustic excitations.

PLASMONIC EXCITATIONS IN TWO-DIMENSIONAL ANISOTROPIC ELECTRON SYSTEMS

4.1 Introduction

As discussed in Sec. 1.2.1, the properties of plasmonic excitations are highly influenced by the geometry of metallic systems [86]. For instance, we have examined the behavior of a Drude metal with bulk plasmon frequency ω_p , revealing that the frequency of the surface plasmon at a planar metal-vacuum interface is $\omega_p/\sqrt{2}$, while in the case of a metallic sphere, this value shifts to $\omega_p/\sqrt{3}$. By carefully selecting the appropriate geometry, the frequency of the plasmonic excitation can be engineered. However, in three-dimensional systems, this frequency tends to converge to a finite value in the $|\mathbf{q}_{\parallel}| \rightarrow 0$ limit. In this context, two-dimensional (2D) materials have emerged as a highly promising alternative. Unlike in their three-dimensional counterparts, plasmons in 2D materials exhibit a dispersion as $\omega \propto \sqrt{|\mathbf{q}_{\parallel}|}$ when the wavevector \mathbf{q}_{\parallel} approaches zero. Consequently, 2D materials can support plasmons with arbitrarily small frequencies in the non-retarded regime, even in the mid-infrared and THz regions of the electromagnetic spectrum.

The investigation of plasmons in two-dimensional materials was pioneered by Stern [48], who initially calculated the $\omega \propto \sqrt{|\mathbf{q}_{\parallel}|}$ -like dispersion, as described in Sec. 2.2.2. This calculation was conducted assuming that the material behaves like a 2D homogeneous electron gas and using the random phase approximation (RPA). Subsequently, further theoretical and experimental investigations confirmed the predicted dispersion of the 2D plasmon in metallic layers (caused by surface electronic states) [173] and in graphene [186]. However, the energy band dispersion

in many other 2D systems can be significantly different from that corresponding to free electrons, leading to the need of further studies to analyze whether 2D plasmons exhibit a similar dispersion in systems with diverse electronic structures. For instance, certain materials exhibit an anisotropic band structure, resulting in an anisotropic 2D plasmon dispersion, as observed in graphene [186, 187], borophene [188, 189], and black phosphorous [190–192], for example.

In this context, some previous works have been focused on investigating the effects of anisotropy on conventional 2D and 3D plasmons. These works have analyzed anisotropy by considering materials with an elliptical band dispersion [193–195] and found modifications on the dispersion of the conventional plasmon, but no additional modes were observed. However, a recent study that considered accurately the anisotropic band structure of graphene predicted the emergence of an acoustic plasmon (AP) in this material [187], due to the presence of electrons with different Fermi velocities in two valleys of the same energy band. The AP has a linear dispersion $\omega \propto |\mathbf{q}_{\parallel}|$ and is associated with even larger wavevectors than the conventional 2D plasmon with $\omega \propto \sqrt{|\mathbf{q}_{\parallel}|}$ -like dispersion, which makes it promising for concentrating light on an even smaller scale than that achieved with usual 2D materials. Nevertheless, according to the current understanding, acoustic plasmons can only appear in systems with two different groups of electrons. For example, these groups of electrons can correspond to states localized in the surface and in the bulk [117], or to $s - p$ and d states with different Fermi velocities [166]. However, such a situation cannot occur in 2D materials with a single band, and there is a lack of studies focusing on the origin of the existence of different groups of electrons in these systems that may lead to acoustic plasmons.

Motivated by the promising potential of anisotropic 2D materials to support acoustic plasmons, this chapter focuses on investigating how the specific form of anisotropy in the band structure of a 2D system can influence its plasmonic characteristics. While previous studies primarily examined materials with elliptical band dispersion and did not observe acoustic plasmons, band structures with other types of anisotropy have been measured in recent years. Some examples are the band structure with triangular form found in borophene [52], the diamond-like structure in the topological nodal semimetal ZrSeS [50, 51, 53], and the hexagonal arrangement in the topological insulator Bi₂Se₃ [49]. Consequently, we analyze the dispersion relations of plasmons in materials featuring such anisotropies. In particular, we study the permittivity and the properties of plasmonic excitations in a free and homogeneous electron gas with a distorted Fermi surface (the band structure of the materials and further details of the calculations are given in Sec. 4.2), considering triangular anisotropy (Sec. 4.3.1), square anisotropy (Sec. 4.3.2), and hexagonal anisotropy (Sec. 4.3.3). Additionally, we discuss the effects of anisotropy on the plasmonic excitations in intermediate situations that lie between isotropic and ideally anisotropic materials (Sec. 4.3.4). These calculations allow us, on the one hand, to analyze how the dispersion of the conventional 2D plasmon is altered depending on the type of anisotropy and, on the other hand, to perform a systematic study of the properties of acoustic plasmons in 2D materials.

4.2 Details of calculations

To obtain the properties of plasmons in 2D anisotropic materials, we first calculate the permittivity of these materials employing the RPA. We follow the methodology outlined in Chapter 2 for this purpose. The initial step involves computing the linear response function for the non-interacting system, denoted as $\chi^0(\mathbf{q}_{\parallel}, \omega)$. In a general system, this function is defined by Eq. (2.11). However, in the case of a non-interacting 2D homogeneous electron gas of surface area S , the corresponding expression simplifies to

$$\begin{aligned}\chi^0(\mathbf{q}_{\parallel}, \omega) &= \lim_{\eta \rightarrow 0} \frac{1}{S} \sum_{\mathbf{k}_{\parallel}} \frac{f_{\text{FD}}(\mathbf{k}_{\parallel}) - f_{\text{FD}}(\mathbf{k}_{\parallel} + \mathbf{q}_{\parallel})}{\omega - (\omega_{\mathbf{k}_{\parallel} + \mathbf{q}_{\parallel}} - \omega_{\mathbf{k}_{\parallel}}) + i\eta} \\ &= \lim_{\eta \rightarrow 0} \frac{1}{(2\pi)^2} \int d\mathbf{k}_{\parallel} \frac{f_{\text{FD}}(\mathbf{k}_{\parallel}) - f_{\text{FD}}(\mathbf{k}_{\parallel} + \mathbf{q}_{\parallel})}{\omega - (\omega_{\mathbf{k}_{\parallel} + \mathbf{q}_{\parallel}} - \omega_{\mathbf{k}_{\parallel}}) + i\eta}.\end{aligned}\quad (4.1)$$

Here, $\omega_{\mathbf{k}_{\parallel}}$ represents the energy of the single electronic band at the two-dimensional wavevector \mathbf{k}_{\parallel} . η is an infinitesimal parameter introduced just to avoid divergences in the calculations, but the actual result is given by the $\eta \rightarrow 0$ limit. We assume that the surface area S is infinitely large, allowing us to treat all \mathbf{k}_{\parallel} as infinitesimally close to each other. This assumption enables us to convert the discrete sum into an integral in Eq. (4.1), simplifying the calculations. Furthermore, to characterize the occupied and unoccupied states in the system, we consider the Fermi-Dirac distribution and specifically focus on the case of zero temperature. Thus, we approximate the Fermi-Dirac occupation factors $f_{\text{FD}}(\mathbf{k}_{\parallel})$ using the Heaviside step function as $f_{\text{FD}}(\mathbf{k}_{\parallel}) \approx \Theta(E_{\text{F}} - \omega_{\mathbf{k}_{\parallel}})$, where E_{F} denotes the Fermi energy.

Importantly, in Eq. (4.1) two different wavevectors are involved: \mathbf{k}_{\parallel} and \mathbf{q}_{\parallel} . While the symbol \mathbf{k}_{\parallel} refers to the wavevector of the electrons in the metal, the symbol \mathbf{q}_{\parallel} gives the dispersion relation of the response function $\chi^0(\mathbf{q}_{\parallel}, \omega)$ and permittivity $\varepsilon(\mathbf{q}_{\parallel}, \omega)$. According to linear response theory, the response function of Eq. (4.1) relates the external potential $V_{\text{ext}}(\mathbf{q}_{\parallel}, \omega)$ with the density induced in the system by this potential as $V_{\text{ext}}(\mathbf{q}_{\parallel}, \omega)\chi^0(\mathbf{q}_{\parallel}, \omega) = \rho_{\text{ind}}(\mathbf{q}_{\parallel}, \omega)$. From this perspective, the result of Eq. (4.1) can be interpreted in the following way: the external potential transfers the momentumⁱ \mathbf{q}_{\parallel} to an electron with initial momentum \mathbf{k}_{\parallel} . Thus, the electron is excited from a state of momentum \mathbf{k}_{\parallel} to another state of momentum $\mathbf{k}_{\parallel} + \mathbf{q}_{\parallel}$, which creates the fluctuations of the induced density $\rho_{\text{ind}}(\mathbf{q}_{\parallel}, \omega)$ given by wavevector \mathbf{q}_{\parallel} . The linear response function $\chi^0(\mathbf{q}_{\parallel}, \omega)$ is therefore given by the contribution of all possible transitions after the momentum transfer \mathbf{q}_{\parallel} , i.e. all transitions from an initial occupied state of momentum \mathbf{k}_{\parallel} [given by the Fermi-Dirac occupation factor $f_{\text{FD}}(\mathbf{k}_{\parallel})$] to a final unoccupied state

ⁱ Since, as described below, in this chapter we adopt units where $\hbar = 1$, the vector \mathbf{q}_{\parallel} is associated with both the wavevector that represents the spatial Fourier transform of the permittivity $\varepsilon(\mathbf{q}_{\parallel}, \omega)$ and the momentum $\hbar\mathbf{q}_{\parallel}$ transferred by an external perturbation to the system. Therefore, we use these two magnitudes to refer to the variable \mathbf{q}_{\parallel} . Similarly, we refer to the parameter ω as both the frequency and the energy $\hbar\omega$ given by the external perturbation.

of momentum $\mathbf{k}_{\parallel} + \mathbf{q}_{\parallel}$ [given by the Fermi-Dirac occupation factor $f_{\text{FD}}(\mathbf{k}_{\parallel} + \mathbf{q}_{\parallel})$].

After performing the integral in Eq. (4.1), we calculate the permittivity $\varepsilon(\mathbf{q}_{\parallel}, \omega)$ within the RPA using Eq. (2.22), which involves the two-dimensional Fourier transform of the Coulomb potential as given by Eq. (2.31). This calculation provides us with both the real part $\varepsilon_{\text{R}}(\mathbf{q}_{\parallel}, \omega)$ and imaginary part $\varepsilon_{\text{I}}(\mathbf{q}_{\parallel}, \omega)$ of the permittivity. From this permittivity, we extract the loss function $-\text{Im}[\varepsilon^{-1}(\mathbf{q}_{\parallel}, \omega)]$, which allows us to obtain the collective excitations of the system that emerge as well-defined peaks in this function. Considering that $-\text{Im}[\varepsilon^{-1}(\mathbf{q}_{\parallel}, \omega)] = \varepsilon_{\text{I}}(\mathbf{q}_{\parallel}, \omega) / [\varepsilon_{\text{R}}(\mathbf{q}_{\parallel}, \omega)^2 + \varepsilon_{\text{I}}(\mathbf{q}_{\parallel}, \omega)^2]$, the peaks in the loss function are given by the zeroes of the real part of the permittivity $\varepsilon_{\text{R}}(\mathbf{q}_{\parallel}, \omega)$. Further, the loss function is also nonzero when $\varepsilon_{\text{R}} \neq 0$, if $\varepsilon_{\text{I}} > 0$. This last condition corresponds to the excitation of electron-hole pairs (Sec. 2.2).

The energy band dispersion $\omega_{\mathbf{k}_{\parallel}}$ is a key parameter to calculate the permittivity according to Eq. (4.1), as it characterizes the specific system under investigation. In this chapter, we consider anisotropic free electron gases with different geometries on the Fermi surfaces. The energy dispersion of the single electronic band of these systems can be expressed using a general form given by the following equation:

$$\omega_{\mathbf{k}_{\parallel}} = \left(\max_{n \in \{1, 2, \dots, N\}} \left\{ k_x \cos\left(2\pi \frac{n}{N}\right) + k_y \sin\left(2\pi \frac{n}{N}\right) \right\} \right)^2, \quad (4.2)$$

which is valid for a 2D material with a band characterized by curves of constant energy that are regular polygons with N sides. Specifically, we focus on three different forms for the anisotropy: triangular anisotropy with $N = 3$, square anisotropy with $N = 4$, and hexagonal anisotropy with $N = 6$. In all the systems we analyze, for any fixed direction $\mathbf{n}_{\mathbf{k}_{\parallel}} = \frac{\mathbf{k}_{\parallel}}{|\mathbf{k}_{\parallel}|}$ in the k -space, the band structure resembles that of a free electron gas, with the energy following the relation $\omega_{\mathbf{k}_{\parallel}} \propto |\mathbf{k}_{\parallel}|^2$. The primary effect of anisotropy is observed in the effective mass m_{eff} of the electrons, which depends on the direction $\mathbf{n}_{\mathbf{k}_{\parallel}}$. This relationship is given by $m_{\text{eff}}^{-1} \propto \nabla_{\mathbf{n}}(\nabla_{\mathbf{n}}\omega_{\mathbf{k}_{\parallel}})$ [129], where $\nabla_{\mathbf{n}}$ represents the directional derivative along $\mathbf{n}_{\mathbf{k}_{\parallel}}$. Notably, in all systems following the dispersion equation of Eq. (4.2), the minimum effective mass occurs in the direction normal to the sides of the Fermi surface, while the maximum value is observed in the direction aligned with the edges of the corresponding polygon. The existence of electrons with different effective masses can result in acoustic plasmons, as we analyze in the following.

Last, we note that in this chapter, we adopt a unit system where $\hbar = 1$ and $m_e = 1$. Consequently, we eliminate these prefactors in the relation between the energy $\omega_{\mathbf{k}_{\parallel}}$ and wavevector \mathbf{k}_{\parallel} , which leads to a more concise expression between these two magnitudes, as described by Eq. (4.2).

4.3 Excitation spectra of two-dimensional anisotropic electron gases

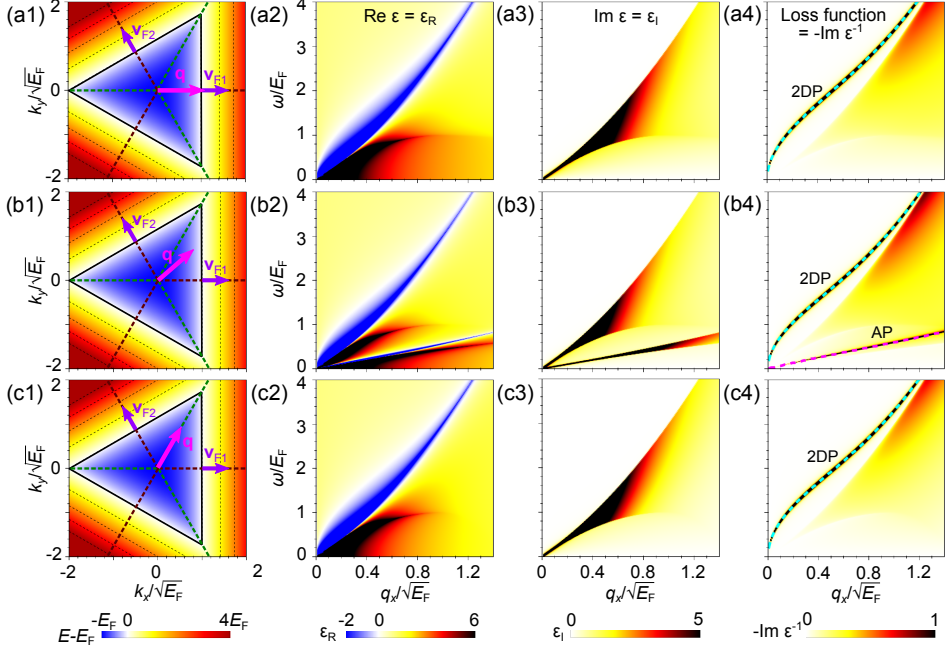


Figure 4.1: Band structure, permittivity, and loss function for a 2D system with triangular band structure. a1) Band structure $\omega_{\mathbf{k}_{\parallel}}$ of the material (contour plot) with the two main symmetry directions of the lowest and the largest effective masses marked by thick brown and green dashed lines, respectively. Thin black dashed lines highlight curves of constant energies, and the black solid line shows the Fermi surface. The momentum \mathbf{q}_{\parallel} along the $q_y = 0$ direction is shown by the magenta arrow. The Fermi velocities \mathbf{v}_{F1} and \mathbf{v}_{F2} of the carriers at the two edges are marked by purple arrows. a2) Real and a3) imaginary parts of the permittivity, and a4) loss function as a function of the momentum component q_x and energy ω . In (a4) the 2D plasmon peak (2DP) is marked by a cyan dashed line. Row b) Same as in the panels of row (a), for momentum transfers \mathbf{q}_{\parallel} with $q_y = \frac{\sqrt{3}}{2}q_x$. Additionally, in (b4) the acoustic plasmon peak AP is highlighted by a magenta dashed line (see labels). Row c) Same as in the panels of row (a), for \mathbf{q}_{\parallel} with $q_y = \sqrt{3}q_x$.

4.3.1 Triangular anisotropy

The permittivity $\varepsilon(\mathbf{q}_{\parallel}, \omega)$ and the loss function $-\text{Im}[\varepsilon^{-1}(\mathbf{q}_{\parallel}, \omega)]$ of the electronic system with triangular anisotropy (where the band dispersion is given by Eq. (4.2) with $N = 3$) are reported in Fig. 4.1. We calculate the permittivity as a function of the x component of the momentum, q_x , for three different directions of the \mathbf{q}_{\parallel} vector given by the equations $q_y = 0$, $q_y = \frac{\sqrt{3}}{2}q_x$, and $q_y = \sqrt{3}q_x$. The momentum transfers \mathbf{q}_{\parallel} along these three directions are indicated by magenta arrows in panels (a1), (b1), and (c1) of Fig. 4.1, respectively, where the contour plot represents the energy band dispersion $\omega_{\mathbf{k}_{\parallel}}$ in the 2D plane (the same in the three panels). The high-symmetry directions of the band structure are indicated by a brown and a

green dashed line, for directions with the lowest and largest effective masses for the electrons, respectively.

The collective excitations characterized by the momentum \mathbf{q}_{\parallel} and energy ω are extracted from the positions of the sharp peaks in the loss function, shown in Fig. 4.1a4. When the momentum of the perturbation lies in the $q_y = 0$ direction, we observe a continuum of electron-hole excitations in the area delimited by $\frac{\omega}{E_F} < \left(\frac{q_x}{\sqrt{E_F}}\right)^2 + 2\left(\frac{q_x}{\sqrt{E_F}}\right)$ (the electron-hole continuum corresponds to the $\varepsilon_I(\mathbf{q}_{\parallel}, \omega) > 0$ region of that can be observed in Fig. 4.1a3 and is the same as the blue area indicated in Fig. 2.2a). This condition corresponds to the range of energies $\omega_{\mathbf{k}_{\parallel}+\mathbf{q}_{\parallel}} - \omega_{\mathbf{k}_{\parallel}}$ where intraband transitions can occur for a given q_x according to Eq. (4.2), as also occurs for systems with an isotropic 2D band dispersion [48] (see Sec. 2.2.2). Besides the area representing the electron-hole continuum, in Fig. 4.1a4 we observe a narrow peak highlighted by a cyan dashed line, corresponding to the 2D plasmon (2DP). This excitation lies outside the electron-hole continuum, and the absence of any decay path into electron-hole pairs leads to an infinite lifetime for the plasmon (for an ideal homogeneous electron gas as assumed in this chapter). The finite thickness of the plasmon peak seen in Fig. 4.1a4 is solely due to the finite parameter η introduced in calculations employing Eq. (4.1) to avoid numerical issues. Interestingly, the dispersion of the 2D plasmon is similar to that in an isotropic free electron gas predicted by Stern [48], with a $\sqrt{q_x}$ -like dependence at small momentum transfers. The triangular energy anisotropy only slightly distorts the dispersion of the plasmon in this symmetry direction, but otherwise, most of the corresponding properties of isotropic materials appear also in the anisotropic case.

At momentum transfers along the direction parameterized by $q_y = \frac{\sqrt{3}}{2}q_x$ (magenta arrow in Fig. 4.1b1), the excitation spectrum of the system exhibits greater complexity compared to the $q_y = 0$ case. This can be observed in Figs. 4.1b2, b3, and b4, which show ε_R , ε_I , and $-\text{Im}[\varepsilon^{-1}]$, respectively. In Fig. 4.1b3, the upper boundary of the electron-hole continuum in ε_I appears nearly identical to the $q_y = 0$ case in Fig. 4.1a3, but an additional sharp peak is visible at low energies ω . The presence of a distinct two-peak structure in ε_I can be explained by the occurrence of intraband transitions near the Fermi surface at two specific energy values. In this system, all electrons have the same magnitude of Fermi velocity $v_F = |\mathbf{v}_F|$, but there are three groups of carriers with Fermi velocity vectors $\mathbf{v}_F \propto \frac{\partial \omega_{\mathbf{k}_{\parallel}}}{\partial \mathbf{k}_{\parallel}}$ pointing in different directions: $\mathbf{v}_{F1} = v_F(1, 0)$, $\mathbf{v}_{F2} = v_F\left(-\frac{1}{2}, \frac{\sqrt{3}}{2}\right)$, and $\mathbf{v}_{F3} = v_F\left(-\frac{1}{2}, -\frac{\sqrt{3}}{2}\right)$. These directions correspond to the three brown dashed lines depicted in Fig. 4.1b1. Each group of electrons occupies one side of the Fermi surface triangle, indicated by the thick black line in Fig. 4.1b1. Considering that the carriers at the Fermi energy level ($\omega_{\mathbf{k}_{\parallel}} = E_F$) are excited to states with energy

$$\omega_{\mathbf{k}_{\parallel}+\mathbf{q}_{\parallel}} = E_F + |\mathbf{q}_{\parallel}|^2 + \mathbf{q}_{\parallel} \cdot \mathbf{v}_F \quad (4.3)$$

[as can be obtained from Eq. (4.2)], the energies of the excited states differ for

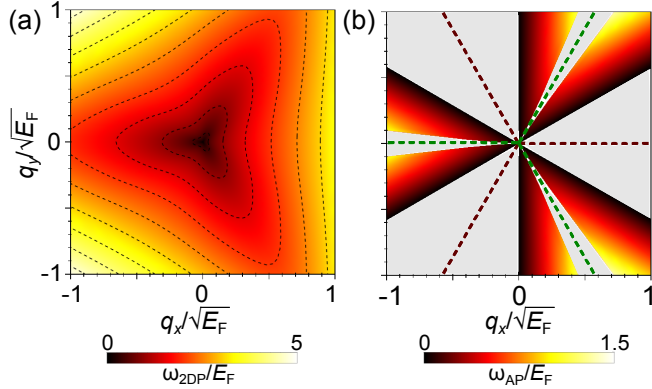


Figure 4.2: Contour plots of the dispersion of a) the 2D plasmon normalized energy $\frac{\omega_{2DP}(\mathbf{q}_{\parallel})}{E_F}$ and b) the acoustic plasmon normalized energy $\frac{\omega_{AP}(\mathbf{q}_{\parallel})}{E_F}$ in the $q_x - q_y$ plane, for a system with a free-electron-like band structure with the triangular anisotropy. The black dashed lines in panel (a) highlight curves of constant energy ω_{2DP} . Brown and green dashed lines in panel (b) indicate the symmetry directions of the band structure with the lowest and the largest effective masses, respectively. The gray regions represent the momentum \mathbf{q}_{\parallel} regions where the acoustic plasmon does not exist.

electrons with Fermi velocities \mathbf{v}_{F1} and \mathbf{v}_{F2} , because $\mathbf{q}_{\parallel} \cdot \mathbf{v}_{F1} \neq \mathbf{q}_{\parallel} \cdot \mathbf{v}_{F2}$ as can be observed in Fig. 4.1b1 (note that for $q_y = 0$, represented in the upper row of Fig. 4.1, only the carriers with Fermi velocity \mathbf{v}_{F1} are excited to a state of higher energy, because $\mathbf{q}_{\parallel} \cdot \mathbf{v}_{F2}$ and $\mathbf{q}_{\parallel} \cdot \mathbf{v}_{F3}$ are negative).

These two distinct excitation channels are behind the two separate regions with high values of ε_I (the two black regions in Fig. 4.1b3). The existence of two groups of carriers moving predominantly with different velocity components along the \mathbf{q}_{\parallel} direction gives rise to two distinct modes: one where both groups oscillate in phase and another where they oscillate out of phase. The former corresponds to the 2D plasmon, which is also observed for momentum transfers with $q_y = 0$. Thus, the dispersion of this plasmon, depicted in Fig. 4.1b4 by the cyan dashed line, closely resembles the dispersion reported in Fig. 4.1a4. The out-of-phase collective oscillation represented by the second peak in the loss function of Fig. 4.1b4, highlighted by the magenta dashed line, arises from an additional zero crossing of the real part of the permittivity ε_R , which is evident in the low-energy region of Fig. 4.1b2. We attribute this peak to an AP, as its dispersion is linear and similar to that of sound waves. However, unlike the 2D plasmon, the AP resides within the electron-hole continuum, where the imaginary part of the permittivity ε_I does not vanish for the corresponding momenta and energies. Consequently, the acoustic plasmon is predicted to have a finite lifetime even within a free-electron model. With increasing momentum $|\mathbf{q}_{\parallel}|$, the width of the AP peak in the loss function gradually expands, accompanied by a decrease in its lifetime.

Last, when considering momentum transfers along the line $q_y = \sqrt{3}q_x$ (panels (c1-4) in Fig. 4.1), the acoustic plasmon is absent. Although two groups of carriers with different Fermi velocities \mathbf{v}_{F1} and \mathbf{v}_{F2} can be excited along this symmetry direction of the system (highlighted by purple arrows in Fig. 4.1c1), these velocities have the same component $\mathbf{q}_{\parallel} \cdot \mathbf{v}_F$ along the direction of momentum \mathbf{q}_{\parallel} , and thus electrons of both groups are excited to the same energy level as indicated by Eq. (4.3). This lack of two different values of $\mathbf{q}_{\parallel} \cdot \mathbf{v}_F$ prevents the appearance of two well-separated peaks in the imaginary part of the permittivity ε_I , which is a necessary condition for the existence of an acoustic plasmon. This absence of two peaks arises because the vector \mathbf{q}_{\parallel} aligns with a symmetry direction of the band structure (green dashed line in Fig. 4.1c1), similar to the case of $q_y = 0$ (brown dashed line in Fig. 4.1a1). Hence, these findings indicate that to excite an acoustic plasmon in an anisotropic 2D electron system, the momentum transferred by the perturbation should not follow the symmetry directions present in the energy band structure.

After examining the permittivity and loss function in three specific momentum transfer directions, let us now generalize the discussion to any direction of \mathbf{q}_{\parallel} . In Fig. 4.2, we plot the energies of the two observed plasmons, $\frac{\omega_{2DP}(\mathbf{q}_{\parallel})}{E_F}$ and $\frac{\omega_{AP}(\mathbf{q}_{\parallel})}{E_F}$, normalized to the Fermi energy, as a function of \mathbf{q}_{\parallel} . Figure 4.2a illustrates the dispersion of the 2D plasmon, with dashed lines highlighting curves of constant energy for this plasmon. The 2D plasmon dispersion is positive in any radial direction of \mathbf{q}_{\parallel} and follows the triangular symmetry of the energy band structure, consistent with the geometry of the considered electron gas. At large magnitudes of $|\mathbf{q}_{\parallel}|$, the curves of constant plasmon energy ω_{2DP} resemble the triangular shape corresponding to the energy of the electronic band (first column in Fig. 4.1). However, for small $|\mathbf{q}_{\parallel}|$, the curves with constant plasmon energy ω_{2DP} deviate significantly from the characteristic triangular shape of the band, leading to a more intricate dependence on the momentum transfer direction.

On the other hand, Fig. 4.2b presents the dispersion of the acoustic plasmon $\frac{\omega_{AP}(\mathbf{q}_{\parallel})}{E_F}$. As already observed in Fig. 4.1, this excitation is prohibited at certain momentum transfers, represented by gray areas in Fig. 4.2b. The energy of the acoustic plasmon can be approximated as $\omega_{AP} \simeq \mathbf{q}_{\parallel} \cdot \mathbf{v}_F$, where \mathbf{v}_F corresponds to the lowest Fermi velocity among the two groups of electrons that are excited with momentum transfer \mathbf{q}_{\parallel} . In a system with triangular anisotropy, where electrons possess three distinct velocity vectors \mathbf{v}_F , for some momentum transfers only one group of carriers exhibits a positive value for $\mathbf{q}_{\parallel} \cdot \mathbf{v}_F$, and thus under this condition a single group of electrons can be excited to a state of larger energy [Eq. (4.3)]. Consequently, the condition for the appearance of an acoustic plasmon (the existence of two distinct groups of electrons) cannot be fulfilled, as it occurs in the gray areas of Fig. 4.2b around $q_y = 0$ and positive q_x , or their symmetry-equivalent directions (along the brown dashed lines). Similarly, in the $q_y = \sqrt{3}q_x$ direction and its symmetry-equivalent directions (indicated by the green dashed lines), although two carrier groups possess a positive value of $\mathbf{q}_{\parallel} \cdot \mathbf{v}_F$, this velocity component is identical for both groups, and no AP is found. Further, while the AP is purely

forbidden by symmetry only in these specific directions, it also does not appear in the extended regions surrounding the brown dashed lines. This absence of an AP occurs because electronic states with just slightly different Fermi velocity components $\mathbf{q}_{\parallel} \cdot \mathbf{v}_F$ are involved in the electron-hole transitions, resulting in two nearby peaks with finite linewidths in ε_1 around $\mathbf{q}_{\parallel} \cdot \mathbf{v}_F$. Consequently, if the two Fermi velocity components are sufficiently close, these peaks in ε_1 overlap, preventing the realization of an AP. In other words, for the appearance of the AP, it is necessary to have an energy range with $\varepsilon_1(\omega) \simeq 0$ between the two peaks so that $\text{Im}[\varepsilon^{-1}]$ contains a clear peak, requiring sufficiently different velocity components along the direction of \mathbf{q}_{\parallel} .

4.3.2 Square anisotropy

After thoroughly analyzing the permittivity and loss function of the system with triangular anisotropy, we now turn our attention to the case where the Fermi surface takes a square shape, corresponding to the band dispersion parameterized by Eq. (4.2) for $N = 4$. Fig. 4.3 shows the permittivity and loss function for such a system, as a function of q_x for \mathbf{q}_{\parallel} in three different directions: (a) $q_y = 0$, (b) $q_y = \frac{q_x}{2}$, and (c) $q_y = q_x$ (these directions are indicated by magenta arrows in the first column of Fig. 4.3, where the colormap represents the energy $\omega_{\mathbf{k}_{\parallel}}$ of the electronic band). The $q_y = 0$ line represents the symmetry direction with the lowest effective mass (indicated by brown dashed lines in the first column of Fig. 4.3), while the $q_y = q_x$ (or $q_y = -q_x$) line corresponds to the direction with the largest effective mass (green dashed lines). On the other hand, we choose the direction $q_y = \frac{q_x}{2}$ because it is halfway between the two different symmetry directions.

The findings in Fig. 4.3 confirm the observations made for the triangular band case. In the $N = 4$ scenario, the conventional 2D plasmon ($\omega \propto \sqrt{|\mathbf{q}_{\parallel}|}$ for small $|\mathbf{q}_{\parallel}|$) exists at momentum transfers in all directions, whereas the momentum space for the appearance of the AP is more limited. Specifically, the acoustic plasmon ($\omega \propto |\mathbf{q}_{\parallel}|$) can only be excited with momentum transfers \mathbf{q}_{\parallel} in directions where two groups of carriers with different Fermi velocity components are present. By symmetry, this condition is not met for $q_y = 0$ (row (a) in Fig. 4.3) and $q_y = q_x$ (row (c) in the same figure). Therefore, the presence of the AP requires \mathbf{q}_{\parallel} not to be parallel to any line of high symmetry (for instance, the AP can be excited at $q_y = \frac{q_x}{2}$, as indicated by row (b) in Fig. 4.3).

Following the previous discussion for the triangular anisotropy, we illustrate in Fig. 4.4 the complete dispersion of the two plasmons that can manifest in materials with a square-shaped band structure, presented in the $q_x - q_y$ plane. In Fig. 4.4a, we present the normalized dispersion of the conventional 2D plasmon, $\frac{\omega_{2\text{DP}}(\mathbf{q}_{\parallel})}{E_F}$. At small $|\mathbf{q}_{\parallel}|$, this dispersion exhibits high isotropy, while at larger distances from $\mathbf{q}_{\parallel} = 0$, the anisotropy increases, resembling the same square shape as that of the energy band. This behavior differs from the dispersion of the 2D plasmon observed in systems with triangular symmetry (Fig. 4.2a), where anisotropy is prominent even at very small momentum transfers.

The dispersion of the AP, $\frac{\omega_{\text{AP}}(\mathbf{q}_{\parallel})}{E_F}$, is reported in Fig. 4.4b. The underlying

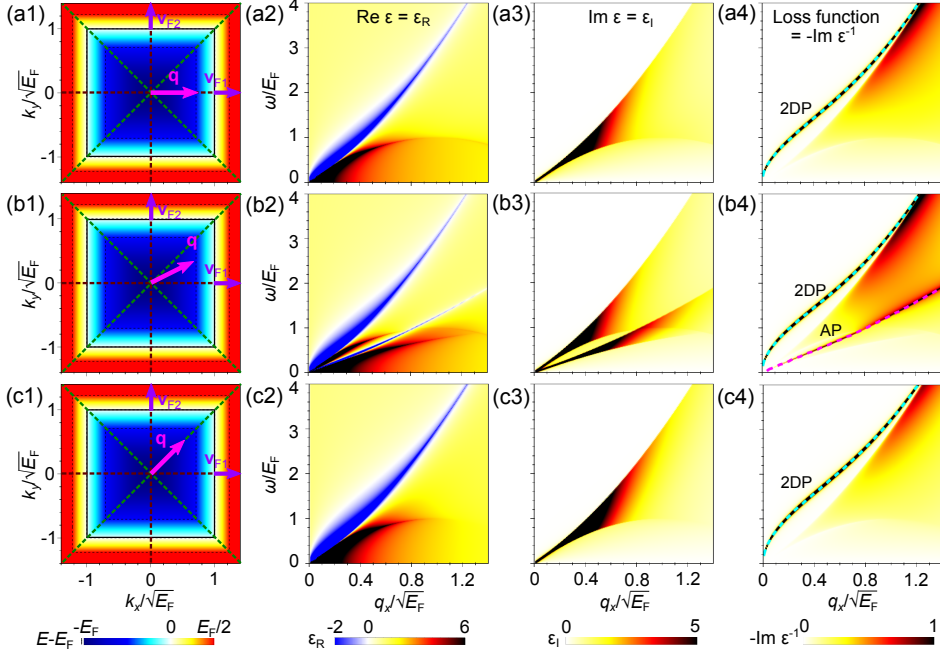


Figure 4.3: Band structure, permittivity, and loss function for a 2D system with square band structure. a1) Band structure $\omega_{\mathbf{k}_{\parallel}}$ of the material (contour plot) with the two main symmetry directions of the lowest and the largest effective masses marked by brown and green dashed lines, respectively. Thin black dashed lines highlight curves of constant energies, and the black solid line shows the Fermi surface. The momentum \mathbf{q}_{\parallel} along the $q_y = 0$ direction is shown by the magenta arrow. The Fermi velocities \mathbf{v}_{F1} and \mathbf{v}_{F2} of the carriers at the two edges are marked by purple arrows. a2) Real and a3) imaginary parts of the permittivity, and a4) loss function as a function of the momentum component q_x and the energy ω . In (a4) the 2D plasmon peak is marked by a cyan dashed line. Row b) Same as in the panels of row (a), for momentum transfers \mathbf{q}_{\parallel} with $q_y = \frac{1}{2}q_x$. Additionally, in (b4) the acoustic plasmon peak AP is highlighted by a magenta dashed line (see labels). Row c) Same as in the panels of row (a), for \mathbf{q}_{\parallel} with $q_y = q_x$.

mechanism for the AP in the system with a square symmetry is fundamentally the same as in the previously studied triangular system. It arises from the existence of two groups of carriers moving in a specific direction with different group velocities. However, in the case of the square band structure, there are only two particular directions where this condition is not met. Nonetheless, as depicted in Fig. 4.4b, the regions around each symmetry line where the AP does not appear have different extensions. In proximity to the directions with the lowest effective mass ($q_x = 0$ and $q_y = 0$, indicated by brown dashed lines), the AP emerges rapidly upon symmetry breaking. Conversely, in the regions near the directions with the largest effective mass ($q_y = \pm q_x$, green dashed lines), the absence of the AP persists over a significantly broader range. This difference can be attributed to the fact that in

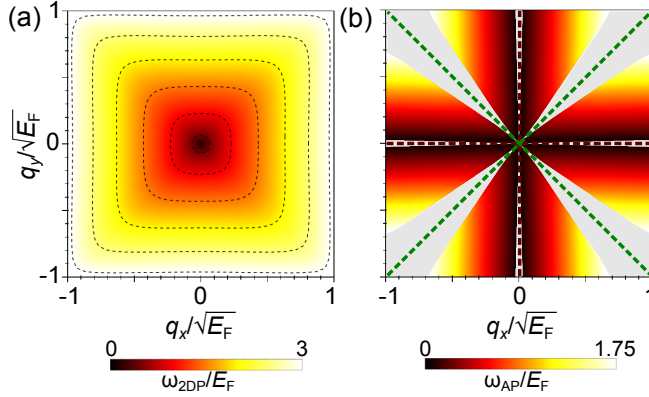


Figure 4.4: Contour plots of the dispersion of a) the 2D plasmon normalized energy $\frac{\omega_{2DP}(\mathbf{q}_{\parallel})}{E_F}$ and b) the acoustic plasmon normalized energy $\frac{\omega_{AP}(\mathbf{q}_{\parallel})}{E_F}$ in the $q_x - q_y$ plane for a system with a free-electron-like band structure with square anisotropy. The black dashed lines in panel (a) highlight curves of constant energy ω_{2DP} . Brown and green dashed lines in panel (b) indicate the symmetry directions of the band structure with the lowest and the largest effective masses, respectively. The gray regions represent the momentum \mathbf{q}_{\parallel} regions where the acoustic plasmon does not exist.

the former case, the AP energy is minimal near the symmetry directions marked by brown dashed lines, with a corresponding low damping rate due to the absence of electron-hole pairs as a decay channel (as can be observed in Fig. 4.3a3, where $\varepsilon_I(\omega) \approx 0$ in the $\omega \rightarrow 0$ limit). In the other scenario, the AP energy becomes maximal as the green dashed lines are approached, leading to a significant decay into electron-hole pairs ($\varepsilon_I(\omega) \gg 0$ if $\omega \gg 0$). Consequently, the emergence of two distinct peaks in ε_I that are associated to the emergence of an acoustic plasmon becomes more challenging in this particular direction.

4.3.3 Hexagonal anisotropy

We now examine the permittivity and loss function of a 2D electron gas with hexagonal anisotropy [corresponding to $N = 6$ in Eq. (4.2)]. These functions are reported in Fig. 4.5 again as a function of the energy ω and the momentum transfer component q_x . In each row of panels (a), (b), and (c), the q_y component of the vector \mathbf{q}_{\parallel} is fixed at $q_y = 0$, $q_y = q_x/2\sqrt{3}$, and $q_y = q_x/\sqrt{3}$, respectively, as indicated by the magenta arrows in the first column. Similar as in the previous cases, these directions correspond to the symmetry directions of lowest ($q_y = 0$) and largest ($q_y = q_x/\sqrt{3}$) effective mass, and to an intermediate non-symmetric direction between the other two ($q_y = q_x/2\sqrt{3}$).

In contrast to materials with triangular and square anisotropic band structures, the hexagonal anisotropy exhibits two distinct peaks in the loss function along

the $q_y = 0$ line (Fig. 4.5a4). Along this symmetry direction, in addition to the conventional 2D plasmon with low- $|\mathbf{q}_{\parallel}|$ dispersion $\omega \propto \sqrt{|\mathbf{q}_{\parallel}|}$, a separate acoustic mode with linear dispersion, denoted as AP1, emerges at lower energies. The appearance of the AP1 can be attributed to the presence of three distinct groups of carriers at the Fermi surface. The carriers located at the Fermi surface edge with Fermi velocity \mathbf{v}_{F1} (see Fig. 4.5a1) constitute a fast-moving group, and their intraband transitions generate a well-defined peak in the imaginary part of the permittivity ε_I above the electron-hole continuum, (the leftmost black region depicted in Fig. 4.5a3). On the other hand, the carriers at the edges corresponding to Fermi velocities \mathbf{v}_{F2} and \mathbf{v}_{F3} (Fig. 4.5a1) move in the direction of the \mathbf{q}_{\parallel} vector with the velocities $\mathbf{q}_{\parallel} \cdot \mathbf{v}_{F2} = \mathbf{q}_{\parallel} \cdot \mathbf{v}_{F3}$ that are half the magnitude of $\mathbf{q}_{\parallel} \cdot \mathbf{v}_{F1}$. Transitions involving these slower carriers give rise to a distinct peak in ε_I at lower energies (the rightmost black region in Fig. 4.5a3), exhibiting an initial dispersion slope that is precisely half the slope of the upper peak. Further, the peaks in ε_I are highly pronounced at low momentum, while an increase in q_x leads to broader peaks. Consequently, the linewidth of the AP1 peak in the loss function (Fig. 4.5a4) increases until it ceases to exist at q_x values larger than $\sim 0.8\sqrt{E_F}$.

When the \mathbf{q}_{\parallel} vector aligns with the $q_y = q_x/2\sqrt{3}$ direction, as shown in Fig. 4.5b1, the components of \mathbf{v}_{F2} and \mathbf{v}_{F3} along this direction become distinct. In combination with the states characterized by the Fermi velocity \mathbf{v}_{F1} , the system now exhibits three groups of carriers with different group velocities, because in this case we obtain $\mathbf{q}_{\parallel} \cdot \mathbf{v}_{F1} \neq \mathbf{q}_{\parallel} \cdot \mathbf{v}_{F2} \neq \mathbf{q}_{\parallel} \cdot \mathbf{v}_{F3}$. Therefore, the electrons are excited to three different energy levels [Eq. (4.3)]. Consequently, the lower-energy peak in ε_I that appears in Fig. 4.5a3 for $q_y = 0$ splits into two well-separated peaks, as observed in Fig. 4.5b3. The presence of three well-separated peaks in ε_I at small $|\mathbf{q}_{\parallel}|$ causes the real part of the permittivity ε_R to cross the zero line six times (Fig. 4.5b2). This, in turn, leads to the appearance of three distinct peaks in the loss function of Fig. 4.5b4, namely, the upper-energy optical branch 2DP and two acoustic branches with linear dispersion, denoted as AP1 and AP2. The AP2 mode, characterized by the lowest energy (smallest group velocity) of the two, corresponds to the out-of-phase oscillation of carriers residing at the Fermi surface edges with velocities \mathbf{v}_{F2} and \mathbf{v}_{F3} . On the other hand, the AP1 mode, with a larger group velocity, involves the out-of-phase motion of carriers with velocities \mathbf{v}_{F1} and \mathbf{v}_{F2} .

Furthermore, for momentum transfers \mathbf{q}_{\parallel} aligned with the $q_y = q_x/\sqrt{3}$ direction (parallel to one of the green lines in Fig. 4.5c1), only transitions involving states associated to Fermi velocities \mathbf{v}_{F1} and \mathbf{v}_{F2} are allowed, because momentum transfers in this direction cannot excite electrons with velocity \mathbf{v}_{F3} from an occupied state to an unoccupied state at small $|\mathbf{q}_{\parallel}|$ [because $\mathbf{q}_{\parallel} \cdot \mathbf{v}_{F3} = 0$ in Eq. (4.3)]. Moreover, the group velocity components of the excited electrons are equal, i.e., both groups of carriers are moving with the same velocity $\mathbf{q}_{\parallel} \cdot \mathbf{v}_{F1} = \mathbf{q}_{\parallel} \cdot \mathbf{v}_{F2}$ and are indistinguishable. As a result, a single peak appears in ε_I as shown in Fig. 4.5c3, resembling the behavior of a conventional one-component electron gas [48]. Consequently, the electron-hole continuum in the loss function depicted in Fig. 4.5c4 remains almost unaffected with respect to that of an isotropic electron gas,

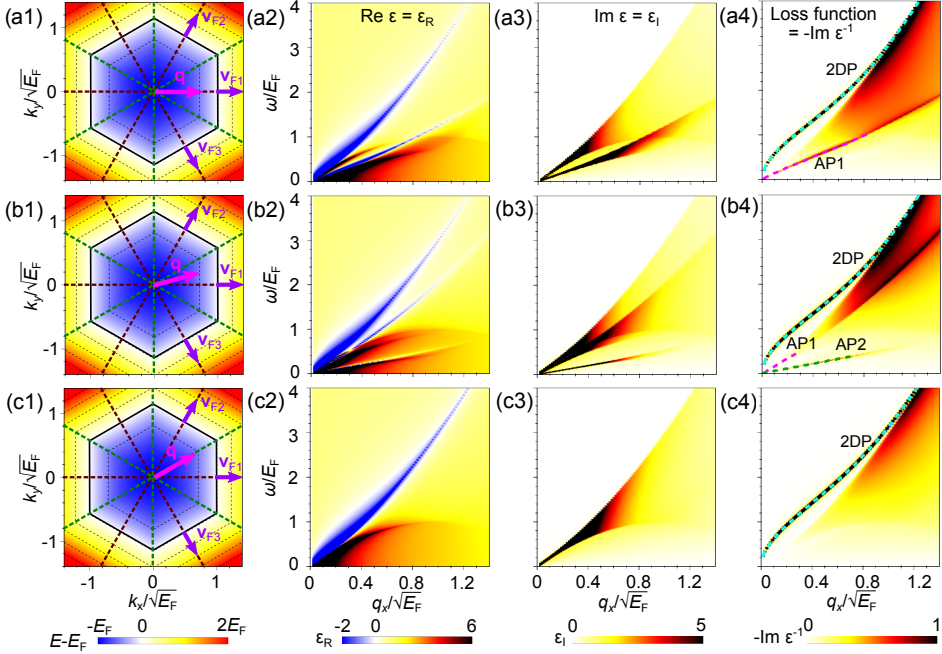


Figure 4.5: Band structure, permittivity, and loss function for a 2D system with hexagonal band structure. a1) Band structure $\omega_{\mathbf{k}_{\parallel}}$ of the material (contour plot) with the two main symmetry directions of the lowest and the largest effective masses marked by brown and green dashed lines, respectively. Thin black dashed lines highlight curves of constant energies, and the black solid line shows the Fermi surface. The momentum \mathbf{q}_{\parallel} along the $q_y = 0$ direction is shown by the magenta arrow. The Fermi velocities \mathbf{v}_{F1} , \mathbf{v}_{F2} , and \mathbf{v}_{F3} of the carriers at the three edges are marked by purple arrows. a2) Real and a3) imaginary parts of the permittivity, and a4) loss function as a function of the momentum component q_x and the energy ω . In (a4) the 2D plasmon (2DP) and the first acoustic plasmon (AP1) peaks are marked by cyan and magenta dashed lines, respectively. Row b) Same as in the panels of row (a), for momentum transfers \mathbf{q}_{\parallel} with $q_y = \frac{1}{2\sqrt{3}}q_x$. Additionally, in (b4) the second acoustic plasmon peak AP2 is highlighted by a green dashed line (see labels). Row c) Same as in the panels of row (a), for \mathbf{q}_{\parallel} with $q_y = \frac{1}{\sqrt{3}}q_x$.

and only a single 2D plasmon peak manifests at higher energies.

To conclude, Fig. 4.6a illustrates the dispersion of the conventional 2D plasmon for momentum transfers \mathbf{q}_{\parallel} in any direction. At small $|\mathbf{q}_{\parallel}|$, its dispersion is highly isotropic, while at larger momenta, it adopts the hexagonal form characteristic of the electronic band dispersion. A similar behavior was displayed in Fig. 4.4 for the system with square anisotropy. However, in the case of a square-shaped band structure, the anisotropic behavior of the 2D plasmon dispersion emerges at smaller $|\mathbf{q}_{\parallel}|$ compared to the hexagonal case. This outcome is expected since the hexagonal form is closer to isotropy than the square one. Only in the case of a triangular band structure is an anisotropic dispersion observed even at very

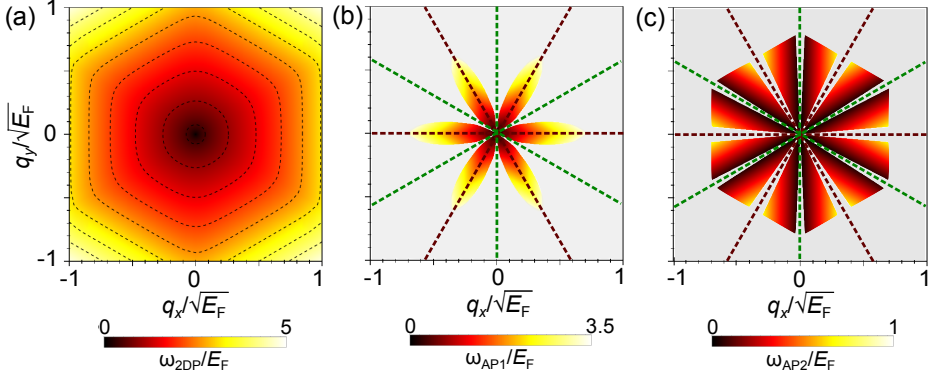


Figure 4.6: Contour plots of the dispersion of a) the 2D plasmon normalized energy $\frac{\omega_{2DP}(\mathbf{q}_{||})}{E_F}$, b) the upper acoustic plasmon normalized energy $\frac{\omega_{AP1}(\mathbf{q}_{||})}{E_F}$ and c) the lower acoustic plasmon normalized energy $\frac{\omega_{AP2}(\mathbf{q}_{||})}{E_F}$ in materials with free-electron-like band structure with hexagonal anisotropy. The black dashed lines in panel (a) highlight curves of constant energy ω_{2DP} . Brown and green dashed lines in panels (b) and (c) indicate the symmetry directions of the band structure of lowest and largest effective mass, respectively. The gray regions represent the wavevectors $\mathbf{q}_{||}$ for which the respective acoustic plasmon does not exist.

small $|\mathbf{q}_{||}|$ (Fig. 4.2a), because this shape represents a regular polygon significantly distinct from a circle.

The dispersions of the two acoustic plasmons AP1 and AP2 corresponding to the system with hexagonal symmetry are plotted in Figs. 4.6b and 4.6c, respectively. In both cases, the initial dispersion is linear in all radial directions of $\mathbf{q}_{||}$ where these plasmons can be excited. The slopes of these dispersions are determined by the two lowest values of the velocity components $\mathbf{q}_{||} \cdot \mathbf{v}_F$ among the three groups of electrons excited by the perturbation. Directions of high symmetry in the band dispersion do not allow the existence of one or two acoustic plasmons since they lack three distinct velocity components $\mathbf{q}_{||} \cdot \mathbf{v}_F$. The importance of the direction has been previously discussed for the triangular and square cases. However, in comparison to those, the acoustic plasmons in the hexagonal system experience a more pronounced damping, and therefore they exist in a smaller $\mathbf{q}_{||}$ region than the corresponding excitations in the triangular and square case, as observed by comparing Fig. 4.6 with Figs. 4.2 and 4.4. Consequently, although the number of plasmons with a sound-like dispersion increases in the hexagonal system, their lifetime diminishes.

We can generalize the discussion about the existence of acoustic plasmons for materials with a band structure in the form of any regular polygon (that is, as given by Eq. (4.2) with any value of N). The number of acoustic plasmons that can be excited for any $\mathbf{q}_{||}$ is determined by the number of distinct Fermi velocity

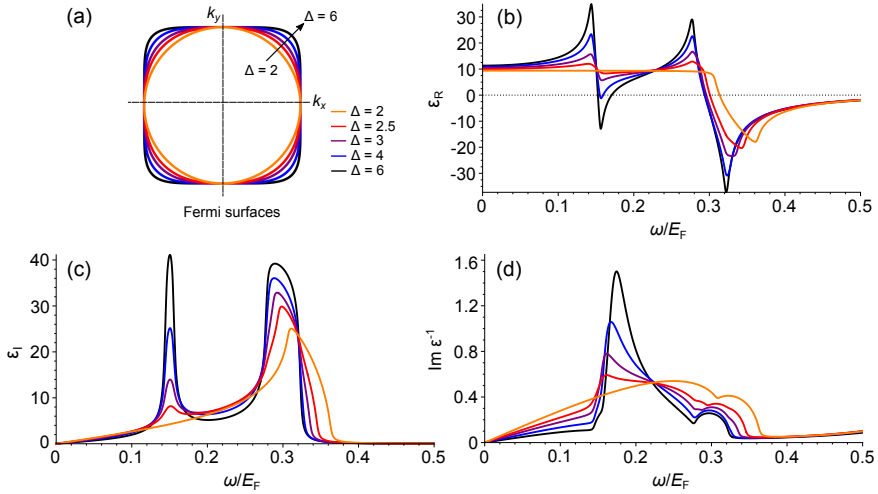


Figure 4.7: Analysis of the effects of the degree of anisotropy on the permittivity and the loss function of 2D materials. a) Sketch of the Fermi surfaces for different anisotropy factors Δ between 2 and 6 [as defined in Eq. (4.4)]. Different values of Δ are represented by solid lines of different color as indicated by the inset. b) Real and c) imaginary parts of the permittivity and d) loss function of an electron system with the square symmetry evaluated at $\mathbf{q}_{\parallel} = (0.15\sqrt{E_F}, 0.075\sqrt{E_F})$ for the same anisotropy factors Δ as in panel (a) (see legend in this panel).

components in the \mathbf{q}_{\parallel} direction, denoted as $\mathbf{q}_{\parallel} \cdot \mathbf{v}_F$. This number increases with larger values of N , where the Fermi surface exhibits more linear sides and the Fermi velocities of the electrons span a greater range of directions, with a maximum of $N/2$ different positive values of $\mathbf{q}_{\parallel} \cdot \mathbf{v}_F$. However, as N increases, the $\mathbf{q}_{\parallel} \cdot \mathbf{v}_F$ components become closer to each other, and the number of electrons associated to each specific \mathbf{v}_F vector decreases. Consequently, the peaks in the imaginary part of the permittivity ϵ_I associated to each group overlap with each other, resulting in a more efficient damping for each acoustic plasmon. This behavior is evident in the $N \rightarrow \infty$ limit of Eq. (4.2), which corresponds to the circular or isotropic case. In this limit, each electron on the Fermi surface possesses a unique value of $\mathbf{q}_{\parallel} \cdot \mathbf{v}_F$, but since there is no distinct group of electrons with a specific Fermi velocity, no acoustic plasmon exists.

4.3.4 Electron gas with non-ideal anisotropic dispersion

The analysis conducted in Secs. 4.3.1, 4.3.2, and 4.3.3 has assumed ideal electronic band dispersions, where the Fermi surfaces form perfect regular polygons as described by Eq. (4.2). However, even though anisotropy with such symmetries has been observed in various materials, real systems often deviate from an ideal shape. To analyze the applicability of our analysis to more realistic cases, we examine how

the permittivity and the properties of plasmons depend on the level of anisotropy in a system. We focus on the specific case of square anisotropy, as it provides a straightforward parameterization of the band structure for different degrees of anisotropy, but the conclusions can be extended to other types of symmetries as well. In this particular case, we consider the following band dispersion:

$$\omega_{\mathbf{k}_{\parallel}} = (|k_x|^{\Delta} + |k_y|^{\Delta})^{\frac{2}{\Delta}}, \quad (4.4)$$

where the parameter Δ quantifies the level of anisotropy in the system. At $\Delta = 2$, the band dispersion corresponds to the isotropic free electron gas. For $\Delta > 2$, some degree of anisotropy is introduced, and as Δ increases, the band dispersion deviates further from the isotropic case. In the $\Delta \rightarrow \infty$ limit, the band dispersion converges to the same form described by Eq. (4.2) for $N = 4$, representing the ideal square anisotropy. We illustrate the effects of the anisotropy factor Δ on the band structure of the system in Fig. 4.7a, where we plot the Fermi surfaces of the system for different Δ values as given by Eq. (4.4).

The dependence of the permittivity and loss function on the anisotropy factor Δ can be observed in Figs. 4.7b, c, and d. These figures show ε_{R} , ε_{I} , and $\text{Im}[\varepsilon^{-1}]$, respectively, as a function of ω at a fixed momentum transfer $\mathbf{q}_{\parallel} = (q_x, q_y) = (0.15\sqrt{E_{\text{F}}}, 0.075\sqrt{E_{\text{F}}})$, for different values of Δ . As expected, in the isotropic case ($\Delta = 2$, orange line) we observe that the electron-hole continuum (the region of $\varepsilon_{\text{I}} > 0$ as shown in Fig. 4.7c) extends up to the energy $\frac{\omega}{E_{\text{F}}} = \left(\frac{|\mathbf{q}_{\parallel}|}{\sqrt{E_{\text{F}}}}\right)^2 + 2\frac{|\mathbf{q}_{\parallel}|}{\sqrt{E_{\text{F}}}} \simeq 0.364$. As Δ increases, the density of states with Fermi velocities in the $q_x = 0$ and $q_y = 0$ directions also increasesⁱⁱ, favoring intraband transitions with energies around $\omega = \mathbf{q}_{\parallel} \cdot \mathbf{v}_{\text{F}} = q_y v_{\text{F}} = 0.15E_{\text{F}}$ and $\omega = \mathbf{q}_{\parallel} \cdot \mathbf{v}_{\text{F}} = q_x v_{\text{F}} = 0.3E_{\text{F}}$. Consequently, two peaks at these energies can be observed in ε_{I} (Fig. 4.7c) for $\Delta > 2$. These two peaks in ε_{I} lead to significant modifications in ε_{R} (Fig. 4.7b) around $\omega = 0.15E_{\text{F}}$, where it reaches zero for Δ exceeding 4. This occurrence is attributed to the appearance of the acoustic plasmons when ε_{R} approaches zero, as observed in the well-defined peak of the loss function in Fig. 4.7d at slightly higher energies. These findings confirm that our results for ideal polygonal band dispersions can be applied to more realistic systems because the acoustic plasmon can also emerge in non-idealized systems

4.4 Summary

We have demonstrated that the permittivity and loss function of a 2D free electron gas can be significantly altered by varying the shape of the energy band. By

ⁱⁱ The fermi velocity is parallel to the gradient of $\omega_{\mathbf{k}_{\parallel}}$, and this gradient is perpendicular to the Fermi surface. As shown in Fig. 4.7a, for $\Delta = 2$, we obtain the same density of electrons for each direction of \mathbf{v}_{F} , due to the isotropy of the Fermi surface. For $\Delta \gg 2$, the shape of the Fermi surface is similar to a square, where the gradient of many points is (almost) parallel to the $q_x = 0$ and $q_y = 0$ directions. Therefore, for $\Delta \gg 2$, the Fermi velocity of most electrons is parallel to the $q_x = 0$ and $q_y = 0$ directions.

considering systems with triangular, square, and hexagonal band shapes, we have observed anisotropy in the dispersion of the conventional 2D plasmon with a characteristic $\omega \propto \sqrt{|\mathbf{q}_{\parallel}|}$ behavior. In the case of the triangular system, a pronounced deviation from isotropic behavior is observed at all momentum transfers. For systems with higher symmetry, the plasmon dispersion becomes nearly isotropic at small momentum transfers, while anisotropy becomes visible only at larger momentum transfers. The threshold for the transition from isotropic to anisotropic dispersion increases as the symmetry of the system increases.

Furthermore, we have shown that the permittivity depends strongly on the direction of the Fermi velocities of the carriers. More importantly, additional plasmon modes with characteristic sound-like dispersion can emerge if the system contains at least two groups of electrons with different Fermi velocities. In systems with triangular and square symmetries, we have identified one acoustic plasmon and determined its dispersion across the entire momentum space. In the case of the hexagonal system, the number of acoustic plasmons increases to two. We anticipate that higher symmetries would lead to an even greater number of such plasmons. However, this process is accompanied by a rapid reduction in the spectral weight of these modes, eventually leading to the well-known result that such modes cannot exist in an isotropic 2D electron gas. In summary, the findings presented in this chapter suggest anisotropy as a possible mechanism for the emergence of acoustic plasmons. While these excitations are predominantly observed in systems with two different types of electronic states (such as surface and bulk states, as discussed in Chapters 2 and 3), our results demonstrate the potential to create systems that consist of a single electronic band and that also support acoustic plasmons.

LIGHT EMISSION FROM TUNNELING JUNCTIONS

5.1 Introduction

After analyzing the properties of plasmons in different metallic systems, we now turn our attention to the study of the excitation process of plasmonic resonances and the resulting emission of light. In particular, we focus on metal-insulator-metal (MIM) junctions, which are a source of electromagnetic radiation as first discovered by Lambe and McCarthy almost half a century ago [131]. In these systems, light emission originates from the excitation of surface plasmon polaritons (SPPs) by electronic injection when a bias potential is applied between the two thin metallic electrodes, inducing a tunneling current in the insulator (see Fig. 5.1a). The first studies of light emission from MIM junctions were carried out in planar junctions, and involved introducing some roughness on the surfaces of the electrodes to enable radiation of the gap SPPs. Subsequently, the role of fast SPPs localized at the metal-vacuum interface, as opposed to the gap SPP, was studied by several authors [57, 196–198]. The interest in light emission by inelastic tunneling was revived when light emission from a scanning tunneling microscope (STM) was first measured [199] and the role of localized plasmons was shown [200]. This localized light emission process has been used as a spectroscopic tool to characterize samples with nanometer, and even subnanometric spatial resolution by measuring the spatial variations of the emitted light [21, 201–203]. After these milestone contributions, light emission in the tunneling regime has been a topic of interest because of its many interesting features for potential applications.

Despite the many potential applications of these systems as optical sources, their development has been hampered by the extremely low electron-to-SPP conversion

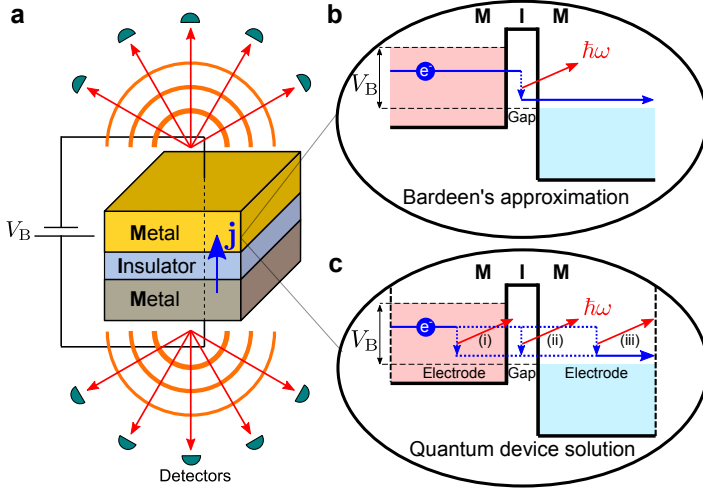


Figure 5.1: Schematics of the light emission process from a MIM tunneling junction due to inelastic tunneling. a) Sketch of a MIM junction. When a bias potential V_B is applied, an electronic current of density \mathbf{j} is induced in the system. An electron excites an electromagnetic mode of energy $\hbar\omega$ due to the inelastic tunneling mechanism. This mode would then emit light towards the detectors. b) Sketch of the inelastic tunneling processes considered by Bardeen's approximation, where the electron decays only in the insulator gap. c) Sketch of the inelastic tunneling processes considered by the quantum device solution (QDS) that we propose in this chapter. The QDS includes inelastic tunneling processes of (i) the first metallic electrode, (ii) the insulator gap and (iii) the second electrode.

rate. It was found that in optimized configurations based on localized plasmons at the tip of a scanning tunneling microscope (STM) [204] or between the edges of two cubes [205], the conversion rates are on the order of 10^{-3} and 10^{-2} , respectively. To explain the light emission by a tunneling junction, two physical mechanisms have been proposed.

The first mechanism was based on inelastic tunneling in the insulator gap. The inelastic process in the gap is illustrated in Fig. 5.1b. When a bias voltage V_B is applied, electrons in one metallic electrode gain an excess energy of $e|V_B|$. These electrons can tunnel through the few-nanometer thick insulator gap between the metals to occupy an unoccupied state in the other electrode. In MIM junctions, the dominant charge transport process is elastic tunneling, which generates a direct current [206, 207]. Alternatively, an electron can use part of its excess energy to excite a SPP (with energy $\hbar\omega < e|V_B|$) in the insulator gap during tunneling. The SPP subsequently relaxes either by absorption or radiation.

Although models of inelastic tunneling in the gap describe experimental data in many systems, it has been reported that this mechanism does not account for the measurements of light emission by MIM junctions. For instance, Kirtley et al. measured light emission from metallic gratings where the electric field of the modes is not mostly concentrated in the insulator gap of the junction. In this case, the

theory based on inelastic tunneling underestimated the light intensity by more than an order of magnitude [57]. Further, it was observed that the radiative intensity depended on the thickness of the top electrode, and models of inelastic tunneling could not explain this dependence because they only considered the interaction between the current and the electric field in the gap. To explain these discrepancies between theory and experiment, the authors suggested a second mechanism of light emission, known as the hot electron decay [208]. In this model, electrons first tunnel elastically and become hot electrons in the second electrode. Then, they thermalize through interactions with other electrons and with phonons. Due to the continuous pumping, a population of hot electrons, not described by a Fermi-Dirac distribution, is maintained. These hot electrons can relax radiatively. On the other hand, Persson and Baratoff analyzed light emission in a STM and found that the inelastic tunneling mechanism overcomes the hot electron mechanism by a factor of approximately 10^3 [209].

At this point, we emphasize that many authors have considered that emission originated in the metallic electrode is necessarily due to the hot electron process [208, 209], and that inelastic tunneling implies emission originated in the gap only (Fig. 5.1b) [208–210]. In what follows, we revisit this point of view by considering a more rigorous description of the inelastic tunneling that indicates how processes in the metal can also lead to emission, as depicted schematically in Fig. 5.1c, without requiring the hot electron mechanism.

Up to now, all the calculations (except Ref. [55]) assume that the light emission process takes place in the gap. This process is typically modelled based on Bardeen’s theory of electron tunneling (Bardeen’s approximation). In this chapter, we introduce an extension of the models of inelastic tunneling that is obtained by solving the Schrödinger equation in the complete MIM device and that we denote the full quantum device solution (QDS). This solution also accounts for processes in the metallic electrodes (Fig. 5.1c), and we show that it includes some features observed experimentally that cannot be predicted by Bardeen’s theory.

Additionally, within the QDS, we show the equivalence of the two main approaches that have been used to describe inelastic light emission. The first one is based on the usual picture of a radiative emission due to an electronic transition between two states. Fermi’s golden rule can then be used to compute the rate of excitation of SPPs [56, 211]. The second one is based on the classical picture of radiation due to time-dependent currents. It relies on the calculation of the power radiated by the time-dependent fluctuations of the current density [55, 212]. Laks and Mills used this viewpoint to model the experiment of Lambe and McCarthy by calculating the emission efficiency of planar junctions with surface roughness in Ref. [55]. A summary of these two methods can be found in the review paper by Parzefall [56]. To our knowledge, no systematic explicit proof of their equivalence has been reported.

The structure of this chapter is the following. In Sec. 5.2, we present the QDS and use it to explain elastic tunneling phenomena, comparing the obtained results with those given by Bardeen’s approximation. In Sec. 5.3, we establish the relation of two different approaches used to describe light emission by inelastic

tunneling, based either i) on the transition rate of electrons between two states, or ii) on the calculation of emission by fluctuating currents. We further emphasize the importance of using these approaches within the QDS. In particular, we use the QDS to compute the cross-spectral density of the current density in a second quantization framework. These results indicate that the QDS accounts for processes of non-local electron-hole recombination within the metallic electrodes that contribute to light emission and that are not considered by Bardeen's approximation. Last, in Sec. 5.4, we calculate the radiative and non-radiative power due to the excitation of different SPPs in planar junctions, analyzing in detail the differences between the results obtained with Bardeen's approximation and the QDS.

5.2 Descriptions of elastic tunneling

We start by reviewing and comparing the frameworks that are used to describe electronic transport in a barrier. We first remind the main results of Bardeen's description of elastic tunneling in MIM junctions (for a more complete discussion see Sec. 2.4), and we then compare Bardeen's approach with the textbook solution of the Schrödinger equation denoted QDS.

The tunneling junction is represented by the potential energy as shown in the inset of Fig. 5.2c (also shown in Fig. 2.4a). Within this description of the junction, the electronic wavefunctions are obtained by solving the Schrödinger equation with the Hamiltonian $\hat{\mathcal{H}}_{\text{el}}$ given by Eq. (2.84). From Bardeen's perspective, the complete Hamiltonian is separated into two approximate expressions, each related to the left or right metallic electrode at potential energy U_L or U_R , respectively. This approximation allows obtaining simple expression of the wavefunctions for electrons in each metal, which are given by Eqs. (2.85) and (2.86) and repeated here for ease of reference (we now use the superscript BA to denote that these wavefunctions are obtained within *Bardeen's approximation*):

$$\Psi_L^{\text{BA}}(\mathbf{r}) = \begin{cases} \frac{1}{\sqrt{L_z}} \frac{1}{\sqrt{S}} \left(e^{ik_{zL}z} + \frac{ik_{zL} + k_{z\text{gap}}}{ik_{zL} - k_{z\text{gap}}} e^{-ik_{zL}z} \right) e^{i\mathbf{k}_{\parallel} \cdot \mathbf{r}_{\parallel}} & z \leq 0 \\ \frac{1}{\sqrt{L_z}} \frac{1}{\sqrt{S}} \left(\frac{2ik_{zL}}{ik_{zL} - k_{z\text{gap}}} e^{-k_{z\text{gap}}z} \right) e^{i\mathbf{k}_{\parallel} \cdot \mathbf{r}_{\parallel}} & z > 0 \end{cases},$$

$$\Psi_R^{\text{BA}}(\mathbf{r}) = \begin{cases} \frac{1}{\sqrt{L_z}} \frac{1}{\sqrt{S}} \left(\frac{2ik_{zR}}{ik_{zR} - k_{z\text{gap}}} e^{k_{z\text{gap}}(z - L_{\text{gap}})} \right) e^{i\mathbf{k}_{\parallel} \cdot \mathbf{r}_{\parallel}} & z \leq L_{\text{gap}} \\ \frac{1}{\sqrt{L_z}} \frac{1}{\sqrt{S}} \left(e^{-ik_{zR}(z - L_{\text{gap}})} + \frac{ik_{zR} + k_{z\text{gap}}}{ik_{zR} - k_{z\text{gap}}} e^{ik_{zR}(z - L_{\text{gap}})} \right) e^{i\mathbf{k}_{\parallel} \cdot \mathbf{r}_{\parallel}} & z > L_{\text{gap}} \end{cases}.$$

In this expression, the wavevectors $k_{zL(R)}$ and $k_{z\text{gap}}$ are given by Eqs. (2.87) and (2.88) for an electron with parallel wavevector \mathbf{k}_{\parallel} , energy $\hbar\omega^{\text{el}}$ and effective mass m_{eff} , i.e.

$$k_{zL(R)}(\omega^{\text{el}}, \mathbf{k}_{\parallel}) = \sqrt{\frac{2m_{\text{eff}}}{\hbar^2} (\hbar\omega^{\text{el}} - U_{L(R)}) - |\mathbf{k}_{\parallel}|^2}$$

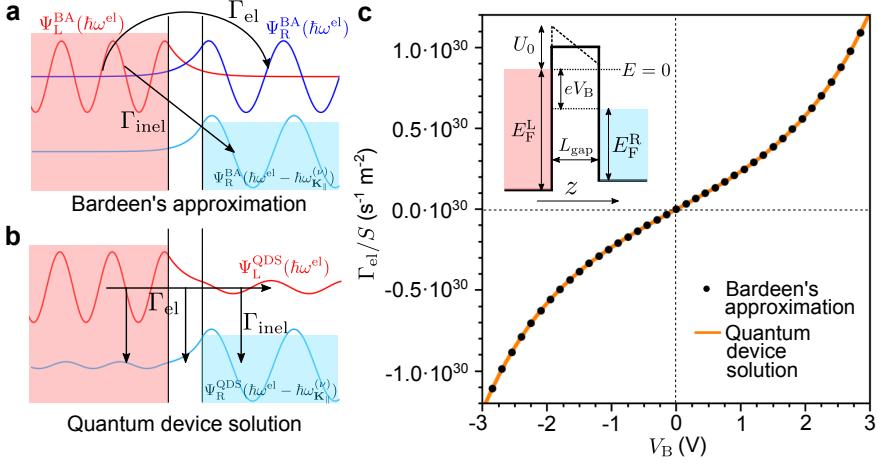


Figure 5.2: Comparison of the Bardeen's and quantum device solution (QDS) approaches for electron tunneling mechanisms. a-b) Schematics of the processes of elastic tunneling (Γ_{el}) and inelastic tunneling (Γ_{inel}) using (a) the wavefunctions Ψ_L^{BA} and Ψ_R^{BA} corresponding to Bardeen's approximation, and (b) the wavefunctions Ψ_L^{QDS} and Ψ_R^{QDS} of the QDS. The wavefunctions are vertically shifted by their energy, where $\hbar\omega^{el}$ is the initial electronic energy and $\hbar\omega_{\mathbf{K}_{\parallel}}^{(\nu)}$ is the energy of a SPP excited by the electron due to inelastic tunneling. c) Elastic tunneling rate Γ_{el} per unit of surface area S of the metallic interfaces, calculated with Bardeen's approximation (black dots) and the QDS (orange line), plotted as a function of the bias potential V_B . The inset is the same figure as Fig. 2.4a and shows the schematics of the potential energy $U(z)$ of electrons in the MIM junction and the occupied states in each metal.

and

$$k_{zgap}(\omega^{el}, \mathbf{k}_{\parallel}) = \sqrt{\frac{2m_{eff}}{\hbar^2}(U_{gap} - \hbar\omega^{el}) + |\mathbf{k}_{\parallel}|^2},$$

where U_{gap} is the potential energy in the insulator gap (see Sec. 2.4 for a more detailed definition of the parameters involving these equations).

According to Bardeen's theory, electrons are initially in an eigenstate of the Hamiltonian of the left metal $\hat{\mathcal{H}}_L$, and the interaction Hamiltonian $\hat{\mathcal{H}}_{el} - \hat{\mathcal{H}}_L$ induces transitions to states corresponding to the right metal (as schematically shown in Fig. 5.2a by the arrow with the Γ_{el} label). Under the assumption of weak tunneling, the calculation of the tunneling rate is done using Fermi's golden rule. We obtain that the elastic tunneling rate per electron in the left metal is given by Eq. (2.95), i.e.

$$\Gamma_L = \frac{\hbar}{m_{eff}L_z} \frac{16k_{zL}^2 k_{zR} k_{zgap}^2}{(k_{zL}^2 + k_{zgap}^2)(k_{zR}^2 + k_{zgap}^2)} e^{-2k_{zgap}L_{gap}}.$$

We now turn to a more rigorous approach that does not use Bardeen's approximation. The eigenstates of the Hamiltonian of Eq. (2.84) for a rectangular barrier are analytically solvable. For a fixed energy $\hbar\omega^{el}$ and parallel wavevector

\mathbf{k}_{\parallel} , the Hamiltonian of a rectangular barrier contains two degenerate states, of the form

$$\Psi_{\text{L}}^{\text{QDS}}(\mathbf{r}) = \begin{cases} \frac{1}{\sqrt{L_z}} \frac{1}{\sqrt{S}} (e^{ik_z L z} + r_{\text{L}} e^{-ik_z L z}) e^{i\mathbf{k}_{\parallel} \cdot \mathbf{r}_{\parallel}} & z \leq 0 \\ \frac{1}{\sqrt{L_z}} \frac{1}{\sqrt{S}} (\alpha_{\text{L}} e^{k_{z\text{gap}} z} + \beta_{\text{L}} e^{-k_{z\text{gap}} z}) e^{i\mathbf{k}_{\parallel} \cdot \mathbf{r}_{\parallel}} & 0 < z \leq L_{\text{gap}}, \\ \frac{1}{\sqrt{L_z}} \frac{1}{\sqrt{S}} t_{\text{L}} e^{ik_z R z} e^{i\mathbf{k}_{\parallel} \cdot \mathbf{r}_{\parallel}} & L_{\text{gap}} < z \end{cases} \quad (5.1)$$

and

$$\Psi_{\text{R}}^{\text{QDS}}(\mathbf{r}) = \begin{cases} \frac{1}{\sqrt{L_z}} \frac{1}{\sqrt{S}} t_{\text{R}} e^{-ik_z L (z - L_{\text{gap}})} e^{i\mathbf{k}_{\parallel} \cdot \mathbf{r}_{\parallel}} & z \leq 0 \\ \frac{1}{\sqrt{L_z}} \frac{1}{\sqrt{S}} (\alpha_{\text{R}} e^{-k_{z\text{gap}} (z - L_{\text{gap}})} + \beta_{\text{R}} e^{k_{z\text{gap}} (z - L_{\text{gap}})}) e^{i\mathbf{k}_{\parallel} \cdot \mathbf{r}_{\parallel}} & 0 < z \leq L_{\text{gap}}, \\ \frac{1}{\sqrt{L_z}} \frac{1}{\sqrt{S}} (e^{-ik_z R (z - L_{\text{gap}})} + r_{\text{R}} e^{ik_z R (z - L_{\text{gap}})}) e^{i\mathbf{k}_{\parallel} \cdot \mathbf{r}_{\parallel}} & L_{\text{gap}} < z \end{cases} \quad (5.2)$$

with coefficients

$$r_{\text{L}} = -\frac{e^{2k_{z\text{gap}} L_{\text{gap}}} (k_{z\text{gap}} + ik_{z\text{L}})(k_{z\text{gap}} - ik_{z\text{R}}) - (k_{z\text{gap}} - ik_{z\text{L}})(k_{z\text{gap}} + ik_{z\text{R}})}{e^{2k_{z\text{gap}} L_{\text{gap}}} (k_{z\text{gap}} - ik_{z\text{L}})(k_{z\text{gap}} - ik_{z\text{R}}) - (k_{z\text{gap}} + ik_{z\text{L}})(k_{z\text{gap}} + ik_{z\text{R}})}, \quad (5.3a)$$

$$\alpha_{\text{L}} = -\frac{2ik_{z\text{L}}(k_{z\text{gap}} + ik_{\text{R}})}{e^{2k_{z\text{gap}} L_{\text{gap}}} (k_{z\text{gap}} - ik_{z\text{L}})(k_{z\text{gap}} - ik_{z\text{R}}) - (k_{z\text{gap}} + ik_{z\text{L}})(k_{z\text{gap}} + ik_{z\text{R}})}, \quad (5.3b)$$

$$\beta_{\text{L}} = -\frac{2ik_{z\text{L}}(k_{z\text{gap}} - ik_{\text{R}}) e^{2k_{z\text{gap}} L_{\text{gap}}}}{e^{2k_{z\text{gap}} L_{\text{gap}}} (k_{z\text{gap}} - ik_{z\text{L}})(k_{z\text{gap}} - ik_{z\text{R}}) - (k_{z\text{gap}} + ik_{z\text{L}})(k_{z\text{gap}} + ik_{z\text{R}})}, \quad (5.3c)$$

$$t_{\text{L}} = -\frac{4ie^{k_{z\text{gap}} L_{\text{gap}}} e^{-ik_{\text{R}} L_{\text{gap}}} k_{z\text{gap}} k_{z\text{L}}}{e^{2k_{z\text{gap}} L_{\text{gap}}} (k_{z\text{gap}} - ik_{z\text{L}})(k_{z\text{gap}} - ik_{z\text{R}}) - (k_{z\text{gap}} + ik_{z\text{L}})(k_{z\text{gap}} + ik_{z\text{R}})}, \quad (5.3d)$$

$$r_{\text{R}} = -\frac{e^{2k_{z\text{gap}} L_{\text{gap}}} (k_{z\text{gap}} - ik_{z\text{L}})(k_{z\text{gap}} + ik_{z\text{R}}) - (k_{z\text{gap}} + ik_{z\text{L}})(k_{z\text{gap}} - ik_{z\text{R}})}{e^{2k_{z\text{gap}} L_{\text{gap}}} (k_{z\text{gap}} - ik_{z\text{L}})(k_{z\text{gap}} - ik_{z\text{R}}) - (k_{z\text{gap}} + ik_{z\text{L}})(k_{z\text{gap}} + ik_{z\text{R}})}, \quad (5.3e)$$

$$\alpha_{\text{R}} = -\frac{2ik_{z\text{R}}(k_{z\text{gap}} + ik_{\text{L}})}{e^{2k_{z\text{gap}} L_{\text{gap}}} (k_{z\text{gap}} - ik_{z\text{L}})(k_{z\text{gap}} - ik_{z\text{R}}) - (k_{z\text{gap}} + ik_{z\text{L}})(k_{z\text{gap}} + ik_{z\text{R}})}, \quad (5.3f)$$

$$\beta_{\text{R}} = -\frac{2ik_{z\text{R}}(k_{z\text{gap}} - ik_{\text{L}}) e^{2k_{z\text{gap}} L_{\text{gap}}}}{e^{2k_{z\text{gap}} L_{\text{gap}}} (k_{z\text{gap}} - ik_{z\text{L}})(k_{z\text{gap}} - ik_{z\text{R}}) - (k_{z\text{gap}} + ik_{z\text{L}})(k_{z\text{gap}} + ik_{z\text{R}})}, \quad (5.3g)$$

$$t_{\text{R}} = -\frac{4ie^{k_{z\text{gap}} L_{\text{gap}}} e^{-ik_{\text{L}} L_{\text{gap}}} k_{z\text{gap}} k_{z\text{R}}}{e^{2k_{z\text{gap}} L_{\text{gap}}} (k_{z\text{gap}} - ik_{z\text{L}})(k_{z\text{gap}} - ik_{z\text{R}}) - (k_{z\text{gap}} + ik_{z\text{L}})(k_{z\text{gap}} + ik_{z\text{R}})}. \quad (5.3h)$$

$r_{L(R)}$ and $t_{L(R)}$ give the reflected and transmitted amplitudes. The wavefunctions $\Psi_L^{\text{QDS}}(\mathbf{r})$ in Eq. (5.1) and $\Psi_R^{\text{QDS}}(\mathbf{r})$ in Eq. (5.2) are the textbook solutions to describe quantum tunneling from the left metal to the right metal and vice versa, respectively. Since the wavefunctions are calculated in the complete MIM device, we refer to these wavefunctions as the quantum device solution (QDS).

It is possible to obtain exactly the elastic tunneling rate using the QDS. Since the electrons under this description are already in an eigenstate of $\hat{\mathcal{H}}_{\text{el}}$ from the beginning, the tunneling properties are included in $\Psi_L^{\text{QDS}}(\mathbf{r})$, as we indicate in Fig. 5.2b by the arrow with the Γ_{el} label. From this wavefunction, we can obtain its associated probability current density from the general definition [213]

$$j_z(\mathbf{r}) = \frac{i\hbar e}{2m_{\text{eff}}} \left[\Psi^*(\mathbf{r}) \frac{\partial \Psi(\mathbf{r})}{\partial z} - \Psi(\mathbf{r}) \frac{\partial \Psi^*(\mathbf{r})}{\partial z} \right], \quad (5.4)$$

which for Eq. (5.1) is constant over space with the value $j_z(z) = -\frac{1}{L_z S} \frac{\hbar e k_{zR}}{m_{\text{eff}}} |t_L|^2$. Since this expression gives the amount of charge that crosses the junction per unit of area and time, the tunneling rate Γ_L^{QDS} is directly calculated as

$$\Gamma_L^{\text{QDS}} = \frac{S}{-e} j_z. \quad (5.5)$$

By introducing the value of the coefficient t_L [Eq. (5.3d)] into Eq. (5.1) and applying Eq. (5.4) to calculate the current density $j_z(z)$, we obtain

$$\begin{aligned} \Gamma_L^{\text{QDS}} &= \frac{\hbar}{m_{\text{eff}} L_z} 16 k_{zL}^2 k_{zR}^2 k_{z\text{gap}}^2 e^{-2k_{z\text{gap}} L_{\text{gap}}} \\ &\times \left\{ (1 + e^{-4k_{z\text{gap}} L_{\text{gap}}}) (k_{z\text{gap}}^2 + k_{zL}^2) (k_{z\text{gap}}^2 + k_{zR}^2) \right. \\ &\quad \left. - 2e^{-2k_{z\text{gap}} L_{\text{gap}}} [(k_{z\text{gap}}^2 - k_{zL}^2) (k_{z\text{gap}}^2 - k_{zR}^2) - 4k_{z\text{gap}}^2 k_{zL} k_{zR}] \right\}^{-1}. \end{aligned} \quad (5.6)$$

The tunneling rate given by Bardeen's approximation [Eq. (2.95)] is identical to the expression that is obtained from the rate of the QDS [Eq. (5.6)] under the assumption of weak tunneling, i.e. for $k_{z\text{gap}} L_{\text{gap}} \gg 1$. To analyze the validity of this assumption, we focus on an Al-AlOx-Au junction as a particular example, which is typically used to analyze elastic and inelastic tunneling phenomena [54, 131, 198]. For these metals, we use through this chapter numerical values of the Fermi energies $E_F^L = 11.5$ eV and $E_F^R = 5.5$ eV [129]. Further, it has been measured that the effective mass of the electrons in junctions with AlOx is $m_{\text{eff}} = 0.23m_e$ (where m_e is the electron mass) [214], and we fix the height of the barrier on a typical value of $U_0 = 2$ eV. Since Bardeen's approximation works accurately for $k_{z\text{gap}} L_{\text{gap}} \gg 1$, the largest mismatch with the QDS occurs in the regime of very thin layers and of high bias potentials, where $k_{z\text{gap}}$ is low according to Eq. (2.88). However, even for values of $L_{\text{gap}} = 1$ nm and $V_B = 3$ V, we have checked that Bardeen's approximation underestimates the tunneling rate Γ_L of the electrons at the Fermi surface only by a factor of 0.4%.

Although the tunneling rate per electron allows us to compare Bardeen's approximation with the QDS by means of an analytical expression [Eqs. (2.95) and (5.6)], the measurable quantity in experiments is the intensity of the electronic current (related to the total tunneling rate Γ_{el}), instead of the individual rate Γ_{L} . In order to model these experiments, we calculate Γ_{el} by summing Eqs. (2.95) and (5.6) over all occupied initial states of the left metal that can tunnel to unoccupied states of the right metal. Specifically, Γ_{el} is calculated by introducing Γ_{L} of Eq. (2.95) (for Bardeen's approximation) or Eq. (5.6) (for the QDS) into Eq. (2.96). To perform this calculation, we have included the probability that a state is occupied in the left metal and unoccupied in the right metal. Since the states described by Bardeen's approximation are localized in a single metal, these probabilities are dictated by the Fermi-Dirac occupation factors of its respective metal $f_{\text{FD}}^{\text{L(R)}}(\mathbf{k}_{\text{L}}) = \left[1 + \exp\left(\frac{\hbar\omega^{\text{el}}(\mathbf{k}_{\text{L}}) - E_{\text{F}}^{\text{L(R)}}}{k_{\text{B}}T}\right) \right]^{-1}$ at temperature T , with Boltzmann constant k_{B} . The assignment of a Fermi-Dirac occupation factor is not so straightforward in the approach of the QDS, because the corresponding electronic states are delocalized over the two metals with different Fermi levels. However, following a similar argument than for Bardeen's approximation, we associate the occupation factor $f_{\text{FD}}^{\text{L}}(\mathbf{k}_{\text{L}})$ to the states $\Psi_{\text{L}}^{\text{QDS}}(\mathbf{r})$ that originate from the left metal, and accordingly the factor $[1 - f_{\text{FD}}^{\text{R}}(\mathbf{k}_{\text{L}})]$ corresponds to the unoccupied states $\Psi_{\text{R}}^{\text{QDS}}(\mathbf{r})$ that tunnel from the right to the left metal.

We plot in Fig. 5.2c the elastic tunneling rate Γ_{el} per surface area S as a function of the applied voltage V_{B} for temperature $T = 0$, where the Fermi-Dirac occupation factors are given by Heaviside step functions (we have checked that the following discussion remains also valid for room and larger temperatures). We compare the results obtained with Bardeen's approximation (black dots) and the QDS (orange line) for a thin gap of width $L_{\text{gap}} = 1$ nm. The two approaches follow a nearly identical trend with a relative error of at most $2.1 \cdot 10^{-3}$ at $V_{\text{B}} = 3$ V. In most experiments, the gap thickness L_{gap} is larger, which decreases the error between the two approaches even more. Therefore, we have shown that Bardeen's approximation gives very reliable results in the description of elastic tunneling. This approach is also easy to use and can be easily extended to barriers with potential energies $U(z)$ for which the Schrödinger equation is not solvable analytically, so that it has been applied successfully to study many systems. Additionally, the agreement between the Bardeen's and QDS approaches indicates that associating single-metal Fermi-Dirac occupation factors $f_{\text{FD}}^{\text{L(R)}}(\mathbf{k}_{\text{L}})$ to the states of the QDS works accurately, and therefore we follow this methodology in the following section where we turn to the inelastic tunneling current.

5.3 Descriptions of inelastic tunneling

The phenomenon of light emission due to inelastic tunneling has been computed using two different models in the literature: a calculation based on Fermi's golden rule and a calculation of the radiated power due to current density fluctuations.

These two models are based on the two usual physical pictures of light emission: the quantum matter picture is based on the radiative relaxation of an excited state, and the classical electromagnetic picture is based on the power radiated by a time-dependent current.

In this section, we aim to provide a comprehensive review of the two models and to prove their equivalence under appropriate conditions. Further, these methods are often used within the framework of Bardeen's approximation, but we emphasize here the consequences of using them within the QDS.

Finally, let us stress that we compute the inelastic transition rate leading to SPP excitation. Once this is known, then the photon emission rate can be deduced by merely multiplying it by the surface plasmon radiative decay yield.

5.3.1 Fermi's golden rule

In the description of light emission from tunneling junctions, it is necessary to include the interaction between electrons and electromagnetic modes. Among different points of view to account for this interaction, one of them is a direct extension of models of elastic tunneling that involves introducing the light-matter coupling in the quantum Hamiltonian of Eq. (2.84). The effects of this coupling are usually treated under the formalism of Fermi's golden rule. This general approach has been used in a large variety of systems, such as in the analysis of photon emission from superconducting junctions [215]. Focusing now on the specific case of planar MIM junctions, the complete Hamiltonian that describes elastic tunneling together with the interaction between electrons and SPPs is

$$\hat{\mathcal{H}}_{\text{el-SPP}} = \hat{\mathcal{H}}_{\text{el}} + \sum_{\mathbf{K}_{\parallel}} \sum_{\nu} \hbar \omega_{\mathbf{K}_{\parallel}}^{(\nu)} \hat{a}_{\mathbf{K}_{\parallel}}^{\dagger(\nu)} \hat{a}_{\mathbf{K}_{\parallel}}^{(\nu)} - \frac{e}{m_{\text{eff}}} \hat{\mathbf{p}} \cdot \hat{\mathbf{A}}. \quad (5.7)$$

Together with the electronic Hamiltonian $\hat{\mathcal{H}}_{\text{el}}$ in Eq. (2.84), the second term on the right handside of this expression is the plasmonic Hamiltonian. The superscript ν refers to all different SPP modes of the system (mostly localized at different interfaces) whose dispersion $\omega_{\mathbf{K}_{\parallel}}^{(\nu)}$ is a function of the parallel component of the wavevector \mathbf{K}_{\parallel} . We have included the corresponding creation operator $\hat{a}_{\mathbf{K}_{\parallel}}^{\dagger(\nu)}$ and annihilation operator $\hat{a}_{\mathbf{K}_{\parallel}}^{(\nu)}$ for each vector \mathbf{K}_{\parallel} . The last term in Eq. (5.7) corresponds to the light-matter interaction $\hat{\mathcal{H}}_{\text{int}}$, which, depending on the system and its mode structure, is described with the vector potential $\hat{\mathbf{A}}$ in the Coulomb gauge as $\hat{\mathcal{H}}_{\text{int}} = -\frac{e}{m_{\text{eff}}} \hat{\mathbf{p}} \cdot \hat{\mathbf{A}}$, or in terms of the scalar potential \hat{V} as $\hat{\mathcal{H}}_{\text{int}} = -e\hat{V}$ [209, 211, 216]. In this work, we use the former interaction term because all transverse modes in planar junctions can be described entirely with the vector potential. The operator $\hat{\mathbf{p}} = -i\hbar\nabla$ acts on the electronic wavefunctions, whereas the field operator $\hat{\mathbf{A}}$ is written after the decomposition into all plasmonic

modes as [217]

$$\begin{aligned} \hat{\mathbf{A}}(\mathbf{r}, t) = & \sum_{\mathbf{K}_{\parallel}} \sum_{\nu} \sqrt{\frac{\hbar}{2\varepsilon_0 S \omega_{\mathbf{K}_{\parallel}}^{(\nu)}}} e^{i\mathbf{K}_{\parallel} \cdot \mathbf{r}_{\parallel}} \mathbf{u}_{\mathbf{K}_{\parallel}}^{(\nu)}(z) \hat{a}_{\mathbf{K}_{\parallel}}^{(\nu)} e^{-i\omega_{\mathbf{K}_{\parallel}}^{(\nu)} t} \\ & + \sqrt{\frac{\hbar}{2\varepsilon_0 S \omega_{\mathbf{K}_{\parallel}}^{(\nu)}}} e^{-i\mathbf{K}_{\parallel} \cdot \mathbf{r}_{\parallel}} \mathbf{u}_{\mathbf{K}_{\parallel}}^{*(\nu)}(z) \hat{a}_{\mathbf{K}_{\parallel}}^{\dagger(\nu)} e^{i\omega_{\mathbf{K}_{\parallel}}^{(\nu)} t}, \end{aligned} \quad (5.8)$$

where $\mathbf{u}_{\mathbf{K}_{\parallel}}^{(\nu)}(z)$ gives the spatial dependence of the vector potential along the z direction for each mode, under the condition $i\mathbf{K}_{\parallel} \cdot \mathbf{u}_{\mathbf{K}_{\parallel}}^{(\nu)}(z) + \frac{\partial}{\partial z} (\mathbf{u}_{\mathbf{K}_{\parallel}}^{(\nu)}(z) \cdot \mathbf{n}_z) = 0$ implied by the Coulomb gauge (\mathbf{n}_z is the unit vector of the z direction). Further, the quantization of each plasmonic mode with energy $\hbar\omega_{\mathbf{K}_{\parallel}}^{(\nu)}$ leads to the following normalization condition of $\mathbf{u}_{\mathbf{K}_{\parallel}}^{(\nu)}(z)$ [217, 218]:

$$\int \frac{1}{2} \left\{ \frac{\partial}{\partial \omega} [\omega \varepsilon(z, \omega)] \left| \mathbf{u}_{\mathbf{K}_{\parallel}}^{(\nu)}(z) \right|^2 + \left| \frac{\varepsilon(z, \omega)}{|\mathbf{K}_{\parallel}|} \frac{\omega}{c} (\mathbf{u}_{\mathbf{K}_{\parallel}}^{(\nu)}(z) \cdot \mathbf{n}_z) \right|^2 \right\} dz = 1. \quad (5.9)$$

To quantize the SPP field, losses have been neglected. This approximation is valid inasmuch as the density of states is not perturbed significantly [217]. It provides an accurate description of the electron-SPP coupling which will be used to compute the SPP emission rate. The photon emission rate will be computed subsequently using the radiative yield of the SPP.

The Hamiltonian of Eq. (5.7) is not exactly solvable in general, and the usual approach to describe inelastic tunneling is to treat $\hat{\mathcal{H}}_{\text{int}} = -\frac{e}{m_{\text{eff}}} \hat{\mathbf{p}} \cdot \hat{\mathbf{A}}$ as a perturbative term under the assumption of weak light-matter interaction. It is first assumed that the electrons come from the left metal and that there is no excited plasmon. Therefore, the initial state is of the form $|\Psi_{\text{L}}\rangle \otimes |0_{\text{pl}}\rangle^{\text{i}}$. Here, the state $|0_{\text{pl}}\rangle$ implies that all modes ν at all wavevectors \mathbf{K}_{\parallel} are in the zero occupation number state. The final plasmonic state is of the form $|1_{\mathbf{K}_{\parallel}}^{(\nu)}\rangle$, where all modes are unoccupied except for a SPP mode ν of parallel wavevector \mathbf{K}_{\parallel} with occupation number 1. On the other hand, the electronic part of the final state can be of the form $|\Psi_{\text{L}}\rangle$ or $|\Psi_{\text{R}}\rangle$, depending on the Fermi-Dirac occupation factor of these states. Due to the applied bias potential, it is expected that, at low temperatures, the number of unoccupied states will be significantly greater in the right metal than in the left metal for final energies lower than that of the initial state. Thus, the transitions to the states of the left metal are highly suppressed, i.e. $\Gamma_{\text{L} \rightarrow \text{L}} \ll \Gamma_{\text{L} \rightarrow \text{R}}$, and in this formalism we only focus on the transitions of the

ⁱ If we do not specify the superscript BA or QDS in the electronic state $\Psi_{\text{L}(\text{R})}$ in this chapter, the expression is valid for both of these approaches.

form $L \rightarrow R$. Specifically, the tunneling rate according to Fermi's golden rule reads

$$\Gamma_{L \rightarrow R} = \frac{2\pi}{\hbar^2} \sum_{\mathbf{K}_{\parallel}} \sum_{\nu} \delta(\omega_L^{\text{el}} - \omega_R^{\text{el}} - \omega_{\mathbf{K}_{\parallel}}^{(\nu)}) \left| \mathcal{M}_{L,R,\mathbf{K}_{\parallel}}^{(\nu)} \right|^2, \quad (5.10)$$

with the matrix element

$$\begin{aligned} \mathcal{M}_{L,R,\mathbf{K}_{\parallel}}^{(\nu)} &= \left\langle \Psi_R, 1_{\mathbf{K}_{\parallel}}^{(\nu)} \left| \hat{\mathcal{H}}_{\text{int}} \right| \Psi_L, 0_{\text{pl}} \right\rangle \\ &= \sqrt{\frac{\hbar}{2\varepsilon_0 S \omega_{\mathbf{K}_{\parallel}}^{(\nu)}}} \frac{i\hbar e}{m_{\text{eff}}} \int_{\mathcal{V}_{\text{gap}} + \mathcal{V}_{\text{met}}} \Psi_R^*(\mathbf{r}) \left[\mathbf{u}_{\mathbf{K}_{\parallel}}^{(\nu)}(z) e^{-i\mathbf{K}_{\parallel} \cdot \mathbf{r}_{\parallel}} \right] \cdot \nabla \Psi_L(\mathbf{r}) \, d\mathbf{r} \\ &= \left\langle \Psi_L, 0_{\text{pl}} \left| \hat{\mathcal{H}}_{\text{int}} \right| \Psi_R, 1_{\mathbf{K}_{\parallel}}^{(\nu)} \right\rangle^* \\ &= \sqrt{\frac{\hbar}{2\varepsilon_0 S \omega_{\mathbf{K}_{\parallel}}^{(\nu)}}} \frac{-i\hbar e}{m_{\text{eff}}} \int_{\mathcal{V}_{\text{gap}} + \mathcal{V}_{\text{met}}} \Psi_L(\mathbf{r}) \left[\mathbf{u}_{\mathbf{K}_{\parallel}}^{(\nu)}(z) e^{-i\mathbf{K}_{\parallel} \cdot \mathbf{r}_{\parallel}} \right] \cdot \nabla \Psi_R^*(\mathbf{r}) \, d\mathbf{r}, \end{aligned} \quad (5.11)$$

where we specify that this integral has to be performed in the volume of the gap \mathcal{V}_{gap} and of the metallic regions, \mathcal{V}_{met} . Note that when accounting for metallic layers with finite thickness, we limit the integration over z but, for the sake of simplicity, we still use the electron wavefunctions given by Eqs. (5.1) and (5.2) established for metals with infinite thickness. Since the contributions of the gap and the metals must be summed, these two terms may produce quantum interferences, as we discuss in Sec. 5.4. Further, combining the two equivalent forms of the matrix element shown in Eq. (5.11), we can write $\mathcal{M}_{L,R,\mathbf{K}_{\parallel}}^{(\nu)}$ in a symmetric form that is similar to the elastic tunneling rate obtained with Bardeen's approximation [Eq. (2.95)], as

$$\begin{aligned} \mathcal{M}_{L,R,\mathbf{K}_{\parallel}}^{(\nu)} &= \sqrt{\frac{\hbar}{2\varepsilon_0 S \omega_{\mathbf{K}_{\parallel}}^{(\nu)}}} \frac{i\hbar e}{2m_{\text{eff}}} \\ &\quad \times \int_{\mathcal{V}_{\text{gap}} + \mathcal{V}_{\text{met}}} \left[\mathbf{u}_{\mathbf{K}_{\parallel}}^{(\nu)}(z) e^{-i\mathbf{K}_{\parallel} \cdot \mathbf{r}_{\parallel}} \right] \cdot [\Psi_R^*(\mathbf{r}) \nabla \Psi_L(\mathbf{r}) - \Psi_L(\mathbf{r}) \nabla \Psi_R^*(\mathbf{r})] \, d\mathbf{r}, \end{aligned} \quad (5.12)$$

where, in analogy with Eq. (5.4), the wavefunctions $\Psi_L(\mathbf{r})$ and $\Psi_R(\mathbf{r})$ appear in the form of the inelastic current density as [211]

$$\mathbf{j}_{L \rightarrow R}(\mathbf{r}) = \frac{i\hbar e}{2m_{\text{eff}}} [\Psi_R^*(\mathbf{r}) \nabla \Psi_L(\mathbf{r}) - \Psi_L(\mathbf{r}) \nabla \Psi_R^*(\mathbf{r})]. \quad (5.13)$$

The experimentally measurable quantity is the intensity of the emitted light due to the total inelastic tunneling rate, which is given by the sum over all occupied initial

states in the left metal and unoccupied final states of the right metal, calculated as $\Gamma_{\text{inel}} = \sum_{\mathbf{k}_L} \sum_{\mathbf{k}_R} \Gamma_{L \rightarrow R} f_{\text{FD}}^L(\mathbf{k}_L) [1 - f_{\text{FD}}^R(\mathbf{k}_R)]$, i.e.

$$\Gamma_{\text{inel}} = \sum_{\mathbf{K}_{\parallel}} \sum_{\nu} \sum_{\mathbf{k}_L} \sum_{\mathbf{k}_R} \frac{2\pi}{\hbar^2} \delta(\omega_L^{\text{el}} - \omega_R^{\text{el}} - \omega_{\mathbf{K}_{\parallel}}^{(\nu)}) f_{\text{FD}}^L(\mathbf{k}_L) [1 - f_{\text{FD}}^R(\mathbf{k}_R)] |\mathcal{M}_{L,R,\mathbf{K}_{\parallel}}^{(\nu)}|^2. \quad (5.14)$$

The corresponding total power transferred by the tunneling current to the SPPs is given by

$$\begin{aligned} \mathcal{P} &= \sum_{\mathbf{K}_{\parallel}} \sum_{\nu} \sum_{\mathbf{k}_L} \sum_{\mathbf{k}_R} \hbar \omega_{\mathbf{K}_{\parallel}}^{(\nu)} \Gamma_{L \rightarrow R}(\omega_{\mathbf{K}_{\parallel}}^{(\nu)}) f_{\text{FD}}^L(\mathbf{k}_L) [1 - f_{\text{FD}}^R(\mathbf{k}_R)], \\ &= \sum_{\mathbf{K}_{\parallel}} \sum_{\nu} \sum_{\mathbf{k}_L} \sum_{\mathbf{k}_R} \frac{2\pi}{\hbar^2} \delta(\omega_L^{\text{el}} - \omega_R^{\text{el}} - \omega_{\mathbf{K}_{\parallel}}^{(\nu)}) f_{\text{FD}}^L(\mathbf{k}_L) [1 - f_{\text{FD}}^R(\mathbf{k}_R)] |\mathcal{M}_{L,R,\mathbf{K}_{\parallel}}^{(\nu)}|^2 \hbar \omega_{\mathbf{K}_{\parallel}}^{(\nu)}. \end{aligned} \quad (5.15)$$

Following the standard procedure of elastic tunneling, the calculation of these transition rates is usually done under Bardeen's approximation, by evaluating the integral of the matrix element [Eq. (5.12)] just in the gap with the wavefunctions from Eqs. (2.85) and (2.86). This approximation assumes that the SPP is excited in the barrier due to the inelastic tunneling processes in the gap. This approach also gives an intuitive understanding on how the optical properties of the MIM junction influence the light emission process. We first notice that in typical gaps of few nanometers, the variation of the electromagnetic field is very smooth and it can be considered as constant in the integration region of Eq. (5.12). This assumption implies that the electronic and optical properties of the junction can be considered separately in Eq. (5.10). On the one hand, $\Gamma_{L \rightarrow R}$ is proportional to the electronic matrix element $|\langle \Psi_R^{\text{BA}} | \mathbf{p} | \Psi_L^{\text{BA}} \rangle + \langle \Psi_L^{\text{BA}} | \mathbf{p} | \Psi_R^{\text{BA}} \rangle|^2 = |-i\hbar \int \Psi_R^{\text{BA}*}(\mathbf{r}) \nabla \Psi_L^{\text{BA}}(\mathbf{r}) - \Psi_L^{\text{BA}}(\mathbf{r}) \nabla \Psi_R^{\text{BA}*}(\mathbf{r}) d\mathbf{r}|^2$. On the other hand, by doing the sum over all plasmonic modes, the tunneling rate is also proportional to the projected local optical density of states $\rho_{\text{opt}}(\mathbf{r}) = \sum_{\mathbf{K}_{\parallel}} \sum_{\nu} \delta(\omega_L^{\text{el}} - \omega_R^{\text{el}} - \omega_{\mathbf{K}_{\parallel}}^{(\nu)}) |\mathbf{u}_{\mathbf{K}_{\parallel}}^{(\nu)}(\mathbf{r}) \cdot \mathbf{n}_z|^2$. Therefore, this analysis suggests that the light emission can be enhanced by choosing optical antennas with large ρ_{opt} .

However, we emphasize that Eq. (5.12) includes processes inside the metals, provided that we use the wavefunctions of Eqs. (5.1) and (5.2) corresponding to the QDS, whereas Bardeen's approximation only considers gap processes (we compare inelastic transitions according to these two perspectives in Figs. 5.2a and b by the arrows with the label Γ_{inel}). When taking the square modulus of Eq. (5.12) within the QDS, we obtain the contributions of the gap, the metal electrodes and a mixed term which is a quantum interference between the two processes. Hence, it appears that it is not necessary to invoke a hot electron mechanism to obtain a contribution of light emission from the metallic electrodes. Further, we emphasize that the inelastic tunneling rate is proportional to the projected local optical density of states only within Bardeen's approximation. This is no longer necessarily true

when considering the QDS, due to the interferences between the amplitudes of the SPP electric field in the gap and in the metal.

5.3.2 Energy-loss model and Poynting vector flux calculation

An alternative model to describe light emission from tunneling junctions has been introduced by Davis [211] and consists in calculating the rate of energy dissipation by the electronic current [66, 67],

$$\mathcal{P} = - \int_{\mathcal{V}} d\mathbf{r} \mathbf{j}(\mathbf{r}, t) \cdot \mathbf{E}(\mathbf{r}, t), \quad (5.16)$$

where $\mathbf{E}(\mathbf{r}, t)$ is the electric field generated by the current density $\mathbf{j}(\mathbf{r}, t)$. This method has also been used by other authors [210, 219, 220]. A slightly different formulation considers the current density as a source that emits light to the far field, and integrate the flux of the Poynting vector. This approach was proposed originally by Hone et al. in Ref. [212] and, since then, it has been a popular method starting from the implementation of Laks and Mills to describe light emission from planar junctions [55], being followed by many works [198, 221–225]. We first show the equivalence of these two points of view using the electromagnetic energy conservation in a volume \mathcal{V} in the stationary regime:

$$\int_{\mathcal{V}} d\mathbf{r} \mathbf{j}(\mathbf{r}, t) \cdot \mathbf{E}(\mathbf{r}, t) + \mathcal{P}_{\text{abs}}(t) + \mathcal{P}_{\text{rad}}(t) = 0, \quad (5.17)$$

where \mathcal{P}_{rad} is the flux of the Poynting vector across a surface enclosing the volume \mathcal{V} and \mathcal{P}_{abs} is the power absorbed by the matter within this volume. Within the approximation of a non-lossy metal $\mathcal{P}_{\text{abs}}(t) = 0$, so that the radiated power is equal to the opposite of the power transferred from the tunneling current to the field. This equality establishes the equivalence between a calculation of the Poynting vector and a calculation of the power transferred from the fluctuating currents to the field. When accounting for the unavoidable metallic losses, the emitted power is then derived by multiplying the power \mathcal{P} transferred to the SPPs [Eq. (5.16)] with the radiative efficiency η_{rad} as discussed previously.

To proceed with the evaluation of Eq. (5.16), we first relate the electric field to the current density using the Green's tensor $\mathbf{G}(\mathbf{r}, \mathbf{r}', \omega)$ of the MIM junction as

$$\mathbf{E}(\mathbf{r}, \omega) = i\omega\mu_0 \int d\mathbf{r}' \mathbf{G}(\mathbf{r}, \mathbf{r}', \omega) \cdot \mathbf{j}(\mathbf{r}', \omega). \quad (5.18)$$

By introducing this last expression into Eq. (5.16), we observe that the power \mathcal{P} transferred from the current to the field can be computed with the expression of the current density $\mathbf{j}(\mathbf{r}, \omega)$ and the Green's tensor $\mathbf{G}(\mathbf{r}, \mathbf{r}', \omega)$. In particular, regarding the dependence on the current, the power \mathcal{P} can be written explicitly in terms of $\mathcal{S}_{j_p j_q}(\mathbf{r}, \mathbf{r}', \omega)$, which is the pq element of the power cross-spectral density tensor of

the current density given by $\overline{j_p(\mathbf{r}, \omega) j_q(\mathbf{r}', \omega')} = 2\pi\delta(\omega + \omega') \mathcal{S}_{j_p j_q}(\mathbf{r}, \mathbf{r}', \omega)$ (where the symbol \bar{x} denotes the ensemble average of x):

$$\mathcal{P} = \int_0^\infty d\omega 2\omega\mu_0 \int d\mathbf{r} \int d\mathbf{r}' \sum_{p,q} \mathcal{S}_{j_p j_q}(\mathbf{r}, \mathbf{r}', \omega) \text{Im}[G_{p,q}(\mathbf{r}, \mathbf{r}', \omega)]. \quad (5.19)$$

It is thus necessary to know $\mathcal{S}_{j_p j_q}(\mathbf{r}, \mathbf{r}', \omega)$ in the nonequilibrium situation of a biased junction, which can be computed using the statistical properties of the two reservoirs on both sides of the junction. In most works [55, 212, 226], the emitted power was calculated by using the form

$$\mathcal{S}_{j_z j_z}(\mathbf{r}, \mathbf{r}', \omega) \approx \frac{eI_{\text{el}}}{S^2} \frac{1 - \frac{\hbar\omega}{eV_B}}{1 - \exp\left(\frac{\hbar\omega - eV_B}{k_B T}\right)} \delta(\mathbf{r} - \mathbf{r}'), \quad (5.20)$$

where I_{el} is the intensity of the elastic current (which can be calculated following the methodology outlined in Sec. 5.2 and using $I_{\text{el}} = -e\Gamma_{\text{el}}$). Typically, the limit of Eq. (5.20) at $T = 0$ has been used, which predicts a linear spectrum proportional to $eV_B - \hbar\omega$. It was further assumed that the correlation function is nonzero in the gap and zero outside. Finally, it was assumed that the correlation function is delta correlated.

All these assumptions prevented a comparison of this model with the Fermi's golden rule result derived in the previous subsection. To obtain an equation that is consistent with the approach presented in Sec. 5.3.1, we now report a calculation of the power cross-spectral density of the current density. We start by introducing the form of the field operator for an arbitrary number of electrons in the conduction band [104]:

$$\hat{\Psi}(\mathbf{r}, t) = \sum_n \Psi_n(\mathbf{r}) \hat{O}_n(t). \quad (5.21)$$

Here, we use the subscript $n = (\mathbf{k}, l)$ where $l = \text{L, R}$ labels the state with wavevector \mathbf{k} and propagation coming from the left or the right metal. \hat{O}_n is the Fermionic annihilation operator of the n state. The current density operator is then given by [104]

$$\hat{\mathbf{j}}(\mathbf{r}, t) = \frac{i\hbar e}{2m_{\text{eff}}} [\hat{\Psi}^\dagger(\mathbf{r}, t) \nabla \hat{\Psi}(\mathbf{r}, t) - \hat{\Psi}(\mathbf{r}, t) \nabla \hat{\Psi}^\dagger(\mathbf{r}, t)]. \quad (5.22)$$

The time dependence of each Fermionic operator can be cast in the form

$$\hat{O}_n(t) = \hat{O}_n \exp(-i\omega_n t). \quad (5.23)$$

where $\hbar\omega_n = \frac{\hbar^2 \mathbf{k}^2}{2m_{\text{eff}}} + U_{\text{L(R)}}$. It follows that the current density in frequency domain is

$$\hat{\mathbf{j}}(\mathbf{r}, \omega) = \sum_{n, n'} \mathbf{j}(\mathbf{r}, n, n') 2\pi\delta(\omega - \omega_{n'n}) \hat{O}_n^\dagger \hat{O}_{n'}, \quad (5.24)$$

where $\mathbf{j}(\mathbf{r}, n, n') = \frac{i\hbar e}{2m_{\text{eff}}} [\Psi_n^*(\mathbf{r}) \nabla \Psi_{n'}(\mathbf{r}) - \Psi_{n'}(\mathbf{r}) \nabla \Psi_n^*(\mathbf{r})]$ and $\omega_{n'n} = \omega_{n'} - \omega_n$.

We can now compute the ensemble average of the current density $\overline{\hat{j}_p(\mathbf{r}, \omega) \hat{j}_q(\mathbf{r}', \omega')}$ where p, q stands for the cartesian components of the current density. To proceed, we assume that the system is a statistical mixture and use the commutation relations satisfied by Fermionic operators $\{\hat{O}_n, \hat{O}_{n'}\} = 0$; $\{\hat{O}_n^\dagger, \hat{O}_{n'}^\dagger\} = 0$; $\{\hat{O}_n^\dagger, \hat{O}_{n'}\} = \delta_{n, n'}$ where $\{a, b\} = ab + ba$. We have to evaluate terms of the form $\overline{\hat{O}_{n_1}^\dagger \hat{O}_{n_2} \hat{O}_{n_3}^\dagger \hat{O}_{n_4}} = \sum_r P_r \langle r | \hat{O}_{n_1}^\dagger \hat{O}_{n_2} \hat{O}_{n_3}^\dagger \hat{O}_{n_4} | r \rangle$ where r denotes a particular Fock state and P_r is the canonical probability that the system is in state r . Given that $\langle r | O_n | r \rangle = \langle r | O_n^\dagger | r \rangle = 0$ and $\langle r | O_n^\dagger O_n | r \rangle = f_{\text{FD}}(n)$, where $f_{\text{FD}}(n)$ is the Fermi-Dirac distribution evaluated at the energy $\hbar\omega_n$, the correlation is of the form:

$$\begin{aligned} \overline{\hat{O}_{n_1}^\dagger \hat{O}_{n_2} \hat{O}_{n_3}^\dagger \hat{O}_{n_4}} &= \delta_{n_1, n_2} \delta_{n_3, n_4} (1 - \delta_{n_1, n_3}) C_1 + \delta_{n_1, n_4} \delta_{n_3, n_2} (1 - \delta_{n_1, n_2}) C_2 \\ &\quad + \delta_{n_1, n_2} \delta_{n_1, n_3} \delta_{n_1, n_4} C_3. \end{aligned} \quad (5.25)$$

Here, $C_1 = f_{\text{FD}}(n_1) f_{\text{FD}}(n_3)$, $C_2 = f_{\text{FD}}(n_1) [1 - f_{\text{FD}}(n_2)]$, $C_3 = f_{\text{FD}}(n_1)$. We note that the terms C_1 and C_3 only contribute to a zero frequencyⁱⁱ so that only the contribution C_2 proportional to $f_{\text{FD}}(n_1) [1 - f_{\text{FD}}(n_2)]$ yields a non-zero contribution to the radiated field at frequencies $\omega > 0$. Furthermore, considering that the Fermi level on the left side is larger than the Fermi level on the right side, Eq. (5.24) selects the terms where $n_1 = (\mathbf{k}_R, R)$ and $n_2 = (\mathbf{k}_L, L)$ so that $\omega = \omega_{n_2} - \omega_{n_1} = \omega_L^{\text{el}} - \omega_R^{\text{el}} > 0$. Hence, the statistical average is only nonzero if there is an electron-hole pair with an electron in a state L and a hole in a state R. Finally, we obtain

$$\mathcal{S}_{j_p j_q}(\mathbf{r}, \mathbf{r}', \omega) = \sum_{\mathbf{k}_L} \sum_{\mathbf{k}_R} j_{p, L \rightarrow R}(\mathbf{r}) j_{q, L \rightarrow R}^*(\mathbf{r}') 2\pi \delta(\omega - \omega_L^{\text{el}} + \omega_R^{\text{el}}) f_{\text{FD}}^L(\mathbf{k}_L) [1 - f_{\text{FD}}^R(\mathbf{k}_R)]. \quad (5.26)$$

This correlation function goes beyond the previous models: i) it is non-zero in the metallic electrodes; and ii) it is correlated in both electrodes in marked contrast with the assumption of a delta-correlated current. In the next subsection, we use this explicit form to establish the equivalence with the Fermi's golden rule result obtained in Sec. 5.3.1. We then discuss in detail the properties of this correlation function and observe that it has all the properties that were missing in previous models and motivated the introduction of a hot electron mechanism [208].

5.3.3 Equivalence of the methods

In order to compute from Eq. (5.19) the power transferred from the electronic tunneling current to the SPPs, we consider the contribution of the SPP modes of

ⁱⁱ By relating the statistical average $\overline{\hat{j}_p(\mathbf{r}, \omega) \hat{j}_q(\mathbf{r}', \omega')}$ and the correlation $\overline{\hat{O}_{n_1}^\dagger \hat{O}_{n_2} \hat{O}_{n_3}^\dagger \hat{O}_{n_4}}$, we observe from Eq. (5.24) that $\omega = \omega_{n_2} - \omega_{n_1}$ and $\omega' = \omega_{n_4} - \omega_{n_3}$. Therefore, the frequencies ω and ω' of the current density average are nonzero only if $n_1 \neq n_2$ and $n_3 \neq n_4$. This condition is only satisfied for the term proportional to C_2 in Eq. (5.25).

all branches ν and all wavevectors \mathbf{K}_{\parallel} in the Green's tensor. Using the expansion of the Green's tensor over these modes [67, 68], we obtain

$$G_{p,q}(\mathbf{r}, \mathbf{r}', \omega) = \sum_{\mathbf{K}_{\parallel}} \sum_{\nu} \frac{c^2}{(\omega_{\mathbf{K}_{\parallel}}^{(\nu)})^2 - \omega^2} \frac{u_{p,\mathbf{K}_{\parallel}}^{*(\nu)}(\mathbf{r}) u_{q,\mathbf{K}_{\parallel}}^{(\nu)}(\mathbf{r}')}{S}. \quad (5.27)$$

We then apply the limit $\lim_{\epsilon \rightarrow 0} \text{Im}[1/(\alpha^2 - (\omega + i\epsilon)^2)] = \pi/(2\alpha)\delta(\omega - \alpha)$, which leads to

$$\text{Im}[G_{p,q}(\mathbf{r}, \mathbf{r}', \omega)] = \sum_{\mathbf{K}_{\parallel}} \sum_{\nu} \frac{\pi c^2}{2\omega_{\mathbf{K}_{\parallel}}^{(\nu)}} \frac{u_{p,\mathbf{K}_{\parallel}}^{*(\nu)}(\mathbf{r}) u_{q,\mathbf{K}_{\parallel}}^{(\nu)}(\mathbf{r}')}{S} \delta(\omega - \omega_{\mathbf{K}_{\parallel}}^{(\nu)}). \quad (5.28)$$

By inserting the above forms of the Green's tensor and the current density cross-spectral density into Eq. (5.19), we recognize the matrix elements $\mathcal{M}_{L,R,\mathbf{K}_{\parallel}}^{(\nu)}$ and recover Eq. (5.15). This establishes the equivalence between the different models provided that the exact current density cross-spectral density given by Eq. (5.26) is used.

5.3.4 Current-density correlation function

We now turn to the discussion of the cross spectral density in Eq. (5.26). In Fig. 5.3a, we plot $\mathcal{S}_{j_z j_z}$ calculated with Eq. (5.26) in the center of the gap, for different bias potentials and in the zero temperature limit. For all considered values of V_B , the results obtained with Bardeen's approximation (dots) agree almost perfectly with those obtained with the QDS (lines). Hence, Bardeen's approximation is a very accurate approach to describe current fluctuations inside the gap. However, we note that a linear behavior with the voltage is only observed for the smallest bias potential considered, $V_B = 0.5$ V. For larger bias potentials ($V_B = 1.5$ V and 2.0 V), $\mathcal{S}_{j_z j_z}$ is not linear with respect to ω as opposed to the prediction of Eq. (5.20) at $T = 0$ K. Therefore, the exact definition of Eq. (5.26) must be used in this approach to calculate the intensity of the emitted light. This issue has been discussed in two recent papers [225, 227].

The QDS allows us to discuss the spatial dependence of the correlation between two arbitrary points of the full device, because we can explore currents in the metals using this approach. With this aim, we plot in Fig. 5.3b the cross-spectral density $\mathcal{S}_{j_z j_z}(z, z', \omega)$ for fixed values $L_{\text{gap}} = 2$ nm, $V_B = 2$ V and $\hbar\omega = 1$ eV, by varying the positions z and z' (for the same position in the parallel direction, $\mathbf{r}_{\parallel} = \mathbf{r}'_{\parallel}$). We observe that there is a peak at $z = z'$ with a width of the order of 1 nm, close to the Fermi wavelengths of the metals, which are around 0.52 nm for gold and 0.36 nm for aluminium [129]. Therefore, the consideration of delta-correlated currents in Eq. (5.20) is accurate enough to describe this feature for most purposes. Nevertheless, we observe a second weaker and broader correlation peak for positions z and z' at opposite metals. Upon inspection (see appendix A), this maximum occurs when the

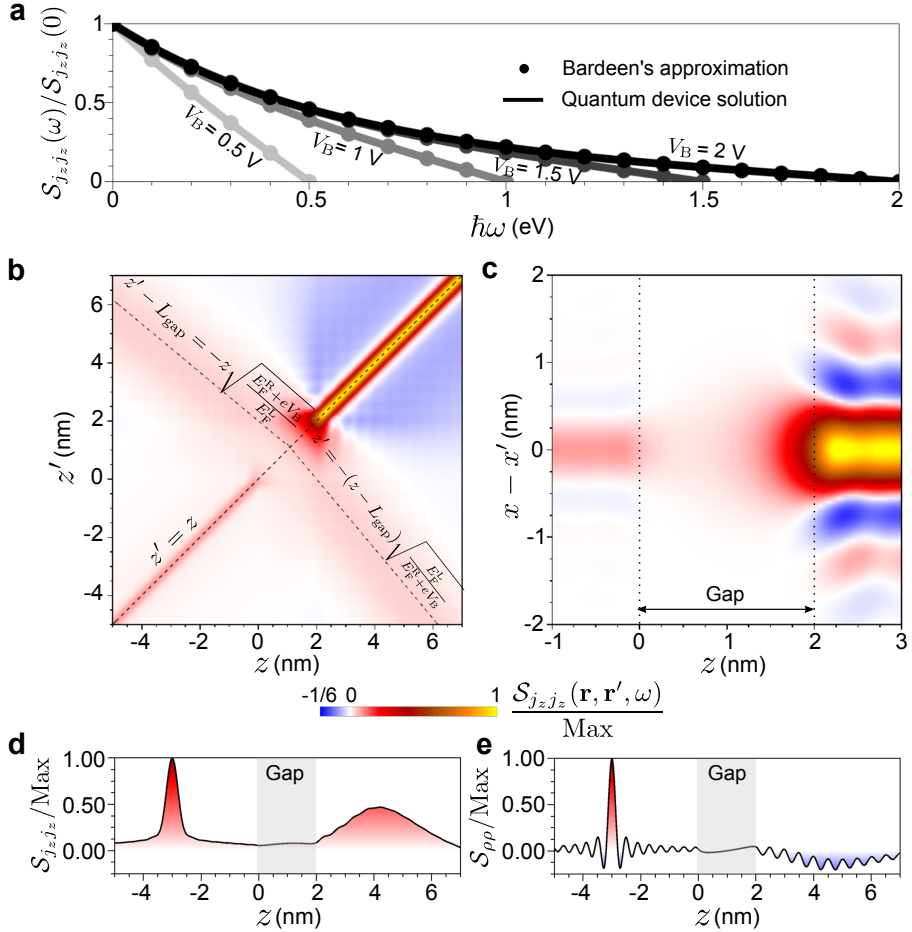


Figure 5.3: Spatial correlations of the current density j_z and charge density ρ . a) Cross-spectral density of the current density fluctuations $S_{j_z j_z}$ in the center of the insulator gap as a function of the energy $\hbar\omega$, for different bias potentials $V_B = 0.5$ V, 1 V, 1.5 V and 2 V. Dots correspond to the calculation with the wavefunctions obtained within Bardeen's approximation, and the solid lines to the QDS. b) Cross-spectral density $S_{j_z j_z}(z, z')$ for points z and z' at the same position in the parallel direction ($\mathbf{r}_{\parallel} = \mathbf{r}'_{\parallel}$), for $L_{\text{gap}} = 2$ nm, $V_B = 2$ V and $\hbar\omega = 1$ eV. The insulator gap is located at values of z and z' between 0 and 2 nm. Dashed lines highlight the two peaks under the conditions $z = z'$ and $z' - L_{\text{gap}} = -z\sqrt{(E_F^R + eV_B)/E_F^L}$ (and its symmetric form). c) Cross-spectral density $S_{j_z j_z}(\mathbf{r}_{\parallel}, \mathbf{r}'_{\parallel})$ for varying positions $z = z'$ and as a function of the distance in the parallel direction $x - x'$, for the same parameters as in panel (b). d-e) Cross-spectral density of the current $S_{j_z j_z}(z, z')$ and charge densities $S_{\rho\rho}(z, z')$, respectively. The point $z' = -3$ nm is fixed and the correlations are calculated for varying second point z (with $\mathbf{r}_{\parallel} = \mathbf{r}'_{\parallel}$), in the same system and for same ω as in panels (b) and (c).

current density $\mathbf{j}_{L \rightarrow R}$ has a similar phase for all $L \rightarrow R$ transitions. The equations describing this condition are i) $\frac{z' - L_{\text{gap}}}{z} = -\frac{k_{zR}}{k_{zL}} = -\sqrt{\frac{E_F^R + eV_B}{E_F^L}}$, if z is in the left metal and z' in the right metal; and ii) $\frac{z - L_{\text{gap}}}{z'} = -\sqrt{\frac{E_F^R + eV_B}{E_F^L}}$ if z is in the right metal and z' in the left metal. Both cases are indicated by dashed lines in Fig. 5.3b.

We further analyze how the currents are correlated for different points in the direction parallel to the interfaces $\mathbf{r}_{\parallel} \neq \mathbf{r}'_{\parallel}$, and for varying values $z = z'$, as shown in Fig. 5.3c (we consider $x \neq x'$ but $y = y'$). The correlations are oscillatory as a function of the difference $x - x'$, and become weaker for distances larger than the Fermi wavelength. The periodicity of these oscillations is of the order of 1 nm. We also observe that the width of the peak of $\mathcal{S}_{j_z j_z}(\mathbf{r}_{\parallel}, \mathbf{r}'_{\parallel}, \omega)$ is not constant for $z = z'$ close to the insulator gap and becomes broader inside the gap. This effect can be easily included in the approximate Eq. (5.20) by broadening the delta function $\delta(\mathbf{r} - \mathbf{r}')$ in the parallel direction. Therefore, the assumption of delta-correlated currents in Eq. (5.20) needs small corrections to describe current correlations along the \mathbf{r}_{\parallel} direction due to the finite thickness of the corresponding peak, but the assumption completely fails to capture the second peak observed for the correlations along the z direction.

In order to understand the physical origin of the current correlations in the two metals, we now focus on the correlations of the electronic charge density fluctuations. The charge density $\rho_{L \rightarrow R}$, associated to each transition from an initial state $\Psi_L^{\text{QDS}}(\mathbf{r})$ to a final state $\Psi_R^{\text{QDS}}(\mathbf{r})$, is obtained from the current density $\mathbf{j}_{L \rightarrow R}$ of Eq. (5.13) by using the continuity equation

$$\nabla \cdot \mathbf{j}_{L \rightarrow R} + \frac{\partial \rho_{L \rightarrow R}}{\partial t} = 0. \quad (5.29)$$

The cross-spectral density $\mathcal{S}_{\rho\rho}$ is then calculated with Eq. (5.26) after substituting $\mathbf{j}_{L \rightarrow R}$ with $\rho_{L \rightarrow R}$.

For the analysis, we fix the point $z' = -3$ nm in the left metal, and observe the cross-spectral density of the current density $\mathcal{S}_{j_z j_z}$ (Fig. 5.3d) and charge density $\mathcal{S}_{\rho\rho}$ (Fig. 5.3e) for any second position z and for $\mathbf{r}_{\parallel} = \mathbf{r}'_{\parallel}$. The latter correlations oscillate more strongly in space as compared to those associated to the current density. In the results of $\mathcal{S}_{\rho\rho}$, we observe a clear peak in the position $z' = z$ as happens for $\mathcal{S}_{j_z j_z}$. More importantly, the second peak in the opposite metal also appears, but whereas the correlation is positive for the current density, we obtain negative values in the case of the charge density. We attribute this result to the presence of a hole with positive charge and opposite velocity. In other words, as a negative charge moves toward the barrier in the left electrode, a positive charge also moves toward the barrier in the right electrode. The double peak in $\mathcal{S}_{\rho\rho}$ and $\mathcal{S}_{j_z j_z}$ disappears inside the gap, where the electron and the hole recombine. These currents in the metal electrodes give a contribution to the light radiation apart from the correlations just inside the gap. Therefore, the QDS introduces in a natural

way a contribution of the currents in the metallic electrodes to the excitation of SPPs without any need to invoke hot electron mechanisms.

To summarize, by starting with the combined Hamiltonian $\hat{\mathcal{H}}_{\text{el-SPP}}$ of electrons and SPPs in Sec. 5.3.1, we have established the exact equivalences between the two models, one based on Fermi's golden rule and the other on the energy dissipation by a tunneling current. When accounting for the contribution of the current in the metal, the assumption of a delta-correlated current does not hold any longer. Furthermore, the emission processes occurring in the gap and in the metals can interfere. In practice, the impact of these effects depends on the spatial structure of the modes. We explore in the next section how significant are these effects for the different plasmonic modes of planar junctions.

5.4 Light emission from planar devices

In this section, we analyze the contribution to light emission from the different SPP modes of a device composed by metallic electrodes of $\approx 10 - 20$ nm thickness at both sides of the gap. The slow mode of the MIM junctions is localized in the insulator gap. Its electric field is strongly confined and it is therefore very large so that it couples efficiently to the tunneling electrons [54, 56, 198, 228]. On the other hand, this mode is characterized by a small group velocity and has no radiative losses unless the surface becomes rough. Other SPP modes are localized at metal-dielectric interfaces few nanometers far from the insulator gap and can also contribute to radiation [196, 208, 225]. Their coupling to the inelastic tunneling mechanism is less efficient, specially at junctions with thick metallic electrodes, because the electric field of the SPP of the corresponding interfaces penetrates weakly into the gap. On the other hand, their radiative losses can be larger. With the objective to analyze the contribution of the coupling in the gap and the coupling in the metal, we choose as a representative system a junction that was considered in the first experiment of light emission from tunneling junctions, consisting in a planar junction formed by an aluminium and a gold electrode separated by a layer of aluminium oxide.

5.4.1 Mode structure of the system

In order to study the intensity of light emission due to inelastic tunneling in Al-AlOx-Au junctions (where electrons tunnel from the Al electrode to the Au electrode), we first analyze the properties of the SPPs of the system. These modes are obtained by assuming that the insulators have a non-dispersive permittivity, with the value $\varepsilon = 3.1$ for aluminium oxide in the gap. Further, the aluminium layer is deposited over a glass substrate with a representative permittivity $\varepsilon = 2.5$, and the insulator in the opposite direction is set to be vacuum. The two metals are represented by a Drude permittivity of the form $\varepsilon^{\text{Dr}}(\omega) = \varepsilon_{\infty} - \omega_{\text{p}}^2/\omega^2$ [Eq. (1.25)], with parameters $\hbar\omega_{\text{p}} = 14.7$ eV and $\varepsilon_{\infty} = 1$ for aluminium [229], whereas we choose $\hbar\omega_{\text{p}} = 9.065$ eV for gold [230]. Further, we consider interband transitions in gold by

setting $\varepsilon_\infty = 9$. The losses in the Drude model are neglected in the calculation of the SPP excitation rates to ensure that the energies of the modes are real and their respective electric fields can be normalized following the quantization rule from Eq. (5.9). We have checked that the dispersion relations in the range of energies considered change only slightly after including losses in the permittivities. Further, we fix the metal thickness of the aluminium layer at $L_{\text{Al}} = 10$ nm and of the gold layer at $L_{\text{Au}} = 20$ nm (unless stated otherwise). Since these two thicknesses are smaller than the electron mean free paths of their respective metal [231], we assume that the electronic wavefunctions given in Sec. 5.2 are valid in the whole metallic regions. A sketch of the system is shown in the inset of Fig. 5.4a.

This system contains three different modes of SPPs, typically referred to as the fast, medium and slow modes, based on their group velocities according to the dispersion relations (shown in Fig. 5.4a) [232]. The group velocities of the fast and the medium modes are very close to the speed of light in vacuum and in the glass, respectively, while it is much smaller for the slow mode. Among these three modes, the slow mode (brown line in Fig. 5.4a) has received significant attention in studies of quantum tunneling due to its large electric field in the gap region. Fig. 5.4b illustrates the large sensitivity of the group velocity on the gap thickness. The normalized electric field distribution $\mathbf{u}_{\mathbf{k}_\parallel}^{(s)}$ of the slow mode at energy $\hbar\omega_{\mathbf{k}_\parallel}^{(s)} = 2$ eV and thickness $L_{\text{gap}} = 3$ nm is shown in Fig. 5.4c, where we plot the field components in the directions (top) parallel and (bottom) perpendicular to the interfacesⁱⁱⁱ. It is apparent that the mode is strongly confined in the gap. However, it is worth noting that the electric fields also penetrate in the metals, which can contribute to the coupling with the electronic current and increase the excitation rate when considering processes in metals within the QDS, as discussed below.

Together with the slow mode, the finite thicknesses of the metallic electrodes lead to the existence of two additional modes localized in the other two metal-insulator interfaces. The fast and medium modes are SPPs mostly localized in the gold-vacuum and aluminium-substrate interfaces, respectively. These modes follow the typical dispersion relations of SPPs calculated with semi-infinite Drude metals [Eq. (1.31)], and the materials at a distance of a few nanometers from these interfaces only cause slight modifications to the dispersion relations.

The dispersion relation (Figs. 5.4a and b) and the field distribution of the modes (Figs. 5.4c, d and e) are useful to analyze which mode may contribute for light emission. The field distributions of the fast and medium modes suggest a smaller electromagnetic energy stored in the gap compared to the slow mode (shown for $\hbar\omega_{\mathbf{k}_\parallel}^{(m)} = \hbar\omega_{\mathbf{k}_\parallel}^{(f)} = 2$ eV and $L_{\text{gap}} = 3$ nm), which results in a smaller excitation rate due to a weaker coupling with tunneling electrons. Despite its small excitation rate, only the fast mode may contribute through leakage in the glass, because it is seen in Fig. 5.4a that it is the only mode whose dispersion relation is inside the light cone of the glass (Fig. 5.4a). On the other hand, if the gold-vacuum interface is rough [212] or periodically structured [221], the slow

ⁱⁱⁱ Since in this chapter we have neglected losses of the Drude permittivities, the electric fields are real or purely imaginary in the whole space.

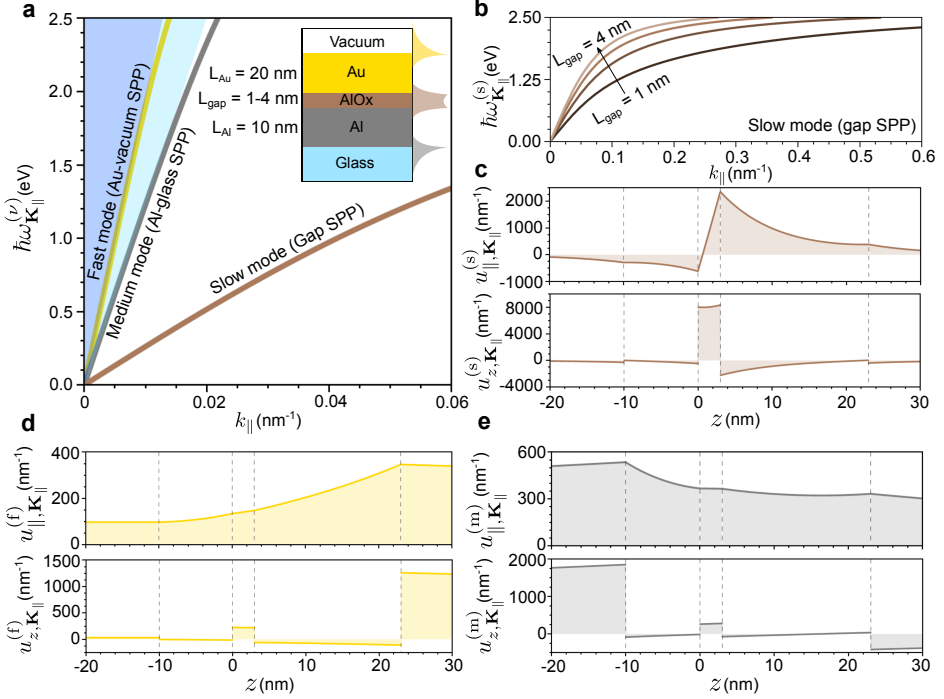


Figure 5.4: SPPs in Al-AIOx-Au tunneling junctions. a) Dispersion relation of the fast (yellow), medium (gray) and slow (brown) modes. The dark blue area indicates the light cone in vacuum, and the light blue area highlights the light cone in the glass substrate. The inset shows a sketch of the device, including the thicknesses of the layers considered in the rest of the panels and in most of the calculations. On the right of the structure we show schematically the field distribution of the different SPP modes, emphasizing the interface where each of them propagates predominantly. Each field distribution is plotted in the same color as the corresponding dispersion (yellow for the fast mode, gray for the medium mode and brown for the slow mode). b) Dispersion relation of the slow mode for different gap thicknesses $L_{\text{gap}} = 1$ nm, 2 nm, 3 nm and 4 nm (from the darkest to the lightest brown). c-e) Electric field distributions at energy $\hbar\omega_{\mathbf{K}_{\parallel}}^{(\nu)} = 2$ eV of the slow (c), fast (d) and medium (e) modes, for $L_{\text{gap}} = 3$ nm. The top panels show the distribution of the electric field component along the direction parallel to the interfaces of the junction $u_{\parallel, \mathbf{K}_{\parallel}}^{(\nu)}$, and the bottom panels show the component in the z direction $u_{z, \mathbf{K}_{\parallel}}^{(\nu)}$. Dashed lines in panels (c-e) indicate the positions of the metal-insulator interfaces.

mode can be coupled into vacuum and it can dominate the light emission process due to its far larger excitation efficiency. In the following subsections, we analyze the effect of the electric field distributions on the theoretical prediction of light emission from the gap and the metal regions.

5.4.2 Excitation rate of the slow mode

We first explore the excitation rate of the slow mode. Within Bardeen's approximation, it amounts to compute an overlap integral between the current density and the SPP field in the gap (i.e. the integral in Eq. (5.12) is calculated only inside the gap volume \mathcal{V}_{gap}). Within the QDS model, we also need to explore the contribution to the excitation rate from the processes in the metal regions and from the quantum interferences due the coupling in the gap and in the metal.

We start by using Bardeen's approximation and the formalism of inelastic tunneling (described in Sec. 5.3) to calculate the excitation rate $\Gamma_{\text{inel}}^{(s)}$ of the slow mode [from Eq. (5.14)]. We plot $\Gamma_{\text{inel}}^{(s)}$ (where the superscript s refers to the slow mode) in the inset of Fig. 5.5a as a function of the bias potential for a fixed gap thickness of $L_{\text{gap}} = 3$ nm. As V_{B} increases, the transition rate grows due to an exponential increase of the matrix element [Eq. (5.12)] and a linear raise of the number of initial and final states. For instance, increasing the bias potential from 0.6 V to 2.4 V causes the number of excited SPPs to increase by three orders of magnitude, from $3.8 \cdot 10^{18}$ to $1.2 \cdot 10^{21}$ SPPs per second and square meter. However, the efficiency of the planar junction does not increase at the same rate because it is measured in terms of the ratio between the elastic and inelastic transition rates, corresponding to the number of excited slow SPPs per tunneling electron. The elastic tunneling rate [Eq. (2.96)] also increases significantly with V_{B} , which means that the efficiency of the tunneling junctions only raises slightly from 10^{-4} to $2 \cdot 10^{-4}$ for the range of V_{B} considered. We have also checked numerically that the efficiency of the junction improves for thinner gaps because the density of states of the slow mode is larger (as can be deduced from the dispersion relations shown in Fig. 5.4b). For example, at $L_{\text{gap}} = 1$ nm, we obtain an efficiency of around $8 \cdot 10^{-4}$ SPPs excited per tunneling electron. Therefore, the efficiency of the planar junctions according to the inelastic tunneling process is not expected to exceed the ratio $\Gamma_{\text{inel}}^{(s)}/\Gamma_{\text{el}} = 10^{-3}$, even for narrower gaps that are experimentally considered in typical light-emission experiments with planar junctions.

To determine whether the inelastic tunneling in the gap can fully account for the excitation of the slow mode, we include the contribution of the metal electrodes according to the QDS model, as explained in Sec. 5.3. After analyzing the SPP excitation rate $\Gamma_{\text{inel}}^{(s)}$ in the inset of Fig. 5.5a, we now focus on the power $\mathcal{P}^{(s)}$ transferred by the current to excite this mode [given by Eq. (5.15)]. With this purpose, we show in Fig. 5.5a the spectral contribution $P^{(s)}(\hbar\omega_{\mathbf{K}_{\parallel}}^{(s)})$ at each energy $\hbar\omega_{\mathbf{K}_{\parallel}}^{(s)}$, which is related to the total non-radiative power $\mathcal{P}^{(s)}$ and to the slow SPP-excitation rate $\Gamma_{\text{inel}}^{(s)}$ as $\mathcal{P}^{(s)} = \int P^{(s)}(\hbar\omega_{\mathbf{K}_{\parallel}}^{(s)})d(\hbar\omega_{\mathbf{K}_{\parallel}}^{(s)}) = \int \hbar\omega_{\mathbf{K}_{\parallel}}^{(s)} \frac{d\Gamma_{\text{inel}}^{(s)}}{d(\hbar\omega_{\mathbf{K}_{\parallel}}^{(s)})} d(\hbar\omega_{\mathbf{K}_{\parallel}}^{(s)})$. We use the electronic states of the QDS [Eqs. (5.1) and (5.2)] to calculate the spectral power $P_{\text{QDS}}^{(s)}$ according to the processes in the whole MIM device (performing the integral of Eq. (5.12) in the volumes \mathcal{V}_{gap} of the gap and \mathcal{V}_{met} of the metals), and we compare it with the contribution of the gap according to Bardeen's approximation,

$P_{\text{BA}}^{(s)}$ (calculating Eq. (5.12) just inside \mathcal{V}_{gap}).

For bias potentials $V_{\text{B}} = 0.6$ V, 1.2 V or 1.8 V, the results of the full QDS (solid line) are nearly identical to those according to Bardeen's approximation (dots) for all energies, with a largest mismatch of 5% in the integrated non-radiative power $\mathcal{P}^{(s)}$. Indeed, for all these values of V_{B} , the negative permittivity of the metals is large for all energies $\hbar\omega_{\mathbf{K}_{\parallel}}^{(s)} \leq eV_{\text{B}}$, resulting in limited penetration of the electric field within these regions. Further, at energies $\hbar\omega_{\mathbf{K}_{\parallel}}^{(s)} > eV_{\text{B}}$, the spectral power vanishes completely, because we assume zero temperature and the Fermi-Dirac occupation factors of the metals do not allow any transition between states at those energies (for $T > 0$ it is possible to excite SPPs at $\hbar\omega_{\mathbf{K}_{\parallel}}^{(s)} > eV_{\text{B}}$ [233], but we take $T = 0$ for simplicity because the main results of this work remain very similar otherwise). Since the calculation within Bardeen's approximation agrees with high accuracy with the calculation of the full QDS at all $\hbar\omega_{\mathbf{K}_{\parallel}}^{(s)}$, the consideration of the inelastic processes only in the insulator gap would be accurate enough to describe the excitation of the slow SPP in the range of V_{B} considered.

For $V_{\text{B}} = 2.4$ V, both calculations still agree with high accuracy at low energies, but the difference becomes considerably larger for $\hbar\omega_{\mathbf{K}_{\parallel}}^{(s)} \gtrsim 1.8$ eV. In this region, $P^{(s)}(\hbar\omega_{\mathbf{K}_{\parallel}}^{(s)})$ is dominated by a peak, where the plasmonic density of states increases considerably (see dispersion relation in Fig. 5.4b). At this peak, the spectral power according to the calculation of the QDS, $P_{\text{QDS}}^{(s)}$, is generally larger than the value obtained within Bardeen's approximation, $P_{\text{BA}}^{(s)}$, suggesting that the metal contribution gains importance under these conditions.

To further showcase the importance of the metal contribution in the high-energy regime, we plot in Fig. 5.5b the ratio $P_{\text{QDS}}^{(s)}/P_{\text{BA}}^{(s)}$ for varying energies and gap thicknesses under a larger bias potential of $V_{\text{B}} = 3$ V. Two distinct regions are observed: one at thin gaps or low energies, where the contribution within the metals reduces the excitation power of the slow mode ($P_{\text{QDS}}^{(s)} < P_{\text{BA}}^{(s)}$), and another at thick gaps and high energies, where it increases ($P_{\text{QDS}}^{(s)} > P_{\text{BA}}^{(s)}$). To clarify this phenomenon, the spatial distribution of the electric field of the slow mode (brown line and background) is shown in Figs. 5.5c-e, together with the inelastic current $\text{Re}(j_{z,L \rightarrow R})$ associated with a $L \rightarrow R$ transition for an electron initially at the highest occupied energy level of aluminium (blue lines), for values of L_{gap} and $\hbar\omega_{\mathbf{K}_{\parallel}}^{(s)}$ indicated by white dots in Fig. 5.5b. For thin gaps (Figs. 5.5c and d for $L_{\text{gap}} = 1$ nm), the electric field is highly concentrated inside the gap, with some penetration into the metals near the gap. Due to the phase difference of the electric field between the insulator and the metal, the metal contributions tend to interfere destructively with the gap contribution. Accordingly, the calculation of the QDS in the full device predicts a smaller excitation rate than Bardeen's approximation, as shown by the region of $P_{\text{QDS}}^{(s)} < P_{\text{BA}}^{(s)}$ in Fig. 5.5b. The effect is more significant at large energies, where the negative electric field in the metal becomes even more concentrated close to the gap leading to a stronger destructive interference (as can

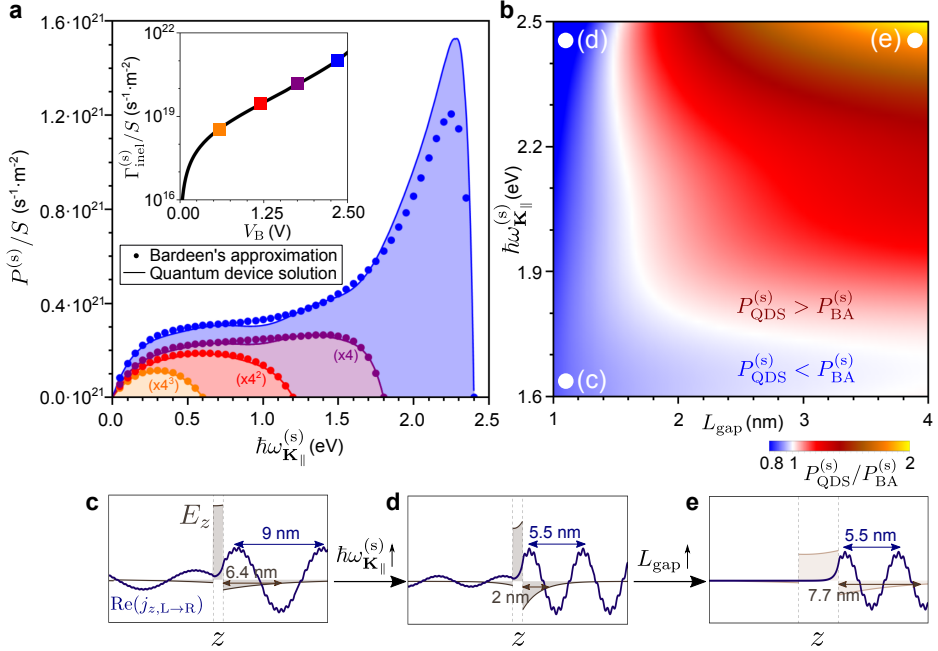


Figure 5.5: Analysis of the power transferred by the tunneling current to the slow mode. a) Spectral power $P^{(s)}$ per surface area S of the junction, with thicknesses $L_{\text{gap}} = 3$ nm, $L_{\text{Al}} = 10$ nm and $L_{\text{Au}} = 20$ nm (see sketch in Fig. 5.4a), and bias potentials $V_B = 0.6$ V (orange), 1.2 V (red), 1.8 V (purple) and 2.4 V (blue). Dots correspond to the gap contribution to the power, $P_{\text{BA}}^{(s)}$, according to Bardeen's approximation, and the solid lines to the joint contribution of processes in the gap and in the metals calculated using the QDS, $P_{\text{QDS}}^{(s)}$. The inset shows the total inelastic tunneling rate $\Gamma_{\text{inel}}^{(s)}$ per surface area in logarithmic scale as a function of the bias potential. Colored squares correspond to the values of V_B that we choose in the main panel. b) Ratio between the spectral power contributions $P_{\text{QDS}}^{(s)}/P_{\text{BA}}^{(s)}$ as a function of the gap thickness L_{gap} and SPP energy $\hbar\omega_{\mathbf{K}_{\parallel}}^{(s)}$. The applied bias voltage is $V_B = 3$ V. The color bar is in linear scale. c-e) Schematics of the distributions of the fluctuating electronic current density $\text{Re}(j_{z,L\rightarrow R})$ for an electron initially in the highest occupied energy level (blue) and the electric field E_z (brown) of the slow mode for gap thicknesses L_{gap} and energies $\hbar\omega_{\mathbf{K}_{\parallel}}^{(s)}$ indicated by the dots in panel (b): c) $\hbar\omega_{\mathbf{K}_{\parallel}}^{(s)} = 1.6$ eV and $L_{\text{gap}} = 1$ nm; d) $\hbar\omega_{\mathbf{K}_{\parallel}}^{(s)} = 2.5$ eV and $L_{\text{gap}} = 1$ nm; and e) $\hbar\omega_{\mathbf{K}_{\parallel}}^{(s)} = 2.5$ eV and $L_{\text{gap}} = 4$ nm. The wavelength of the electronic current density and the decay length of the SPP are indicated in each panel.

be observed by comparing Fig. 5.5d for $\hbar\omega_{\mathbf{K}_{\parallel}}^{(s)} = 2.5$ eV with 5.5c for $\hbar\omega_{\mathbf{K}_{\parallel}}^{(s)} = 1.6$ eV).

On the other hand, the inelastic electronic current $\mathbf{j}_{L\rightarrow R}$ oscillates in space. For larger L_{gap} these oscillations can give not only destructive interferences between the processes in the gap and the metals, but also constructive ones under some

circumstances. Due to the oscillations of $\mathbf{j}_{L \rightarrow R}$ (whose wavelength varies between 5 and 9 nm in the energy range considered in Fig. 5.5b), the integrand of the matrix element of Eq. (5.12) has the same sign in some regions of the metal as in the gap, leading to a constructive interference. Since the contribution close to the gap leads to a destructive interference, the wavelength of the electronic current should be small compared to the SPP decay length to have an overall constructive interference, which happens for large L_{gap} (Fig. 5.5e), because the SPP decay length increases with the gap thickness. After accounting for all constructive and destructive interferences within the metal according to the QDS, the interference averages to be constructive for all electrons in junctions with $L_{\text{gap}} \gtrsim 1.6$ nm, and the excitation power at 2.5 eV can be even twice as high as that predicted by Bardeen's approximation. At larger energies, the slow mode contains significant losses, and thus the description based of non-lossy Hermitian Hamiltonians that we present in this work loses its accuracy.

In general, Fig. 5.5b illustrates that Bardeen's approximation can underestimate or overestimate the excitation power of the slow mode up to a factor of two. Importantly, while the slow mode is non-radiative in perfectly planar junctions, it can dominate light emission in other systems, such as in localized gap tunneling junctions [209], commonly used in STM, or in planar junctions with sufficient surface roughness. In these systems, the QDS gives a more appropriate description of radiation than Bardeen's approximation that only considers the gap contribution.

5.4.3 Excitation rate of the fast mode

The formalism of inelastic tunneling predicts that the excitation of the fast mode is far less efficient than for the slow mode, due to the considerably weaker electric field inside the gap (see Fig. 5.4d). In particular, as shown in Fig. 5.6a, the spectral power $P_{\text{BA}}^{(\text{f})}$ of the fast mode at $V_{\text{B}} = 0.6$ V is of the order of 10^{11} s⁻¹ m⁻², which is 10^7 times smaller than $P_{\text{BA}}^{(\text{s})}$ for the slow mode. However, the study of the excitation rate of the fast mode is important, because in perfectly planar junctions it is the only process that leads to radiation. Although for many systems with surface roughness, or in situations where a localized gap mode is produced, the slow mode can be dominant, its radiative efficiency depends on the roughness and on the details of the geometry. It was estimated that in gratings with a periodicity of hundreds of nanometers, the emission of the fast mode may overcome the emission by the slow mode by a factor of 10^2 [196]. Indeed, the main discrepancy between the theory of inelastic tunneling and experiments was firstly observed for gratings [57, 197]. The results that we present for planar junctions can be generalized to describe the contribution of Bardeen's approximation and the QDS in other kinds of systems where the fast mode is the leading mechanism of light emission.

Interestingly, when the QDS is applied, we already observe a difference from Bardeen's approximation at $V_{\text{B}} = 0.6$ V in the calculation of the spectra $P^{(\text{f})}$. Although this variation is only 18% in the integrated power $\mathcal{P}^{(\text{f})}$, it is considerably larger than for the slow mode at the same bias potential. This suggests that

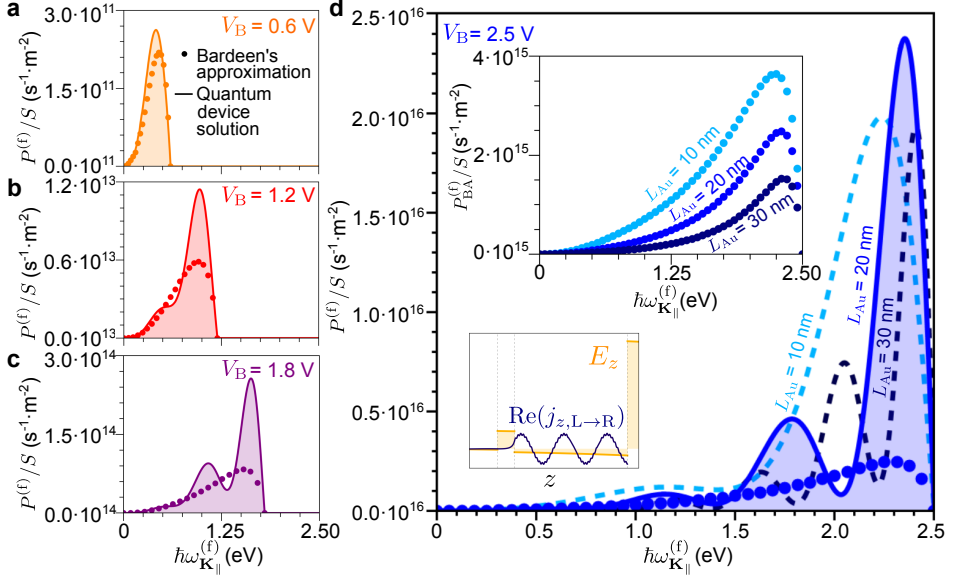


Figure 5.6: Analysis of the power transferred by the tunneling current to the fast mode. a-c) Spectral radiative power $P^{(f)}$ per surface area S of the junction, with thicknesses $L_{\text{gap}} = 3 \text{ nm}$, $L_{\text{Al}} = 10 \text{ nm}$ and $L_{\text{Au}} = 20 \text{ nm}$, and bias potentials $V_B = 0.6 \text{ V}$ (a), 1.2 V (b) and 1.8 V (c). Dots indicate the contribution of the gap according to Bardeen's approximation, and the solid lines refer to the full results of the QDS. d) Spectral radiative power $P^{(f)}$ per surface area S under bias potential $V_B = 2.5 \text{ V}$. We compare the results obtained using Bardeen's approximation (dots) and the QDS (solid line) for $L_{\text{Au}} = 20 \text{ nm}$. Dashed lines indicate the results according to the QDS for $L_{\text{Au}} = 10 \text{ nm}$ and $L_{\text{Au}} = 30 \text{ nm}$. The upper inset shows the results within Bardeen's approximation for $L_{\text{Au}} = 10 \text{ nm}$, 20 nm and 30 nm . The lower inset shows the electric field of the fast mode at energy 1.8 eV for $L_{\text{Au}} = 20 \text{ nm}$ and the corresponding fluctuating inelastic current density of one electron. All results in this panel have been obtained for $L_{\text{Al}} = 10 \text{ nm}$ and $L_{\text{gap}} = 3 \text{ nm}$.

including the metal contribution is significant for the fast mode as pointed out by Kirtley et al. [208]. The discrepancy between Bardeen's approximation and the QDS increases considerably for $V_B = 1.2 \text{ V}$ (Fig. 5.6b) and continues to grow with V_B . Further, at $V_B = 1.8 \text{ V}$ (Fig. 5.6c), local minima and maxima in $P_{\text{QDS}}^{(f)}$ are observed at different energies, which is related to the oscillatory behavior of the inelastic current density for each electron, as shown in the lower inset of Fig. 5.6d together with the electric field of the fast mode. The wavelength of the oscillations inside the metal depends on the energy of the electrons, leading to constructive or destructive interference with the contribution of the insulator gap in the integral of Eq. (5.12), which relates the current density according to Eq. (5.13) with the field distribution of the mode [Eq. (5.8)]. However, we do not expect these oscillations to be as predominant in experiments, because the position of the maxima and minima in the spectra $P_{\text{QDS}}^{(f)}$ is very sensitive to the thicknesses of the metals and the gap. In real systems, metallic surfaces present small roughness, and thus the contribution

of different thicknesses will cancel out these oscillations and the measured power would be the average between thicknesses. Finally, we remind that the calculation of the matrix element uses a very simple model which may produce artefacts. Specifically, to compute the overlap integral between the electronic wavefunction and the SPP electric field, we use the electronic wavefunction computed for an infinite metal [Eqs. (5.1) and (5.2)] and perform the integral over a finite thickness.

The increased importance of the metal contribution to light emission at larger energies becomes more evident in Fig. 5.6d. The comparison between the results obtained with Bardeen's approximation (dots) and QDS (solid line) for $V_B = 2.5$ V demonstrates that, for most energies, the results of the latter calculation are significantly larger than for the former. Therefore, despite the oscillations in the calculation for the full system, the integrated power $\mathcal{P}_{\text{QDS}}^{(f)}$ is notably larger than $\mathcal{P}_{\text{BA}}^{(f)}$.

The role of the thickness of the metallic electrodes is also highlighted in Fig. 5.6d. The upper inset indicates the result $P_{\text{BA}}^{(f)}$ according to Bardeen's approximation for $L_{\text{Au}} = 10$ nm, 20 nm and 30 nm (the values of $L_{\text{Au}} = 20$ nm are the same as in the main panel). We obtain that $P_{\text{BA}}^{(f)}$ decreases significantly by increasing L_{Au} , because the electric field inside the gap becomes smaller due to the exponential decay from the Au-vacuum interface where the fast SPP is mostly localized. Therefore, the decrease of the inelastic tunneling rate according to Bardeen's approximation is dictated by the decay length of the SPP. However, experimental measurements from Ref. [57] indicate that the intensity of the light emitted by the fast mode decreases with L_{Au} more slowly than the decay length of the SPP. Indeed, by increasing L_{Au} , the electric field inside the metal gets stronger and it could be expected that the contribution from the metal compensates the decrease of the gap contribution. To verify this, we plot in Fig. 5.6d the results predicted by the QDS for the same thicknesses, $L_{\text{Au}} = 10$ nm, 20 nm and 30 nm. The obtained radiative power decreases more slowly as a function of L_{Au} than expected from Bardeen's approximation, indicating that the latter cannot provide the correct dependence of the intensity of the emitted light on the thicknesses of the electrodes. In general, Figs. 5.6a-d show that under different circumstances, the QDS can lead to a value of the power $\mathcal{P}_{\text{QDS}}^{(f)}$ two or three times larger than $\mathcal{P}_{\text{BA}}^{(f)}$ for intermediate bias potentials, or even an order of magnitude larger at high energies and thick metallic layers.

Together with the inelastic processes in the metallic regions, Kirtley et al. argued that processes close to vacuum-metal interfaces placed far from the insulator gap could also contribute significantly to the excitation of the fast mode [208]. To verify this, we first observe in Fig. 5.4d that the electric field changes drastically from the bulk metal to vacuum at the interface. Therefore, one could expect indeed that under a non-local description of the electromagnetic response, the electrons placed close to the interface interact with the strong electric fields outside the metal and that a large contribution to the electron-SPP matrix element corresponds to this region. This feature cannot be explained by Bardeen's approximation.

In the QDS approach to calculate the SPP excitation rate in planar junctions,

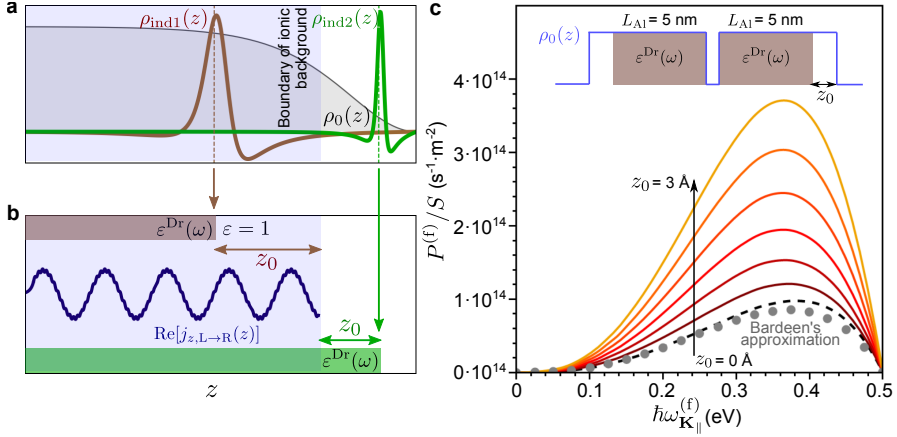


Figure 5.7: Consideration of the non-local optical response in the light emission induced by the excitation of the fast mode. a) Schematics of the ground state density $\rho_0(z)$ (gray) and the induced charge densities for two different possible metals ($\rho_{\text{ind}1}(z)$ in brown and $\rho_{\text{ind}2}(z)$ in green). The dashed lines indicate the position of the centroid of the induced charge density of the same color. The blue area indicates the step-like positive charge background that is considered in the jellium model of metals. b) Schematics of the distribution of the electronic current density $j_{z,L \rightarrow R}(z)$ considered in the calculations, up to the boundary of the ionic positive background. We also show the spatial distribution of the permittivities considered in our non-local approach for each $\rho_{\text{ind}}(z)$ distribution shown in panel (a). c) Spectral radiative power per surface area S for different distances z_0 from the boundary between the aluminium and vacuum permittivities (corresponding to the position of the centroid of charge) to the boundary of the step-like ionic positive background. z_0 is indicated in panel (b) and in the inset of panel (c), and we consider that the boundary between permittivities is inside the ionic background [brown color in (a) and (b)]. All these calculations are done for a junction with two aluminium layers of thickness $L_{\text{Al}1} = 5$ nm, and parameters $L_{\text{gap}} = 2$ nm and $V_{\text{B}} = 0.5$ V.

we need to calculate the integral of Eq. (5.12). The regions of this integral are delimited by the volumes of the insulator gap (\mathcal{V}_{gap}) and of the metals (\mathcal{V}_{met}). In all the calculations shown up to this point, we consider a local approach of electromagnetism to calculate the electric field of the SPPs. This perspective implies that in the metallic regions (inside the volume \mathcal{V}_{met}) the system has a Drude permittivity, and that outside this region the permittivity is constant over frequency and positive. Accordingly, the electromagnetic fields drop strongly exactly at the interface between these two regions, so that the electronic current interacts with the electric field of the gap and the weaker electric field inside the metallic regions, while it does not interact with the strong electric fields in vacuum and in the substrate (see Fig. 5.4).

However, according to the non-local theory of optical response of metals, the tunneling electrons could interact with the strong electric fields close to the metal-vacuum boundary. To visualize this, we show in Fig. 5.7a a sketch of the electronic density distribution close to this boundary. As an example, we consider a simple jellium model for the metal, where the ions create an uniform

density of positive charge (indicated by the blue area). This uniform background leads to the calculation of the electronic ground state density $\rho_0(z)$ that decays gradually at the boundary between the jellium charge density and vacuum. $\rho_0(z)$ indicates the region where the wavefunctions of the tunneling electrons are well defined. Regarding the fields at optical frequency, the discontinuity of the normal fields takes place across a finite but narrow region where an oscillating charge density is induced. This region of strong induced charges is called the centroid of charge. The position of the centroid of charge does not coincide with the interface between the jellium and vacuum. It can be either inside (case 1 indicated by $\rho_{\text{ind1}}(z)$, brown curve) or outside (case 2 indicated by $\rho_{\text{ind2}}(z)$, green curve) the jellium depending on the metal (inside for noble metals including d -band excitations, such as Au or Ag, and outside for s -like metals such as Na or Al). The positions of the centroid of the charge density are highlighted by vertical dashed lines in Fig. 5.7a. From the optical point of view, a simple model to obtain the optical response amounts to shifting the position of the metal interface to the position given by the charge centroid. This shift is given by the so-called Feibelman parameters [35, 138, 234–237]. The key point regarding the interaction between tunneling electrons and optical modes is that in case 1 (brown curve), the tunneling electrons (present in the jellium) can interact with an electric field lying outside the centroid of charge and therefore, much larger.

To account for this electron-SPP interaction, we use a very simple approach. We consider that the electronic current is defined in the region delimited by the metallic volume \mathcal{V}_{met} of the ionic background in the jellium model, as shown by the blue curve (current density $j_{z,\text{L}\rightarrow\text{R}}$) and the blue area (ionic background) in Fig. 5.7b. On the other hand, when calculating the electric fields of the SPPs, we assume that the boundary between the metallic permittivity $\varepsilon^{\text{Dr}}(\omega)$ and the vacuum permittivity $\varepsilon = 1$ is given by the centroid of the induced charge density (as shown by brown and green). Importantly, the boundary between permittivities generally does not coincide with the integration boundary of Eq. (5.12) given by \mathcal{V}_{met} (blue area), and the difference z_0 between them lies within few angstroms (in our calculations, \mathcal{V}_{met} extends from the boundary between permittivities).

We show the consequences of considering this simple model of non-local optical response by examining a system composed of two aluminium electrodes of thickness $L_{\text{Al}} = 5$ nm separated by an insulator gap of thickness $L_{\text{gap}} = 2$ nm. These values are taken from Ref. [225], where it was noted that the gap contribution alone does not explain all the light emitted by the fast mode of this system, even at low bias potentials. We show in Fig. 5.7c the spectral radiative power $P^{(\text{f})}$ of the fast SPP of the mentioned junction for $V_{\text{B}} = 0.5$ V. In these circumstances, the calculation of the excitation power with the QDS $P_{\text{QDS}}^{(\text{f})}$ and in the absence of any non-local effect (dashed line), is very similar to the gap contribution $P_{\text{BA}}^{(\text{f})}$ according to Bardeen's approximation (dots), because i) at such low bias potentials, the field penetration is small at all energies $\hbar\omega_{\mathbf{K}_{\parallel}}^{(\text{f})} < eV_{\text{B}}$ due to the large negative permittivities of the metals, so that the fields at the gap are comparatively large; and ii) at so thin metallic layers, the space to excite the fast SPP in the metals

is minimal compared to the gap where the electric fields are confined. However, these two calculations assume that the electron density is nonzero only up to the interfaces between the aluminium and vacuum permittivities, where the limits of the integrals in Eq. (5.12) are set.

We now consider that the electronic current shifts by a maximum distance z_0 with respect to the boundary between permittivities, as shown in the inset of Fig. 5.7c, according to the simple model of non-locality introduced above. This model results in electrons tunneling from the first electrode and reaching positions near the metal-vacuum interface of the other second electrode where the electric field is strong, which efficiently boosts the coupling to electrons. Specifically, we consider that electrons can interact with the electric field outside the electrode in a region of different widths $z_0 = 0.5 \text{ \AA}, 1 \text{ \AA}, 1.5 \text{ \AA}, 2 \text{ \AA}, 2.5 \text{ \AA}$ and 3 \AA (from brown to yellow lines in Fig. 5.7c). The power transferred to the fast SPP becomes considerably larger for increasing z_0 . For example, for $z_0 = 3 \text{ \AA}$, the QDS predicts an excitation power $P_{\text{QDS}}^{(f)}$ four times larger than $P_{\text{BA}}^{(f)}$. We have thus shown that the QDS can account not only for processes in the gap and in the bulk metal, but also for those at the interface. The model is thus able to describe systems where any contribution, and not only from inelastic tunneling processes in the gap, is relevant.

5.4.4 Excitation rate of the medium mode

To complete the results obtained for the slow and fast modes in the previous subsections, we last analyze briefly the excitation of the medium SPP mode. Figure 5.8 shows the emission rate of the medium mode under varying bias potentials ($V_{\text{B}} = 0.6 \text{ V}, 1.2 \text{ V}, 1.8 \text{ V},$ and 2.4 V), for a junction with thicknesses $L_{\text{Al}} = 10 \text{ nm}, L_{\text{Au}} = 20 \text{ nm}$ and $L_{\text{gap}} = 3 \text{ nm}$. The calculation with the QDS ($P_{\text{QDS}}^{(m)}$, results shown by solid lines) in the complete device reveals some oscillations as a function of the SPP energy. These oscillations are due to constructive or destructive interferences between the metal and gap contributions, as we have already discussed for the slow and fast modes. Curiously, the QDS predicts a smaller power transferred to the medium mode than Bardeen's approximation ($P_{\text{BA}}^{(m)}$, results shown by dots). This is the opposite behavior found for the slow and fast modes (Figs. 5.5 and 5.6), where the QDS gives a larger contribution than Bardeen's approximation. Further, the medium mode excitation rate is much smaller than the slow mode excitation rate. In addition, it can only be coupled radiatively by roughness as opposed to the fast mode. Therefore, the medium mode is likely negligible regarding light emission from a planar junction, so that the contribution of the metallic electrodes can be expected to increase the total emission rate once all SPP modes are considered.

5.5 Summary

In this chapter, we have introduced a theoretical approach to describe light emission from planar tunneling junctions. The proposed quantum device solution (QDS) solves the Schrödinger equation in the complete system with the metallic layers and

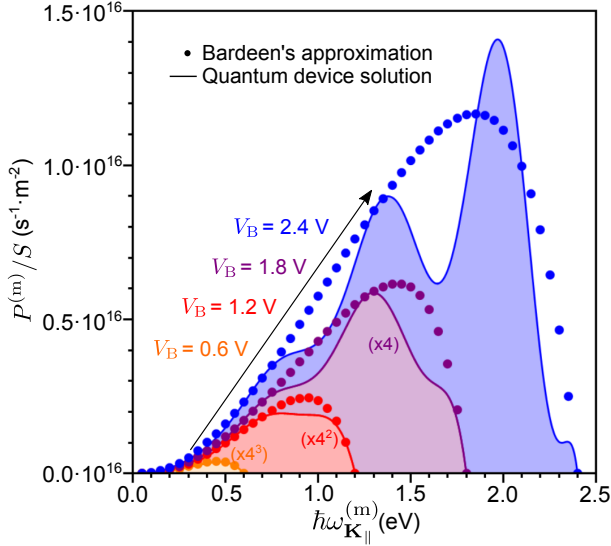


Figure 5.8: Spectral non-radiative power $P^{(m)}$ per surface area S of the junction caused by the excitation of the medium SPP mode, with thicknesses $L_{\text{Al}} = 10$ nm, $L_{\text{Au}} = 20$ nm and $L_{\text{gap}} = 3$ nm, and bias potentials $V_{\text{B}} = 0.6$ V (orange), 1.2 V (red), 1.8 V (purple) and 2.4 V (blue). Dots indicate the calculation using Bardeen's approximation, and the solid lines refer to the full calculation by the QDS.

the insulator gap, unlike Bardeen's approximation that considers electronic states in each electrode separately. While Bardeen's approximation accurately describes elastic tunneling, we show that it can only model accurately the excitation of the slow SPP mode for small energies. For the other cases, and particularly when the fast mode plays a significant role, a more general approach is needed in order to account for the excitation of SPPs by the electrons in the metallic electrodes.

To describe inelastic tunneling accurately, we revisit two approaches that model this mechanism: a Hamiltonian description of light-matter interaction based on Fermi's golden rule, and the calculation of the power radiated by fluctuating currents. These models were used independently in the past. Here, we have established explicitly their equivalence so that they lead to the same theoretical predictions under appropriate circumstances. We have stressed that these descriptions are mostly used under Bardeen's approximation and a current density correlation model that neglects non-local correlations of the current density. We have extended their domain of applicability by abandoning Bardeen's approximation using the exact wavefunctions of the QDS. Interestingly, with this model, we have shown that the electronic current density is strongly correlated in the opposite metals. These strong correlations can be interpreted as an electron-hole pair that recombines in the gap and include a contribution to light emission from metallic electrodes.

Last, we evaluate the difference between the QDS and Bardeen's approximation

to calculate the excitation rate of SPPs in planar junctions and the corresponding light emission. We find that these differences are negligible for the slow mode at small energies. In contrast, we have found that the processes in the metallic electrodes contribute mostly to the excitation of the fast mode, which is known to dominate in the case of periodically corrugated planar junctions. Further, under a non-local description of optical response in the metallic electrodes, processes close to the metal-vacuum interfaces can also contribute to light emission significantly. Since the QDS accounts for these processes in the electrodes and close to the interfaces, and improves the results of Bardeen's approximation considerably, it does no longer appear necessary to invoke a different hot electron mechanism to account for additional light emission.

In summary, the approach presented here generalizes the current theoretical framework of light emission by inelastic tunneling, and could be extended to many other systems with different geometries.

COMPARISON OF CLASSICAL AND CAVITY-QED MODELS IN THE ULTRA-STRONG COUPLING REGIME

6.1 Introduction

The results presented in Chapters 3, 4 and 5 have been devoted to the properties and excitation of plasmons, without considering their interaction with any external optical resonance. However, a rich variety of phenomena can be observed when matter excitations (in molecules, quantum dots, two-dimensional materials...) interact with the electromagnetic modes of an optical cavity or resonator. As discussed in Sec. 1.3, an important interaction regime occurs when the coupling strength g between the cavity modes and the matter excitations exceeds the losses. In this strong coupling regime [41, 238], hybrid modes appear that are known as polaritons and have a different frequency and properties compared to those of the uncoupled resonances.

In order to characterize the properties of the hybrid modes, we need to use appropriate descriptions of light-matter interaction. These descriptions can be based on classical or quantum models, which have been discussed in Secs. 1.3.1 and 1.3.2, respectively. Models based on cavity quantum electrodynamics (QED) have been successfully used to evaluate the frequencies of the hybrid modes and also to explain phenomena related to strong coupling beyond the classical realm, such as nonlinearities due to the Jaynes-Cummings ladder [239], emission of strongly correlated light [240], and changes on the chemical reactivity [62] or on the conductivity [241] of molecules situated in optical resonators.

Further, cavity-QED models can be particularly interesting in the ultrastrong

coupling regime, where the coupling strength of the system overcomes the 10% of the frequencies of the uncoupled excitations, because additional quantum phenomena emerge in this situation. For instance, a shift of the energy of the ground state is predicted, together with the appearance of virtual excitations in this state [242]. These effects are attributed to the breakdown of the rotating-wave approximation (RWA), which makes necessary to include the counter-rotating terms [i.e. the combined operators $\hat{a}\hat{b}$ and $\hat{a}^\dagger\hat{b}^\dagger$ from Eq. (1.48)] in the Hamiltonian. However, two different Hamiltonians have been considered when studying the ultrastrong coupling regime, where the difference stems from the presence or absence of a contribution to the energy called diamagnetic term, corresponding to the term $\hat{\mathcal{H}}_{\text{Hop}}^{\text{dia}}$ in Eq. (1.48). This diamagnetic term is also known as the A^2 term, where A refers to the transverse vector potential of the electromagnetic mode. Introducing this term avoids a superradiant phase transition [102], for example. However, the inclusion of the diamagnetic contribution is still under discussion [95, 103, 243–245] and it depends on the system [246, 247].

We focus on three situations of interest. First, we consider conventional dielectric cavities. In this case, the electromagnetic fields of the cavity modes are transverse and expressed with the vector potential. As a consequence, the diamagnetic term is necessary to model the interaction of these modes with excitations of molecules introduced in the cavity (see schematics for a dielectric Fabry-Pérot cavity in Fig. 6.1a). On the other hand, if molecules interact with a cavity via Coulomb coupling, the interaction is mediated by longitudinal fields. This type of interaction occurs, for instance, in systems with plasmonic cavities of nanometric dimensions (such as metallic nanospheres, as shown in Fig. 6.1b). In this case, we can use the quasistatic approximation that neglects the effect of all transverse modes, leading to the disappearance of the diamagnetic term. In a general system, both transverse and longitudinal fields may appear. By decomposing the total electric field into these components, the incorporation of the diamagnetic term for each component depends on whether it exhibits transverse or longitudinal characteristics. We illustrate in Fig. 6.1c the case of an ensemble of molecules inside a Fabry-Pérot cavity. In this system, each molecule couples with the transverse electromagnetic modes of the cavity and with other molecules via longitudinal Coulomb interactions (we discuss in Sec. 6.5.3 how this system can be treated in a simplified case).

On the other hand, light-matter interaction can also be modelled with fully classical models based on coupled harmonic oscillators [60, 248, 249]. These systems are appropriate when linear phenomena dominate, e.g. when many molecules are introduced in a cavity to obtain large coupling strengths. These classical coupled harmonic oscillator models have successfully described the avoided crossing of the hybrid modes [250], Fano resonances [251], stimulated Raman [252] and electromagnetic induced transparency [253–255]. Further, they are used to fit experimental data and to extract the coupling strength g , the frequencies of the hybrid modes and the fraction of light and matter corresponding to each mode [256, 257]. However, it is often not clear the exact physical magnitude that each oscillator represents, which can make it difficult to determine the value of a given observable in an experiment. Further, in a similar way as we have described

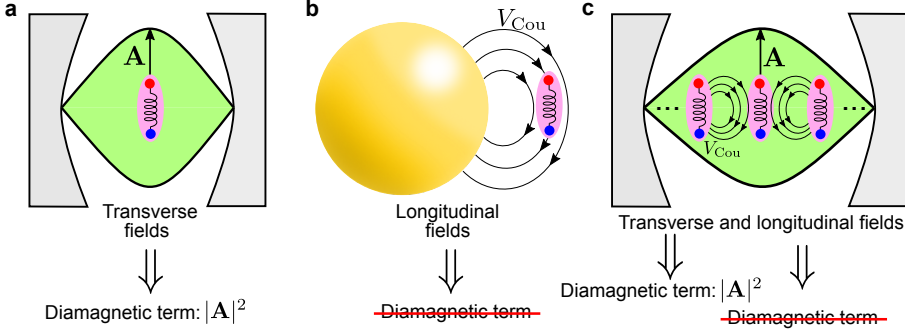


Figure 6.1: Schematics of the interaction between molecular excitations and cavity modes in the three systems considered in this chapter. a) A molecule placed inside a dielectric (Fabry-Pérot) cavity. The transverse field of the single cavity mode considered is described with the vector potential \mathbf{A} , which leads to the presence of the diamagnetic term $\propto |\mathbf{A}|^2$ in the cavity-QED Hamiltonian that describes this system. b) A molecule close to a metallic nanosphere and coupled to a single plasmonic mode. Within the quasistatic approximation, the molecule only interacts with the longitudinal fields of the nanosphere, via the Coulomb potential V_{Cou} . Since the vector potential \mathbf{A} is not considered, the diamagnetic term is absent in the corresponding cavity-QED description. c) An ensemble of molecules placed inside a Fabry-Pérot cavity. In this system, each molecule interacts with the transverse cavity modes indicated by the vector potential \mathbf{A} and with the longitudinal fields associated with the Coulomb potential V_{Cou} induced by the other molecules. Whereas the interaction with cavity modes requires a diamagnetic term in the cavity-QED description, the coupling with other molecules is described without this term.

the possibility to use two cavity-QED Hamiltonians to model light-matter coupling with or without diamagnetic term, different classical models have been used to analyze the strong and ultrastrong coupling regimes. These classical models are almost equivalent in the strong coupling but not in the ultrastrong coupling regime, leading e.g. to different frequencies of the hybrid modes and of the corresponding mode splitting. However, the choice of the model is often not clearly justified [258]. Therefore, it can be useful to analyze in detail the relation between these classical models with the cavity-QED formalism, in order to understand better how to use and interpret the classical harmonic oscillator models and how each classical oscillator is related with physical magnitudes of the system. In this analysis, it is again critical to consider if the matter excitations couple with either the transverse electromagnetic fields (e.g. in conventional dielectric cavities) or the longitudinal fields characteristic of Coulomb coupling with plasmonic cavities.

In this chapter, we present a pedagogical overview of the different classical models of coupled harmonic oscillators that can be used to describe ultrastrong coupling in nanophotonics, and their connection with cavity-QED descriptions. We establish that the main light-matter coupling mechanism, i.e. either the coupling occurs via transverse electromagnetic fields or via Coulomb interactions, is the key to determine the right model of the system. In Sec. 6.2, we present in detail the two main classical coupled harmonic oscillator models under consideration and

show that they lead to different dispersions of the hybrid modes as a function of the frequency of the cavity mode. We then show in Sec. 6.3 how these classical equations can be derived from a Lagrangian description of electrodynamics. In Sec. 6.4, we use the classical Lagrangian to derive the corresponding quantum Hamiltonian, and in this way we establish the connection of each classical coupled harmonic oscillator model with the cavity-QED descriptions. In Sec. 6.5, we determine how to calculate physical observables of the system, such as the electric field of the cavity mode or the induced dipole moment of the matter excitation, using the amplitudes of the classical oscillators. With this aim, we consider in this section the three specific examples shown in Fig. 6.1. Specifically, we first discuss the application of coupled harmonic oscillator models in systems with transverse (molecule in a dielectric cavity, Sec. 6.5.1) and longitudinal (molecule coupled to a metallic nanoparticle via Coulomb interactions, Sec. 6.5.2) fields. We then consider a system of large relevance in studies of strong and ultrastrong coupling, which consists in an ensemble of molecules inside a Fabry-Pérot cavity [259–261] and where both components of the electromagnetic fields (transverse and longitudinal) need to be considered (Sec. 6.5.3). Last, although in this chapter we mainly focus on two different models of classical coupled harmonic oscillators, we show in Sec. 6.6 how to use alternative classical models that lead to equivalent results.

6.2 Classical models of coupled harmonic oscillators in nanophotonics

We have discussed in Sec. 1.3.1 that light-matter interaction can be modelled classically using two coupled harmonic oscillators. While the previous discussion has been focused on the strong coupling regime, we now turn our attention to the ultrastrong coupling regime, and in this section we compare two different harmonic oscillator models that are mainly used in this context.

According to one of the main classical models, the interchange of energy between the matter and light degrees of freedom can be described by making an analogy with the widely-used spring mass model, as it is schematically shown in Fig. 6.2a. This model is able to capture the dynamics of strongly-coupled light-matter systems, such as Rabi oscillations [60]. In this approach, the cavity mode is replaced by a mass m_{cav} attached to a spring with spring constant k_{cav} , while the matter excitation is modelled in the same way with a mass m_{mat} and spring constant k_{mat} . These two masses are coupled with each other by a spring of spring constant k_{SPC} . The equations of motion for the displacements X_{cav} and X_{mat} of the oscillators from the equilibrium positions are

$$m_{\text{cav}}\ddot{X}_{\text{cav}} + k_{\text{cav}}X_{\text{cav}} + k_{\text{SPC}}(X_{\text{cav}} - X_{\text{mat}}) = 0, \quad (6.1a)$$

$$m_{\text{mat}}\ddot{X}_{\text{mat}} + k_{\text{mat}}X_{\text{mat}} - k_{\text{SPC}}(X_{\text{cav}} - X_{\text{mat}}) = 0. \quad (6.1b)$$

As will be analyzed in detail below, the displacements of the oscillators can in

principle refer to different magnitudes of the nanophotonic system that oscillate during the Rabi oscillations. For instance, X_{mat} can be related to the charges inside the matter structure, and X_{cav} to the transverse electromagnetic fields of a dielectric cavity mode or to moving electrons inside a plasmonic nanocavity. Similarly, m_{cav} and m_{mat} can be seen as effective parameters whose meaning depends on the system and, at this stage, are not well defined. By defining the frequency of the cavity $\omega_{\text{cav}} = \sqrt{\frac{k_{\text{cav}} + k_{\text{SpC}}}{m_{\text{cav}}}}$, the frequency of the matter excitation $\omega_{\text{mat}} = \sqrt{\frac{k_{\text{mat}} + k_{\text{SpC}}}{m_{\text{mat}}}}$ and the coupling strength $g_{\text{SpC}} = \frac{k_{\text{SpC}}}{2\sqrt{m_{\text{cav}}m_{\text{mat}}}\sqrt{\omega_{\text{cav}}\omega_{\text{mat}}}}$, Eq. (6.1) can be rewritten as

$$\ddot{x}_{\text{cav}} + \omega_{\text{cav}}^2 x_{\text{cav}} + 2g_{\text{SpC}}\sqrt{\omega_{\text{cav}}\omega_{\text{mat}}}x_{\text{mat}} = 0, \quad (6.2a)$$

$$\ddot{x}_{\text{mat}} + \omega_{\text{mat}}^2 x_{\text{mat}} + 2g_{\text{SpC}}\sqrt{\omega_{\text{cav}}\omega_{\text{mat}}}x_{\text{cav}} = 0, \quad (6.2b)$$

where we have used the renormalized displacements $x_{\text{cav}} = \sqrt{m_{\text{cav}}}X_{\text{cav}}$ and $x_{\text{mat}} = \sqrt{m_{\text{mat}}}X_{\text{mat}}$. This transformation allows us to write the equations in a simpler way without indicating the masses of the oscillators m_{cav} and m_{mat} explicitly, and leaves the eigenfrequencies of the system invariant. We discuss in Secs. 6.3 and 6.5 how to connect x_{cav} and x_{mat} with the parameters governing specific systems. Further, we have not included losses (friction terms proportional to the time derivatives \dot{x}_{cav} and \dot{x}_{mat}) in these equations in order to facilitate the comparison with Hermitian Hamiltonians of cavity-QED modelsⁱ. Neglecting losses is usually an excellent approximation for the calculation of the eigenfrequencies and eigenvectors of the system in the ultrastrong coupling regime, where the coupling strength can be much larger than the losses of the system. The eigenmodes of this model are obtained by writing Eq. (6.2) in the frequency domain and diagonalizing the matrix associated with the resulting equations, which leads to the eigenfrequencies

$$\omega_{\pm, \text{SpC}} = \frac{1}{\sqrt{2}} \sqrt{\omega_{\text{cav}}^2 + \omega_{\text{mat}}^2 \pm \sqrt{(\omega_{\text{cav}}^2 - \omega_{\text{mat}}^2)^2 + 16g_{\text{SpC}}^2 \omega_{\text{cav}}\omega_{\text{mat}}}}. \quad (6.3)$$

This simple coupled harmonic oscillator model has been used to extract the coupling strength g_{SpC} by fitting the spectra of the hybrid modes obtained from experimental data or from simulations [91, 262–267]. We refer to this model as the Spring Coupling (SpC) model, as it assumes that the coupling is mathematically equivalent to a spring attached to two masses. We emphasize that the SpC model is defined as the coupled harmonic oscillator model that satisfies two important properties as indicated in Eq. (6.2): i) the coupling terms (third term in the left handside) are proportional to the amplitudes x_{cav} and x_{mat} ; and ii) the frequencies that appear in the second term in the left handside are the bare frequencies ω_{cav} and ω_{mat} corresponding to the uncoupled oscillators (without any renormalization of these frequencies, which is discussed in Sec. 6.6).

ⁱ An accurate approach to include losses in a system under ultrastrong coupling consists in generalized master equations [98, 99].

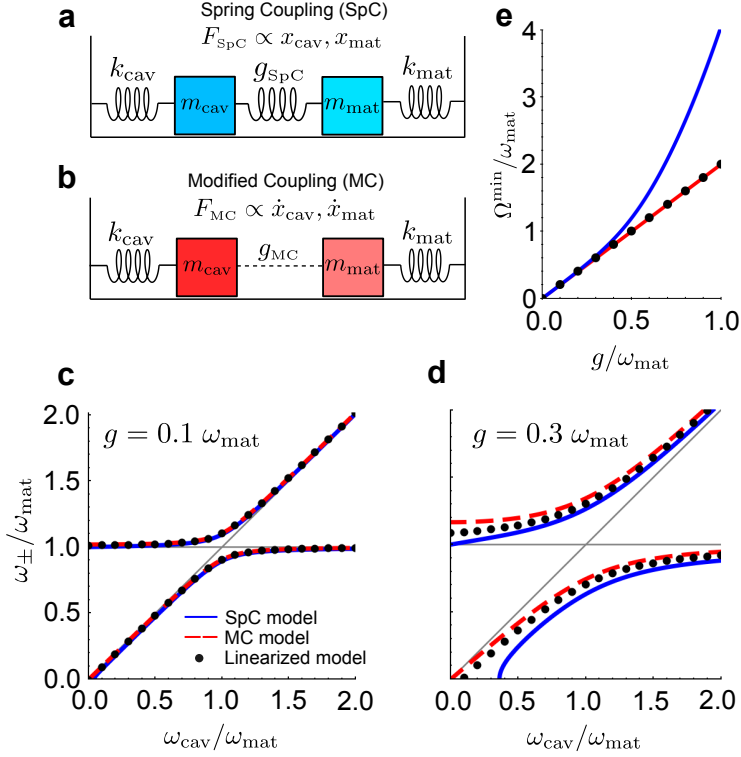


Figure 6.2: Comparison of the Spring Coupling (SpC), Modified Coupling (MC) and linearized models. a) Schematics of the SpC model in analogy to an oscillator model in classical mechanics. The coupling mechanism of strength g_{SpC} is analogous to a force $F_{\text{SpC}} \propto x_{\text{cav}}, x_{\text{mat}}$. b) Schematics of the MC model. The coupling mechanism of strength g_{MC} is analogous to a force $F_{\text{MC}} \propto \dot{x}_{\text{cav}}, \dot{x}_{\text{mat}}$. c) Eigenfrequencies ω_{\pm} as a function of the cavity frequency ω_{cav} , obtained from the SpC model [blue solid line, corresponding to Eq. (6.3)], MC model [red dashed line, Eq. (6.6)] and the approximate linearized model [black dots, Eq. (6.8)], for coupling strength $g = 0.1 \omega_{\text{mat}}$. The thin gray lines correspond to the bare cavity frequency ω_{cav} and the bare frequency of the matter excitation, ω_{mat} . d) Same as panel (c), for coupling strength $g = 0.3 \omega_{\text{mat}}$. e) Minimum splitting between the hybrid modes $\Omega^{\text{min}} = \omega_{+} - \omega_{-}$, as a function of the coupling strength g for the SpC model (blue solid line), the MC model (red solid line) and the linearized model (black dots). All frequencies in panels (c-e) are normalized with respect to the fixed frequency of the matter excitation ω_{mat} .

On the other hand, a different classical coupled harmonic oscillator model is also used [268–270]:

$$\ddot{x}_{\text{cav}} + \omega_{\text{cav}}^2 x_{\text{cav}} - 2g_{\text{MC}} \dot{x}_{\text{mat}} = 0, \quad (6.4a)$$

$$\ddot{x}_{\text{mat}} + \omega_{\text{mat}}^2 x_{\text{mat}} + 2g_{\text{MC}} \dot{x}_{\text{cav}} = 0. \quad (6.4b)$$

These equations are very similar to Eq. (6.2), but in this case the coupling terms are proportional to the time derivatives of the displacements \dot{x}_{cav} and \dot{x}_{mat} (i.e. to the velocities of the oscillators, in the analogy with the coupled masses). Equivalently, the coupling terms are proportional to the frequency ω in the frequency domain [258]:

$$(\omega_{\text{cav}}^2 - \omega^2)x_{\text{cav}} + 2i\omega g_{\text{MC}}x_{\text{mat}} = 0, \quad (6.5a)$$

$$(\omega_{\text{mat}}^2 - \omega^2)x_{\text{mat}} - 2i\omega g_{\text{MC}}x_{\text{cav}} = 0. \quad (6.5b)$$

Due to the modification of the coupling term with respect to the simple picture of coupled mechanical oscillators, we call this model the Modified Coupling (MC) model (Fig. 6.2b). Similarly to the case of the SpC model, we emphasize that the frequencies in the MC model [appearing in the second term in the left handside in Eq. (6.4)] are the bare frequencies ω_{cav} and ω_{mat} , as renormalizing these frequencies is equivalent to a change in the coupling term (see Sec. 6.6) and thus it would correspond to a different type of model. The frequencies of the hybrid modes according to the MC model are

$$\omega_{\pm, \text{MC}} = \frac{1}{\sqrt{2}} \sqrt{\omega_{\text{cav}}^2 + \omega_{\text{mat}}^2 + 4g_{\text{MC}}^2 \pm \sqrt{(\omega_{\text{cav}}^2 + \omega_{\text{mat}}^2 + 4g_{\text{MC}}^2)^2 - 4\omega_{\text{cav}}^2\omega_{\text{mat}}^2}}. \quad (6.6)$$

At moderate coupling strengths g , corresponding to a system in the strong but not in the ultrastrong coupling regime, the frequencies of the hybrid modes are very similar for the two models. In this regime, by considering that the eigenfrequencies ω_{\pm} do not differ too strongly from the bare frequencies ω_{α} ($\alpha = \text{'cav'}$ or $\alpha = \text{'mat'}$), we can make the approximation $\omega_{\alpha} + \omega \approx 2\omega$ to solve the equations for ω_{\pm} . The frequency-domain equations of both the SpC and MC models become linear in ω :

$$(\omega_{\text{cav}} - \omega)x_{\text{cav}} + g_{\text{in}}x_{\text{mat}} = 0 \quad (6.7a)$$

$$(\omega_{\text{mat}} - \omega)x_{\text{mat}} + g_{\text{in}}^*x_{\text{cav}} = 0, \quad (6.7b)$$

with $g_{\text{in}} = g_{\text{SpC}}$ (SpC model) or $g_{\text{in}} = ig_{\text{MC}}$ (MC model). The resulting eigenfrequencies are in both cases

$$\omega_{\pm, \text{lin}} = \frac{\omega_{\text{cav}} + \omega_{\text{mat}} \pm \sqrt{(\omega_{\text{cav}} - \omega_{\text{mat}})^2 + 4|g_{\text{in}}|^2}}{2}. \quad (6.8)$$

The validity of these linearized equations for $g = 0.1\omega_{\text{mat}}$ (conventionally defined as the onset of the ultrastrong coupling regime) is analyzed in Fig. 6.2c, where we

compare the eigenfrequencies of the SpC model (blue solid line), the MC model (red dashed line) and the linearized model (black dots). These eigenfrequencies are given by Eqs. (6.3), (6.6) and (6.8), respectively, and plotted as a function of the cavity frequency ω_{cav} (all values in Fig. 6.2 are given as the ratio with the frequency ω_{mat} , which remains fixed in all the panels of this figure). We find that the three curves follow a nearly identical dependence on the cavity frequency ω_{cav} , and the agreement is even better for $g < 0.1 \omega_{\text{mat}}$. Thus, for systems not in the ultrastrong coupling regime, the three models can often be used equally with very small implications to the results.

In contrast, for even larger coupling strengths, corresponding to a system well into the ultrastrong coupling regime, the choice of the model is crucial. The differences between the three models are illustrated in Fig. 6.2d for coupling strength $g = 0.3 \omega_{\text{mat}}$. In this case, the three models predict significantly different eigenfrequencies of the coupled system. The difference is smaller for large cavity frequencies, $\omega_{\text{cav}} \gg \omega_{\text{mat}}$, because the oscillators become uncoupled and the eigenfrequencies approach the bare frequencies ω_{cav} and ω_{mat} in all models. However, even for a relatively large $\omega_{\text{cav}}/\omega_{\text{mat}} = 1.5$, the difference between the values of ω_{\pm} according to the different models is around 10%.

Further, comparing the three models in resonant conditions at zero detuning, $\omega_{\text{cav}} = \omega_{\text{mat}}$, the splitting $\Omega = \omega_{+} - \omega_{-}$ between the two eigenmodes is equal to twice the coupling strength in the linearized and in the MC model, i.e. $\Omega = 2g$. This is the minimum splitting in these two models [271, 272]. On the other hand, in the SpC model the relation between Ω and the coupling strength for zero detuning is different:

$$\Omega_{\text{SpC}} = \omega_{+, \text{SpC}} - \omega_{-, \text{SpC}} = \omega_{\text{mat}} \left(\sqrt{1 + \frac{2g_{\text{SpC}}}{\omega_{\text{mat}}}} - \sqrt{1 - \frac{2g_{\text{SpC}}}{\omega_{\text{mat}}}} \right). \quad (6.9)$$

We find $\Omega_{\text{SpC}} = 2.11 g_{\text{SpC}}$ for the values used in Fig. 6.2d. Further, according to this model the minimum splitting between the branches does not happen at zero detuning, but at cavity frequencies larger than the matter excitation frequencies. To further emphasize the difference in the splitting between the models, we plot in Fig. 6.2e the minimum splitting Ω^{min} for the SpC model (blue solid line) as a function of the coupling strength, as compared to the $\Omega^{\text{min}} = 2g$ linear relationship of the MC (red solid line) and the linearized model (black dots). For couplings too small to reach the ultrastrong coupling regime ($g/\omega_{\text{mat}} \lesssim 0.1$), the splitting of the three models follows the same linear tendency. However, for larger values of g , within the ultrastrong coupling regime, the minimum splitting according to the SpC model deviates strongly from linearity, and close to the so-called deep strong coupling regime ($g/\omega_{\text{mat}} \approx 1$), $\Omega_{\text{SpC}}^{\text{min}}$ is approximately the double than for the other two models. Last, Fig. 6.2d shows that a striking difference appears for small cavity frequencies, $\omega_{\text{cav}} \ll \omega_{\text{mat}}$. According to the MC model, for decreasing ω_{cav} the lower mode frequency $\omega_{-, \text{MC}}$ tends towards ω_{cav} , but the upper branch approaches the limit $\omega_{+, \text{MC}} = \sqrt{\omega_{\text{mat}}^2 + 4g_{\text{MC}}^2}$ instead of the bare matter frequency, and thus this hybrid mode is affected by the coupling even in this highly detuned

situation.

The behavior of ω_- and ω_+ in the asymptotic limits of ω_{cav} has an interesting consequence on the range of energies where hybrid modes can exist according to each model. The dispersion of the MC model shows two hybrid modes for all values of the detuning and indicates that there is a band between ω_{mat} and $\sqrt{\omega_{\text{mat}}^2 + 4g_{\text{MC}}^2}$ with no modes available (as can be appreciated from the limits of the eigenfrequencies for $\omega_{\text{cav}} \rightarrow 0$ and $\omega_{\text{cav}} \rightarrow \infty$). For the SpC model, the upper mode approaches the bare frequency ω_{mat} for vanishing ω_{cav} , but the lower mode ceases to exist ($\omega_{-, \text{SpC}}$ becomes imaginary) under the condition $\frac{\omega_{\text{cav}}}{\omega_{\text{mat}}} < \left(\frac{2g_{\text{SpC}}}{\omega_{\text{mat}}}\right)^2$. Further, by considering the total dispersion of the SpC model, we emphasize that we obtain hybrid modes at any frequency $\omega_{\pm, \text{SpC}}$ by tuning the bare frequencies ω_{cav} and ω_{mat} , and thus there is no forbidden band as opposed to the MC model. Last, the dispersion of the linearized model lies between the dispersions of the other two models. In this case, there is a band of forbidden modes of spectral width half the value given by the MC model, and the lower mode disappears as in the SpC model but under a different inequality, because $\omega_{-, \text{lin}}$ becomes negative for frequencies $\frac{\omega_{\text{cav}}}{\omega_{\text{mat}}} < \left(\frac{g_{\text{lin}}}{\omega_{\text{mat}}}\right)^2$. The finding of these bands has important consequences on describing the optical response of materials supporting vibrational excitations, as done in Chapter 7. Specifically, in Sec. 7.5 we connect the bands observed in Fig. 6.2d with the Reststrahlen band of polar materials (Sec. 1.2.2), and show that we can only reproduce the experimental dispersion with the correct width of the Reststrahlen band by using the MC model.

The analysis of Fig. 6.2d thus emphasizes that the three classical models considered can lead to distinctly different predictions of the eigenfrequencies of light-matter coupled systems in the ultrastrong coupling regime. These differences imply that the coupling terms of the SpC and MC models are related to different types of interactions between light and matter, and that not all electromagnetic interactions are mathematically equivalent to two coupled mechanical springs (i.e. to the SpC model). In order to better understand the origins of the SpC and MC models and their relation with Coulomb interactions and with interactions based on transverse electromagnetic modes, we derive in the next section the corresponding classical equations from a general Lagrangian description of electrodynamics. Further, this section has focused on the eigenfrequencies, which can be extracted directly from the equations of coupled harmonic oscillators without an exact knowledge of what the displacements x_{cav} and x_{mat} represent. However, a clear physical interpretation of these parameters often becomes necessary to evaluate magnitudes of interest such as the electric field at a given position. We discuss in Sec. 6.5 how x_{cav} and x_{mat} relate to relevant physical quantities for representative systems.

6.3 Derivation of the equations of motion in the classical coupled harmonic oscillator models

We have presented the classical SpC and MC harmonic oscillator models based on an intuitive perspective of classical mechanics. We show in this section that these models can be obtained in a more rigorous way from the Euler-Lagrange equations of motion associated to the Lagrangian of electrodynamics. To particularize this discussion, we focus on the specific systems shown in Figs. 6.1a and b, which consist in a molecular excitation interacting with a transverse electromagnetic mode or with the near field of a plasmonic nanoparticle.

We start considering the general Lagrangian description of electrodynamics. The form of this Lagrangian depends on the gauge. We first choose the Coulomb gauge, which leads to the expression given by Eq. (1.18):

$$\mathcal{L}_{\text{Cou}} = \sum_i \frac{1}{2} m_i \dot{\mathbf{r}}_i^2 - \sum_{i,j>i} \frac{Q_i Q_j}{4\pi\epsilon_0 |\mathbf{r}_i - \mathbf{r}_j|} + \int \left[\frac{\epsilon_0}{2} (|\dot{\mathbf{A}}|^2 - c^2 |\nabla \times \mathbf{A}|^2) + \mathbf{j}_f \cdot \mathbf{A} \right] d\mathbf{r}.$$

In this Lagrangian, the electromagnetic degrees of freedom are encapsulated in the dynamical field variable $\mathbf{A}(\mathbf{r})$, which represents the vector potential of the fields, with the condition $\nabla \cdot \mathbf{A} = 0$ due to the choice of gauge. On the other hand, all the dynamics related to the matter structure are expressed by the spatial positions \mathbf{r}_i of each point-like charge indexed by i . Each point charge, of mass m_i and charge Q_i , interacts with all the others according to the Coulomb potential energy (second term in the right handside) and with the transverse electromagnetic fields as indicated in the last term of the Lagrangian (of the form $\mathbf{j}_f \cdot \mathbf{A}$), where $\mathbf{j}_f(\mathbf{r}) = \sum_i Q_i \dot{\mathbf{r}}_i \delta(\mathbf{r} - \mathbf{r}_i)$ is the current density at any position \mathbf{r} [Eq. (1.13)].

We have proven in Sec. 1.1.2 that the equations of motion for the variables $\mathbf{A}(\mathbf{r})$ and \mathbf{r}_i obtained from the Lagrangian in Eq. (1.18) are completely equivalent to Maxwell's equation for a general system. We are interested in obtaining the equations of motion that describe the dynamics of systems formed by molecules interacting with cavity modes in the strong and the ultrastrong coupling regimes. First, we focus on the terms of the Lagrangian related to the transverse electromagnetic field (which in the Coulomb gauge is entirely described with the vector potential \mathbf{A}), in order to separate them into the contribution of different cavity modes. The vector potential is separated into the components $\mathbf{A}_\alpha(\mathbf{r})$ of all transverse modes α of the cavity as $\mathbf{A}(\mathbf{r}) = \sum_\alpha \mathbf{A}_\alpha(\mathbf{r}) = \sum_\alpha \mathcal{A}_\alpha \Xi_\alpha(\mathbf{r}) \mathbf{n}_\alpha$. For each α index, the field is polarized in the direction determined by the unit vector \mathbf{n}_α , the amplitude is given by \mathcal{A}_α and the fields have spatial distribution $\Xi_\alpha(\mathbf{r})$, normalized so that $\Xi_\alpha(\mathbf{r}) = 1$ in the position where the field is maximum. Further, we consider that the α modes form an orthogonal basis and the integral of the field distribution over space gives the effective volume $\mathcal{V}_{\text{eff},\alpha}$ of the mode, i.e.

$$\int \Xi_\alpha(\mathbf{r}) \Xi_{\alpha'}^*(\mathbf{r}) d\mathbf{r} = \mathcal{V}_{\text{eff},\alpha} \delta_{\alpha,\alpha'}. \quad (6.10)$$

By taking into account the decomposition of the modes and their orthogonality, the terms of the Lagrangian of Eq. (1.18) only related to the electromagnetic fields are written as

$$\begin{aligned} & \int \frac{\varepsilon_0}{2} \left(\left| \sum_{\alpha} \dot{\mathcal{A}}_{\alpha} \Xi_{\alpha}(\mathbf{r}) \mathbf{n}_{\alpha} \right|^2 - c^2 \left| \nabla \times \sum_{\alpha} \mathcal{A}_{\alpha} \Xi_{\alpha}(\mathbf{r}) \mathbf{n}_{\alpha} \right|^2 \right) d\mathbf{r} \\ &= \sum_{\alpha} \frac{\varepsilon_0 \mathcal{V}_{\text{eff},\alpha}}{2} (\dot{\mathcal{A}}_{\alpha} \dot{\mathcal{A}}_{\alpha}^* - \omega_{\text{cav},\alpha}^2 \mathcal{A}_{\alpha} \mathcal{A}_{\alpha}^*). \end{aligned} \quad (6.11)$$

We now focus on the terms of the Lagrangian associated to the matter degrees of freedom, so that we can describe the matter excitations. We model the material as an ensemble of dipoles indexed by j , each formed by two point charges that have the same mass m_j and opposite charges, and are placed in positions \mathbf{r}_{j+} and \mathbf{r}_{j-} . The two point charges are at equilibrium if they are placed at a distance $|\mathbf{r}_{j+} - \mathbf{r}_{j-}| = |\mathbf{r}_{\text{eq}}|$. We make the harmonic approximation to the Coulomb potential of each dipole with respect to the equilibrium position: $\frac{Q_j^2}{4\pi\varepsilon_0|\mathbf{r}_{j+} - \mathbf{r}_{j-}|} = \frac{1}{2} m_{\text{red}} \omega_{\text{mat}}^2 |\mathbf{r}_{j+} - \mathbf{r}_{j-} - \mathbf{r}_{\text{eq}}|^2 + \mathcal{O}(|\mathbf{r}_{j+} - \mathbf{r}_{j-} - \mathbf{r}_{\text{eq}}|^3) \approx \frac{1}{2} m_{\text{red}} \omega_{\text{mat}}^2 |\mathbf{r}_{j+} - \mathbf{r}_{j-} - \mathbf{r}_{\text{eq}}|^2$, where $m_{\text{red}} = \frac{m_j}{2}$ is the reduced mass of the dipole. We also assume that the mass center of the dipole is static at position $\mathbf{r}_j = \frac{\mathbf{r}_{j+} + \mathbf{r}_{j-}}{2}$. Therefore, the only variable that evolves in time for each dipole is the distance between point charges from the equilibrium position, i.e., $\mathbf{l}_j = \mathbf{r}_{j+} - \mathbf{r}_{j-} - \mathbf{r}_{\text{eq}}$ or, equivalently, the induced dipole moment $\mathbf{d}_j = Q_j \mathbf{l}_j$. From these assumptions, the Coulomb potential energy in Eq. (1.18) includes the harmonic potential corresponding to the charges in each dipole, and also the potential energy due to the interaction between different dipoles. Accordingly, the terms related to the matter degrees of freedom in the Lagrangian transform as

$$\begin{aligned} \sum_j \frac{1}{2} m_j \dot{\mathbf{r}}_j^2 - \sum_{i,j>i} \frac{Q_i Q_j}{4\pi\varepsilon_0 |\mathbf{r}_i - \mathbf{r}_j|} &= \sum_i \left(\frac{1}{2} \frac{m_{\text{red},i}}{Q_i^2} \dot{d}_i^2 - \frac{1}{2} \frac{m_{\text{red},i}}{Q_i^2} \omega_{\text{mat},i}^2 d_i^2 \right) \\ &\quad - \sum_{i,j>i} \frac{1}{4\pi\varepsilon_0 |\mathbf{r}_j - \mathbf{r}_i|^3} [\mathbf{d}_i \cdot \mathbf{d}_j - 3(\mathbf{d}_i \cdot \mathbf{n}_{rij})(\mathbf{d}_j \cdot \mathbf{n}_{rij})], \end{aligned} \quad (6.12)$$

with $d_j = |\mathbf{d}_j|$ and the unit vector $\mathbf{n}_{rij} = \frac{\mathbf{r}_j - \mathbf{r}_i}{|\mathbf{r}_j - \mathbf{r}_i|}$.

Equation (6.12) has been derived using the harmonic approximation of the dipolar potential, and as a consequence all terms of the Lagrangian that do not account for light-matter interaction are quadratic with respect to the amplitudes of the vector potential and their time derivatives [Eq. (6.11)], or with respect to the dipole moments and their time derivatives [Eq. (6.12)]. Therefore, if light and matter were uncoupled, the dynamical evolution of these variables would be the same as that of free harmonic oscillators. We now discuss how the interaction between the cavity modes and the dipoles affects the equations of motion. The

coupling of each dipole with the transverse fields of the cavity appears in the Lagrangian as

$$\begin{aligned} \int \mathbf{j}_f \cdot \mathbf{A} \, d\mathbf{r} &= \int \left(\sum_j Q_j \dot{\mathbf{r}}_{j+} \delta(\mathbf{r} - \mathbf{r}_{j+}) - Q_j \dot{\mathbf{r}}_{j-} \delta(\mathbf{r} - \mathbf{r}_{j-}) \right) \left(\sum_\alpha \mathcal{A}_\alpha \Xi_\alpha(\mathbf{r}) \mathbf{n}_\alpha \right) d\mathbf{r} \\ &= \sum_{j,\alpha} Q_j [\mathbf{r}_{j+} \Xi_\alpha(\dot{\mathbf{r}}_{j+}) - \dot{\mathbf{r}}_{j-} \Xi_\alpha(\mathbf{r}_{j-})] \mathcal{A}_\alpha \mathbf{n}_\alpha \approx \sum_{j,\alpha} \mathcal{A}_\alpha \Xi_\alpha(\mathbf{r}_j) \dot{\mathbf{d}}_j \cdot \mathbf{n}_\alpha \end{aligned} \quad (6.13)$$

In the last step, we have performed the long-wavelength approximation, so that in the length scale of each dipole the fields do not vary, i.e. $\Xi(\mathbf{r}_{j+}) \approx \Xi(\mathbf{r}_{j-})$ for all j . The total Lagrangian of the system in the Coulomb gauge reads

$$\begin{aligned} \mathcal{L}_{\text{Cou}}(d_j, \dot{d}_j, \mathcal{A}_\alpha, \dot{\mathcal{A}}_\alpha, \mathcal{A}_\alpha^*, \dot{\mathcal{A}}_\alpha^*) &= \sum_\alpha \frac{\varepsilon_0 \mathcal{V}_{\text{eff},\alpha}}{2} (\dot{\mathcal{A}}_\alpha \dot{\mathcal{A}}_\alpha^* - \omega_{\text{cav},\alpha}^2 \mathcal{A}_\alpha \mathcal{A}_\alpha^*) \\ &+ \sum_j \frac{1}{2} \frac{1}{f_{\text{mat},j}} (\dot{d}_j^2 - \omega_{\text{mat},j}^2 d_j^2) + \sum_{j,\alpha} \mathcal{A}_\alpha \dot{d}_j \Xi_\alpha(\mathbf{r}_j) \cos \theta_{\alpha,j} \\ &- \sum_{i,j} d_i d_j \frac{\mathbf{n}_{\mathbf{d}i} \cdot \mathbf{n}_{\mathbf{d}j} - 3(\mathbf{n}_{\mathbf{d}i} \cdot \mathbf{n}_{\mathbf{r}ij})(\mathbf{n}_{\mathbf{d}j} \cdot \mathbf{n}_{\mathbf{r}ij})}{4\pi\varepsilon_0 |\mathbf{r}_i - \mathbf{r}_j|^3}, \end{aligned} \quad (6.14)$$

where $\mathbf{n}_{\mathbf{d}j} = \frac{\mathbf{d}_j}{|\mathbf{d}_j|}$, $\theta_{\alpha,j}$ is the angle between the dipole moment \mathbf{d}_j and the direction \mathbf{n}_α of the electric field in the mode α , and $f_{\text{mat}} = \frac{Q_j^2}{m_{\text{red}}}$ is the oscillator strength of the j^{th} dipole.

From the Lagrangian \mathcal{L}_{Cou} of Eq. (6.14), we can easily derive the equations of motion of the classical coupled harmonic oscillators by calculating the Euler-Lagrange equations, $\frac{d}{dt} \frac{\partial \mathcal{L}_{\text{Cou}}}{\partial \dot{x}} - \frac{\partial \mathcal{L}_{\text{Cou}}}{\partial x} = 0$, for $x \in \{d_j, \mathcal{A}_\alpha^*\}$. The resulting equations of motion are

$$\ddot{\mathcal{A}}_\alpha + \omega_{\text{cav},\alpha}^2 \mathcal{A}_\alpha - \sum_j \dot{d}_j \frac{\Xi_\alpha(\mathbf{r}_j) \cos \theta_{\alpha,j}}{\varepsilon_0 \mathcal{V}_{\text{eff},\alpha}} = 0, \quad (6.15a)$$

$$\begin{aligned} \ddot{d}_j + \omega_{\text{mat},j}^2 d_j + f_{\text{mat},j} \sum_{i \neq j} \frac{\mathbf{n}_{\mathbf{d}i} \cdot \mathbf{n}_{\mathbf{d}j} - 3(\mathbf{n}_{\mathbf{d}i} \cdot \mathbf{n}_{\mathbf{r}ij})(\mathbf{n}_{\mathbf{d}j} \cdot \mathbf{n}_{\mathbf{r}ij})}{4\pi\varepsilon_0 |\mathbf{r}_i - \mathbf{r}_j|^3} d_i \\ + \sum_\alpha \dot{\mathcal{A}}_\alpha f_{\text{mat},j} \Xi_\alpha^*(\mathbf{r}_j) \cos \theta_{\alpha,j} = 0. \end{aligned} \quad (6.15b)$$

These equations account for all interactions of the system, which consist in dipole-dipole interactions and the interaction of dipoles with cavity modes. To show how each of these two types of interaction is connected with the MC and SpC models, we focus on two canonical scenarios, which are sketched in Figs. 6.1a and b:

- Coupling between a molecular excitation and a transverse mode of a

dielectric cavity: By considering a single transverse mode α of the cavity interacting with one molecular excitation represented by the induced dipole moment d , all Coulomb interactions in Eq. (6.15) are eliminated. The equations of motion become

$$\ddot{\mathcal{A}} + \omega_{\text{cav}}^2 \mathcal{A} - d \frac{\dot{\Xi}(\mathbf{r}_{\text{mat}}) \cos \theta}{\varepsilon_0 \mathcal{V}_{\text{eff}}} = 0, \quad (6.16a)$$

$$\ddot{d} + \omega_{\text{mat}}^2 d + \dot{\mathcal{A}} f_{\text{mat}} \Xi^*(\mathbf{r}_{\text{mat}}) \cos \theta = 0. \quad (6.16b)$$

By replacing here the oscillator amplitudes $x_{\text{cav}} = \mathcal{A} \sqrt{\varepsilon_0 \mathcal{V}_{\text{eff}}}$ and $x_{\text{mat}} = \frac{d}{\sqrt{f_{\text{mat}}}}$, together with the coupling strength

$$g_{\text{MC}} = \frac{1}{2} \sqrt{\frac{f_{\text{mat}}}{\varepsilon_0 \mathcal{V}_{\text{eff}}}} \Xi(\mathbf{r}_{\text{mat}}) \cos \theta, \quad (6.17)$$

we recover the equations of motion of the MC model [Eq. (6.4)].

- Coupling between a molecule and a plasmonic nanoparticle via Coulomb interactions: We consider a molecule close to a metallic nanoparticle that supports a plasmonic mode. Under the quasistatic approximation of the plasmonic response, the vector potential components of all transverse modes are neglected, and the nanoparticle can be described as a polarizable dipole of induced dipole moment d_{cav} (Sec. 1.2.1). Equation (6.15) is then written as

$$\ddot{d}_{\text{cav}} + \omega_{\text{cav}}^2 d_{\text{cav}} + f_{\text{cav}} \frac{\mathbf{n}_{\text{dcav}} \cdot \mathbf{n}_{\text{dmat}} - 3(\mathbf{n}_{\text{dcav}} \cdot \mathbf{n}_{\text{rrel}})(\mathbf{n}_{\text{dmat}} \cdot \mathbf{n}_{\text{rrel}})}{4\pi\varepsilon_0 |\mathbf{r}_{\text{cav}} - \mathbf{r}_{\text{mat}}|^3} d_{\text{mat}} = 0, \quad (6.18a)$$

$$\ddot{d}_{\text{mat}} + \omega_{\text{mat}}^2 d_{\text{mat}} + f_{\text{mat}} \frac{\mathbf{n}_{\text{dcav}} \cdot \mathbf{n}_{\text{dmat}} - 3(\mathbf{n}_{\text{dcav}} \cdot \mathbf{n}_{\text{rrel}})(\mathbf{n}_{\text{dmat}} \cdot \mathbf{n}_{\text{rrel}})}{4\pi\varepsilon_0 |\mathbf{r}_{\text{cav}} - \mathbf{r}_{\text{mat}}|^3} d_{\text{cav}} = 0, \quad (6.18b)$$

where d_{mat} is the induced dipole moment of the molecule and $\mathbf{n}_{\text{rrel}} = \frac{\mathbf{r}_{\text{cav}} - \mathbf{r}_{\text{mat}}}{|\mathbf{r}_{\text{cav}} - \mathbf{r}_{\text{mat}}|}$ is the unitary vector of the relative direction between the nanocavity and the molecule. By replacing $x_{\text{cav}} = \frac{d_{\text{cav}}}{\sqrt{f_{\text{cav}}}}$ and $x_{\text{mat}} = \frac{d_{\text{mat}}}{\sqrt{f_{\text{mat}}}}$, together with the coupling strength g_{SpC} defined as

$$g_{\text{SpC}} = \frac{1}{2} \frac{\sqrt{f_{\text{cav}}} \sqrt{f_{\text{mat}}}}{4\pi\varepsilon_0 |\mathbf{r}_{\text{cav}} - \mathbf{r}_{\text{mat}}|^3 \sqrt{\omega_{\text{cav}} \omega_{\text{mat}}}} \times [\mathbf{n}_{\text{dcav}} \cdot \mathbf{n}_{\text{dmat}} - 3(\mathbf{n}_{\text{dcav}} \cdot \mathbf{n}_{\text{rrel}})(\mathbf{n}_{\text{dmat}} \cdot \mathbf{n}_{\text{rrel}})], \quad (6.19)$$

we recover the equations of the SpC model [Eq. (6.2)].

Hence, this derivation confirms that the SpC model is well suited to describe the interaction of matter excitations with longitudinal Coulomb fields, whereas the

MC model is appropriate when transverse cavity modes dominate the interaction, as in the case of conventional dielectric cavities. This derivation also shows that the oscillator displacements x_{cav} and x_{mat} defined in Sec. 6.2 are related to physical magnitudes of the system such as the dipole moment or the vector potential. In Sec. 6.5, we analyze in more detail how these relations can be used to calculate physical observables in different systems under ultrastrong coupling. Additionally, we have focused until here on the two classical models that are most used in the literature, but we discuss other alternatives in Sec. 6.6. Specifically, we show that renormalizing the cavity frequency by the right amount in the model with coupling terms proportional to the time derivatives \dot{x}_{cav} and \dot{x}_{mat} leads to the same frequencies as for the SpC model without renormalization, or vice versa.

6.3.1 Spring coupling model with external laser illumination

Up to now, we have not considered in this chapter any external illumination. We now discuss briefly how to introduce an incident laser field in the model of nanocavity-molecule interaction. We focus on the case of a single metallic nanoparticle that supports one plasmonic mode and interacts with only one nearby molecule, but this derivation can be generalized to systems with more molecules and with metallic nanoparticles supporting more plasmonic modes, and also to a dielectric cavity supporting transverse cavity modes.

The incident field has associated a vector potential of the form $\mathbf{A}_{\text{inc}}(\mathbf{r}, t) = \mathcal{A}_{\text{inc}} e^{i\mathbf{k}_{\text{inc}} \cdot \mathbf{r}} e^{-i\omega t}$, which is a planewave of wavevector \mathbf{k}_{inc} , amplitude \mathcal{A}_{inc} and frequency ω . Under the quasistatic approximation, all transverse modes α of the system are neglected, and thus the only component of the vector potential considered in the Lagrangian of Eq. (6.14) corresponds to the external laser $\mathbf{A}_{\text{inc}}(\mathbf{r}, t)$. With these considerations, the Lagrangian of Eq. (6.14) becomes

$$\begin{aligned} \mathcal{L}_{\text{Cou}}^{\text{dip-dip}}(d_{\text{cav}}, \dot{d}_{\text{cav}}, d_{\text{mat}}, \dot{d}_{\text{mat}}) &= \frac{1}{2} \frac{1}{f_{\text{cav}}} (\dot{d}_{\text{cav}}^2 - \omega_{\text{cav}}^2 d_{\text{cav}}^2) + \frac{1}{2} \frac{1}{f_{\text{mat}}} (\dot{d}_{\text{mat}}^2 - \omega_{\text{mat}}^2 d_{\text{mat}}^2) \\ &\quad - d_{\text{cav}} d_{\text{mat}} \frac{\mathbf{n}_{\text{dcav}} \cdot \mathbf{n}_{\text{dmat}} - 3(\mathbf{n}_{\text{dcav}} \cdot \mathbf{n}_{\text{rrel}})(\mathbf{n}_{\text{dmat}} \cdot \mathbf{n}_{\text{rrel}})}{4\pi\epsilon_0 |\mathbf{r}_{\text{cav}} - \mathbf{r}_{\text{mat}}|^3} \\ &\quad + \mathcal{A}_{\text{inc}} e^{-i\omega t} (\dot{d}_{\text{cav}} \cos \theta_{\text{inc,cav}} + \dot{d}_{\text{mat}} \cos \theta_{\text{inc,mat}}), \end{aligned} \quad (6.20)$$

where $\theta_{\text{inc,cav}}$ and $\theta_{\text{inc,mat}}$ are the angles between the incident field and the dipole moments of the cavity and molecule, respectively. The superscript "dip-dip" emphasizes that we only consider dipole-dipole interactions for this system (under the quasistatic approximation). The dynamics of the variables d_{cav} and d_{mat} are obtained within the Euler-Lagrange equations from Eq. (6.20). By calculating these equations of motion and transforming the variables into the oscillator amplitudes $x_{\text{cav}} = \frac{d_{\text{cav}}}{\sqrt{f_{\text{cav}}}}$ and $x_{\text{mat}} = \frac{d_{\text{mat}}}{\sqrt{f_{\text{mat}}}}$, the resulting equations are

$$\ddot{x}_{\text{cav}} + \omega_{\text{cav}}^2 x_{\text{cav}} + \frac{\mathbf{n}_{\text{dcav}} \cdot \mathbf{n}_{\text{dmat}} - 3(\mathbf{n}_{\text{dcav}} \cdot \mathbf{n}_{\text{rrel}})(\mathbf{n}_{\text{dmat}} \cdot \mathbf{n}_{\text{rrel}})}{4\pi\epsilon_0 |\mathbf{r}_{\text{cav}} - \mathbf{r}_{\text{mat}}|^3} x_{\text{mat}}$$

$$= i\omega\mathcal{A}_{\text{inc}}\sqrt{f_{\text{cav}}}\cos\theta_{\text{inc,cav}}e^{-i\omega t}, \quad (6.21a)$$

$$\begin{aligned} \ddot{x}_{\text{mat}} + \omega_{\text{mat}}^2 x_{\text{mat}} + \frac{\mathbf{n}_{\text{dcav}} \cdot \mathbf{n}_{\text{dmat}} - 3(\mathbf{n}_{\text{dcav}} \cdot \mathbf{n}_{\text{rrel}})(\mathbf{n}_{\text{dmat}} \cdot \mathbf{n}_{\text{rrel}})}{4\pi\epsilon_0|\mathbf{r}_{\text{cav}} - \mathbf{r}_{\text{mat}}|^3} x_{\text{cav}} \\ = i\omega\mathcal{A}_{\text{inc}}\sqrt{f_{\text{mat}}}\cos\theta_{\text{inc,mat}}e^{-i\omega t}. \end{aligned} \quad (6.21b)$$

Therefore, the incident field is incorporated into the SpC equations of motion [Eq. (6.2)] by adding time-dependent forces of amplitude $F_{\text{cav}} = i\omega\mathcal{A}_{\text{inc}}\sqrt{f_{\text{cav}}}\cos\theta_{\text{inc,cav}}$ and $F_{\text{mat}} = i\omega\mathcal{A}_{\text{inc}}\sqrt{f_{\text{mat}}}\cos\theta_{\text{inc,mat}}$ to the nanocavity and the molecule, respectively.

6.4 Comparison between cavity-QED Hamiltonians and classical models

We have derived in Sec. 6.3 the SpC and MC harmonic oscillator models from a fully classical Lagrangian description. We show next how the classical Lagrangian is related first to the classical and then to the different cavity-QED Hamiltonians with or without the diamagnetic term [i.e. with or without the term $\hat{\mathcal{H}}_{\text{Hop}}^{\text{dia}}$ in Eq. (1.48)]. In this way, we establish a key result of this chapter, which is the connection of the SpC and MC models with the cavity-QED Hamiltonians. We further note that all the connections established in this section are summarized in Table 6.1 at the end of the chapter.

6.4.1 Modified coupling model

We have shown in Sec. 6.3 that the MC model corresponds to the coupling between a dipole (which can be associated to a molecular excitation, for example) and a transverse electromagnetic mode of a cavity, as depicted schematically in Fig. 6.1a. We now focus in this particular system to derive its corresponding cavity-QED Hamiltonian. In this derivation, we start with the Lagrangian of Coulomb gauge given by Eq. (6.14), which for a single dipole interacting with only one transverse mode becomes

$$\mathcal{L}_{\text{Cou}}^{\text{min-c}}(d, \dot{d}, \mathcal{A}, \dot{\mathcal{A}}) = \frac{\epsilon_0\mathcal{V}_{\text{eff}}}{2}(\dot{\mathcal{A}}^2 - \omega_{\text{cav}}^2\mathcal{A}^2) + \frac{1}{2f_{\text{mat}}}(\dot{d}^2 - \omega_{\text{mat}}^2d^2) + \mathcal{A}\dot{d}. \quad (6.22)$$

To simplify the analytical expressions in the following discussion, Eq. (6.22) considers a specific case where the molecule is placed in the position of maximum field of the mode and oriented in the same direction as the field polarization, so that $\Xi(\mathbf{r}_{\text{mat}})\cos\theta = 1$ in Eq. (6.14). However, the discussion of this section remains valid for other values of $\Xi(\mathbf{r}_{\text{mat}})\cos\theta$.

The next step is to derive the classical Hamiltonian of the system. With this aim, we obtain the canonical momenta related to the vector potential (of amplitude \mathcal{A})

of the transverse electromagnetic mode and to the dipole moment in the Coulomb gauge as

$$\Pi_{\text{Cou}} = \frac{\partial \mathcal{L}_{\text{Cou}}}{\partial \dot{\mathcal{A}}} = \varepsilon_0 \mathcal{V}_{\text{eff}} \dot{\mathcal{A}}, \quad (6.23a)$$

$$p_{\text{Cou}} = \frac{\partial \mathcal{L}_{\text{Cou}}}{\partial \dot{d}} = \frac{\dot{d}}{f_{\text{mat}}} + \mathcal{A}. \quad (6.23b)$$

According to these expressions, the dynamical variable Π_{Cou} expresses the transverse electric field of the cavity mode from the relation $\mathbf{E} = -\frac{\partial \mathbf{A}}{\partial t}$. On the other hand, the relation between the dipole moment d and its canonical momentum p_{Cou} is more complicated because p_{Cou} depends not only on d but also on the vector potential. Using Eq. (6.23), the calculation of the Hamiltonian $\mathcal{H}_{\text{Cou}}^{\text{min-c}} = \dot{\mathcal{A}} \Pi_{\text{Cou}} + \dot{d} p_{\text{Cou}} - \mathcal{L}_{\text{Cou}}^{\text{min-c}}$ is straightforward:

$$\mathcal{H}_{\text{Cou}}^{\text{min-c}} = \frac{\Pi_{\text{Cou}}^2}{2\varepsilon_0 \mathcal{V}_{\text{eff}}} + \frac{1}{2} \varepsilon_0 \mathcal{V}_{\text{eff}} \omega_{\text{cav}}^2 \mathcal{A}^2 + \frac{f_{\text{mat}}}{2} p_{\text{Cou}}^2 + \frac{1}{2} \frac{\omega_{\text{mat}}^2}{f_{\text{mat}}} d^2 - f_{\text{mat}} p_{\text{Cou}} \mathcal{A} + \frac{1}{2} f_{\text{mat}} \mathcal{A}^2. \quad (6.24)$$

This expression has the well-known form of the minimal-coupling Hamiltonian [Eq. (1.22)], and thus we refer to this form of the coupling with the superindex "min-c" in the Lagrangian of Eq. (6.22) and in the Hamiltonian of Eq. (6.24).

On the other hand, the Hamiltonian of Eq. (6.24) is not the only one that can be used to describe the interaction of a molecular excitation with a transverse electromagnetic mode, because the form of the Hamiltonian depends on the gauge. In particular, besides the Coulomb gauge used up to this point, the dipole gauge [273] is also widely used in cavity QED. We now derive the classical Hamiltonian in this new gauge, so that we can then apply the canonical quantization procedure in both gauges and establish a complete connection between the classical coupled harmonic oscillator models and commonly used Hamiltonians.

To obtain the new Hamiltonian, we first note that the Lagrangian in the Coulomb gauge \mathcal{L}_{Cou} of Eq. (6.22) can be transformed to any other Lagrangian \mathcal{L}' with the operation $\mathcal{L}' = \mathcal{L}_{\text{Cou}} + \frac{d\mathcal{G}(\mathcal{A}, d, t)}{dt}$, by using a general function $\mathcal{G}(\mathcal{A}, d, t)$. The particular choice that leads to the dipole gauge is $\mathcal{G} = -d\mathcal{A}$, which is equivalent to the Power-Zienau-Woolley transformation [274] in cavity QED, with the unitary operator

$$\hat{U} = \exp \left\{ \frac{i}{\hbar} \int \mathbf{P} \cdot \mathbf{A} \, d\mathbf{r} \right\}, \quad (6.25)$$

where \mathbf{P} is the polarization density. After applying the gauge transformation to Eq. (6.22), the Lagrangian of the system in the dipole gauge is

$$\mathcal{L}_{\text{Dip}}^{\text{min-c}}(d, \dot{d}, \mathcal{A}, \dot{\mathcal{A}}) = \frac{\varepsilon_0 \mathcal{V}_{\text{eff}}}{2} (\dot{\mathcal{A}}^2 - \omega_{\text{cav}}^2 \mathcal{A}^2) + \frac{1}{2f_{\text{mat}}} (\dot{d}^2 - \omega_{\text{mat}}^2 d^2) - \dot{\mathcal{A}} d. \quad (6.26)$$

We repeat the procedure implemented in the Coulomb gauge to obtain the

classical Hamiltonian in the dipole gauge, so that the canonical momenta are calculated as

$$\Pi_{\text{Dip}} = \frac{\partial \mathcal{L}_{\text{Dip}}}{\partial \dot{\mathbf{A}}} = \varepsilon_0 \mathcal{V}_{\text{eff}} \dot{\mathbf{A}} - d, \quad (6.27a)$$

$$p_{\text{Dip}} = \frac{\partial \mathcal{L}_{\text{Dip}}}{\partial \dot{d}} = \frac{d}{f_{\text{mat}}}. \quad (6.27b)$$

In the dipole gauge, p_{Dip} is only related to the time derivative of the dipole moment. However, the canonical momentum associated with the cavity mode, Π_{Dip} , depends on both d and the vector potential, in contrast to the result of the Coulomb gauge. Thus, in the dipole gauge this variable represents the displacement vector $\Pi_{\text{Dip}} \propto |\mathbf{D}| = |\varepsilon_0 \mathbf{E} + \mathbf{P}|$ instead of the transverse electric field of the cavity mode as happens in the Coulomb gauge, i.e. $\Pi_{\text{Cou}} \propto |\mathbf{E}|$. The resulting Hamiltonian in the dipole gauge is

$$\mathcal{H}_{\text{Dip}}^{\text{min-c}} = \frac{\Pi_{\text{Dip}}^2}{2\varepsilon_0 \mathcal{V}_{\text{eff}}} + \frac{1}{2} \varepsilon_0 \mathcal{V}_{\text{eff}} \omega_{\text{cav}}^2 \mathcal{A}^2 + \frac{f_{\text{mat}}}{2} p_{\text{Dip}}^2 + \frac{1}{2} \frac{\omega_{\text{mat}}^2}{f_{\text{mat}}} d^2 + \frac{\Pi_{\text{Dip}} d}{\varepsilon_0 \mathcal{V}_{\text{eff}}} + \frac{d^2}{2\varepsilon_0 \mathcal{V}_{\text{eff}}}. \quad (6.28)$$

We have thus shown that the coupling between a molecule and a transverse electromagnetic mode of a cavity is described by the minimal-coupling Hamiltonian, which for the Coulomb gauge has the classical form of Eq. (6.24) and for the dipole gauge it is given by Eq. (6.28). To obtain the quantum Hopfield Hamiltonian of the form of Eq. (1.48), we use the following quantization relations that are used in cavity QED [72, 94, 275]:

$$\hat{\mathbf{A}}(\mathbf{r}) = \sqrt{\frac{\hbar}{2\omega_{\text{cav}}\varepsilon_0\mathcal{V}_{\text{eff}}}} \Xi(\mathbf{r})(\hat{a} + \hat{a}^\dagger), \quad (6.29a)$$

$$\hat{\Pi}(\mathbf{r}) = -i\sqrt{\frac{\hbar\omega_{\text{cav}}\varepsilon_0\mathcal{V}_{\text{eff}}}{2}} \Xi(\mathbf{r})(\hat{a} - \hat{a}^\dagger), \quad (6.29b)$$

$$\hat{d} = \sqrt{\frac{\hbar f_{\text{mat}}}{2\omega_{\text{mat}}}} (\hat{b} + \hat{b}^\dagger), \quad (6.29c)$$

$$\hat{p} = -i\sqrt{\frac{\hbar\omega_{\text{mat}}}{2f_{\text{mat}}}} (\hat{b} - \hat{b}^\dagger). \quad (6.29d)$$

Following the quantization procedure in Eqs. (6.24) and (6.28), we obtain

$$\begin{aligned} \hat{\mathcal{H}}_{\text{Cou}}^{\text{min-c}} = & \hbar\omega_{\text{cav}} \left(\hat{a}^\dagger \hat{a} + \frac{1}{2} \right) + \hbar\omega_{\text{mat}} \left(\hat{b}^\dagger \hat{b} + \frac{1}{2} \right) + i\hbar g_{\text{MC}} \sqrt{\frac{\omega_{\text{mat}}}{\omega_{\text{cav}}}} (\hat{a} + \hat{a}^\dagger)(\hat{b} - \hat{b}^\dagger) \\ & + \hbar \frac{g_{\text{MC}}^2}{\omega_{\text{cav}}} (\hat{a} + \hat{a}^\dagger)^2, \end{aligned} \quad (6.30a)$$

$$\begin{aligned} \hat{\mathcal{H}}_{\text{Dip}}^{\text{min-c}} = & \hbar\omega_{\text{cav}} \left(\hat{a}^\dagger \hat{a} + \frac{1}{2} \right) + \hbar\omega_{\text{mat}} \left(\hat{b}^\dagger \hat{b} + \frac{1}{2} \right) - i\hbar g_{\text{MC}} \sqrt{\frac{\omega_{\text{cav}}}{\omega_{\text{mat}}}} (\hat{a} - \hat{a}^\dagger)(\hat{b} + \hat{b}^\dagger) \\ & + \hbar \frac{g_{\text{MC}}^2}{\omega_{\text{mat}}} (\hat{b} + \hat{b}^\dagger)^2, \end{aligned} \quad (6.30b)$$

for the Coulomb and dipole gauges, respectively. In these Hamiltonians, \hat{a} and \hat{a}^\dagger are the annihilation and creation operators of the cavity mode, while \hat{b} and \hat{b}^\dagger are the corresponding operators of the molecular excitation. The coupling strength g_{MC} is given by Eq. (6.17). The main difference between Eqs. (6.30a) and (6.30b) is the last quadratic term, which is originated from the vector potential of the electromagnetic mode in the Coulomb gauge, while it comes from the dipole moment of the molecule in the dipole gauge. However, in both cases, we obtain a Hopfield Hamiltonian with the diamagnetic term that is proportional to g_{MC}^2 (i.e. Eq. (1.48) with $D \propto g_{\text{MC}}^2$).

Despite the different forms of Eqs. (6.30a) and (6.30b), we emphasize that they are equivalent. On the one hand, by solving the Schrödinger equation with both Hamiltonians, the same eigenvalues are obtained. Further, although the expectation values of the operators \hat{a} , \hat{a}^\dagger , \hat{b} and \hat{b}^\dagger are not the same for each Hamiltonian, this occurs because they are defined differently in each gauge due to their relation with a different set of canonical momenta: Π_{Cou} and p_{Cou} given by Eq. (6.23) for the Hamiltonian of Eq. (6.30a), or Π_{Dip} and p_{Dip} given by Eq. (6.27) for the Hamiltonian of Eq. (6.30b). Thus, the relation between the operators and the physical magnitudes of the system are different. Once these differences are considered, the same values for all physical observables (such as the amplitude of the vector potential, \mathcal{A} , or the dipole moment d) can be obtained with both Hamiltonians because they have been derived from the same starting point.

Importantly, the classical MC model has been obtained from the same Lagrangian [Eq. (6.22)] as the Hamiltonians of Eq. (6.30), which demonstrates that the MC model leads to the same description as the cavity-QED Hamiltonians with the diamagnetic term. This equivalence implies that the same values of the hybrid mode frequencies [given by Eq. (6.6)] and of other physical observables are obtained with either a classical or a quantum description. However, we note that there is a slight difference between the meaning of the eigenfrequencies of Eq. (6.6) in the classical and quantum models. By solving the Schrödinger equation, we observe that cavity QED predicts a g_{MC} -dependent shift of the ground-state energy from zero, which is a fully quantum phenomenon and is not captured by the classical MC model: the eigenvalues of the classical MC model are equivalent to the transition energies between the ground and excited states in the cavity-QED descriptions, and not to the absolute values of the excited state energies. The transitions between energetic levels (and not the absolute energies) govern most current optical experiments in nanophotonics, so that the classical models are equivalent to the quantum approach except in very specific circumstances where the results are affected by the ground-state energy.

6.4.2 Spring coupling model

We now focus on studying the cavity-QED Hamiltonian that is equivalent to the classical SpC model. As shown in Sec. 6.3, this classical model represents dipole-dipole interactions, and the example that we consider through this section is a molecule placed close to a metallic nanoparticle and coupled with each other via Coulomb interactions (sketch in Fig. 6.1b). This system is described in the quasistatic approximation by the Lagrangian of Eq. (6.20) (here we do not include laser excitation, i.e. $\mathcal{A}_{\text{inc}} = 0$). From this Lagrangian, and proceeding like in the previous section, we obtain the classical Hamiltonian of the system $\mathcal{H}^{\text{dip-dip}} = \dot{d}_{\text{cav}} p_{\text{cav}} + \dot{d}_{\text{mat}} p_{\text{mat}} - \mathcal{L}_{\text{Cou}}^{\text{dip-dip}}$, which is

$$\begin{aligned} \mathcal{H}^{\text{dip-dip}} = & \frac{1}{2} f_{\text{cav}} p_{\text{cav}}^2 + \frac{1}{2} \frac{\omega_{\text{cav}}^2}{f_{\text{cav}}} d_{\text{cav}}^2 + \frac{1}{2} f_{\text{mat}} p_{\text{mat}}^2 + \frac{1}{2} \frac{\omega_{\text{mat}}^2}{f_{\text{mat}}} d_{\text{mat}}^2 \\ & + d_{\text{cav}} d_{\text{mat}} \frac{\mathbf{n}_{\text{dcav}} \cdot \mathbf{n}_{\text{dmat}} - 3(\mathbf{n}_{\text{dcav}} \cdot \mathbf{n}_{\text{rrel}})(\mathbf{n}_{\text{dmat}} \cdot \mathbf{n}_{\text{rrel}})}{4\pi\epsilon_0 |\mathbf{r}_{\text{cav}} - \mathbf{r}_{\text{mat}}|^3}, \end{aligned} \quad (6.31)$$

with the canonical momenta $p_{\text{cav}} = \frac{\dot{d}_{\text{cav}}}{f_{\text{cav}}}$ and $p_{\text{mat}} = \frac{\dot{d}_{\text{mat}}}{f_{\text{mat}}}$. The Hamiltonian of Eq. (6.31) has been obtained using the Coulomb gauge, but the dipole gauge leads to the same Hamiltonian for this specific system.

We apply next the quantization rules given by Eq. (6.29). Since both the cavity and the molecule are described with the induced dipole moments d_{cav} and d_{mat} , all the operators (\hat{a} and \hat{a}^\dagger of the cavity mode, and \hat{b} and \hat{b}^\dagger of the molecular excitation) are related to the corresponding dipole moment following Eq. (6.29c) and the canonical momentum as given by Eq. (6.29d). The quantization of the Hamiltonian in Eq. (6.31) leads to the expression

$$\hat{\mathcal{H}}^{\text{dip-dip}} = \hbar\omega_{\text{cav}} \left(\hat{a}^\dagger \hat{a} + \frac{1}{2} \right) + \hbar\omega_{\text{mat}} \left(\hat{b}^\dagger \hat{b} + \frac{1}{2} \right) + \hbar g_{\text{SpC}} (\hat{a} + \hat{a}^\dagger) (\hat{b} + \hat{b}^\dagger). \quad (6.32)$$

This Hamiltonian does not have any diamagnetic term (i.e. it satisfies the form of Eq. (1.48) with $D = 0$). Thus, we have shown that the classical SpC model and the Hopfield Hamiltonian without diamagnetic term are equivalent. Indeed, solving the Schrödinger equation with Eq. (6.32), we obtain the same eigenvalues as the classical SpC model given by Eq. (6.3) (except for the shift of the ground state energy in the classical model) and also the same values for other physical magnitudes.

6.5 Physical observables obtained from classical models

In Sec. 6.3, we have derived the classical SpC and MC models starting from a general Lagrangian of electrodynamics. This derivation allows us to determine how the oscillator amplitudes x_{cav} and x_{mat} , which in Sec. 6.2 have been defined

arbitrarily, are related to the vector potential and to the dipole moment of the matter excitation. We now exploit this connection to show in detail how several physical observables in systems under ultrastrong coupling (e.g. the spatial distribution of the electric field) can be obtained with classical models (in an equivalent way as with cavity-QED models, due to the equivalence shown in Sec. 6.4). To illustrate the procedure, we analyze the same three canonical examples in nanophotonics that we have already introduced (Fig. 6.1) and for which different classical or quantum (with and without the diamagnetic term) models are appropriate. In Sec. 6.5.1, we focus in the textbook case of a single molecule interacting with transverse electromagnetic modes of a resonant dielectric cavity (Fig. 6.1a). As the next example, we analyze in Sec. 6.5.2 a molecule close to a small metallic nanoparticle, where the coupling is governed by longitudinal Coulomb interactions (Fig. 6.1b). The last example (Sec. 6.5.3) consists in an ensemble of molecules (representing a bulk material) inside a Fabry-Pérot cavity, where the molecules couple with each other as well as with the transverse electromagnetic modes of the cavity (Fig. 6.1c).

6.5.1 A molecular excitation interacting with a transverse mode of a dielectric cavity

We consider first the canonical quantum-optics system consisting in one dipole interacting with a single transverse mode of a resonant dielectric cavity. The dipole is associated to matter excitations, and it can represent an excitonic transition of a molecule or a transition between vibrational states, for example. Cavity-QED models of this system have successfully described phenomena such as the modification of the spontaneous emission rate of a molecule [93,276], of the photon statistics of the emitted light [277,278] or of the coherence time of the quantum states [279].

To analyze how the physical observables associated with this system can be described classically, we first note that it has been demonstrated in Sec. 6.3 that this system is described with the MC model. Further, we have obtained that the cavity oscillator amplitude x_{cav} in the MC model [Eq. (6.4)] is given by $x_{\text{cav}} = \mathcal{A}\sqrt{\varepsilon_0\mathcal{V}_{\text{eff}}}$. Therefore, the oscillator amplitude x_{cav} can be used to calculate the spatial distribution of this potential as $A(\mathbf{r}) = \mathcal{A}\Xi(\mathbf{r}) = \frac{x_{\text{cav}}}{\sqrt{\varepsilon_0\mathcal{V}_{\text{eff}}}}\Xi(\mathbf{r})$. Equivalently, the amplitude of the oscillator corresponding to the matter excitation is directly connected with the induced classical dipole moment d as $x_{\text{mat}} = \frac{d}{\sqrt{f_{\text{mat}}}}$. These relations are schematically shown in Fig. 6.3a and allow us to obtain physical magnitudes in the system from the classical harmonic MC model, such as the electric field at any position inside the cavity.

We first show how to obtain the spatial distribution of the electric fields corresponding to each hybrid mode. The transverse cavity mode field [given by

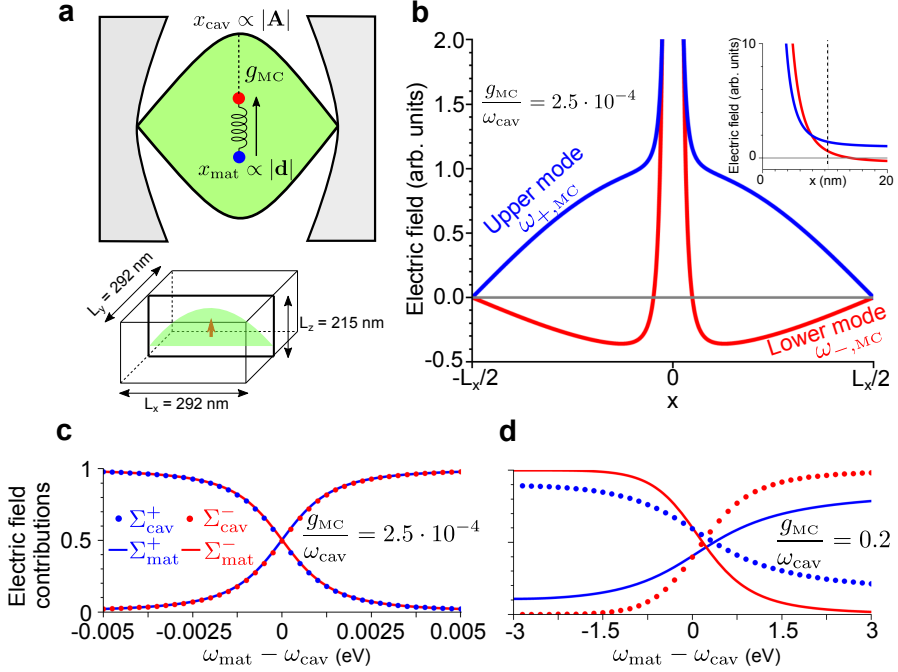


Figure 6.3: Interaction of a molecule with a transverse cavity mode within the classical MC model. a) Schematics of the system. The two oscillators are associated with the vector potential \mathbf{A} of the cavity mode and the induced dipole moment \mathbf{d} of the molecular excitation. The oscillators are coupled with each other with strength g_{MC} . The bottom sketch indicates the dimensions of the cavity that we analyze in the rest of the panels. The dipole is placed at the center of the cavity. The green shaded areas in the sketches represent the field distribution of the cavity mode. b) Spatial distribution of the electric field for the upper (blue) and the lower (red) hybrid modes at frequencies $\omega_{+,MC}$ and $\omega_{-,MC}$, respectively, for coupling strength $g_{MC} = 2.5 \cdot 10^{-4} \omega_{cav}$. The electric field is calculated along the axis of the cavity (along the x direction in panel (a), with $x = y = z = 0$ corresponding to the cavity center). The inset is a zoom of the region near the molecule. c) Contribution to the electric field from the cavity Σ_{cav}^{\pm} (dots) and from the molecule Σ_{mat}^{\pm} (solid lines), for the hybrid mode at frequency $\omega_{+,MC}$ (blue) and the hybrid mode at frequency $\omega_{-,MC}$ (red), as a function of the detuning $\omega_{mat} - \omega_{cav}$. The fields are evaluated at the position $(x, y, z) = (10.5 \text{ nm}, 0, 0)$, i.e. at 10.5 nm distance from the center of the cavity where the molecule is situated (see sketch in (a) for directions), which corresponds to the position indicated by the dashed line in the inset of panel (b). The coupling strength is $g_{MC} = 2.5 \cdot 10^{-4} \omega_{cav}$. d) Same as in (c), for $g_{MC} = 0.2 \omega_{cav}$.

$\mathbf{A}(\mathbf{r}, t)$] must be added to the longitudinal near field induced by the dipoleⁱⁱ, which is obtained from the scalar Coulomb potential

$$V_{\text{Coul}}(\mathbf{r}, t) = \frac{1}{4\pi\epsilon_0} \frac{d(t)\mathbf{n}_d \cdot \mathbf{n}_r}{|\mathbf{r}|^2}, \quad (6.33)$$

with the unit vectors $\mathbf{n}_d = \frac{\mathbf{d}}{|\mathbf{d}|}$ and $\mathbf{n}_r = \frac{\mathbf{r}}{|\mathbf{r}|}$. The total electric field is therefore given as

$$\mathbf{E}(\mathbf{r}, t) = -\nabla V_{\text{Coul}}(\mathbf{r}, t) - \frac{\partial \mathbf{A}(\mathbf{r}, t)}{\partial t},$$

and the electric field at frequencies $\omega_{\pm, \text{MC}}$ of each hybrid mode [given by Eq. (6.6)] corresponds to

$$\begin{aligned} \mathbf{E}(\mathbf{r}, \omega_{\pm, \text{MC}}) &= \frac{3(\mathbf{n}_d \cdot \mathbf{n}_r)\mathbf{n}_r - \mathbf{n}_d}{4\pi\epsilon_0 r^3} d(\omega_{\pm, \text{MC}}) + i\omega_{\pm, \text{MC}} A(\mathbf{r}, \omega_{\pm, \text{MC}}) \mathbf{n}_\alpha \\ &= \underbrace{\frac{3(\mathbf{n}_d \cdot \mathbf{n}_r)\mathbf{n}_r - \mathbf{n}_d}{4\pi\epsilon_0 r^3} \sqrt{f_{\text{mat}}} x_{\text{mat}}(\omega_{\pm, \text{MC}})}_{\mathbf{E}_{\text{mat}}(\mathbf{r}, \omega_{\pm, \text{MC}})} + \underbrace{\frac{i\Xi(\mathbf{r})}{\sqrt{\epsilon_0 \mathcal{V}_{\text{eff}}}} \omega_{\pm, \text{MC}} x_{\text{cav}}(\omega_{\pm, \text{MC}}) \mathbf{n}_\alpha}_{\mathbf{E}_{\text{cav}}(\mathbf{r}, \omega_{\pm, \text{MC}})}. \end{aligned} \quad (6.34)$$

According to this equation, the oscillator amplitude of the cavity mode x_{cav} gives directly the contribution of the cavity to the electric field [$\mathbf{E}_{\text{cav}}(\mathbf{r}, \omega_{\pm, \text{MC}})$], whereas the oscillator amplitude x_{mat} is related to the contribution of the matter excitation [$\mathbf{E}_{\text{mat}}(\mathbf{r}, \omega_{\pm, \text{MC}})$]. Further, we use Eq. (6.5) to obtain the ratio between the amplitudes x_{cav} and x_{mat} of the classical harmonic oscillators:

$$\frac{x_{\text{cav}}(\omega_{\pm, \text{MC}})}{x_{\text{mat}}(\omega_{\pm, \text{MC}})} = \frac{-2i\omega_{\pm, \text{MC}} g_{\text{MC}}}{\omega_{\text{cav}}^2 - \omega_{\pm, \text{MC}}^2}. \quad (6.35)$$

Inserting Eq. (6.35) into Eq. (6.34), we obtain the ratio between the electric field contribution of the cavity and of the matter excitation.

Equations (6.34) and (6.35) are the main result of this subsection and are valid to obtain the electric field at any position and for an arbitrary transverse mode with field distribution given by $\Xi(\mathbf{r})$. We consider for illustration the particular case of a molecule introduced in the center of a rectangular vacuum box enclosed in the three dimensions by perfect mirrors, as sketched in Fig. 6.3a. The cross section of the box is square, with size $L_x = L_y = 292$ nm and its height is $L_z = 215$ nm, which results in a fundamental lowest-order mode at frequency $\omega_{\text{cav}} = 3$ eV and an effective volume $\mathcal{V}_{\text{eff}} = 4.483 \cdot 10^6$ nm³. This value of \mathcal{V}_{eff} is calculated

ⁱⁱ To satisfy the boundary conditions in a closed cavity, additional terms due to image dipoles should be included. However, for simplicity, here we neglect these terms, since their contribution is typically small compared to the near field of the dipole $\propto \frac{1}{r^3}$ and of the field of the cavity mode.

from the general expression of dielectric structures [280]

$$\mathcal{V}_{\text{eff}} = \frac{\int \varepsilon(\mathbf{r}) |\Xi(\mathbf{r})|^2 d\mathbf{r}}{\max[\varepsilon(\mathbf{r}) |\Xi(\mathbf{r})|^2]}, \quad (6.36)$$

and in this particular case we consider $\varepsilon(\mathbf{r}) = 1$ inside the cavity. The molecular excitation is nearly resonant with the cavity, $\omega_{\text{mat}} \approx \omega_{\text{cav}} = 3$ eV, but its exact frequency is changed to study the effects of the detuning. The transition dipole moment $\mu_{\text{mat}} = \sqrt{\frac{\hbar f_{\text{mat}}}{2\omega_{\text{mat}}}}$ [corresponding to the transition from the ground state to the first excited state, as observed in Eq. (6.29c)] is parallel to the z axis and is relatively strong, $\mu_{\text{mat}} = 15$ Debye, achievable with nonacene, for example [281]. This value of the transition dipole moment implies that this molecule has an oscillator strength of $f_{\text{mat}} = \frac{(118.74e)^2}{m_p}$, where e is the electron charge and m_p the mass of the proton. By placing the molecule in the center of the cavity where the electric field of the mode is maximum, this choice of parameters leads to a coupling strength $g_{\text{MC}} \approx 2.5 \cdot 10^{-4} \omega_{\text{cav}}$, far from the ultrastrong coupling regime (a larger value of g_{MC} is considered at the end of this subsection).

We show in Fig. 6.3b the distribution of the z component of the electric field inside this cavity for the upper hybrid mode $E_z(x, \omega_{+, \text{MC}})$ and for the lower hybrid mode $E_z(x, \omega_{-, \text{MC}})$, as obtained from Eq. (6.34). We plot the fields as a function of the position in the x direction with respect to the location of the dipole at the center of the cavity. To highlight the differences between the contributions of the cavity and the dipole in the two modes, we choose a slight detuning of $\omega_{\text{cav}} - \omega_{\text{mat}} = 1.5$ meV. Since the classical MC model does not give the absolute value of the eigenmode fields, we choose arbitrary units so that the contribution of the cavity mode to the electric field of the upper hybrid mode [$\mathbf{E}_{\text{cav}}(\mathbf{r}, \omega_{+, \text{MC}})$ in Eq. (6.34)] has a maximum absolute value of 1, and this choice fixes all the other values according to Eq. (6.35)ⁱⁱⁱ. The field distribution shows a clear difference in the behavior of the two hybrid modes, where for the upper mode the dipole points in the same direction as the cavity field ($\frac{x_{\text{cav}}(\omega_{+, \text{MC}})}{x_{\text{mat}}(\omega_{+, \text{MC}})} > 0$), but in the inverse direction for the lower mode ($\frac{x_{\text{cav}}(\omega_{-, \text{MC}})}{x_{\text{mat}}(\omega_{-, \text{MC}})} < 0$). Further, at the chosen detuning, the relative contribution of the cavity to the fields is larger for the upper than the lower mode, as indicated by the values of the electric field far from the molecule at $\omega_{+, \text{MC}}$ and $\omega_{-, \text{MC}}$. In contrast, as shown in the inset, the relative contribution from the dipole to the field close to the molecule ($x = 0$) is stronger for the lower mode. Figure 6.3b thus confirms that the classical harmonic oscillator model allows for the calculation of the relative contribution of cavity and matter for each mode, as desired.

ⁱⁱⁱ The eigenstates of the Hopfield Hamiltonian from Eq. (6.30) have a symmetry where the cavity contribution of one hybrid mode is the same as the matter contribution of the other mode and vice versa, satisfying the equality $\langle \hat{a} + \hat{a}^\dagger \rangle(\omega_{\pm, \text{MC}}) = \langle \hat{b} + \hat{b}^\dagger \rangle(\omega_{\mp, \text{MC}})$. This property allows us to connect the amplitudes of the classical oscillators for the two hybrid eigenmodes as $\sqrt{\omega_{\text{cav}}} x_{\text{cav}}(\omega_{\pm, \text{MC}}) = \sqrt{\omega_{\text{mat}}} x_{\text{mat}}(\omega_{\mp, \text{MC}})$ (from $x_{\text{cav}} = \langle \hat{x}_{\text{cav}} \rangle = \sqrt{\hbar/2\omega_{\text{cav}}} \langle \hat{a} + \hat{a}^\dagger \rangle$ and $x_{\text{mat}} = \langle \hat{x}_{\text{mat}} \rangle = \sqrt{\hbar/2\omega_{\text{mat}}} \langle \hat{b} + \hat{b}^\dagger \rangle$).

In addition to the spatial distribution of the electric field of the two hybrid modes, Eqs. (6.34) and (6.35) also enable to plot the dependence of the field $\mathbf{E}(\mathbf{r}, \omega_{\pm, \text{MC}})$ inside the same cavity on the detuning $\omega_{\text{mat}} - \omega_{\text{cav}}$. Figure 6.3c shows for each mode the contributions to this electric field of the cavity and the molecule, normalized with respect to the sum of both contributions, according to $\Sigma_{\text{cav}}^{\pm} = \frac{|\mathbf{E}_{\text{cav}}(\omega_{\pm, \text{MC}})|^2}{|\mathbf{E}_{\text{cav}}(\omega_{\pm, \text{MC}})|^2 + |\mathbf{E}_{\text{mat}}(\omega_{\pm, \text{MC}})|^2}$ (dots) and $\Sigma_{\text{mat}}^{\pm} = \frac{|\mathbf{E}_{\text{mat}}(\omega_{\pm, \text{MC}})|^2}{|\mathbf{E}_{\text{cav}}(\omega_{\pm, \text{MC}})|^2 + |\mathbf{E}_{\text{mat}}(\omega_{\pm, \text{MC}})|^2}$ (solid lines). These ratios play a similar role as the Hopfield coefficients from cavity QED. The blue (red) dots and solid lines correspond to the upper (lower) hybrid mode. We obtain $\mathbf{E}_{\text{cav}}(\omega_{\pm, \text{MC}})$ and $\mathbf{E}_{\text{mat}}(\omega_{\pm, \text{MC}})$ by replacing Eq. (6.35) into Eq. (6.34), for a fixed coupling strength $g_{\text{MC}} = 2.5 \cdot 10^{-4} \omega_{\text{cav}}$ and for a distance of 10.5 nm from the dipole in the x direction. This position (indicated by the dashed line in the inset of Fig. 6.3b) is chosen because it is where the contributions of the matter and cavity have the same weight for the two hybrid modes at zero detuning for such small coupling strengths ($\Sigma_{\text{cav}}^{\pm} = \Sigma_{\text{mat}}^{\pm} \approx 0.5$, as shown in Fig. 6.3c). For detunings such that $\omega_{\text{cav}} > \omega_{\text{mat}}$ the field of the lower mode is predominantly given by the matter excitation ($\Sigma_{\text{mat}}^{-} > \Sigma_{\text{cav}}^{-}$ as indicated by the red dots and the red solid line), while for the upper mode the cavity contribution dominates ($\Sigma_{\text{cav}}^{+} > \Sigma_{\text{mat}}^{+}$, blue). Further, already at detunings as small as $\omega_{\text{cav}} - \omega_{\text{mat}} \gtrsim 15 \text{ meV} = 5 \cdot 10^{-3} \omega_{\text{cav}}$, the modes are essentially uncoupled for this small coupling strength ($\Sigma_{\text{mat}}^{+} \ll \Sigma_{\text{cav}}^{+}$ and $\Sigma_{\text{mat}}^{-} \gg \Sigma_{\text{cav}}^{-}$).

The coupling strength that we have considered up to now in this subsection corresponds to the strong coupling regime (we have neglected losses), far from the ultrastrong coupling regime, so that the phenomena studied can also be explained with the classical linearized model. On the other hand, we consider again in Fig. 6.3d the contributions to the electric field $\Sigma_{\text{cav}}^{\pm}$ and $\Sigma_{\text{mat}}^{\pm}$ as a function of the detuning, but in this case for a considerably larger coupling strength $g_{\text{MC}} = 0.2 \omega_{\text{cav}}$. This value of g_{MC} is not currently achievable with dielectric cavities at the single molecule level, but we choose it to illustrate the analysis of a ultrastrongly-coupled systems within the classical MC model. Further, such large g_{MC} can be achieved in systems with many molecules, as discussed in Sec. 6.5.3. For zero detuning $\omega_{\text{cav}} = \omega_{\text{mat}}$, the contributions of the dipole and the cavity are no longer identical in the ultrastrong coupling regime, with $\Sigma_{\text{cav}}^{+} \approx 0.6$ and $\Sigma_{\text{mat}}^{+} \approx 0.4$ for the upper hybrid mode at frequency $\omega_{+, \text{MC}}$ (and the opposite for the lower hybrid mode). More strikingly, the results in Fig. 6.3d indicate a qualitatively very different tendency of the modes at large detunings as compared to strong coupling, especially in the case of the upper hybrid mode. In ultrastrong coupling, in the $\omega_{\text{mat}} \rightarrow 0$ limit ($\omega_{\text{mat}} - \omega_{\text{cav}} \rightarrow -3 \text{ eV}$), this mode at frequency $\omega_{+, \text{MC}}$ (blue solid line and dots) has significant contributions from both the cavity and the matter ($\Sigma_{\text{cav}}^{+} \approx 0.9$ and $\Sigma_{\text{mat}}^{+} \approx 0.1$), and thus these two excitations do not decouple in this limit. This behavior is consistent with the discussion of the dispersion in Fig. 6.2d, where at large detunings the upper mode frequency does not reach the bare frequency ω_{cav} or ω_{mat} . The SpC, as well as the linearized model (not shown), do not reproduce this behavior, because in the SpC model the modes become uncoupled ($\Sigma_{\text{cav}}^{+} \approx 1$ and $\Sigma_{\text{mat}}^{+} \approx 0$), while in the linearized model we obtain intermediate values between

those corresponding to the SpC and MC models. In summary, we have shown in this section how to use the classical MC model to characterize the fields in a hybrid system composed by a molecule coupled to a transverse mode of a cavity. The methodology described enables to obtain equivalent results to the cavity-QED description (Hopfield Hamiltonian with diamagnetic term) by using an intuitive classical model of coupled harmonic oscillators.

6.5.2 A molecule interacting with the longitudinal field of a metallic nanoparticle

As an alternative system to analyze how to obtain physical observables in the strong and ultrastrong coupling regimes, we now consider a molecule placed close to a metallic nanoparticle (Fig. 6.4a). These nanoparticles are attractive in nanophotonics because they support localized surface plasmon modes characterized by very low effective volumes [85, 264, 281–283]. Since the coupling strength is inversely proportional to the square root of the effective mode volume, large coupling strengths can be obtained even when the nanoparticle interacts with a single molecule, as desired to reach the ultrastrong coupling regime.

In order to analyze the interaction of the nanoparticle with a molecular (bosonic) excitation of dipole moment d_{mat} , we consider that the size of the nanoparticle and the molecule-nanoparticle distance are much smaller than the light wavelength, and treat the system within the quasistatic approximation. We have shown in Sec. 6.3 that, under this approximation, the only interactions of the system are Coulomb interactions. Therefore, while in the previous subsection we have analyzed the coupling of molecular excitations with transverse electromagnetic fields, here we focus on the interaction with longitudinal fields. Accordingly, instead of the MC model that has been used in Sec. 6.5.2, the SpC model has to be considered, as shown in Eq. (6.18).

For simplicity, we consider small spherical particles of radius R_{cav} that are composed by a Drude metal with plasma frequency ω_{p} . These particles present a dipolar plasmonic resonance of Lorentzian lineshape at frequency $\omega_{\text{cav}} = \frac{\omega_{\text{p}}}{\sqrt{3}}$ (Sec. 1.2.1), oscillator strength $f_{\text{cav}} = 4\pi\epsilon_0 R_{\text{cav}}^3 \omega_{\text{cav}}^2$ and dipole moment d_{cav} [86]. Further, we consider that this dipolar mode is illuminated by an external field of amplitude \mathbf{E}_{inc} and frequency ω . We have shown in Sec. 6.3.1 that this field can be introduced in the SpC model as a forcing term acting both into the nanoparticle and into the molecule, by adding terms $F_{\alpha} e^{-i\omega t} = \sqrt{f_{\alpha}} |\mathbf{E}_{\text{inc}}| e^{-i\omega t}$ ($\alpha = \text{'cav'}$ or $\alpha = \text{'mat'}$) in the right handside of Eq. (6.2), i.e. the amplitude F_{α} of the time-dependent force is proportional to the dipole moments d_{α} and to the electric field of the illumination. By solving the equations of motion of the SpC model [Eq. (6.2)] with this external force included, we can calculate the induced dipole moments of the cavity and the matter excitation:

$$d_{\text{cav}}(\omega) = \sqrt{f_{\text{cav}}} x_{\text{cav}}(\omega) = \sqrt{f_{\text{cav}}} \frac{F_{\text{cav}}(\omega_{\text{mat}}^2 - \omega^2) - F_{\text{mat}} 2g_{\text{SpC}} \sqrt{\omega_{\text{cav}} \omega_{\text{mat}}}}{(\omega_{\text{cav}}^2 - \omega^2)(\omega_{\text{mat}}^2 - \omega^2) - 4g_{\text{SpC}}^2 \omega_{\text{cav}} \omega_{\text{mat}}}, \quad (6.37a)$$

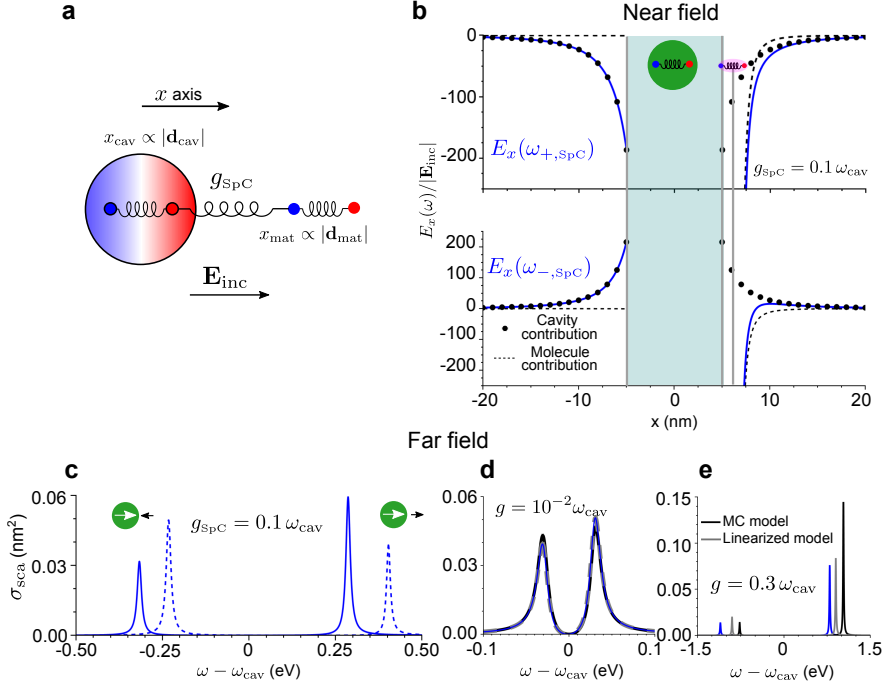


Figure 6.4: Modelling of the coupling between a molecule and a spherical nanoparticle (a nanocavity) within the classical SpC model. a) Schematics of the system. The molecular excitation (of induced dipole moment \mathbf{d}_{mat}) and the dipolar mode of the plasmonic nanocavity (of induced dipole moment \mathbf{d}_{cav}) are described as two harmonic oscillators (with oscillation amplitudes x_{mat} and x_{cav}) that are coupled with strength g_{SpC} . The system is excited by a laser with electric field \mathbf{E}_{inc} . The radius of the spherical nanocavity is 5 nm and the dipole is placed at 1 nm distance from the surface of the nanoparticle along the x axis (the center of the nanoparticle corresponds to $x = y = z = 0$). \mathbf{d}_{cav} , \mathbf{d}_{mat} and \mathbf{E}_{inc} are polarized along x . b) Electric field distribution along the x axis ($y = z = 0$) when the system is excited at the frequency of the upper hybrid mode $\omega_{+, \text{SpC}}$ (top panel) and of the lower hybrid mode $\omega_{-, \text{SpC}}$ (bottom panel). The fields are evaluated only outside the nanocavity, with the positions inside highlighted by the green-shaded area. The position of the molecule is indicated by the vertical gray line. We evaluate the fields for coupling strength $g_{\text{SpC}} = 0.1 \omega_{\text{cav}}$ and the following parameters: $f_{\text{mat}} = (118.74e)^2/m_{\text{p}}$, $f_{\text{cav}} = (4345e)^2/m_{\text{p}}$, $F_{\text{cav}} = \sqrt{f_{\text{cav}}}|\mathbf{E}_{\text{inc}}|$, $F_{\text{mat}} = \sqrt{f_{\text{mat}}}|\mathbf{E}_{\text{inc}}|$, $\kappa = 20$ meV and $\gamma = 10$ meV. For each hybrid mode, the cavity contribution to the field is highlighted by dots, the molecular contribution is indicated by dashed lines and the total field by blue solid lines. c) Scattering cross section of the same system, with $g_{\text{SpC}} = 0.1 \omega_{\text{cav}}$, as a function of the detuning of the laser $\omega - \omega_{\text{cav}}$. Solid lines: tuned system with frequencies $\omega_{\text{cav}} = \omega_{\text{mat}} = 3$ eV. Dashed lines: detuned system with frequencies $\omega_{\text{cav}} = 3$ eV and $\omega_{\text{mat}} = 3.2$ eV. d) Scattering cross section of the tuned system ($\omega_{\text{cav}} = \omega_{\text{mat}} = 3$ eV), comparing the result of the SpC model (blue line) to the results of the MC model (black) and the linearized model (gray), in the strong coupling regime, $g = 10^{-2} \omega_{\text{cav}}$. e) Same as in (d) for the ultrastrong coupling regime, $g = 0.3 \omega_{\text{cav}}$.

$$d_{\text{mat}}(\omega) = \sqrt{f_{\text{mat}}} x_{\text{mat}}(\omega) = \sqrt{f_{\text{mat}}} \frac{F_{\text{mat}}(\omega_{\text{cav}}^2 - \omega^2) - F_{\text{cav}} 2g_{\text{SpC}} \sqrt{\omega_{\text{cav}} \omega_{\text{mat}}}}{(\omega_{\text{cav}}^2 - \omega^2)(\omega_{\text{mat}}^2 - \omega^2) - 4g_{\text{SpC}}^2 \omega_{\text{cav}} \omega_{\text{mat}}}. \quad (6.37b)$$

These expressions are consistent with an alternative classical approach that models the nanocavity and the molecule as polarizable objects (see Appendix B), which supports the validity of the general approach presented in this chapter. We further note that in the absence of losses the dipole moments d_{cav} and d_{mat} diverge at the eigenfrequencies $\omega_{\pm, \text{SpC}}$ of the SpC model [Eq. (6.3)]. To avoid these divergences, in this section we add an imaginary part to the bare cavity and matter frequencies. These imaginary parts are related to the decay rates κ and γ of the cavity and the matter excitation, respectively, as $\text{Im}(\omega_{\text{cav}}) = -\frac{\kappa}{2}$ and $\text{Im}(\omega_{\text{mat}}) = -\frac{\gamma}{2}$.

As an example, we consider a metallic spherical nanoparticle of radius $R_{\text{cav}} = 5$ nm and with a cavity mode of frequency $\omega_{\text{cav}} = 3$ eV. We consider the same molecule of Sec. 6.5.1, with a strong transition dipole moment of magnitude $\mu_{\text{mat}} = 15$ Debye. As indicated by Eq. (6.19), the coupling strength of the system can be adjusted depending on the position and the orientation of the molecule. The coupling strength is maximized if the induced dipole moments \mathbf{d}_{cav} and \mathbf{d}_{mat} and their relative position \mathbf{n}_{rrel} are oriented in the same direction, parallel to the incident field. With this choice (as indicated in Fig. 6.4a) and placing the molecule at 1 nm from the surface of the nanoparticle, we obtain a coupling strength $g_{\text{SpC}} \approx 300$ meV = $0.1 \omega_{\text{cav}}$ and thus reach the limit of ultrastrong coupling regime. This large value of g_{SpC} is possible due to the small size of the nanoparticle (large field confinement) and to the strong transition dipole moment considered for the molecule, which lies slightly beyond the values of $\mu_{\text{mat}} = 3-5$ Debyes corresponding to typical molecules used in plasmonic systems. Even larger field confinement is possible in current non-spherical experimental configurations that exploit very narrow gaps [264]. To ensure that the system is also in the strong coupling regime when considering lower values of g_{SpC} below, we choose $\gamma = 10$ meV and a damping rate of the plasmonic cavity $\kappa = 20$ meV that is small compared to those of usual plasmonic metals.

The induced dipole moments obtained from Eq. (6.37) can be used, for example, to calculate the near-field distribution for excitation at frequency ω . The total electric field is the sum of the cavity \mathbf{E}_{cav} and molecular or matter contribution \mathbf{E}_{mat} . Under the quasistatic approximation, with $d_{\text{cav}}(\omega) = \sqrt{f_{\text{cav}}} x_{\text{cav}}(\omega)$ and $d_{\text{mat}}(\omega) = \sqrt{f_{\text{mat}}} x_{\text{mat}}(\omega)$ we obtain that the fields at position \mathbf{r} outside the metallic nanoparticle, $|\mathbf{r} - \mathbf{r}_{\text{cav}}| > R_{\text{cav}}$, depend on the amplitude of the harmonic oscillators as

$$\begin{aligned} \mathbf{E}(\mathbf{r}, \omega) = & \underbrace{\frac{3(\mathbf{n}_{\text{dcav}} \cdot \mathbf{n}_{\text{rcav}}) \mathbf{n}_{\text{rcav}} - \mathbf{n}_{\text{dcav}}}{4\pi\epsilon_0 |\mathbf{r} - \mathbf{r}_{\text{cav}}|^3} \sqrt{f_{\text{cav}}} x_{\text{cav}}(\omega)}_{\mathbf{E}_{\text{cav}}(\mathbf{r}, \omega)} \\ & + \underbrace{\frac{3(\mathbf{n}_{\text{dmat}} \cdot \mathbf{n}_{\text{rmat}}) \mathbf{n}_{\text{rmat}} - \mathbf{n}_{\text{dmat}}}{4\pi\epsilon_0 |\mathbf{r} - \mathbf{r}_{\text{mat}}|^3} \sqrt{f_{\text{mat}}} x_{\text{mat}}(\omega)}_{\mathbf{E}_{\text{mat}}(\mathbf{r}, \omega)}. \end{aligned} \quad (6.38)$$

From this expression, the fields at the frequency of each hybrid mode are calculated by replacing into Eq. (6.38) the dipole moments of Eq. (6.37) induced at the mode frequencies $\omega_{\pm, \text{SpC}}$.

The electric fields associated to the upper and lower mode frequencies, which at both frequencies are real and polarized along the x direction, are plotted in the top and bottom panels of Fig. 6.4b (blue lines), respectively. We further show the decomposition of the fields into the contribution of the cavity (black dots) and the molecule (black dashed line) as given by the first and second terms in the right handside of Eq. (6.38), respectively, which is useful to characterize the different properties of each mode. In particular, it can be appreciated from Fig. 6.4b that when the upper hybrid mode is excited, the dipoles associated to the cavity and the molecule are oriented to the same direction (same sign). In contrast, for the lower mode, the dipoles point towards the opposite direction.

The near field plotted in Fig. 6.4b is useful to analyze the behavior of the hybrid modes but is difficult to measure, and most experiments focus on the far-field spectra, such as the scattering cross-section spectra σ_{sca} . Neglecting retardation effects due to the small molecule-nanocavity distance that we consider, σ_{sca} is related to the total dipole moment of the system as [67]

$$\begin{aligned} \sigma_{\text{sca}}(\omega) &= \frac{\omega^4}{6\pi\epsilon_0^2 c^4} \left| \frac{\mathbf{d}_{\text{cav}}(\omega)}{|\mathbf{E}_{\text{inc}}|} + \frac{\mathbf{d}_{\text{mat}}(\omega)}{|\mathbf{E}_{\text{inc}}|} \right|^2 \\ &= \frac{\omega^4}{6\pi\epsilon_0^2 c^4} \left| \frac{\sqrt{f_{\text{cav}}} x_{\text{cav}}(\omega)}{|\mathbf{E}_{\text{inc}}|} \mathbf{n}_{\text{d}_{\text{cav}}} + \frac{\sqrt{f_{\text{mat}}} x_{\text{mat}}(\omega)}{|\mathbf{E}_{\text{inc}}|} \mathbf{n}_{\text{d}_{\text{mat}}} \right|^2. \end{aligned} \quad (6.39)$$

We show in Fig. 6.4c the scattering cross section for the same nanoparticle-molecule system in the outset of the ultrastrong coupling regime ($g_{\text{SpC}} = 0.1 \omega_{\text{cav}}$). Since the oscillator strength of the cavity is much larger than that of the molecule ($f_{\text{cav}} \gg f_{\text{mat}}$), the spectrum is fully dominated by the contribution of the cavity, given by Eq. (6.37a) [however, in other systems, where both oscillator strengths are similar, $f_{\text{cav}} \approx f_{\text{mat}}$, it is crucial to consider both contributions in Eq. (6.39)]. The scattering cross-section spectra are shown for two different detunings between the nanocavity and the molecule. At zero detuning ($\omega_{\text{cav}} = \omega_{\text{mat}} = 3$ eV, solid lines in Fig. 6.4c) the upper hybrid mode has a (moderately) larger cross section than the lower hybrid mode, mostly due to the ω^4 factor in Eq. (6.39). However, when the molecular excitation is blue detuned with respect to the cavity ($\omega_{\text{cav}} = 3$ eV and $\omega_{\text{mat}} = 3.2$ eV, dashed line), the strength of the peak in the cross-section spectra associated to the lower hybrid mode increases and the upper hybrid mode becomes weaker. This behavior occurs because, for this detuning, the lower hybrid mode acquires a larger contribution of the cavity resonance that dominates the scattering spectra, while the predominantly molecule-like behavior of the upper mode results in a smaller cross section due to $f_{\text{mat}} \ll f_{\text{cav}}$.

To assess the importance of using the classical SpC model to describe this system, we compare the results of the scattering cross-section spectra calculated with this model with those obtained using the MC and linearized models. For this

purpose, it is first necessary to obtain the expressions of the scattering cross section for the latter two models under external illumination. By introducing forcing terms in the equations of motion of the MC model [Eq. (6.4)] to account for the external field, we obtain the corresponding oscillator amplitudes

$$x_{\text{cav}}(\omega) = \frac{F_{\text{cav}}(\omega_{\text{mat}}^2 - \omega^2) - F_{\text{mat}}2ig_{\text{MC}}\omega}{(\omega_{\text{cav}}^2 - \omega^2)(\omega_{\text{mat}}^2 - \omega^2) - 4g_{\text{MC}}^2\omega^2}, \quad (6.40a)$$

$$x_{\text{mat}}(\omega) = \frac{F_{\text{cav}}2ig_{\text{MC}}\omega + F_{\text{mat}}(\omega_{\text{mat}}^2 - \omega^2)}{(\omega_{\text{cav}}^2 - \omega^2)(\omega_{\text{mat}}^2 - \omega^2) - 4g_{\text{MC}}^2\omega^2}. \quad (6.40b)$$

On the other hand, by repeating the procedure with the linearized model [Eq. (6.7)], we obtain

$$x_{\text{cav}}(\omega) = \frac{1}{4\omega} \frac{F_{\text{cav}}(\omega_{\text{mat}} - \omega) - F_{\text{mat}}g_{\text{lin}}}{(\omega_{\text{cav}} - \omega)(\omega_{\text{mat}} - \omega) - g_{\text{lin}}^2}, \quad (6.41a)$$

$$x_{\text{mat}}(\omega) = \frac{1}{4\omega} \frac{F_{\text{mat}}(\omega_{\text{cav}} - \omega) - F_{\text{cav}}g_{\text{lin}}}{(\omega_{\text{cav}} - \omega)(\omega_{\text{mat}} - \omega) - g_{\text{lin}}^2}. \quad (6.41b)$$

We calculate the scattering cross section according to each classical model by introducing the corresponding values of $x_{\text{cav}}(\omega)$ and $x_{\text{mat}}(\omega)$ in Eq. (6.39). Figure 6.4d shows the spectra for the system at zero detuning ($\omega_{\text{cav}} = \omega_{\text{mat}} = 3$ eV) in the strong coupling regime but far from the ultrastrong coupling regime, with $g = 10^{-2}\omega_{\text{cav}}$. The spectra calculated from the three models overlap almost perfectly, as expected (black line: MC model; gray line: linearized model; blue line: SpC model). Concretely, the difference between the three calculations is less than 10% at the hybrid mode frequencies $\omega_{\pm, \text{SpC}}$. This small error is consistent with the good agreement of the eigenfrequencies in Sec. 6.2 for this relatively low value of g .

In contrast, if the system is well into the ultrastrong coupling regime, with coupling strength $g = 0.3\omega_{\text{cav}}$, the spectra obtained with the three models are very different (Fig. 6.4e). There is a clear disagreement in the peak positions, due to the difference in the eigenfrequencies of the three models (see Fig. 6.2d). Further, the MC model predicts that the strength of the peak corresponding to the excitation of the upper hybrid mode is two times larger than the equivalent value for the SpC model. These significant differences emphasize the importance of the choice of the model in this regime. We note, however, that for such large coupling, higher-order modes of the nanocavity likely play an important role in the coupling in realistic systems, which would need to be taken into account [284]. Further, it would be interesting to examine how this analysis is modified by going beyond the quasistatic description.

6.5.3 An ensemble of interacting molecules in a Fabry-Pérot cavity

The previous two examples were chosen to illustrate the procedure to connect the oscillators of the SpC and MC models to physical observables. In both cases, the optical cavity was coupled to a single molecule, which makes it very challenging to reach the ultrastrong coupling regime experimentally. An alternative approach to reach the necessary coupling strengths consists in filling a cavity with many molecules or a material supporting a well-defined excitation (such as a phononic resonance) [63,64]. We consider in this section a homogeneous ensemble of molecules interacting with resonant transverse electromagnetic modes of a Fabry-Pérot cavity (left sketch in Fig. 6.5), a system of large relevance to experiments [260]. Each molecule presents a vibrational excitation that is modelled as a dipole of induced dipole moment \mathbf{d}_i (we focus here on the case of molecules for specificity, but the same derivation can also be applied to phononic or similar materials by focusing on the dipole moment associated to each unit cell). We consider that all molecules are identical, and thus have the same oscillator strength f_{mat} and resonant frequency ω_{mat} . For simplicity, we assume that there are N_{mat} molecules distributed homogeneously. The electromagnetic modes of the Fabry-Pérot cavity are standing waves with vector potential \mathbf{A}_α and frequency $\omega_{\text{cav},\alpha}$, where all α modes are orthogonal.

Following the relations between the observables and oscillators given in Sec. 6.3, we represent each vibrational dipole as a harmonic oscillator with oscillation amplitude $x_{\text{mat},i} = \frac{|\mathbf{d}_i|}{\sqrt{f_{\text{mat}}}}$ and each cavity mode with the variable $x_{\text{cav},\alpha} = \sqrt{\varepsilon_0 \mathcal{V}_{\text{eff}}} \mathcal{A}_\alpha$. Notably, this system encompasses the two types of interaction discussed in the previous subsections: (i) each dipole i is coupled to all other dipoles j (i.e. direct longitudinal molecule-molecule interaction) following the SpC model, where the coupling strength $g_{\text{SpC}}^{(i,j)}$ is given by Eq. (6.19); (ii) each dipole i is coupled to all transverse cavity modes α according to the MC model with coupling strength $g_{\text{MC}}^{(\alpha,i)} = \frac{1}{2} \sqrt{\frac{f_{\text{mat}}}{\varepsilon_0 \mathcal{V}_{\text{eff}}}} \Xi_\alpha(\mathbf{r}_i) \cos \theta_{\alpha,i}$ [Eq. (6.17)], where the normalized amplitude value Ξ_α of the cavity field is evaluated at the position of molecule i . We assume for simplicity that all molecules are oriented in the same direction as the cavity field, and thus $\cos \theta_{\alpha,i} = 1$ for all α and i . All the interactions that are present in this system are shown schematically in the left panel of Fig. 6.5. To combine all couplings in a single model, we just include in the harmonic oscillator equations the coupling terms associated with the longitudinal dipole-dipole interactions [SpC model, Eq. (6.2)] and those describing the interaction of the molecules with the transverse cavity modes [MC model, Eq. (6.4)]. The resulting equations are

$$\ddot{x}_{\text{mat},i} + \omega_{\text{mat}}^2 x_{\text{mat},i} + \sum_{\alpha} 2g_{\text{MC}}^{(\alpha,i)} \dot{x}_{\text{cav},\alpha} + \sum_{j \neq i} 2\omega_{\text{mat}} g_{\text{SpC}}^{(i,j)} x_{\text{mat},j} = 0, \quad (6.42a)$$

$$\ddot{x}_{\text{cav},\alpha} + \omega_{\text{cav},\alpha}^2 x_{\text{cav},\alpha} - \sum_i 2g_{\text{MC}}^{(\alpha,i)*} \dot{x}_{\text{mat},i} = 0, \quad (6.42b)$$

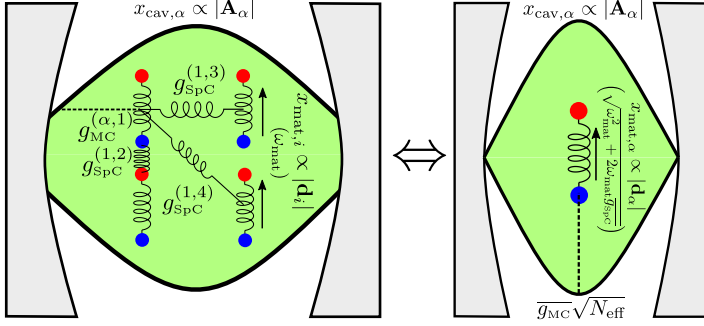


Figure 6.5: Interaction between matter excitations within a homogeneous material (here a homogeneous ensemble of molecules) and the transverse modes of a dielectric cavity. (Left) Schematic of the system. The oscillators $x_{\text{cav},\alpha} \propto |\mathbf{A}_\alpha|$ represent the vector potential \mathbf{A}_α associated to all modes α in the cavity, and the matter oscillators $x_{\text{mat},i}$ represent the dipole moments \mathbf{d}_i of each molecule. The cavity-molecule interactions are modelled with the MC model and coupling strength $g_{\text{MC}}^{(\alpha,i)}$, and the molecule-molecule interactions with the SpC model and coupling strength $g_{\text{SpC}}^{(i,j)}$. We indicate all the interactions of the molecule with index $i = 1$. (Right) Schematic indicating that the description of the full system is equivalent to the coupling, within the MC model, of the cavity mode α with a single molecular excitation of dipole moment \mathbf{d}_α , modified frequency $\sqrt{\omega_{\text{mat}}^2 + 2\omega_{\text{mat}}g_{\text{SpC}}}$ and modified coupling strength $\overline{g_{\text{MC}}}\sqrt{N_{\text{eff}}}$.

where we sum over all molecules and all cavity modes.

The direct calculation of the whole dynamics of the system requires solving $N_{\text{mat}} \times N_{\text{cav}}$ equations, where N_{cav} is the number of cavity modes. However, due to the homogeneity of the material and of the orthogonality of the cavity modes, each cavity mode α only couples with a collective matter excitation (represented by an oscillator of oscillation amplitude $x_{\text{mat},\alpha} \propto \sum_i \Xi_\alpha(\mathbf{r}_i)x_{\text{mat},i}$, i.e. the amplitude of each individual oscillator in the collective mode α is weighted by the cavity mode field at the same position), which allows us to strongly simplify Eq. (6.42). The equations of motion for this new variable are (see Appendix C for the derivation of these equations and of the value of the different parameters)

$$\ddot{x}_{\text{mat},\alpha} + (\omega_{\text{mat}}^2 + 2\omega_{\text{mat}}\overline{g_{\text{SpC}}})x_{\text{mat},\alpha} + 2\overline{g_{\text{MC}}}\sqrt{N_{\text{eff}}}\dot{x}_{\text{cav},\alpha} = 0, \quad (6.43a)$$

$$\ddot{x}_{\text{cav},\alpha} + \omega_{\text{cav},\alpha}^2 x_{\text{cav},\alpha} - 2\overline{g_{\text{MC}}}\sqrt{N_{\text{eff}}}\dot{x}_{\text{mat},\alpha} = 0. \quad (6.43b)$$

In these equations, $\overline{g_{\text{SpC}}}$ is a parameter that describes effectively the effect of the molecule-molecule interactions within the α collective matter excitation, and $\overline{g_{\text{MC}}}$ is the maximum coupling strength between a single molecule and the transverse cavity mode, obtained for a molecule placed at the antinodes of the mode. N_{eff} is the effective number of molecules that are coupled to the mode ($N_{\text{eff}} = N_{\text{mat}}/2$ for a Fabry-Pérot mode). Equation (6.43) indicates that it is possible to describe the coupling between a cavity mode and a collective molecular excitation by considering only two harmonic oscillators, which are independent of the other

cavity and collective modes. The coupling strength between each collective matter excitation and the corresponding cavity mode increases with N_{eff} as $\overline{g}_{\text{MC}}\sqrt{N_{\text{eff}}}$. This scaling with $\sqrt{N_{\text{eff}}}$ is consistent with the quantum Dicke model [285], and explains the large coupling strengths that have been demonstrated in these systems [286, 287]. Further, the dipole-dipole interaction between the molecules just renormalizes the frequency of the collective excitation from ω_{mat} to $\sqrt{\omega_{\text{mat}}^2 + 2\omega_{\text{mat}}\overline{g}_{\text{SpC}}}$ (except when the cavity mode presents extremely fast spatial variations, where more complex effects can occur [288]).

In this description, each cavity mode α only couples to the collective molecular mode where the dipoles are polarized following the orientation and spatial distribution $\Xi_{\alpha}(\mathbf{r})$ of the cavity field. This collective mode thus has a dipole moment $\mathbf{d}_{\alpha} = \frac{1}{\sqrt{N_{\text{eff}}}} \sum_i \Xi_{\alpha}(\mathbf{r}_i) \mathbf{d}_i$, where \mathbf{d}_i are the single-molecule induced dipole moments (see Appendix C). Importantly, as can be observed in Eq. (6.43), the interaction between each cavity mode with the corresponding collective matter mode is described classically within the MC model. As a consequence, the description of this coupling is fully equivalent to the analysis of the coupling between the same cavity mode and an individual dipole of frequency $\sqrt{\omega_{\text{mat}}^2 + 2\omega_{\text{mat}}\overline{g}_{\text{SpC}}}$ and increased coupling strength $\overline{g}_{\text{MC}}\sqrt{N_{\text{eff}}}$, as indicated schematically in Fig. 6.5. Accordingly, the response of the cavity filled by a large number of molecules can be described by adapting the analysis and conclusions in Sec. 6.5.1. For example, the expression of the eigenmodes as a function of the cavity and collective molecular modes can be obtained using Eq. (6.35). The electric field inside the cavity corresponding to each hybrid mode can be obtained by noticing that i) $x_{\text{cav},\alpha}$ gives the amplitude of the vector potential \mathcal{A}_{α} , ii) the oscillator $x_{\text{mat},\alpha}$ is proportional to the dipole moment \mathbf{d}_{α} , which enables to calculate the individual induced dipole moments \mathbf{d}_i and iii) these single-molecule quantities lead to the polarization density $\mathbf{P}(\mathbf{r}) = \frac{\mathbf{d}_i(\mathbf{r})}{\Delta\mathcal{V}}$, where $\Delta\mathcal{V}$ is the volume that each individual dipole occupies.

We have thus shown that the MC model constitutes the proper description of the coupling between transverse cavity modes and matter excitations in homogeneous materials. An alternative approach that further verifies the validity of this model to describe the system is to demonstrate that it allows for recovering the typical bulk permittivity of ensembles of molecules or phononic materials, which cannot be correctly done with the SpC and linearized models. We discuss this issue in more detail in Chapter 7.

6.6 Alternative classical models of coupled harmonic oscillators

The discussion of Sec. 6.3 led us to conclude that the classical MC model relates matter excitations with transverse electromagnetic modes, while the SpC model can express dipole-dipole interactions. In this section, we show that there are other classical coupled harmonic oscillator models that are equivalent to the MC and the SpC models. These alternative models depend on the gauge chosen for the classical

Lagrangian and Hamiltonian descriptions, and we discuss oscillator models in two of the most vastly used gauges: the Coulomb and dipole gauges.

6.6.1 Interaction of a molecular excitation with a transverse cavity mode described within the Coulomb gauge

We first focus on the description of the coupling between a transverse electromagnetic mode and a molecular excitation in the Coulomb gauge. This system is described with the Lagrangian of Eq. (6.22) in this gauge, and it has been shown in Sec. 6.3 that it leads to the MC model. Alternatively, here we use Hamilton's equations to obtain another equivalent classical model of harmonic oscillators, starting from the classical minimal-coupling Hamiltonian of Eq. (6.24) corresponding to the Coulomb gauge. In this section we focus again on the situation of maximum coupling strength with $\Xi(\mathbf{r}_{\text{mat}}) \cos \theta = 1$ (as in Sec. 6.4), so that the equations are written in a more concise way. From Eq. (6.24), we can directly derive the Hamilton's equations of motion of all canonical variables:

$$\dot{\mathcal{A}} = \frac{\partial \mathcal{H}_{\text{Cou}}^{\text{min-c}}}{\partial \Pi_{\text{Cou}}} = \frac{\Pi_{\text{Cou}}}{\varepsilon_0 \mathcal{V}_{\text{eff}}}, \quad (6.44a)$$

$$\dot{\Pi}_{\text{Cou}} = -\frac{\partial \mathcal{H}_{\text{Cou}}^{\text{min-c}}}{\partial \mathcal{A}} = -\varepsilon_0 \mathcal{V}_{\text{eff}} \omega_{\text{cav}}^2 \mathcal{A} + f_{\text{mat}} (p_{\text{Cou}} - \mathcal{A}), \quad (6.44b)$$

$$\dot{d} = \frac{\partial \mathcal{H}_{\text{Cou}}^{\text{min-c}}}{\partial p_{\text{Cou}}} = f_{\text{mat}} (p_{\text{Cou}} - \mathcal{A}), \quad (6.44c)$$

$$\dot{p}_{\text{Cou}} = -\frac{\partial \mathcal{H}_{\text{Cou}}^{\text{min-c}}}{\partial d} = -\frac{\omega_{\text{mat}}^2}{f_{\text{mat}}} d_j. \quad (6.44d)$$

Hamilton's equations can be used to obtain classical harmonic oscillator models by eliminating two variables, which leads to two second-order differential equations. By choosing the variables \mathcal{A} and d to describe the dynamics of the system, we obtain

$$\ddot{\mathcal{A}} + \omega_{\text{cav}}^2 \mathcal{A} - \frac{\dot{d}}{\varepsilon_0 \mathcal{V}_{\text{eff}}} = 0, \quad (6.45a)$$

$$\ddot{d} + \omega_{\text{mat}}^2 d + f_{\text{mat}} \dot{\mathcal{A}} = 0. \quad (6.45b)$$

As discussed in detail in Sec. 6.3, these equations have the form of the MC model, because the coupling terms are proportional to the time derivatives $\dot{\mathcal{A}}$ and \dot{d} . However, there are other possible ways to represent the response of this system with harmonic oscillators. An alternative is to choose the variable p_{Cou} for the matter excitation and \mathcal{A} for the cavity mode. By eliminating the rest of variables in Eq. (6.44), the equations of motion for the chosen variables are written as

$$\ddot{\mathcal{A}} + \left(\omega_{\text{cav}}^2 + \frac{f_{\text{mat}}}{\varepsilon_0 \mathcal{V}_{\text{eff}}} \right) \mathcal{A} - \frac{f_{\text{mat}}}{\varepsilon_0 \mathcal{V}_{\text{eff}}} p_{\text{Cou}} = 0, \quad (6.46a)$$

$$\ddot{p}_{\text{Cou}} + \omega_{\text{mat}}^2 p_{\text{Cou}} - \omega_{\text{mat}}^2 \mathcal{A} = 0. \quad (6.46b)$$

With the transformation $x_{\text{cav}} = \sqrt{\varepsilon_0 \mathcal{V}_{\text{eff}}} \mathcal{A}$ used in Sec. 6.5.1, and with the new transformation $x'_{\text{mat}} = \frac{\sqrt{f_{\text{mat}}}}{\omega_{\text{mat}}} p_{\text{Cou}}$, Eq. (6.46) becomes

$$\ddot{x}_{\text{cav}} + (\omega_{\text{cav}}^2 + 4g_{\text{MC}}^2)x_{\text{cav}} - 2g_{\text{MC}}\omega_{\text{mat}}x'_{\text{mat}} = 0, \quad (6.47a)$$

$$\ddot{x}'_{\text{mat}} + \omega_{\text{mat}}^2 x'_{\text{mat}} - 2g_{\text{MC}}\omega_{\text{mat}}x_{\text{cav}} = 0, \quad (6.47b)$$

with the same coupling strength $g_{\text{MC}} = \frac{1}{2}\sqrt{\frac{f_{\text{mat}}}{\varepsilon_0 \mathcal{V}_{\text{eff}}}}$ that is used to describe the cavity-dipole coupling within the MC model.

Equations (6.45) and (6.47) (the former corresponding to the MC model) have been derived for the same system, and thus must result in the same response of the system. However, several interesting aspects can be observed. First, in Eq. (6.47) x'_{mat} is related to p_{Cou} , while x_{mat} is related to d in the MC model. Thus, it is important to consider this difference when calculating physical observables as in Sec. 6.5.1. Second, Eq. (6.47) contains coupling terms proportional to the oscillator displacements x_{cav} and x'_{mat} (as in the SpC model) instead of to the time derivatives \dot{x}_{cav} and \dot{x}_{mat} (as in the MC model). Last, in Eq. (6.47) the frequency of the cavity mode is renormalized from ω_{cav} to $\sqrt{\omega_{\text{cav}}^2 + 4g_{\text{MC}}^2}$. The different coupling term and the frequency renormalization compensate each other, so that Eq. (6.47) gives the same result as the MC model. Therefore, the molecule-dielectric cavity system can be equivalently described with coupling terms proportional to the oscillator displacements or to their time derivatives, if the frequency of the cavity mode and the oscillator amplitudes are modified appropriately.

6.6.2 Interaction of a molecular excitation with a transverse cavity mode described within the dipole gauge

We have shown that the results of the MC model can be recovered by equations with a different coupling term and a renormalized frequency of the cavity mode. Here, we use the dipole gauge to show that we can also obtain equivalent equations by renormalizing the frequency of the matter excitation. In this case, we start from the Hamiltonian of Eq. (6.28) and obtain the following Hamilton's equations of motion:

$$\dot{\mathcal{A}} = \frac{\partial \mathcal{H}_{\text{Dip}}^{\text{min-c}}}{\partial \Pi_{\text{Dip}}} = \frac{\Pi_{\text{Dip}} + d}{\varepsilon_0 \mathcal{V}_{\text{eff}}}, \quad (6.48a)$$

$$\dot{\Pi}_{\text{Dip}} = -\frac{\partial \mathcal{H}_{\text{Dip}}^{\text{min-c}}}{\partial \mathcal{A}} = -\varepsilon_0 \mathcal{V}_{\text{eff}} \omega_{\text{cav}}^2 \mathcal{A}, \quad (6.48b)$$

$$\dot{d} = \frac{\partial \mathcal{H}_{\text{Dip}}^{\text{min-c}}}{\partial p_{\text{Dip}}} = f_{\text{mat}} p_{\text{Dip}}, \quad (6.48c)$$

$$\dot{p}_{\text{Dip}} = -\frac{\partial \mathcal{H}_{\text{Dip}}^{\text{min-c}}}{\partial d} = -\frac{\omega_{\text{mat}}^2}{f_{\text{mat}}} d - \frac{\Pi_{\text{Dip}} + d}{\varepsilon_0 \mathcal{V}_{\text{eff}}}. \quad (6.48d)$$

The choice of variables \mathcal{A} and d to obtain second-order differential equations leads to the transformation from Eq. (6.48) to Eq. (6.45). Therefore, for these variables the MC model is obtained independently of the considered gauge. On the other hand, with the choice of the variables d and Π_{Dip} , we obtain

$$\ddot{\Pi}_{\text{Dip}} + \omega_{\text{cav}}^2 \Pi_{\text{Dip}} + \omega_{\text{cav}}^2 d = 0 \quad (6.49a)$$

$$\ddot{d} + \left(\omega_{\text{mat}}^2 + \frac{f_{\text{mat}}}{\varepsilon_0 \mathcal{V}_{\text{eff}}} \right) d + \frac{f_{\text{mat}}}{\varepsilon_0 \mathcal{V}_{\text{eff}}} \Pi_{\text{Dip}} = 0. \quad (6.49b)$$

This equation can be rewritten in terms of oscillator amplitudes. By using the matter oscillator amplitude $x_{\text{mat}} = \frac{d}{\sqrt{f_{\text{mat}}}}$ and the new cavity oscillator amplitude $x'_{\text{cav}} = \frac{\Pi_{\text{Dip}}}{\sqrt{\varepsilon_0 \mathcal{V}_{\text{eff}} \omega_{\text{cav}}}}$, the equations are

$$\ddot{x}'_{\text{cav}} + \omega_{\text{cav}}^2 x'_{\text{cav}} + 2g_{\text{MC}} \omega_{\text{cav}} x_{\text{mat}} = 0, \quad (6.50a)$$

$$\ddot{x}_{\text{mat}} + (\omega_{\text{mat}}^2 + 4g_{\text{MC}}^2) x_{\text{mat}} + 2g_{\text{MC}} \omega_{\text{cav}} x'_{\text{cav}} = 0. \quad (6.50b)$$

The last system of equations gives the same results as the MC model, but with the coupling term proportional to the oscillator displacements x'_{cav} and x_{mat} and with the frequency of the matter excitation renormalized from ω_{mat} to $\sqrt{\omega_{\text{mat}}^2 + 4g_{\text{MC}}^2}$.

6.6.3 Interaction of a molecule with a metallic nanoparticle

In Secs. 6.6.1 and 6.6.2 we have shown that the coupling between a molecular excitation and a transverse cavity mode can be described equivalently with the MC model (coupling terms proportional to the time derivatives \dot{x}'_{cav} and \dot{x}_{mat}) or with models where the coupling terms are proportional to the oscillator displacements and the frequencies of the oscillators are modified. Here, we show a similar result for dipole-dipole interactions: they can be described by the SpC model (coupling terms proportional to the amplitudes x_{cav} and x_{mat}) or with alternative equations that contain coupling terms proportional to the time derivatives \dot{x}'_{cav} and \dot{x}_{mat} (as they appear in the MC model), together with renormalized frequencies.

To show the alternative model to describe this system, we consider the Hamiltonian of dipole-dipole interactions given by Eq. (6.31) (which is the same in the Coulomb and dipole gauges). By calculating the equations of motion for the oscillator variables $x_{\text{cav}} = \frac{d_{\text{cav}}}{\sqrt{f_{\text{cav}}}}$ and $x_{\text{mat}} = \frac{d_{\text{mat}}}{\sqrt{f_{\text{mat}}}}$ as in previous subsections, we recover the equations of the SpC model [Eq. (6.2)]. However, we can again make another choice for the variables to obtain an alternative model of harmonic oscillators. Using the oscillator $x_{\text{cav}} = \frac{d_{\text{cav}}}{\sqrt{f_{\text{cav}}}}$ as considered previously and the new oscillator $x'_{\text{mat}} = \frac{\sqrt{f_{\text{mat}}}}{\omega_{\text{mat}}} p_{\text{mat}}$, the equations of motion are

$$\ddot{x}'_{\text{cav}} + (\omega_{\text{cav}}^2 - 4g_{\text{SpC}}'^2) x_{\text{cav}} - 2g'_{\text{SpC}} \dot{x}'_{\text{mat}} = 0, \quad (6.51a)$$

$$\ddot{x}'_{\text{mat}} + \omega_{\text{mat}}^2 x'_{\text{mat}} + 2g'_{\text{SpC}} \dot{x}_{\text{cav}} = 0, \quad (6.51b)$$

with the coupling strength $g'_{\text{SpC}} = g_{\text{SpC}} \sqrt{\frac{\omega_{\text{cav}}}{\omega_{\text{mat}}}}$, slightly modified compared to the SpC value g_{SpC} used in Eq. (6.19). We have thus shown that the results of the SpC model can also be obtained with a model where the coupling terms are proportional to the time derivatives \dot{x}_{cav} and \dot{x}'_{mat} , but in this case the cavity frequency has been renormalized from ω_{cav} to $\sqrt{\omega_{\text{cav}}^2 - 4g_{\text{SpC}}'^2}$.

6.7 Summary

We have analyzed the application of classical coupled harmonic oscillator models to describe nanophotonic systems under ultrastrong coupling and the connection of these models with quantum descriptions. The study mainly focuses on the two classical models typically used in this context, here referred to as the Spring Coupling (SpC) and Modified Coupling (MC) models, where the difference relies on whether the coupling term is proportional to the displacement of the oscillators (SpC model) or to their velocities (MC model). The choice between these models typically does not have significant consequences in the weak and strong coupling regimes, where both can be approximated to the same linearized model (this approximation is equivalent to the rotating-wave approximation in quantum models). However, the SpC model and the MC model result in very different eigenvalues in the ultrastrong coupling regime. We demonstrate that the SpC model represents light-matter coupling via Coulomb interactions, such as those governing the interaction between different molecules and between molecules and small plasmonic nanoparticles, and that this model results in the same eigenvalue spectra as the quantum Hopfield Hamiltonian without diamagnetic term. On the other hand, the MC model reproduces the spectra of systems for which the diamagnetic term should be present in the Hamiltonian, corresponding to systems where matter excitations interact with transverse electromagnetic fields (for example, in conventional dielectric cavities). We thus show that the SpC and MC models are capable of capturing the same information than a cavity-QED description about the spectra of nanophotonic systems under ultrastrong coupling, but using a simpler framework. We generalize this discussion in Sec. 6.6 to other alternative models of classical oscillators. We summarize in Table 6.1 all the correspondences between classical and cavity-QED models that we have discussed in this chapter.

Additionally, classical oscillator models are typically used to calculate the eigenvalues of the system, but we also discuss how they provide other experimentally measurable magnitudes in three canonical systems of nanophotonics. We first show that the MC model can be applied to calculate the electric field distribution of each hybrid mode in a dielectric cavity filled by a single molecule. On the other hand, for the SpC model, we consider a molecule situated near a metallic nanoparticle and calculate the near-field distribution and the far-field scattering spectra. Last, the two models are combined when considering an ensemble of molecules that interact with each other due to Coulomb interactions (SpC model) and also with

Diarmagnetic term	Included		Not included
Type of interaction	Transverse cavity mode-dipole interaction		Dipole-dipole Coulomb interaction
Cavity QED Hamiltonian	Coulomb gauge	Dipole gauge	Coulomb and dipole gauge
Cavity QED Hamiltonian	$\hat{H}_{\text{Coul}}^{\text{cav}} = h\omega_{\text{cav}} \left(\hat{a}^\dagger \hat{a} + \frac{1}{2} \right) + h\omega_{\text{mat}} \left(\hat{b}^\dagger \hat{b} + \frac{1}{2} \right) + ihg_{\text{SpC}} \sqrt{\frac{\omega_{\text{mat}}}{\omega_{\text{cav}}}} \left(\hat{a} + \hat{a}^\dagger \right) \left(\hat{b} - \hat{b}^\dagger \right) + h\frac{g_{\text{MC}}}{\omega_{\text{cav}}} \left(\hat{a} + \hat{a}^\dagger \right)^2$	$\hat{H}_{\text{Dip}}^{\text{cav}} = h\omega_{\text{cav}} \left(\hat{a}^\dagger \hat{a} + \frac{1}{2} \right) + h\omega_{\text{mat}} \left(\hat{b}^\dagger \hat{b} + \frac{1}{2} \right) - ihg_{\text{SpC}} \sqrt{\frac{\omega_{\text{cav}}}{\omega_{\text{mat}}}} \left(\hat{a} - \hat{a}^\dagger \right) \left(\hat{b} + \hat{b}^\dagger \right) + h\frac{g_{\text{MC}}}{\omega_{\text{mat}}} \left(\hat{b} + \hat{b}^\dagger \right)^2$	$\hat{H}^{\text{cav-dip}} = h\omega_{\text{cav}} \left(\hat{a}^\dagger \hat{a} + \frac{1}{2} \right) + h\omega_{\text{mat}} \left(\hat{b}^\dagger \hat{b} + \frac{1}{2} \right) + ihg_{\text{SpC}} \left(\hat{a} + \hat{a}^\dagger \right) \left(\hat{b} + \hat{b}^\dagger \right)$
Classical model with coupling term $\propto \hat{x}_{\text{cav}}, \hat{x}_{\text{mat}}$	<p>Alternative model 1</p> $\ddot{x}_{\text{cav}} + (\omega_{\text{cav}}^2 + 4g_{\text{MC}}^2)x_{\text{cav}} - 2g_{\text{SpC}}\omega_{\text{mat}}x'_{\text{mat}} = 0$ $\ddot{x}_{\text{mat}} + \omega_{\text{mat}}^2 x'_{\text{mat}} - 2g_{\text{SpC}}\omega_{\text{mat}}x_{\text{cav}} = 0$	<p>Alternative model 2</p> $x'_{\text{cav}} + \omega_{\text{cav}}^2 x_{\text{cav}} + 2g_{\text{SpC}}\omega_{\text{cav}}x_{\text{mat}} = 0$ $\ddot{x}_{\text{mat}} + (\omega_{\text{mat}} + 4g_{\text{MC}})x_{\text{mat}} + 2g_{\text{SpC}}\omega_{\text{cav}}x_{\text{cav}} = 0$	<p>SpC model</p> $\ddot{x}_{\text{cav}} + \omega_{\text{cav}}^2 x_{\text{cav}} + 2g_{\text{SpC}}\sqrt{\omega_{\text{cav}}\omega_{\text{mat}}}x_{\text{mat}} = 0$ $\ddot{x}_{\text{mat}} + \omega_{\text{mat}}^2 x_{\text{mat}} + 2g_{\text{SpC}}\sqrt{\omega_{\text{cav}}\omega_{\text{mat}}}x_{\text{cav}} = 0$
Classical model with coupling term $\propto \hat{x}_{\text{cav}}, \hat{x}_{\text{mat}}$	<p>MC model</p> $\ddot{x}_{\text{cav}} + \omega_{\text{cav}}^2 x_{\text{cav}} + 2g_{\text{MC}}\dot{x}_{\text{mat}} = 0$ $\ddot{x}_{\text{mat}} + \omega_{\text{mat}}^2 x_{\text{mat}} - 2g_{\text{MC}}\dot{x}_{\text{cav}} = 0$		<p>Alternative model 3</p> $\ddot{x}'_{\text{mat}} + \omega_{\text{mat}}^2 x'_{\text{mat}} + 2g_{\text{SpC}}\sqrt{\frac{\omega_{\text{mat}}}{\omega_{\text{cav}}}}x_{\text{cav}} = 0$ $\ddot{x}_{\text{cav}} + (\omega_{\text{cav}}^2 - 4g_{\text{MC}}^2\frac{\omega_{\text{mat}}}{\omega_{\text{cav}}})x_{\text{cav}} - 2g_{\text{SpC}}\sqrt{\frac{\omega_{\text{mat}}}{\omega_{\text{cav}}}}x'_{\text{mat}} = 0$
Magnitudes of the oscillators	$x_{\text{cav}} = \sqrt{\varepsilon_0} \mathcal{V}_{\text{eff}} \mathcal{A} \frac{x'_{\text{mat}}}{d}$ $x_{\text{mat}} = \sqrt{f_{\text{mat}}} \left(p_{\text{Cou}} + \frac{d}{f_{\text{mat}}} \right)$	$x_{\text{cav}} = \sqrt{\varepsilon_0} \mathcal{V}_{\text{eff}} \mathcal{A} \frac{x'_{\text{cav}}}{d}$ $x_{\text{mat}} = \sqrt{f_{\text{mat}}} \left(\Pi_{\text{Dip}} + \varepsilon_0 \mathcal{V}_{\text{eff}} \mathcal{A} - d \right)$	$x_{\text{cav}} = \frac{d_{\text{cav}}}{\sqrt{f_{\text{cav}}}}$ $x'_{\text{mat}} = \frac{\sqrt{f_{\text{mat}}}}{\omega_{\text{mat}}} p_{\text{mat}}$ $x_{\text{mat}} = \frac{d_{\text{mat}}}{\sqrt{f_{\text{mat}}}}$
Frequencies of the hybrid modes	$\omega_{\pm} = \frac{1}{\sqrt{2}} \sqrt{\omega_{\text{cav}}^2 + \omega_{\text{mat}}^2 + 4g_{\text{MC}}^2} \pm \sqrt{(\omega_{\text{cav}}^2 + \omega_{\text{mat}}^2 + 4g_{\text{MC}}^2)^2 - 4\omega_{\text{cav}}^2 \omega_{\text{mat}}^2}$		$\omega_{\pm} = \frac{1}{\sqrt{2}} \sqrt{\omega_{\text{cav}}^2 + \omega_{\text{mat}}^2} \pm \sqrt{(\omega_{\text{cav}}^2 - \omega_{\text{mat}}^2)^2 + 16g_{\text{SpC}}^2 \omega_{\text{cav}} \omega_{\text{mat}}}$

Table 6.1: Summary of the correspondences between the classical coupled harmonic oscillator models and the cavity-QED Hamiltonians. We consider the coupling between a dipole (representing e.g. a molecular excitation) and a dielectric cavity (with transverse electromagnetic modes) or a plasmonic nanocavity (dipole-dipole coupling via Coulomb interactions). The coupling with transverse modes is described in the Coulomb (second column) and dipole (third column) gauges, while the dipole-dipole coupling is described in the same way in both gauges as indicated in the fourth column. The fourth row shows the cavity-QED Hamiltonians that describe each of these situations. The fifth and the sixth rows indicate the corresponding equations of motion. The fifth mode corresponds to the models associated with coupling terms proportional to oscillator amplitudes, and the sixth row to models with coupling terms proportional to the time derivatives \dot{x}_{cav} and \dot{x}_{mat} [with coupling strengths g_{MC} given by Eq. (6.17) and g_{SpC} given by Eq. (6.19)]. We highlight in green the SpC and MC models, which are the main focus of this chapter except for Sec. 6.6, and for which the frequencies ω_{cav} and ω_{mat} are considered. We indicate with the yellow background the alternative models where we use renormalized frequencies, which also changes the coupling term. The seventh row includes the association between the amplitudes of the oscillators and physical magnitudes of the system, which is different for the models in the fifth and in the sixth row. The last row gives the frequencies of the two hybrid modes due to each type of interaction.

transverse electromagnetic modes of a cavity (MC model). In this case, we show that the response of the system can be obtained by considering that each transverse cavity mode interacts with a collective molecular excitation. The only effect of the molecule-molecule interactions is to modify the effective frequency of these collective excitations, and the MC model describes the relevant ultrastrong coupling between these collective excitations and the cavity modes.

MICROCAVITY PHONON POLARITONS IN THE WEAK, STRONG AND ULTRA STRONG COUPLING REGIMES

7.1 Introduction

We have discussed the phenomenology behind the strong and ultrastrong light-matter coupling regimes in Sec. 1.3 and in Chapter 6. In particular, strong coupling between cavity modes and vibrations can be achieved by filling classical Fabry-Pérot microcavities with molecules. We have further shown in Sec. 6.5.3 that the coupling between Fabry-Pérot modes and molecular vibrations can be described by simple models based on classical coupled harmonic oscillators or on cavity QED. Vibrational strong coupling has emerged as a new intriguing research topic, specially after it has been reported that it can lead to modification of fundamental material properties, triggering, for example, phase transitions [289] or modifying chemical reactions [61,62]. Recently, it was shown that molecular vibrational strong coupling could be achieved even on the nanometre scale, by exploiting localized phonon polaritons in hexagonal boron nitride (hBN) nanoresonators [91] and slabs [290] (localized phonon polaritons are excitations similar to localized plasmon polaritons that emerge due to the coupling between photons and collective vibrations of the ions of a polar material).

Remarkably, a detailed study and control of the coupling strength between photons and phonons in classical Fabry-Pérot microcavities is relatively unexplored terrain. Phonons have significant influence on many physical properties of crystals

[129], such as on the electrical and thermal conductivity, ferroelectricity [291], and superconductivity [292], so that controlling the coupling strength between infrared photons and phonons in microcavities may become an interesting platform for future fundamental and applied studies. For example, recent studies suggest that cavity-mediated strong light-phonon coupling may trigger quantum phase transitions without the need of an external pump [289].

In this chapter, we demonstrate that infrared microcavities comprising polar van der Waals materials are a versatile test bench to study the interaction of optical phonons and photons. Specifically, we study microcavities containing layers of hBN, which is an insulating polar material exhibiting phonons in the mid-infrared spectral range [87]. This system is described in more detail in Sec. 7.2. The theoretical analysis of the coupling between cavity modes and phonons is then performed in Sec. 7.3. We first calculate in Sec. 7.3.1 the coupling strength g of the system from the reflectivity calculated by transfer-matrix simulations. The value of g is extracted from the spectra by describing the system using a classical coupled harmonic oscillator model, based on the analysis of Chapter 6. We demonstrate that strong coupling can be achieved for layers as thin as a few nanometres, leading to the formation of microcavity phonon polaritons. Ultrastrong coupling is possible for thick layers, and we systematically trace the evolution from the weak to the ultrastrong coupling regime. Further, in Sec. 7.3.2 we show that a microscopic model that accounts for the interaction of phonons with Fabry-Pérot modes leads to an analytical expression of the coupling strength that agrees with the results of transfer-matrix simulations. The theoretical results presented in this chapter have also been verified experimentally by the groups of Luis Hueso and Rainer Hillenbrand from CIC nanoGUNE, and we show the comparison between the theoretical predictions and experimental data in Sec. 7.4. Last, we discuss in Sec. 7.5 how the dispersion of the cavity fully filled with hBN is directly connected with the intrinsic properties of hBN, such as with its bulk permittivity and dispersion.

7.2 Description of the system

In this section, we describe in more detail the hBN microcavities that we analyze in this chapter. We use Fabry-Pérot cavities containing hBN layers of variable thickness. A schematic diagram is shown in Fig. 7.1. The cavities are formed by planar layers, and all the interfaces are perpendicular to the z axis, as shown by the coordinates axes included in the scheme. In all the calculations the incident medium (i.e. the medium from which the system is illuminated) is vacuum, the substrate is CaF_2 and the mirrors are 20 nm-thick gold layers. The inside of the cavity, i.e. without considering the mirrors, extends from $z = 0$ to $z = L_{\text{cav}}$ (L_{cav} is the total thickness), and it contains a layer of thickness L_{hBN} placed between $z = L_1$ and $z = L_2$. Unless stated otherwise, we consider that the layer is in the center of the cavity, between $L_1 = \frac{L_{\text{cav}}}{2} - \frac{L_{\text{hBN}}}{2}$ and $L_2 = \frac{L_{\text{cav}}}{2} + \frac{L_{\text{hBN}}}{2}$. In many of the transfer-matrix simulations, and also in all the experiments shown in Sec. 7.4, the material of this layer is hBN, and we refer to this particular case as a

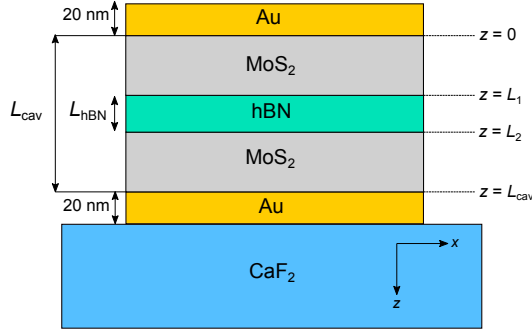


Figure 7.1: Schematic diagram of the hBN microcavities. We indicate the coordinates axes and the material and thickness of each layer. In some simulations, hBN is substituted by a material with constant permittivity $\varepsilon_{\text{hBN},\infty}$, PMMA or a material which has vibrations characterized by a weak oscillator strength.

hBN-filled cavity. In other simulations, we replace hBN by a material with constant permittivity $\varepsilon_{\text{hBN},\infty}$, which corresponds to the high-frequency permittivity of hBN. We refer to these cavities as *bare cavities*, because the contribution of the hBN phonons is eliminated. The rest of the cavity (the layers between $z = 0$ and $z = L_1$ and between $z = L_2$ and $z = L_{\text{cav}}$) is filled by MoS₂, which does not show any resonant feature in the analyzed range of frequencies.

In the transfer-matrix simulations, we have modelled the materials of the system as follows. For the incident medium we use the vacuum permittivity, and the (relative) permittivity of the substrate material CaF₂ is $\varepsilon_{\text{CaF}_2} = 1.882$. The gold mirrors are described by a Drude function that fits the low-frequency experimental data from Ref. [71], i.e. the permittivity follows Eq. (1.25) with plasma frequency $\omega_{\text{p,Au}} = 73114.15 \text{ cm}^{-1}$ and damping frequency $\gamma_{\text{Au}} = 571.04 \text{ cm}^{-1}$ [230].

We model hBN with a diagonal permittivity tensor $\overset{\leftrightarrow}{\varepsilon}_{\text{hBN}}(\omega)$, in order to take into account the anisotropy of this material. hBN is characterized by a layered atomic structure, so that the phonons that are polarized along the plane of the atomic layers (in-plane phonons) have different frequencies compared to those polarized in the normal direction, i.e. parallel to the anisotropic axis (\parallel , out-of-plane phonons). In our configuration, the plane of the atomic layers is parallel to all the Fabry-Pérot interfaces ($x - y$ plane). We thus have $\overset{\leftrightarrow}{\varepsilon}_{\text{hBN}}(\omega) = \text{diag}(\varepsilon_{\text{hBN}}(\omega), \varepsilon_{\text{hBN}}(\omega), \varepsilon_{\text{hBN},\parallel}(\omega))$, where we omit a second subscript in the x and y components for brevity (notice that the x and y components are identical). The in-plane permittivity tensor component $\varepsilon_{\text{hBN}}(\omega)$ follows a Lorentzian function given by Eq. (1.42). For our analysis, the exact value of the TO phonon frequency ω_{TO} determines the detuning between the cavity mode and the phonon, which is a crucial parameter when analyzing strong coupling. Therefore, to obtain the value of this parameter that is consistent with the experimental samples, the

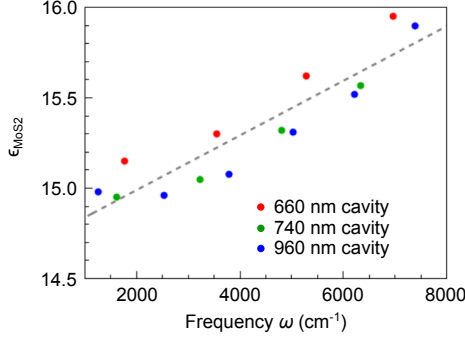


Figure 7.2: Linear fitting of the permittivity of MoS₂. The dots indicate the experimental resonant frequency of the different Fabry-Pérot modes and the corresponding permittivity extracted from these values according to the procedure described in the text, for three cavities fully filled by MoS₂ of nominal thickness $L_{\text{cav}} = 660$ nm (red dots), $L_{\text{cav}} = 740$ nm (green dots) and $L_{\text{cav}} = 960$ nm (blue dots). The dashed line corresponds to the linear fitting of all dots, given by Eq. (7.1).

experimental collaborators measured the reflectivity spectra of a 100 nm-thick hBN layer. A clear resonance was observed at $\omega_{\text{TO}} = 1364$ cm $^{-1}$, which is the value that we consider in the simulations. This frequency is very close to the value $\omega_{\text{TO}} = 1360$ cm $^{-1}$ reported in Ref. [91]. For all the other parameters in Eq. (1.42) we use the values of Ref. [91]: the high-frequency permittivity $\epsilon_{\text{hBN},\infty} = 4.52$, the LO phonon frequency $\omega_{\text{LO}} = 1610$ cm $^{-1}$ and damping frequency $\gamma = 5$ cm $^{-1}$.

Equation (1.42) properly describes the optical response of hBN in most of the results of this chapter, because we focus on calculating the response of the system to normal incident light. In this case, the electric fields are directed along the x direction and thus hBN can be treated as an isotropic material of permittivity $\epsilon_{\text{hBN}}(\omega)$. However, in Sec. 7.4.1 we consider focused illumination to describe experimental data, where it is necessary to take the anisotropy of hBN into account. In this case, the permittivity tensor component along the z axis $\epsilon_{\text{hBN},\parallel}(\omega)$ follows the same Lorentzian function as in Eq. (1.42), except that the values of the parameters are $\epsilon_{\text{hBN},\infty} = 4.52$, $\omega_{\text{TO},\parallel} = 746$ cm $^{-1}$, $\omega_{\text{LO},\parallel} = 819$ cm $^{-1}$ and $\gamma_{\parallel} = 4$ cm $^{-1}$ (taken from Ref. [91]).

In order to obtain the permittivity of MoS₂, the experimental collaborators fabricated three microcavities fully filled by MoS₂ of different nominal thickness: $L_{\text{cav}} = 660$ nm, 740 nm and 960 nm. The geometry is the same as in Fig. 7.1 but without the hBN layer. The reflectivity spectra was measured to obtain the frequencies of the Fabry-Pérot modes for each cavity up to 8000 cm $^{-1}$. We then perform transfer-matrix simulations (Sec. 1.1.1) of the cavities and find the value of the permittivity ϵ_{MoS_2} required to reproduce the position of the experimental dips. We show in Fig. 7.2 the experimental frequencies of the dips for the three cavities and the corresponding value of ϵ_{MoS_2} that we obtain from the theoretical

analysis. A linear fitting of these results (dashed line) gives the permittivity that we use in the simulations:

$$\varepsilon_{\text{MoS}_2}(\omega) = 14.689 + 0.000151\omega, \quad (7.1)$$

where ω is in units of cm^{-1} .

Last, in some simulations in Sec. 7.5, we replace hBN with poly(methyl methacrylate) (PMMA) or with a molecule presenting a vibration of low oscillator strength. For PMMA, we use the permittivity given by Eq. (1.41), with high-frequency permittivity $\varepsilon_\infty = 1.99$, vibrational frequency $\omega_{\text{vib}} = 1742 \text{ cm}^{-1}$, damping frequency $\gamma = 13 \text{ cm}^{-1}$ and oscillator strength $f = (223.76 \text{ cm}^{-1})^2$ [293]. When we consider molecules with weak oscillator strength in Sec. 7.5, we use the same values as for PMMA, except for a 100 times smaller oscillator strength: $f = (22.376 \text{ cm}^{-1})^2$.

7.3 Evolution of the coupling strength with the cavity filling factor

7.3.1 Transfer-matrix simulations and classical coupled harmonic oscillator model

In this section, we explore the coupling between phonons in hBN and Fabry-Pérot cavity modes. With this purpose, we first calculate the evolution of the reflectivity spectra as the cavity resonance is detuned from the phonon frequencies, and then analyze these results using a coupled harmonic oscillator model that gives the coupling strength g between phonons and cavity modes. To obtain the spectra, we perform transfer-matrix simulations of the reflectivity spectra under a normal incident planewave as a function of the total cavity length, L_{cav} , while keeping fixed the thickness of the hBN layer (L_{hBN}) that is placed in the middle of the cavity. The frequencies of the modes of the system are obtained from the poles of the reflection and transmission coefficients of the system, which are calculated from the analytical expressions of $r_{\text{total}}^{s(p)}$ and $t_{\text{total}}^{s(p)}$ by extending the permittivities of the materials to complex frequencies (as explained in Sec. 1.1.1). The mode frequencies are very close to the dips in the reflectivity spectra (see, e.g., Fig. 1.1), and therefore, we can also identify the modes of the system by the frequencies of minimum reflectivity. This method is particularly useful to obtain modes from experimental data.

We first consider a thin layer of $L_{\text{hBN}} = 10 \text{ nm}$, and compare calculations for the bare cavity (i.e. with the hBN layer substituted by a medium with permittivity $\varepsilon_{\text{hBN},\infty}$, Fig. 7.3a) and the hBN-filled cavity (Fig. 7.3b). We observe that the first ($j = 1$) and the third ($j = 3$) modes of the bare cavity ($\omega_{\text{cav}}^{(j)}$ indicated by colored dashed lines in Fig. 7.3a) split into an upper and a lower branch when the hBN layer is included ($\omega_+^{(j)}$ and $\omega_-^{(j)}$ in Fig. 7.3b). Importantly, the anticrossing of the branches at the TO phonon frequency manifests the typical signature of

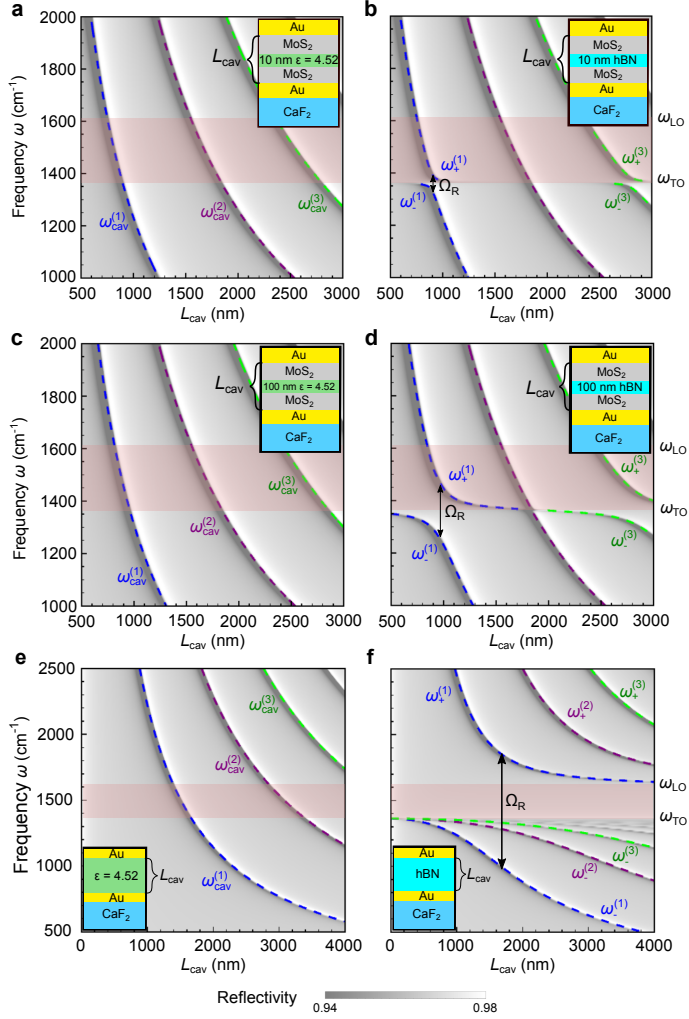


Figure 7.3: Reflectivity spectra calculated with transfer-matrix simulations. a-b) Theoretical calculations of the reflectivity spectra of a cavity embedding in its center a 10 nm layer of (a) a material with the high-frequency-permittivity of hBN, $\epsilon_{\text{hBN},\infty}$, and (b) hBN. The reflectivity spectra is calculated for normal incidence and plotted as a function of the frequency of the incident light and the total thickness of the cavity, L_{cav} . The shadowed area highlights the Reststrahlen band of the in-plane phonon, delimited by the ω_{TO} and ω_{LO} frequencies. The dashed lines represent the frequencies (a) of the bare cavity modes $\omega_{\text{cav}}^{(j)}$ and (b) of the polariton modes $\omega_{\pm}^{(j)}$ and $\omega_{-}^{(j)}$, as obtained from the poles of the reflection and transmission coefficients. The Rabi splitting Ω_{R} in panel (b) is indicated by the arrow. c-d) Same as in panels (a) and (b), for a 100 nm layer of a material with permittivity $\epsilon_{\text{hBN},\infty}$ or of hBN. e-f) Same as in panels (a) and (b), for a cavity fully filled by a material with permittivity $\epsilon_{\text{hBN},\infty}$ or with hBN. The structures analyzed are sketched in the insets.

coupling between two modes. The second cavity mode, in contrast, does not show any splitting of the reflection dips and thus reveals the absence of coupling, which can be explained by the vanishing electric field intensity of this mode in the cavity center (for further details see the discussion of Fig. 7.5).

In Figs. 7.3c and d, we show the reflectivity spectra of a bare cavity and a hBN-filled cavity embedding a thicker layer of 100 nm, respectively. While the spectra of the bare cavity is very similar for layers of thickness of 10 nm and 100 nm (compare Figs. 7.3a and c), we observe for the hBN-filled cavity a much larger anticrossing in the first and third modes for $L_{\text{hBN}} = 100$ nm than for $L_{\text{hBN}} = 10$ nm. Specifically, the Rabi splitting Ω_{R} of the first mode, corresponding to the minimum splitting between the polaritonic modes $\omega_{+}^{(1)} - \omega_{-}^{(1)}$, increases from 63 cm^{-1} to 211 cm^{-1} . We corroborate the increase of the Rabi splitting for thicker hBN layers by considering cavities fully filled by this material (Fig. 7.3e for the bare cavity and Fig. 7.3f for the hBN-filled cavity). We can identify an anticrossing between the hBN TO phonon and all cavity modes, yielding the polaritonic modes $\omega_{\pm}^{(j)}$ for all j [260], contrary to Figs. 7.3b and d, where coupling is observed only for odd j . Further, a much larger spectral separation of the upper and lower polariton branches occurs as compared to the previous cases. Indeed, there is not any polaritonic mode in the spectral range $\omega_{\text{TO}} \lesssim \omega \lesssim \omega_{\text{LO}}$ that corresponds to the Reststrahlen band (purple area in Fig. 7.3f). We determine a Rabi splitting of $\Omega_{\text{R}} = 856 \text{ cm}^{-1}$, which is larger than the Reststrahlen band (246 cm^{-1}).

For a quantitative analysis of the coupling between the hBN phonons and the microcavity photons in the transfer-matrix calculations, we model the phonon-photon interaction with two coupled harmonic oscillators. We have discussed in detail in Sec. 6.5.3 that the interaction between Fabry-Pérot modes and the collective excitation of molecular vibrations can be described classically with the modified coupling (MC) model, obtaining the same results as for a description based on cavity QED. We use the same classical model to describe the photon-phonon coupling in the system of this chapter, as phonons are collective oscillations of ions of each unit cell, with the vibrations of the ions in each cell playing a similar role than the vibrations of molecules (see also Sec. 7.3.2). On the other hand, in Chapter 6, we do not consider losses in the harmonic oscillator models for a simpler comparison with the Hermitian cavity-QED Hamiltonians. However, in the analysis of this chapter we need to include losses because the Rabi splitting is comparable to the width of the reflectivity dips for thin hBN layers (Fig. 7.3b), which implies that losses are not negligible. We include losses of the cavity modes and the phonon into the MC model by adding a friction term proportional to the oscillator velocities $\dot{x}_{\text{cav}}^{(j)}$ and \dot{x}_{mat} as

$$\ddot{x}_{\text{cav}}^{(j)} + \kappa \dot{x}_{\text{cav}}^{(j)} + (\omega_{\text{cav}}^{(j)})^2 x_{\text{cav}}^{(j)} - 2g \dot{x}_{\text{mat}} = 0, \quad (7.2a)$$

$$\ddot{x}_{\text{mat}} + \gamma \dot{x}_{\text{mat}} + \omega_{\text{TO}}^2 x_{\text{mat}} + 2g \dot{x}_{\text{cav}}^{(j)} = 0. \quad (7.2b)$$

In general, the eigenfrequencies of Eq. (7.2) cannot be expressed by a simple analytical expression, but such expression can be obtained for two typical situations.

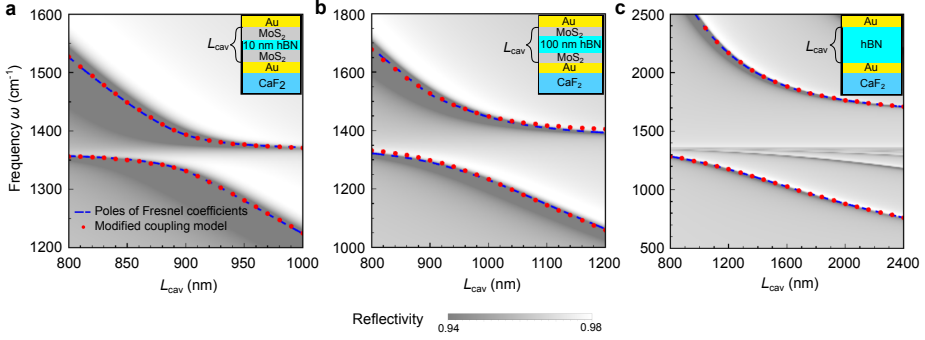


Figure 7.4: Frequency of the polaritonic states formed by the TO phonon and the first cavity mode, for a cavity (a) filled with a 10 nm layer of hBN, (b) filled with a 100 nm layer of hBN and (c) fully filled with hBN. The layers are placed at the center of the cavity. The contour plot shows the reflectivity spectra under normal incidence as a function of the incident frequency ω and the total thickness L_{cav} calculated with transfer-matrix simulations. Red dots show the polariton frequencies given by the MC model for (a) $g = 34 \text{ cm}^{-1}$, (b) $g = 105 \text{ cm}^{-1}$ and (c) $g = 428 \text{ cm}^{-1}$, and the blue dashed lines show the frequencies extracted from the poles of the Fresnel coefficients.

For small values of g , the polaritonic frequencies are (Sec. 1.3.1)

$$\omega_{\pm}^{(j)} = \frac{1}{2}(\omega_{\text{cav}}^{(j)} + \omega_{\text{TO}}) \pm \frac{1}{2} \text{Re} \left[\sqrt{\left(\omega_{\text{cav}}^{(j)} - \omega_{\text{TO}} + i \frac{\gamma - \kappa}{2}\right)^2 + 4g^2} \right].$$

On the other hand, if the losses κ and γ are negligible compared to g , we obtain the eigenfrequencies of the MC model analyzed in Sec. 6.2:

$$\omega_{\pm}^{(j)} = \frac{1}{\sqrt{2}} \sqrt{(\omega_{\text{cav}}^{(j)})^2 + \omega_{\text{TO}}^2 + 4g^2} \pm \sqrt{\left((\omega_{\text{cav}}^{(j)})^2 + \omega_{\text{TO}}^2 + 4g^2\right)^2 - 4(\omega_{\text{cav}}^{(j)})^2 \omega_{\text{TO}}^2}.$$

The purpose of using the MC model in this system is to determine the coupling strength g . With this aim, for a fixed thickness of the hBN layer, L_{hBN} , we choose the total thickness L_{cav} so that the cavity mode is resonant with the TO phonon, $\omega_{\text{cav}}^{(j)} = \omega_{\text{TO}}$, and we extract the polaritonic frequencies $\omega_{\pm}^{(j)}$ from the transfer-matrix simulations. Then, we obtain the value of g that minimizes the difference between the two frequencies obtained from this simulation and the analytical solution. For the latter, we use either between the two equations for $\omega_{\pm}^{(j)}$ above, depending on the coupling regime (we have verified that the results from these equations are a very good approximation of the exact Eq. (7.2) in their corresponding regimes of application). We follow this procedure to calculate all the values of g for the systems illustrated in Fig. 7.3. The coupling strength that we obtain for the first cavity mode is $g = 34 \text{ cm}^{-1}$ for the cavity embedding a 10 nm-thick hBN layer,

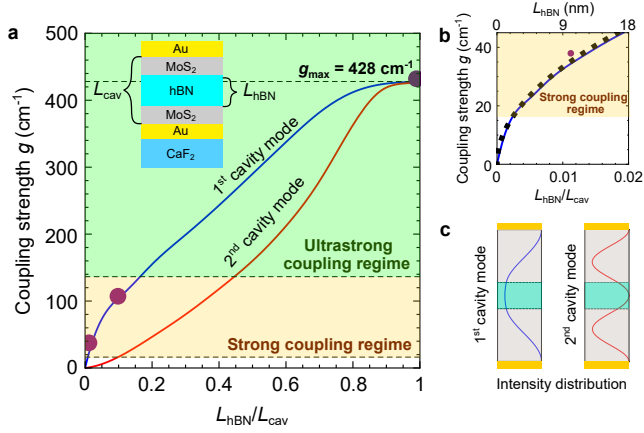


Figure 7.5: Evolution of the coupling strength as a function of the cavity filling factor. a) Calculated coupling strength g between the TO phonon and the bare-cavity modes, for an hBN layer of thickness L_{hBN} in the middle of a cavity of thickness L_{cav} , as sketched in the inset. The evolution of g for varying L_{hBN} is shown for the first (blue solid line) and the second (red solid line) cavity modes. The coupling strengths corresponding to the strong coupling regime are highlighted by the beige area, and the green area corresponds to the ultrastrong coupling regime. b) Zoom into the panel (a) for small filling factors $L_{\text{hBN}}/L_{\text{cav}}$ for the first cavity mode (blue line). The analytical approximation $g = 332\sqrt{L_{\text{hBN}}/L_{\text{cav}}}$ cm⁻¹ [according to Eq. (7.20)] is shown by black dots. Purple dots in panels (a) and (b) indicate the experimental coupling strengths g_{exp} . c) Sketch of the intensity distribution of the electric field of the first and second cavity modes. We note that the hBN layer is placed at the maximum of the intensity of the first cavity mode and at the minimum for the second cavity mode.

$g = 105$ cm⁻¹ for the 100 nm-thick layer and $g = 428$ cm⁻¹ for the cavity fully filled by hBN. These values are very close to half the Rabi splitting Ω_{R} , as expected from the analysis of Chapter 6.

Further, although we have calculated g for the particular case where the cavity is tuned to the TO phonon, we show in Fig. 7.4 that these values of g enable to fully describe the evolution of the polaritonic frequencies as the cavity is detuned. Specifically, Fig. 7.4 shows the polaritonic frequencies obtained from the MC model with (a) $g = 34$ cm⁻¹, (b) $g = 105$ cm⁻¹ and (c) $g = 428$ cm⁻¹ (red dots) compared with those given by the poles of the total reflection and transmission coefficients for (a) a cavity with a 10 nm-thick hBN layer, (b) a cavity with a 100 nm-thick hBN layer, and (c) a fully filled cavity (dashed blue lines), as a function of the total cavity thickness L_{cav} . These values are superimposed to the contour plot of the calculated reflectivity of the cavity. The frequencies obtained from the MC model, from the poles of the Fresnel coefficients and from the reflectivity minima are almost identical for all L_{cav} and for the three cavities considered. This agreement shows the adequacy of the MC model in the description of this system.

We generalize next this calculation and study systematically the evolution of the coupling strength with the thickness L_{hBN} of the hBN layer. We plot in Fig.

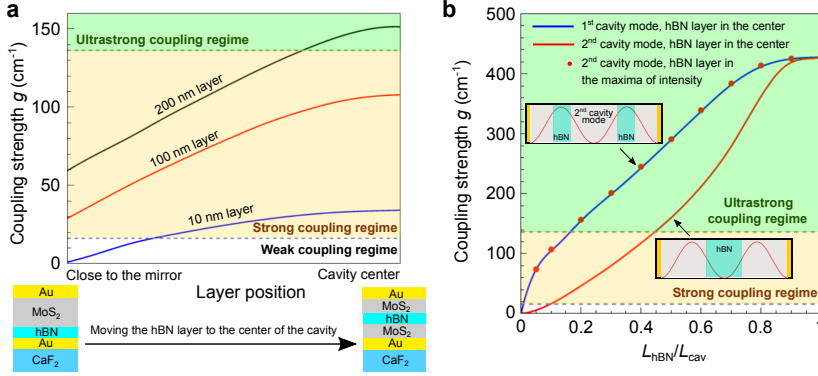


Figure 7.6: Dependence of the coupling strength on the hBN layer position. a) Coupling strength g between the TO phonon and the first cavity mode as a function of the hBN layer position, for $L_{\text{hBN}} = 10$ nm (blue line), $L_{\text{hBN}} = 100$ nm (red line) and $L_{\text{hBN}} = 200$ nm (black line). The layer is moved from the position closest to the bottom gold mirror (corresponding to the left of the x axis in the figure, see sketch) to the center of the cavity (right of the x axis). b) Evolution of the coupling strength g as a function of the filling factor $L_{\text{hBN}}/L_{\text{cav}}$. Blue line: the hBN layer is placed in the middle of the cavity, interacting with the first cavity mode. Red line: the hBN layer is placed in the middle of the cavity, interacting with the second cavity mode. Red dots: the hBN layer is separated into two equally thick hBN layers, which are centered at the intensity maxima of the second cavity mode, interacting with this mode. The insets show the intensity distribution of the second cavity mode interacting with either a single hBN layer of thickness L_{hBN} in the center of the cavity or two hBN layers of thickness $\frac{L_{\text{hBN}}}{2}$. Solid lines correspond to the results shown in Fig. 7.5. The beige area indicates the values of g in the strong coupling regime, while the green area corresponds to the ultrastrong coupling regime.

7.5a the resulting coupling strength g as a function of the filling factor $L_{\text{hBN}}/L_{\text{cav}}$ for the first (blue line) and the second (red line) cavity modes. We observe that g increases with the filling factor for both modes, more strongly for the first mode, which is a consequence of the intensity distribution of the electric field across the cavity (Fig. 7.5c). The second cavity mode exhibits an intensity minimum in the center of the cavity, where the hBN layer is located. Thus, the coupling between hBN phonons and the second cavity mode is generally much smaller than for the first cavity mode, that exhibits its intensity maximum in the cavity center. This observation is consistent with the absence of a polariton gap for the second cavity mode in Figs. 7.3b and d. The interaction between the TO phonon and the second cavity mode remains weak until the hBN layer is thick enough to sufficiently overlap with the off-center intensity maxima of the cavities (shown in the right panel of Fig. 7.5c).

We can identify the weak and strong coupling regimes in Fig. 7.5a according to the fulfillment of the conditions $\frac{g}{\kappa+\gamma} < \frac{1}{4}$ (blank area) and $\frac{g}{\kappa+\gamma} > \frac{1}{4}$ (beige area), respectively (see Sec. 1.3.1). For the first cavity mode, remarkably, the strong coupling regime starts for $L_{\text{hBN}}/L_{\text{cav}} \approx 0.0025$, which corresponds to hBN slabs for about 3 nm thickness (about four atomic hBN layers, see Fig. 7.5b for

a zoom into Fig. 7.5a for small filling factors). Moreover, the usual condition for ultrastrong coupling, $g/\omega_{\text{TO}} > 0.1$ (highlighted by the green area in Fig. 7.5a), is fulfilled for hBN layers of thickness $L_{\text{hBN}} > 148$ nm. Interestingly, we find that g saturates for the first-order mode when $L_{\text{hBN}}/L_{\text{cav}} \gtrsim 0.8$ and for the second-order mode when $L_{\text{hBN}}/L_{\text{cav}} \gtrsim 0.9$. The maximum coupling strength is obtained for both modes when the cavity is fully filled with hBN, with $g_{\text{max}} = 428$ cm⁻¹. In this case, the ratio $g_{\text{max}}/\omega_{\text{TO}}$ reaches up to 0.31. These results show the versatility of the hBN-filled microcavities to explore the light-matter coupling regimes, ranging from weak to ultrastrong coupling.

The influence of the position of the hBN layer on the coupling strength is emphasized in Fig. 7.6. We show in Fig. 7.6a the dependence of g on the position of a 10 nm hBN layer (blue line), a 100 nm hBN layer (red line) and a 200 nm hBN layer (black line) placed inside the cavity. The total thickness of the cavity is chosen so that the first cavity mode is resonant with the TO phonon frequency, and MoS₂ is again chosen as the spacer material (see sketches). Displacing the 10 nm hBN layer from a position near a mirror (left of the x axis in the figure) to the center of the cavity (right of the axis) induces a transition from the weak to the strong coupling regime. In a similar way, the coupling strength for the cavity containing a 100 nm hBN layer is tuned along a range of values corresponding to the strong coupling regime. Last, for $L_{\text{hBN}} = 200$ nm, the system is tuned from the strong to the ultrastrong coupling regime. Therefore, the results in Fig. 7.6a show that displacing a hBN layer of fixed thickness inside the cavity also makes possible to control the coupling strength [294].

Further, in Fig. 7.6b we plot the coupling strength g as a function of the filling factor $L_{\text{hBN}}/L_{\text{cav}}$ for different situations. As we have already shown in Fig. 7.5a, when the hBN layer is placed in the center of the cavity, the coupling strength with the second cavity mode (red line) is generally much smaller than with the first mode (blue line), because in this position the intensity of the cavity mode vanishes for the former and is maximum for the latter. For comparison, we consider a situation that maximizes the coupling strength with the second cavity mode (red dots). To obtain these results, we calculate the intensity distribution associated with the mode and place two identical hBN layers of thickness $\frac{L_{\text{hBN}}}{2}$ centered in the maxima (antinodes). We observe that the evolution of g is almost identical for the first cavity mode with a hBN layer in the center of the cavity and for the second mode with the layers in the positions of maximum intensity of this mode.

Last, we note that the MC model used here treats each cavity mode of order j independently, i.e. that different cavity modes do not interact with each other and thus the coupling between hBN and each cavity mode is described by a separate Eq. (7.2). For the cavities that we analyze in this work, which are designed so that the TO phonon interacts mostly with the first cavity mode, the results in Fig. 7.4 show that this approach is appropriate. However, we have found that for thicker cavities where higher-order modes are tuned to the TO phonon, the MC model does not always describe well the position of the polaritonic frequencies as obtained from the transfer-matrix simulations. We believe that solving this discrepancy requires to include in the MC model the possibility of coupling different

modes with each other, for instance following an approach based on quasinormal modes [295, 296]. However, the analysis in this and the following section would be only weakly affected by these effects.

7.3.2 Microscopic model of interaction between phonons and Fabry-Pérot modes

Coupling strength of a TO phonon with a Fabry-Pérot cavity mode

In Sec. 7.3.1, we have described how the coupling strength g in hBN cavities can be calculated numerically from transfer-matrix simulations and the classical MC model. We now present an alternative approach based on the microscopic interaction between the phononic material and the modes of a Fabry-Pérot cavity, which allows for a derivation of an approximate analytical expression for g , and can give additional physical insight about the coupling. An analogous approach has been followed in Ref. [297] to model the coupling strength between molecules and guided nanowire modes.

In this derivation, we consider a simplified picture where we model each unit cell of hBN as a harmonic oscillator characterized by a transition dipole moment \mathbf{d}_n . The dipole is induced by the vibrations of the ions. From this perspective, the material is a collection of N_{cell} dipoles interacting with the cavity mode. Due to the homogeneity of the material, the transition dipole moments of all unit cells are the same: $\mathbf{d}_n = \mathbf{d}$. All dipoles are oriented parallel to the electric field, and in order to deduce the magnitude $d_n = |\mathbf{d}_n|$, we first consider the electric susceptibility χ_{pol} , which for a polar material such as hBN is

$$\chi_{\text{pol}}(\omega) = \varepsilon_{\infty} \frac{\omega_{\text{LO}}^2 - \omega_{\text{TO}}^2}{\omega_{\text{TO}}^2 - \omega^2 - i\omega\gamma}. \quad (7.3)$$

From this expression, we can directly obtain the polarizability α_n of each dipole induced in an unit cell of volume $\mathcal{V}_{\text{cell}}$. We consider that the polarization density \mathbf{P} is related to the electric field \mathbf{E} as $\mathbf{P} = \frac{\alpha_n}{\mathcal{V}_{\text{cell}}} \mathbf{E} = \varepsilon_0 \chi_{\text{pol}} \mathbf{E}$, and we therefore obtain

$$\alpha_n(\omega) = \varepsilon_0 \mathcal{V}_{\text{cell}} \chi_{\text{pol}}(\omega). \quad (7.4)$$

We can now relate the transition dipole moment d_n and the classical polarizability by [67]

$$\alpha_n(\omega) = \frac{2\omega_{\text{TO}}}{\hbar} \frac{d_n^2}{\omega_{\text{TO}}^2 - \omega^2 - i\omega\gamma}, \quad (7.5)$$

and, from Eqs. (7.3)–(7.5):

$$d_n = \sqrt{\frac{\hbar}{2\omega_{\text{TO}}} \mathcal{V}_{\text{cell}} \varepsilon_0 \varepsilon_{\infty} (\omega_{\text{LO}}^2 - \omega_{\text{TO}}^2)}. \quad (7.6)$$

This expression allows us to characterize the coupling strength g_n between the dipole associated to a particular unit cell and the cavity mode with quantized

electric field $\hat{\mathbf{E}}(\mathbf{r})$. This electric field corresponds to a bare cavity where hBN is substituted by a material of frequency-independent, real permittivity ε_∞ (i.e., without considering the resonant polarizability of the unit cells). In this derivation, we consider normal incidence of the excitation light, as done for all transfer-matrix simulations in Sec. 7.3.1 (however, the following derivation can be easily generalized for light incident at an arbitrary angle). For the quantization of the field, we further assume that the mirrors of the cavity are perfect, so that the electric and magnetic energy of the modes are equal and the fields do not penetrate into the mirrors. The electric field of the Fabry-Pérot mode of order j resonant at frequency $\omega_{\text{cav}}^{(j)}$ is quantized as [273]

$$\hat{\mathbf{E}} = \mathbf{E}(\hat{a} + \hat{a}^\dagger) = \sqrt{\frac{\hbar\omega_{\text{cav}}^{(j)}}{2\varepsilon_0\mathcal{V}_{\text{eff}}}}\Xi(z)(\hat{a} + \hat{a}^\dagger)\mathbf{n}_x. \quad (7.7)$$

\hat{a} and \hat{a}^\dagger are the annihilation and creation operators of the cavity mode, respectively. The fields only vary along the z direction normal to the flat interfaces of the system, as given by the field profile $\Xi(z)$ (normalized so that $\Xi(z) = 1$ in the position where the field amplitude is maximum). The electric field is assumed to be polarized along the x axis, with unit vector \mathbf{n}_x . $\mathcal{V}_{\text{eff}} = S \int \varepsilon(z)|\Xi(z)|^2 dz$ is the effective volume of the field, where S is the effective surface area of the cavity and $\varepsilon(z)$ indicates the spatial distribution of the permittivities of the system. The value of the electric field $\mathbf{E}(\mathbf{r})$ of a Fabry-Pérot mode is related to the coupling strength g_n between that mode and the dipole excited in the unit cell at position \mathbf{r}_n , according to

$$\hbar g_n = -\mathbf{d}_n \cdot \mathbf{E}(\mathbf{r}_n). \quad (7.8)$$

Taking into account that the dipole moments and the electric field are parallel, we write this coupling strength as

$$g_n = -\sqrt{\frac{\omega_{\text{cav}}^{(j)} \omega_{\text{LO}}^2 - \omega_{\text{TO}}^2}{\omega_{\text{TO}} \cdot 4} \frac{\mathcal{V}_{\text{cell}} \varepsilon_\infty \Xi(z_n)^2}{S \int \varepsilon(z)|\Xi(z)|^2 dz}}. \quad (7.9)$$

As discussed in Sec. 6.4, the interaction of cavity modes with molecules can be done with the Hopfield Hamiltonian in the cavity-QED framework. We next consider the following Hopfield Hamiltonian associated with all the dipoles induced at the unit cells in the phononic material:

$$\hat{\mathcal{H}}_{\text{Hop}} = \hbar\omega_{\text{cav}}^{(j)}\hat{a}^\dagger\hat{a} + \hbar\omega_{\text{TO}} \sum_{n=1}^{N_{\text{cell}}} \hat{b}_n^\dagger \hat{b}_n + i\hbar(\hat{a} + \hat{a}^\dagger) \sum_{n=1}^{N_{\text{cell}}} (g_n \hat{b}_n - g_n^* \hat{b}_n^\dagger) + \frac{\hbar g^2}{\omega_{\text{TO}}} (\hat{a} + \hat{a}^\dagger)^2. \quad (7.10)$$

where \hat{b}_n and \hat{b}_n^\dagger are the annihilation and creation operator of the harmonic oscillator that represents each vibrational dipole, respectively. The next step is to write the Hamiltonian of the system in terms of the annihilation \hat{b}_c and creation \hat{b}_c^\dagger operators

of the bright collective excitation that represents the TO phonon,

$$\hat{\mathcal{H}}_{\text{Hop}} = \hbar\omega_{\text{cav}}^{(j)}\hat{a}^\dagger\hat{a} + \hbar\omega_{\text{TO}}\hat{b}_c^\dagger\hat{b}_c + \hbar\omega_{\text{TO}} \sum_{n=1}^{N_{\text{cell}}-1} \hat{c}_n^\dagger\hat{c}_n - i\hbar g(\hat{a} + \hat{a}^\dagger)(\hat{b}_c - \hat{b}_c^\dagger) + \frac{\hbar g^2}{\omega_{\text{TO}}}(\hat{a} + \hat{a}^\dagger)^2, \quad (7.11)$$

where we have also added the annihilation \hat{c}_n and creation \hat{c}_n^\dagger operators of the $N_{\text{cell}} - 1$ dark collective modes that are uncoupled to the cavity mode. Equation (7.11) can be derived from Eq. (7.10) by using the Dicke transformation

$$\sum_{n=1}^{N_{\text{cell}}} \hat{b}_n^\dagger\hat{b}_n = \hat{b}_c^\dagger\hat{b}_c + \sum_{n=1}^{N_{\text{cell}}-1} \hat{c}_n^\dagger\hat{c}_n, \quad \sum_{n=1}^{N_{\text{cell}}} g_n\hat{b}_n = g\hat{b}_c, \quad \sum_{n=1}^{N_{\text{cell}}} g_n^*\hat{b}_n^\dagger = g^*\hat{b}_c^\dagger, \quad (7.12)$$

where g takes the value [298]

$$g = \sqrt{\sum_{n=1}^{N_{\text{cell}}} |g_n|^2} \quad (7.13)$$

so that the commutation relation $[\hat{b}_c, \hat{b}_c^\dagger] = 1$ is fulfilled. The operators of the dark modes fulfill the commutation relations $[\hat{c}_{n_1}, \hat{c}_{n_2}^\dagger] = \delta_{n_1, n_2}$ and $[\hat{b}_c, \hat{c}_n^\dagger] = 0$. Thus, Eq. (7.13) gives the coupling strength between the cavity mode and the collective excitation (the TO phonon) in terms of the coupling strengths g_n associated to the individual dipoles of each unit cell. g is evaluated by introducing Eq. (7.9) into Eq. (7.13), and transforming the sum into an integral (since the dipoles are distributed in a continuous way). The result is

$$\begin{aligned} |g|^2 &= \sum_{n=1}^{N_{\text{cell}}} \frac{\omega_{\text{cav}}^{(j)}}{\omega_{\text{TO}}} \frac{\omega_{\text{LO}}^2 - \omega_{\text{TO}}^2}{4} \frac{\mathcal{V}_{\text{cell}}\varepsilon_\infty |\Xi(z_n)|^2}{S \int \varepsilon(z') |\Xi(z')|^2 dz'} \\ &= \int \frac{\omega_{\text{cav}}^{(j)}}{\omega_{\text{TO}}} \frac{\omega_{\text{LO}}^2 - \omega_{\text{TO}}^2}{4} \frac{\mathcal{V}_{\text{cell}}\varepsilon_\infty |\Xi(z)|^2}{S \int \varepsilon(z') |\Xi(z')|^2 dz'} \frac{dN_{\text{cell}}}{d\mathcal{V}} d\mathcal{V} \\ &= \frac{\omega_{\text{cav}}^{(j)}}{\omega_{\text{TO}}} \frac{\omega_{\text{LO}}^2 - \omega_{\text{TO}}^2}{4} \frac{\int \varepsilon_\infty |\Xi(z)|^2 dz}{\int \varepsilon(z') |\Xi(z')|^2 dz'}, \end{aligned} \quad (7.14)$$

where in the last step we have taken into account that the density of dipoles is $\frac{dN_{\text{cell}}}{d\mathcal{V}} = \frac{1}{\mathcal{V}_{\text{cell}}}$ and the effective surface area S of the mode is eliminated after the integration in the $x - y$ plane. The integral of the denominator in Eq. (7.14) is evaluated in the entire cavity, while the integral of the numerator is bounded to the region of the phononic material. Therefore, in this subsection we have obtained an expression that enables to calculate the coupling strength between the TO phonon of a polar material and a Fabry-Pérot mode of a cavity with an arbitrary spatial distribution of the permittivity $\varepsilon(z)$ [and thus arbitrary field distribution $\Xi(z)$].

Application to hBN microcavities

We now focus on the particular system that we analyze in this chapter, a cavity of thickness L_{cav} with MoS₂ as a spacer and containing a layer of hBN (Sec. 7.2). First, we need to calculate the field profile $\Xi(z)$ of the modes of the bare cavity, in order to evaluate the coupling strength g through Eq. (7.14). Labelling the positions of the MoS₂-hBN interfaces as L_1 and L_2 (indicated in Fig. 7.1), the spatial distribution of the permittivity $\varepsilon(z)$ of the bare cavity is described by the function

$$\varepsilon(z) = \begin{cases} \varepsilon_{\text{MoS}_2}, & 0 < z < L_1 \\ \varepsilon_{\text{hBN},\infty}, & L_1 < z < L_2 \\ \varepsilon_{\text{MoS}_2}, & L_2 < z < L_{\text{cav}} \end{cases} . \quad (7.15)$$

In each interval with constant permittivity ε_n , the field profile $\Xi(z)$ satisfies the Helmholtz equation

$$\frac{d^2\Xi(z)}{dz^2} + \frac{\varepsilon_n(\omega_{\text{cav}}^{(j)})^2}{c^2}\Xi(z) = 0, \quad (7.16)$$

Further, since the cavity is assumed to be bounded by perfect mirrors and we only consider modes at normal incidence (so that the electric field is completely polarized in the direction parallel to the mirror planes), the electric field vanishes at both ends: $\Xi(0) = \Xi(L_{\text{cav}}) = 0$. In order to verify the boundary conditions, $\Xi(z)$ needs to be continuous and differentiable in all interfaces, which leads to the solution

$$\Xi(z) = \begin{cases} \mathcal{A} \frac{\sin\left(\frac{\omega_{\text{cav}}^{(j)}}{c} \sqrt{\varepsilon_{\text{hBN},\infty} L_1 + \phi^{(j)}}\right)}{\sin\left(\frac{\omega_{\text{cav}}^{(j)}}{c} \sqrt{\varepsilon_{\text{MoS}_2} L_1}\right)} \sin\left(\frac{\omega_{\text{cav}}^{(j)}}{c} \sqrt{\varepsilon_{\text{MoS}_2} z}\right) & 0 < z < L_1 \\ \mathcal{A} \sin\left(\frac{\omega_{\text{cav}}^{(j)}}{c} \sqrt{\varepsilon_{\text{hBN},\infty} z + \phi^{(j)}}\right) & L_1 < z < L_2 \\ \mathcal{A} \frac{\sin\left(\frac{\omega_{\text{cav}}^{(j)}}{c} \sqrt{\varepsilon_{\text{hBN},\infty} L_1 + \phi^{(j)}}\right)}{\sin\left(\frac{\omega_{\text{cav}}^{(j)}}{c} \sqrt{\varepsilon_{\text{MoS}_2} L_1}\right)} \sin\left(\frac{\omega_{\text{cav}}^{(j)}}{c} \sqrt{\varepsilon_{\text{MoS}_2} (z - L_{\text{cav}})}\right), & L_2 < z < L_{\text{cav}} \end{cases} . \quad (7.17)$$

\mathcal{A} is the normalization constant chosen so that the maximum of the field profile is $\Xi(z) = 1$, while $\omega_{\text{cav}}^{(j)}$ and $\phi^{(j)}$ are the j^{th} solution of the system of equations

$$\sqrt{\varepsilon_{\text{MoS}_2}} \cot\left(\frac{\omega_{\text{cav}}^{(j)}}{c} \sqrt{\varepsilon_{\text{MoS}_2} L_1}\right) = \sqrt{\varepsilon_{\text{hBN},\infty}} \cot\left(\frac{\omega_{\text{cav}}^{(j)}}{c} \sqrt{\varepsilon_{\text{hBN},\infty} L_1 + \phi^{(j)}}\right) \quad (7.18a)$$

$$\sqrt{\varepsilon_{\text{MoS}_2}} \cot\left(\frac{\omega_{\text{cav}}^{(j)}}{c} \sqrt{\varepsilon_{\text{MoS}_2} (L_2 - L_{\text{cav}})}\right) = \sqrt{\varepsilon_{\text{hBN},\infty}} \cot\left(\frac{\omega_{\text{cav}}^{(j)}}{c} \sqrt{\varepsilon_{\text{hBN},\infty} L_2 + \phi^{(j)}}\right). \quad (7.18b)$$

We can obtain g by inserting Eq. (7.17) into Eq. (7.14), with the integral

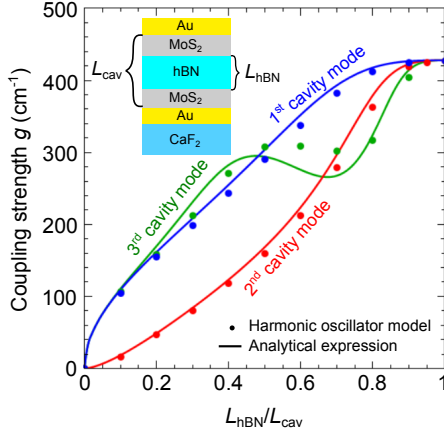


Figure 7.7: Evolution of the coupling strength g as a function of the ratio $\frac{L_{\text{hBN}}}{L_{\text{cav}}}$ (shown in the inset) for the first (blue), the second (red) and the third (green) cavity modes. Solid lines represent the solution of Eq. (7.19), and the dots correspond to the values obtained from fitting the mode frequencies given by the poles of the Fresnel coefficients with the classical MC harmonic oscillator model (blue and red dots correspond to the values shown in Fig. 7.5). The cavity thickness L_{cav} is changed so that the cavity mode being analyzed is always resonant with the TO phonon frequency.

extending over the phononic material (between L_1 and L_2), i.e. we evaluate

$$|g|^2 = \frac{\omega_{\text{LO}}^2 - \omega_{\text{TO}}^2}{4} \frac{\int_{L_1}^{L_2} \varepsilon_{\text{hBN},\infty} |\Xi(z)|^2 dz}{\int_0^{L_{\text{cav}}} \varepsilon(z') |\Xi(z')|^2 dz'}. \quad (7.19)$$

In this calculation, we always assume that the cavity mode of order j is resonant with the TO phonon, $\omega_{\text{TO}} = \omega_{\text{cav}}^{(j)}$, so that the cavity thickness L_{cav} is different for each order and the permittivity of MoS₂ is evaluated at that frequency ($\varepsilon_{\text{MoS}_2} \equiv \varepsilon_{\text{MoS}_2}(\omega_{\text{TO}})$ in this subsection). Adjusting the cavity parameters (specially the thickness of the hBN layer) enables to vary g from 0 to a maximum value g_{max} corresponding to the fully filled cavity that can be evaluated to be $g_{\text{max}} = \sqrt{\frac{\omega_{\text{LO}}^2 - \omega_{\text{TO}}^2}{4}} = 428 \text{ cm}^{-1}$. The analytical model therefore confirms the value of g_{max} obtained from transfer-matrix simulations (Fig. 7.5) and shows that g_{max} is fully determined by the Reststrahlen band of the material defined by the TO and LO phonon frequencies.

Further, we can also obtain a simple analytical expression of g for thin layers of hBN placed in the middle of the cavity and interacting with the first cavity mode. In order to obtain the field profile $\Xi(z)$ in this regime, we consider that the thin layer of hBN disturbs very weakly the electric field of the cavity fully filled with MoS₂ and with the same total thickness L_{cav} . Under this assumption, we obtain

that $\Xi(z) \approx \sin\left(\frac{\omega_{\text{cav}}^{(1)}}{c} \sqrt{\varepsilon_{\text{MoS}_2}} z\right)$, with $\omega_{\text{cav}}^{(1)} = \frac{\pi c}{\sqrt{\varepsilon_{\text{MoS}_2}} L_{\text{cav}}}$. Moreover, since the thin layer is located in the position of the maximum amplitude of the electric field, this amplitude varies slowly inside the hBN layer, and we can assume that the field is constant between L_1 and L_2 ($\Xi(z) \approx 1$). By evaluating the integrals in Eq. (7.19) for $L_1 = \frac{L_{\text{cav}}}{2} - \frac{L_{\text{hBN}}}{2}$ and $L_2 = \frac{L_{\text{cav}}}{2} + \frac{L_{\text{hBN}}}{2}$, we obtain

$$g \approx \sqrt{\frac{\omega_{\text{LO}}^2 - \omega_{\text{TO}}^2}{2} \frac{\varepsilon_{\text{hBN},\infty} L_{\text{hBN}}}{\varepsilon_{\text{MoS}_2} L_{\text{cav}}}} \approx 332 \text{ cm}^{-1} \sqrt{\frac{L_{\text{hBN}}}{L_{\text{cav}}}}. \quad (7.20)$$

This result is consistent with the Dicke model [285, 299] that has been often applied to quantify the coupling strength between a cavity mode and an ensemble of N identical molecules [300–302]. Since in our case the thickness of the hBN layer L_{hBN} is proportional to the amount of dipoles interacting with the cavity mode, we obtain the same dependency of g on the number of matter excitations $g \propto \sqrt{N}$ as predicted by Dicke. The agreement between the analytical approximation obtained in Eq. (7.20) and the coupling strength obtained from transfer-matrix simulation for thin layers is indicated in Fig. 7.5b.

We further assess in Fig. 7.7 the validity of our analytical model by comparing the result of Eq. (7.19) with the coupling strengths calculated by applying the classical MC model to the polaritonic frequencies calculated with the transfer-matrix method. For the calculation of the polaritonic frequencies, we always choose the thickness L_{cav} so that the frequency of the cavity mode considered is resonant with the TO phonon frequency. We show the evolution of the coupling strength g as a function of the filling factor $\frac{L_{\text{hBN}}}{L_{\text{cav}}}$ for the first three cavity modes. As discussed in Sec. 7.3.1, g generally increases with the filling factor, particularly strongly for thin layers and odd modes, until for all modes it saturates at the same value g_{max} for fully filled cavities. The third mode also shows a non-intuitive tendency of the coupling strength which decreases with an increase of $\frac{L_{\text{hBN}}}{L_{\text{cav}}}$ (in the interval $0.5 \lesssim \frac{L_{\text{hBN}}}{L_{\text{cav}}} \lesssim 0.7$). The reason is that changing L_{hBN} also modifies L_{cav} (to keep the cavity resonant with the TO phonon) and the field distribution inside the cavity, which leads to a complex tendency. Importantly, for the coupling strength of the first two modes, we observe that the agreement between the analytical expression (solid lines) and the MC model of classical harmonic oscillators (dots) is very good, with only a slight overestimation by the analytical Eq. (7.19) for intermediate values of the filling factor. The agreement becomes worse for the third cavity mode and intermediate filling factors. This small discrepancy may be related to the assumption made in the MC harmonic oscillator model that the cavity modes are independent of each other [Eq. (7.2)] and could be solved by considering the interaction between different cavity modes. However, even without this consideration the agreement between the results shown in Fig. 7.7 remains generally reasonable. Thus, we confirm that the simple analytical model presented here is able to explain the evolution of the coupling strength with the filling factor, particularly for the first two cavity modes considered in this chapter.

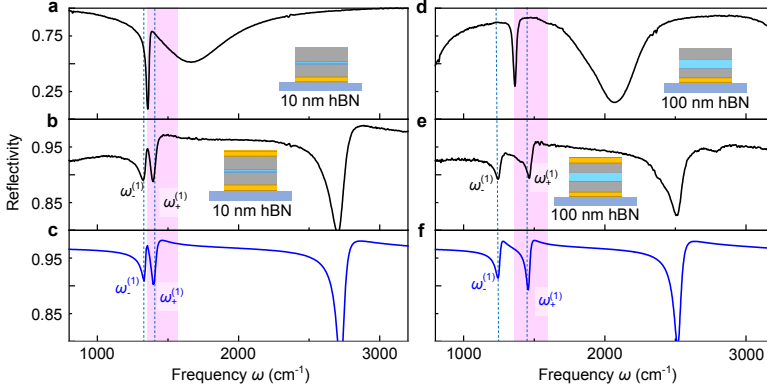


Figure 7.8: Experimental and theoretical spectra at frequencies close to the TO phonon. a) Experimental reflectivity spectrum of the MoS₂/hBN/MoS₂ heterostructure placed on the bottom gold mirror (illustrated by the inset), measured before the evaporation of the top gold mirror. Measured thicknesses are 510 nm/10 nm/370 nm. b) Experimental reflectivity spectrum of the stack of the panel (a) after closing it with the top Au layer (illustrated by the inset). $\omega_{-}^{(1)}$ and $\omega_{+}^{(1)}$ mark the dips emerging for the coupling between the TO phonon and the cavity mode. c) Theoretical reflectivity spectrum of the cavity in panel (b), using layer thicknesses of 510 nm/10 nm/370 nm and calculated for a normal incident planewave. d-f) Same as panels (a-c) for a MoS₂/hBN/MoS₂ heterostructure with measured thicknesses 520 nm/100 nm/430 nm and simulated thicknesses 480 nm/100 nm/390 nm.

7.4 Comparison with experimental reflectivity data

The theoretical predictions discussed in Sec. 7.3 have been verified experimentally by the groups of Luis Hueso and Rainer Hillenbrand in CIC nanoGUNE. Experimental reflectivity measurements in several cavities of different L_{hBN} and L_{cav} thicknesses were performed. With this aim, the collaborators first fabricated a gold mirror of 20 nm thickness with thermal evaporation. The MoS₂/hBN/MoS₂ heterostructure was then fabricated over the bottom mirror, following several steps of mechanical exfoliation and deterministic transfer [303]. The thickness of all layers was characterized with a profilometer of experimental accuracy of about 5%. The last step of fabrication consisted in closing the cavity by evaporating the top gold mirror over the stack. Once the samples were fabricated, their reflectivity was measured with a Fourier transform infrared microspectroscopy setup that operates with a Cassegrainian objective with numerical aperture of $NA = 0.4$. More details can be found in Ref. [304].

We show in Fig. 7.8 the comparison between theoretical calculations and experimental results for cavities filled with hBN layers of 10 and 100 nm. For the fabrication of each cavity, after fixing the hBN layer thickness L_{hBN} , the value of L_{cav} was adjusted so that the fundamental cavity resonance $\omega_{\text{cav}}^{(1)}$ approximately

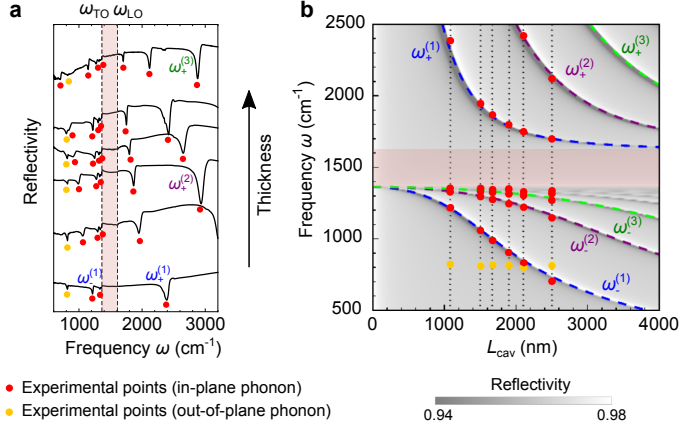


Figure 7.9: Experimental measurements of ultrastrong coupling in cavities fully filled with hBN. a) Experimental reflectivity spectra of fully filled cavities (plotted with a vertical offset). Cavity thicknesses (from bottom to top) are: 1080 nm, 1500 nm, 1665 nm, 1900 nm, 2100 nm, 2500 nm. b) Reflectivity spectra of a cavity fully filled with hBN as a function of the cavity thickness L_{cav} and obtained with transfer-matrix simulations (same results as in Fig. 7.3f). Red and yellow symbols show the spectral position of the experimental reflectivity dips extracted from panel (a). The shadowed area highlights the Reststrahlen band.

coincides with the frequency of the in-plane TO phonon, ω_{TO} , according to transfer-matrix simulations of the bare cavity.

First, it was verified that the hBN flakes in both samples exhibit a sharp phonon line at $\omega_{\text{TO}} = 1364 \text{ cm}^{-1}$, by measuring the reflection spectra prior to the fabrication of the top mirror (Figs. 7.8a and d). Additional to the narrow phonon lines, we observe broader dips, which indicate that the stacks act as detuned open cavities of a low quality factor. By closing the cavities (i.e. fabricating the top gold mirror), we clearly see a splitting of the reflection dip at the TO phonon frequency into two dips that are shifted to a lower and a higher frequency, $\omega_{-}^{(1)}$ and $\omega_{+}^{(1)}$, respectively (Figs. 7.8b and e). Transfer-matrix calculations match well the experimental reflection spectra (Figs. 7.8c and f) upon slight modification of the nominal values of the cavity parameter (see caption of Fig. 7.8). The need for such modification is attributed to uncertainties in the thickness and permittivity measurements. Further, the agreement between theory and experiments is also observed in the values of the splitting between reflectivity dips associated to polaritonic modes, because in experiments we observe splittings of 76 cm^{-1} and 215 cm^{-1} for 10 nm- and 100 nm-thick hBN layers, respectively, while the corresponding theoretical values are 68 cm^{-1} and 213 cm^{-1} . From the analysis of Sec. 7.3, we know that the double dip observed in experiments appears due to the strong coupling between the cavity mode and the TO phonon. Further, since the cavity and phonon resonances match reasonably well, i.e. $\omega_{\text{cav}}^{(1)} \approx \omega_{\text{TO}}$, we can estimate the coupling strength

of the system from experimental data, according to $g_{\text{exp}} = (\omega_+^{(1)} - \omega_-^{(1)})/2$, where $\omega_+^{(1)} - \omega_-^{(1)}$ is the experimental dip splitting (indicated in Figs. 7.8b and e). The corresponding values of $g_{\text{exp}} = 34 \text{ cm}^{-1}$ and $g_{\text{exp}} = 106 \text{ cm}^{-1}$ for $L_{\text{hBN}} = 10 \text{ nm}$ and 100 nm , respectively, are plotted in Fig. 7.5 by purple dots, showing good agreement with the theoretical results. Therefore, the experimental measurements shown in Fig. 7.8 verify that strong coupling between microcavity photons and phonons can be indeed achieved with layers of a polar material as thin as 10 nm , and that larger coupling strengths can be obtained by increasing the layer thickness.

To further explore the regime of maximum coupling strength, a thorough experimental study of cavities fully filled with hBN has also been performed. We show in Fig. 7.9a the reflectivity spectra of six samples of different thicknesses (indicated in the caption). The spectral positions of the reflectivity dips are also plotted in Fig. 7.9b, as the dots superimposed to the colormap of the reflectivity spectra. The latter is obtained from transfer-matrix simulations as a function of the thickness L_{cav} . Interestingly, we observe that the frequencies of most of the experimental dips approximately coincide with the theoretical frequencies of the polariton modes $\omega_-^{(j)}$ and $\omega_+^{(j)}$ (these experimental frequencies are indicated by red dots). This agreement allows us to associate each experimental dip with a particular polaritonic mode. The large dip splittings that we observe in experimental data confirm that the ultrastrong coupling regime can be reached in Fabry-Pérot cavities filled with polar materials. We further note that the experimental reflectivity spectra exhibit a set of almost thickness-independent dips at around 819 cm^{-1} (yellow dots in Fig. 7.9) that do not appear in the theoretical calculations. This frequency corresponds to the out-of-plane LO phonon of hBN. In the following subsection, we show that this dip appears in the experimental spectra due to the use of focused illumination of the cavity (using a Cassegrainian objective) instead of illumination by normal incident light.

7.4.1 Reflectivity of the system under focused illumination

In the transfer-matrix calculations performed up to this point, we assume that the propagation direction of the incident light is normal to the surface of the mirrors and the substrate (z direction). However, the experiments have been performed using a microscope with focused illumination. The total reflectivity \mathcal{R}_{foc} for focused illumination is obtained theoretically by decomposing the incident light as an integral over planewaves incident at different angles. We then obtain (for more details, see Chapter 3.9 in Ref. [67]):

$$\mathcal{R}_{\text{foc}} = \frac{I_{\text{ref}}}{I_{\text{in}}} = \frac{\int_{\sin \theta_{\text{min}}}^{\sin \theta_{\text{max}}} \frac{|r_{\text{total}}^s(\xi)|^2 + |r_{\text{total}}^p(\xi)|^2}{2} \xi d\xi}{\int_{\sin \theta_{\text{min}}}^{\sin \theta_{\text{max}}} \xi d\xi}, \quad (7.21)$$

where I_{in} and I_{ref} correspond to the intensity of the incident and reflected focused beam, respectively, $\xi = \frac{\sqrt{k_x^2 + k_y^2}}{k_0} = \frac{k_{\parallel}}{k_0}$ is the normalized parallel wavevector and

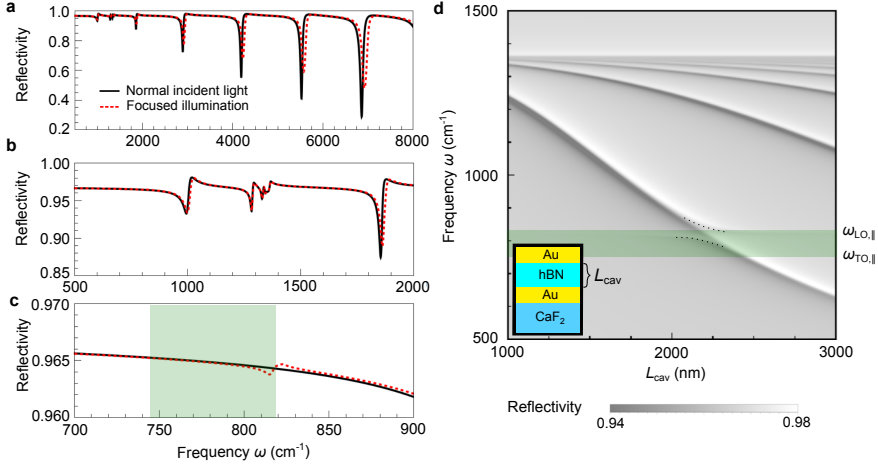


Figure 7.10: Reflectivity spectra calculated for cavities fully filled with hBN under focused illumination. a-c) Comparison between the spectra of a cavity with thickness $L_{\text{cav}} = 1665$ nm obtained for normal incident light (black solid lines) and focused illumination (red dashed lines). (b) and (c) correspond to zooms of different regions of the spectra in (a). d) Reflectivity spectra under focused illumination as a function of the total cavity thickness L_{cav} and frequency ω of the incident light. Dots are a guide to the peak positions in the region near the anticrossing that occurs due to the coupling of the cavity mode of order 1 and the out-of-plane phonons. The green shadowed area in (c) and (d) represents the Reststrahlen band of the out-of-plane phonon, limited by frequencies $\omega_{\text{TO},\parallel}$ and $\omega_{\text{LO},\parallel}$.

$r_{\text{total}}^{s(p)}$ is the ξ -dependent reflection coefficient of the full system for a $s(p)$ -polarized planewave, which is discussed thoroughly in Sec. 1.1.1. The upper limit of the integral is given by the numerical aperture of the microscope used to focus light, $\text{NA} = \sin \theta_{\text{max}}$. In the experiments performed in this work, the corresponding value is $\text{NA} = 0.4$, and thus, $\theta_{\text{max}} \approx 23.5^\circ$. Furthermore, we set $\theta_{\text{min}} = 10^\circ$ for the lower bound of the integral, because the microscope used in the experiments obstructs the propagation of the central part of the light incoming to the focusing lens, which eliminates the contribution from the small-angle components.

We have verified that, for cavities embedding a 10 nm layer of hBN, the results of the transfer-matrix simulations using focused illumination are nearly identical compared to the spectra for normal incidence. Crucially, light travels at considerably smaller angles inside this cavity than in free space, due to the high permittivity of MoS_2 , ϵ_{MoS_2} , which fills most of the cavity for such a thin hBN layer. In particular, the angles inside MoS_2 range from 2.6° to 5.9° , and thus the difference with the case of normal incidence is very small.

We next consider a fully filled hBN cavity of thickness $L_{\text{cav}} = 1665$ nm (whose first cavity mode is resonant with the TO phonon frequency) and show in Fig. 7.10a-c the reflectivity spectra under focused (red dashed line) and normal-incidence illumination (black solid line), both calculated by transfer-matrix simulations. The

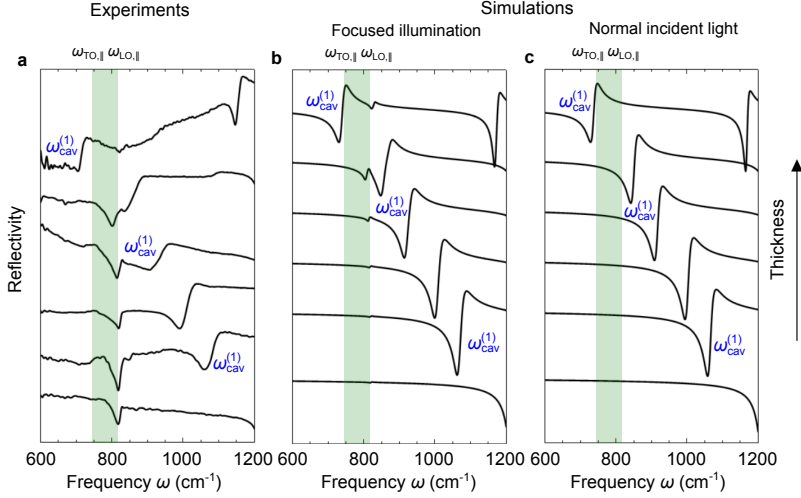


Figure 7.11: Reflectivity spectra of the fully filled hBN cavities at low frequencies, obtained from a) the experiments; b) transfer-matrix simulations under focused illumination; and c) transfer-matrix simulations when the illumination is a plane wave incoming in the normal direction. The Reststrahlen band of the out-of-plane phonon is highlighted by the green area. The (a) nominal and (b,c) simulated thicknesses L_{cav} of the cavities (from bottom to top) are: 1080 nm, 1500 nm, 1665 nm, 1900 nm, 2100 nm and 2500 nm. Panel a is a zoom of Fig. 7.9a in the region of low frequencies.

effect of using focused light becomes larger for the cavity fully filled by hBN, as the high-frequency permittivity of hBN $\epsilon_{\text{hBN},\infty}$ is smaller than ϵ_{MoS_2} , and thus the angle of light propagation inside the cavity can be larger. A small but appreciable difference between normal incident light and focused illumination is observed for high frequencies, as shown in panel a. The reflectivity dips obtained under focused illumination are displaced towards larger frequencies compared to the normal-incidence spectra, because the frequencies of the Fabry-Pérot cavity modes depend on the angle of propagation. Furthermore, the widths of the dips are larger for focused illumination because they are the result of the sum of different contributions, each corresponding to a different angle and thus resonant at a slightly different frequency [Eq. (7.21)]. However, these differences remain small, and the agreement between the two spectra improves further for frequencies close to $\omega_{\text{TO}} = 1364 \text{ cm}^{-1}$ (see zoom in panel b), which is the main region of interest in this work. Thus, the use of normal incidence in our calculations of Sec. 7.3.1 is justified.

Possibly the most interesting feature of the results obtained under focused illumination is observed in Fig. 7.10c, which shows the reflectivity spectra at low frequencies (near the frequencies of the out-of-plane phonons). An additional reflectivity dip for focused illumination (red dashed line) appears compared to the normal-incidence spectra (black solid line), which is due to the anisotropy of

hBN. For normal incidence, the illumination only couples with the in-plane TO phonon, which is polarized in the parallel direction to all planar interfaces. On the other hand, for focused illumination it becomes possible to excite the phonons that are polarized in the out-of-plane direction and that are found at significantly lower frequencies ($\omega_{\text{TO},\parallel} = 746 \text{ cm}^{-1}$ and $\omega_{\text{LO},\parallel} = 819 \text{ cm}^{-1}$, the Reststrahlen band of the out-of-plane phonons limited by these frequencies is highlighted by the green area in Fig. 7.10). These phonons strongly affect the z component of the permittivity tensor, and thus they can couple with the electric field components in the z direction of the focused light, which explains the extra dip.

For a more detailed analysis of this coupling, we show in Fig. 7.10d the calculated reflectivity spectra under focused illumination as a function of the total cavity thickness L_{cav} , for illumination frequencies between 600 and 1200 cm^{-1} . When the frequency of the bare-cavity mode gets close to the Reststrahlen band of the out-of-plane phonon, an anticrossing characterized by a relatively small splitting is observed, as indicated by the dots as a guide. Hence, the use of a focused beam makes possible to observe the coupling of the cavity modes with in-plane and out-of-plane phonons.

We now compare the theoretical spectra under focused illumination with the experimental measurements. Figure 7.11a shows the experimental reflectivity spectra for all six cavities. This figure corresponds to a zoom of Fig. 7.9a on the region near the Reststrahlen band associated with the out-of-plane phonons (green area). We observe a dip labelled by $\omega_{\text{cav}}^{(1)}$ that changes strongly with the thickness of the cavity and it is mostly associated to the bare-cavity mode. The other dip is close to $\omega_{\text{LO},\parallel}$, and its frequency is also indicated by the yellow dots in Fig. 7.9b. In order to confirm the nature of the dips at frequency $\approx \omega_{\text{LO},\parallel}$, we also show in Fig. 7.11 the results from the transfer-matrix simulations under focused illumination (panel b) and normal incident light (panel c). For panel c, we only see the dip associated to the bare-cavity mode at frequency $\omega_{\text{cav}}^{(1)}$. On the other hand, once we consider focused illumination, we can observe the second feature near $\omega_{\text{LO},\parallel}$ that was identified in the experiments. We thus confirm that the extra peak only appears in the calculations when the polarization has a nonzero z component and thus the illumination couples also with the out-of-plane phonons. However, we notice that the size of the experimental dips is significantly larger than the simulated ones, and we attribute this discrepancy to experimental imperfections such as rugosities (which can scatter light at high angles) or non-perfect planarity of the fabricated cavities. Despite this difference, the good agreement on the spectral positions of the dips indicates that they are indeed a result of the coupling between the first cavity mode and the out-of-plane phonons.

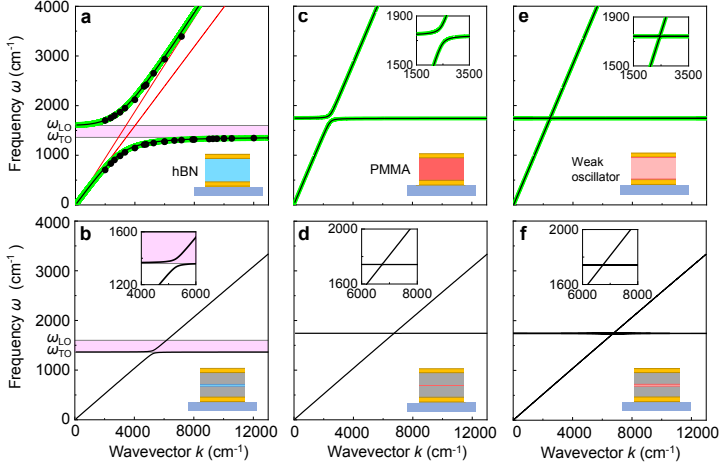


Figure 7.12: Polariton dispersions. a) Measured (black symbols) and calculated (black curves) phonon polariton dispersion obtained from hBN layers that fully fill the cavity. Green curves show the bulk phonon polariton dispersion of hBN. Red dashed lines indicate the light lines $\omega(k) = \frac{ck}{\sqrt{\varepsilon(\omega=0)}}$ and $\omega(k) = \frac{ck}{\sqrt{\varepsilon_{\text{hBN},\infty}}}$, where $\varepsilon(\omega = 0) = 6.29$ and $\varepsilon_{\text{hBN},\infty} = 4.52$ are the low- and high-frequency permittivities of hBN. The Reststrahlen band of bulk hBN is marked by the purple area. b) Calculated (black curves) phonon polariton dispersion obtained from cavities that are filled with a 10 nm thick hBN layer. c) Calculated (black curves) polariton dispersion obtained for cavities that are fully filled with molecules exhibiting a C=O vibration. Green curves show the bulk polariton dispersion of the filling material. d) Dispersion for a 10 nm thick molecular layer embedded in the cavity. e) Calculated (black curves) polariton dispersion obtained for cavities fully filled with hypothetical molecules exhibiting a vibration of arbitrarily reduced oscillator strength. Green curves show the dispersion of the filling material. f) Dispersion for a 10 nm thick hypothetical molecular layer of arbitrarily reduced coupling strength embedded in the cavity. Schematics illustrate the cross section of the cavities.

7.5 Dispersion relation of microcavity phonon polaritons

After emphasizing the agreement between theory and experiments in the polaritonic modes of the fully filled cavity (Fig. 7.9), we now use these data to establish a connection between the dispersion relation $\omega(k)$ of microcavity phonon polaritons and inherent bulk properties of hBN, such as the dispersion of bulk phonon polaritons and the bulk permittivity. To obtain the dispersion relation $\omega(k)$ of microcavity phonon polaritons, we extract the wavevector k from the reflectivity spectra according to [Eq. (1.11)]

$$k = \frac{j\pi}{L_{\text{cav}}}, \quad (7.22)$$

assuming perfect metal mirrors and where L_{cav} is the cavity length at which the cavity eigenmode of order j and frequency ω is found. In Figs. 7.12a and b, we compare $\omega(k)$ for the cavity that is fully filled with hBN (obtained from Fig. 7.3f) and the cavity embedding a 10 nm thick hBN layer (obtained from Fig. 7.3b), respectively (calculations are shown by black curves and experimental values by black symbols). Note that for the fully filled cavity, the hybrid modes resulting from the coupling with all cavity modes j were considered, whereas for the cavity filled with 10 nm of hBN we considered only the first mode ($j = 1$). Both dispersions feature anticrossing, separating into a lower and upper microcavity phonon polariton branch, with large Rabi splitting amounting to $\Omega_{\text{R}} \approx 856 \text{ cm}^{-1}$ and $\Omega_{\text{R}} \approx 63 \text{ cm}^{-1}$, respectively.

To appreciate the dramatic coupling strengths between infrared microcavity modes and phonons with respect to typical molecular vibrations [259], we show in Figs. 7.12c and d the calculated polariton dispersions obtained (analogous to Figs. 7.3b and f) for cavities embedding molecules that possess C=O vibrations. Specifically, we consider the ensemble of C=O oscillators of PMMA, whose electromagnetic response is described as specified in Sec. 7.2. Clear anticrossing can be observed for the cavity fully filled with PMMA (Fig. 7.12c), but the Rabi splitting $\Omega_{\text{R}} \approx 159 \text{ cm}^{-1}$ is more than five times smaller than that of the cavity fully filled with hBN. For the cavity filled with a 10 nm thick PMMA layer, we do not find anticrossing (Fig. 7.12d), revealing that the system is in the weak coupling regime, in contrast to the strong coupling regime achieved with a 10 nm thick hBN layer (Fig. 7.12b). We note that the C=O vibrations are rather strong and that many molecular vibrations can be much weaker. To demonstrate the coupling between microcavity modes and weak molecular oscillators by way of an example, we reduce the oscillator strength in the permittivity model of PMMA by a factor of 100 and recalculate the dispersions. In both the partially and fully filled cavity we do not observe anticrossing (Figs. 7.12e and f), highlighting that for weak molecular oscillators strong coupling cannot be achieved by placing them into a microcavity.

We now compare the dispersions of the material in the fully filled cavities with the bulk polariton dispersion of the same material, $\omega(k) = \frac{ck}{\sqrt{\varepsilon(\omega)}}$ [Eq. (1.26)], where $\varepsilon(\omega)$ is the permittivity of the filling material (green solid lines in Figs. 7.12a, c and e). Interestingly, we find that the polariton dispersion obtained from fully filled cavities is identical to that of the bulk phonon polariton dispersion of the filling material, independent of whether phonon or molecule oscillators (weak or strong) are embedded into the cavity. The maximum splitting is determined exclusively by the material properties as clearly shown by the analytical expression of g in Eq. (7.19) and is also highlighted in Refs. [258, 297, 305]. These results show that the maximum coupling strength between a cavity mode and a dipolar excitation is governed by that of photons and bulk, implying that fully filling a resonant cavity with a specific material does not enhance the coupling strength between light and matter. The cavity merely enforces the strongly coupled state by selecting the corresponding wavevector. Importantly, strong coupling in a cavity

can only be achieved in the case that the bulk dispersion of the filling material already exhibits strong coupling, i.e. anticrossing. In the case that the dispersion of light in the bulk material does not exhibit polaritonic behavior, the coupling of this bulk material with a cavity mode will remain weak. In other words, placing a material into a cavity will not make the coupling strength to exceed that of the bulk material. Interestingly, it has been reported that vibrational strong coupling in cavities can modify physical and chemical properties of the material filling the cavity [62, 306–308]. Since the coupling strength is not enhanced, another effect, such as a modification of the density of states, may be needed to explain this intriguing phenomenon.

To reinforce the idea that the bulk permittivity contains all the information of the ultrastrong coupling between microcavity photons and phonons in this system, we last demonstrate that the classical MC model used in this chapter allows for recovering the bulk permittivity. We first note that the modes of the bare cavity follow the dispersion relation $\omega_{\text{cav}}^{(j)} = \frac{ck}{\sqrt{\varepsilon_{\text{hBN},\infty}}}$, with the wavevector determined by Eq. (7.22). For the cavity filled with hBN, the frequency of each cavity mode of wavevector k is modified to $\omega(k) = \frac{ck}{\sqrt{\varepsilon(\omega)}} = \omega_{\text{cav}}^{(j)} \sqrt{\frac{\varepsilon_{\text{hBN},\infty}}{\varepsilon(\omega)}}$. Therefore, from the relation between the frequencies of the polaritonic modes ($\omega_{\pm}^{(j)}$) and the bare-cavity modes ($\omega_{\text{cav}}^{(j)}$) of the MC model in the ultrastrong coupling regime (Eq. (6.6), where we neglect losses for simplicity), we obtain that the permittivity of the material inside the cavity must be

$$\varepsilon_{\text{MC}}(\omega) = \varepsilon_{\text{hBN},\infty} \left(1 + \frac{4g^2}{\omega_{\text{TO}}^2 - \omega^2} \right). \quad (7.23)$$

Considering next the maximum coupling strength given by Eq. (7.19), $g_{\text{max}} = \sqrt{\frac{\omega_{\text{LO}}^2 - \omega_{\text{TO}}^2}{4}}$, we recover the permittivity of polar materials given by Eq. (1.42).

Furthermore, we emphasize that only the MC model can appropriately describe the permittivity of polar materials, while the other harmonic oscillator models discussed in Chapter 6 lead to incorrect results. To demonstrate it, we derive the permittivities $\varepsilon_{\text{SpC}}(\omega)$ and $\varepsilon_{\text{MC}}(\omega)$ obtained within the SpC model and the linearized model of harmonic oscillators, by repeating the same procedure with Eqs. (6.3) and (6.8), respectively. We obtain:

$$\varepsilon_{\text{SpC}}(\omega) = \varepsilon_{\text{hBN},\infty} \left(\frac{2g^2\omega_{\text{TO}}}{\omega(\omega_{\text{TO}}^2 - \omega^2)} + \sqrt{1 + \left(\frac{2g^2\omega_{\text{TO}}}{\omega(\omega_{\text{TO}}^2 - \omega^2)} \right)^2} \right)^2, \quad (7.24)$$

$$\varepsilon_{\text{lin}}(\omega) = \varepsilon_{\text{hBN},\infty} \left(1 + \frac{g^2}{\omega(\omega_{\text{TO}} - \omega)} \right), \quad (7.25)$$

which do not follow the standard form of the permittivity of polar materials [Eq. (1.42)].

For a comparison, we plot in Fig. 7.13 the permittivities obtained with the MC

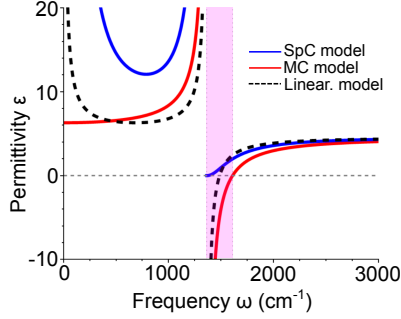


Figure 7.13: Permittivity of the material filling the Fabry-Pérot cavity, obtained from the classical SpC model [blue solid line, Eq. (7.24)], MC model [red solid line, Eq. (7.23)] and the linearized model [black dashed line, Eq. (7.25)], with $\omega_{\text{TO}} = 1364 \text{ cm}^{-1}$, $g = 428 \text{ cm}^{-1}$ and $\varepsilon_{\text{hBN},\infty} = 4.52$. The Reststrahlen band of hBN is highlighted by the purple area.

model [red solid line, Eq. (7.23)], SpC model [blue solid line, Eq. (7.24)] and the linearized model [black dashed line, Eq. (7.25)], with the TO phonon frequency $\omega_{\text{TO}} = 1364 \text{ cm}^{-1}$, coupling strength $g = 428 \text{ cm}^{-1}$ and high-frequency permittivity $\varepsilon_{\text{hBN},\infty} = 4.52$ of hBN. The different behavior of the calculation according to the three models can be clearly observed by comparing the permittivity in the range of frequencies with negative permittivity for each case, i.e., the Reststrahlen band. The MC model describes the Reststrahlen band appropriately, because the permittivity is negative in the range $\omega \in (\omega_{\text{TO}}, \omega_{\text{LO}})$ (highlighted by the purple area in Fig. 7.13). In contrast, the permittivity ε_{SpC} associated to the SpC model is non-negative for all frequencies, and thus is unable to describe the presence of a Reststrahlen band. Last, the linearized model does give a Reststrahlen band, as can be appreciated in Fig. 7.13, but the width of this band is half of that obtained with the MC model. As an additional difference between the models, only the MC model results in a permittivity that does not diverge in the $\omega \rightarrow 0$ limit, in agreement with the expected behavior [Eq. (1.42)]. Hence, the equations of motion of the MC model contain the equivalent information as the bulk permittivity of polar materials.

7.6 Summary

We have demonstrated that classical microcavities can be applied for studying and tuning the coupling between photons and optical phonons in thin layers of polar van der Waals materials. For the studied material hBN, our theoretical analysis predicts strong coupling for hBN layers between 3 and 148 nm thickness and ultrastrong coupling for hBN thicknesses larger than 148 nm. Experimental reflection spectra of cavities embedding 10 and 100 nm thick hBN layers show excellent agreement with theoretical calculations and confirm strong coupling. For fully filled cavities ultrastrong coupling was also demonstrated experimentally. In comparison with

typical molecular vibrational strong coupling in fully filled cavities, the coupling strength is about five times larger due to the high oscillator strength of crystal phonons. Notably, we have shown that for Fabry-Pérot microcavities, the coupling strength between the cavity modes and the vibrations depends on the amount of material inside the cavity, but the maximum coupling strength achievable is solely determined by the oscillator strength of the material. Following the analysis of this chapter, by using van der Waals materials with even larger oscillator strength than hBN, the deep strong coupling regime may be reached [309–311].

CONCLUSIONS AND OUTLOOK

This thesis addresses the importance of quantum descriptions in nanophotonic systems. To achieve this goal, three primary areas of study have been chosen: i) how quantum calculations based on the framework of condensed matter theory lead to an accurate first-principles description of plasmonic excitations in metals by considering their electronic structure; ii) how a complete solution of the Schrödinger equation in tunneling junctions allows for a more accurate calculation of the light emitted by the system; and iii) how equivalences can be established between models based on cavity quantum electrodynamics (QED) and on classical coupled harmonic oscillators that are used to describe the strong and ultrastrong coupling between cavity modes and matter excitations. We summarize in the following the main findings obtained throughout this thesis.

First-principles description of plasmonic excitations in metallic systems (Chapters 3 and 4)

- We employ Time Dependent Density Functional Theory (TDDFT) to investigate the properties of plasmonic excitations on the Pd(110) surface. Our analysis focuses on calculating the surface loss function, which reveals a dominant peak corresponding to the surface plasmon. The frequency of the surface plasmon in the classical limit of small wavevectors aligns with existing experimental data. Nevertheless, we observe a weak positive dispersion in the study of non-local optical response when the associated wavevectors are of the order of 1 nm^{-1} , contrary to the previously reported negative dispersion observed in experiments on this surface. Further, we report that this system displays bulk and surface electronic states with distinct Fermi velocities. However, although previous studies have suggested that metallic surfaces with such electronic states can support acoustic plasmons, we do not identify any acoustic excitation with linear dispersion for the Pd(110) surface. This finding indicates that the mere existence of bulk and surface states close to the Fermi level is insufficient to generate acoustic plasmons. Instead, a consideration of the complete band structure is essential to identify all excitations of a metallic surface.
- We investigate the plasmonic excitations in anisotropic two-dimensional (2D) electron gases with band structure of triangular, square, and hexagonal

shapes. With this aim, we calculate the loss function in these systems. For all geometries, we observe a plasmon characterized by a dispersion proportional to the square root of the wavevector. This excitation is also present in isotropic 2D metals. However, we discover an additional, acoustic plasmon with linear dispersion that does not exist in the isotropic case. The number of these acoustic plasmons varies depending on the shape of the band structure of the material. Triangular and square-shaped systems exhibit a single acoustic plasmon, while the hexagonal system displays two such excitations with reduced lifetime compared to those corresponding to the other two geometries. The number of plasmons is related to the number of groups of electrons with the same Fermi velocity in each system. Previously, the presence of acoustic plasmons was predominantly observed in systems with distinct types of electronic states. Our findings thus suggest that anisotropy serves as an additional mechanism for the emergence of acoustic plasmons, even in materials characterized by a single electronic band.

Light emission from tunneling junctions (Chapter 5)

- We develop theoretical approaches to model the light emission that results from the excitation of surface plasmon polaritons (SPP) in tunneling junctions. Specifically, we revisit two methods commonly employed in the literature to evaluate the SPP excitation rate, consisting in calculations within Fermi's golden rule and in the calculation of the power radiated by fluctuating currents. We establish the relationship between these two methods, which reveals that they provide equivalent results. Moreover, we show that the accurate calculation of the SPP excitation rate requires the use of appropriate wavefunctions for the tunneling electrons, obtained from the solution of the Schrödinger equation of the entire device by considering both the insulator gap and metallic electrodes. We call this approach the quantum device solution (QDS). The QDS is an improvement of the widely utilized Bardeen's approximation that considers the wavefunctions just in the insulator gap region. We find that the QDS predicts a significantly larger excitation rate for the fast SPPs localized at interfaces several nanometers away from the gap, in comparison to the result obtained within Bardeen's approximation. Further, the QDS provides additional qualitative insights into light emission compared to Bardeen's approximation. In particular, the QDS shows strong correlations in the tunneling current between opposite metals, which Bardeen's approximation fails to capture. These strong correlations can be interpreted as an electron-hole pair that recombines in the gap and that gives an additional contribution to light emission that Bardeen's approximation does not consider. In general, this analysis extends the current framework of light emission from tunneling junctions.

Coupling between cavity modes and matter excitations (Chapters 6 and 7)

- We perform a comprehensive study of cavity-QED models and classical coupled harmonic oscillator models that describe light-matter interaction in the ultrastrong coupling regime. By deriving these two types of models from the Lagrangian of electromagnetic fields, we establish the connections between them and show that the same eigenvalue spectra and values of experimentally measurable observables can be obtained classically and quantum mechanically, but that care is required when defining the models. In particular, we focus on two main classical models and two cavity-QED Hamiltonians. The first classical model is the spring coupling (SpC) model, which mathematically corresponds to two coupled mechanical springs. We demonstrate that this model accurately represents longitudinal Coulomb interactions (for example, the coupling between a molecule and a plasmonic nanoparticle within the quasistatic approximation) and that it reproduces the behavior described with a cavity-QED Hamiltonian that does not include a diamagnetic term. The second model that we investigate is the modified coupling (MC) model, where the coupling term is proportional to the time derivatives of the oscillator amplitudes. This model is shown to be appropriate to analyze the coupling of matter excitations with transverse electromagnetic modes in dielectric cavities and is equivalent to the cavity-QED Hamiltonian with the diamagnetic term.
- We study the coupling between optical phonons and Fabry-Pérot cavity modes within cavities filled with layers of hexagonal boron nitride (hBN). We demonstrate that the strong coupling regime can be achieved even with a hBN layer only 3 nm thick and that the coupling strength increases rapidly as the hBN layers become thicker. The ultrastrong coupling regime is obtained with a hBN layer of approximately 150 nm thickness, and for fully filled cavities the coupling strength is more than 30% the bare phonon frequency. A numerical study of the coupling strength based on transfer-matrix simulations is supplemented by a microscopic model that leads to an analytical expression. Notably, this analytical model emphasizes that in fully filled cavities the coupling strength is solely determined by the bulk properties of the material, rather than by the cavity properties. As a consequence, a coupling strength larger than that determined by the bulk properties of the material cannot be obtained in Fabry-Pérot cavities. Further, we demonstrate that the dispersion of the hybrid modes that emerge due to the phonon-photon ultrastrong coupling in fully filled cavities is directly related to the bulk permittivity and the bulk phonon polariton dispersion of hBN. These findings indicate that microcavities filled with polar materials are a promising platform for studying the influence of strong and ultrastrong light-matter coupling on the properties of polar materials.

The findings presented in this thesis also raise new questions for future research. For instance, an immediate question raised by the results of Chapter 3 is the origin of the discrepancy between the theoretical and experimental dispersions of the surface plasmon on the Pd(110) surface. Answering this question would require future work from both a theoretical and an experimental perspective. Regarding

the theoretical description, we note that our treatment has not fully captured the accurate dynamics of the electrons that excite the surface plasmon. Instead, the results have been evaluated with a simpler description based on the surface loss function. Additionally, while our investigations of Chapter 4 have revealed that anisotropy in the band structure serves as a mechanism for the emergence of acoustic plasmons, the calculations in this thesis have utilized idealized band structures. Thus, it would be intriguing to explore whether our findings are confirmed in realistic metals, after performing calculations with more rigorous approaches such as TDDFT.

In addition, Chapter 5 has emphasized the significance of considering the QDS to accurately describe light emission from tunneling junctions. However, we have limited this study to the specific case of planar junctions. Thus, future work can generalize the QDS to other systems, such as gratings or nanoantennas that include narrow junctions. Furthermore, our model for describing tunneling electrons could be further improved. The metallic layers in our calculations possess finite thickness, which is considered in the calculation of the electric field distribution of the SPPs but not in the calculation of the electronic wavefunctions of the QDS. Future work may investigate how to implement more appropriate boundary conditions to the Schrödinger equation to obtain more accurate wavefunctions within the QDS approach.

Last, regarding the chapters exploring ultrastrong coupling between cavity modes and matter excitations, a first open question is how losses can be rigorously incorporated in classical coupled harmonic oscillator models in an equivalent manner as in cavity-QED models. Although the implementation of losses in classical and cavity-QED models is well understood in the strong coupling regime, it has been recently shown that the usual method to consider losses in cavity QED (based on Lindblad operators) fails in the ultrastrong coupling regime. As a result, a more rigorous procedure to consider losses in the cavity-QED approach has been adopted, which uses generalized master equations. Future work could shed light on the implications, if any, of these improvements on the classical approach. Another noteworthy question relates to the study of ultrastrong coupling in microcavities filled with polar materials, as presented in Chapter 7. In particular, according to previous studies, strong coupling with electromagnetic modes can alter the chemical reactivity of molecules introduced inside a cavity. Future work could find whether modifications of other physical properties can occur in the case of polar materials coupled to a cavity. Further, we have found that the maximum coupling strength in the cavity is not larger than the intrinsic coupling strength in a bulk material, which emphasizes the interest of exploring reasons of the modification of the physical and chemical properties that go beyond the value of the coupling strength.

In conclusion, we hope that this thesis contributes to improving the understanding of a large variety of quantum effects in nanophotonics.

Appendices

Appendix A

Origin of the strong current correlations at opposite metals in tunneling junctions

In Fig. 5.3b, we plot the cross-spectral density $\mathcal{S}_{j_z j_z}(z, z', \omega_{\mathbf{k}_{\parallel}}^{(\nu)})$ associated with the spatial correlations of the current density due to electrons tunneling through a narrow gap (for $\mathbf{r}_{\parallel} = \mathbf{r}'_{\parallel}$). This calculation is performed by introducing the wavefunctions of the quantum device solution (QDS) in the definition of $\mathcal{S}_{j_z j_z}(z, z', \omega_{\mathbf{k}_{\parallel}}^{(\nu)})$ from Eq. (5.26) and then solving the integral numerically over the wavevectors \mathbf{k}_L and \mathbf{k}_R (corresponding to electronic states of the metals in the left and the right, respectively). We discussed that the electronic currents are strongly correlated for $z = z'$ but also for points satisfying the condition $z' - L_{\text{gap}} = -z\sqrt{\frac{E_F^R + V_B}{E_F^L}}$ at opposite metals. In this appendix, we analyse analytically the origin of the latter strong correlations.

The cross-spectral density $\mathcal{S}_{j_z j_z}(z, z', \omega_{\mathbf{k}_{\parallel}}^{(\nu)})$ depends on the expression for the current density $\mathbf{j}_{L \rightarrow R}$ associated to each particular transition [Eq. (5.13)]. We consider the QDS and thus use Eq. (5.1) for the wavefunction $\Psi_L(\mathbf{r})$ of the initial state for an electron that tunnels from the left metal, and Eq. (5.2) for the wavefunction $\Psi_R(\mathbf{r})$ of the final state associated with an electron tunneling from the right metal. The final state $\Psi_R(\mathbf{r})$ has a lower energy than the initial state $\Psi_L(\mathbf{r})$. By introducing their corresponding expression in Eq. (5.13), we obtain the following expressions for the z component of the current density:

- For $z \leq 0$,

$$j_{z, L \rightarrow R}(z) = \frac{i\hbar e}{2m_{\text{eff}} L_z S} t_R^* e^{-ik_{zL}^- L_{\text{gap}}} \left[e^{i(k_{zL}^+ + k_{zL}^-)z} i(k_{zL}^+ - k_{zL}^-) - r_L e^{-i(k_{zL}^+ - k_{zL}^-)z} i(k_{zL}^+ + k_{zL}^-) \right]$$

$$\approx \frac{\hbar e}{2m_{\text{eff}}} \frac{1}{L_z S} t_{\text{R}}^* e^{-ik_{z\text{L}}^- L_{\text{gap}}} r_{\text{L}} e^{-i(k_{z\text{L}}^+ - k_{z\text{L}}^-)z} (k_{z\text{L}}^+ + k_{z\text{L}}^-). \quad (\text{A.1})$$

- For $0 < z \leq L_{\text{gap}}$,

$$j_{z,\text{L} \rightarrow \text{R}}(z) = \frac{i\hbar e}{2m_{\text{eff}}} \frac{1}{L_z S} \left[(k_{z\text{gap}}^+ + k_{z\text{gap}}^-) \alpha_{\text{R}}^* \alpha_{\text{L}} e^{(k_{z\text{gap}}^+ - k_{z\text{gap}}^-)z} e^{k_{z\text{gap}}^- L_{\text{gap}}} \right. \\ - (k_{z\text{gap}}^+ + k_{z\text{gap}}^-) \beta_{\text{R}}^* \beta_{\text{L}} e^{-(k_{z\text{gap}}^+ - k_{z\text{gap}}^-)z} e^{-k_{z\text{gap}}^- L_{\text{gap}}} \\ - (k_{z\text{gap}}^+ - k_{z\text{gap}}^-) \alpha_{\text{R}}^* \beta_{\text{L}} e^{-(k_{z\text{gap}}^+ + k_{z\text{gap}}^-)z} e^{k_{z\text{gap}}^- L_{\text{gap}}} \\ \left. + (k_{z\text{gap}}^+ - k_{z\text{gap}}^-) \beta_{\text{R}}^* \alpha_{\text{L}} e^{(k_{z\text{gap}}^+ + k_{z\text{gap}}^-)z} e^{-k_{z\text{gap}}^- L_{\text{gap}}} \right]. \quad (\text{A.2})$$

- For $z > L_{\text{gap}}$,

$$j_{z,\text{L} \rightarrow \text{R}}(z) = \frac{i\hbar e}{2m_{\text{eff}}} \frac{1}{L_z S} t_{\text{L}} \left[e^{i(k_{z\text{R}}^+ + k_{z\text{R}}^-)z} e^{-ik_{z\text{R}}^- L_{\text{gap}}} i(k_{z\text{R}}^+ - k_{z\text{R}}^-) \right. \\ \left. + t_{\text{R}}^* e^{i(k_{z\text{R}}^+ - k_{z\text{R}}^-)z} e^{ik_{z\text{R}}^- L_{\text{gap}}} i(k_{z\text{R}}^+ + k_{z\text{R}}^-) \right] \\ \approx -\frac{\hbar e}{2m_{\text{eff}}} \frac{1}{L_z S} t_{\text{L}} r_{\text{R}}^* e^{i(k_{z\text{R}}^+ - k_{z\text{R}}^-)z} e^{ik_{z\text{R}}^- L_{\text{gap}}} (k_{z\text{R}}^+ + k_{z\text{R}}^-). \quad (\text{A.3})$$

In these expressions, the superscripts + and - in $k_{z\text{L}}$, $k_{z\text{R}}$ and $k_{z\text{gap}}$ mean that these wavevectors are associated to the state of the initial state (at higher energy) or to the final state (at lower energy), respectively. Further, in Eqs. (A.1) and (A.3), we have assumed that $k_{z\text{L}(\text{R})}^+ + k_{z\text{L}(\text{R})}^- \gg |k_{z\text{L}(\text{R})}^+ - k_{z\text{L}(\text{R})}^-|$.

To calculate the cross-spectral density $\mathcal{S}_{j_z j_z}(z, z', \omega_{\mathbf{k}_{\parallel}}^{(\nu)})$, we need to integrate the product of the current density of Eqs. (A.1), (A.2) and (A.3) at two points z and z' , over all initial (with wavevector \mathbf{k}_{L}) and final (with wavevector \mathbf{k}_{R}) states, as indicated by Eq. (5.26). Crucially, to obtain strong correlations at different points z and z' , the relation between the phases of the current density $j_{z,\text{L} \rightarrow \text{R}}(z)$ at these two points must be equal for all transitions between $\Psi_{\text{L}}(z)$ and $\Psi_{\text{R}}(z)$ states, so that contributions with different phases do not cancel out with each other. For each transition, we obtain the following phase relations of the current density over spaceⁱ:

$$\arg\{j_{z,\text{L} \rightarrow \text{R}}(z)\} \approx \begin{cases} \arg(t_{\text{R}}^*) + \arg(r_{\text{L}}) - k_{z\text{L}}^- L_{\text{gap}} - (k_{z\text{L}}^+ - k_{z\text{L}}^-)z & z \leq 0 \\ \text{constant} & 0 < z \leq L_{\text{gap}} \\ \pi + \arg(t_{\text{L}}) + \arg(r_{\text{R}}^*) + k_{z\text{R}}^- L_{\text{gap}} + (k_{z\text{R}}^+ - k_{z\text{R}}^-)z & L_{\text{gap}} < z \end{cases}. \quad (\text{A.4})$$

In the length scales of usual insulator gaps, the argument of Eq. (A.2) changes

ⁱ In all equations involving the arg function in this appendix, the equalities are satisfied under $\text{mod}(2\pi)$.

very slightly, and thus we have considered in the derivation of Eq. (A.4) that it is constant over the gap region. Importantly, the phase of the current density changes linearly with z in the metals, due to the exponential terms $e^{-i(k_{zL}^+ - k_{zL}^-)z}$ and $e^{i(k_{zR}^+ - k_{zR}^-)z}$ in Eqs. (A.1) and (A.3), respectively. Further, the continuity of the wavefunctions $\Psi_L(z)$ and $\Psi_R(z)$ implies that $j_{z,L \rightarrow R}(z)$ must be also continuous. By defining ζ as the argument of the current density in the two metal-insulator boundaries at the gap, we rewrite Eq. (A.4) as

$$\arg\{j_{z,L \rightarrow R}(z)\} \approx \begin{cases} \zeta - (k_{zL}^+ - k_{zL}^-)z & z \leq 0 \\ \zeta & 0 < z \leq L_{\text{gap}} \\ \zeta + (k_{zR}^+ - k_{zR}^-)(z - L_{\text{gap}}) & L_{\text{gap}} < z \end{cases} \quad (\text{A.5})$$

An important consequence of Eq. (A.5) is that the values of $\arg\{j_{z,L \rightarrow R}(z)\}$ are related in the two metals. Indeed, at two points z and z' satisfying the condition

$$z = -\frac{k_{zR}^+ - k_{zR}^-}{k_{zL}^+ - k_{zL}^-}(z' - L_{\text{gap}}) \quad (\text{A.6})$$

the current density has the same argument. Considering a transition from an initial state of energy $\hbar\omega^{\text{el}}$ and parallel wavevector \mathbf{k}_{\parallel}^+ to a final state of corresponding values $\hbar\omega^{\text{el}} - \hbar\omega_{\mathbf{K}_{\parallel}}^{(\nu)}$ and \mathbf{k}_{\parallel}^- , the denominator of Eq. (A.6) is evaluated as

$$\begin{aligned} k_{zL}^+ - k_{zL}^- &= \sqrt{\frac{2m_{\text{eff}}(\hbar\omega^{\text{el}} + E_{\text{F}}^{\text{L}})}{\hbar^2} - |\mathbf{k}_{\parallel}^+|^2} - \sqrt{\frac{2m_{\text{eff}}(\hbar\omega^{\text{el}} - \hbar\omega_{\mathbf{K}_{\parallel}}^{(\nu)} + E_{\text{F}}^{\text{L}})}{\hbar^2} - |\mathbf{k}_{\parallel}^-|^2} \\ &= \sqrt{\frac{2m_{\text{eff}}E_{\text{F}}^{\text{L}}}{\hbar^2}} \left(\sqrt{1 + \frac{\hbar\omega^{\text{el}} - \frac{\hbar|\mathbf{k}_{\parallel}^+|^2}{2m_{\text{eff}}}}{E_{\text{F}}^{\text{L}}}} - \sqrt{1 + \frac{\hbar\omega^{\text{el}} - \hbar\omega_{\mathbf{K}_{\parallel}}^{(\nu)} - \frac{\hbar|\mathbf{k}_{\parallel}^-|^2}{2m_{\text{eff}}}}{E_{\text{F}}^{\text{L}}}} \right) \\ &\approx \sqrt{\frac{2m_{\text{eff}}E_{\text{F}}^{\text{L}}}{\hbar^2}} \frac{\hbar\omega_{\mathbf{K}_{\parallel}}^{(\nu)} + \frac{\hbar(|\mathbf{k}_{\parallel}^-|^2 - |\mathbf{k}_{\parallel}^+|^2)}{2m_{\text{eff}}}}{E_{\text{F}}^{\text{L}}}, \end{aligned} \quad (\text{A.7})$$

where in the last step we have made a first-order Taylor expansion under the assumption that the electronic energies $\hbar\omega^{\text{el}} - \frac{\hbar|\mathbf{k}_{\parallel}^+|^2}{2m_{\text{eff}}}$ are considerably smaller than the Fermi energy E_{F}^{L} in the transitions considered. Following the same calculation for $k_{zR}^+ - k_{zR}^-$, we obtain the same expression of Eq. (A.7) with the substitution $E_{\text{F}}^{\text{L}} \rightarrow E_{\text{F}}^{\text{R}} + eV_{\text{B}}$. Accordingly, we can evaluate the fraction in Eq. (A.6), which leads to the condition

$$z = -\sqrt{\frac{E_{\text{F}}^{\text{R}} + eV_{\text{B}}}{E_{\text{F}}^{\text{L}}}}(z' - L_{\text{gap}}). \quad (\text{A.8})$$

Notably, under the approximations considered in this appendix, Eq. (A.8) does

not depend on the transition frequency $\omega_{\mathbf{k}_{\parallel}}^{(\nu)}$ and on the parallel wavevectors $\mathbf{k}_{\parallel}^{+}$ and $\mathbf{k}_{\parallel}^{-}$ of the initial and final quantum states. This means that for all possible transitions from a state $\Psi_{\text{L}}(z)$ to a state $\Psi_{\text{R}}(z)$, the current density has a similar argument at points z and z' that satisfy Eq. (A.8). Therefore, all transitions act constructively in the integral of Eq. (5.26) at these two points, leading to a strong peak in the correlations of the current density.

Appendix B

Classical description of the coupling between a molecule and a plasmonic nanocavity based on their polarizability

The interaction of a small metallic nanoparticle with a molecular excitation can be described classically by using polarizabilities α_{cav} and α_{mat} for both particles, so that the dipole moment induced by the electric field at each position \mathbf{r}_{cav} and \mathbf{r}_{mat} is given by $\mathbf{d}_{\text{cav}} = \alpha_{\text{cav}}\mathbf{E}(\mathbf{r}_{\text{cav}})$ and $\mathbf{d}_{\text{mat}} = \alpha_{\text{mat}}\mathbf{E}(\mathbf{r}_{\text{mat}})$, respectively. In this appendix, we briefly show that this approach leads to the same equations as the SpC model obtained from the electromagnetic Lagrangian [Eq. (6.21)], which supports the validity of the general approach used in Chapter 6.

For the cavity (metallic nanoparticle) and the molecular excitation (or any matter excitation in general), we consider the polarizability given by the Lorentz oscillator model. In the case of the molecule, we focus on a single excitation with Lorentzian polarizability centered at resonant frequency ω_{mat} , linewidth determined by the damping frequency γ and oscillator strength f_{mat} . Similarly, we also model the nanocavity response as given by a single plasmonic resonance that follows a Lorentzian-like lineshape, which is the typical lineshape in the quasistatic regime. This resonance is centered at frequency ω_{cav} , and is characterized by losses κ and oscillator strength f_{cav} . The polarizabilities of the plasmonic nanocavity and the molecule are then given by

$$\alpha_{\text{cav}}(\omega) = \frac{f_{\text{cav}}}{\omega_{\text{cav}}^2 - \omega^2 - i\omega\kappa}, \quad (\text{B.1a})$$

$$\alpha_{\text{mat}}(\omega) = \frac{f_{\text{mat}}}{\omega_{\text{mat}}^2 - \omega^2 - i\omega\gamma}. \quad (\text{B.1b})$$

The dipole moment of each particle is induced by the electric field \mathbf{E}_{inc} of

the external laser and also by the electric field generated by the other particle (\mathbf{E}_{cav} and \mathbf{E}_{mat} corresponding to the fields induced by the nanocavity and the matter excitation, respectively). We then have $\mathbf{d}_{\text{cav}} = \alpha_{\text{cav}}[\mathbf{E}_{\text{mat}}(\mathbf{r}_{\text{cav}}) + \mathbf{E}_{\text{inc}}]$ and $\mathbf{d}_{\text{mat}} = \alpha_{\text{mat}}[\mathbf{E}_{\text{cav}}(\mathbf{r}_{\text{mat}}) + \mathbf{E}_{\text{inc}}]$. By inserting in these expressions the polarizabilities given by Eq. (B.1) and the fields induced by the dipoles excited at the cavity and the molecule,

$$\mathbf{E}_{\text{mat}}(\mathbf{r}_{\text{cav}}) = \frac{\mathbf{n}_{\text{dmat}} - 3(\mathbf{n}_{\text{dmat}} \cdot \mathbf{n}_{\text{rrel}})\mathbf{n}_{\text{rrel}}}{4\pi\epsilon_0|\mathbf{r}_{\text{cav}} - \mathbf{r}_{\text{mat}}|^3}, \quad (\text{B.2a})$$

$$\mathbf{E}_{\text{cav}}(\mathbf{r}_{\text{mat}}) = \frac{\mathbf{n}_{\text{dcav}} - 3(\mathbf{n}_{\text{dcav}} \cdot \mathbf{n}_{\text{rrel}})\mathbf{n}_{\text{rrel}}}{4\pi\epsilon_0|\mathbf{r}_{\text{cav}} - \mathbf{r}_{\text{mat}}|^3}, \quad (\text{B.2b})$$

we obtain the expressions of the induced dipole moments

$$\begin{aligned} & (\omega_{\text{cav}}^2 - \omega^2 - i\omega\kappa)d_{\text{cav}} \\ &= f_{\text{cav}} \left[\frac{\mathbf{n}_{\text{dcav}} \cdot \mathbf{n}_{\text{dmat}} - 3(\mathbf{n}_{\text{dcav}} \cdot \mathbf{n}_{\text{rrel}})(\mathbf{n}_{\text{dmat}} \cdot \mathbf{n}_{\text{rrel}})}{4\pi\epsilon_0|\mathbf{r}_{\text{cav}} - \mathbf{r}_{\text{mat}}|^3} + \mathbf{E}_{\text{inc}} \cdot \mathbf{n}_{\text{dcav}} \right], \end{aligned} \quad (\text{B.3a})$$

$$\begin{aligned} & (\omega_{\text{mat}}^2 - \omega^2 - i\omega\gamma)d_{\text{mat}} \\ &= f_{\text{mat}} \left[\frac{\mathbf{n}_{\text{dcav}} \cdot \mathbf{n}_{\text{dmat}} - 3(\mathbf{n}_{\text{dcav}} \cdot \mathbf{n}_{\text{rrel}})(\mathbf{n}_{\text{dmat}} \cdot \mathbf{n}_{\text{rrel}})}{4\pi\epsilon_0|\mathbf{r}_{\text{cav}} - \mathbf{r}_{\text{mat}}|^3} + \mathbf{E}_{\text{inc}} \cdot \mathbf{n}_{\text{dmat}} \right]. \end{aligned} \quad (\text{B.3b})$$

These equations are equivalent to Eq. (6.21) in frequency domain, with $x_{\text{cav}} = \frac{d_{\text{cav}}}{\sqrt{f_{\text{cav}}}}$, $x_{\text{mat}} = \frac{d_{\text{mat}}}{\sqrt{f_{\text{mat}}}}$ and using the relation $|\mathbf{E}_{\text{inc}}| = |i\omega\mathcal{A}_{\text{inc}}|$ that follows from the definition of the vector potential.

Appendix C

Transformation from individual to collective oscillators in the description of homogeneous materials in Fabry-Pérot cavities

In Sec. 6.5.3, we analyze how classical models of harmonic oscillators describe an ensemble of N_{mat} molecules introduced in a Fabry-Pérot cavity. Each molecule couples with all the other molecules and also with the transverse modes of the cavity, and all these interactions can be modelled through Eq. (6.42). In this appendix, we show how to describe this system by considering the coupling of each Fabry-Pérot mode with a single collective mode of matter oscillators. Specifically, here we demonstrate how to transform Eq. (6.42), written in terms of harmonic oscillators of individual molecular excitations, into Eq. (6.43), which considers collective modes. This derivation can be generalized to other cavities by following the same procedure but using the spatial distribution of the transverse electric field of the corresponding cavity modes.

We assume that the Fabry-Pérot cavity contains perfect mirrors in the planes $z = 0$ and $z = L_{\text{cav}}$ (L_{cav} is the thickness of the cavity), so that the cavity has transverse electric (TE) modes with field distributionⁱ

$$\Xi_{n\mathbf{k}_{\parallel}}(\mathbf{r}) = \sin\left(\frac{n\pi z}{L_{\text{cav}}}\right) e^{i\mathbf{k}_{\parallel} \cdot \mathbf{r}_{\parallel}}. \quad (\text{C.1})$$

All modes of the cavity are indexed by the integer n and the wavevector in the parallel direction \mathbf{k}_{\parallel} , which can be any two-dimensional vector [we consider a

ⁱTo simplify the discussion, here we show explicitly the transformation under the field distribution of TE modes. However, Fabry-Pérot cavities also have transverse magnetic (TM) modes, and all the transformations are equivalent after substituting the field distribution of these modes into Eq. (C.1).

discrete set of \mathbf{k}_{\parallel} by assuming that the cavity has a long but finite size in the lateral dimensions and using Born-von Karman periodic boundary conditions for Eq. (C.1)]. We further assume that the direction of the transition dipole moments of the molecules is the same as that of the electric field of the mode (parallel to the mirror planes). As a consequence, the coupling strength between each molecule placed in the position $\mathbf{r}_i = (\mathbf{r}_{\parallel,i}, z_i)$ and the $n\mathbf{k}_{\parallel}$ Fabry-Pérot mode is calculated with the expression $g_{\text{MC}}^{(n\mathbf{k}_{\parallel},i)} = \frac{1}{2} \sqrt{\frac{f_{\text{mat}}}{\varepsilon_0 V_{\text{eff}}}} \Xi_{n\mathbf{k}_{\parallel}}(\mathbf{r}_i)$ [Eq. (6.17)]. By introducing the field distribution of Eq. (C.1) in the expression of the coupling strength explicitly, the equations of motion of the system [Eq. (6.42)] become

$$\ddot{x}_{\text{cav},n\mathbf{k}_{\parallel}} + \omega_{\text{cav},n\mathbf{k}_{\parallel}}^2 x_{\text{cav},n\mathbf{k}_{\parallel}} - \sum_i \sqrt{\frac{f_{\text{mat}}}{\varepsilon_0 V_{\text{eff}}}} \sin\left(\frac{n\pi z_i}{L_{\text{cav}}}\right) e^{-i\mathbf{k}_{\parallel} \cdot \mathbf{r}_{\parallel,i}} \dot{x}_{\text{mat},i} = 0, \quad (\text{C.2a})$$

$$\begin{aligned} \ddot{x}_{\text{mat},i} + \omega_{\text{mat}}^2 x_{\text{mat},i} + \sum_{n',\mathbf{k}'_{\parallel}} \sqrt{\frac{f_{\text{mat}}}{\varepsilon_0 V_{\text{eff}}}} \sin\left(\frac{n'\pi z_i}{L_{\text{cav}}}\right) e^{i\mathbf{k}'_{\parallel} \cdot \mathbf{r}_{\parallel,i}} \dot{x}_{\text{cav},n'\mathbf{k}'_{\parallel}} \\ + \sum_{j \neq i} 2\omega_{\text{mat}} g_{\text{SpC}}^{(i,j)} x_{\text{mat},j} = 0. \end{aligned} \quad (\text{C.2b})$$

In Eq. (C.2a), we already observe that the oscillator $x_{\text{cav},n\mathbf{k}_{\parallel}}$ of the $n\mathbf{k}_{\parallel}$ cavity mode is coupled to a collective matter operator. By defining the collective oscillator of the $n\mathbf{k}_{\parallel}$ matter mode as

$$x_{\text{mat},n\mathbf{k}_{\parallel}} = \frac{1}{\sqrt{N_{\text{eff}}}} \sum_i e^{-i\mathbf{k}_{\parallel} \cdot \mathbf{r}_{\parallel,i}} \sin\left(\frac{n\pi z_i}{L_{\text{cav}}}\right) x_{\text{mat},i}, \quad (\text{C.3})$$

Equation (C.2a) becomes

$$\ddot{x}_{\text{cav},n\mathbf{k}_{\parallel}} + \omega_{\text{cav},n\mathbf{k}_{\parallel}}^2 x_{\text{cav},n\mathbf{k}_{\parallel}} - \sqrt{N_{\text{eff}} g_{\text{MC}}} \dot{x}_{\text{mat},n\mathbf{k}_{\parallel}} = 0. \quad (\text{C.4})$$

where $\overline{g_{\text{MC}}} = \frac{1}{2} \sqrt{\frac{f_{\text{mat}}}{\varepsilon_0 V_{\text{eff}}}}$ is the maximum achievable coupling strength in this system between a single molecule and a cavity mode, for molecules placed in the antinodes of the mode. As discussed below, $N_{\text{eff}} = \sum_i |\Xi_{n\mathbf{k}_{\parallel}}(\mathbf{r}_i)|^2$ is the effective number of molecules that couple with the cavity mode, whose exact relation with the total number of molecules N_{mat} depends on the system and the spatial distribution of the modes. Further, we observe in Eq. (C.4) that the coupling strength between the cavity mode and the collective oscillator mode increases as $\overline{g_{\text{MC}}} \sqrt{N_{\text{eff}}}$. This scaling of the coupling strength [together with the scaling as $1/\sqrt{N_{\text{eff}}}$ of the collective oscillator in Eq. (C.3)] is the same as in the quantum Dicke model [285], showing that the classical oscillator models are consistent with descriptions based on cavity QED.

The next step is to transform Eq. (C.2b), which requires considering N_{mat} equations simultaneously, one per molecule at position \mathbf{r}_i . To do the transformation,

we multiply Eq. (C.2b) by $\frac{1}{\sqrt{N_{\text{eff}}}} \sin\left(\frac{n\pi z_i}{L_{\text{cav}}}\right) e^{-i\mathbf{k}_{\parallel} \cdot \mathbf{r}_{\parallel i}}$ for each i molecule and sum the N_{mat} resulting terms. With this procedure, the transformation of the first two terms is straightforward as

$$\frac{1}{\sqrt{N_{\text{eff}}}} \sum_i \sin\left(\frac{n\pi z_i}{L_{\text{cav}}}\right) e^{-i\mathbf{k}_{\parallel} \cdot \mathbf{r}_{\parallel i}} (\ddot{x}_{\text{mat},i} + \omega_{\text{mat}}^2 x_{\text{mat},i}) = \ddot{x}_{\text{mat},n\mathbf{k}_{\parallel}} + \omega_{\text{mat}}^2 x_{\text{mat},n\mathbf{k}_{\parallel}}. \quad (\text{C.5})$$

Repeating the procedure with the third term of Eq. (C.2b), we obtain

$$\begin{aligned} & \frac{1}{\sqrt{N_{\text{eff}}}} \overline{g_{\text{MC}}} \sum_{n', \mathbf{k}'_{\parallel}} \dot{x}_{\text{cav}, n' \mathbf{k}'_{\parallel}} \sum_i \sin\left(\frac{n' \pi z_i}{L_{\text{cav}}}\right) \sin\left(\frac{n \pi z_i}{L_{\text{cav}}}\right) e^{i(\mathbf{k}_{\parallel} - \mathbf{k}'_{\parallel}) \cdot \mathbf{r}_{\parallel i}} \\ &= \frac{1}{\sqrt{N_{\text{eff}}}} \overline{g_{\text{MC}}} \sum_{n', \mathbf{k}'_{\parallel}} \dot{x}_{\text{cav}, n \mathbf{k}_{\parallel}} \frac{N_{\text{mat}}}{2} \delta_{n, n'} \delta_{\mathbf{k}_{\parallel}, \mathbf{k}'_{\parallel}} = \overline{g_{\text{MC}}} \frac{N_{\text{mat}}}{2} \frac{1}{\sqrt{N_{\text{eff}}}} \dot{x}_{\text{cav}, n \mathbf{k}_{\parallel}}. \end{aligned} \quad (\text{C.6})$$

Equation (C.6) shows that, although each molecule couples with all Fabry-Pérot modes, the collective matter oscillator of amplitude $x_{\text{mat}, n \mathbf{k}_{\parallel}}$, described by the indexes n and \mathbf{k}_{\parallel} , only couples with the cavity mode of same indexes due to the orthogonality of all these modes. Further, the coupling strength between the cavity mode and the collective matter mode, which is the term multiplying $\dot{x}_{\text{cav}, n \mathbf{k}_{\parallel}}$ in Eq. (C.6), must be equal to the coupling strength that multiplies $\dot{x}_{\text{mat}, n \mathbf{k}_{\parallel}}$ in Eq. (C.4). This equality implies that $N_{\text{eff}} = \sum_i |\Xi_{n \mathbf{k}_{\parallel}}(\mathbf{r}_i)|^2 = N_{\text{mat}}/2$ for the Fabry-Pérot cavity.

Last, we transform the fourth term of Eq. (C.2b), which involves molecule-molecule interactions. To perform this transformation, we consider the SpC coupling strength between molecules as given by Eq. (6.19) explicitly, which leads to

$$\begin{aligned} & \frac{1}{\sqrt{N_{\text{eff}}}} \sum_i \sum_{j \neq i} 2\omega_{\text{mat}} g_{\text{SpC}}^{(i,j)} \sin\left(\frac{n\pi z_i}{L_{\text{cav}}}\right) e^{-i\mathbf{k}_{\parallel} \cdot \mathbf{r}_{\parallel i}} x_{\text{mat},j} \\ &= \frac{1}{\sqrt{N_{\text{eff}}}} \sum_j 2\omega_{\text{mat}} x_{\text{mat},j} e^{-i\mathbf{k}_{\parallel} \cdot \mathbf{r}_{\parallel j}} \sum_{i \neq j} g_{\text{SpC}}^{(i,j)} \sin\left(\frac{n\pi z_i}{L_{\text{cav}}}\right) e^{-i\mathbf{k}_{\parallel} \cdot (\mathbf{r}_{\parallel i} - \mathbf{r}_{\parallel j})} \\ &= \frac{1}{\sqrt{N_{\text{eff}}}} \sum_j 2\omega_{\text{mat}} x_{\text{mat},j} e^{-i\mathbf{k}_{\parallel} \cdot \mathbf{r}_{\parallel j}} \\ & \quad \times \left[\sum_{i \neq j} \frac{1}{2} \frac{f_{\text{mat}} e^{-i\mathbf{k}_{\parallel} \cdot (\mathbf{r}_{\parallel i} - \mathbf{r}_{\parallel j})}}{4\pi \varepsilon_0 |\mathbf{r}_i - \mathbf{r}_j|^3 \omega_{\text{mat}}} [1 - 3(\mathbf{n}_{\mathbf{d}} \cdot \mathbf{n}_{\mathbf{r}_{ij}})] \sin\left(\frac{n\pi z_i}{L_{\text{cav}}}\right) \right] \\ &\approx \frac{1}{\sqrt{N_{\text{eff}}}} \sum_j 2\omega_{\text{mat}} x_{\text{mat},j} e^{-i\mathbf{k}_{\parallel} \cdot \mathbf{r}_{\parallel j}} \sin\left(\frac{n\pi z_j}{L_{\text{cav}}}\right) \end{aligned}$$

$$\times \underbrace{\left[\sum_{i \neq j} \frac{1}{2} \frac{f_{\text{mat}} e^{-i\mathbf{k}_{\parallel} \cdot (\mathbf{r}_{\parallel i} - \mathbf{r}_{\parallel j})}}{4\pi\epsilon_0 |\mathbf{r}_i - \mathbf{r}_j|^3 \omega_{\text{mat}}} [1 - 3(\mathbf{n}_{\mathbf{d}} \cdot \mathbf{n}_{\mathbf{r}_{ij}})] \right]}_{\overline{g_{\text{SpC}}^{(n\mathbf{k}_{\parallel})}}} \quad (\text{C.7})$$

$$= 2\omega_{\text{mat}} \overline{g_{\text{SpC}}^{(n\mathbf{k}_{\parallel})}} x_{\text{mat}, n\mathbf{k}_{\parallel}}. \quad (\text{C.8})$$

To obtain Eq. (C.7), we have considered that the dipole-dipole coupling strength between different molecules, which depends over their distance as $|\mathbf{r}_i - \mathbf{r}_j|^{-3}$, decays much faster over z than the term $\sin(n\pi z_i/L_{\text{cav}})$ changes (unless n is so large that it has very fast oscillations, which we do not consider here). Due to this fast decay, we have checked numerically that the term $\sin(n\pi z_i/L_{\text{cav}})$ can be taken outside the sum over molecules i as a constant. The sum over the variable i in Eq. (C.7) can be then performed numerically to obtain the collective molecule-molecule coupling strength $\overline{g_{\text{SpC}}^{(n\mathbf{k}_{\parallel})}}$.

Therefore, by gathering all transformed terms in Eqs. (C.5), (C.6) and (C.8), Eq. (C.2b) becomes

$$\ddot{x}_{\text{mat}, n\mathbf{k}_{\parallel}} + \left(\omega_{\text{mat}}^2 + 2\omega_{\text{mat}} \overline{g_{\text{SpC}}^{(n\mathbf{k}_{\parallel})}} \right) x_{\text{mat}, n\mathbf{k}_{\parallel}} + \overline{g_{\text{MC}}} \sqrt{N_{\text{eff}}} \dot{x}_{\text{cav}, n\mathbf{k}_{\parallel}} = 0. \quad (\text{C.9})$$

Equations (C.4) and (C.9) correspond to Eq. (6.43). Importantly, the derivation carried out in this appendix shows two important features of light-matter coupling in this system: i) although each $n\mathbf{k}_{\parallel}$ cavity mode is coupled to all individual molecules, it is only coupled to the $n\mathbf{k}_{\parallel}$ collective mode due to the orthogonality of the modes, and ii) the only consequence of the molecule-molecule coupling for the interaction between the $n\mathbf{k}_{\parallel}$ cavity and matter modes is to renormalize the bare frequency of the matter oscillator from ω_{mat} to $\sqrt{\omega_{\text{mat}}^2 + 2\omega_{\text{mat}} \overline{g_{\text{SpC}}^{(n\mathbf{k}_{\parallel})}}}$ [288].

List of publications

This thesis has been based on the following publications:

Chapter 3:

1. **U. Muniain**, R. Esteban, I. P. Chernov, J. Aizpurua, and V. M. Silkin: “Surface plasmons on Pd(110): An *ab initio* calculation”, *Physical Review B* **103**, 045407 (2021).
<https://doi.org/10.1103/PhysRevB.103.045407>

Chapter 4:

2. **U. Muniain** and V. M. Silkin: “Impact of the energy dispersion anisotropy on the plasmonic structure in a two-dimensional electron system”, *Physical Chemistry Chemical Physics* **24**, 17885-17894 (2022).
<https://doi.org/10.1039/d2cp02050e>

Chapter 5:

3. **U. Muniain**, R. Esteban, J. Aizpurua and J.-J. Greffet: “Unified treatment of light emission by inelastic tunneling: interaction of electrons and photons beyond the gap”, In preparation.

Chapter 6:

4. **U. Muniain**, J. Aizpurua, R. Hillenbrand, L. Martín-Moreno and R. Esteban: “Description of ultrastrong light-matter interaction through coupled harmonic oscillator models and their connection with cavity-QED Hamiltonians”, In preparation.

Chapter 7:

5. M. Barra-Burillo*, **U. Muniain***, S. Catalano, M. Autore, F. Casanova, L. E. Hueso, J. Aizpurua, R. Esteban, and R. Hillenbrand: “Microcavity phonon polaritons from the weak to the ultrastrong phonon-photon coupling regime”, *Nature Communications* **12**, 6206 (2021).
<https://doi.org/10.1038/s41467-021-26060-x>

* These authors contributed equally to this work.

Other publications related to this thesis:

1. J. J. Baumberg, R. Esteban, S. Hu, **U. Muniain**, I. V. Silkin, J. Aizpurua, and V. M. Silkin: “Quantum plasmonics in sub-atom-thick optical waveguides”, Submitted.
2. Á. Nodar, R. Esteban, **U. Muniain**, M. J. Steel, J. Aizpurua, and M. K. Schmidt: “Identifying unbound strong bunching and the breakdown of the Rotating Wave Approximation in the quantum Rabi model”, Submitted. ArXiv preprint, arXiv:2211.13249 (2022).
<https://arxiv.org/abs/2211.13249>
3. S. Ribeiro, **U. Muniain**, J. Aizpurua and R. Esteban: “Theoretical description of Raman scattering from molecular vibrations strongly coupled to infrared cavity modes”, In preparation.

Bibliography

- [1] A. Van Helden, The invention of the telescope, *Trans. Am. Philos. Soc.* **67**, 1 (1977).
- [2] P. Mazzeo, A unifying concept: the history of cell theory, *Nat. Cell Biol.* **1**, E13 (1999).
- [3] E. Abbe, Beiträge zur Theorie des Mikroskops und der mikroskopischen Wahrnehmung, *Arch. für Mikrosk. Anat.* **9**, 413 (1873).
- [4] D. K. Gramotnev and S. I. Bozhevolnyi, Plasmonics beyond the diffraction limit, *Nat. Photon.* **4**, 83 (2010).
- [5] H. Raether, *Surface plasmons on smooth and rough surfaces and on gratings*, Springer, 2006.
- [6] P. Mühlischlegel, H.-J. Eisler, O. J. F. Martin, B. Hecht, and D. W. Pohl, Resonant Optical Antennas, *Science* **308**, 1607 (2005).
- [7] I. Romero, J. Aizpurua, G. W. Bryant, and F. J. García de Abajo, Plasmons in nearly touching metallic nanoparticles: singular response in the limit of touching dimers, *Opt. Express* **14**, 9988 (2006).
- [8] D. O. Sigle et al., Monitoring Morphological Changes in 2D Monolayer Semiconductors Using Atom-Thick Plasmonic Nanocavities, *ACS Nano* **9**, 825 (2015).
- [9] J. J. Baumberg, J. Aizpurua, M. H. Mikkelsen, and D. R. Smith, Extreme nanophotonics from ultrathin metallic gaps, *Nat. Mater.* **18**, 668 (2019).
- [10] S. Shen, A. Narayanaswamy, and G. Chen, Surface Phonon Polaritons Mediated Energy Transfer between Nanoscale Gaps, *Nano Lett.* **9**, 2909 (2009).
- [11] Y. Xu, L. Wu, and L. Ang, Surface Exciton Polaritons: A Promising Mechanism for Refractive-Index Sensing, *Phys. Rev. Appl.* **12**, 024029 (2019).

- [12] P. Roelli, C. Galland, N. Piro, and T. J. Kippenberg, Molecular cavity optomechanics as a theory of plasmon-enhanced Raman scattering, *Nat. Nanotechnol.* **11**, 164 (2016).
- [13] M. K. Schmidt, R. Esteban, A. González-Tudela, G. Giedke, and J. Aizpurua, Quantum mechanical description of Raman scattering from molecules in plasmonic cavities, *ACS Nano* **10**, 6291 (2016).
- [14] T. Neuman, R. Esteban, G. Giedke, M. K. Schmidt, and J. Aizpurua, Quantum description of surface-enhanced resonant Raman scattering within a hybrid-optomechanical model, *Phys. Rev. A* **100**, 043422 (2019).
- [15] A. I. Pérez-Jiménez, D. Lyu, Z. Lu, G. Liu, and B. Ren, Surface-enhanced Raman spectroscopy: benefits, trade-offs and future developments, *Chem. Sci.* **11**, 4563 (2020).
- [16] F. Neubrech et al., Resonant Plasmonic and Vibrational Coupling in a Tailored Nanoantenna for Infrared Detection, *Phys. Rev. Lett.* **101**, 157403 (2008).
- [17] F. Neubrech, C. Huck, K. Weber, A. Pucci, and H. Giessen, Surface-Enhanced Infrared Spectroscopy Using Resonant Nanoantennas, *Chem. Rev.* **117**, 5110 (2017).
- [18] H.-L. Wang, E.-M. You, R. Panneerselvam, S.-Y. Ding, and Z.-Q. Tian, Advances of surface-enhanced Raman and IR spectroscopies: from nano/microstructures to macro-optical design, *Light Sci. Appl.* **10**, 161 (2021).
- [19] R. Zhang et al., Chemical mapping of a single molecule by plasmon-enhanced Raman scattering, *Nature* **498**, 82 (2013).
- [20] F. Benz et al., Single-molecule optomechanics in “picocavities”, *Science* **354**, 726 (2016).
- [21] A. Rosławska et al., Mapping Lamb, Stark, and Purcell Effects at a Chromophore-Picocavity Junction with Hyper-Resolved Fluorescence Microscopy, *Phys. Rev. X* **12**, 011012 (2022).
- [22] D. J. de Aberasturi, A. B. Serrano-Montes, and L. M. Liz-Marzán, Modern Applications of Plasmonic Nanoparticles: From Energy to Health, *Adv. Opt. Mater.* **3**, 602 (2015).
- [23] S. K. Cushing and N. Wu, Progress and Perspectives of Plasmon-Enhanced Solar Energy Conversion, *J. Phys. Chem. Lett.* **7**, 666 (2016).
- [24] S. Carretero-Palacios, A. Jiménez-Solano, and H. Míguez, Plasmonic Nanoparticles as Light-Harvesting Enhancers in Perovskite Solar Cells: A User’s Guide, *ACS Energy Lett.* **1**, 323 (2016).

-
- [25] R. Bardhan, S. Lal, A. Joshi, and N. J. Halas, Theranostic nanoshells: from probe design to imaging and treatment of cancer, *Acc. Chem. Res.* **44**, 936 (2011).
- [26] T. L. Doane and C. Burda, The unique role of nanoparticles in nanomedicine: imaging, drug delivery and therapy, *Chem. Soc. Rev.* **41**, 2885 (2012).
- [27] B. de Nijs et al., Inhibiting Analyte Theft in Surface-Enhanced Raman Spectroscopy Substrates: Subnanomolar Quantitative Drug Detection, *ACS Sens.* **4**, 2988 (2019).
- [28] I. Alonso Calafell et al., Quantum computing with graphene plasmons, *Npj Quantum Inf.* **5**, 37 (2019).
- [29] S. A. Maier, *Plasmonics: fundamentals and applications*, Springer, 2007.
- [30] M. S. Tame et al., Quantum plasmonics, *Nat. Phys.* **9**, 329 (2013).
- [31] W. Zhu et al., Quantum mechanical effects in plasmonic structures with subnanometre gaps, *Nat. Commun.* **7**, 1 (2016).
- [32] F. Marquier, C. Sauvan, and J.-J. Greffet, Revisiting Quantum Optics with Surface Plasmons and Plasmonic Resonators, *ACS Photonics* **4**, 2091 (2017).
- [33] A. Liebsch, *Electronic excitations at metal surfaces*, Springer Science & Business Media, 1997.
- [34] N. A. Mortensen, Mesoscopic electrodynamics at metal surfaces, *Nanophotonics* **10**, 2563 (2021).
- [35] A. Babaze et al., Quantum surface effects in the electromagnetic coupling between a quantum emitter and a plasmonic nanoantenna: time-dependent density functional theory vs. semiclassical Feibelman approach, *Opt. Express* **30**, 21159 (2022).
- [36] R. Esteban, A. G. Borisov, P. Nordlander, and J. Aizpurua, Bridging quantum and classical plasmonics with a quantum-corrected model, *Nat. Commun.* **3**, 825 (2012).
- [37] L. Mao, Z. Li, B. Wu, and H. Xu, Effects of quantum tunneling in metal nanogap on surface-enhanced Raman scattering, *Appl. Phys. Lett.* **94**, 243102 (2009).
- [38] J. Zuloaga, E. Prodan, and P. Nordlander, Quantum Description of the Plasmon Resonances of a Nanoparticle Dimer, *Nano Letters* **9**, 887 (2009).
- [39] H. J. Kimble, M. Dagenais, and L. Mandel, Photon Antibunching in Resonance Fluorescence, *Phys. Rev. Lett.* **39**, 691 (1977).
- [40] B. Lounis and M. Orrit, Single-photon sources, *Rep. Prog. Phys.* **68**, 1129 (2005).

- [41] P. Törmä and W. L. Barnes, Strong coupling between surface plasmon polaritons and emitters: a review, *Rep. Prog. Phys.* **78**, 013901 (2014).
- [42] M. Marques and E. Gross, Time-dependent density functional theory, *Annu. Rev. Phys. Chem.* **55**, 427 (2004).
- [43] S. Botti, A. Schindlmayr, R. D. Sole, and L. Reining, Time-dependent density-functional theory for extended systems, *Rep. Prog. Phys.* **70**, 357 (2007).
- [44] V. M. Silkin et al., Novel low-energy collective excitation at metal surfaces, *EPL* **66**, 260 (2004).
- [45] B. Diaconescu et al., Low-energy acoustic plasmons at metal surfaces, *Nature* **448**, 57 (2007).
- [46] L. Vattuone et al., Correlated Motion of Electrons on the Au(111) Surface: Anomalous Acoustic Surface-Plasmon Dispersion and Single-Particle Excitations, *Phys. Rev. Lett.* **110**, 127405 (2013).
- [47] C. Tegenkamp, H. Pfñür, T. Langer, J. Baringhaus, and H. W. Schumacher, Plasmon electron-hole resonance in epitaxial graphene, *J. Phys. Condens. Matter* **23**, 012001 (2010).
- [48] F. Stern, Polarizability of a Two-Dimensional Electron Gas, *Phys. Rev. Lett.* **18**, 546 (1967).
- [49] K. Kuroda et al., Hexagonally Deformed Fermi Surface of the 3D Topological Insulator Bi₂Se₃, *Phys. Rev. Lett.* **105**, 076802 (2010).
- [50] M. Neupane et al., Observation of topological nodal fermion semimetal phase in ZrSiS, *Phys. Rev. B* **93**, 201104 (2016).
- [51] L. M. Schoop et al., Dirac cone protected by non-symmorphic symmetry and three-dimensional Dirac line node in ZrSiS, *Nat. Commun.* **7**, 11696 (2016).
- [52] B. Feng et al., Discovery of 2D anisotropic Dirac cones, *Adv. Mater.* **30**, 1704025 (2018).
- [53] S. Xue et al., Observation of Nodal-Line Plasmons in ZrSiS, *Phys. Rev. Lett.* **127**, 186802 (2021).
- [54] S. McCarthy and J. Lambe, Enhancement of light emission from metal-insulator-metal tunnel junctions, *Appl. Phys. Lett.* **30**, 427 (1977).
- [55] B. Laks and D. L. Mills, Photon emission from slightly roughened tunnel junctions, *Phys. Rev. B* **20**, 4962 (1979).
- [56] M. Parzefall and L. Novotny, Optical antennas driven by quantum tunneling: a key issues review, *Rep. Prog. Phys.* **82**, 112401 (2019).

-
- [57] J. Kirtley, T. N. Theis, and J. C. Tsang, Light emission from tunnel junctions on gratings, *Phys. Rev. B* **24**, 5650 (1981).
- [58] A. Frisk Kockum, A. Miranowicz, S. De Liberato, S. Savasta, and F. Nori, Ultrastrong coupling between light and matter, *Nat. Rev. Phys.* **1**, 19 (2019).
- [59] P. Forn-Díaz, L. Lamata, E. Rico, J. Kono, and E. Solano, Ultrastrong coupling regimes of light-matter interaction, *Rev. Mod. Phys.* **91**, 025005 (2019).
- [60] L. Novotny, Strong coupling, energy splitting, and level crossings: A classical perspective, *Am. J. Phys.* **78**, 1199 (2010).
- [61] J. A. Hutchison, T. Schwartz, C. Genet, E. Devaux, and T. W. Ebbesen, Modifying chemical landscapes by coupling to vacuum fields, *Angew. Chem. Int. Ed.* **51**, 1592 (2012).
- [62] A. Thomas et al., Tilting a ground-state reactivity landscape by vibrational strong coupling, *Science* **363**, 615 (2019).
- [63] S. Kéna-Cohen, S. A. Maier, and D. D. C. Bradley, Ultrastrongly Coupled Exciton–Polaritons in Metal-Clad Organic Semiconductor Microcavities, *Adv. Opt. Mater.* **1**, 827 (2013).
- [64] S. Brodbeck et al., Experimental Verification of the Very Strong Coupling Regime in a GaAs Quantum Well Microcavity, *Phys. Rev. Lett.* **119**, 027401 (2017).
- [65] J. C. Maxwell, A dynamical theory of the electromagnetic field, *Philos. Trans. R. Soc.* **155**, 459 (1865).
- [66] J. D. Jackson, *Classical electrodynamics*, Wiley, New York, NY, 1999.
- [67] L. Novotny and B. Hecht, *Principles of Nano-Optics*, Cambridge University Press, 2012.
- [68] H. Benisty, J.-J. Greffet, and P. Lalanne, *Introduction to Nanophotonics*, Oxford University Press, 2022.
- [69] D. J. Griffiths, *Introduction to electrodynamics*, Cambridge University Press, 2005.
- [70] N. C. Passler and A. Paarmann, Generalized 4×4 matrix formalism for light propagation in anisotropic stratified media: study of surface phonon polaritons in polar dielectric heterostructures, *J. Opt. Soc. Am. B* **34**, 2128 (2017).
- [71] P. B. Johnson and R. W. Christy, Optical Constants of the Noble Metals, *Phys. Rev. B* **6**, 4370 (1972).

- [72] C. Cohen-Tannoudji, J. Dupont-Roc, and G. Grynberg, *Photons and atoms: introduction to quantum electrodynamics*, Wiley, New York, NY, 1989.
- [73] D. L. Andrews, G. A. Jones, A. Salam, and R. G. Woolley, *Perspective: Quantum Hamiltonians for optical interactions*, *J. Chem. Phys.* **148**, 040901 (2018).
- [74] Y. Li, *Plasmonic optics: theory and applications*, SPIE Press, 2017.
- [75] J. M. Pitarke, V. M. Silkin, E. V. Chulkov, and P. M. Echenique, *Theory of surface plasmons and surface-plasmon polaritons*, *Rep. Prog. Phys.* **70**, 1 (2006).
- [76] A. Otto, *Excitation of nonradiative surface plasma waves in silver by the method of frustrated total reflection*, *Z. Phys.* **216**, 398 (1968).
- [77] E. Kretschmann and H. Raether, *Radiative Decay of Non Radiative Surface Plasmons Excited by Light*, *Z. Naturforsch. A* **23**, 2135 (1968).
- [78] W. Gao, J. Shu, C. Qiu, and Q. Xu, *Excitation of Plasmonic Waves in Graphene by Guided-Mode Resonances*, *ACS Nano* **6**, 7806 (2012).
- [79] S. Joseph, S. Sarkar, and J. Joseph, *Grating-Coupled Surface Plasmon-Polariton Sensing at a Flat Metal-Analyte Interface in a Hybrid-Configuration*, *ACS Appl. Mater. Interfaces* **12**, 46519 (2020).
- [80] B. Hecht, H. Bielefeldt, L. Novotny, Y. Inouye, and D. W. Pohl, *Local Excitation, Scattering, and Interference of Surface Plasmons*, *Phys. Rev. Lett.* **77**, 1889 (1996).
- [81] F. De Angelis et al., *Nanoscale chemical mapping using three-dimensional adiabatic compression of surface plasmon polaritons*, *Nat. Nanotechnol.* **5**, 67 (2010).
- [82] C. C. Neacsu et al., *Near-Field Localization in Plasmonic Superfocusing: A Nanoemitter on a Tip*, *Nano Lett.* **10**, 592 (2010).
- [83] B. N. J. Persson and E. Zaremba, *Electron-hole pair production at metal surfaces*, *Phys. Rev. B* **31**, 1863 (1985).
- [84] J. J. Baumberg et al., *Quantum plasmonics in sub-atom-thick optical slot waveguides*, Submitted (2023).
- [85] E. Waks and D. Sridharan, *Cavity QED treatment of interactions between a metal nanoparticle and a dipole emitter*, *Phys. Rev. A* **82**, 043845 (2010).
- [86] W. L. Barnes, *Particle plasmons: Why shape matters*, *Am. J. Phys.* **84**, 593 (2016).
- [87] J. D. Caldwell et al., *Photonics with hexagonal boron nitride*, *Nat. Rev. Mater.* **8**, 1 (2019).

-
- [88] J. D. Caldwell et al., Low-Loss, Extreme Subdiffraction Photon Confinement via Silicon Carbide Localized Surface Phonon Polariton Resonators, *Nano Lett.* **13**, 3690 (2013).
- [89] J. Kulda, D. Strauch, P. Pavone, and Y. Ishii, Inelastic-neutron-scattering study of phonon eigenvectors and frequencies in Si, *Phys. Rev. B* **50**, 13347 (1994).
- [90] J. D. Caldwell et al., Low-loss, infrared and terahertz nanophotonics using surface phonon polaritons, *Nanophotonics* **4**, 44 (2015).
- [91] M. Autore et al., Boron nitride nanoresonators for phonon-enhanced molecular vibrational spectroscopy at the strong coupling limit, *Light Sci. Appl.* **7**, 17172 (2018).
- [92] M. Cardona and P. Y. Yu, *Fundamentals of semiconductors*, Springer, 2005.
- [93] E. M. Purcell, H. C. Torrey, and R. V. Pound, Resonance absorption by nuclear magnetic moments in a solid, *Phys. Rev.* **69**, 37 (1946).
- [94] J. J. Hopfield, Theory of the Contribution of Excitons to the Complex Dielectric Constant of Crystals, *Phys. Rev.* **112**, 1555 (1958).
- [95] T. Tufarelli, K. R. McEnery, S. A. Maier, and M. S. Kim, Signatures of the A^2 term in ultrastrongly coupled oscillators, *Phys. Rev. A* **91**, 063840 (2015).
- [96] G. Lindblad, On the generators of quantum dynamical semigroups, *Commun. Math. Phys.* **48**, 119 (1976).
- [97] H. Carmichael, *Statistical methods in quantum optics 1: master equations and Fokker-Planck equations*, Springer Science & Business Media, 1999.
- [98] F. Beaudoin, J. M. Gambetta, and A. Blais, Dissipation and ultrastrong coupling in circuit QED, *Phys. Rev. A* **84**, 043832 (2011).
- [99] A. Settineri et al., Dissipation and thermal noise in hybrid quantum systems in the ultrastrong-coupling regime, *Phys. Rev. A* **98**, 053834 (2018).
- [100] R. Stassi, A. Ridolfo, O. Di Stefano, M. J. Hartmann, and S. Savasta, Spontaneous Conversion from Virtual to Real Photons in the Ultrastrong-Coupling Regime, *Phys. Rev. Lett.* **110**, 243601 (2013).
- [101] S. De Liberato, Virtual photons in the ground state of a dissipative system, *Nat. Commun.* **8**, 1465 (2017).
- [102] K. Rzażewski, K. Wódkiewicz, and W. Żakowicz, Phase Transitions, Two-Level Atoms, and the A^2 Term, *Phys. Rev. Lett.* **35**, 432 (1975).
- [103] D. De Bernardis, T. Jaako, and P. Rabl, Cavity quantum electrodynamics in the nonperturbative regime, *Phys. Rev. A* **97**, 043820 (2018).

- [104] G. L. Giuliani and G. Vignale, Quantum theory of the electron liquid, Cambridge University Press, 2005.
- [105] P. Coleman, Introduction to many-body physics, Cambridge University Press, 2015.
- [106] D. Pines and P. Nozieres, The Theory of Quantum Liquids: Normal Fermi Liquids, W. A. Benjamin, New York, 1966.
- [107] R. de L. Kronig, On the Theory of Dispersion of X-Rays, J. Opt. Soc. Am. **12**, 547 (1926).
- [108] G. D. Mahan, Many-particle physics, Springer Science & Business Media, 2000.
- [109] J. Lindhard, On the properties of a gas of charged particles, Dan. Vid. Selsk Mat.-Fys. Medd. **28**, 8 (1954).
- [110] F. J. García de Abajo, Optical excitations in electron microscopy, Rev. Mod. Phys. **82**, 209 (2010).
- [111] K. Sturm, Electron energy loss in simple metals and semiconductors, Adv. Phys. **31**, 1 (1982).
- [112] F. J. García de Abajo, Graphene Plasmonics: Challenges and Opportunities, ACS Photonics **1**, 135 (2014).
- [113] T. Stauber, Plasmonics in Dirac systems: from graphene to topological insulators, J. Phys. Condens. Matter **26**, 123201 (2014).
- [114] A. Politano et al., Interplay of Surface and Dirac Plasmons in Topological Insulators: The Case of Bi₂Se₃, Phys. Rev. Lett. **115**, 216802 (2015).
- [115] V. M. Silkin, J. M. Pitarke, E. V. Chulkov, and P. M. Echenique, Acoustic surface plasmons in the noble metals Cu, Ag, and Au, Phys. Rev. B **72**, 115435 (2005).
- [116] K. Pohl et al., Acoustic surface plasmon on Cu(111), EPL **90**, 57006 (2010).
- [117] J. M. Pitarke et al., Theory of acoustic surface plasmons, Phys. Rev. B **70**, 205403 (2004).
- [118] M. Born and R. Oppenheimer, Zur quantentheorie der molekeln, Ann. Phys. **389**, 457 (1927).
- [119] P. Hohenberg and W. Kohn, Inhomogeneous Electron Gas, Phys. Rev. **136**, B864 (1964).
- [120] W. Kohn and L. J. Sham, Self-Consistent Equations Including Exchange and Correlation Effects, Phys. Rev. **140**, A1133 (1965).

-
- [121] C. A. Ullrich, Time-dependent density-functional theory: concepts and applications, (2011).
- [122] C. Fiolhais, F. Nogueira, and M. A. Marques, A primer in density functional theory, Springer Science & Business Media, 2003.
- [123] D. M. Ceperley and B. J. Alder, Ground State of the Electron Gas by a Stochastic Method, *Phys. Rev. Lett.* **45**, 566 (1980).
- [124] J. P. Perdew and A. Zunger, Self-interaction correction to density-functional approximations for many-electron systems, *Phys. Rev. B* **23**, 5048 (1981).
- [125] E. Runge and E. K. U. Gross, Density-Functional Theory for Time-Dependent Systems, *Phys. Rev. Lett.* **52**, 997 (1984).
- [126] A. A. Quong and A. G. Eguiluz, First-principles evaluation of dynamical response and plasmon dispersion in metals, *Phys. Rev. Lett.* **70**, 3955 (1993).
- [127] B.-O. Kim, G. Lee, E. W. Plummer, P. A. Dowben, and A. Liebsch, Mercury surface-plasmon dispersion: Experiment and theory, *Phys. Rev. B* **52**, 6057 (1995).
- [128] M. Cazzaniga et al., Dynamical response function in sodium and aluminum from time-dependent density-functional theory, *Phys. Rev. B* **84**, 075109 (2011).
- [129] N. W. Ashcroft and N. D. Mermin, *Solid State Physics*, Saunders College Publishing, 1976.
- [130] V. U. Nazarov, Electronic excitations in quasi-2D crystals: what theoretical quantities are relevant to experiment?, *New J. Phys.* **17**, 073018 (2015).
- [131] J. Lambe and S. L. McCarthy, Light Emission from Inelastic Electron Tunneling, *Phys. Rev. Lett.* **37**, 923 (1976).
- [132] J. Bardeen, Tunnelling from a Many-Particle Point of View, *Phys. Rev. Lett.* **6**, 57 (1961).
- [133] C. B. Duke, *Tunneling in solids*, Academic Press, 1969.
- [134] A. D. Gottlieb and L. Wesoloski, Bardeen's tunnelling theory as applied to scanning tunnelling microscopy: a technical guide to the traditional interpretation, *Nanotechnology* **17**, R57 (2006).
- [135] M. Rocca, Low-energy EELS investigation of surface electronic excitations on metals, *Surf. Sci. Rep.* **22**, 1 (1995).
- [136] E. Prodan, C. Radloff, N. J. Halas, and P. Nordlander, A hybridization model for the plasmon response of complex nanostructures, *Science* **302**, 419 (2003).

- [137] R. H. Ritchie, Plasma Losses by Fast Electrons in Thin Films, *Phys. Rev.* **106**, 874 (1957).
- [138] P. J. Feibelman, Surface electromagnetic fields, *Prog. Surf. Sci.* **12**, 287 (1982).
- [139] A. R. Echarri et al., Optical response of noble metal nanostructures: quantum surface effects in crystallographic facets, *Optica* **8**, 710 (2021).
- [140] P. J. Feibelman, Microscopic calculation of surface-plasmon dispersion and damping, *Phys. Rev. B* **9**, 5077 (1974).
- [141] P. J. Feibelman, Microscopic calculation of electromagnetic fields in refraction at a jellium-vacuum interface, *Phys. Rev. B* **12**, 1319 (1975).
- [142] A. Liebsch, Dynamical screening at simple-metal surfaces, *Phys. Rev. B* **36**, 7378 (1987).
- [143] K. Kempa and W. L. Schaich, Nonlocal corrections to Fresnel optics: Model calculations from first principles for flat jellium, *Phys. Rev. B* **37**, 6711 (1988).
- [144] K.-D. Tsuei, E. W. Plummer, and P. J. Feibelman, Surface-plasmon dispersion in simple metals, *Phys. Rev. Lett.* **63**, 2256 (1989).
- [145] K.-D. Tsuei et al., The normal modes at the surface of simple metals, *Surf. Sci.* **247**, 302 (1991).
- [146] M. Rocca and U. Valbusa, Angular dependence of dipole scattering cross section: Surface-plasmon losses on Ag(100), *Phys. Rev. Lett.* **64**, 2398 (1990).
- [147] M. Rocca, F. Biggio, and U. Valbusa, Surface-plasmon spectrum of Ag(001) measured by high-resolution angle-resolved electron-energy-loss spectroscopy, *Phys. Rev. B* **42**, 2835 (1990).
- [148] M. Rocca, M. Lazzarino, and U. Valbusa, Surface plasmon on Ag(110): Observation of linear and positive dispersion and strong azimuthal anisotropy, *Phys. Rev. Lett.* **69**, 2122 (1992).
- [149] M. Rocca, L. Yibing, F. Buatier de Mongeot, and U. Valbusa, Surface plasmon dispersion and damping on Ag(111), *Phys. Rev. B* **52**, 14947 (1995).
- [150] A. Liebsch, Surface plasmon dispersion of Ag, *Phys. Rev. Lett.* **71**, 145 (1993).
- [151] P. J. Feibelman, Perturbation of surface plasmon dispersion by “extra” electrons near a surface, *Surf. Sci.* **282**, 129 (1993).
- [152] V. M. Silkin, P. Lazić, N. Došlić, H. Petek, and B. Gumhalter, Ultrafast electronic response of Ag(111) and Cu(111) surfaces: From early excitonic transients to saturated image potential, *Phys. Rev. B* **92**, 155405 (2015).

-
- [153] V. M. Silkin, E. V. Chulkov, and P. M. Echenique, Band Structure versus Dynamical Exchange-Correlation Effects in Surface Plasmon Energy and Damping: A First-Principles Calculation, *Phys. Rev. Lett.* **93**, 176801 (2004).
- [154] J. Yan, K. W. Jacobsen, and K. S. Thygesen, First-principles study of surface plasmons on Ag(111) and H/Ag(111), *Phys. Rev. B* **84**, 235430 (2011).
- [155] J. Yan, K. W. Jacobsen, and K. S. Thygesen, Conventional and acoustic surface plasmons on noble metal surfaces: A time-dependent density functional theory study, *Phys. Rev. B* **86**, 241404 (2012).
- [156] A. Politano and G. Chiarello, The influence of electron confinement, quantum size effects, and film morphology on the dispersion and the damping of plasmonic modes in Ag and Au thin films, *Prog. Surf. Sci.* **90**, 144 (2015).
- [157] K. Okuno, T. Ito, M. Iwami, and A. Hiraki, Low energy electron loss spectroscopic study of Pd-Si(111) system, *Solid State Commun.* **44**, 209 (1982).
- [158] J. L. Robins, Characteristic Electron Energy Loss Spectra of the Noble Metals and their Neighbours, *Proc. Phys. Soc.* **78**, 1177 (1961).
- [159] H. A. Hagelin, J. F. Weaver, G. B. Hoflund, and G. N. Salaita, Electron energy loss spectroscopic investigation of palladium metal and palladium(II) oxide, *J. Electron Spectrosc. Relat. Phenom.* **124**, 1 (2002).
- [160] H. A. Hagelin-Weaver, J. F. Weaver, G. B. Hoflund, and G. N. Salaita, Electron energy loss spectroscopic investigation of polycrystalline Au, Pd and a Pd–Au alloy, *J. Alloys Compd.* **393**, 93 (2005).
- [161] M. Nishijima, M. Jo, Y. Kuwahara, and M. Onchi, Electron energy loss spectra of a Pd(110) clean surface, *Solid State Commun.* **58**, 75 (1986).
- [162] T. Bornemann, J. Eickmans, and A. Otto, Interaction of d-electron excitations and plasmons in Pd, Ag, Cd, In, Sn and Sb, *Solid State Commun.* **65**, 381 (1988).
- [163] F. Netzer and M. El Gomati, Electronic excitations on clean and adsorbate covered Pd(111) by angle resolved electron energy loss spectroscopy, *Surf. Sci.* **124**, 26 (1983).
- [164] M. Rocca et al., The influence of d electrons on surface plasmon dispersion: Pd(110), *J. Phys. Condens. Matter* **7**, L611 (1995).
- [165] M. Rocca and F. Moresco, Hreels and els-leed studies of surface plasmons on Ag and Pd single crystals, *Prog. Surf. Sci.* **53**, 331 (1996).
- [166] V. M. Silkin, I. P. Chernov, Y. M. Koroteev, and E. V. Chulkov, Low-energy collective electronic excitations in Pd metal, *Phys. Rev. B* **80**, 245114 (2009).

- [167] V. M. Silkin, V. U. Nazarov, A. Balassis, I. P. Chernov, and E. V. Chulkov, Temperature effect on acoustic plasmons, *Phys. Rev. B* **94**, 165122 (2016).
- [168] V. M. Silkin, E. V. Chulkov, and P. M. Echenique, First-principles calculation of the electron inelastic mean free path in Be metal, *Phys. Rev. B* **68**, 205106 (2003).
- [169] C. Kittel, *Introduction to solid state physics*, John Wiley & Sons, 1953.
- [170] M. Skottke, R. J. Behm, G. Ertl, V. Penka, and W. Moritz, LEED structure analysis of the clean and (2×1)H covered Pd(110) surface, *J. Chem. Phys.* **87**, 6191 (1987).
- [171] N. Troullier and J. L. Martins, Efficient pseudopotentials for plane-wave calculations, *Phys. Rev. B* **43**, 1993 (1991).
- [172] J. P. Echeverry, E. V. Chulkov, P. M. Echenique, and V. M. Silkin, Low-energy collective electronic excitations in LiC₆, SrC₆, and BaC₆, *Phys. Rev. B* **100**, 115137 (2019).
- [173] T. Nagao, T. Hildebrandt, M. Henzler, and S. Hasegawa, Dispersion and Damping of a Two-Dimensional Plasmon in a Metallic Surface-State Band, *Phys. Rev. Lett.* **86**, 5747 (2001).
- [174] H. Ishida and A. Liebsch, Lifetime of surface plasmons of simple metals: Volume versus surface contributions, *Phys. Rev. B* **54**, 14127 (1996).
- [175] B.-O. Kim, G. Lee, E. W. Plummer, P. A. Dowben, and A. Liebsch, Mercury surface-plasmon dispersion: Experiment and theory, *Phys. Rev. B* **52**, 6057 (1995).
- [176] N. Memmel, G. Rangelov, and E. Bertel, Surface electronic structure of Pt(110): comparison with Ni and Pd, *Prog. Surf. Sci.* **74**, 239 (2003).
- [177] N. V. Smith, C. T. Chen, J. M. Tranquada, and P. D. Johnson, Unoccupied states on Pd(110) and the surface potential barrier, *Phys. Rev. B* **38**, 12259 (1988).
- [178] W. Dong, V. Ledentu, P. Sautet, A. Eichler, and J. Hafner, Hydrogen adsorption on palladium: a comparative theoretical study of different surfaces, *Surf. Sci.* **411**, 123 (1998).
- [179] X. Zubizarreta et al., Quantum-size effects in the loss function of Pb(111) thin films: An ab initio study, *Phys. Rev. B* **95**, 235405 (2017).
- [180] E. D. Palik, *Handbook of optical constants of solids*, Academic press, 1998.
- [181] V. Olevano, M. Palummo, G. Onida, and R. D. Sole, Exchange and correlation effects beyond the LDA on the dielectric function of silicon, *Phys. Rev. B* **60**, 14224 (1999).

-
- [182] D.-R. Liu and L. Brown, Characterization of palladium hydride films by electron energy loss spectroscopy and electron diffraction, *Acta Metall.* **36**, 2597 (1988).
- [183] D. Liu, Extraction of electronic structural information on the grain-boundaries of Pd-based polycrystalline specimens with transmission electron energy loss spectroscopy, *Ultramicroscopy* **29**, 44 (1989).
- [184] V. U. Nazarov, Multipole surface-plasmon-excitation enhancement in metals, *Phys. Rev. B* **59**, 9866 (1999).
- [185] V. U. Nazarov, V. M. Silkin, and E. E. Krasovskii, Role of the kinematics of probing electrons in electron energy-loss spectroscopy of solid surfaces, *Phys. Rev. B* **93**, 035403 (2016).
- [186] A. Hill, S. A. Mikhailov, and K. Ziegler, Dielectric function and plasmons in graphene, *EPL* **87**, 27005 (2009).
- [187] M. Pisarra, A. Sindona, P. Riccardi, V. M. Silkin, and J. M. Pitarke, Acoustic plasmons in extrinsic free-standing graphene, *New J. Phys.* **16**, 083003 (2014).
- [188] K. Sadhukhan and A. Agarwal, Anisotropic plasmons, Friedel oscillations, and screening in 8-*Pmmn* borophene, *Phys. Rev. B* **96**, 035410 (2017).
- [189] Z. Torbatian, D. Novko, and R. Asgari, Hyperbolic plasmon modes in tilted Dirac cone phases of borophene, *Phys. Rev. B* **104**, 075432 (2021).
- [190] J. S. Gomez-Diaz and A. Alù, Flatland Optics with Hyperbolic Metasurfaces, *ACS Photonics* **3**, 2211 (2016).
- [191] Z. Torbatian and R. Asgari, Optical absorption properties of few-layer phosphorene, *Phys. Rev. B* **98**, 205407 (2018).
- [192] E. van Veen et al., Tuning Two-Dimensional Hyperbolic Plasmons in Black Phosphorus, *Phys. Rev. Appl.* **12**, 014011 (2019).
- [193] J. A. Budagosky and E. E. Krasovskii, All-electron product basis set: Application to plasmon anisotropy in simple metals, *Phys. Rev. B* **99**, 245149 (2019).
- [194] S. Ahn and S. Das Sarma, Theory of anisotropic plasmons, *Phys. Rev. B* **103**, L041303 (2021).
- [195] R. Hayn, T. Wei, V. M. Silkin, and J. van den Brink, Plasmons in anisotropic Dirac systems, *Phys. Rev. Mater.* **5**, 024201 (2021).
- [196] B. Laks and D. L. Mills, Light emission from tunnel junctions: The role of the fast surface polariton, *Phys. Rev. B* **22**, 5723 (1980).

- [197] P. Dawson, D. G. Walmsley, H. A. Quinn, and A. J. L. Ferguson, Observation and explanation of light-emission spectra from statistically rough Cu, Ag, and Au tunnel junctions, *Phys. Rev. B* **30**, 3164 (1984).
- [198] S. Ushioda, J. E. Rutledge, and R. M. Pierce, Theory of prism-coupled light emission from tunnel junctions, *Phys. Rev. B* **34**, 6804 (1986).
- [199] J. K. Gimzewski, B. Reihl, J. H. Coombs, and R. R. Schlittler, Photon emission with the scanning tunneling microscope, *Z. Phys. B* **72**, 497 (1988).
- [200] J. K. Gimzewski, J. K. Sass, R. R. Schlitter, and J. Schott, Enhanced Photon Emission in Scanning Tunnelling Microscopy, *EPL* **8**, 435 (1989).
- [201] R. Berndt et al., Photon Emission at Molecular Resolution Induced by a Scanning Tunneling Microscope, *Science* **262**, 1425 (1993).
- [202] C. Chen, C. A. Bobisch, and W. Ho, Visualization of Fermi's Golden Rule Through Imaging of Light Emission from Atomic Silver Chains, *Science* **325**, 981 (2009).
- [203] Y. Zhang et al., Visualizing coherent intermolecular dipole-dipole coupling in real space, *Nature* **531**, 623 (2016).
- [204] J. H. Coombs, J. K. Gimzewski, B. Reihl, J. K. Sass, and R. R. Schlittler, Photon emission experiments with the scanning tunnelling microscope, *J. Microsc.* **152**, 325 (1988).
- [205] H. Qian et al., Efficient light generation from enhanced inelastic electron tunnelling, *Nat. Photon.* **12**, 485 (2018).
- [206] A. Vilan, Analyzing Molecular Current-Voltage Characteristics with the Simmons Tunneling Model: Scaling and Linearization, *J. Phys. Chem. C* **111**, 4431 (2007).
- [207] S. Banerjee and P. Zhang, A generalized self-consistent model for quantum tunneling current in dissimilar metal-insulator-metal junction, *AIP Adv.* **9**, 085302 (2019).
- [208] J. R. Kirtley, T. N. Theis, J. C. Tsang, and D. J. DiMaria, Hot-electron picture of light emission from tunnel junctions, *Phys. Rev. B* **27**, 4601 (1983).
- [209] B. N. J. Persson and A. Baratoff, Theory of photon emission in electron tunneling to metallic particles, *Phys. Rev. Lett.* **68**, 3224 (1992).
- [210] P. Johansson, R. Monreal, and P. Apell, Theory for light emission from a scanning tunneling microscope, *Phys. Rev. B* **42**, 9210 (1990).
- [211] L. C. Davis, Theory of surface-plasmon excitation in metal-insulator-metal tunnel junctions, *Phys. Rev. B* **16**, 2482 (1977).

-
- [212] D. Hone, B. Mühlischlegel, and D. J. Scalapino, Theory of light emission from small particle tunnel junctions, *Appl. Phys. Lett.* **33**, 203 (1978).
- [213] J. J. Sakurai, *Modern quantum mechanics*, Addison-Wesley, 1994.
- [214] M. Groner, J. Elam, F. Fabreguette, and S. George, Electrical characterization of thin Al₂O₃ films grown by atomic layer deposition on silicon and various metal substrates, *Thin Solid Films* **413**, 186 (2002).
- [215] G.-L. Ingold and Y. V. Nazarov, *Charge Tunneling Rates in Ultrasmall Junctions*, Springer US, Boston, MA, 1992.
- [216] A. Downes, M. E. Taylor, and M. E. Welland, Two-sphere model of photon emission from the scanning tunneling microscope, *Phys. Rev. B* **57**, 6706 (1998).
- [217] A. Archambault, F. Marquier, J.-J. Greffet, and C. Arnold, Quantum theory of spontaneous and stimulated emission of surface plasmons, *Phys. Rev. B* **82**, 035411 (2010).
- [218] A. Archambault, *Optique des ondes de surface: super-résolution et interaction matière-rayonnement*, Theses, Université Paris Sud - Paris XI, 2011.
- [219] P. Johansson and R. Monreal, Theory for photon emission from a scanning tunneling microscope, *Z. Phys. B* **84**, 269 (1991).
- [220] J. Aizpurua, S. P. Apell, and R. Berndt, Role of tip shape in light emission from the scanning tunneling microscope, *Phys. Rev. B* **62**, 2065 (2000).
- [221] C. Zhang et al., Antenna surface plasmon emission by inelastic tunneling, *Nat. Commun.* **10**, 1 (2019).
- [222] K. Arya and R. Zeyher, Light emission from tunnel junctions: The role of multiple scattering of surface polaritons, *Phys. Rev. B* **28**, 4080 (1983).
- [223] Y. Uehara, Y. Kimura, and S. U. Takeuchi, Theory of Visible Light Emission from Scanning Tunneling Microscope, *Jpn. J. Appl. Phys.* **31**, 2465 (1992).
- [224] F. Bigourdan, J.-P. Hugonin, F. Marquier, C. Sauvan, and J.-J. Greffet, Nanoantenna for Electrical Generation of Surface Plasmon Polaritons, *Phys. Rev. Lett.* **116**, 106803 (2016).
- [225] P. Février and J. Gabelli, Tunneling time probed by quantum shot noise, *Nat. Commun.* **9**, 4940 (2018).
- [226] J. Lambe and R. Jaklevic, Molecular Vibration Spectra by Inelastic Electron Tunneling, *Phys. Rev.* **165**, 821 (1968).
- [227] A. Martin-Jimenez et al., Unveiling the radiative local density of optical states of a plasmonic nanocavity by STM, *Nat. Commun.* **11**, 1021 (2020).

- [228] M. Parzefall and L. Novotny, Light at the End of the Tunnel, *ACS Photonics* **5**, 4195 (2018).
- [229] M. A. Ordal, R. J. Bell, R. W. Alexander, L. L. Long, and M. R. Querry, Optical properties of fourteen metals in the infrared and far infrared: Al, Co, Cu, Au, Fe, Pb, Mo, Ni, Pd, Pt, Ag, Ti, V, and W., *Appl. Opt.* **24**, 4493 (1985).
- [230] R. Esteban et al., A classical treatment of optical tunneling in plasmonic gaps: extending the quantum corrected model to practical situations, *Faraday Discuss.* **178**, 151 (2015).
- [231] D. Gall, Electron mean free path in elemental metals, *J. Appl. Phys.* **119**, 085101 (2016).
- [232] E. N. Economou, Surface Plasmons in Thin Films, *Phys. Rev.* **182**, 539 (1969).
- [233] G. Shalem, O. Erez-Cohen, D. Mahalu, and I. Bar-Joseph, Light Emission in Metal–Semiconductor Tunnel Junctions: Direct Evidence for Electron Heating by Plasmon Decay, *Nano Lett.* **21**, 1282 (2021).
- [234] P. Gonçalves et al., Plasmon–emitter interactions at the nanoscale, *Nat. Commun.* **11**, 366 (2020).
- [235] N. A. Mortensen et al., Surface-response functions obtained from equilibrium electron-density profiles, *Nanophotonics* **10**, 3647 (2021).
- [236] J. Aizpurua, G. Hoffmann, S. P. Apell, and R. Berndt, Electromagnetic Coupling on an Atomic Scale, *Phys. Rev. Lett.* **89**, 156803 (2002).
- [237] T. V. Teperik, P. Nordlander, J. Aizpurua, and A. G. Borisov, Robust Subnanometric Plasmon Ruler by Rescaling of the Nonlocal Optical Response, *Phys. Rev. Lett.* **110**, 263901 (2013).
- [238] D. S. Dovzhenko, S. V. Ryabchuk, Y. P. Rakovich, and I. R. Nabiev, Light–matter interaction in the strong coupling regime: configurations, conditions, and applications, *Nanoscale* **10**, 3589 (2018).
- [239] J. Fink et al., Climbing the Jaynes–Cummings ladder and observing its nonlinearity in a cavity QED system, *Nature* **454**, 315 (2008).
- [240] R. Sáez-Blázquez, J. Feist, A. I. Fernández-Domínguez, and F. J. García-Vidal, Enhancing photon correlations through plasmonic strong coupling, *Optica* **4**, 1363 (2017).
- [241] E. Orgiu et al., Conductivity in organic semiconductors hybridized with the vacuum field, *Nat. Mater.* **14**, 1123 (2015).

-
- [242] C. Ciuti, G. Bastard, and I. Carusotto, Quantum vacuum properties of the intersubband cavity polariton field, *Phys. Rev. B* **72**, 115303 (2005).
- [243] P. Nataf and C. Ciuti, No-go theorem for superradiant quantum phase transitions in cavity QED and counter-example in circuit QED, *Nat. Commun.* **1**, 72 (2010).
- [244] A. Vukics and P. Domokos, Adequacy of the Dicke model in cavity QED: A counter-no-go statement, *Phys. Rev. A* **86**, 053807 (2012).
- [245] C. Schäfer, M. Ruggenthaler, V. Rokač, and A. Rubio, Relevance of the Quadratic Diamagnetic and Self-Polarization Terms in Cavity Quantum Electrodynamics, *ACS Photonics* **7**, 975 (2020).
- [246] J. Galego, C. Climent, F. J. Garcia-Vidal, and J. Feist, Cavity Casimir-Polder Forces and Their Effects in Ground-State Chemical Reactivity, *Phys. Rev. X* **9**, 021057 (2019).
- [247] J. Feist, A. I. Fernández-Domínguez, and F. J. García-Vidal, Macroscopic QED for quantum nanophotonics: emitter-centered modes as a minimal basis for multiemitter problems, *Nanophotonics* **10**, 477 (2021).
- [248] S. R. K. Rodriguez, Classical and quantum distinctions between weak and strong coupling, *Eur. J. Phys.* **37**, 025802 (2016).
- [249] S. Rudin and T. L. Reinecke, Oscillator model for vacuum Rabi splitting in microcavities, *Phys. Rev. B* **59**, 10227 (1999).
- [250] A. B. Lockhart, A. Skinner, W. Newman, D. B. Steinwachs, and S. A. Hilbert, An experimental demonstration of avoided crossings with masses on springs, *Am. J. Phys.* **86**, 526 (2018).
- [251] Y. S. Joe, A. M. Satanin, and C. S. Kim, Classical analogy of Fano resonances, *Phys. Scr.* **74**, 259 (2006).
- [252] P. R. Hemmer and M. G. Prentiss, Coupled-pendulum model of the stimulated resonance Raman effect, *J. Opt. Soc. Am. B* **5**, 1613 (1988).
- [253] C. L. Garrido Alzar, M. A. G. Martinez, and P. Nussenzveig, Classical analog of electromagnetically induced transparency, *Am. J. Phys.* **70**, 37 (2002).
- [254] J. Harden, A. Joshi, and J. D. Serna, Demonstration of double EIT using coupled harmonic oscillators and RLC circuits, *Eur. J. Phys.* **32**, 541 (2011).
- [255] J. A. Souza, L. Cabral, R. R. Oliveira, and C. J. Villas-Boas, Electromagnetically-induced-transparency-related phenomena and their mechanical analogs, *Phys. Rev. A* **92**, 023818 (2015).
- [256] X. Liu et al., Strong light–matter coupling in two-dimensional atomic crystals, *Nat. Photon.* **9**, 30 (2014).

- [257] M. Harder and C.-M. Hu, Cavity spintronics: An early review of recent progress in the study of magnon–photon level repulsion, *Solid State Phys.* **69**, 47 (2018).
- [258] D. Yoo et al., Ultrastrong plasmon–phonon coupling via epsilon-near-zero nanocavities, *Nat. Photon.* **15**, 125 (2021).
- [259] J. George, A. Shalabney, J. A. Hutchison, C. Genet, and T. W. Ebbesen, Liquid-Phase Vibrational Strong Coupling, *J. Phys. Chem. Lett.* **6**, 1027 (2015).
- [260] J. George et al., Multiple Rabi Splittings under Ultrastrong Vibrational Coupling, *Phys. Rev. Lett.* **117**, 153601 (2016).
- [261] K. Nagarajan, A. Thomas, and T. W. Ebbesen, Chemistry under Vibrational Strong Coupling, *J. Am. Chem. Soc.* **143**, 16877 (2021).
- [262] P. Vasa et al., Ultrafast Manipulation of Strong Coupling in Metal-Molecular Aggregate Hybrid Nanostructures, *ACS Nano* **4**, 7559 (2010).
- [263] C. Symonds et al., Particularities of surface plasmon–exciton strong coupling with large Rabi splitting, *New J. Phys.* **10**, 065017 (2008).
- [264] R. Chikkaraddy et al., Single-molecule strong coupling at room temperature in plasmonic nanocavities, *Nature* **535**, 127 (2016).
- [265] S. Wang et al., Coherent Coupling of WS₂ Monolayers with Metallic Photonic Nanostructures at Room Temperature, *Nano Lett.* **16**, 4368 (2016).
- [266] D. Zheng et al., Manipulating Coherent Plasmon–Exciton Interaction in a Single Silver Nanorod on Monolayer WSe₂, *Nano Lett.* **17**, 3809 (2017).
- [267] M. Stührenberg et al., Strong Light–Matter Coupling between Plasmons in Individual Gold Bi-pyramids and Excitons in Mono- and Multilayer WSe₂, *Nano Lett.* **18**, 5938 (2018).
- [268] X. Wu, S. K. Gray, and M. Pelton, Quantum-dot-induced transparency in a nanoscale plasmonic resonator, *Opt. Express* **18**, 23633 (2010).
- [269] N. Liu et al., Plasmonic analogue of electromagnetically induced transparency at the Drude damping limit, *Nat. Mater.* **8**, 758 (2009).
- [270] S. R. K. Rodriguez et al., From weak to strong coupling of localized surface plasmons to guided modes in a luminescent slab, *Phys. Rev. B* **90**, 235406 (2014).
- [271] G. Khitrova, H. Gibbs, M. Kira, S. W. Koch, and A. Scherer, Vacuum Rabi splitting in semiconductors, *Nat. Phys.* **2**, 81 (2006).

-
- [272] J. Bellessa, C. Bonnard, J. C. Plenat, and J. Mugnier, Strong Coupling between Surface Plasmons and Excitons in an Organic Semiconductor, *Phys. Rev. Lett.* **93**, 036404 (2004).
- [273] Y. Todorov and C. Sirtori, Intersubband polaritons in the electrical dipole gauge, *Phys. Rev. B* **85**, 045304 (2012).
- [274] R. G. Woolley, Power-Zienau-Woolley representations of nonrelativistic QED for atoms and molecules, *Phys. Rev. Res.* **2**, 013206 (2020).
- [275] R. Esteban, J. Aizpurua, and G. W. Bryant, Strong coupling of single emitters interacting with phononic infrared antennae, *New J. Phys.* **16**, 013052 (2014).
- [276] M. Pelton, Modified spontaneous emission in nanophotonic structures, *Nat. Photon.* **9**, 427 (2015).
- [277] J. McKeever, A. Boca, A. D. Boozer, J. R. Buck, and H. J. Kimble, Experimental realization of a one-atom laser in the regime of strong coupling, *Nature* **425**, 268 (2003).
- [278] R. Sáez-Blázquez, J. Feist, F. J. García-Vidal, and A. I. Fernández-Domínguez, Photon statistics in collective strong coupling: Nanocavities and microcavities, *Phys. Rev. A* **98**, 013839 (2018).
- [279] M. Thorwart, L. Hartmann, I. Goychuk, and P. Hänggi, Controlling decoherence of a two-level atom in a lossy cavity, *J. Mod. Opt.* **47**, 2905 (2000).
- [280] J. S. Foresi et al., Photonic-bandgap microcavities in optical waveguides, *Nature* **390**, 143 (1997).
- [281] M. Kuisma et al., Ultrastrong Coupling of a Single Molecule to a Plasmonic Nanocavity: A First-Principles Study, *ACS Photonics* **9**, 1065 (2022).
- [282] M. Pelton, S. D. Storm, and H. Leng, Strong coupling of emitters to single plasmonic nanoparticles: exciton-induced transparency and Rabi splitting, *Nanoscale* **11**, 14540 (2019).
- [283] A. Trügler and U. Hohenester, Strong coupling between a metallic nanoparticle and a single molecule, *Phys. Rev. B* **77**, 115403 (2008).
- [284] A. Delga, J. Feist, J. Bravo-Abad, and F. J. Garcia-Vidal, Quantum Emitters Near a Metal Nanoparticle: Strong Coupling and Quenching, *Phys. Rev. Lett.* **112**, 253601 (2014).
- [285] R. H. Dicke, Coherence in Spontaneous Radiation Processes, *Phys. Rev.* **93**, 99 (1954).
- [286] T. Schwartz, J. A. Hutchison, C. Genet, and T. W. Ebbesen, Reversible Switching of Ultrastrong Light-Molecule Coupling, *Phys. Rev. Lett.* **106**, 196405 (2011).

- [287] F. Barachati et al., Tunable Third-Harmonic Generation from Polaritons in the Ultrastrong Coupling Regime, *ACS Photonics* **5**, 119 (2018).
- [288] S. Ribeiro, J. Aizpurua, and R. Esteban, Influence of direct dipole-dipole interactions on the optical response of 2D materials in extremely inhomogeneous infrared cavity fields, Submitted (2023).
- [289] Y. Ashida et al., Quantum Electrodynamic Control of Matter: Cavity-Enhanced Ferroelectric Phase Transition, *Phys. Rev. X* **10**, 041027 (2020).
- [290] A. Bylinkin et al., Real-space observation of vibrational strong coupling between propagating phonon polaritons and organic molecules, *Nat. Photon.* **15**, 197 (2021).
- [291] H. J. Bakker, S. Hunsche, and H. Kurz, Coherent phonon polaritons as probes of anharmonic phonons in ferroelectrics, *Rev. Mod. Phys.* **70**, 523 (1998).
- [292] Y. He et al., Rapid change of superconductivity and electron-phonon coupling through critical doping in Bi-2212, *Science* **362**, 62 (2018).
- [293] K. S. Menghrajani, G. R. Nash, and W. L. Barnes, Vibrational Strong Coupling with Surface Plasmons and the Presence of Surface Plasmon Stop Bands, *ACS Photonics* **6**, 2110 (2019).
- [294] F. Wall, O. Mey, L. M. Schneider, and A. Rahimi-Iman, Continuously-tunable light-matter coupling in optical microcavities with 2D semiconductors, *Sci. Rep.* **10**, 8303 (2020).
- [295] C. Sauvan, J. P. Hugonin, I. S. Maksymov, and P. Lalanne, Theory of the Spontaneous Optical Emission of Nanosize Photonic and Plasmon Resonators, *Phys. Rev. Lett.* **110**, 237401 (2013).
- [296] S. Franke et al., Quantization of Quasinormal Modes for Open Cavities and Plasmonic Cavity Quantum Electrodynamics, *Phys. Rev. Lett.* **122**, 213901 (2019).
- [297] D. R. Abujetas, J. Feist, F. J. García-Vidal, J. G. Rivas, and J. A. Sánchez-Gil, Strong coupling between weakly guided semiconductor nanowire modes and an organic dye, *Phys. Rev. B* **99**, 205409 (2019).
- [298] Y. Zhang, J. Aizpurua, and R. Esteban, Optomechanical Collective Effects in Surface-Enhanced Raman Scattering from Many Molecules, *ACS Photonics* **7**, 1676 (2020).
- [299] B. M. Garraway, The Dicke model in quantum optics: Dicke model revisited, *Philos. Trans. R. Soc. A* **369**, 1137 (2011).

-
- [300] Y. Kaluzny, P. Goy, M. Gross, J. M. Raimond, and S. Haroche, Observation of Self-Induced Rabi Oscillations in Two-Level Atoms Excited Inside a Resonant Cavity: The Ringing Regime of Superradiance, *Phys. Rev. Lett.* **51**, 1175 (1983).
- [301] M. G. Raizen, R. J. Thompson, R. J. Brecha, H. J. Kimble, and H. J. Carmichael, Normal-mode splitting and linewidth averaging for two-state atoms in an optical cavity, *Phys. Rev. Lett.* **63**, 240 (1989).
- [302] R. J. Thompson, G. Rempe, and H. J. Kimble, Observation of normal-mode splitting for an atom in an optical cavity, *Phys. Rev. Lett.* **68**, 1132 (1992).
- [303] A. Castellanos-Gomez et al., Deterministic transfer of two-dimensional materials by all-dry viscoelastic stamping, *2D Mater.* **1**, 011002 (2014).
- [304] M. Barra-Burillo, Micro and Nano Fabrication of Structures for Light-Matter Interaction, PhD thesis, Euskal Herriko Unibertsitatea/Universidad del País Vasco, 2023.
- [305] A. Canales, D. G. Baranov, T. J. Antosiewicz, and T. Shegai, Abundance of cavity-free polaritonic states in resonant materials and nanostructures, *J. Chem. Phys.* **154** (2021).
- [306] J. Flick, N. Rivera, and P. Narang, Strong light-matter coupling in quantum chemistry and quantum photonics, *Nanophotonics* **7**, 1479 (2018).
- [307] O. Kapon, R. Yitzhari, A. Palatnik, and Y. R. Tischler, Vibrational Strong Light-Matter Coupling Using a Wavelength-Tunable Mid-infrared Open Microcavity, *J. Phys. Chem. C* **121**, 18845 (2017).
- [308] A. Bisht et al., Collective Strong Light-Matter Coupling in Hierarchical Microcavity-Plasmon-Exciton Systems, *Nano Lett.* **19**, 189 (2019).
- [309] N. S. Mueller et al., Deep strong light-matter coupling in plasmonic nanoparticle crystals, *Nature* **583**, 780 (2020).
- [310] J. Casanova, G. Romero, I. Lizuain, J. J. García-Ripoll, and E. Solano, Deep Strong Coupling Regime of the Jaynes-Cummings Model, *Phys. Rev. Lett.* **105**, 263603 (2010).
- [311] S. De Liberato, Light-Matter Decoupling in the Deep Strong Coupling Regime: The Breakdown of the Purcell Effect, *Phys. Rev. Lett.* **112**, 016401 (2014).